

HOST-GUEST CHEMISTRY OF ACRIDONE- BASED COORDINATION CAGES

This dissertation is submitted for the degree of “Doctor rerum naturalium”
within the PhD program of the Georg – August – University School of
Science (GAUSS)



Susanne Löffler

from Dresden

Göttingen, February 2018

*To my family and everyone who supported me
during the past years.*

If you want to go fast, go alone.
If you want to go far, go in a group.
-African Proverb-

BETREUUNGS-AUSSCHUSS

Prof. Dr. Guido H. Clever

Institut für Chemie und Chemische Biologie,
Technische Universität Dortmund, Otto-Hahn-Str. 6, 44227 Dortmund

Prof. Dr. Franc Meyer

Institut für Anorganische Chemie,
Georg-August-Universität Göttingen, Tammannstr. 4, 37077 Göttingen

MITGLIEDER DER PRÜFUNGSKOMMISSION

Referent: **Prof. Dr. Guido H. Clever**

Institut für Chemie und Chemische Biologie,
Technische Universität Dortmund, Otto-Hahn-Str.6, 44227 Dortmund

Koreferent: **Prof. Dr. Franc Meyer**

Institut für Anorganische Chemie, Georg-August-Universität Göttingen,
Tammannstr. 4, 37077 Göttingen

WEITERE MITGLIEDER DER PRÜFUNGSKOMMISSION

Prof. Dr. Ricardo A. Mata

Institut für Physikalische Chemie,
Georg-August-Universität Göttingen, Tammannstr 6, 37077 Göttingen

Prof. Dr. Manuel Alcarazo

Institut für Organische und Biomolekulare Chemie,
Georg-August-Universität Göttingen, Tammannstr. 2, 37077 Göttingen

Dr. Michael John

Institut für Organische und Biomolekulare Chemie,
Georg-August-Universität Göttingen, Tammannstr. 2, 37077 Göttingen

Dr. Holm Frauendorf

Institut für Organische und Biomolekulare Chemie,
Georg-August-Universität Göttingen, Tammannstr. 2, 37077 Göttingen

Tag der mündlichen Prüfung: 09.03.2018

DECLARATION

I hereby declare that I wrote this dissertation entitled: "*Host-Guest Chemistry of Acridone-based Coordination Cages*" on my own, without the use of any other than the cited sources and tools. All explanations that I copied directly or in their sense are marked as such. Furthermore, I declare that this thesis has not yet been handed in neither in this nor in equal form at any other official examination commission.

Eidesstattliche Erklärung:

Ich versichere hiermit, dass ich die Doktorarbeit mit dem Titel: „*Host-Guest Chemistry of Acridone-based Coordination Cages*“ selbstständig und ohne Benutzung anderer als der angegebenen Quellen und Hilfsmittel angefertigt habe und alle Ausführungen, die wörtlich oder sinngemäß übernommen wurden, als solche gekennzeichnet sind, sowie dass diese Doktorarbeit in gleicher oder ähnlicher Form noch keiner anderen Prüfungsbehörde vorgelegt wurde.



Susanne Löffler

Göttingen, February 19, 2018

ABSTRACT

Supramolecular coordination cages, assembled from organic ligands and metal cations, are of broad interest due to their versatile topologies and properties. Discrete cages often possess a secluded cavity, which allows the inclusion of various guest molecules (anions, cations and neutral molecules). These structures are stabilized by non-covalent interactions and commonly referred to as host-guest complexes.

The here presented thesis entitled “Host-Guest Chemistry of Acridone-based Coordination Cages” focuses on the synthesis, self-assembly and host-guest chemistry of novel coordination cages based on acridone-derived ligands **L** and square-planar Pd(II) metal ions. In the first part of this thesis, the preparation and characterization of an interpenetrated coordination cage from eight bispyridyl ligands **L**¹ and four Pd(II) cations was studied. This [Pd₄**L**₈] assembly shows the unique ability to encapsulate neutral guest molecules after activation through addition of halide anions. It is the first example of an interpenetrated coordination cage that shows this feature. In this project, the range of encapsulated neutral molecules was explored. In particular, the size, shape as well as the amount and positions of heteroatoms within the guests were varied and the influence of dispersion interactions in the formation of the host-guest complexes was investigated (Chapter 2). Additionally, the interpenetrated coordination cage has the unique ability to function as a photosensitizer by exciting triplet oxygen into singlet oxygen. The reactivity of the coordination cage was discovered as the guest 1,3-cyclohexadiene was transformed into the Hetero-Diels-Alder product 2,3-dioxabicyclo[2.2.2]oct-5ene in presence of oxygen and light (Chapter 3). The uptake of halide anions in the interpenetrated coordination cage occurs after an allosteric mechanism with positive cooperativity. The chloride-binding ability of the acridone-based [Pd₄**L**₈] was compared with previously reported interpenetrated coordination cages based on dibenzosuberone and phenothiazine (Chapter 6).

Introduction of a bulky adamantyl group in the novel ligand **L**² prevents dimerization and results in the formation of the monomeric cage [Pd₂**L**₄]. Owing to steric crowding, the adamantyl substituent is considerably bent sideways with respect to the ligand backbone and an unprecedented flipping motion of the free ligand was observed. Surprisingly, this unique dynamic also occurs in the coordination cage. Despite the very dense packing within the self-assembled structure, the cage is able to encapsulate a series of bis-anionic guests in an induced-fit fashion. Additionally, electronic structure calculations revealed a substantial contribution from dispersion interactions between the guest and the surrounding adamantyl groups that stabilize the host-guest complex (Chapter 4).

The variation of ligand length, through introduction of different linkers between the acridone backbone and the coordinating pyridyl groups, illustrated the remarkable influence of this ligand feature. Depending on the length, the formation of monomeric or dimeric interpenetrated coordination cages was achieved (Chapter 5).

The formation and characterization of these novel structures were verified with the help of NMR spectroscopic studies, HR-MS spectrometric data and X-ray diffraction analysis of several obtained crystal structures. The collected results give a deeper insight in the understanding of supramolecular coordination cages, especially their formation *via* self-assembly, their ability to form host-guest complexes with a variety of different guest molecules and the influence of dispersion interactions on the stability of the systems. It broadens the scope of supramolecular assemblies and is the basis for further applications in the field of selective recognition, tunable guest uptake and catalysis.

LIST OF PUBLICATIONS AND CONFERENCE CONTRIBUTIONS

Publications

- “*Influence of Size, Shape, Heteroatom Content and Dispersive Contributions on Guest Binding in a Coordination Cage*” S. Löffler, A. Wuttke, B. Zhang, J. J. Holstein, R. A. Mata, G. H. Clever, *ChemComm* **2017**, 53, 11933.
- “*Internal Dynamics and Guest Binding of a Sterically Overcrowded Host*” S. Löffler, J. Lüb- ben, A. Wuttke, R. A. Mata, M. John, B. Dittrich, G. H. Clever, *Chem. Sci.* **2016**, 7, 4676.
- “*Triggered Exchange of Anionic for Neutral Guests inside a Cationic Coordination Cage*“, S. Löffler, J. Lüb- ben, L. Krause, D. Stalke, B. Dittrich, G. H. Clever, *J. Am. Chem. Soc.* **2015**, 137, 1060.
- “*Electron Transfer between Hydrogen-Bonded Pyridylphenols and a Photoexcited Rhenium(I) Complex*” W. Herzog, C. Bronner, S. Löffler, B. He, D. Kratzert, D. Stalke, A. Hauser, O. S. Wenger, *ChemPhysChem* **2013**, 14, 1168.

Award

- “MS-CEC Young Researcher Award 2016“ at the 7th Münster Symposium on Cooperative Effects in Chemistry. DFG SFB 858.

Conference Contributions

- *Talk*, 11.Tag der Chemie, **2018**, *Dortmund*, Germany
- *Poster*, 10.Tag der Chemie, **2017**, *Dortmund*, Germany
- *Poster*, SupraChem, **2017**, *Aachen*, Germany
- *Talk*, Jung Chemiker Symposium, **2016**, *Dortmund*, Germany
- *Poster*, The 11th International Symposium on Macrocyclic and Supramolecular Chemistry (ISMSC), **2016**, *Seoul*, South Korea
- *Talk*, 7th Münster Symposium on Cooperative Effects in Chemistry, **2016**, *Münster*, Ger- many
- *Poster*, 9.Tag der Chemie, **2016**, *Dortmund*, Germany
- *Poster*, 1st SPP1807 Meeting, **2015**, *Göttingen*, Germany
- *Talk*, 18. Norddeutsches Doktorandenkolloquium, **2015**, *Goslar*, Germany
- *Poster*, SupraChem, **2015**, *Berlin*, Germany
- *Poster*, Niedersächsisches Katalyse Symposium, **2014**, *Göttingen*, Germany
- *Poster*, The 9th International Symposium on Macrocyclic and Supramolecular Chemistry (ISMSC), **2014**, *Shanghai*, China

ACKNOWLEDGEMENTS

First of all, I would like to thank my supervisor Prof. Guido Clever for giving me the opportunity to conduct my PhD thesis in his lab and to give access to so many great techniques and opportunities. Moreover, I would like to thank him for his motivation, teaching and encouragement. I am very grateful for all his helpful discussions and advices in research as well as writing scientific publications.

I would like to thank my secondary supervisor Prof. Meyer for his support during my research time. I am thankful to Prof. Mata, Prof. Alcarazo, Dr. John and Dr. Frauendorf for taking part in my defense examination team.

Special thanks goes to Dr. Michael John for all his support in NMR related problems, especially for all the time he spent measuring my samples and for discussing and analyzing the results. Likewise, I like to thank Prof. Dr. Wolf Hiller for his patience, his help with various temperature measurements and his dedication to run the 500er Varian spectrometer.

Dr. Holm Frauendorf, Mrs. Györgyi Sommer-Udvarnoki and Mrs. Christiane Heitbrink I like to thank for measuring and analyzing mass samples.

For measuring and solving X-ray data I like to thank Dr. Julian Holstein, Dr. Jens Lübben, PD Dr. Birger Dittrich, Dr. Lennard Krause and Prof. Dietmar Stalke. Thank you for your hard work!

Alexander Wuttke and Prof. Ricardo Mata I am grateful for conducting time-consuming computations and for their valuable contribution to the resulting publications.

I like to thank Gabi Trötscher-Kaus, Birgit Thormann and Kristian Surich for the welcoming atmosphere in Dortmund and for all the help over the last two years. Special thanks goes to Gabi Trötscher-Kaus for her help with organizational issues (e.g. contract details, christmas parties, group trips and Thermomix events) as well as personal advice and support.

I would like to thank my bachelor student Markus Gilles and all my research students, namely Jochen Jung, Marlene Költer, Lianrong Liu, Anja Hausmann, Henning Hemmen, Nico Graw, Sebastian Kampling and Jan Gierok for their time, hard work and dedication to this project.

I like to thank all current and former members of the Clever-lab for creating such a nice and supporting work atmosphere. I thank everyone for contribution to our social activities by helping to organize movie nights, group activities and bringing cakes for our coffee break. I hope, you will continue these traditions after I left the group.

Special thanks goes to Thorben Schulte, David Engelhard and Marcel Krick for helping me with any kind of software problem. I like to thank Fernanda Pereira, Marcel Krick and David Engelhard

for having a fun time in the “Dungeon Lab” in Göttingen. Huge thanks goes to Bin Chen for sharing the office, for discussions and for all the offered snacks during the last two years in Dortmund.

Thanks to Marcel Krick, Kristina Ebbert, Bin Chen, Rujin Li and everyone else for short brainstorming discussions during my weeks of writing. For proof reading, I like to thank Marina Versäumer, Fernanda Pereira, Mark Johnstone, David Engelhard, Rujin Li, Kristina Ebbert, Marcel Krick and Bo Zhang.

Furthermore, I would like to thank Ulrike Kroesen for reminding me to focus on the important part: “writing and finishing” as well as her support during my recovery. I like to thank Isabell Kappen, Irene Regeni, Renee Bloch and Ulrike Kroesen for their friendship. I will always remember our girl nights in Dortmund with a lot of tasty food, wine, girl talks and fun.

Furthermore, I thank Julian Holstein for motivating me (and several others) to play Volleyball, for discussions about X-ray or any other problems and for invitations to pizza and beer evenings. I also like to thank Thorben Schulte for his friendship, his support during my recovery and for testing my patience.

Last but not least, I would like to thank my parents and my sister Christiane for always believing in me, for supporting my decision and listening to my problems and worries. Without you, I would not be where I am.

TABLE OF CONTENT

1	Introduction	1
1.1	General Introduction and History	1
1.2	Concepts in Supramolecular Chemistry	4
1.3	Supramolecular Coordination Cages	8
2	Neutral Guest Uptake in Interpenetrated Coordination Cages	17
2.1	Introduction	18
2.2	Ligand Synthesis and Cage Assembly	19
2.3	Encapsulation of Anionic Guest Molecules	22
2.4	X-ray Structure Analysis	24
2.5	Neutral Guest Uptake	27
2.6	Guest Release	34
2.7	Dispersive Contribution	35
2.8	Conclusion	36
3	Coordination Cage as Photosensitizer	39
3.1	Introduction	40
3.2	NMR and HR-MS Studies	40
3.3	X-ray Structure Analysis	43
3.4	Conclusion	46
4	Endohedral Functionalization and Dynamics	46
4.1	Introduction	47
4.2	Ligand Synthesis and Cage Assembly	49
4.3	Flipping Dynamics in Ligand L ² and [Pd ₂ L ₂] ₄ Coordination Cage	52
4.4	Host-guest Chemistry	56
4.5	Guest Effect on Flipping Dynamics	59
4.6	X-ray Structure Analysis	60

4.7	Analyses of Non-covalent Interactions-----	62
4.8	Conclusion-----	64
5	Influence of Ligand Length on Cage Formation	65
5.1	Introduction-----	66
5.2	Results and Discussion-----	66
5.3	Conclusion and Prospects-----	76
6	Anion Binding Competition Experiments	77
6.1	Introduction and Objectives-----	78
6.2	Anion Exchange between Interpenetrated Coordination Cages-----	79
6.3	Chloride Competition Experiments-----	80
6.4	Conclusion and Prospects-----	82
7	Experimental Section	83
7.1	Instrumentation-----	83
7.2	General Procedures-----	84
7.3	Part A – Neutral Guest Uptake in Interpenetrated Coordination Cages-----	85
7.4	Part B – Coordination Cage as Photosensitizer-----	134
7.5	Part C – Endohedral Functionalization and Dynamics-----	139
7.6	Part D – Influence of Ligand Length on Cage Formation-----	165
7.7	Part E – Anion Binding Competitions Experiments-----	192
8	Abbreviations	199
9	List of Figures	201
10	List of Tables	223
11	References	224

1 INTRODUCTION

1.1 General Introduction and History

The field of supramolecular chemistry focusses on the construction of highly complex, functional systems held together by intermolecular forces and is referred to as the “chemistry beyond the molecule”.^[1] For a long time, chemists solely concentrated on connecting atoms by covalent bonds, whereas the field of supramolecular chemistry investigates non-covalent interactions between molecules.^[2] Examples for these weak and reversible interactions include hydrogen bonds, metal coordination, van-der-Waals forces (dispersion), π - π stacking interactions, hydrophobic effects and electrostatic interactions (e.g. ion-ion, ion-dipole).^[3]

In nature, a vast number of examples can be found, in which non-covalent interactions play an important role. For example, the DNA (deoxyribonucleic acid) double helix, which carries our genetic information, is stabilized by complementary hydrogen bonds between the nucleobases and π - π stacking interactions.^[4] Proteins and enzymes are folded into unique three-dimensional structures due to stabilizing non-covalent forces (e.g. hydrogen bonds, ionic interactions).^[5] Due to dispersion interactions, lizards are able to climb up a straight wall.^[6] These biological examples serve as an inspiration and motivation for chemists in all fields. Supramolecular chemistry is an interdisciplinary research area, which includes aspects from fields such as physics, biochemistry, biology, crystallography as well as (in-)organic and computational chemistry.^[3,7]

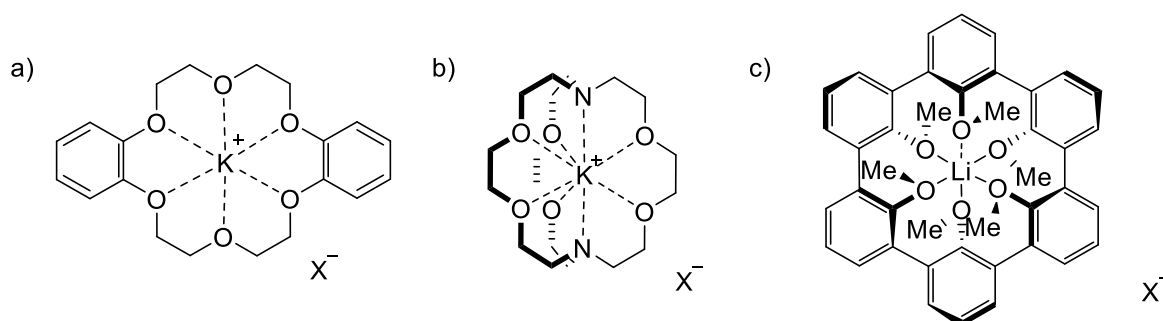


Figure 1.1 Schematic representation of a) Dibenzo-[18]crown-6 complex by *Pederson*^[8] b) [2.2.2]cryptand complex by *Lehn*^[9] and c) spherand-6 complex by *Cram*.^[10]

The field of supramolecular chemistry is one of the most vigorous and fast developing areas of chemistry with the foundation being laid in the early 1960s with the discovery of crown ethers^[8] and cryptands^[9] by *Pedersen* and *Lehn*. The discovered compounds showed an unexpected and diverse ability to bind alkaline and alkaline earth metals (e.g. Li, Na, K, Rb, Cs) and led to the realization, that small, complementary molecules can be designed to recognize each other by non-

covalent interactions. Soon after, in 1979, *Cram* studied the metal binding ability of rigid and pre-organized spherands^[10] and found a stronger metal binding ability than that of the crown ether or cryptand systems.

When in 1987 the Nobel Prize in Chemistry was awarded jointly to *Donald J. Cram*, *Jean-Marie Lehn* and *Charles J. Pederson* for “their development and use of molecules with structure-specific interactions of high selectivity” the phrase “chemistry beyond the molecule” was coined by *Jean-Marie Lehn* in the Nobel lecture in Stockholm.^[1] At that time, supramolecular chemistry has been accepted as an interdisciplinary but independent field of contemporary research. In the following years, the field of supramolecular chemistry experienced a rapid expansion and the number of supramolecular systems and unique structures increased continuously. With the rising interest and development of new analytical techniques,^[11] novel chemical systems with high diversity and complexity were developed.

A fascinating approach was performed by *Sauvage* in order to form a so-called catenane^[12] (see Figure 1.2a), which consist of two (or more) mechanically interlocked molecules that cannot be separated without breaking a bond.^[13,14,15] *Wassermann* already synthesized a similar system in an earlier study. However, the synthesis by pure organic chemistry was tedious and nerve-wracking.^[16] *Sauvage*'s strategy improved the yield and accessibility of catenanes by using a metal ion (e.g. copper) as a template. With this strategy, fascinating new intertwined structures like links and knots could be formed. Some stunning examples are the Borromean rings^[17], tre^[18]- or pentafoil^[19] knots and the Solomon's knot^[20] (see Figure 1.2b-c).

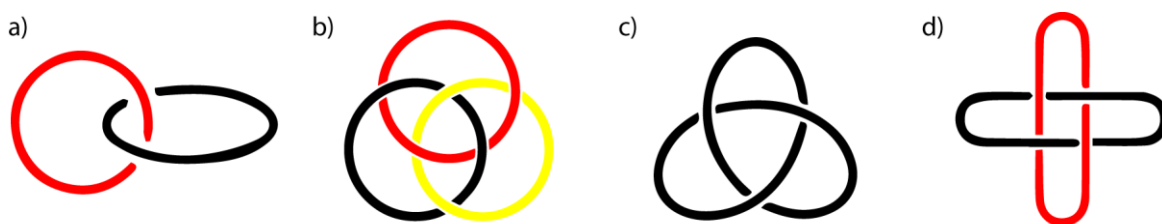


Figure 1.2 Schematic representation of different links and knots: a) Catenane, b) Borromean rings, c) trefoil knot, and d) Solomon knot.

Another class of supramolecular structures are the so-called “Rotaxanes”,^[13] which consists of a dumbbell shaped molecule, which is threaded through a macrocycle. High yields of rotaxanes could be obtained by preorganizing the components utilizing non-covalent interactions (e.g. hydrogen bonds, metal coordination, coulomb interactions etc.). In 1991, *Stoddard* showed, that the ring can be moved along the rod^[21] (see Figure 1.3a). Controlled movement or switching of the macrocycle along the thread was achieved by applying an external trigger, for example: oxidation/reduction, irradiation with light, pH variation or addition of a chemical trigger (e.g. metals, crown ether).^[13] With the use of these principles, the formation of a shuttlebus rotaxane^[22] or the mimicry of a molecular muscle^[23] (see Figure 1.3b) was realized.

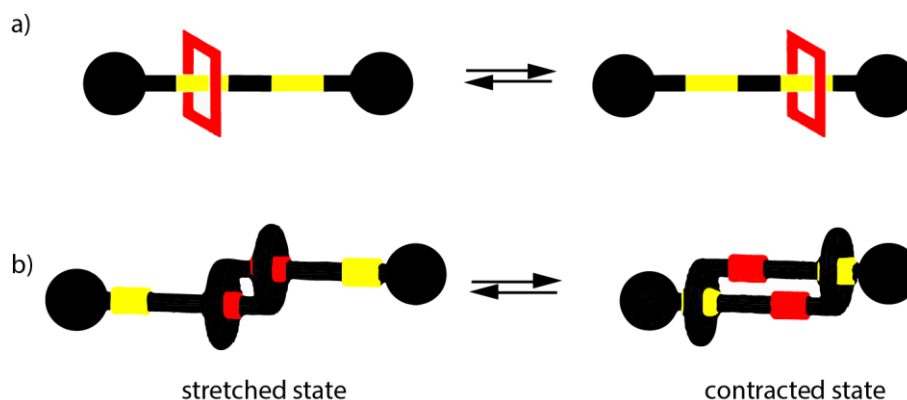


Figure 1.3 Schematic representation of a) molecular shuttle^[22] and b) molecular muscle.^[23]

In 2004, *Stoddard* could enhance the complexity of the rotaxane chemistry by synthesizing a molecular machine that behaves similar to an elevator (see Figure 1.4).^[24] The supramolecular assembly consists of a platform-like component interlocked with a trifurcated ring-like component and operated by pH variation. The traveled distance of this nano elevator is 0.7 nm.

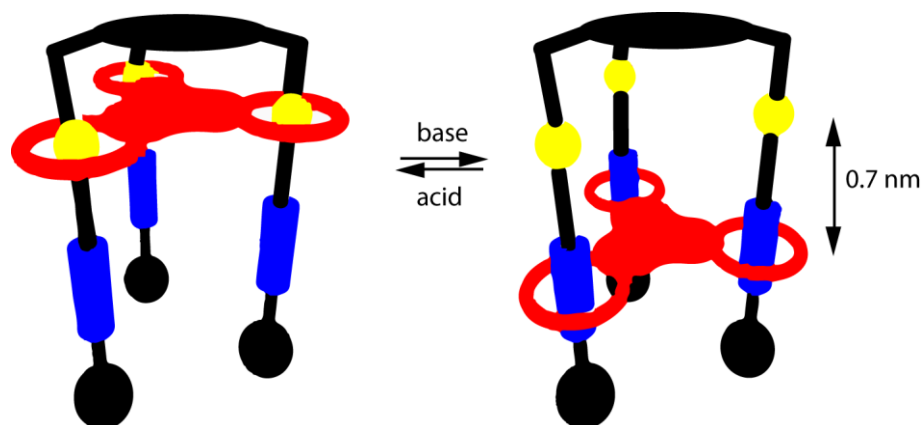


Figure 1.4 Schematic representation of a molecular elevator.^[24] Addition of base causes the platform (red) to move to the lower level. Addition of acid results in a lift of the platform to the upper level.

Feringa introduced the first unidirectional molecular rotor in 1999.^[25] Irradiation with light resulted in a rotation around a central bond and by variation of temperature, the direction of this rotation was controlled. In 2011, this principle helped in the synthesis of the smallest car on earth. This 4-wheeled “vehicle” is only 1 nm long and can move in one direction along a copper-surface.^[26]

In 2016, the achievements of *Jean-Pierre Sauvage*, *Sir Frazer Stoddard* and *Bernard L. Feringa* were awarded jointly with the Nobel Prize in chemistry for “the design and synthesis of molecular machines”. This shows, that the fascinating field of supramolecular chemistry is of high impact and of broad interest.^[27] The developed molecular machines and other supramolecular structures are only of fundamental research interest, but applications in medicine, computer science, as smart materials or as energy storage devices are just one-step away.

1.2 Concepts in Supramolecular Chemistry

In supramolecular chemistry or the “chemistry beyond the molecules” non-covalent interactions play a major role in the formation and the properties of supramolecular systems. Formation occurs *via* self-assembly and the resulting structure often possess the ability to form so-called host-guest complexes.

1.2.1 Non-covalent Interactions

Non-covalent interactions are attractive forces between different molecules or different groups within one molecule.^[3] They are categorized into electrostatic attraction, hydrogen bonds, π - π stacking interactions, Van-der-Waals forces and hydrophobic effects (see Figure 1.5). In contrast, to covalent bond with bond energies of 300-400 kJ·mol⁻¹, non-covalent interactions are significantly weaker. One of the strongest interactions with bond energies of 50-250 kJ·mol⁻¹ are electrostatic interactions, which occur between charged ions or dipoles (e.g. ion-ion, ion-dipole, and dipole-dipole). Hydrogen bonds are formed between polarized “acidic” hydrogens and an electron pair donor atom. Although the binding energy of one single hydrogen bond is low (10-30 kJ·mol⁻¹), the presence of several hydrogen bridges can add up to high bond energies and systems containing multiple hydrogen bonds show high stability (e.g. DNA). In aromatic systems, π - π stacking interactions can be found with bond energies of up to 50 kJ·mol⁻¹. One of the weakest interaction are Van-der-Waals forces with energies of less than 5 kJ·mol⁻¹. They include London forces (between induced dipoles), Debye forces (interactions between permanent dipoles and induces dipoles) and dispersion forces (attractive interaction between non-polarized molecules). Furthermore, under specific conditions metal coordination is considered a non-covalent interaction. On the one hand, the formed complex needs to be thermodynamically stable with the system in its lowest energy state with its environment. On the other hand, the metal-ligand bonds should be kinetically labile, to allow ligand exchange in the formation process (see *Self-assembly* in Chapter 1.2.2). Therefore, transition metals, alkaline, earth alkaline or lanthanide metal cations are frequently used in metallo-supramolecular chemistry.^[28]

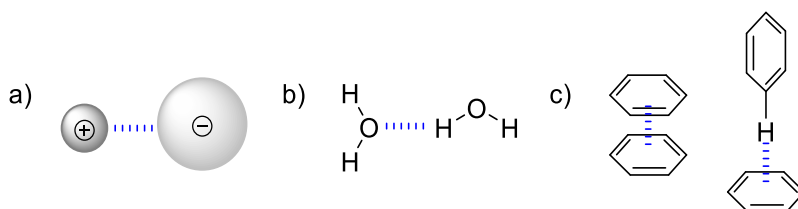


Figure 1.5 Non-covalent interactions: a) ion-ion b) hydrogen bonding c) π - π and CH- π stacking.

While the bond energy of a typical covalent bond is around ~350 kJ·mol⁻¹, non-covalent interactions are usually weaker ranging from 5 kJ·mol⁻¹ for dispersion forces to 250 kJ·mol⁻¹ for ion-ion interactions (see Table 1.1).^[3] Despite the low binding energy, rather stable systems can be formed due

to an interplay of different interactions and the sum of individual contributions. Non-covalent interactions are highly reversible and can be broken easily, which is important in the formation of supramolecular assemblies (see Chapter 1.2.2).

Table 1.1 Supramolecular interaction and their energy contribution.^[2]

Interaction	E [kJ·mol ⁻¹]
ion-ion	200-250
ion-dipole	50-200
dipole-dipole	5-50
hydrogen bonds	4-100
cation- π	5-80
π - π	0-50
Van-der-Waals	< 5
hydrophobic	solvent dependence

1.2.2 Self-assembly

Supramolecular systems are often built with the help of molecular self-assembly.^[28] Thereby, pre-existing components arrange themselves spontaneously into one ordered structure. The self-assembled product is stabilized through non-covalent interactions, which are highly reversible.^[29] This reversibility is important in the formation process, because any error that may have occurred during the assembly can be corrected immediately (“self-healing”). Less stable products or mismatched bonds are broken in favor of more stable ones. During self-assembly processes, many reversible reactions may occur simultaneously until the system reaches equilibrium and a thermodynamic product is formed in nearly quantitative yield. The used starting compounds are often quite simple and the resulting product can be of complex architecture and topology. *Via* self-assembly chemists were able to form fascinating structures,^[30] whose synthesis was difficult or unsuccessful by the utilization of traditional organic synthesis. Examples of supramolecular assemblies are links and knots (see Chapter 1.1), Platonic and Archimedean solids,^{[31],[32]} micelles and vesicles^[33] as well as capsules^[34] and cages (see Chapter 1.3 for more details). Despite sophisticated planning of reaction conditions and starting components, supramolecular chemists are often surprised by their self-assembled products. Due to the reversibility and the weakness of the non-covalent interactions, a precise prediction of the formed structure can be difficult.

Self-assembly processes are distinguished into two types (see Figure 1.6).^[35] The most common one is *strict self-assembly*, where all added compounds are directly used in the formation of the supramolecular aggregate. Whereas, in the *directed self-assembly* process, another species or template (e.g.: counter ions, cations or solvent molecules) accompanies the formation. The template can be essential for the assembly of one discrete species or drive the assembly to a product, that is inaccessible by *strict self-assembly* (see Figure 1.6).

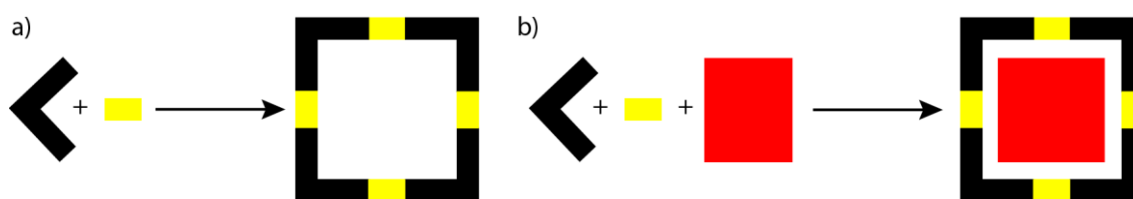


Figure 1.6 Types of self-assembly: a) strict self-assembly and b) directed (templated) self-assembly.

The driving force of supramolecular assemblies is controlled by thermodynamics. Based on the Gibbs-Helmholtz equation $\Delta G = \Delta H - T\Delta S$ enthalpic (ΔH) and entropic (ΔS) contributions have to be considered for the total free energy of the system. The enthalpic contribution is the deliberation of energy by forming non-covalent interactions within the supramolecular aggregate. The assembly of one highly organized species out of several individual components gives the idea, that the entropic contribution is less favorable. However, the release of solvent molecules, organized around the starting components, needs to be considered as well. This dissociation process is so prominent, that the disfavored contribution of the formation process may be negligible and the overall entropic contribution is in favor of the supramolecular assembly process.

1.2.3 Host-Guest Chemistry

Besides the synthesis of unique supramolecular structures with exceptional topologies and architectures, chemists are further interested in investigating the host-guest chemistry of these systems.^[2,7,36] Supramolecular assemblies are often able to incorporate smaller molecules or ions in their structure. The larger supramolecular aggregate is referred to as “host” (abbreviated **H**), while the encapsulated molecule is named “guest” (**G**). The resulting structure is the host-guest complex [**G@H**] (see Figure 1.7).^[2] Driving force for the encapsulation process is an attractive interaction between the guest and the interior of the host molecules based on electrostatic attractions and/or solvophobic effects (see Chapter 1.2.1).

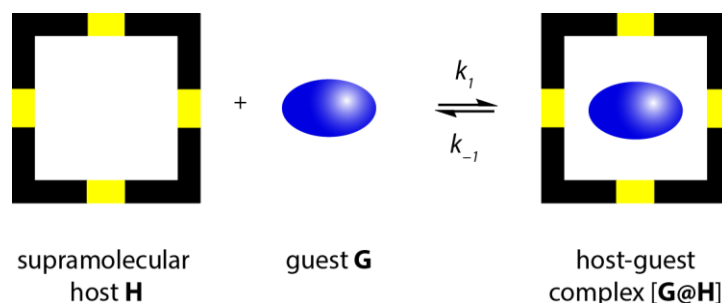


Figure 1.7 Schematic representation of a supramolecular host, which can encapsulate another molecule in its cavity and form a host-guest complex.

Requirement for the formation of the host-guest complex is the presence of a sizeable central cavity of the supramolecular assembly. Researchers found numerous supramolecular systems, which are able to incorporate guests such as (in)organic anions, cations, or even larger neutral guest molecules.^[2,36] Among these, cages and capsules are of particular interest due to their ability to host, protect, transport and release guest molecules (for further information about supramolecular cages

see Chapter 1.3). Furthermore, guest molecules can act as a template in the self-assembly process of the supramolecular structure (see Chapter 1.2.2). Charged molecules are usually used as templates, due to their directional electrostatic interactions, which help to organize the starting molecules prior to the final assembly.

Due to the stabilization of the host-guest complex through non-covalent interactions, the formation is reversible and the complex is in equilibrium with its starting components (see Figure 1.7). The association- or binding constant K_a expresses the thermodynamic stability of the host-guest complex:

$$K_a = \frac{[\mathbf{G@H}]}{[\mathbf{G}] \cdot [\mathbf{H}]} = \frac{k_1}{k_{-1}}$$

A high binding constant correlates to a high equilibrium concentration of the host-guest complex $[\mathbf{G@H}]$ in comparison to free host and guest. The binding constant can be expressed *via* the rate constant of the complexation (k_1) and decomplexation (k_{-1}) process. Determination of K_a is possible *via* NMR-, UV/Vis-, fluorescence spectroscopy, ITC or any other technique whose response signals correlates to the concentration of the involved components.^[37]

Some supramolecular assemblies are able to incorporate more than one guest molecule. This binding of several guest molecules towards a supramolecular host can occur in an allosteric fashion with positive or negative cooperativity (see Figure 1.8).

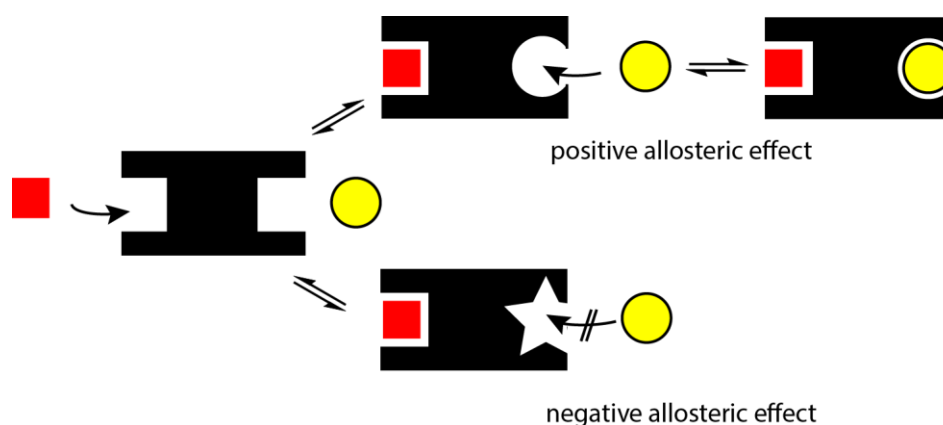


Figure 1.8 Schematic representation of positive and negative allosteric effect.

In case of positive cooperativity, the binding of the first guest molecule enhances the binding affinity of the second uptake, resulting in a higher value for the second association constant K_{a2} . Negative cooperativity decreases the association affinity for further guest binding, resulting in a lower value for the second association constant. In nature, positive cooperativity is observed for example in the binding of dioxygen towards hemoglobin. Binding of one oxygen molecule to one of hemoglobin's four binding sites induces a structural change, which increases the binding affinity towards another oxygen molecule.^[5]

1.3 Supramolecular Coordination Cages

1.3.1 General Concept

The topologies and architecture of supramolecular structures are highly diverse. Among them, supramolecular coordination cages are of high interest.^[31,34,38,39–45] A coordination cage is described as a discrete, three-dimensional coordination compound with cavities that can engage in host-guest chemistry. A coordination cage is composed of several metal centers joined by organic ligands. Through openings in the structure, guest molecules can enter and exit the central cavity of the assembly. Several examples of supramolecular coordination cages were the result of serendipity, but many structures are the outcome of careful planning and understanding of geometric properties of metal ions and individual ligands. The utilization of metal cations introduces a number of geometric topologies in supramolecular assemblies, which would be impossible to obtain by solely applying conventional organic synthesis. Depending on the metal ion, different coordination geometries can be addressed such as linear for silver(I) cations, square planar for palladium(II) or octahedral for iron(II),^[46] which directs the self-assembly of the resulting coordination cage (see Figure 1.9 for coordination geometries). Due to the formation of kinetically labile metal-ligand bonds with bond energies between 40 – 125 kJ·mol⁻¹ the assembly of metal-based coordination cages is highly reversible, which enables the immediate self-healing of wrongly connected bonds.^[41] The formation of coordination cages is an equilibrium reaction between the starting compounds (free ligand and metal ion) and the supramolecular assembly, with the equilibrium position shifted towards the product side.

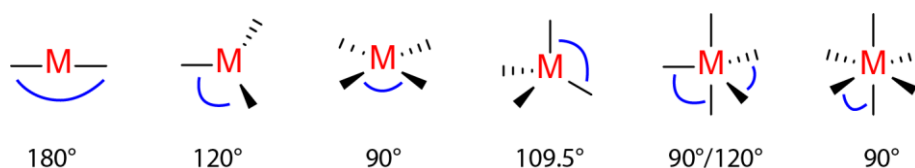


Figure 1.9 Coordination geometries of metal cations including angles. *From left to right:* linear, trigonal planar, square planar, tetrahedral, trigonal bipyramidal and octahedral (M = metal cation).

Besides directionality of the metal cation, the shape and topology of the organic ligand plays an important role in the self-assembly of coordination cages. Ligand length, bending angle, choice of coordinating groups, denticity (bidentate, tridentate etc.), flexibility and other structural features have a major impact on formation and properties of the formed aggregate. On top of this, the reaction conditions such as metal/ligand ratio, choice of counter anions, solvent, temperature, and reaction time will affect the cage formation.^[47] Overall, coordination cages can be created in a highly diverse way with various resulting shapes and topologies. Typical geometries are highly symmetric, often resembling Platonic and Archimedean solids,^[31] e.g. tetrahedra, octahedra or cubes (see Figure 1.10). Nevertheless, many other geometries (e.g. trigonal bipyramidal, adamantoids, trigonal prism, boxes, bowls etc.) could be observed in the last years.

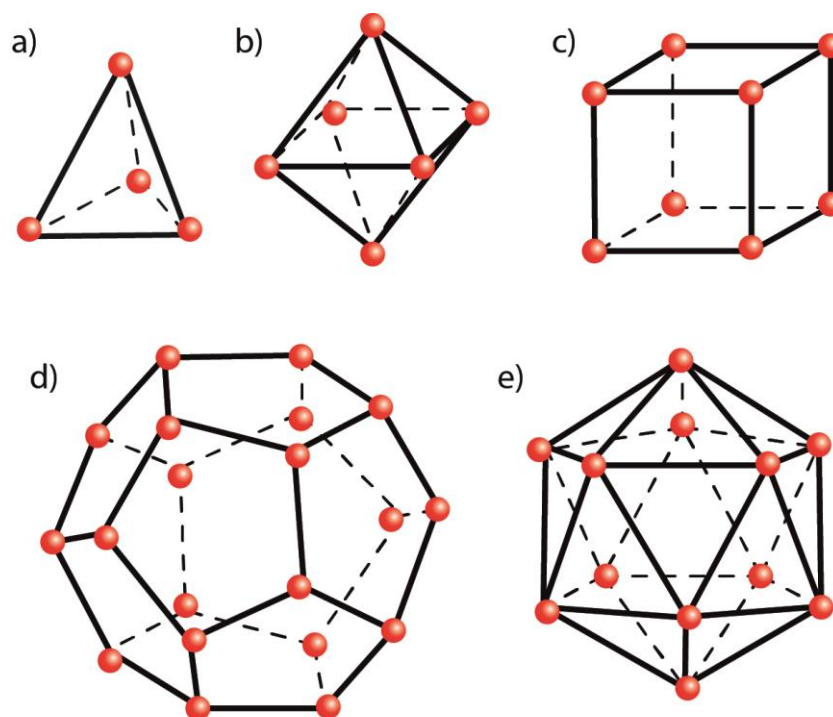


Figure 1.10 Schematic representation of Platonic solids: a) tetrahedron, b) octahedron c) cube, d) dodecahedron and e) icosahedron.

The assembled coordination cages have a discrete cavity, which imparts unique properties to the structure leading to novel functions and characteristics. A large number of coordination cages is positively charged (formation from neutral ligands and positively charged metal ions) and anions can be encapsulated inside the void.^[39] Additionally, neutral ^[40,48] and reactive guests can be stabilized^[49,50] or unreactive molecules were activated for further reactions.^[51] Furthermore, catalytic reactivity,^[52–58] gas sequestration^[59] or separation of species from mixtures^[40,60] can be achieved by the utilization of supramolecular coordination cages.

1.3.2 Coordination Cages based on Banana-shaped Ligands

One class of supramolecular cages are assembled from banana-shaped ligands and various metal cations.^[42] Reported metal ions are copper, nickel, palladium, platinum, cobalt or different lanthanides (La, Ce, Sm, Eu, Tb).^[61] In general, diamagnetic and relatively inert metal ions are preferred. The utilized ligands have a symmetric, concave shape with the donor groups positioned at the end of the molecule. The ligand backbones are usually rigid, aromatic and connected *via* single bonds, alkyne units or flexible sp^3 linkers. Resulting cage assemblies are mostly charged, thus polar solvents (e.g. acetonitrile) are preferably used in formation reaction and analysis.

In the group of *Prof. Clever*, the research of supramolecular cages is focused on the self-assembled structures from banana-shaped bis-monodentate pyridine ligands and square-planar d^8 metal centers [Pd(II) or Pt(II)].^[42] The metal cations offer four coordination sides, which are coordinated by the nitrogen atom of the pyridine-containing ligands. Self-assembly between these metal cations and different ligand resulted in the formation of structures with diverse topologies (see Figure 1.11).

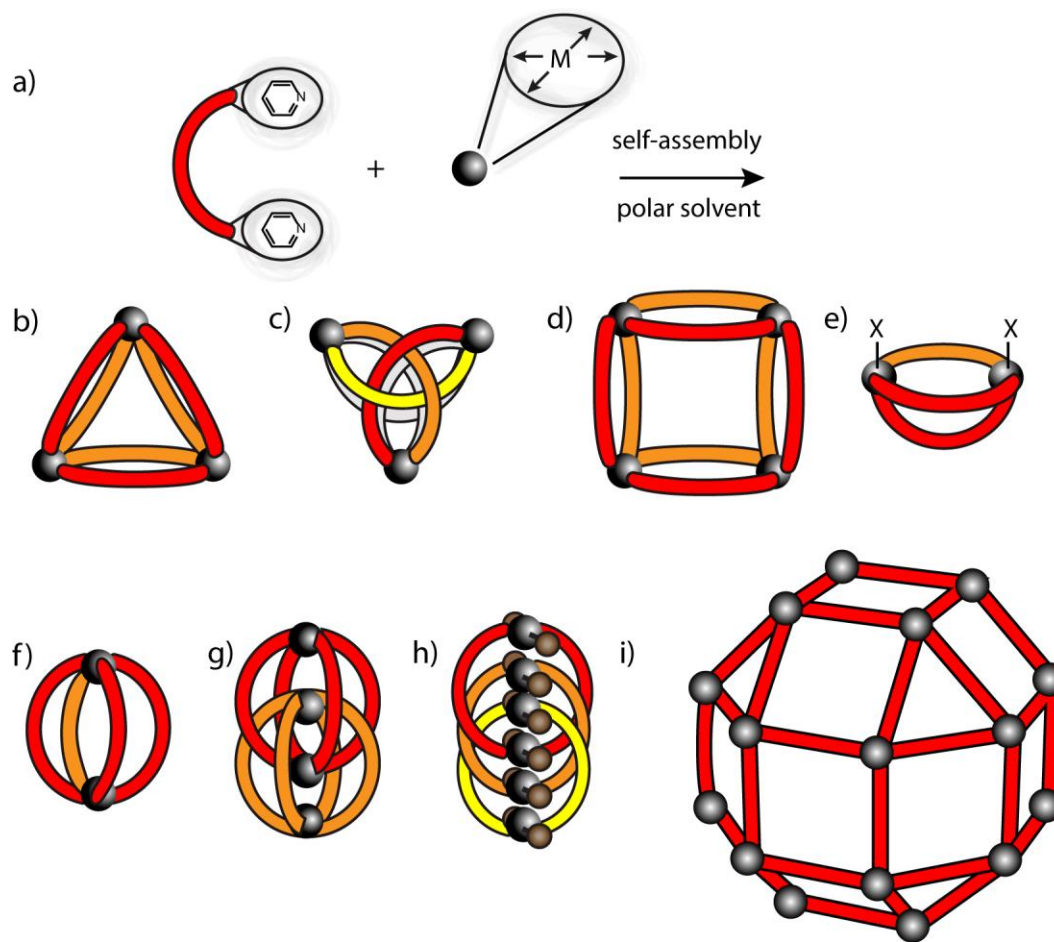


Figure 1.11 a) Schematic representation of self-assembled architectures based on metal(II) cations (e.g. Pd^(II) or Pt^(II)) and banana-shaped bispyridyl ligands **L**. Resulting products are b) [M₃L₆] ring, c) [M₃L₆] double-trefoil knot, d) [M₄L₈] ring, e) [M₂L₃X₂] bowl (X = solvent), f) [M₂L₄] coordination cage, g) [M₄L₈] interpenetrated coordination cage, h) triple catenane {trans-[(MBr₂)₂L₂]₃} and i) rhombicuboctahedral sphere [M₂₄L₄₈].

The most common structure is the monomeric [M₂L₄] cage, where two metal cations are bridged by four banana-shaped ligands occupying all possible metal coordination sides (see Figure 1.11f). Due to the concave shape of the ligands, the coordination cage contains a spherical void, in which guest molecules can be encapsulated. Resulting host-guest structures can contain anionic^[39,62] or neutral guests^[63] and even pairs of small metal-complexes revealing an alternating cation-anion arrangement.^[45] Under specific conditions, interpenetration of the monomeric cages and formation of the dimeric [M₄L₈] cage is observed.^[64] (Conditions and influencing factors of the assembly process will be discussed in Chapter 1.3.3). An excess of halide anions (e.g. Br) in the solution can result in the formation of a triple catenane, namely {trans-[(MBr₂)₂L₂]₃} (Figure 1.11h).^[65] Substitution of the pyridine donor group by a quinoline group yielded a bowl shaped [M₂L₃X₂]-structure (X = solvent, see Figure 1.11e). Due to the sterically more demanding donor group, only three ligands can coordinate to the two metal centers and surrounding solvent molecules (e.g. acetonitrile) occupy the other two coordination sides. Furthermore, a light switchable dithienylethene (DTE) based ligand forms a mixture of three- or four membered rings ([Pd₃L₆] or [Pd₄L₈]) in their open form (Figure 1.11b and d). After irradiation, the ligand undergoes a photo induced conformation change and the

subsequently “closed” ligand forms the rhombicuboctahedral sphere $[\text{Pd}_{24}\text{L}_{48}]$ in presence of palladium(II) cations (Figure 1.11i).^[66]

All described examples, assembled from palladium(II) cations and bispyridyl ligands, show the diversity of accessible architectures by simple variation of some structural parameters or reaction conditions. The complexity of the assembled systems is increased by mixing two or more kinds of different ligands in presence of metal cations. Self-assembly can result in the formation of one discrete species containing both types of ligands with $[\text{Pd}_2\text{L}^a_2\text{L}^b_2]$ stoichiometry.^[67] Another outcome can be a statistical mixture with $[\text{Pd}_2\text{L}^a_x\text{L}^b_y]$ species ($x = 0 \leq 4, y = 4 - x$) or a self-sorted system following the principle of narcissistic self-sorting, generating several discrete species ($[\text{Pd}_2\text{L}^a_4]$ and $[\text{Pd}_2\text{L}^b_4]$) containing only one type of ligand.^[68,69]

The outcome of self-assembly from one type of banana-shaped ligands and square planar coordinating metal centers is usually predictable, but occasionally the resulting structures are surprising, such as formation of an entangled double-trefoil knot (Figure 1.11c)^[70] from an elongated ligand or the assembly of a butterfly shaped complex from a longer flexible bispyridyl ligand.^[71] This diversity results in supramolecular coordination cages being an exciting research topic and scientist all around the world are fascinated by it.

1.3.3 Interpenetrated Coordination Cages based on Banana-shaped Ligands and Pd(II) cations

Interpenetrated coordination cages^[64] are classified as three-dimensional catenanes, which assemble from organic ligands and metal cations. In this thesis, the focus on interpenetrated structures will be reduced to assemblies from banana-shaped bispyridyl ligands with palladium(II) metal centers (see Figure 1.12).

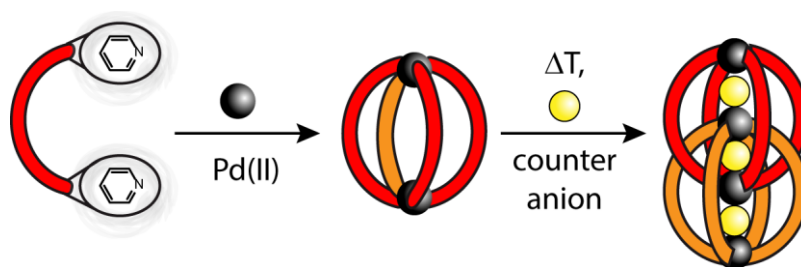


Figure 1.12 Schematic representation of the self-assembly of interpenetrated $[\text{Pd}_4\text{L}_8]$ coordination cages.

Mixing the organic ligand with a palladium(II) salt in a 2:1 ratio leads to the immediate formation of the monomeric $[\text{Pd}_2\text{L}_4]$ cage as the kinetically favored product. The monomeric cage can dimerize to the thermodynamically stable interpenetrated $[\text{Pd}_4\text{L}_8]$ cage, after prolonged heating of the mixture. The dimer consists of two monomeric cages, which are quadruple intertwined and cannot be separated without cleaving several coordination bonds within the individual cages. The interpenetrated coordination cages possess three individual cavities filled by guest molecules (e.g. non-coordinating counter anions). The assembled structures are formed in nearly quantitative yields,

which makes further purification redundant. During the assembly process, several factors play an important role. First, the reversibility of the formed metal-coordination bonds are vital for the formation of the interpenetrated structure. Immediate breaking of improperly connected and thus unfavorable bonds leads to rearrangement into correct positions (see Chapter 1.2.2) and allows the formation of one distinct final product. Second, the presence of a non-coordinating counter anion as a template is necessary for the dimerization process. For the best of my knowledge, there are no interpenetrated cages containing banana-shaped ligands without a templating anion. During self-assembly, the anions pre-organize the palladium centers in an alternating fashion (Pd(II)-anion-Pd(II)) and are incorporated in the resulting structure (see Figure 1.12). In the final product, the templating anion weakens the repulsion of the double positively charged palladium centers. Tetrafluoroborate (BF_4^-), hexafluorophosphate (PF_6^-) or nitrate (NO_3^-) are commonly used templating anions. Furthermore, the choice of solvent is crucial for the formation process. Utilization of acetonitrile or acetone leads to the interpenetrated product, while in dimethylsulfoxid (DMSO) the formation of the monomeric cage is preferred.^[47]

The stability of the interpenetrated coordination cage results from a combination of enthalpic and entropic effects. Enthalpic contributions are electrostatic interactions between the metal centers and the anions, the coordination bonds between the ligand and the metal as well as π - π and van-der-Waals interactions between the ligands. Whereas the release of organized solvent molecules contributes to a favorable entropic effect and thus, to the total free energy of the system.

In 2008, *Kuroda* and coworkers introduced the first example of an interpenetrated coordination cage containing bis-monodentate banana-shaped ligands (see Figure 1.13).^[72] Mixing benzophenone based ligand **1.1** and $\text{Pd}(\text{NO}_3)_2$ in a 2:1 ratio resulted in formation of the monomeric $[\text{Pd}_2\mathbf{1.1}_4]$ cage after stirring for 1 h at ambient temperature. Heating the sample for 24 h at elevated temperature yielded the interlocked $[\text{Pd}_4\mathbf{1.1}_8]$ dimer as the thermodynamic product. The three voids of the $[\text{Pd}_4\mathbf{1.1}_8]$ cage are occupied by non-coordinating nitrate (NO_3^-) anions as an auxiliary template. In later studies *Kuroda* showed, that addition of different anionic guest molecules triggers an interconversion between the monomeric and dimeric cages and therefore a precise control over the formation process was achieved.^[73,74]

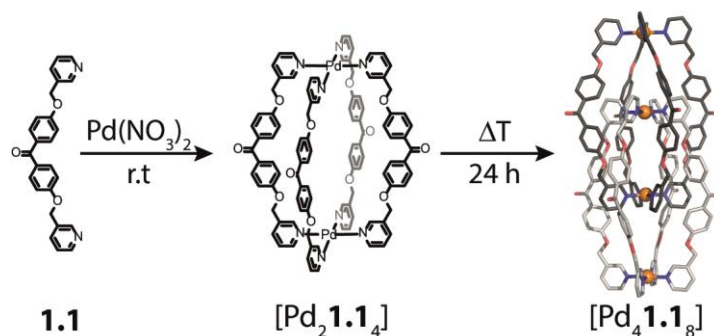


Figure 1.13 Schematic illustration of the formation of the monomeric $[\text{Pd}_2\mathbf{1.1}_4]$ coordination cage from benzophenone-based ligand **1.1** and $\text{Pd}(\text{NO}_3)_2$. Prolonged heating yielded the interpenetrated dimer $[\text{Pd}_4\mathbf{1.1}_8]$.^[72] Color scheme: C: light/dark gray; N: blue; O: red; Pd: orange.

In 2012, *Clever* and coworkers synthesized a banana-shaped ligand **1.2** based on dibenzosuberone.^[75] In contrast to the previous system, the ligand **1.2** is rigid due to a bridging ethynyl group between the backbone and the pyridine units. Nevertheless, formation of the interpenetrated dimer was observed, after heating the sample for several hours (see Figure 1.14a). The presence of the kinetic, monomeric $[\text{Pd}_2\mathbf{1.2}_4]$ cage was observed immediately after mixing the ligands and the palladium cations, but isolation was not possible due to rapid transformation into the thermodynamically stable dimer. Non-coordinating tetrafluoroborate counter anions occupy the three cavities of the interpenetrated coordination cage $[\text{3BF}_4@\text{Pd}_4\mathbf{1.2}_8]$. ^{19}F NMR experiments showed that one of these BF_4^- anions is tightly encapsulated in the central pocket of the cage dimer, while the two BF_4^- anions in the outer cavities are weakly bound.^[76] Addition of halide anions (e.g. Cl^- , Br^-) results in an anion exchange of the loosely bound tetrafluoroborate anions *via* an allosteric mechanism with positive cooperativity (see Chapter 1.2.3). The halide binding results in the overall shrinkage of the dimer along the Pd_4 -axis and a torsion of the monomeric cages towards each other. Adding an excess of silver(I) cations to the halide-filled host-guest assembly leads to the precipitation of silver halide (such as AgCl) and regeneration of the tetrafluoroborate-containing $[\text{3BF}_4@\text{Pd}_4\mathbf{1.2}_8]$ cage.^[75]

The dibenzosuberone backbone, which consists of a central, seven-membered ring carrying a carbonyl functionality, can be easily modified. A Grignard reaction allowed the introduction of a bulky aryl substituent to the ligands center. Addition of $[\text{Pd}(\text{CH}_3\text{CN})_4](\text{BF}_4)_2$ to a solution of ligand **1.3** in acetonitrile gave the monomeric $[\text{Pd}_2\mathbf{1.3}_4]$ cage as the thermodynamic product in quantitative yields. No evidence of the interpenetrated dimer was found in presence of tetrafluoroborate counter anions. Only, after the addition of 0.5 equivalents chloride anions as a template, the interpenetrated dimer $[\text{Cl}@\text{Pd}_4\mathbf{1.3}_8]$ forms in quantitative yields. The chloride anion is occupying the central pocket of the interpenetrated coordination cage and arranging the palladium(II) centers in a linear fashion ($\text{Pd}-\text{Cl}-\text{Pd}$). Due to the small templating chloride in the central void of the dimer, the outer cavities are enlarged. Thus, incorporation of larger perrhenate anions (ReO_4^-) in the outer pockets of the cage and formation of the host-guest complex $[\text{2ReO}_4+\text{Cl}@\text{Pd}_4\mathbf{1.3}_8]$ is possible (see Figure 1.14b). The attachment of the bulky aryl group prevents the formation of the tetrafluoroborate-templated double cage and only a smaller templating anion such as chloride can induce the dimerization process.^[77]

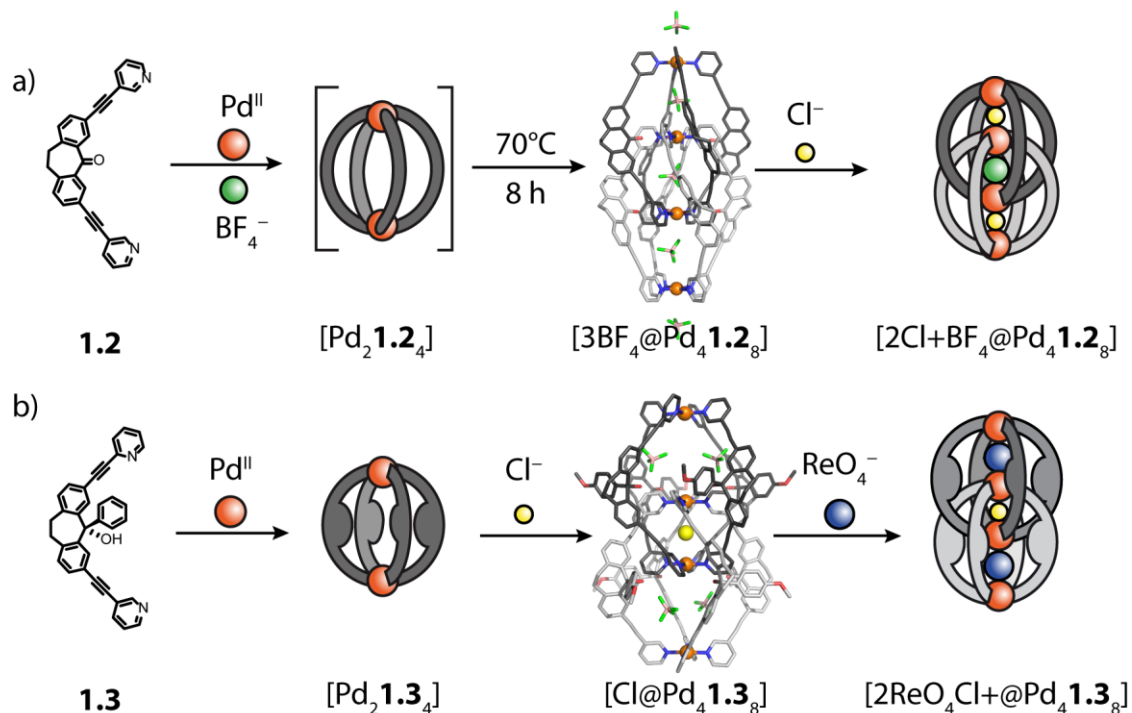


Figure 1.14 a) Addition of $[\text{Pd}(\text{CH}_3\text{CN})_4](\text{BF}_4)_2$ to dibenzosuberone-based ligand **1.2** leads to formation of the thermodynamically unstable monomeric $[\text{Pd}_2 \mathbf{1.2}_4]$ cage. Heating the mixture for 8 h at 70°C gave the interpenetrated coordination cage $[3\text{BF}_4 @ \text{Pd}_4 \mathbf{1.2}_8]$, which can encapsulate chloride anions in its outer pockets in an allosteric fashion and form $[2\text{Cl} + \text{BF}_4 @ \text{Pd}_4 \mathbf{1.2}_8]$. b) Ligand **1.3** forms the stable monomeric $[\text{Pd}_2 \mathbf{1.3}_4]$ cage after addition of $[\text{Pd}(\text{CH}_3\text{CN})_4](\text{BF}_4)_2$. In presence of chloride anions (0.5 eq.) the interpenetrated dimer $[\text{Cl} @ \text{Pd}_4 \mathbf{1.3}_8]$ is formed, which can incorporate two perchlorate anions in the outer pockets.^[77] *Color scheme:* C: light/dark gray; N: blue; O: red; Cl: yellow; F: green; B: salmon; Pd: orange. Hydrogens, solvent molecules and disordered counter anions were removed for clarity.

Similar to the previous example, a carbazole based-ligand (**1.4**) is transformed into the monomeric $[\text{Pd}_2 \mathbf{1.4}_4]$ cage after heating the sample in presence of $[\text{Pd}(\text{CH}_3\text{CN})_4](\text{BF}_4)_2$ in acetonitrile. Addition of halide anions and subsequent heating for 5 h induced the dimerization of the individual cages and the assembly of the interpenetrated $[3\text{X} @ \text{Pd}_4 \mathbf{1.4}_8]$ cages ($\text{X} = \text{Cl}^-, \text{Br}^-$, see Figure 1.15). In this example, all three voids of the structure are occupied by halide anions such as bromide or chloride. In contrast to the system described in Figure 1.14b, the formation of the thermodynamically stable monomeric $[\text{Pd}_2 \mathbf{1.4}_4]$ cage does not result from an attached sterically demanding residue. Instead, monomer formation is preferred due to the size of the ligand. The backbone of the carbazole ligand contains a five-membered ring with a nitrogen-nitrogen distance of 13.60 \AA . This is too short for the formation of the dimeric cage in presence of the rather large non-coordinating tetrafluoroborate anion (in comparison: ligand **1.2** contains a seven-membered ring and has a N-N distance of 16.34 \AA). Only in presence of a smaller templating halide anion, dimerization is possible. Interestingly, the dimer can transform into triple catenane $[(\text{PdBr}_2)_6 \mathbf{1.4}_6]$ if an excess of halide is added (see Figure 1.15). This example shows that the concentration of only one chemical trigger (such as halides) can direct the outcome of the self-assembly and the topology of the supramolecular product (monomeric cage, interpenetrated dimer or triple catenane).^[65]

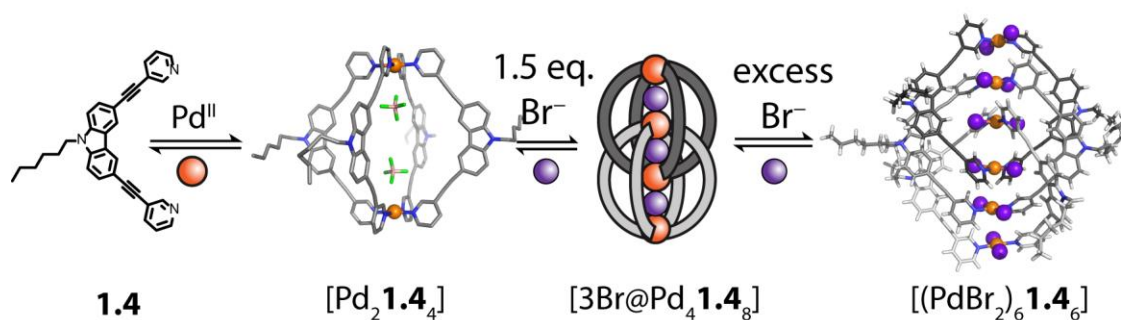


Figure 1.15 Self-assembly of the carbazole-based ligand **1.4** to the monomeric $[Pd_2 \mathbf{1.4}_4]$ cage. Addition of 1.5 eq. of halide (e.g. bromide or chloride) forms the dimer $[3Br@Pd_4 \mathbf{1.4}_8]$ with all three pockets occupied by bromide anions. Upon addition of larger amounts of halide the triple catenane $[(PdBr_2)_6 \mathbf{1.4}_6]$ is formed.^[65] *Color scheme:* C: light/dark gray; N: blue; O: red; Br: purple F: green; B: salmon; Pd: orange. Hydrogens, solvents and disordered counter anions have been removed for clarity.

Besides cage formation from the five- and seven-membered ring containing ligand backbones (carbazole and dibenzosuberone), the self-assembly from similar ligands containing a six-membered ring in the backbone structure was investigated. Thus, phenothiazine or anthraquinone were easily transformed into corresponding bispyridyl ligands **1.5** and **1.8**. Addition of Pd(II) cations and heating for several hours at 70 °C lead to the quantitative formation of the corresponding interpenetrated coordination cages $[3BF_4@Pd_4 \mathbf{1.5}_8]$ and $[3BF_4@Pd_4 \mathbf{1.8}_8]$ containing tetrafluoroborate anions in all three pockets (see Figure 1.16). The electron rich phenothiazine backbone was chosen due to the well-known redox activity of the organic compound. It was shown, that the ligand **1.5** oxidizes to the mono- and di-oxygenated ligands **1.6** and **1.7**, which also assemble into the corresponding interpenetrated dimers in presence of palladium(II).^[78] Even though all three phenothiazine-based interpenetrated coordination cages have the same topology, the palladium-palladium distances and the size of the cavities are quite different. Due to the steric demand of the oxygen substituents, which are attached to the ligand's central positions, the ring fold of the phenothiazine system (angle between two benzene planes) is decreased in the oxygenated systems, resulting in a decrease of the Pd-Pd distances. All phenothiazine and anthraquinone based interpenetrated coordination cages are able to bind halide anions *via* an allosteric mechanism.^[79] Due to the small structural differences between these derivatives, the size of the cavities and consequently the binding affinities towards the halides are influenced.^[79] Mixing two different phenothiazine or anthraquinone based ligands in solution with $[Pd(CH_3CN)_4](BF_4)_2$ resulted in the formation of interpenetrated coordination cages comprising a statistically distribution of the ligands as the thermodynamic product.^[68] These mixed dimers containing electron-rich ligand **1.5** and electron-deficient ligand anthraquinone **1.6** shows light-induced charge separation from donor to acceptor upon photoexcitation.^[69]

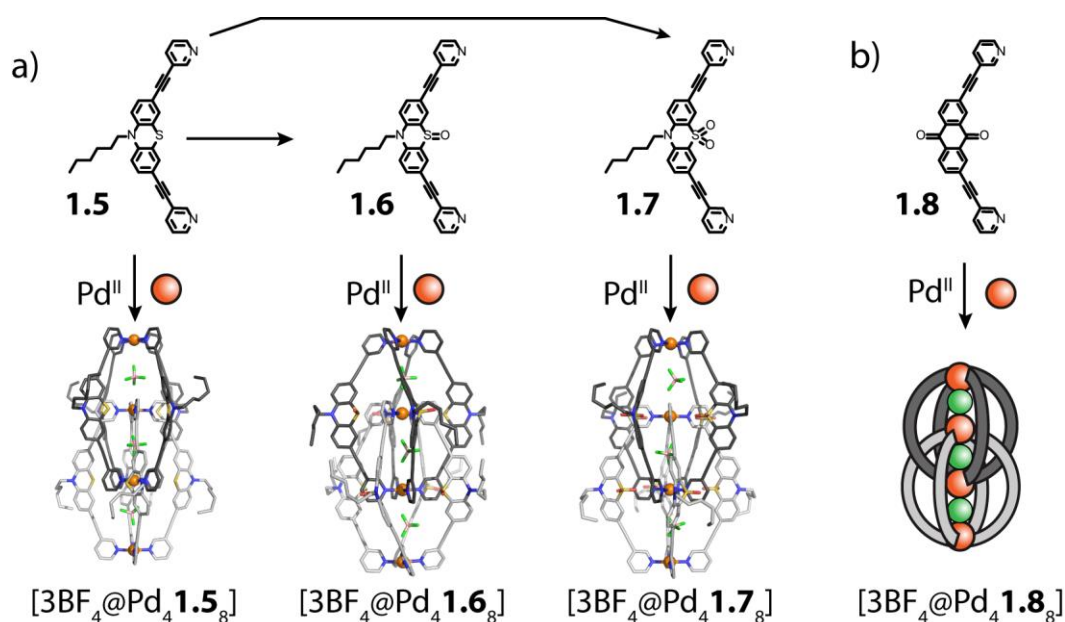
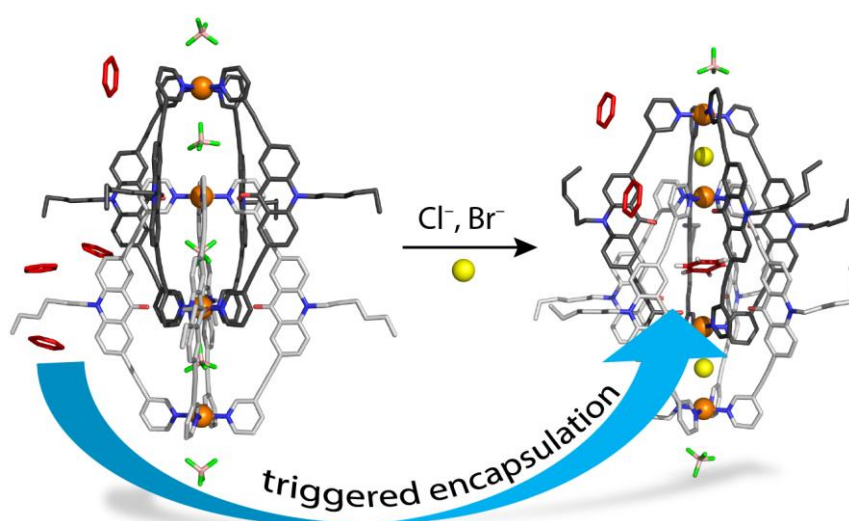


Figure 1.16 a) Self-assembly of phenothiazine-based interpenetrated coordination cages $[3\text{BF}_4@Pd_4\mathbf{1.5}_8]$, $[3\text{BF}_4@Pd_4\mathbf{1.6}_8]$ and $[3\text{BF}_4@Pd_4\mathbf{1.7}_8]$ in presence of palladium(II) cations. b) Addition of palladium(II) to anthraquinone-based ligand **1.8** results in the formation of the thermodynamic driven product $[3\text{BF}_4@Pd_4\mathbf{1.8}_8]$ cage.^[76] *Color scheme:* C: light/dark gray; N: blue; O: red; F: green; B: salmon; S: yellow; Pd: orange. Hydrogens, solvents molecules and disordered counter anions have been removed for clarity.

The previous examples could show, that the dimerization of monomeric $[\text{Pd}_2\text{L}_4]$ cages into the interpenetrated $[\text{Pd}_4\text{L}_8]$ dimer depends on several factors. The most important ones are length, bending angle and steric demand of the organic ligands. Furthermore, the choice of the solvent, the size of the templating counter anions as well as the type of metal cation^[80] play an important role in the dimerization process.

2 NEUTRAL GUEST UPTAKE IN INTER-PENETRATED COORDINATION CAGES



This Chapter correspond to the following publications:

"Triggered Exchange of Anionic for Neutral Guests inside a Cationic Coordination Cage", S. Löffler, J. Lübber, L. Krause, D. Stalke, B. Dittrich, G. H. Clever, *J. Am. Chem. Soc.* **2015**, 137, 1060.

"Influence of Size, Shape, Heteroatom Content and Dispersive Contributions on Guest Binding in a Coordination Cage" S. Löffler, A. Wuttke, B. Zhang, J. J. Holstein, R. A. Mata, G. H. Clever, *Chem. Comm.* **2017**, 53, 11933.

2.1 Introduction

In supramolecular chemistry, one field of research focusses on the investigation of host-guest chemistry in self-assembled structures.^[2] The topologies and architectures of the supramolecular hosts are highly diverse, just as their host-guest chemistry. Supramolecular coordination architectures were in the beginning solely constructed to create a pool of novel architectures such as rings, knots, links, rotaxanes, catenanes and cages.^[13] In recent studies, the focus was shifted towards the implementation of functionalities such as light-switch ability,^[81] chirality and redox activity^[78] as well as the integration of endohedral anchor groups.^[82,83] Furthermore, controlled uptake of the guest molecules inside the supramolecular coordination cages has become a central interest.

One class of supramolecular assemblies, which were intensively studied in the past years are the interpenetrated coordination cages based on banana-shaped bispyridyl ligands and square planar palladium(II) metal cations.^[64] In the formation process of these special catenanes, several factors play an important role, such as length, torsion angle and steric demand of the ligand. Furthermore, solvent, type of metal cation and concentration of counter anion are important factors in the assembly process (see Figure 2.1).^[47]

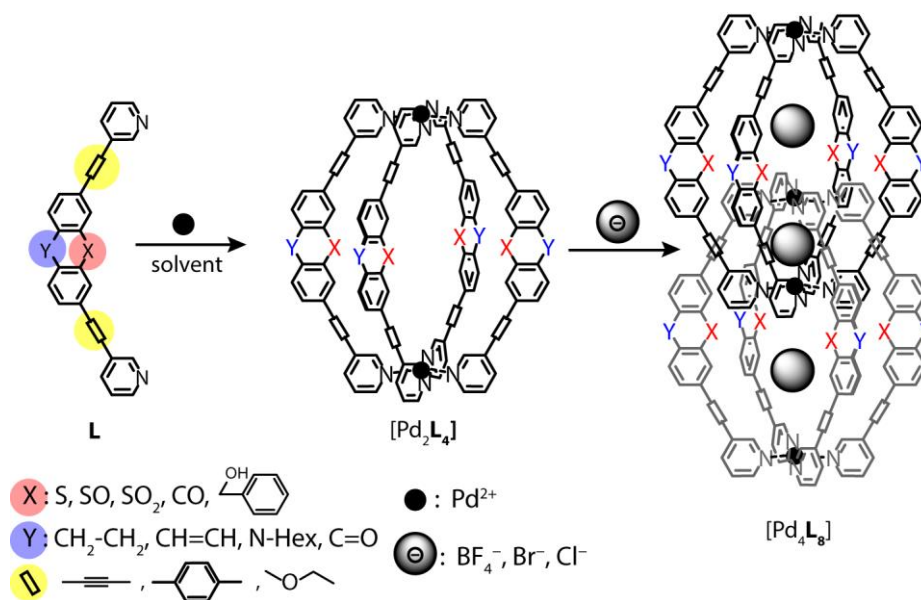


Figure 2.1 Schematic representation of influencing factors of the ligand modification on the self-assembly of the interpenetrated [M₄L₈] cage dimer.

As an intermediate, the monomeric [Pd₂L₄] cage is formed and in presence of a suitable templating anion, the [Pd₄L₈] dimer is yielded as the thermodynamic product (see Figure 2.1). Interpenetrated [Pd₄L₈] coordination cages consist of two interlocked monomeric [Pd₂L₄] cages stabilized through non-covalent interactions (electrostatic forces, metal-ligand coordination bonds, π - π stacking). The assembled structures contain three pockets, which can incorporate different kinds of anions. Variation of the ligand backbone, such as different length or attachment of bulky residues, enabled the control over the type of encapsulated anion. It was found, that BF₄⁻, Cl⁻, Br⁻ or ReO₄⁻ are encapsulated in the cavities of the interpenetrated structures.^[64]

In previous studies, interpenetrated coordination cages containing benzophenone,^[72–74] dibenzosuberone,^[47,75,77] phenothiazine,^[68,69,78,79] or carbazole-based^[65] ligands and palladium(II) cations were synthesized and their host-guest chemistry intensively investigated. It was found, that tetrafluoroborate-containing interpenetrated coordination cages $[3\text{BF}_4@Pd_4L_8]$ from dibenzosuberone and phenothiazine could encapsulate halide anions in their outer cavities according to an allosteric binding mechanism with strong positive cooperativity.

The focus in this Chapter is set on the design and characterization of a new type of interpenetrated coordination cage built from acridone-based bispyridyl ligands and palladium(II) nodes. The new ligand, containing a central six-membered ring and a carbonyl functionality in the acridone backbone has a similar size as the previous reported dibenzosuberone and phenothiazine systems and is expected to form the interpenetrated cage dimer in presence of tetrafluoroborate counter anions. The dimer formation as well as the ability to incorporate molecules (e.g. halide anions and neutral guests) inside the cavities of the supramolecular coordination cage was studied.

2.2 Ligand Synthesis and Cage Assembly

Starting from commercially available 10*H*-acridin-9-one, the new ligand **L**¹ was synthesized in three steps (see Figure 2.3). To increase the solubility, a hexyl chain was attached to the nitrogen atom by a S_N2 reaction using potassium-*tert*-butoxide and 1-bromohexane.^[84] Thereafter, reaction with *N*-bromosuccinimide (2.0 eq.) leads to the bromination at positions 2 and 7 of *N*-hexylacridone.^[85] Subsequent, a sonogashira cross coupling^[86] with 3-ethynylpyridine gave ligand **L**¹ in adequate yields.

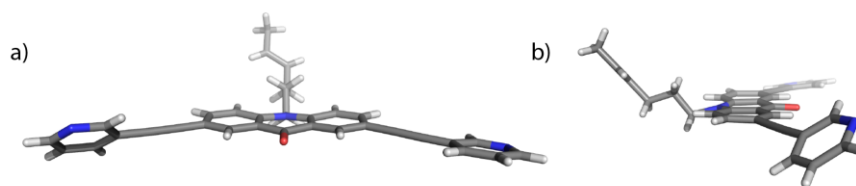


Figure 2.2 a) Front and b) side view of the preliminary X-ray crystal structure of ligand **L**¹. Color scheme: C: gray; N: blue; O: red.

Single crystals of ligand **L**¹, suitable for X-ray determination, were obtained by slow vapor diffusion (for further details see Chapter 7.3.5). The crystal structure indicated that the backbone based on acridone is planar and the pyridine residues are slightly twisted. One pyridine residue is disordered either with the nitrogen atom pointing towards or away from the acridone backbone (see Figure 2.2 and Figure 7.85).

After successful purification and characterization, ligand **L**¹ was tested for its ability to form supramolecular cages. Hence, the ligand was suspended in deuterated acetonitrile and 0.5 equivalents of tetrakis(acetonitrile)palladium(II) tetrafluoroborate were added. After heating the resulting solution for 24 h at 70 °C in a closed vial, the interpenetrated coordination cage $[3\text{BF}_4@Pd_4L_8]$ was

obtained in quantitative yields (see Figure 2.3, and for synthetic protocols and characterization data see Chapter 7.3.1). Due to the complete conversion to the supramolecular coordination cage, no further purification was necessary. The ligand and the interpenetrated coordination cage were characterized *via* NMR spectroscopy, high resolution ESI mass spectrometry and X-ray structure determination.

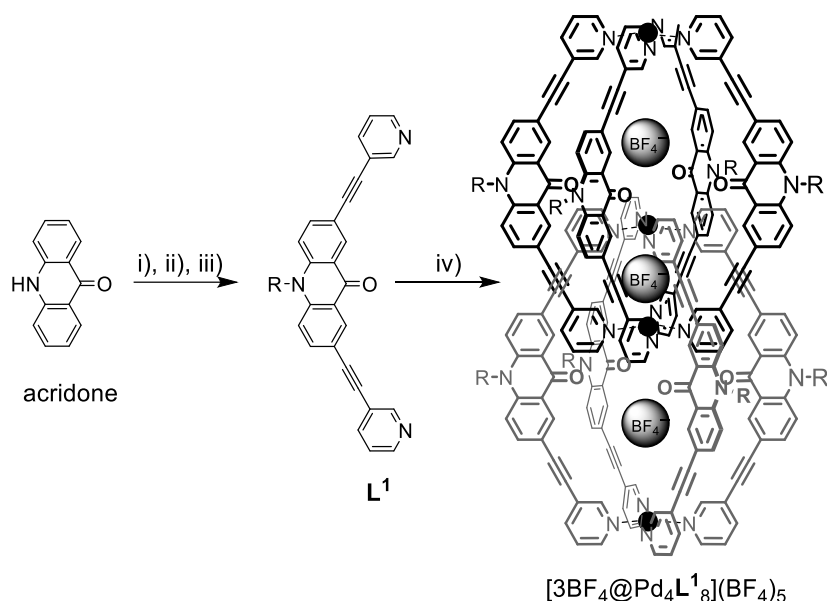


Figure 2.3 Synthesis of ligand L^1 and assembly to cage $[3\text{BF}_4@Pd_4L^1_8](\text{BF}_4)_5$: i) 1-bromohexane, KO^tBu , THF; ii) NBS, DMF; iii) 3-ethynylpyridine, CuI , $[\text{Pd}(\text{PPh}_3)_2\text{Cl}_2]$, NEt_3 ; iv) $[\text{Pd}(\text{CH}_3\text{CN})_4](\text{BF}_4)_2$, CD_3CN , 24 h, 70°C . Reprinted with permission from reference ^[87] Copyright © 2015 American Chemical Society.

The free ligand L^1 shows seven equivalent signals in the aromatic region of the ^1H NMR spectrum. Incorporation of this ligand into the highly symmetric cage structure $[3\text{BF}_4@Pd_4L^1_8](\text{BF}_4)_5$ (further abbreviated as $[3\text{BF}_4@Pd_4L^1_8]$) results in splitting of all ^1H NMR signals into two sets of equal intensity, indicating different environments of the two sides of the ligand within the cage structure. Furthermore, metal coordination leads to a strong downfield shift of pyridine signals H_g and H_f . In contrast, the signals of the N-CH_2 groups of the hexyl chain and the acridone backbone (H_a , H_b and H_c) show an upfield shift in the ^1H NMR spectrum (see Figure 2.4 and experimental section).

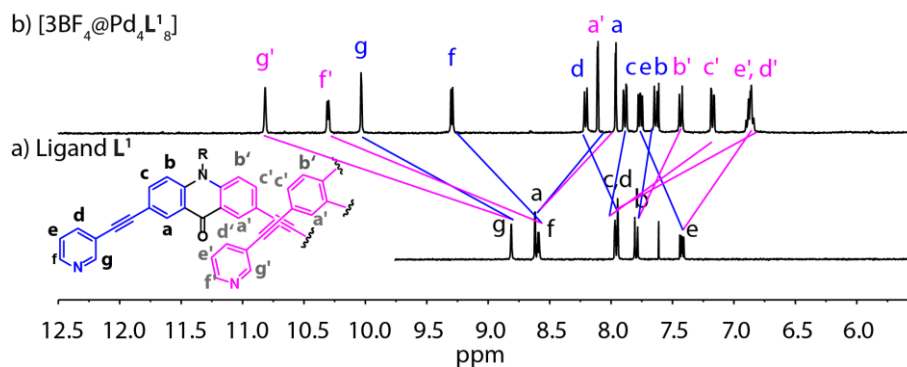


Figure 2.4 ^1H NMR spectra of (a) ligand L^1 and (b) the interpenetrated double cage $[3\text{BF}_4@Pd_4L^1_8]$ (400 MHz, 298 K, CD_3CN). Reprinted with permission from reference ^[87] Copyright © 2015 American Chemical Society.

Tetrakis(acetonitrile)palladium(II) tetrafluoroborate was used as a palladium source to form the interpenetrated coordination cage. It was chosen due to its good solubility in the used solvent (acetonitrile) and the presence of the non-coordinating counter anion (BF_4^-).^[88] The tetrafluoroborate counter anion only weakly interacts with the palladium(II) cation, which allows the formation of the slightly stronger palladium-nitrogen coordination bond.^[3] Furthermore, the anion is crucial for the formation of the interpenetrated coordination cage due to the template effect (see Chapter 1.2.2).^[2] Three BF_4^- anions are encapsulated inside the supramolecular assembly between two palladium(II) cations resulting in an alternating arrangement of positive and negative charges ($\text{Pd}^{2+}/\text{BF}_4^-$). A formation of the interpenetrated coordination cage without any encapsulated counter anions was not observed. Also usage of tetrakis(acetonitrile)palladium(II) hexafluorophosphate did not result in the formation of the $[\text{3PF}_6@\text{Pd}_4\text{L}_8](\text{PF}_6)_5$ coordination cage. It seemed that the PF_6^- anion is too large to be encapsulated in such an intertwined supramolecular structure. This indicates the importance of the volume occupied by the non-coordinating counter anion within the interpenetrated structure during its formation.

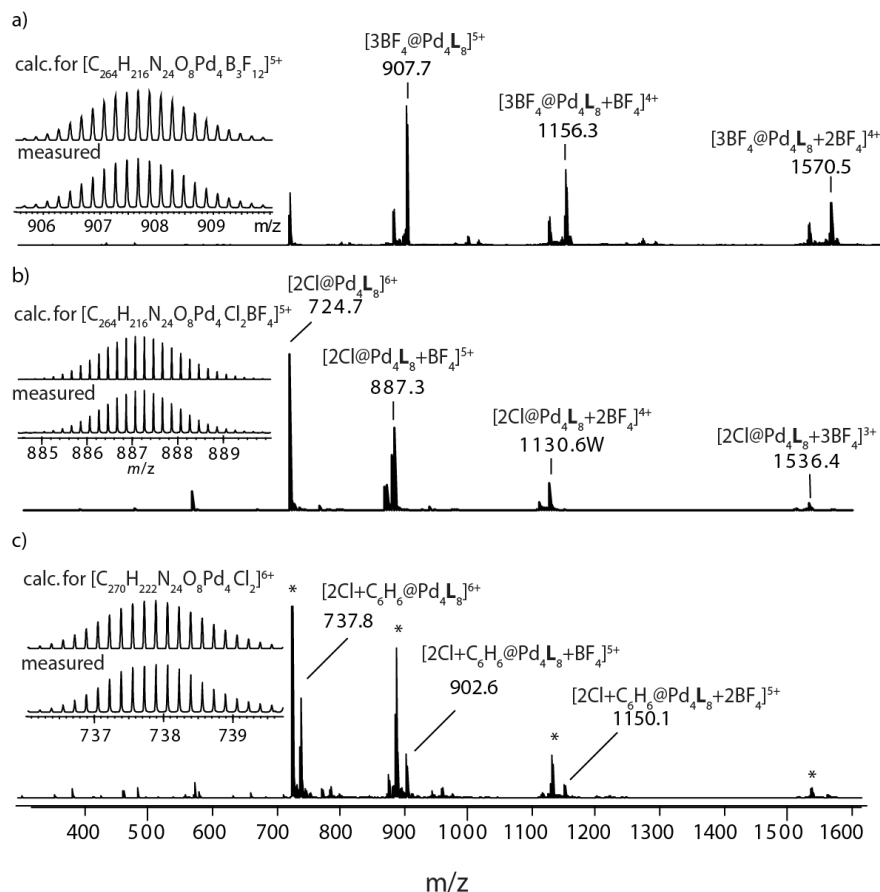


Figure 2.5 ESI mass spectra of (a) $[\text{3BF}_4@\text{Pd}_4\text{L}_8]$, (b) $[\text{2Cl}@\text{Pd}_4\text{L}_8]$, and (c) $[\text{2Cl}+\text{C}_6\text{H}_6@\text{Pd}_4\text{L}_8]$ (* = free host). Reprinted with permission from reference ^[87] Copyright © 2015 American Chemical Society.

The presence of the BF_4^- anions inside the coordination cage was verified by NMR spectroscopy. At room temperature, the ^{19}F NMR spectrum showed three sets of signals. The signal with a chemical shift of $\delta = -151.70$ ppm can be assigned to free tetrafluoroborate in the solution. Encapsulated BF_4^- in the inner pocket of the interpenetrated dimer is found at a chemical shift of $\delta = -143.32$ ppm

and the two BF_4^- enclosed in the outer pockets at $\delta = -144.85$ ppm (see Figure 7.77 in the appendix section 7.3.4). In addition, a ^{19}F NMR based exchange experiment (EXSY) showed that the encapsulated BF_4^- anion in the outer pockets could be exchanged with the exterior tetrafluoroborate ions. In contrast, the BF_4^- anion in the central pocket of the structure is tightly bound and no exchange occurs (see Figure 7.80).

The high resolution ESI mass spectrum of the interpenetrated cage solution showed a series of species with varying number of counter anions, which could be identified as $[\text{3BF}_4@\text{Pd}_4\text{L}^1_8+n\text{BF}_4]^{(5-n)+}$ ($n=0-2$) (see Figure 2.5a). The peak with the highest intensity found at $m/z = 907.7$ corresponds to the $[\text{3BF}_4@\text{Pd}_4\text{L}^1_8]^{5+}$ species. No species with less than three BF_4^- anions could be found in the HR-ESI-MS spectra, indicating the importance of the encapsulated counter anions.

2.3 Encapsulation of Anionic Guest Molecules

Similar to previously reported interpenetrated coordination cages with banana-shaped ligands^[42] based on dibenzosuberone^[75] and phenothiazine,^[79] the acridone based $[\text{3BF}_4@\text{Pd}_4\text{L}^1_8]$ coordination cage features three small inner voids, which are able to bind small anionic molecules. Originally, all three pockets are filled with tetrafluoroborate anions. Addition of two equivalents of halide anions, e.g. F^- , Cl^- , Br^- and I^- leads to the replacement of the loosely bound BF_4^- in the outer two voids. As a consequence, the host-guest complexes $[\text{2X}+\text{BF}_4@\text{Pd}_4\text{L}^1_8]$ ($\text{X} = \text{F}^-$, Cl^- , Br^- , I^-) are formed. The formation of this new species were confirmed with NMR spectroscopy and high-resolution mass spectrometry (see Chapter 7.3). The exchange of the encapsulated anion in the interpenetrated coordination cage follows an allosteric binding mechanism with a strong positive cooperativity. This conclusion could be drawn from the ^1H NMR titrations, where the addition of halide anions (as their tetrabutylammonium salts) to the $[\text{3BF}_4@\text{Pd}_4\text{L}^1_8]$ system, does not result in a gradual shifting of all signals. Instead, the intensity of signals corresponding to $[\text{3BF}_4@\text{Pd}_4\text{L}^1_8]$ are decreasing, while a set of new signals appear and rise in intensity with increasing amounts of halides. After the addition of 2 equivalents of halide only one set of signals were observed in the ^1H NMR spectrum, which were assigned to $[\text{2X}+\text{BF}_4@\text{Pd}_4\text{L}^1_8]$ ($\text{X} = \text{F}^-$, Cl^- , Br^- , I^-) (see Figure 2.6). No evidence of species with the composition $[\text{1X}+\text{2BF}_4@\text{Pd}_4\text{L}^1_8]$ ($\text{X} = \text{F}^-$, Cl^- , Br^- , I^-) could be found. The addition of halides results in a downfield shift of the ^1H NMR signals of the inward pointing protons H_g , H_f and H_e in the outer pockets (e.g. for Cl^- : $\Delta\delta = 1.63$ ppm for H_g , $\Delta\delta = 1.22$ ppm for H_f ; $\Delta\delta = 0.61$ ppm for H_e). Reason is the close proximity of these protons to the negatively charged halides, which as a monoatomic anion shows a larger charge density as the pentaatomic BF_4^- anion. In case of the addition of chloride anions, a very strong upfield shift of the backbone proton H_a , due to the proximity to neighboring ligands is observed ($\Delta\delta = 2.08$ ppm; Figure 2.6).

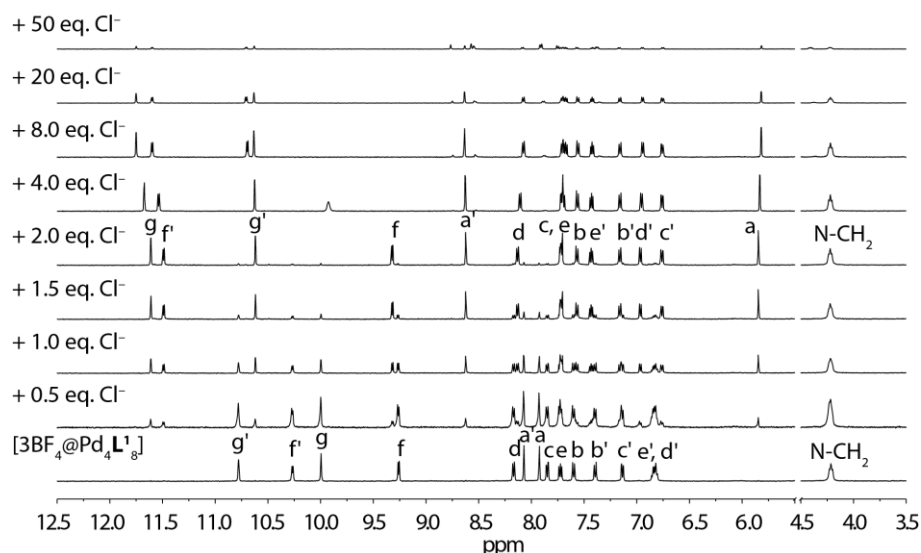


Figure 2.6 ^1H NMR titration (500 MHz, 298 K, CD_3CN) of $[\text{3BF}_4@\text{Pd}_4\text{L}^{18}]$ with NBu_4Cl . Upon addition of two equivalents of chloride ions; $[\text{3BF}_4@\text{Pd}_4\text{L}^{18}]$ transforms into $[\text{2Cl}@\text{Pd}_4\text{L}^{18}]$, indicated by strong downfield shifts of the protons pointing inside the outer two cavities. Further addition of halide results in a strong downfield shift of protons f, caused by the interaction of chloride anions with the periphery of the cage. Addition of further amounts of NBu_4Cl leads to a partial decomposition of the double cage.

Similar trends in shifting of the ^1H NMR signals occur for the other halides (F^- , Br^- and I^-) (see Chapter 7.3.2 for experimental details).

It was assumed, that the replacement of the tetrafluoroborate anions by halides result in drastic changes in the ^{19}F NMR spectrum. Indeed, the ^{19}F NMR spectrum of the bromide-filled cage $[\text{2Br}+\text{BF}_4@\text{Pd}_4\text{L}^{18}]$ at various temperatures shows the expected two signals; one corresponding to encapsulated BF_4^- in the central pocket of the interpenetrated cage ($\delta = -152.23$ ppm) and one for free BF_4^- in solution ($\delta = -151.70$ ppm; values for measurement at room temperature) (Figure 7.79). No signals corresponding to encapsulated tetrafluoroborate anion in the outer pocket of the supramolecular assembly were found. An exchange between the tightly bound BF_4^- in the cage and free BF_4^- in solution can be excluded, due to a ^{19}F EXSY NMR experiment (probing a millisecond time scale) (Figure 7.80). This result is in accordance with the previously reported interpenetrated coordination cages in our group.^[76] In contrast, only one signal at a chemical shift of $\delta = -151.00$ ppm was observed in the ^{19}F NMR spectrum of the chloride containing coordination cage at 298 K (Figure 7.78). Even decreasing the temperature to 273 K or 243 K shows only one signal in the ^{19}F NMR spectrum. The observed signal corresponds to free tetrafluoroborate in solution and therefore, a strong encapsulation of the non-coordinating counter anion in the central pocket of the coordination cage is unlikely. Nevertheless, quickly exchanging tetrafluoroborate anions between the central pocket of the coordination cage and the exterior solvent cannot be excluded. Due to this experimental observation, the chloride-filled coordination cage will be further abbreviated as $[\text{2Cl}@\text{Pd}_4\text{L}^{18}]$.

The presence of the halide-containing coordination cages were further verified *via* high-resolution ESI mass spectrometry. The spectrum of the chloride-filled cage $[\text{2Cl}@\text{Pd}_4\text{L}^{18}]$ shows a series of species $[\text{2Cl}@\text{Pd}_4\text{L}^{18}+n\text{BF}_4^-]^{(6-n)+}$ ($n = 0-3$) which contain a variable number of tetrafluoroborate

anions (Figure 2.5b). The molecule peak at $m/z = 727.7$ could be assigned to the hexacationic $[2\text{Cl}@Pd_4L^1_8]^{6+}$ cage without any tetrafluoroborate counter anions. The HR-ESI-MS spectrum of the bromide-filled coordination cage shows a series of species with a varying number of counter anions, which were identified as $[2\text{Br}+\text{BF}_4@Pd_4L^1_8+n\text{BF}_4^-]^{(5-n)+}$ ($n = 0-3$). The molecule peak is the pentacationic $[2\text{Br}+\text{BF}_4@Pd_4L^1_8]^{5+}$ species at $m/z = 904.8$ (see Figure 7.17). A hexacationic species corresponding to $[2\text{Br}@Pd_4L^1_8]^{6+}$ without any tetrafluoroborate counter anion in the central pocket was observed in only small amounts. This indicates a stronger binding affinity of the BF_4^- anion towards the bromide- in comparison to the chloride-containing cage. The observation in the HR-MS spectra match the results from the ^{19}F NMR experiments.

Furthermore, cyclic voltammetry (CV) measurements show that the redox potential of the halides (Cl^- and Br^-) are anodically shifted upon encapsulation in the outer pockets of the interpenetrated coordination cage $[Pd_4L^1_8]$ (see Figure 7.89). This suggest that the cationic coordination cage disfavors the removal of one electron from the halides.

Addition of larger anions e.g. hexafluorophosphate (PF_6^-) or perrhenate (ReO_4^-) to the interpenetrated coordination cage $[3\text{BF}_4@Pd_4L^1_8]$ does not result in any changes in the ^1H NMR spectrum (see Figure 7.19 and Figure 7.20). Hence, an encapsulation of these anions does not occur. Only the smaller nitrate (NO_3^-) anion is incorporated inside the coordination cage (see Figure 7.21). This observation lead to the conclusion, that the size of the encapsulated anion is crucial for the uptake inside the outer pockets of the coordination cage. Smaller anions e.g. F^- , Cl^- , Br^- , I^- , NO_3^- are incorporated in the cage assembly, while bigger anions do not interact.

2.4 X-ray Structure Analysis

Single crystals of $[3\text{BF}_4@Pd_4L^1_8]$ suitable for X-ray diffraction were obtained *via* slow vapor diffusion of benzene into an acetonitrile solution of the interpenetrated cage. The supramolecular assembly crystallizes in the tetragonal space group $P4/n$ with unit cell dimension of $a = b = 22.065(4)$ Å and $c = 33.491(6)$ Å. The structure consists of four square planar coordinated Pd(II) cations aligned in one axis and eight banana-shaped ligands L^1 . The interpenetrated double cage structure is composed of two monomeric cages with the formula $[Pd_2L^1_4]$, which are quadruply interpenetrated to form the thermodynamically stable $[3\text{BF}_4@Pd_4L^1_8]$ cage. Looking at the topology of the assembly, the $[3\text{BF}_4@Pd_4L^1_8]$ cage belongs to the class of “catenanes” (see Chapter 1.1 and Figure 1.2), which are defined as “a molecules which contain two or more intertwined rings.”^[15] The structure features three internal pockets, which are all filled with one tetrafluoroborate anion. Further BF_4^- anions are located at the outside of the interpenetrated cage in close proximity to the palladium(II) cations. The distance between the palladium cations in the outer voids was measured to be 8.24 and 8.26 Å and the Pd–Pd distance in the inner cavity was determined to be 8.44 Å (Figure 2.7a). These values are in accordance with the previously reported dibenzosuberone and phenothiazine containing interpenetrated cages.^[75,78]

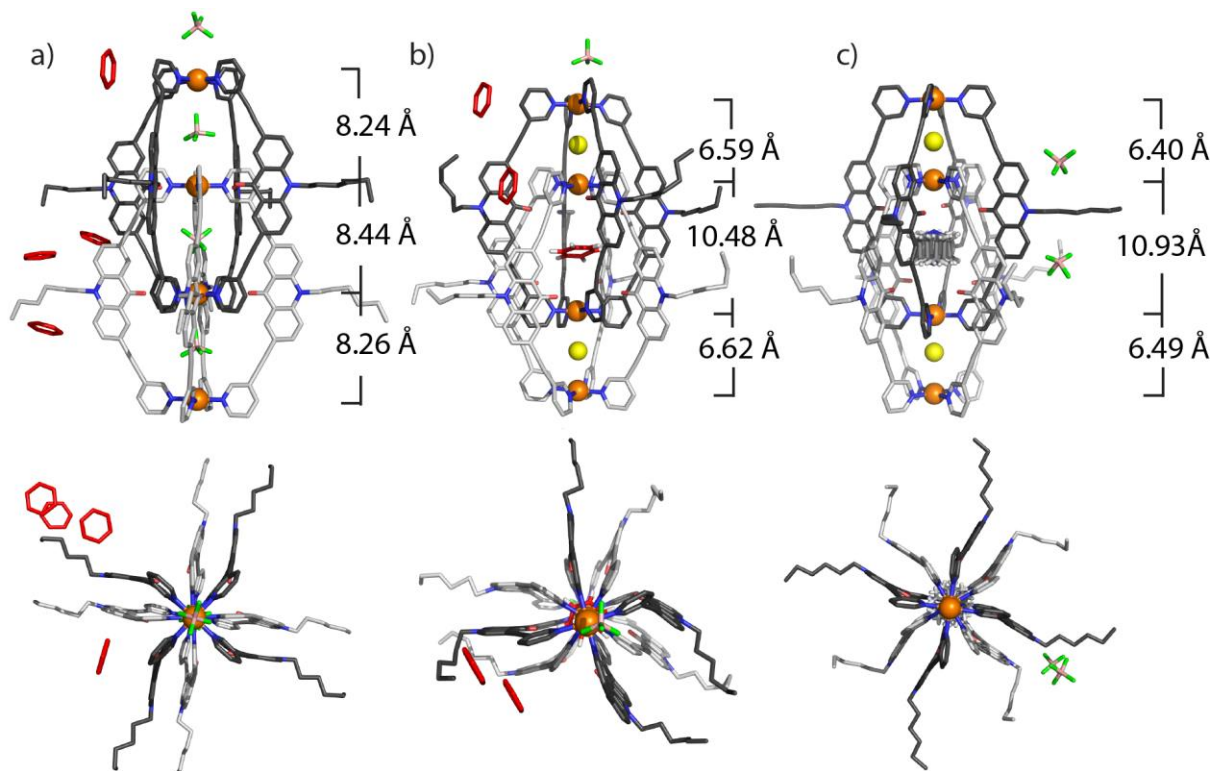


Figure 2.7 X-ray crystal structures of cage (a) $[3\text{BF}_4@Pd_4L^1_8]$, (b) $[2\text{Cl}+\text{benzene}@Pd_4L^1_8]$ and (c) $[2\text{Cl}+\text{DABCO}@Pd_4L^1_8]$ with disordered DABCO guest. *Color scheme*: C: light/dark gray; N: blue; O: red; Cl: yellow; F: green; B: salmon; Pd: orange. Hydrogen atoms, some of the solvent molecules and disordered components have been removed for clarity. Benzene molecules were highlighted in red.

Slow vapor diffusion of benzene into an acetonitrile solution of the chloride-incorporated coordination cage $[2\text{Cl}@Pd_4L^1_8]$ gave suitable crystals for X-ray determination. The halide containing coordination cage crystallized in the monoclinic space group $P2_1/n$, with cell dimensions of $a = b = 22.065(4)$ Å and $c = 33.491(5)$ Å. Due to the smaller size of the chloride anion in comparison to the larger tetrafluoroborate anion, the overall size of the coordination cage is decreased from 24.94 Å for $[3\text{BF}_4@Pd_4L^1_8]$ to 23.69 Å in the $[2\text{Cl}@Pd_4L^1_8]$ cage (distance measured between the outer two palladium cations). The Pd–Pd distance in the outer cavities of the interpenetrated double cage decreases to 6.59 Å and 6.62 Å. In contrast, the central cavity enlarges, which is indicated by the increase of the Pd–Pd distance from 8.44 Å to 10.48 Å (see Figure 2.7b). Surprisingly, benzene molecules were not only found at the exterior of the cage, but also one benzene molecule is encapsulated in the central pocket of the interpenetrated coordination cage, thereby forming the host-guest complex $[2\text{Cl}+\text{benzene}@Pd_4L^1_8]$. Stabilizing cation- π interaction between the cationic coordination cage and the neutral guest molecule can be excluded, because the closest distance between one of the central palladium cations and the benzene ring center was measured to be 4.64 Å (and 5.02 Å to the center of the ring). Furthermore, the closest distance from the benzene hydrogen atoms to the next carbonyl oxygen is 2.68 Å and all pyridine hydrogen atoms are more than 3.0 Å away. Consequently, substantial CH- π or hydrogen bond interaction are unlikely to contribute to the stabilization of the benzene molecule. Based on the position of the benzene molecule in the interior of the coordination cage, it is assumed, that the main interaction for stabilizing the neutral

guest molecule in the cationic coordination cage are dispersion interaction, with further contribution of solvophobic effects.^[89]

A closer look at the crystal structure of $[2\text{Cl}+\text{benzene}@\text{Pd}_4\text{L}^1_8]$ along the Pd_4 -axis shows a quite asymmetric arrangement of the eight ligands around the palladium centers. It therefore can be assumed, that the acridone-based ligands are to some degree flexible. This observation is in contrast with the previously reported interpenetrated cage structures based on dibenzosuberone and phenothiazine. Those ligands have twisted or bent backbones, which result in more rigidly interlocked cage structures. The conformational flexibility of the acridone-derived ligand might be an important requirement of the interpenetrated coordination cage to enable the uptake of the relatively large neutral guest molecule in its central cavity (Figure 2.7b). On the basis of the unique guest-uptake behavior of the interpenetrated coordination cage, a series of neutral guest molecules was tested for their capability to be encapsulated in the chloride-containing coordination cage $[2\text{Cl}@\text{Pd}_4\text{L}^1_8]$ (see Chapter 2.5 about *Neutral Guest Uptake* for a more detailed description).

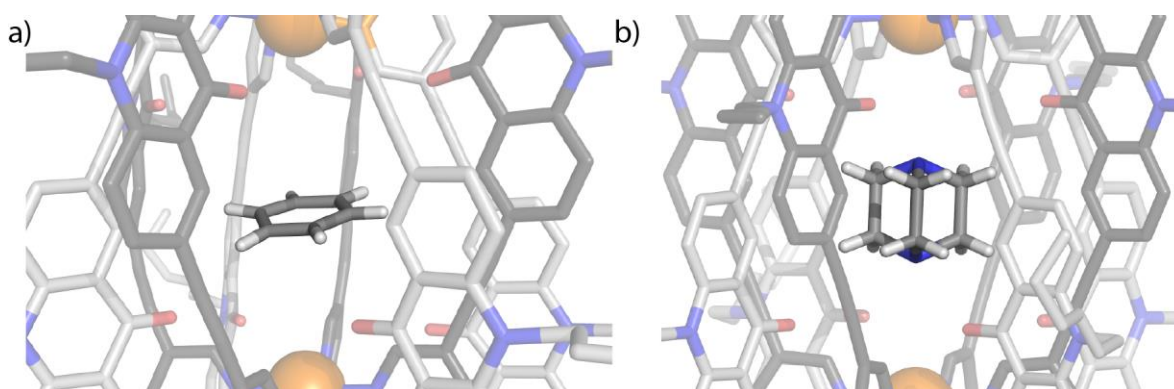


Figure 2.8 Central pockets of the X-ray structure of the host-guest complexes $[2\text{Cl}+\text{NG}@\text{Pd}_4\text{L}^1_8]$ (NG = neutral guest) with a) benzene and b) one selected orientation of DABCO. While the benzene molecules is oriented perpendicular to the Pd_4 axis, the DABCO molecules stands upright in the central pocket of the interpenetrated coordination cage. Reproduced from reference ^[90] with permission from The Royal Society of Chemistry.

Further crystals suitable for X-ray structure determination were obtained for the host-guest complex $[2\text{Cl}+\text{DABCO}@\text{Pd}_4\text{L}^1_8]$ from slow vapor diffusion of ethanol into an acetonitrile solution of the complex (see Figure 2.7c) (DABCO = 1,4-Diazabicyclo[2.2.2]octane). The supramolecular assembly crystallizes in the tetragonal space group $P4/ncc$ with unit cell dimension of $a = b = 22.064(3)$ Å and $c = 62.075(1)$ Å. The structure has a fourfold crystallographic symmetry axis along the Pd_4 – axis, which complicated the modeling of the axially disordered D_{3h} symmetric DABCO molecule. Nevertheless, refinement showed clearly, that the DABCO molecule stands upright inside the central cavity with its nitrogen-axis aligned with the Pd_4 -axis of the interpenetrated coordination cage (see Figure 2.7c for visualization of the disordered DABCO molecule). Comparison with the benzene-containing complex, the binding mode of these two neutral guest are quite different. The benzene molecular plane is oriented perpendicular to the Pd_4 -axis, exposing its π -surface towards the palladium(II) cations (see Figure 2.8a), while DABCO stands upright in the central pocket (see Figure 2.8b). A close contact of 4.13 Å between the positively-charged palladium cation and the nitrogen atom of the DABCO molecule indicates an interaction of the free lone pair (from DABCO)

with the Pd(II) cation from the interpenetrated coordination cage. Furthermore, close contacts of ~ 2.5 Å between the hydrogen atoms of the encapsulated neutral guest molecule and the ligands of the coordination cage were found in the crystal structure. One can assume that both of these interactions contribute to the stability of the host-guest system.

The distances between the palladium cations in the outer voids of $[2\text{Cl}+\text{DABCO}@\text{Pd}_4\text{L}^1_8]$ were measured to be 6.40 Å and 6.49 Å and the Pd-Pd distance in the central cavity is 10.93 Å (Figure 2.7c, top). These values are in a similar range compared to the benzene-containing coordination cage. Nevertheless, it is noteworthy that the central pocket of the DABCO-containing cage (Pd-Pd: 10.93 Å) is larger compared to the host-guest complex incorporating benzene (Pd-Pd: 10.48 Å) (see Figure 2.7b and c), while the outer pockets are smaller. This change in size might be due to the overall size of the encapsulated neutral guest. While benzene is a rather small, plate-like neutral molecule ($V_{\text{benzene}} = 99.0$ Å³), DABCO has a larger and three-dimensional shape ($V_{\text{DABCO}} = 126.4$ Å³). Due to the observed trends, it seems that the interpenetrated coordination cage is able to adapt to a certain extent towards the size and shape of the neutral guest molecule.

2.5 Neutral Guest Uptake

After the discovery of one encapsulated benzene molecule inside the central pocket of the interpenetrated coordination cage with X-ray structure analysis (Chapter 2.4 and Figure 2.9), further experiments were conducted to proof the formation of this unexpected host-guest complex in solution. Addition of an excess of benzene to an acetonitrile solution of $[2\text{Cl}@\text{Pd}_4\text{L}^1_8]$ leads to strong shifting of significant signals in the ¹H NMR spectrum (see Figure 2.10). Specially, protons pointing towards the inside of the central cavity (H_{G} and H_{A}) were affected by the encapsulation of the neutral guest molecule. While proton H_{G} is shifted upfield by $\Delta\delta = 0.68$ ppm, proton H_{A} is shifted downfield by $\Delta\delta = 0.33$ ppm. In addition, a new signal at $\delta = 10.12$ ppm was observed, which could be assigned to the encapsulated benzene molecule. It is noteworthy, that the signal for the incorporated guest molecule is shifted downfield by $\Delta\delta = 2.8$ ppm in comparison to the free benzene ($\delta = 7.37$ ppm) (Figure 2.4c). In addition, 2D NOESY NMR spectroscopy showed contacts between the encapsulated benzene molecule ($\delta = 10.12$ ppm) and the inward pointing cage protons H_{G} and H_{A} (Figure 7.83).

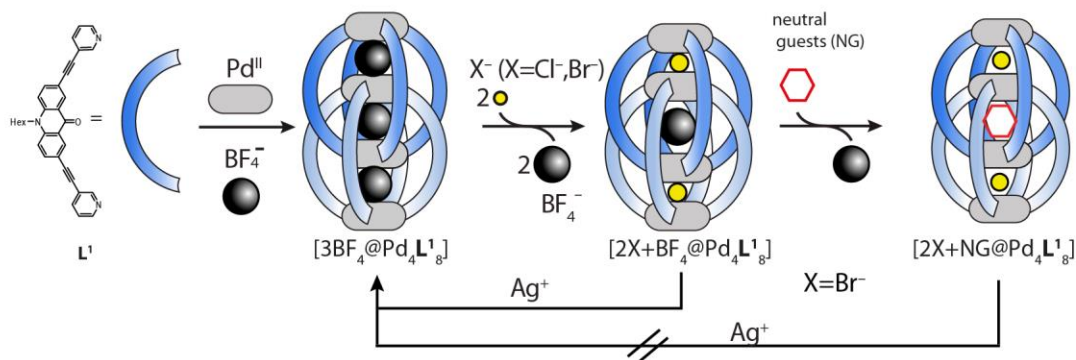


Figure 2.9 Schematic representation of formation of the interpenetrated coordination cage [3BF₄@Pd₄L₁₈]. Addition of halide anions triggers the exchange of neutral guest molecules inside the central pocket of the structure.

The high resolution ESI mass spectrum shows species, which could be assigned to the host guest complex [2Cl+C₆H₆@Pd₄L₁₈+nBF₄]⁽⁶⁻ⁿ⁾⁺ (*n* = 0–2) with a varying number of counter ions (Figure 2.5 c). Besides the expected host guest complex [2Cl+C₆H₆@Pd₄L₁₈], the mass spectrum also shows signals of the parent [2Cl@Pd₄L₁₈] cage (highlighted with * in Figure 2.5), which might be due to a relatively low binding constant of the neutral guest molecule in the interpenetrated coordination cage.

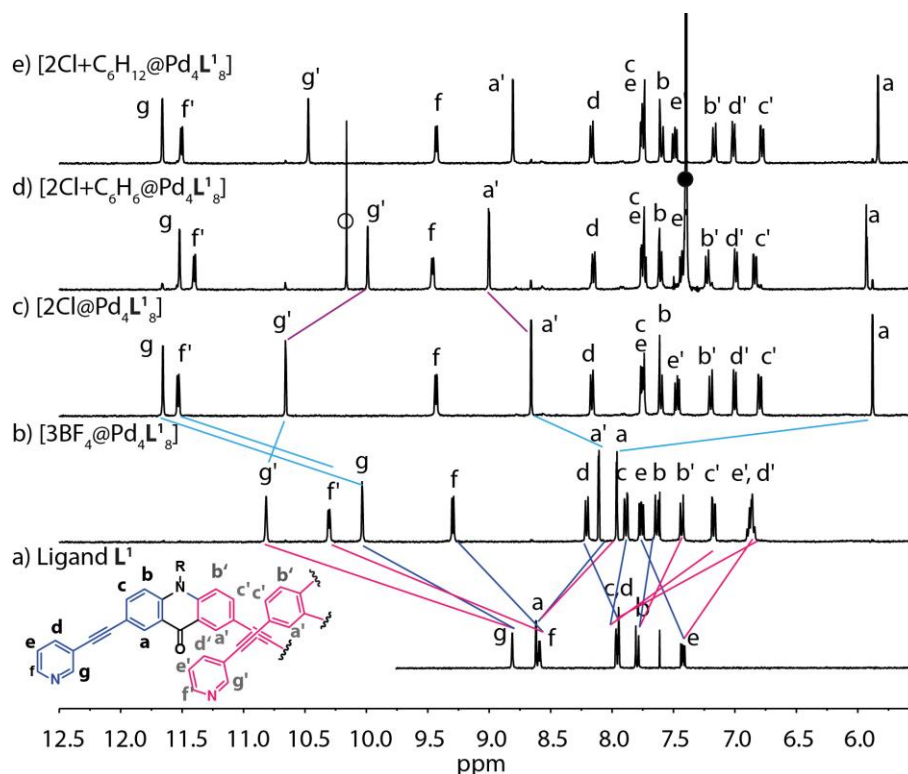


Figure 2.10 ¹H NMR spectra of a) Ligand **L**¹, b) double cage [3BF₄@Pd₄L₁₈] (c) [2Cl@Pd₄L₁₈] which forms upon addition of 2.0 eq. of *n*-NBu₄Cl, (d) [2Cl+C₆H₆@Pd₄L₁₈] and e) [2Cl+C₆H₁₂@Pd₄L₁₈] which form after addition of 20 eq. of neutral guest (benzene or cyclohexane; 400 MHz, 298 K, CD₃CN). Filled circle: free benzene, empty circle: encapsulated benzene (the cyclohexane signals are out of the depicted range, see Figure 7.84). Reprinted with permission from reference [87]. Copyright © 2015 American Chemical Society.

Further studies focused on the exploration of the ability of the halide-containing cages for the encapsulation of other neutral guest molecules. Neutral guest uptake inside the central pocket of the

bromide or fluoride-filled coordination cages $[2\text{Br}+\text{BF}_4@Pd_4L^1_8]$ and $[2F+\text{BF}_4@Pd_4L^1_8]$ was observed and studied for a few guest molecules (e.g. benzene, and norbornadiene) (see Chapter 7.3.3 for experimental results). However, formation of unidentified side products complicated the analysis of the ^1H NMR spectra and therefore the investigation of neutral guest uptake was mainly focused on the chloride-containing cage $[2\text{Cl}@Pd_4L^1_8]$. In total 64 different neutral guest molecules were tested for their uptake inside the supramolecular assembly. Of these, 36 were encapsulated while 22 did not show any interaction with the $[2\text{Cl}@Pd_4L^1_8]$ cage (Figure 2.11 and Chapter 7.3.3). Furthermore, six of the tested neutral guests lead to the disassembly of the coordination cage and the release of free ligand L^1 (Figure 2.11 in blue). Reason for the decomposition of the supramolecular structure are a higher affinity for complex formation with the Pd(II) cation or the presence of traces of chloride anions (e.g. acetyl chloride).

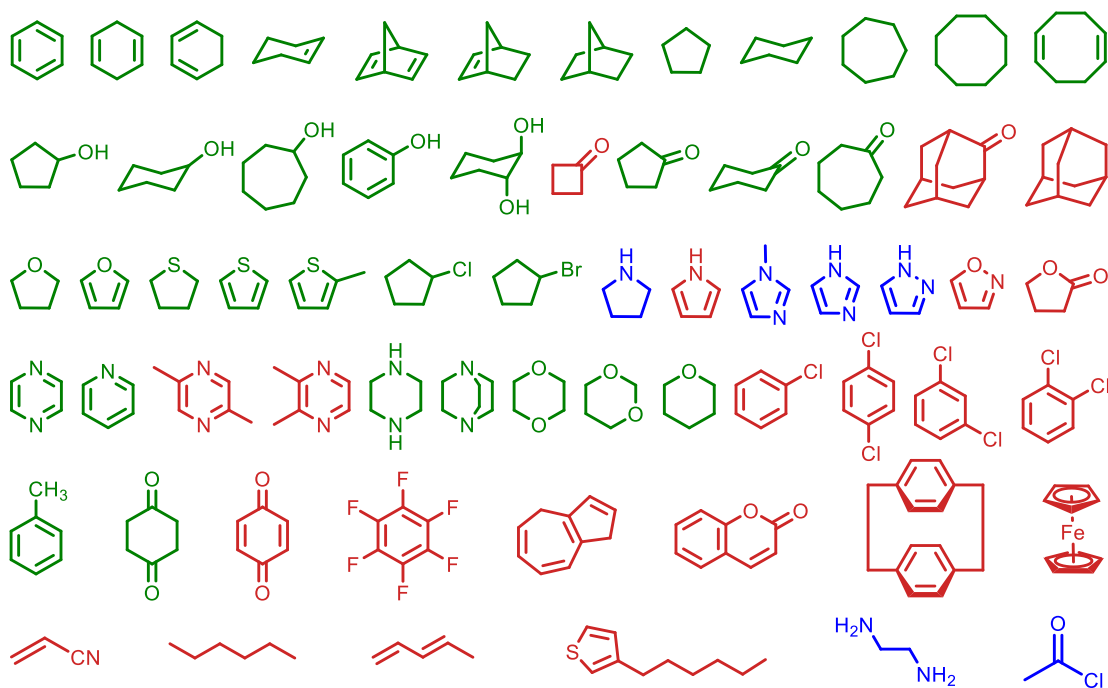


Figure 2.11 Overview of tested neutral guest for encapsulation inside the chloride-containing coordination cages $[2\text{Cl}@Pd_4L^1_8]$. *Color Scheme:* **green:** encapsulation, **red:** no interaction between neutral guest and $[2\text{Cl}@Pd_4L^1_8]$ host, **blue:** disassembly of coordination cage under release of free ligand L^1 .

Interestingly, addition of neutral guest molecules to the parental cage $[3\text{BF}_4@Pd_4L^1_8]$ does not lead to the formation of a host guest complex with a neutral guest (Figure 7.26 and Figure 2.7). Thus, the addition of halide anions seems to activate the interpenetrated coordination cage for binding neutral guest molecules in its central pocket.

In further studies, the binding constants of the encapsulated neutral guest molecules inside the central pocket of the chloride-containing interpenetrated coordination cage were determined. For this reason, an excess (~2-100 eq.) of the dissolved neutral guest compound (in CD_3CN) was added to the solution of $[2\text{Cl}@Pd_4L^1_8]$ in deuterated acetonitrile (0.3 mM). The sample was stored at 23 °C (in an air-conditioned room) and ^1H NMR spectra were recorded after several days until

full equilibration of the reaction mixture was reached (3 days to up to 2 month) and no further spectral change was observed.

Table 2.1 Experimental and computed binding free enthalpies, volumes and packing coefficients for all tested guests. a) Volume of the neutral guest was gained from Spartan via EDF2/6-31G* computation b) The packing coefficient (PC) was calculated as the quotient of $V_{\text{guest}}/V_{\text{cavity}} * 100$. The volume of the cavity was calculated using VOIDOO (details see experimental section 7.3.7). (This table does not include all neutral guest, which are encapsulated inside the coordination cage. Further experiments need to be performed to give reliable results for the missing molecules). Reproduced from Reference [90] with permission from The Royal Society of Chemistry.

Guest	M/g-mol	V/A ^{3a}	PC/% ^b	$\Delta G_{\text{exp}}/$ kJ·mol ⁻¹	$\Delta G_{\text{theo}}/$ kJ·mol ⁻¹
1,3-dioxane	88.1	93.2	47.2	- 12.3	
1,3 cyclohexadiene	80.13	104.2	54.3	- 20.2	
1,4-cyclohexadiene	80.13	104.0	54.3	- 19.4	
1,4-cyclohexanedione	117.4	117.5	58.4	- 8.8	
1,4-dioxan	88.1	93.8	47.3	- 25.4	
2-methylthiophene	98.2	104.9	52.2	- 10.8	
benzene	78.1	99.0	49.5	- 17.4	- 34.9
bromocyclopentane	149.0	113.6	56.8	- 11.5	
chlorocyclopentane	104.6	109.2	54.2	- 12.6	
cycloheptane	98.2	129.5	64.5	- 19.3	
cycloheptanone	112.2	132.2	65.8	- 13.4	
cyclohexane	80.7	111.8	55.9	- 20.2	- 18.9
cyclohexanone	98.2	114.5	57.1	- 13.4	
cyclooctane	112.2	147.2	73.6	- 15.6	
cyclopentane	70.1	95.2	47.5	- 12.8	- 19.5
cyclopentanone	84.1	97.8	48.7	- 10.5	
DABCO	112.2	126.4	63.8	- 27.1	- 31.0
furan	68.1	77.7	38.9	- 6.1	- 1.4
norbornadiene	92.1	113.2	56.2	- 20.2	- 28.4
norbornane	96.2	120.1	60.1	- 18.9	
norbornene	94.2	116.3	58.2	- 19.2	
phenol	94.1	106.1	53.0	- 12.8	- 13.1
piperazine	86.1	100.1	50.7	- 22.8	
pyrazine	80.1	86.3	43.5	- 21.8	
pyridine	79.1	92.6	46.5	- 12.3	
tetrahydropyran	86.1	102.8	51.6	- 17.2	
tetrahydrofuran	72.1	86.0	43.1	- 14.3	
tetrahydrothiophene	88.2	95.6	47.6	- 16.9	
thiophene	84.1	86.5	43.1	- 13.4	
toluene	92.1	117.2	58.4	- 7.5	

The concentrations of the individual species could be determined by relative integration of characteristic ¹H NMR signals (see appendix section 7.3.3) and thermodynamic constants were determined by applying the law of mass action with the concentrations of free host and host-guest complexes at known concentrations, which were derived from the ¹H NMR spectra by signal integration. From this, binding free enthalpies were calculated using equation 2.1.

$$\Delta G^{exp} = -RT \ln K \quad (2.1)$$

The experimental binding free enthalpies range from - 6.1 kJ·mol⁻¹ for the weakest (furan) to - 27.1 kJ·mol⁻¹ for the strongest binding guest (DABCO) (see Table 2.1 for an overview). Trying to understand and visualize this range in binding affinity, the binding free enthalpies were plotted

against the volume of the neutral guests (Figure 2.12). The volume of the guest was calculated as the CPK volume of EDF2/6-31G* optimized molecular models using the software SPARTAN.^[91] In addition the packing coefficient (PC) of the neutral guest were determined as quotient of the CPK volumes (of the neutral guests) and the volume of the empty pockets as calculated using the software VOIDOO^[92] (Chapter 7.3.7 for further details).

Analyzing this plot and the results from the NMR experiments helped in understanding the binding affinity. Oversized (ferrocene, azulene, coumarin, [2.2]paracyclophane) and non-cyclic neutral guest (hexane, 1,3-butadiene, acrylonitrile) are not encapsulated in the central pocket of [2Cl@Pd₄L₃] cage. Smaller aromatic 5-rings (furan, thiophene) with packing coefficients between 39 and 48 % and more voluminous neutral guest molecules with one substituent such as a methyl or hydroxyl group (e.g. toluene, 2-methoxythiophene) showed weak binding. In contrast, molecules carrying two substituents, e.g. dichlorobenzenes (*o*, *m*, *p*) or dimethylpyrazine (2,5 or 2,6-substituted) do not form host-guest complexes. Cyclic six-membered rings such as benzene, cyclohexadiene (1,3 and 1,4-substituted), cyclohexane and bridged 6-rings e.g. norbornadiene and its relative bind rather strongly with free energies of binding of around $\Delta G = -19 \text{ kJ}\cdot\text{mol}^{-1}$. This shows that a three dimensional extension of the guest structure is not detrimental to the encapsulation process. In general, the PC does not exceed 74 %, which is the PC for the largest encapsulated guest molecule: cyclooctane. As an example, adamantane with a PC of 81 % is not incorporated in the supramolecular cage.

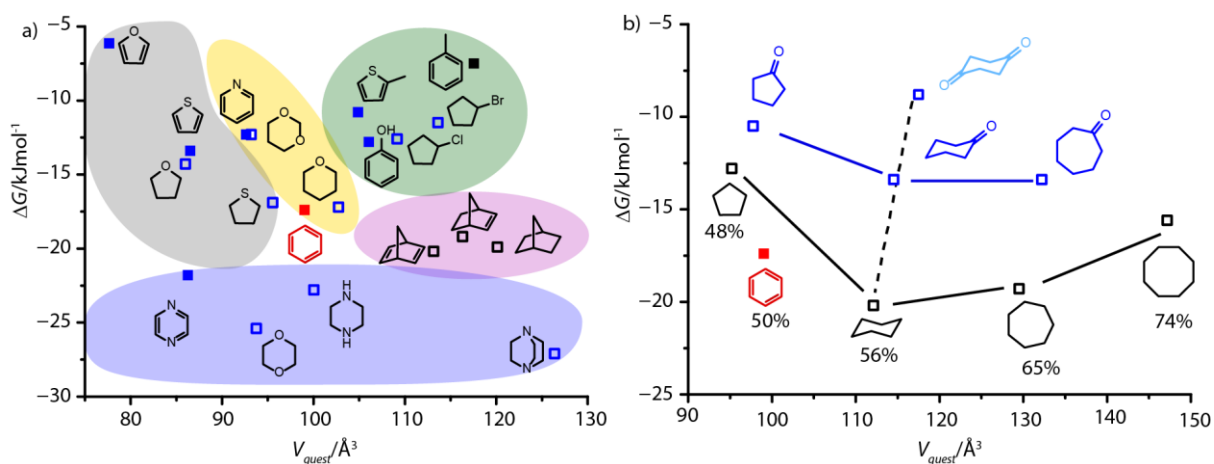


Figure 2.12 Binding free enthalpies over guest volume for a) various guest families with different ring sizes, 3D structures and heteroatom content and b) selected series of cyclic alkanes and alkanones (packing coefficients are shown for the alkanes). Reprinted with permission from reference^[90] Copyright © 2017 The Royal Society of Chemistry.

The strongest binding with free enthalpies below $\Delta G = -21 \text{ kJ}\cdot\text{mol}^{-1}$ are shown by molecules, which possess two heteroatoms in opposite position (highlighted in blue in Figure 2.12a). These molecules are DABCO, 1,4-pyrazine, 1,4-piperazine and 1,4-dioxane. The position of the heteroatoms is crucial for the high binding affinity, which indicates a comparison between 1,4-dioxane and 1,3-dioxane. While the 1,4-isomer binds with $\Delta G = -26.6 \text{ kJ}\cdot\text{mol}^{-1}$ the free enthalpy for 1,3-dioxane is decreased to $\Delta G = -12.6 \text{ kJ}\cdot\text{mol}^{-1}$ (difference of $\Delta\Delta G = 14 \text{ kJ}\cdot\text{mol}^{-1}$). Furthermore, similar six

membered rings containing only one heteroatom show lower binding enthalpies than their analogues carrying two heteroatoms. For comparison; while 1,4-pyrazine binds with $\Delta G = -21.8 \text{ kJ}\cdot\text{mol}^{-1}$ the free enthalpy for pyridine is decreased to $\Delta G = -12.3 \text{ kJ}\cdot\text{mol}^{-1}$ (difference of $\Delta\Delta G = 9.5 \text{ kJ}\cdot\text{mol}^{-1}$).

Reason for the significant differences in free binding energies are due to the position and the number of the heteroatoms. High binding affinities of molecules with two heteroatoms in 1,4-position might result from an interaction of the free lone pair of the nitrogen or oxygen atom and the two cationic palladium(II) centers of the coordination cage. This assumption is confirmed by the X-ray crystal structure of the DACBO-containing cage structure $[\text{DACBO}+2\text{Cl}@Pd_4L^1_8]$ as elaborated in Chapter 2.4. The neutral guest molecule is arranged upright inside the central cavity, with the nitrogen atoms pointing towards the Pd(II) cations (Figure 2.7).

Comparison of binding affinities in a series of cycloalkanes (C_5-C_8), cyclic ketones (C_5-C_7)^[93] and 1,4-cyclohexanedione (Figure 2.12b) illustrated further trends. One important factor for the encapsulation process is the size of the ring. Small 5-membered rings bind weaker than their 6-ring analogue, while further expansion of the ring size results in decrease of binding affinity. Surprisingly, the voluminous cyclooctane, with a PC of approximately 74 % was found to be encapsulated in the coordination cage. This indicated a structural flexibility, which allows the guest to adapt a favorable conformation inside the supramolecular assembly. Furthermore, the presence of substituents has a tremendous effect on the binding affinity. While cyclohexane (PC = 54 %) binds rather strong with $\Delta G = -20.2 \text{ kJ}\cdot\text{mol}^{-1}$, the binding affinity of 1,4-cyclohexanedione (PC = 58 %) is decreased to $\Delta G = -8.6 \text{ kJ}\cdot\text{mol}^{-1}$, even though the PC only changes by 4 % (dotted line in Figure 2.12b).

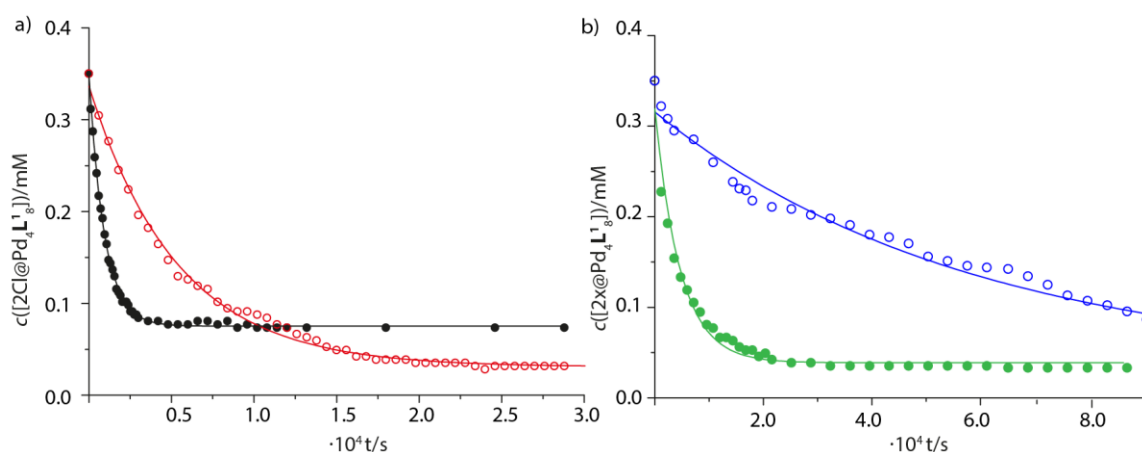


Figure 2.13 Uptake kinetics of (a) $[\text{2Cl}@Pd_4L^1_8]$ with benzene (black) and cyclohexane (red); (b) addition of norbornadiene to $[\text{2Cl}@Pd_4L^1_8]$ (green) and $[\text{2Br}+\text{BF}_4@Pd_4L^1_8]$ (blue). Reprinted with permission from reference ^[87] Copyright © 2015 American Chemical Society.

Subsequently, the uptake kinetics of different neutral guests into the halide-containing cages were investigated. Hence, a solution of the neutral guest (~10 eq.) was added to a solution of the coordination cage in deuterated acetonitrile. The encapsulation process was monitored by arrayed ¹H NMR experiment at 298 K and the rate constants were determined with the help of the software *MestReNova*.^[94] The uptake of benzene inside the central cavity of the coordination cage ($k = (1.07 \pm 0.02) \times 10^{-3} \text{ s}^{-1}$) is significantly faster (6x) than the incorporation of cyclohexane

($k = (1.87 \pm 0.04) \times 10^{-4} \text{ s}^{-1}$) (Figure 2.13a). The reason for this observation is the size difference of these two guests. The larger, more flexible cyclohexane with a molecular volume of 111.8 \AA^3 is sterically hindered and therefore shows a slower uptake than the smaller rigid benzene molecule with $V = 99.0 \text{ \AA}^3$ (Table 2.1). Interestingly, the binding affinity of cyclohexane ($\Delta G = -20.2 \text{ kJ/mol}$) is higher than the binding affinity of benzene ($\Delta G = -17.4 \text{ kJ/mol}$) towards the chloride-containing coordination cage $[2\text{Cl}@Pd_4L^1_8]$. Since cyclohexane is an unfunctionalized alkane and benzene an aromatic compound, it is assumed that dispersion interactions play a crucial role in the stabilization of the neutral guest inside the interpenetrated coordination cage. (For a detailed explanation on determination of kinetic constants from NMR experiments see experimental section Chapter 7.3.3)

Furthermore, a competition experiment was performed to verify the difference in kinetic uptake and thermodynamic stability of benzene and cyclohexane towards the chloride-containing coordination cage. Hence, to a solution of the $[2\text{Cl}@Pd_4L^1_8]$ in deuterated acetonitrile, a mixture of two guest molecules was added (benzene and cyclohexane; 20 eq. each) and the progress of the uptake was monitored *via* arrayed ^1H NMR spectroscopy. After 5 min benzene was immediately encapsulated inside the coordination cage, with only trace amount of parental $[2\text{Cl}@Pd_4L^1_8]$ cage remaining in the mixture. Over time, the intensity of $[\text{benzene}+2\text{Cl}@Pd_4L^1_8]$ decreased (blue highlighted), while signals of $[\text{cyclohexane}+2\text{Cl}@Pd_4L^1_8]$ increased (highlighted in red in Figure 2.14). This experiment showed, that weaker binding guests can be replaced by stronger (slowly) binding neutral molecules.

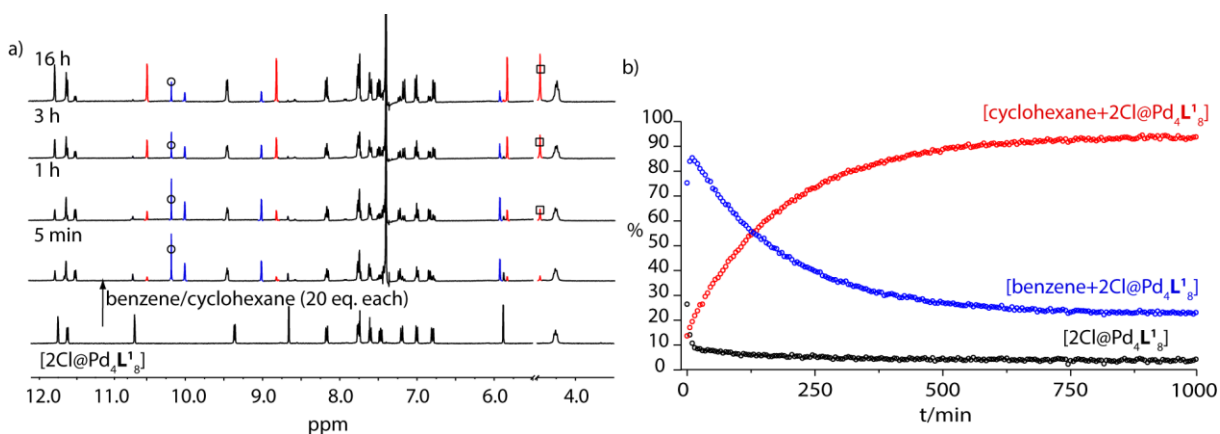


Figure 2.14 a) ^1H NMR competition experiment (400 MHz, 298 K, CD_3CN) of cyclohexane and benzene (each 20 equivalent) into the $[2\text{Cl}@Pd_4L^1_8]$ cage, b) kinetic plot of the competition experiment. *Color Scheme:* black: $[2\text{Cl}@Pd_4L^1_8]$, blue: $[\text{benzene}+2\text{Cl}@Pd_4L^1_8]$ and red: $[\text{cyclohexane}+2\text{Cl}@Pd_4L^1_8]$. Reproduced from Reference [90] with permission from The Royal Society of Chemistry.

Further studies focused on the uptake of the same neutral guest in different halide-filled cages. It was chosen to compare the encapsulation of norbornadiene in $[2\text{Cl}@Pd_4L^1_8]$ and $[2\text{Br}+\text{BF}_4@Pd_4L^1_8]$ (Figure 2.13b). Norbornadiene is incorporated with a rate constant of $k = (2.15 \pm 0.04) \times 10^{-4} \text{ s}^{-1}$ in the chloride-filled cage. In contrast, the uptake in the bromide-containing cage is 12 times slower with $k = (1.73 \pm 0.14) \times 10^{-5} \text{ s}^{-1}$. The reason for this different behavior is the fact that the central cavity of the chloride-containing interpenetrated cage is larger than of the bromide-containing cage, due to a smaller ionic radius of the chloride anion compared to bromide.

2.6 Guest Release

In addition, the relative binding affinity of the halide anions in the outer voids of the interpenetrated coordination cages before and after encapsulation of neutral guest were examined by silver(I) back-titrations.^[76] Addition of two equivalents of AgBF_4 to $[\text{2Br}+\text{BF}_4@\text{Pd}_4\text{L}^1_8]$ resulted in the immediate formation of $[\text{3BF}_4@\text{Pd}_4\text{L}^1_8]$ (Figure 2.15a). In contrast, no regeneration of $[\text{3BF}_4@\text{Pd}_4\text{L}^1_8]$, was observed after titrating silver(I)-tetrafluoroborate to $[\text{2Cl}@\text{Pd}_4\text{L}^1_8]$. Even after the addition of 50 equivalents of AgBF_4 and subsequent heating to 70 °C for 24 h, no change in the ^1H NMR spectrum could be observed. This shows that the interpenetrated coordination cage has an enormous binding affinity for chloride anions. In contrast, the encapsulation of neutral guest molecules inside the central void of the coordination cage changes the behavior of the bromide-containing cage. The addition of silver(I) cations did not lead to an immediate regeneration of the $[\text{3BF}_4@\text{Pd}_4\text{L}^1_8]$ cage. Instead, regeneration of the parental cage could be obtained after subsequent heating the sample to 70 °C for 24 h or leaving the sample at room temperature for a longer period of time (several days). To demonstrate this effect, silver(I) ions were added to a 1:1 mixture of $[\text{2Br}+\text{BF}_4@\text{Pd}_4\text{L}^1_8]$ and $[\text{2Br}+\text{norbornadiene}@\text{Pd}_4\text{L}^1_8]$ (Figure 2.15c). Immediately, after addition of two equivalents of the silver(I) salt, the bromide-containing cage transforms into $[\text{3BF}_4@\text{Pd}_4\text{L}^1_8]$, while the host-guest complex incorporating norbornadiene remains (marked in green in Figure 2.15c). After heating the sample to 70 °C overnight, only the parental tetrafluoroborate-containing coordination cage is observed in the ^1H NMR spectra, while signals from the $[\text{2Br}+\text{norbornadiene}@\text{Pd}_4\text{L}^1_8]$ host-guest-complex disappeared. This experiment indicates that the encapsulated neutral-guest in the central cavity kinetically hinders the removal of the halide anions in the outer voids of the coordination cages.

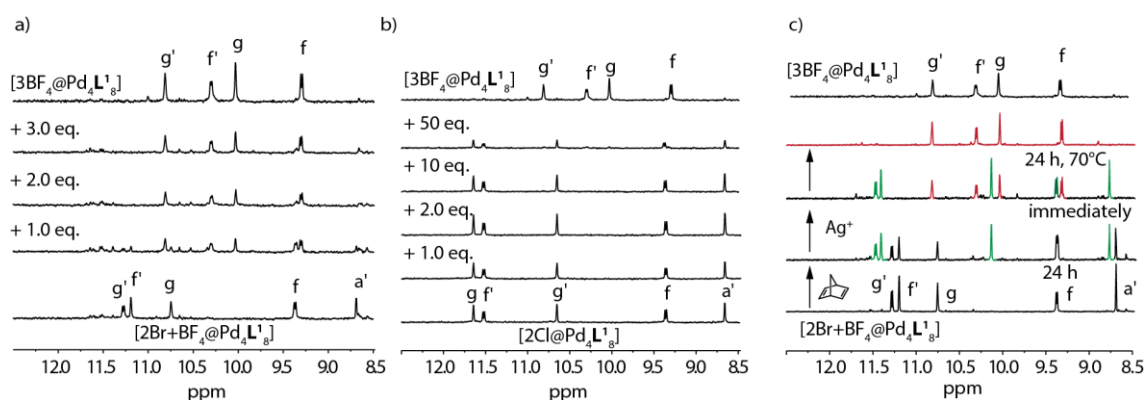


Figure 2.15 ^1H NMR titrations (400 MHz, 298 K, CD_3CN) with silver(I) ions to a) $[\text{2Br}+\text{BF}_4@\text{Pd}_4\text{L}^1_8]$, b) $[\text{2Cl}@\text{Pd}_4\text{L}^1_8]$ and c) $[\text{norbornadiene}+\text{2Cl}@\text{Pd}_4\text{L}^1_8]$.

2.7 Dispersive Contribution

Prof. Dr. R. Mata and coworkers carried out electronic structure calculations on a set of selected guest molecules and the host structure. To reduce the computational time, a model of the interpenetrated cage was used, where only the central pocket was represented (see Figure 7.91b). Even using this simplification the overall systems contains more than 300 atoms. For each neutral guest, different orientations were tested at the DFT level, followed by an optimization with a frozen cage geometry. This approach is based on the assumption that the chloride–palladium interaction in the outer pockets of the interpenetrated coordination cage is much stronger, than the binding of the neutral guest molecules in the central pocket and thus rules the host-geometry. *Mata* and coworker were not able to fit the cyclooctane guest within the fixed cage geometry and subsequent calculation were not possible to conduct. For a detailed explanation about computational procedures, see Chapter 7.3.8.

Table 2.2 Experimental and computed binding free enthalpies, dispersive contributions, volumes and packing coefficients for selected guests (solvent: acetonitrile). a: CPK volume of EDF2/6-31G* optimized model; b: Packing Coefficients, see Chapter 7.3.8 for detailed information on calculations; c: in kJ/mol; d: not computed. Reproduced from Reference [90] with permission from The Royal Society of Chemistry.

Guest	M/gmol^{-1}	$V/\text{\AA}^3$ ^a	PC% ^b	$\Delta G^{296\text{c}}$	$\Delta G_{\text{theo}}^{\text{c}}$	$\Delta E_{\text{disp}}^{\text{c}}$
furan	68.1	77.7	39	− 6.1	1.4	− 77.6
cyclopentane	70.1	95.2	48	− 12.8	− 19.5	− 88.6
benzene	78.1	99.0	50	− 17.4	− 34.9	− 86.0
cyclohexane	84.2	111.8	56	− 20.2	− 18.9	− 107.1
norbornadiene	92.1	113.2	56	− 20.2	− 28.4	− 110.5
phenol	94.1	106.8	53	− 12.8	− 13.1	− 100.5
cyclooctane	112.2	147.2	74	− 15.6	--- ^d	--- ^d
DABCO	112.2	126.4	64	− 27.1	− 31.0	− 134.4

From the optimized structures, the dispersion interactions between host and guest were calculated (SCS-LMP2/cc-pVTZ level, with effective core potential for Pd).^[95–98] Some of the results of these calculations are summarized in Table 2.2 and illustrated in Figure 2.16 (for further data see Figure 7.92 and Chapter 7.3.8.). The computed results showed, that the dispersion contributions are increased with increasing size of the neutral guest. While 5-members rings show a $\Delta E_{\text{disp}} = 70\text{--}90 \text{ kJ}\cdot\text{mol}^{-1}$, the 6-ring analogues have a contribution of $\Delta E_{\text{disp}} = 100 \text{ kJ}\cdot\text{mol}^{-1}$. These calculated values are in the expected range. The DFT D3 corrections^[99] could not be used to interpret the forces in this systems, because the contacts between the host and the guest are too close and would results in unrealistic values of more than $300 \text{ kJ}\cdot\text{mol}^{-1}$.

The dispersion interaction density (DID) profiles, show that close contacts between the neutral guest molecules and the interior of the central pocket dominates the profiles. Similar results were observed in systems similar to coupled diamondoids.^{[100],[101]} Individually, these contributions are very small, but for the entire system they add up significantly, what also explains the difference in

ΔE_{dis} between benzene and cyclohexane, since the latter has a larger number of C-H contacts. It was found, that the dispersion contribution for the selection of computed neutral guest correlates with the experimental binding affinity derived from the NMR experiments (see Table 2.2 and Figure 2.16c). The slope of the least-squares fit is 0.41, reflecting the attenuation from solvent effects, for example stabilizing dispersion interactions with solvent in the unbound state.

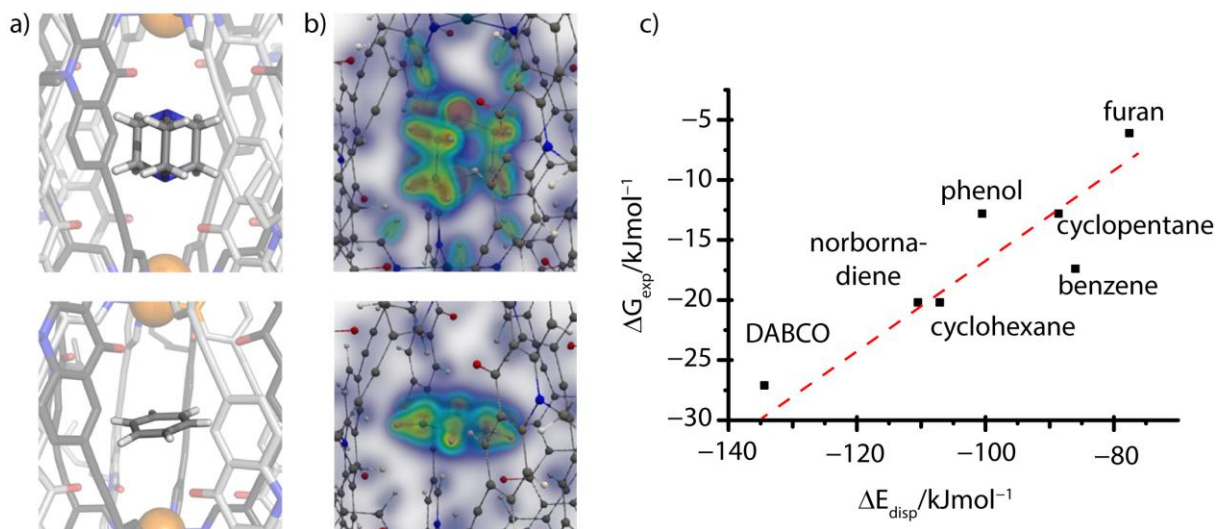


Figure 2.16 a) central pocket of the X-ray structure of [DABCO+2Cl @Pd₄L₁₈] (top) and [benzene+2Cl @Pd₄L₁₈] (bottom). b) calculated dispersion interaction density (DIDs) profile of DABCO (top) compared to benzene (bottom; from X-ray structure [2Cl+benzene@Pd₄L₁₈]; CCDC 1035009). Color scheme: red = strong; blue = weak interacting regions. c) Correlation of experimental guest affinities listed in Table 2.2 with computed dispersion contributions. Reproduced from Reference [90] with permission from The Royal Society of Chemistry.

Additionally, a composite approach for the calculation of the free enthalpy of binding was devised (For a detailed explanation, see experimental section *Computational Details* in Chapter 7.3.8.) Generally, all computed values are in good agreement with the experimental results, the only outlier is benzene. The mean absolute deviation of the computed binding affinity is 6.5 kJ·mol⁻¹. This value is acceptable given the size and complexity of the system.^[102]

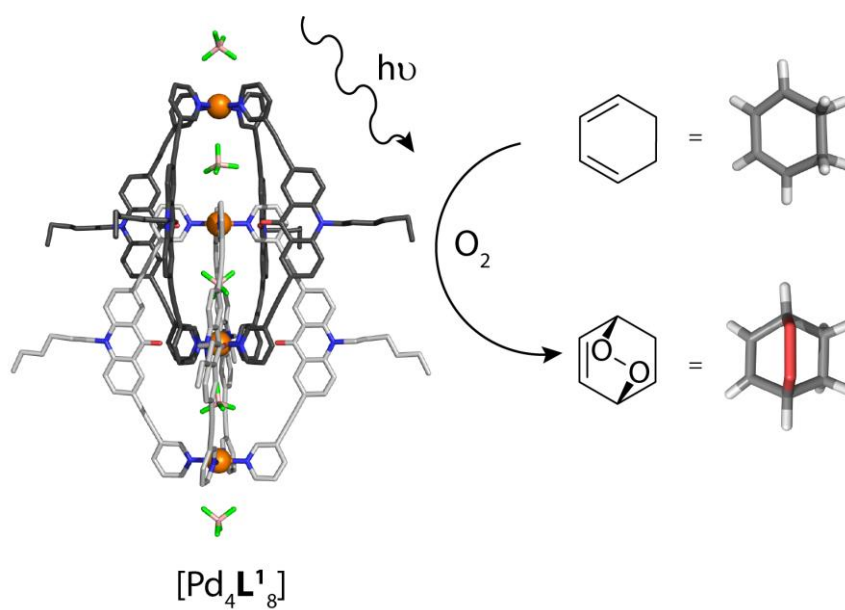
2.8 Conclusion

In this Chapter, the quantitative preparation of the highly symmetric supramolecular structure [3BF₄@Pd₄L₁₈] constructed from eight acridone based ligands **L**¹ and four square planar palladium(II) cations was described. Addition of halides anions (F⁻, Cl⁻, Br⁻, I⁻) leads to the replacement of the initially contained BF₄⁻ anions in the outer two pockets of the interpenetrated coordination cage. The binding occurs in an allosteric fashion with an enhanced affinity for the binding of the second halide (positive cooperativity) and is accompanied by compression of the entire structure along the Pd₄-axis. The addition of the halide anions activates the supramolecular assembly to incorporate neutral guest molecules inside the central cavity and form novel host-guest complexes. A wide variety of neutral guest molecules was tested for their ability to be encapsulated inside the chloride-containing coordination cage [2Cl@Pd₄L₁₈]. It was found, that six-membered rings (e.g. cyclohexane, benzene) and norbornene-type compounds are favored. Molecules containing one

substituent in the size of a methyl group, e.g. toluene, 2-methyltoluene are tolerated, while guests with two substituents (e.g. dichlorobenzene) or linear molecules are not incorporated. The opposite arrangement of heteroatoms in bridge or unbridged six-ring guest (e.g. DABCO, pyrazine) are favorable. The X-ray structure of $[\text{DABCO}+2\text{Cl}@\text{Pd}_4\text{L}^1_8]$ showed, that the nitrogen atoms of the neutral guest DABCO point towards the Pd(II) cations, indicating that this arrangement stabilizes the host-guest complex. Furthermore, the encapsulation of neutral guests inside the central pocket stabilizes the halide anions in the outer pockets. Electronic structure calculation showed, that the binding of neutral guest molecules inside these systems are strongly favored by dispersion interactions.

This presented system is the first example of an interpenetrated coordination cages containing banana-shaped ligand and palladium(II) cations, which is able to incorporate neutral guest molecules inside its central cavity.

3 COORDINATION CAGE AS PHOTOSENSITIZER



3.1 Introduction

In discrete cavities of supramolecular coordination cages, guest molecules can be encapsulated,^[39] stabilized^[49,50] and even catalytically reacted.^[52–58] Catalytic functions inside the protected voids of the cages can vary from acceleration of the reaction^[57] to the formation of products with surprising topology.^[44,53] Interpenetrated coordination cages based on banana-shaped ligands and palladium(II) cations are of special interest, because these structures have three voids, in which guest molecules can be incorporated.^[64] The interpenetrated coordination cage $[\text{Pd}_4\text{L}_8]$ based on an acridone-derived ligand can incorporate a variety of neutral guest molecules inside the central pocket after being activated by halide anions (see Chapter 2).^[87] Among the tested guests, the organic compound 1,3-cyclohexadiene was found to be encapsulated. These molecule is a common starting compound for Diels-Alder reactions in organic synthesis.^[103]

The following Chapter will focus on the encapsulation of 1,3-cyclohexadiene inside the central cavity of the halide-containing interpenetrated coordination cage $[\text{2Cl}@\text{Pd}_4\text{L}_8]$ and the ability to further undergo a Diels-Alder reactions inside the void of the cage is studied.

3.2 NMR and HR-MS Studies

As discussed in Chapter 2, the interpenetrated coordination cage $[\text{2Cl}@\text{Pd}_4\text{L}_8]$ can encapsulate a broad range of neutral guest molecules in the central pocket of the supramolecular cage. After the addition of 10 equivalents of 1,3-cyclohexadiene to the chloride-containing cage and incubating the sample at room temperature, a new set of signals was observed in the ^1H NMR spectrum after 24 h (see Figure 3.1b, highlighted in green). Protons H_g and H_a , which point inside the central pocket of the interpenetrated coordination cage, are shifted significantly; H_g shifted upfield by $\Delta\delta = 0.25$ ppm and H_a downfield by $\Delta\delta = 0.16$ ppm.

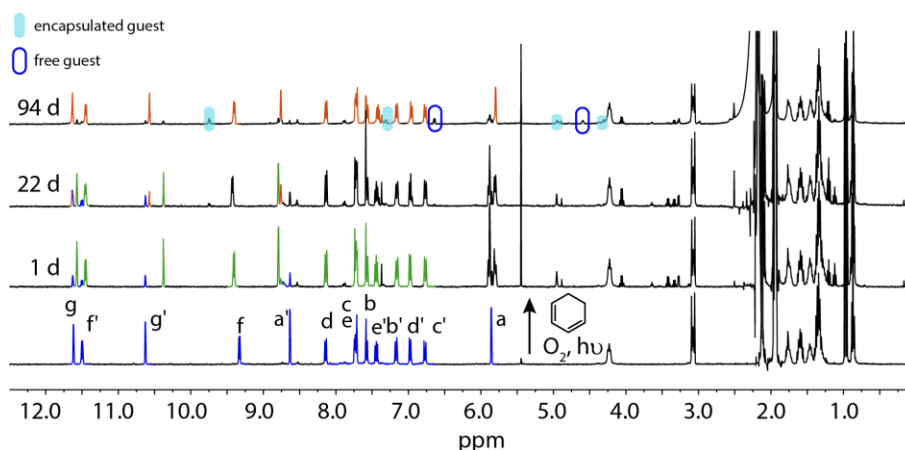


Figure 3.1 ^1H NMR spectra (400 MHz, 298 K, CD_3CN) of $[\text{2Cl}@\text{Pd}_4\text{L}_8]$ and after the addition of 1,3-cyclohexadiene (10 eq.) and an incubation time of 1 day, 22 days and 94 days. 1 day after the addition, the neutral guest molecule is encapsulated inside the cationic cage and the host-guest complex $[\text{2Cl}+\text{C}_6\text{H}_8@\text{Pd}_4\text{L}_8]$ is formed (highlighted in green). After 22 days a new set of signals arise (highlighted in orange), which is the main species after 94 days. This NMR spectrum corresponds to the host-guest complex $[\text{2Cl}+\text{C}_6\text{H}_8\text{O}_2@\text{Pd}_4\text{L}_8]$.

Based on the shifting of these proton signals, the encapsulation of the 1,3-cyclohexadiene inside the central cavity of the supramolecular coordination cage was indicated. High-resolution ESI mass spectrometry showed a series of species $[2\text{Cl}+\text{C}_6\text{H}_8@\text{Pd}_4\text{L}^1_8+n\text{BF}_4]^{(6-n)+}$ ($n=0-3$) containing a variable number of tetrafluoroborate counter anions, confirming the formation of the host-guest complex (see Figure 3.3b).

To determine the binding constant of the neutral guest encapsulation, the sample was left at room temperature for an extended period of time and ^1H NMR spectra were measured in periodic time intervals. Surprisingly, after 22 days a new set of signals appeared in the ^1H NMR spectrum (Figure 3.1c, highlighted in orange). After a time period of more than 90 days this new compound was the main species in the solution and only small amounts of the chloride-containing cage $[2\text{Cl}@\text{Pd}_4\text{L}^1_8]$ remained (Figure 3.1, highlighted in blue). The overall interpenetrated cage structure is still intact and only the inward pointing protons (H_g and H_a) experience a change in their chemical environments. Furthermore, the signals of the guest molecule 1,3-cyclohexadiene at $\delta = 5.81-5.93$ ppm disappeared, indicating that a reaction with the guest molecule had occurred. High-resolution ESI mass spectrometry showed signals corresponding to $[2\text{Cl}+\text{C}_6\text{H}_8\text{O}_2@\text{Pd}_4\text{L}^1_8+n\text{BF}_4]^{(6-n)+}$ ($n=0-3$) with a series of tetrafluoroborate counter anions (Figure 3.3c). This confirms the stability of the coordination cage and the change of the guest molecule from 1,3-cyclohexadiene (C_6H_8) to a species with a chemical formula of $\text{C}_6\text{H}_8\text{O}_2$.

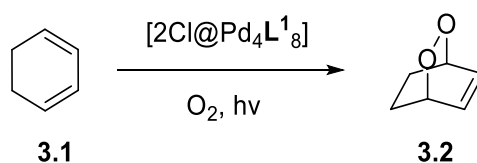


Figure 3.2 In the presence of the interpenetrated coordination cage $[2\text{Cl}@\text{Pd}_4\text{L}^1_8]$, atmospheric oxygen and ambient light, 1,3-cyclohexadiene **3.1** transforms into 2,3-dioxabicyclo[2.2.2]oct-5-ene **3.2**.

A closer look at the ^1H NMR spectra shows a new species with signals at chemical shifts ranging from 9.79–1.36 ppm. ^1H - ^1H NOESY NMR measurement showed strong correlation between the protons pointing towards the inside of the central cavity of the interpenetrated cage (H_g and H_a) and proton signals of the new species at a chemical shift of $\delta = 9.78, 7.31, 4.94$ and 4.29 ppm (highlighted in light blue in Figure 7.94). Furthermore, signals of the reaction product were found outside of the coordination cage in the acetonitrile solution at chemical shifts of $\delta = 6.63, 4.60, 2.22$ and 1.43 ppm (see Figure 7.93).

Based on the NMR spectroscopy, HR ESI mass spectrometry and X-ray data (see Chapter 3.3) the new compound with a chemical formula of $\text{C}_6\text{H}_8\text{O}_2$ was identified as 2,3-dioxabicyclo[2.2.2]oct-5-ene (see Figure 3.2).^{[104][105]}

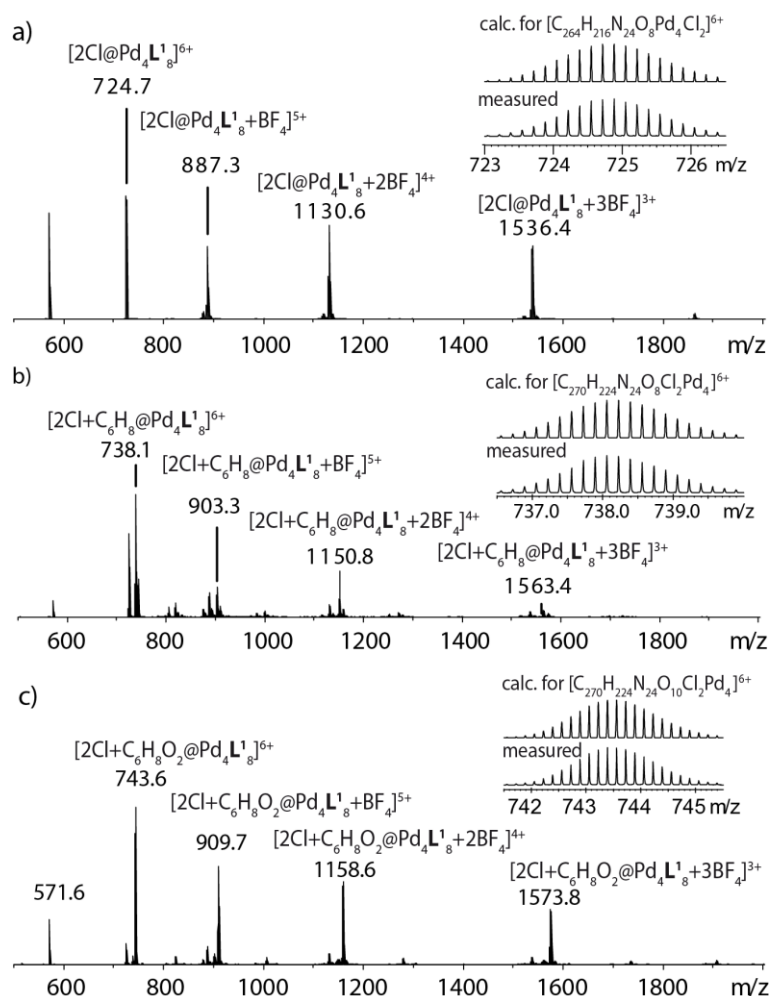


Figure 3.3 HR-MS of a) [2Cl@Pd₄L¹₈], b) [2Cl+C₆H₈@Pd₄L¹₈] and c) [2Cl+C₆H₈O₂@Pd₄L¹₈].

1,3-cyclohexadiene (**3.1**) as a common starting material for Diels–Alder reactions^[103] is known to undergo a [4+2] cycloaddition in the presence of a photosensitizer (e.g. Rose Bengal or tetraphenylporphyrin), oxygen and irradiation and forming the peroxide **3.2**. The role of the photosensitizer in this reaction is to generate singlet oxygen from triplet oxygen.^[106] It seems that the chloride-containing coordination cage [2Cl@Pd₄L¹₈] is working as a photosensitizer. To confirm this presumption, a series of control experiments were performed. Addition of 1,3-cyclohexadiene to the chloride-containing host-guest complex in absence of atmospheric oxygen or ambient light shows no formation of the peroxide **3.2** (Figure 7.95 and Figure 7.96), which indicates that a light induced [4+2] cycloaddition is taking place. The presence of oxygen and light are an essential preconditions for the reaction.

Furthermore, no product formation was observed in the presence of only tetrabutylammonium chloride, tetrakis(acetonitrile)palladium(II) tetrafluoroborate, acetonitrile or free ligand (Table 3.1 entries 6–9).

Table 3.1 Conditions and results for control experiments. **3.1**: 1,3-cyclohexadiene, **3.2**: 2,3-dioxabicyclo[2.2.2]oct-5ene, **3**: 1,4-cyclohexadiene. 10 eq. of **3.1** or **3.3**, CD₃CN, ambient temperature. *Results obtained from a mixture of **3.1** and free ligand in various temperatures were not reproducibly. However, formation of **3.2** can be ruled out. Currently, the influence of the ligand is under further investigation.

Entry	Conditions	Results
1	[2Cl@Pd ₄ L ¹ ₈], O ₂ , hv, 3.1	formation of peroxide 3.2
2	[2Cl@Pd ₄ L ¹ ₈], O ₂ , 3.1	-
3	[2Cl@Pd ₄ L ¹ ₈], hv, 3.1	-
4	[3BF ₄ @Pd ₄ L ¹ ₈], O ₂ , hv, 3.1	formation of peroxide 3.2
5	[2Cl@Pd ₄ L ¹ ₈], O ₂ , hv, 3.3	-
6	NBu ₄ Cl, O ₂ , hv, 3.1	-
7	[Pd(CH ₃ CN) ₄](BF ₄) ₂ , O ₂ , hv, 3.1	degradation
8	CD ₃ CN, O ₂ , hv, 3.1	-
9	Ligand L ¹ , O ₂ , hv, 3.1	*

A central question regarding this reaction was whether it was necessary for the guest to be bound in the central cavity of the interpenetrated coordination cage or if the reaction can proceed when the substrate is in free solution. Therefore, 10 equivalents of 1,3-cyclohexadiene **3.1** were added to a solution of [3BF₄@Pd₄L¹₈]. After several days at room temperature in the presence of ambient light and atmospheric oxygen, the formation of the peroxide **3.2** was observed (see Figure 7.101 and Table 3.1 entry 4). Since the tetrafluoroborate-containing coordination cage [3BF₄@Pd₄L¹₈] does not have any free pockets (see Figure 2.7a) it can be concluded, that the Hetero-Diels–Alder reaction does not occur inside of the [3BF₄@Pd₄L¹₈] coordination cage. However, what about the chloride-containing [2Cl@Pd₄L¹₈] cage? Addition of 1,3-cyclohexadiene **3.1** (10 eq.) to a solution of peroxide encapsulated coordination cage [2Cl+C₆H₈O₂@Pd₄L¹₈], shows no exchange of the neutral guests inside the central cavity of the coordination cage (see Figure 7.102). The binding affinity of the product **3.2** towards the cationic coordination cage seems to be stronger compared to compound **3.1**. This would inhibit the cage from performing a catalytic reaction (product inhibition). However, after 94 days no traces of the in excess added substrate **3.1**. was present in the solution of the chloride-containing coordination cage (see Figure 3.1). Thus, the formation of the peroxide **3.2** must be due to the ability of the cage to act as a photosensitizer to the free guest in solution. Therefore, there is no evidence that the reaction occurs exclusively in the central cavity of the interpenetrated coordination cage.

3.3 X-ray Structure Analysis

Single crystals of [2Cl+C₆H₈@Pd₄L¹₈] and [2Cl+C₆H₈O₂@Pd₄L¹₈] suitable for X-ray diffraction were obtained *via* slow vapor diffusion of diethyl ether into an acetonitrile solution of the host-guest complexes (see Figure 3.4). Both interpenetrated cage structures crystallized in the space group *P4/n*. The host-guest complexes consist of two monomeric cage units with the formula [Pd₂L¹₄], which interlace to the interpenetrated [Pd₄L¹₈] cage. The structure features three pockets, the outer two

occupied by a chloride anion and the inner void occupied by the neutral guest molecules 1,3-cyclohexadiene **3.1** (C_6H_8) or 2,3-dioxabicyclo[2.2.2]oct-5-ene **3.2** ($C_6H_8O_2$).

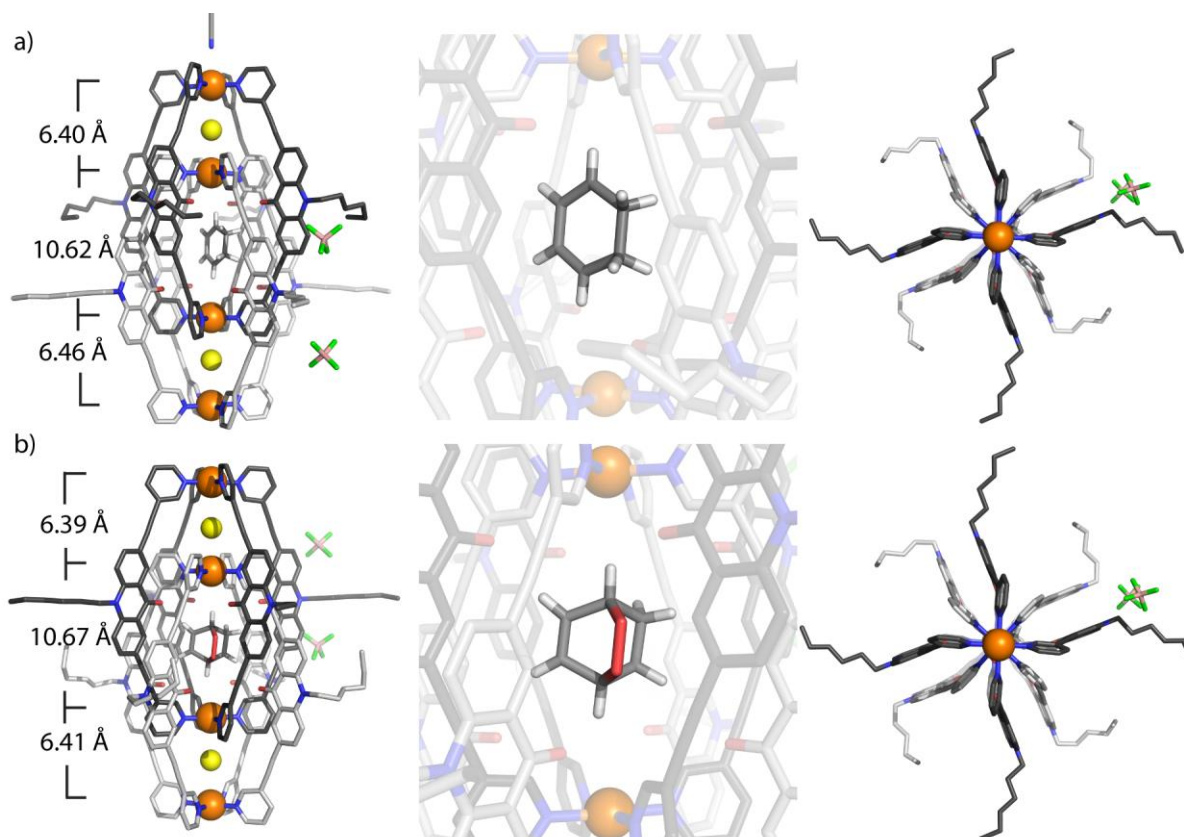


Figure 3.4 Preliminary X-ray crystal structures of cage (a) $[2Cl+C_6H_8@Pd_4L^1_8]$ and (b) $[2Cl+C_6H_8O_2@Pd_4L^1_8]$. *Color scheme:* C: light/dark gray; N: blue; O: red; Cl: yellow; F: green; B: salmon; Pd: orange; H: white. For clarity, the hydrogen atoms of the coordination cage and some of the solvent molecules were removed. The depicted neutral guest molecules in the central pockets of the cavity are one of four symmetry equivalent positions.

In the host-guest complex $[2Cl+C_6H_8@Pd_4L^1_8]$ the distance between the palladium cations for the outer pockets are 6.40 Å and 6.46 Å and for the inner void 10.62 Å (see Figure 3.4a). Compared with the benzene-containing interpenetrated cage structure $[2Cl+C_6H_6@Pd_4L^1_8]$ it is striking, that all distances change around 0.14–0.20 Å (see Figure 2.7b). While the central cavity increased (from 10.48 Å to 10.62 Å) and the outer pockets decreased in size (6.59 and 6.62 Å in the benzene vs. 6.40 and 6.46 Å in the 1,3-cyclohexadiene-containing host-guest complex). An explanation for this observation might be the larger size of the 1,3-cyclohexadiene **3.1** in comparison to the benzene molecule. Another remarkable difference is the arrangement of the neutral guest molecules inside the central pocket of the coordination cage. While the benzene molecule is positioned horizontal with the π -system pointing towards the palladium centers, 1,3-cyclohexadiene **3.1** is arranged vertically between the two palladium cations of the inner void of the cage similar to the DABCO-containing structure (see Figure 2.7c). A comparison between the interpenetrated coordination cages containing DABCO and 1,3 cyclohexadiene **3.1** revealed similar Pd-Pd distances for the outer cavities with 6.40 and 6.49 Å for $[2Cl+DABCO@Pd_4L^1_8]$ vs. 6.40 and 6.46 Å for $[2Cl+C_6H_8@Pd_4L^1_8]$. Interestingly, the Pd-Pd distance for the central pocket are slightly different. While for the 1,3-cyclohexadiene-incorporated complex a palladium-palladium distance of 10.62 Å was measured, the

distance in the DACO structure is 10.93 Å. The observed differences in the Pd-Pd distances of all three neutral guest incorporated host-guest complexes might be a result of the varying steric demand of the encapsulated neutral guest molecules.

Furthermore, a close contact between the neutral guest **3.1** and the palladium cation was measured to be ~3.00 Å. Additionally, close contacts with the hydrogen atoms of the surrounding coordination cage were found in the crystal structure ranging from 1.96–3.90 Å.

The crystal structure of the interpenetrated coordination cage encapsulating the peroxide product **3.2** [2Cl+C₆H₈O₂@Pd₄L₈] is very similar to the structure of the 1,3-cyclohexadiene encapsulated [2Cl+C₆H₈@Pd₄L₈] complex. The palladium-palladium distances in the [2Cl+C₆H₈O₂@Pd₄L₈] complex are with 6.39 Å and 6.41 Å for the outer and 10.67 Å for the inner pockets very similar to the described [2Cl+C₆H₈@Pd₄L₈] complex (see Figure 3.4). The guest molecule **3.2** is aligned vertically between the palladium cations in the central cavity of the interpenetrated coordination cage with the shortest palladium-guest distance of ~3.16–3.05 Å. Close intermolecular contacts between the acridone ligands of the cage and the neutral guest molecule **3.2** were measured to range from 1.99 to 3.92 Å.

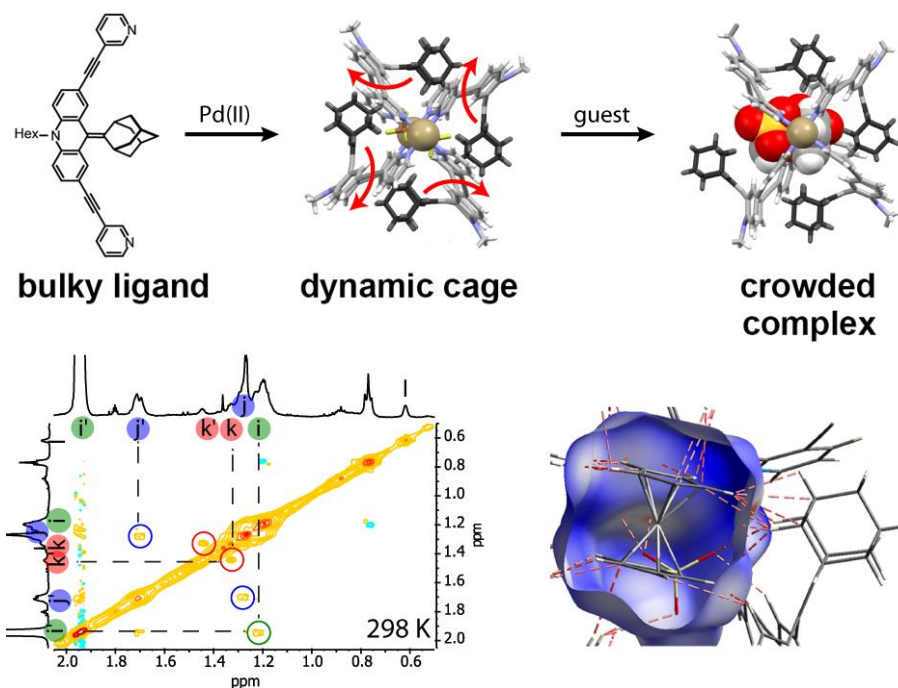
It is worth mentioning, that both encapsulated guest molecules **3.1** and **3.2** sit on a crystallographic 4-fold axis of the Pd-Pd axis. This results in four symmetry-equivalent positions of the guest inside the interpenetrated coordination cage. In Figure 3.4 only one possibility is depicted.

As already discussed in Chapter 2.4 it was assumed, that the main driving force for the encapsulation of the neutral guest are dispersion interaction with further contribution of a solvophobic effect.

3.4 Conclusion

This Chapter describes the unique ability of the interpenetrated coordination cages [2Cl@Pd₄L₈] and [3BF₄@Pd₄L₈] to convert 1,3-cyclohexadiene **3.1** in presence of atmospheric oxygen and light into the peroxide 2,3-dioxabicyclo[2.2.2]oct-5-ene **3.2**. A requirement for Hetero [4+2] Diels–Alder reactions is singlet oxygen. As the reaction requires a photosensitizer, it is assumed, that the supramolecular coordination cages excites triplet oxygen to singlet oxygen and can therefore enable the reaction to the peroxide **3.2**. The formation of **3.2** was verified *via* NMR spectroscopy, high-resolution mass spectrometry and X-ray structure analysis.

4 ENDOHEDRAL FUNCTIONALIZATION AND DYNAMICS



Reprinted with permission from reference ^[107]. Copyright © 2016 Royal Society of Chemistry.

Results of this Chapter are published in “*Internal Dynamics and Guest Binding of a Sterically Overcrowded Host*” S. Löffler, J. Lübben, A. Wuttke, R. A. Mata, M. John, B. Dittrich, G. H. Clever, *Chem. Sci.* **2016**, 7, 4676.

4.1 Introduction

Dynamic processes are widely observed phenomena in nature, in particular in biomolecular systems. The binding of a substrate to a protein can lead to a structural rearrangement of the entire protein (e.g. binding of molecular oxygen to hemoglobin). Another example is the DNA double helix, which unfolds to be transcribed into RNA.^[108] Inspired by nature, supramolecular chemists are interested in studying dynamic features in smaller artificial systems and over the last decades, numerous examples of dynamic systems were reported. In 2016, the achievements of *Sauvage*, *Stoddard* and *Feringa* for “the design and synthesis of molecular machines”^[109] was rewarded with the Nobel Prize in chemistry. The aforementioned scientists investigated the dynamic motions in different systems. They developed molecular elevators,^[24] muscles,^[23] light-powered rotors,^[25] unidirectional walkers^[27] and “cars”.^[26] Nevertheless, they were not the only ones interested in this topic. Other groups reported propellers,^[110] scissors,^[111] caterpillars,^[112] molecular valves^[113] and controlled motions in catenanes and rotaxanes.^[13,114]

In the field of supramolecular cages, dynamic examples are rare. The supramolecular host often consists of a rigid ligand backbone, which does not allow flexible motion. Up to date, only few examples are described, where flexible units are incorporated in the ligand structure.^[11,115] One prominent example from the group of *Clever* is the light-switchable ligand, based on dithienylethene (DTE), which can be transformed from a flexible, open conformation to a rigid, closed-ring isomer upon irradiation (see Figure 4.1). This ligand yields a photo-switchable cage systems, which shows significant differences in guest binding affinity for its two photo-isomeric states.^[66,81]

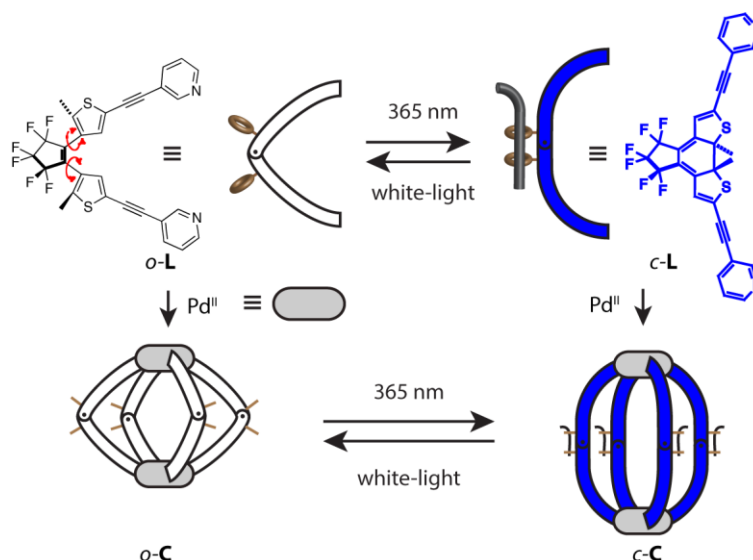


Figure 4.1 Photo-induced conformation switching of the dithienylethene-based ligands and their self-assembly to monomeric $[Pd_2L_4]$ coordination cages. Figure redrawn and adapted from reference ^[81].

Clever and coworkers introduced another example for a dynamic motion in a coordination cage in 2016. Attachment of an endohedral functionality in the central backbone of the acridone-based ligand resulted in an interesting rotational dynamic (see Figure 4.2). Although, the residue is bound *via* a C=C double bond, the rotation around this bond is possible due to a donor-acceptor character

of the entire backbone, which lowers the rotational barriers. The rotational velocity is influenced by the cage assembly, the polarity and derivatization of the attached electron-withdrawing residue ($R = \text{CN}, \text{COOEt}, \text{COO}^t\text{Bu}, \text{COOPh}$). Furthermore, encapsulation of an anionic guest molecule reduces the rotational rate.^[116]

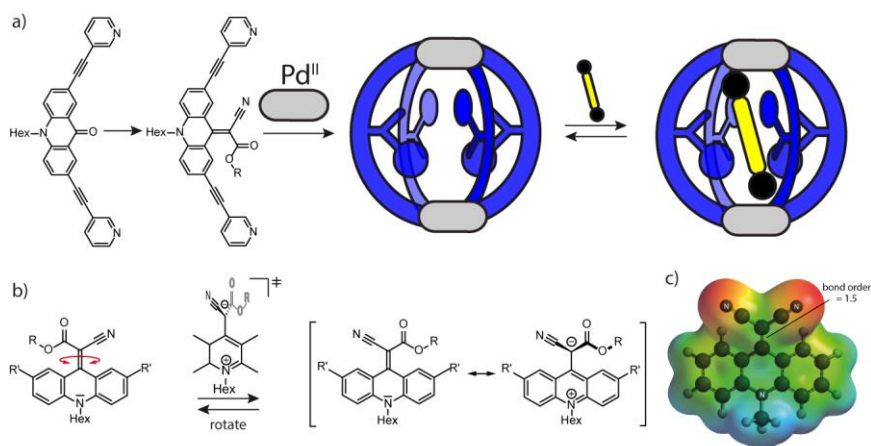


Figure 4.2 a) Endohedral ligand modification, cage assembly and guest uptake, b) rotation of the endohedral functionality via a charge-separated transition state, c) electrostatic potential map of the endohedral functionalized ligand backbone, highlighted the partial charge separation and C=C double-bond weakening in the push-pull backbone ($R = \text{CN}, \text{COOEt}, \text{COO}^t\text{Bu}, \text{COOPh}$). Figure redrawn and adapted from reference ^[116].

Further studies on dynamic processes in supramolecular systems focused on the uptake/release kinetics of guest molecules as well as the mobility of the guest inside the cavity of the host. Thereby tumbling, rotation and flipping motions of guest molecules were observed.^[110,117]

Endohedral functionalization of organic ligands lead to the introduction of a steric bulk in the resulting supramolecular assembly. *Hooley* and coworker could enable the formation of heteroleptic cages, containing two different ligands, through implementation of endohedral functional groups.^[82,83] Attachment of a bulky phenyl-substituent to the previously described dibenzosuberone ligand by *Clever* helped to control the dimerization into interpenetrated coordination cages and binding affinity towards anionic guest molecules (see Chapter 1.3.3).^[77] In addition, implementation of bulky groups affects the uptake/release kinetics and the thermodynamic stability of encapsulated guest molecules. An example introduced by *Yoshizawa* and coworkers shows a molecular capsule with an anthracene shell. Due to the sterically demanding residues, the central cavity is completely shielded from the external environment and larger neutral guest molecules (e.g. C_{60} , adamantane or pyrene derivatives) are found to be encapsulated in quantitative yields.^[118] Furthermore, *Fujita* attached the light-switchable azobenzene group to the center of a bispyridyl ligand. Addition of palladium(II) cations results in the assembly of a $[\text{Pd}_{12}\text{L}_{24}]$ sphere, with all azobenzenes concentrated in the interior of the assembly. By photoisomerization of the endohedral moiety, the hydrophobicity and consequently the host-guest affinity of the supramolecular cage is regulated.^[119]

In general, the introduction of sterically demanding residues into host systems has two direct consequences. First, size reduction of the internal cavity of the supramolecular assembly and secondly, the (partially) blockage of the portals that allow the uptake and release of the encapsulated guest

molecules. Thus, decelerated exchange kinetics in bulky systems are often observed.^[120] Nevertheless, the idea that steric crowding is always repulsive and thus disadvantageous for guest binding seems to be incorrect. Attractive interactions between closely associated molecules, without any functional groups, are attributed to London dispersion interactions.^[121] Individually, dispersion forces are quite weak in comparison to other intermolecular interactions (see Chapter 1.2.1 on *Non-covalent Interactions*). In larger systems, such as supramolecular assemblies, they can add up to a substantial value, which contributes to the overall stability.^[122] Dispersion interactions are known since the 1930's, but only recently chemists realized their significance leading to an intense discussion by a broad community that has only just started. The introduction of the term "dispersion energy donors" (DEDs) and the implementation of dispersion contribution in modern methods of electronic structure calculations are the first steps towards an intense research.^[123]

Therefore, the following Chapter will be focused on the synthesis and characterization of a self-assembled coordination cage equipped with a bulky, but otherwise unfunctionalized adamantyl group at the ligand backbone. The influence of the steric residue on the assembly process and the host-guest chemistry as well as the effect of non-covalent dispersion interactions on the stability of the host and the host-guest complex will be discussed.

4.2 Ligand Synthesis and Cage Assembly

Initially, ligand **L**¹ was synthesized motivated by the presence of the carbonyl group at the acridone backbone and the possibility to easily modify the organic compound under mild reaction conditions. It turned out, that condensation reactions with different amines were not successful.^[124] Instead, applying harsher reaction conditions resulted in the modification of the acridone backbone at the carbonyl functionality. The novel ligand **L**² was synthesized from ligand **L**¹ via a McMurry^[125] coupling with 2-adamantone (1.0 eq.) using titanium(III)-chloride (17 eq.), lithium aluminum hydride (5 eq.) and trimethylamine (5.0 eq.), yielding the desired product in 85 % yield (see Figure 4.3).

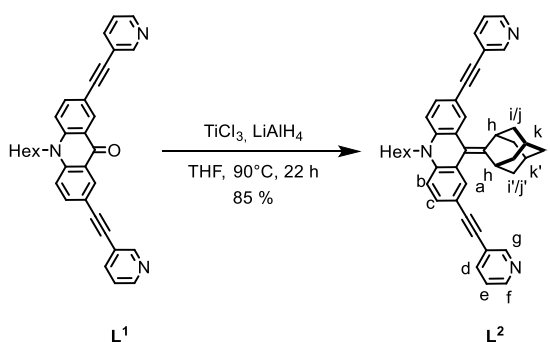


Figure 4.3 Synthesis of ligand **L**² from ligand **L**¹.

The aromatic region of the ¹H NMR spectrum of the ligand **L**² shows the expected seven signals of the tricyclic backbone and the pyridine moieties. In the aliphatic region, six signals for the hexyl

chain and eight signals for the adamantyl group were observed (see Figure 4.5a). Initially, a symmetric structure with the adamantyl residue and the acridone backbone in the same plane was expected. This would give rise to five different signals in the ^1H NMR spectrum for the adamantyl group. The observed results from the NMR experiment contradicts this assumption and indicates a reduced symmetry of the attached group, due to a bent shape of the ligand with the adamantyl residue pointing to one side.

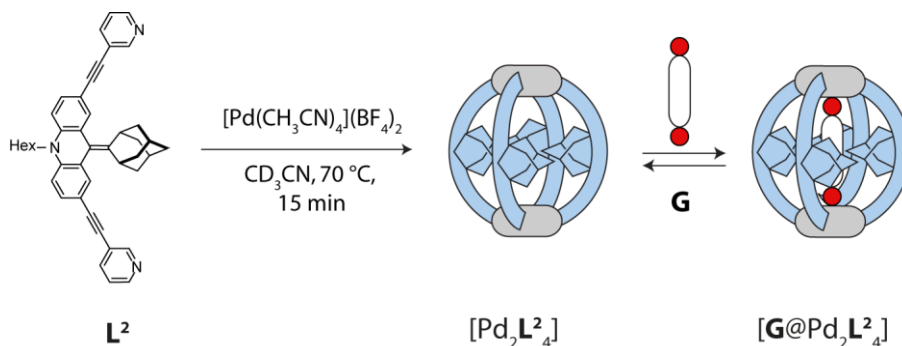


Figure 4.4 Self-assembly of the monomeric coordination cage $[\text{Pd}_2\text{L}_2^4]$. Addition of a guest **G** to $[\text{Pd}_2\text{L}_2^4]$ leads to the formation of a host-guest complex $[\text{G}@\text{Pd}_2\text{L}_2^4]$. Reprinted with permission from reference ^[107]. Copyright © 2016 Royal Society of Chemistry.

Ligand L^2 was suspended in deuterated acetonitrile and 0.5 equivalents of tetrakis(acetonitrile)palladium(II) tetrafluoroborate were added to the solution. Heating the reaction mixture in a closed vial at 70 °C for 15 min resulted in the quantitative formation of the monomeric $[\text{Pd}_2\text{L}_2^4]$ cage. The formation of the coordination cage was accompanied by a change in color from a dull, slightly yellow suspension to a clear, orange solution.

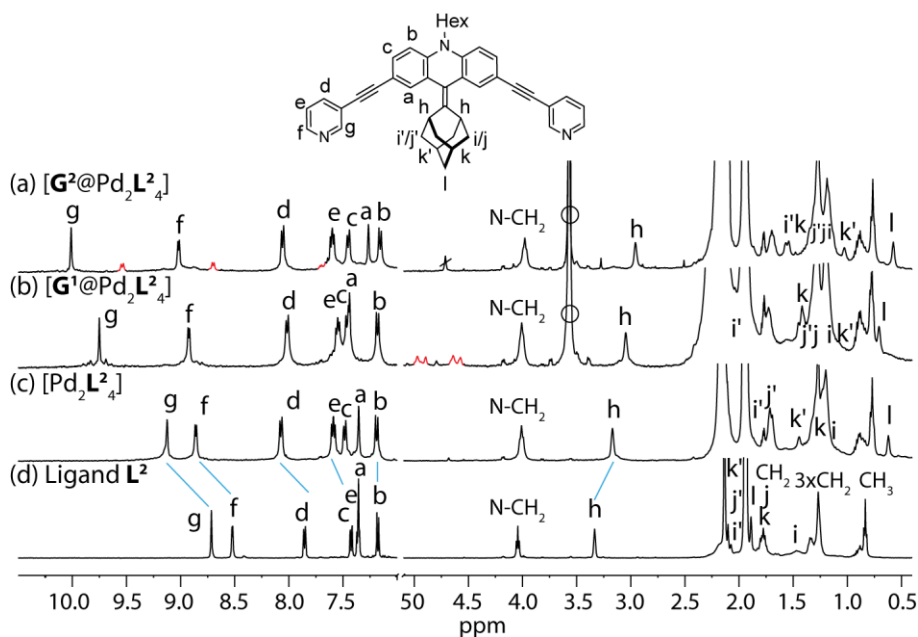


Figure 4.5 ^1H NMR spectra of (a) free ligand L^2 , (b) cage $[\text{Pd}_2\text{L}_2^4]$ and the corresponding host-guest complexes (c) $[\text{G}^1@\text{Pd}_2\text{L}_2^4]$ and (d) $[\text{G}^2@\text{Pd}_2\text{L}_2^4]$ (400 MHz, 298 K, CD_3CN). The signals of the encapsulated guest molecules are highlighted in red. H_i , H_j and H_k represent outside (*exo*) and H_i' , H_j' and H_k' inside (*endo*) pointing hydrogen atoms of the adamantyl substituent with respect to the acridone backbone (compare Figure 4.9). Empty circle: $[\text{K}(18\text{-crown-6})]^+$. Reprinted with permission from reference ^[107]. Copyright © 2016 Royal Society of Chemistry.

Following ^1H NMR analysis of the resulting solution showed a shifting of all signals in the spectrum. Signals that were assigned to the pyridine protons shifted downfield. This change results from the coordination of the positively charged palladium(II) cation to the nitrogen donor and the accompanied reduction of electron density at the ligand due to the complexation^[126] ($\Delta\delta = 0.44$ ppm for H_g , $\Delta\delta = 0.34$ ppm for H_f). In contrast, all adamantyl signals shifted upfield. Reason for this change is the ring current effect^[103] of the aromatic backbone of the neighboring ligand on the adamantyl substituent ($\Delta\delta = 1.27$ ppm for H_i) (Figure 4.5a and b). Prolonged heating (for 24 h) or addition of smaller templating anions (e.g. chloride) did not lead to dimerization and the formation of an interpenetrated coordination cage $[\text{Pd}_4\text{L}_8]$. The adamantyl-group of the ligand L^2 seems to be sterically too demanding and therefore prevents the dimerization process.

Next, high-resolution ESI mass spectrometric analysis was performed, which clearly showed the formation of the self-assembled $[\text{Pd}_2\text{L}_4]^{4+}$ coordination cage. A series of species was detected, which can be assigned to $[\text{Pd}_2\text{L}_4+n\text{BF}_4]^{(4-n)+}$ ($n = 0-2$) containing a variable number of tetrafluoroborate counter anions (Figure 4.6a). The molecule peak at $m/z = 899.7$ is the trivalent species $[\text{Pd}_2\text{L}_4+\text{BF}_4]^{3+}$ with one BF_4 counter anion.

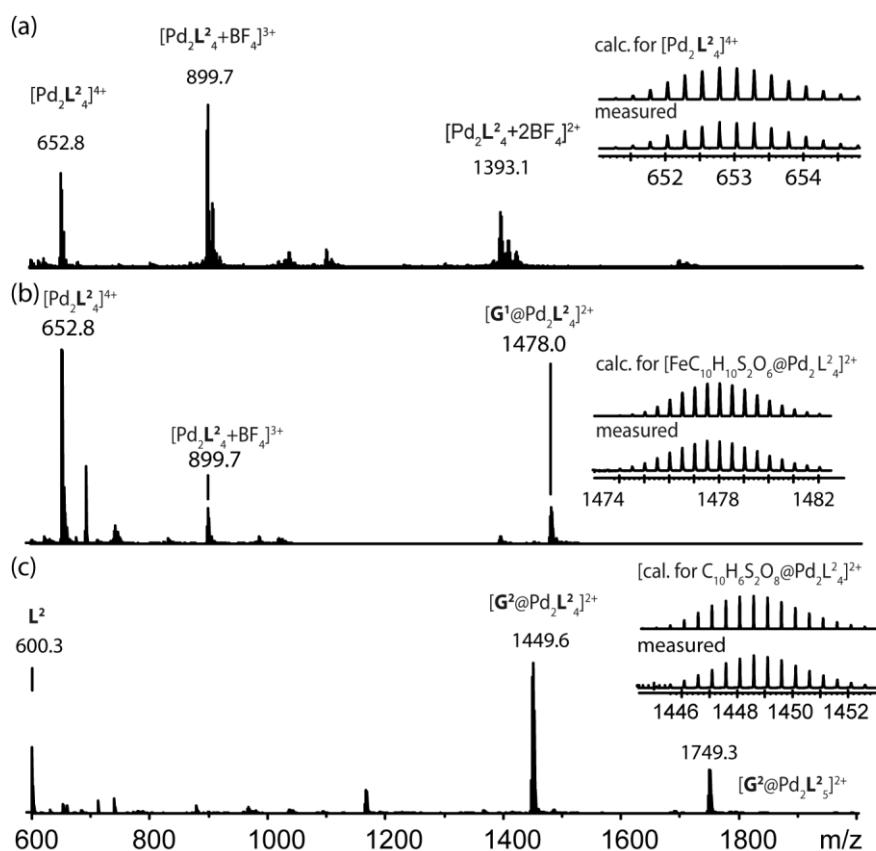


Figure 4.6 ESI(+)-mass spectra of (a) $[\text{Pd}_2\text{L}_4]$ coordination cage and the host-guest complexes: (b) $[\text{G}^1@[\text{Pd}_2\text{L}_4]]$ and (c) $[\text{G}^2@[\text{Pd}_2\text{L}_4]]$. Reprinted with permission from reference ^[107]. Copyright © 2016 Royal Society of Chemistry.

4.3 Flipping Dynamics in Ligand L^2 and $[Pd_2L^2_4]$ Coordination Cage

Attachment of the sterically demanding adamantyl group to the central carbon of the acridone backbone results in a change of the structural arrangement of the ligand L^2 . While ligand L^1 shows a planar configuration (see Chapter 2 and Figure 7.85), ligand L^2 is bent. The sterically demanding adamantyl residue bends to one side to avoid close contacts between the hydrogen atoms of the adamantyl residue (H_h) and the acridone backbone (H_a) (Figure 4.9a).

Correlation between *exo* (H_i , H_j , H_k , pointing “outside”/towards the acridone backbone) and the *endo* protons ($H_{i'}$, $H_{j'}$, $H_{k'}$, pointing “inside”/towards the pyridine residues of the ligand structure) of the adamantyl group could be observed in an 1H - 1H NOESY NMR experiment of the free ligand (see Figure 4.7). With increasing temperature, the corresponding cross-peak intensities increase, therefore indicating a dynamic movement (such as rotation or flipping) of the adamantyl group within the ligand configuration. Rotation was observed in a similar system reported by *Clever* and *Krick*.^[116,127] The endohedral attached residue was found to rotate around the attached double bond due a weakening of the C=C bond as a result of the push-pull character of the conjugated system (see Figure 4.2 in Chapter 4.1). The adamantyl group in Ligand L^2 is attached *via* a double bond to the acridone backbone, without a push-pull character. Therefore, a rotation as in the previously reported system^[116,127] can be excluded. Hence, it can be assumed that a flipping motion occurs in the ligand, which allows the *endo* and *exo* sides of the adamantyl residue to change the position (Figure 4.7 and Figure 4.9a).

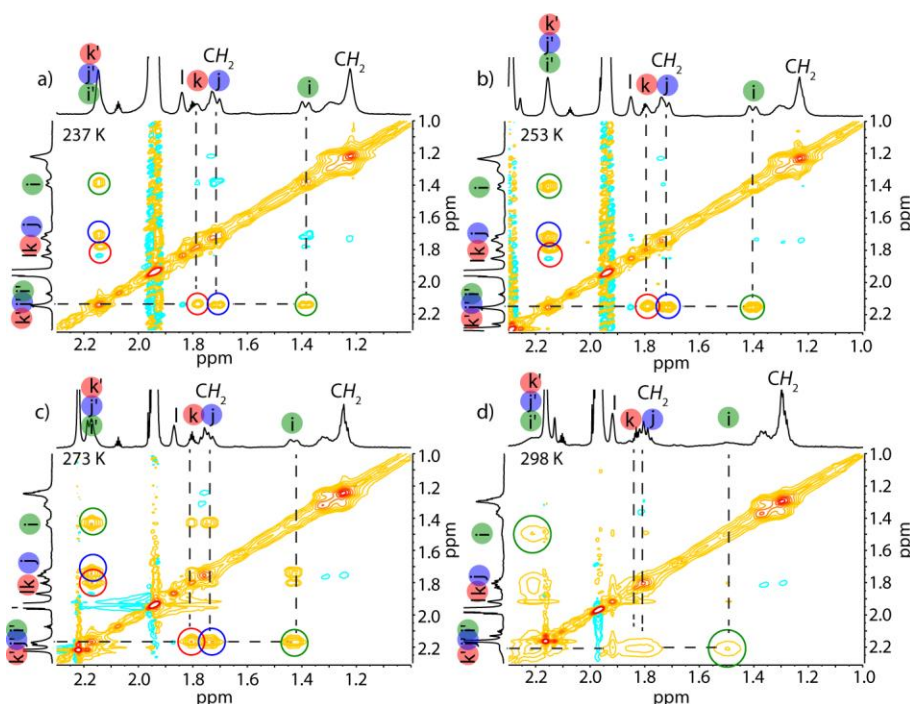


Figure 4.7 1H - 1H NOESY spectrum of ligand L^2 (500 MHz, CD_3CN) at different temperatures: a) 237 K, b) 253 K, c) 273 K and d) 298 K. The highlighted cross-peaks indicate the exchange between the inward (i' , j' and k') and outward (i , j , k) pointing hydrogen atoms and are increasing with rising temperature. This indicates the adamantyl group is undergoing a rapid flipping motion. Reprinted with permission from reference ^[107]. Copyright © 2016 Royal Society of Chemistry.

From the 2D NMR measurement the rate constant for the dynamic motion of the adamantyl group was calculated to be $k \approx 150 \text{ s}^{-1}$ at 298 K. For comparison, all further discussed rate constants were determined at the same temperature of 298 K.

In further experiments, the presence of the dynamic motion in the palladium-containing coordination cage was investigated. To our surprise, the flipping movement of the adamantyl group occurs also in the self-assembled $[\text{Pd}_2\text{L}^2_4]$ coordination cage (see Figure 4.8).

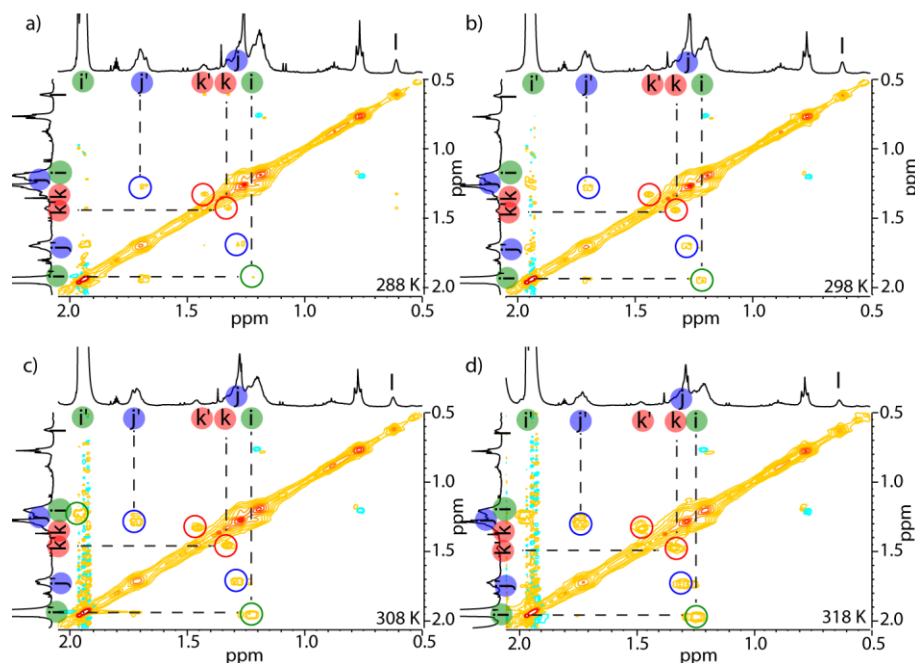


Figure 4.8 ^1H - ^1H NOESY spectra of cage $[\text{Pd}_2\text{L}^2_4]$ (500 MHz, CD_3CN , 0.5 s mixing time) at different temperatures: a) 288 K, b) 298 K, c) 308 K and d) 318 K. The intensities of the highlighted exchange signals between inward (i' , j' and k') and outward (i , j , k) pointing protons are increasing with rising temperature. Reprinted with permission from reference ^[107]. Copyright © 2016 Royal Society of Chemistry.

The rate constant of the dynamic movement could be determined *via* variable temperature (VT) ^1H - ^1H NOESY NMR measurements and the activation parameters were calculated by the Eyring plot method (see *Experimental Section*). The flipping motion inside the coordination cage is with $k \approx 0.32 \text{ s}^{-1}$ (see Figure 4.9 b and section 7.5.4.2) significantly slowed down with respect to the free ligand. Due to the crowded environment in the coordination cage, a decrease of the flipping rate is understandable. Reason for this deceleration is an unfavorable entropic contribution in the cage ($\Delta S_{\text{cage}}^\ddagger = -164.5 \text{ J}\cdot\text{mol}^{-1}\cdot\text{K}^{-1}$) in comparison to the free ligand ($\Delta S_{\text{ligand}}^\ddagger = 11.4 \text{ J}\cdot\text{mol}^{-1}\cdot\text{K}^{-1}$). Considering the enthalpic contribution, the flipping process inside the cage seems to be favored over flipping in the free ligand ($\Delta H_{\text{ligand}}^\ddagger = 64.0 \text{ kJ}\cdot\text{mol}^{-1}$ vs. $\Delta H_{\text{cage}}^\ddagger = 26.9 \text{ kJ}\cdot\text{mol}^{-1}$). A computational study performed by *Prof. Mata* and coworkers supported the experimental results. The activation barrier for the flipping movement in the free ligand L^2 could be calculated to be $\Delta G_{298,\text{calc}}^\ddagger = 56.6 \text{ kJ}\cdot\text{mol}^{-1}$, which is in good agreement with the experimental value of $\Delta G_{298,\text{exp}} = 60.6 \text{ kJ}\cdot\text{mol}^{-1}$, which was extracted from the NMR data. Furthermore, the two degenerate minimum conformations of ligand L^2 and the transition state of the flipping mechanism were computed and are illustrated in Figure 4.9a (left side). The computed transition state showed a

nearly planar configuration of ligand L^2 , where the acridone backbone, the attached pyridine arms and the adamantyl groups are arranged in the same plane. In contrast, the degenerate minima show a twisted structure, where the adamantyl group is bent to one side and the pyridine residues are bent towards the opposite side.

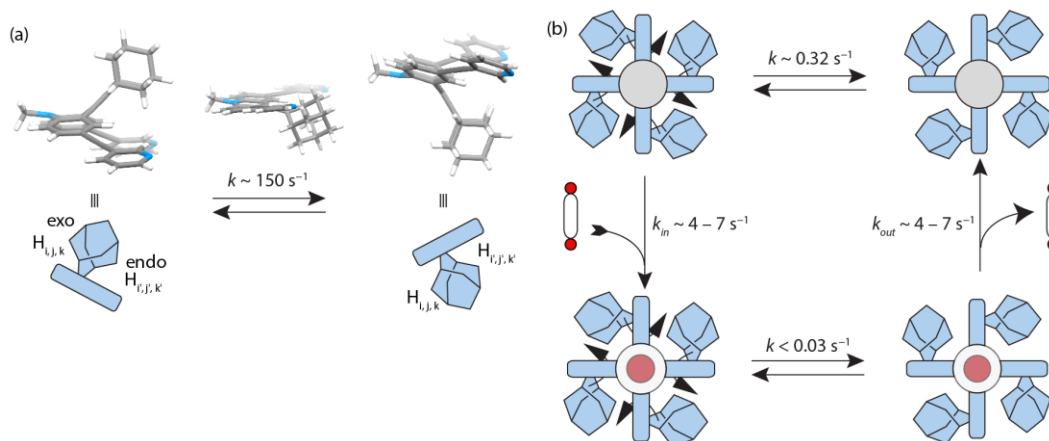


Figure 4.9 Flipping rate constants in ligand L^2 , coordination cage $[Pd_2L^2_4]$ and host-guest complexes $[G^1@Pd_2L^2_4]$ and $[G^2@Pd_2L^2_4]$. (a) Depiction of the degenerate minimum conformations of ligand L^2 and the calculated transition state. The flipping rate constant of the free ligand L^2 was experimentally determined to $k \approx 150 \text{ s}^{-1}$ at 298 K. (b) The flipping rate constant in the 'empty' $[Pd_2L^2_4]$ cage was determined to $k \approx 0.32 \text{ s}^{-1}$. After addition of bis-anionic guests G^1 or G^2 , the rate constant decreased to $k < 0.03 \text{ s}^{-1}$. Reprinted with permission from reference ^[107]. Copyright © 2016 Royal Society of Chemistry.

To understand the mechanism of the flipping dynamics of the adamantyl group within the densely packed coordination cages, four possible mechanisms are plausible (see Figure 4.10):

- full dissociation of one ligand, followed by flipping of all adamantyl groups in the temporary, sterically relaxed $[Pd_2L^2_3]$ fragment and finally recomplexation of the free ligand and reformation of the $[Pd_2L^2_4]$ cage
- one side detachment of one ligand, subsequent flipping of all adamantyl groups and recomplexation
- concerted flipping of all four adamantyl groups passing each other simultaneously in the center of the cage
- sequential flipping of each adamantyl groups in the complete cage

To deduce the most likely mechanism, several experiments were performed. First, a 1H EXSY experiment of a mixture of L^2 and $[Pd_2L^2_4]$ was performed and evaluated. Since no exchange between these two species could be observed on the NMR time scale, a complete decomplexation of one of the ligands (suggestion a) can be excluded (see Figure 7.134 in the experimental section).

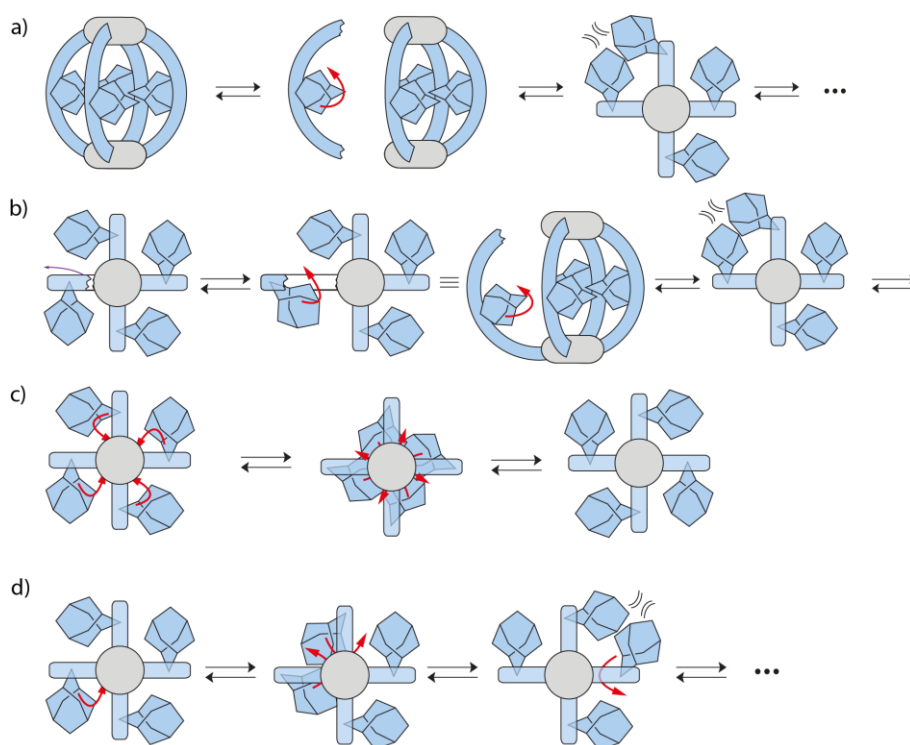


Figure 4.10 Possible mechanism for flipping movement a) full decomplexation of one ligand b) one-side decomplexation c) concerted flipping and d) sequential flipping.

For a square-planar coordinated palladium complexes, ligand exchange proceeds *via* an associative mechanism.^[128] The addition of a competing ligand would increase the ligand exchange mechanism. If the flipping mechanism of the adamantyl group occurred after a one-side dissociation of one of the ligands, the addition of a competing ligand would accelerate the rate. Therefore, pyridine (1 or 5 equivalents) was added as a competing ligand to the $[\text{Pd}_2\text{L}^2_4]$ coordination cage and ^1H - ^1H NOESY NMR measurements were performed. The determined rate constant of the flipping dynamic in this mixture was determined to be $k \approx 0.25 \text{ s}^{-1}$ at 298 K (see Figure 7.135). Compared to the rate constant of the “empty” coordination cage $[\text{Pd}_2\text{L}^2_4]$ ($k \approx 0.32 \text{ s}^{-1}$ at 298 K) the values are very similar, indicating a negligible influence of the competing pyridine ligand.

Furthermore, the influence of the coordination cation on the flipping dynamic was studied. As already know, the pyridine-platinum bond is kinetically more stable than the palladium analogue,^[129] so the rate constant of the flipping dynamic was investigated for the analogue platinum coordination cage. The $[\text{Pt}_2\text{L}^2_4]$ cage was prepared by heating a solution of ligand L^2 with *cis*-bis(acetonitrile)dichloroplatinum(II) and silver(I) perchlorate at 80 °C in deuterated acetonitrile for 3 days. The ^1H - ^1H NOESY NMR measurements at different temperatures proved the occurrence of the flipping dynamic even in the $[\text{Pt}_2\text{L}^2_4]$ cage. The flipping rate at 298 K was determined to be $k \approx 0.13 \text{ s}^{-1}$, which is similar in magnitude to that of the palladium cage (see Figure 7.128). Taken together, these performed experiments rule out that a partial dissociation pathway is involved in the flipping mechanism of the adamantyl groups in the cationic coordination cage (suggestion b).

Further experimental proof which could differentiate between a concerted (suggestion c) or sequential flipping (suggestion d) is hard to give. Nevertheless, a concerted flipping of all adamantyl

groups at the same time is very unlikely due to the steric bulk of the residues. It seems that there is not enough space in the interior of the cage to host all four adamantyl groups. Therefore, a flipping in a sequential movement (suggestion d) seems most likely (see Figure 4.10).

4.4 Host-guest Chemistry

Generally, $[\text{Pd}_2\text{L}_4]^{2+}$ coordination cages with banana-shaped ligands are known to encapsulate guest molecules in their central cavity and form host-guest complexes. Mostly, incorporation of anionic guests were observed and investigated in various systems.^{[42][43]} Therefore, the next step was to explore the host-guest chemistry of the novel $[\text{Pd}_2\text{L}_4]^{2+}$ coordination cage with different mono- and bis-anionic guests **G** (**G**¹-**G**⁹) (see Figure 4.11)

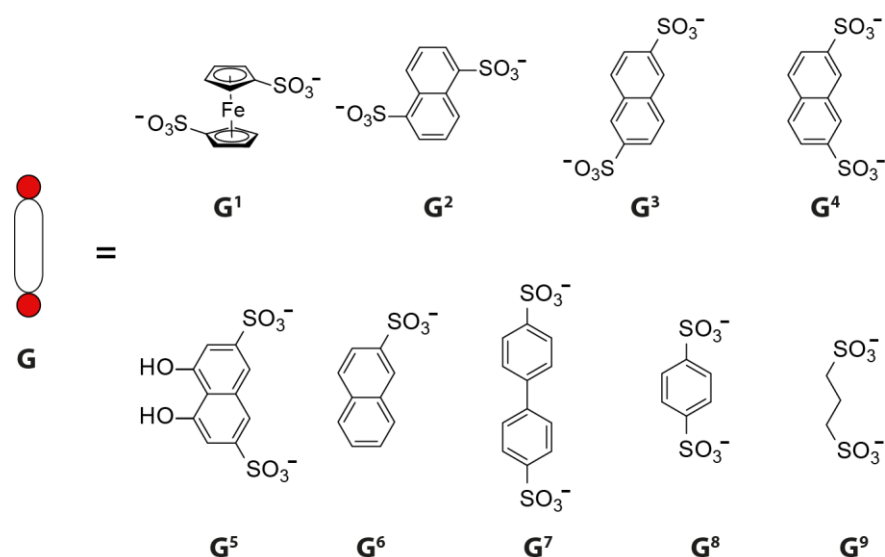


Figure 4.11 Structures of various guest molecules encapsulated by coordination cage $[\text{Pd}_2\text{L}_4]$. Reprinted with permission from reference ^[107]. Copyright © 2016 Royal Society of Chemistry.

The cavity volume of the novel $[\text{Pd}_2\text{L}_4]$ coordination cage was calculated with the software VOIDOO^[92] to be $\sim 321 \text{ \AA}^3$ (for further information on the calculation, see Chapter 7.5.7.4). Visualization with the software PyMol^[130] showed a dumbbell-shaped molecular volume of the cavity, with a smaller diameter around the center of the coordination cage in the immediate vicinity of the adamantyl groups (see Figure 4.12).

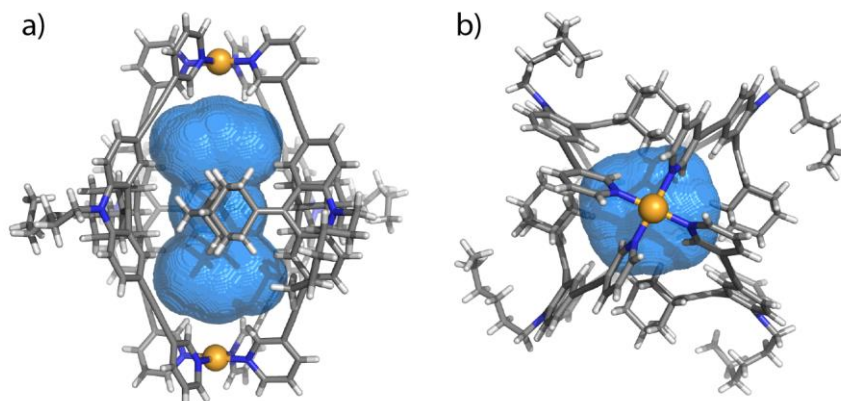


Figure 4.12 Visualization of the central cavity of the $[\text{Pd}_2\text{L}^{24}]$ coordination cages: a) side and b) top view. *Color scheme:* C: gray; N: blue; Pd: orange, H: white.

Due to this calculation and the tremendous steric bulk of the four equatorial adamantyl groups inside the host structure, it was expected, that only thin guest molecules (e.g. based on an alkyl chain) could be incorporated inside the self-assembled coordination cage. Surprisingly, also quite bulky guests were found to bind inside the host. NMR spectroscopy (see Figure 4.5 and experimental Chapter 7.5.2), HR ESI mass spectrometry (Figure 4.6) and single X-ray analysis (see Chapter 4.6) verified the formation of the individual host-guest complexes $[\mathbf{G}@\text{Pd}_2\text{L}^{24}]$.

The binding behavior is influenced by the size and the charge of the tested guest molecule. After addition of the respected bis-anionic guest ($\mathbf{G}^1\text{-}\mathbf{G}^5$) to the preassembled cage, a new set of signals could be observed in the ^1H NMR spectra, which corresponds to the formed host-guest complex $[\mathbf{G}^{1-5}@\text{Pd}_2\text{L}^{24}]$. In all cases, the ^1H NMR spectrum showed noticeable changes of the chemical shift of all inward pointing protons (H_g , H_i , H_j and H_k), which indicated the encapsulation of the anionic guest molecules inside the cationic coordination cage (see Figure 4.5c-d, and Chapter 7.5.2). Furthermore, a set of new signals appeared in the ^1H NMR spectrum, which corresponds to the encapsulated guest. It is noteworthy, that all signals of the incorporated guest molecules are sharp and shifted downfield in comparison to the free guest. The high-resolution ESI(+) mass spectra showed signals corresponding to the host-guest systems $[\mathbf{G}^{1-5}@\text{Pd}_2\text{L}^{24}]^{2+}$ which was further confirmed by the corresponding experimental isotopic patterns in perfect agreement with the calculated peak distributions (see Figure 4.6b–c and experimental section 7.5.2 for further analytical data). In the following paragraph, the incorporation of guest molecule \mathbf{G}^1 (1,1'-ferrocene bis(sulfonate)) will be discussed in greater detail. The addition of the bis-anionic ferrocene guest leads to a shift of all proton signals of the coordination cage. Signals assigned to protons H_g , H_i and H_j are shifted downfield ($\Delta\delta = 0.63$ ppm for H_g ; and $\Delta\delta = 0.08$ ppm for H_i) and H_h , H_j , and H_k are shifted upfield ($\Delta\delta = 0.12$ ppm for H_h ; and $\Delta\delta = 0.27$ ppm for H_k). The free guest \mathbf{G}^1 shows two signals in the ^1H NMR spectra (see Figure 7.110 and Figure 7.111), assigned to the cyclopentadienyl protons in α and β position relative to the sulfonate substituent. Upon encapsulation of the guest \mathbf{G}^1 inside the $[\text{Pd}_2\text{L}^{24}]$ -host, the signals are split twofold. The reason for this splitting is the loss of symmetry

of the C_{2h} -symmetric ferrocene derivate (*anti* conformation) once incorporated inside the coordination cage. However, the number of cage signals in the NMR spectrum does not change after encapsulation of the bis-anionic guest, indicating a fast rotation of the anionic guest molecule G^1 inside the cavity of the host relative to the NMR time scale.

Ferrocene is a common compound which is used as an internal standard for electrochemical measurements.^[131] Therefore, cyclic voltammetry (CV) measurements of the free anionic ferrocene guest G^1 and the host-guest complex $[G^1@Pd_2L_2^4]$ were performed. It could be shown, that the Fe(II)/Fe(III) redox-potential of G^1 is anodically shifted upon encapsulation in the $[Pd_2L_2^4]$ cage (see Figure 4.13). This suggests that the cationic coordination cage disfavors the removal of one electron from the encapsulated ferrocene guest molecule G^1 . This observation is in accordance with a previously conducted study on a similar host-guest complex.^[62]

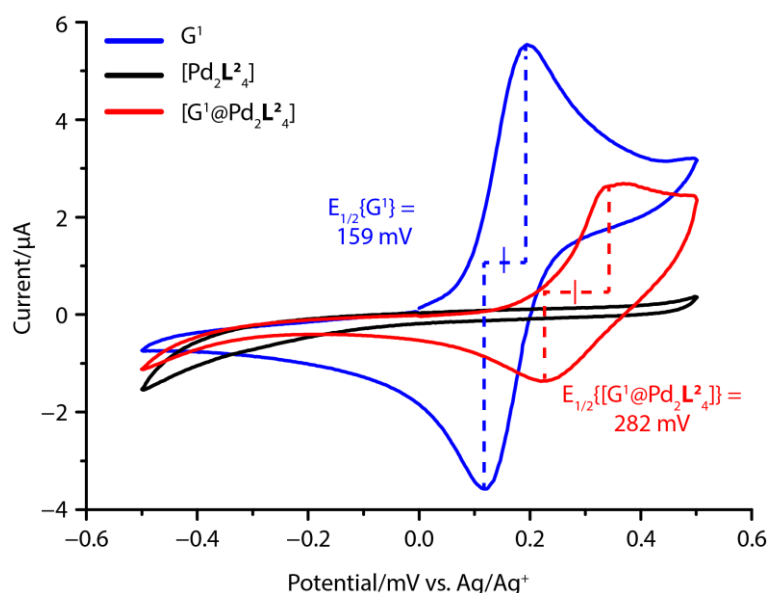


Figure 4.13 Cyclic voltammograms (CV) of the free guest G^1 (blue), the coordination cage $[Pd_2L_2^4]$ (black) and the host-guest complex $[G^1@Pd_2L_2^4]$ (red) at 298 K, 0.07 mM, 0.1 M NBu_4PF_6 , scan rate 0.1 Vs^{-1} (potentials given against an $Ag/AgNO_3$ reference electrode; $[AgNO_3] = 0.001 \text{ M}$). While the cage $[Pd_2L_2^4]$ does not show a redox reaction in the examined potential range, the encapsulated guest G^1 shows an anodic shift of 123 mV for $E_{1/2}(Fe^{II/III})$ with respect to free guest G^1 . Inside the cationic coordination cage $[Pd_2L_2^4]$ it becomes more difficult to oxidize the guest.

Due to the steric bulk of the cationic coordination cage and the substantial size of the bis-anionic guest molecules (G^1 - G^5) close contacts between the host and the guest are expected. Indeed, 1H - 1H NOESY NMR measurements and X-ray structural analysis reveal close contacts between the guest molecules and the adamantyl groups in the equatorial region of the cage cavity. Figure 7.130 in the experimental section highlights close contacts between the protons of the guest G^2 (H_A , H_B , H_C) and the inward pointing protons of the adamantyl group (H_i , H_j , H_k).

After addition of one equivalent of guest molecules G^1 - G^5 to the coordination cage, all signals of the empty $[Pd_2L_2^4]$ cage disappear and only signals of the host-guest complexes $[G^{1-5}@Pd_2L_2^4]$ are observed in the 1H NMR spectrum. Thus, guests G^1 - G^5 are strongly bound in the host. The association constant is estimated to be larger than 10^4 to 10^5 L mol^{-1} and the exchange between free and encapsulated guest is slow on the NMR timescale.

In contrast, guests **G**⁶-**G**⁹ show fast exchange with the solution and the interior of the [Pd₂L₂]₄ cage, which is indicated by gradual shifting of all proton signals upon addition of increasing amount of guest solution to the coordination cage. Because more than one equivalent of guest (**G**⁶-**G**⁹) is necessary to saturate the cage, one can conclude that the binding affinity of these guests is lower than that of the guests **G**¹-**G**⁵. Determination of reliable association constants was not possible, because the addition of more than 1.5 equivalents of the respective guest resulted in decomposition of the cage and the precipitation of free ligand L².

The different binding behaviors of the investigated anionic guests in the coordination cage can be rationalized by the differences in the guest structures. Guest molecules **G**¹-**G**⁵ possess two sulfonate groups (bis-anionic) and have an adequate size for uptake inside the host structure.^[62] In contrast, the other guest are either too small (**G**⁸ and **G**⁹), too large (**G**⁷) or lack a second sulfonate group (**G**⁶) to be encapsulated strongly inside the [Pd₂L₂]₄ cage (see Figure 4.11 for schematic representation of the guest molecules).

The exchange rates of the guest molecules **G**¹ and **G**², respectively were determined via an EXSY NMR experiment. From a sample of a 50:50 mixture of the empty [Pd₂L₂]₄ cage and the host guest complex [**G**¹/**G**²@Pd₂L₂]₄ the rate constant could be determined to be $k \approx 7 \text{ s}^{-1}$ for [**G**¹@Pd₂L₂]₄ and $k \approx 4 \text{ s}^{-1}$ for [**G**²@Pd₂L₂]₄ (see Figure 4.9b and Experimental section 7.5.4.6 about EXSY Measurements). This result is compared with the exchange kinetics of guest **G**¹ in the previously reported monomeric coordination cage, composed of the dibenzocycloheptatriene-based ligand L^{2*}.^[47] This ligand is of similar length and backbone structure, but does not have a bulky adamantyl group like ligand L². The exchange rate of the 1,1'-ferrocene bis(sulfonate) (**G**¹) was determined via an ¹H NMR titration experiment to be $k \approx 90 \text{ s}^{-1}$ (see Figure 7.124). Thus, it is assumed, that the sterically demanding adamantyl groups block the access to the inner cavity of the coordination cage resulting in a decrease of the exchange rate of guest molecules **G**¹. Furthermore, it is hypothesized, that the adamantyl groups also contribute to the thermodynamic stabilization of the guest molecule inside the host. Further discussion about the contribution of non-covalent interaction are explicated in Chapter 4.7.

4.5 Guest Effect on Flipping Dynamics

As described in the previous Chapters, the self-assembled [Pd₂L₂]₄ cage shows an interesting dynamic motion of the adamantyl groups and a rich host-guest chemistry (encapsulation of a large selection of bis-anionic guest molecules, see Chapter 4.4). In a further study, the influence of the guest uptake on the flipping rate of the steric adamantyl groups was investigated. The rate constant of the dynamic motion in the [**G**¹@Pd₂L₂]₄ and [**G**²@Pd₂L₂]₄ host-guest complexes was measured via high resolution NMR spectroscopy on a 900 MHz machine from Dr. M. John (2D NOESY measurement at 298 K, see Figure 7.129 and Figure 7.130). As a counter cation [K(18-crown-6)]⁺ was used, since the ¹H NMR signals of the NBu₄⁺ species overlapped with relevant ligand signals. The

rate constants of the flipping motion of the adamantyl groups in the host-guest systems $[\mathbf{G}^1@Pd_2L_2^4]$ and $[\mathbf{G}^2@Pd_2L_2^4]$ were determined to be $k < 0.03 \text{ s}^{-1}$ and $k < 0.02 \text{ s}^{-1}$, respectively. When compared, with the rate constant in the tetrafluoroborate-containing $[Pd_2L_2^4]$ cage ($k < 0.32 \text{ s}^{-1}$), the flipping dynamics in the host guest systems are more than ten times slower. The exchange rate of the guests \mathbf{G}^1 and \mathbf{G}^2 were determined to be in the range of $k \approx 4\text{-}7 \text{ s}^{-1}$ (see Chapter 4.4), which is several hundred times faster than the flipping motion. Thus, it can be assumed that a flipping of the adamantyl groups does not occur while the host-guest complex is intact. Instead, the bis-anionic guest will leave the cage, before the adamantyl groups undergo the flipping motion.

4.6 X-ray Structure Analysis

The formation of the supramolecular $[Pd_2L_2^4]$ coordination cage and the corresponding host-guest complexes $[\mathbf{G}^{1-5}@Pd_2L_2^4]$ in solution were confirmed *via* intensive NMR spectroscopy and HR-MS spectrometry. Furthermore, the presence of these structures in the solid state were examined with X-ray radiation. Single crystals of $[Pd_2L_2^4]$ suitable for X-ray structure determination were grown by slow vapor diffusion of diethyl ether into an acetonitrile solution (0.7 mM) of the self-assembled cage. *PD Dr. B. Dittrich* and co-workers collected diffraction data for all crystals at the SLS synchrotron source.

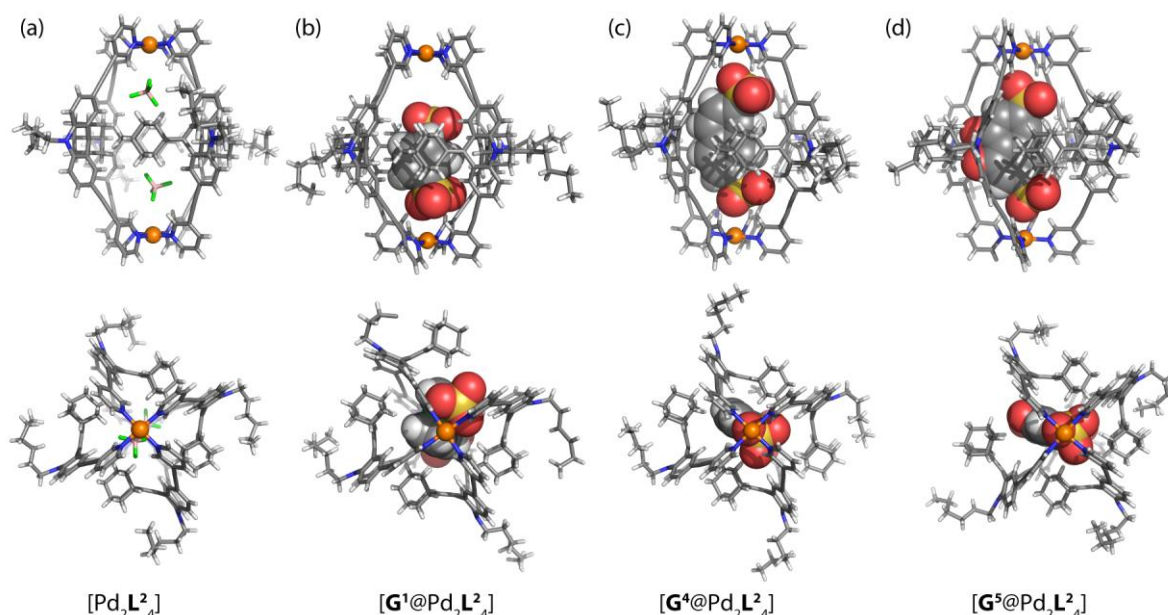


Figure 4.14 X-ray crystal structures of (a) $[Pd_2L_2^4]$, (b) $[\mathbf{G}^1@Pd_2L_2^4]$, (c) $[\mathbf{G}^4@Pd_2L_2^4]$ and (d) $[\mathbf{G}^5@Pd_2L_2^4]$. *Color scheme:* C, grey; N: blue; O: red; S: yellow; F: green; B: salmon; Pd: orange Fe: forest green. For clarity, solvent molecules and free (non encapsulated) anions are omitted. Appendix section 7.5.5 and CCDC numbers 1053080-83 contain details of the crystallographic data. Reprinted with permission from reference ^[107]. Copyright © 2016 Royal Society of Chemistry.

The cationic coordination cage $[Pd_2L_2^4]$ crystalized in the triclinic space group $P\bar{1}$ with unit cell dimension of $a = 16.196(3)$, $b = 16.375(3) \text{ \AA}$ and $c = 17.065(3) \text{ \AA}$. The central cavity of the supramolecular assembly is occupied by two tetrafluoroborate anions, which are positioned in close

proximity to the Pd(II) cation (~ 4.1 Å from Pd(II) to the boron atom). The Pd-Pd distance in the monomeric coordination cage was measured to be 16.20 Å (see Figure 4.14). A fact worth discussing is the arrangement of the ligand within the cage structure. Due to the attachment of the sterically demanding adamantyl group, the ligand shows a remarkable bent shape. This arises from a strong deformation of the tricyclic acridone backbone, in which the central ring arranges in a boat conformation. The connecting double bond between the acridone backbone and the adamantyl residue is not bent. Thus, all six carbon atoms constituting the tetra-substituted double bond system occupy a common plane.

In the cage structure, all adamantyl groups are bent to one side with radial symmetry and block the openings of the supramolecular assembly. The crystal structure is highly packed and short inter-ligand distances are found. For example, proton H_a from one ligand and proton H_j from the neighboring ligand are only 3.11 Å apart.

The central cavity of the coordination cage provides a rather spacious environment close to the Pd(pyridine)₄-planes. These spaces are occupied by the tetrafluoroborate counter anions. In contrast, the bulky adamantyl groups reach into the center of the cage cavity, which results in a quite narrow channel with a diameter of about 6.3 Å (see appendix section 7.5.5 for further views of the X-ray structure).

In addition, single crystals of the host-guest systems [**G**¹@Pd₂L₂⁴], [**G**⁴@Pd₂L₂⁴] and [**G**⁵@Pd₂L₂⁴] were obtained by slow vapor diffusion of methanol (for [**G**¹@Pd₂L₂⁴]), benzene (for [**G**⁴@Pd₂L₂⁴]) and diethyl ether (for [**G**⁵@Pd₂L₂⁴]) into acetonitrile solutions (0.7 M) of these supramolecular assemblies. The crystal structures of the host-guest complexes confirm the encapsulation of the bis-anionic guest molecules **G**¹, **G**⁴ and **G**⁵ (see Figure 4.14b-d). The negatively charged sulfonate groups of the guest molecules are in close proximity to the positively charged Pd(II) cations. The palladium-sulphur distances in the [**G**⁵@Pd₂L₂⁴] host-guest complex are 4.42 Å and 4.03 Å (similar values were measured for [**G**⁴@Pd₂L₂⁴]). Due to the smaller size of the ferrocene-based guest **G**¹, only one sulfonate group shows a close Pd-S contact of 4.12 Å. The distance between the second sulfonate group and the palladium(II) cation was measured to be 6.73 Å. Surprisingly, the encapsulation of the ionic guest molecules inside the central cavity of the coordination cage forced the adamantyl groups of the ligand to bend further towards the outside of the cage (see Figure 4.14 b-d and Table 4.1). According to DFT computational results (performed from *Prof. Dr. R. Mata* and coworkers), this guest-induced overstretching of the ligand should not cost an energetic penalty of more than 4 kJ·mol⁻¹. In the “empty” [Pd₂L₂⁴] cage, the average distance between the adamantyl sp²-carbon atom and the center of the cage is 5.3 Å, while in the host-guest complex [**G**¹@Pd₂L₂⁴] the distance is 6.0 Å. In addition, the size of the cage shrinks along the Pd-Pd axis. For example from 16.2 Å for [Pd₂L₂⁴] to 16.0 Å in the [**G**¹@Pd₂L₂⁴] complex. The packing coefficient (PC) of the three encapsulated guest molecules **G**^{1,4,5} are calculated to be PC ~ 70-80 %, which exceeds Rebek’s rule of 55 %, ^[132] indicating the formation of a densely packed complex.

In conclusion, the more bulky guests push the adamantyl groups further away from the center of the cage, which results in an overall shortening of the cage along the palladium axis. The cage

seems to be a flexible container, which can adapt to the size and shape of the “cargo” (see Table 4.1 for selected distances extracted from the X-ray structure analysis).

Table 4.1 Selected distances extracted from the X-ray structures of $[\text{Pd}_2\text{L}_2^4]$ and some of its host-guest complexes.

	$[\text{Pd}_2\text{L}_2^4]$	$[\text{G}^4@ \text{Pd}_2\text{L}_2^4]$	$[\text{G}^5@ \text{Pd}_2\text{L}_2^4]$	$[\text{G}^1@ \text{Pd}_2\text{L}_2^4]$
$V_{\text{guest}} [\text{\AA}^3]^a$	109.7	226.2	239.0	256.1
$d_{\text{ada}}-d_{\text{center}} [\text{\AA}]^b$	5.4^d	6.1	6.9	6.8
	5.3	5.5	5.5	5.8
	5.2	5.0	5.4	5.7
	5.2	5.0	5.1	5.6
average distance [\AA]	5.3	5.4	5.7	6.0
Pd–Pd distance [\AA]	16.2	16.2	15.9	16.0
PC [%] ^c	34	70	74	80

^a calculated from the DFT (B3LYP/6-31G*)^[133] structure of the anions, ^b distance between adamantyl sp^2 -C atom and the center of the cage as defined by the middle of the line connecting the two palladium atoms, ^c The packing coefficient (PC) was calculated as the quotient of $V_{\text{guest}}/V_{\text{cavity}} \cdot 100$. The volume of the cavity was calculated using VOIDOO (details see experimental section p. 162), ^d the longest distance each is highlighted in bold font.

4.7 Analyses of Non-covalent Interactions

As already described in Chapter 4.6, short interactions between the coordination cage and the encapsulated guest were observed in the X-ray structure, with intermolecular distances between 2.0 and 3.0 \AA . These close contacts in the supramolecular host-guest complex were visualized *via* a *Hirshfeld* surface analysis with the software *Crystal Explorer*.^[134] The *Hirshfeld* surfaces were mapped with a *Van-der-Waals*-radius-normalized distance d_{norm} around the guest molecules for host-guest complexes $[\text{G}^1@ \text{Pd}_2\text{L}_2^4]$ and $[\text{G}^5@ \text{Pd}_2\text{L}_2^4]$, respectively (see Figure 4.15a and b).

Close contacts, contributing to the stabilization of the host-guest complex are highlighted in red. Major contacts between the sulfonate oxygen atoms and the inward pointing pyridine hydrogen atoms were found. Formation of the metal containing coordination complex leads to the polarization of the pyridine protons, which can serve as hydrogen bond donors (which is also expressed by the changes in their ^1H NMR chemical shifts upon guest binding, see Figure 4.5). Furthermore, close contacts between the guests' hydrogen substituents or π -faces and the surrounding adamantyl hydrogens were observed. This is no surprise, since close contacts could be detected *via* ^1H - ^1H NOESY measurements and X-ray structure analysis. The *Hirshfeld* surface analysis supports the experimental results for this dense packing inside the sterically congested cage. Further element-filtered surface pictures and fingerprint plots are given in the experimental section to further visualize the range of non-covalent interactions at the interface of the guest and the surrounding host.

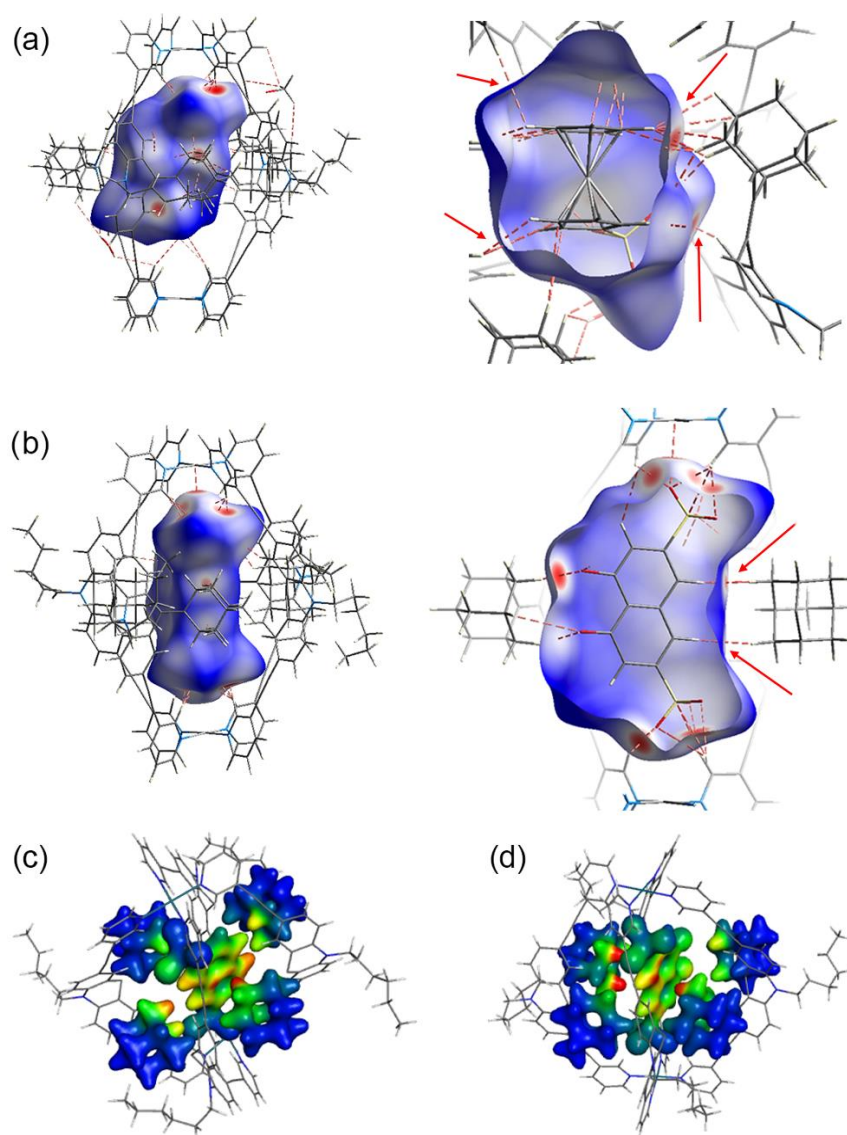


Figure 4.15 Visualization of non-covalent host-guest interaction. *Hirshfeld* d_{norm} surfaces for the guest molecules in (a) $[\mathbf{G}^1@Pd_2L_4]$ and (b) $[\mathbf{G}^5@Pd_2L_4]$ (plotted with isovalues from -0.4 (red: short contact) to 1.4 (blue: long contact); red dotted lines and arrows indicate some close non-hydrogen bond interactions that are shorter than 3.0 \AA). Below: Depiction of dispersion interaction densities (DIDs) between the guests and the surrounding adamantyl groups in (c) $[\mathbf{G}^4@Pd_2L_4]$ and (d) $[\mathbf{G}^5@Pd_2L_4]$ (red: high DID; blue: low DID). Reprinted with permission from reference ^[107]. Copyright © 2016 Royal Society of Chemistry.

Furthermore, *Prof. Dr. R. Mata* and coworkers carried out electronic structure calculations. Aim of these calculations was to obtain a deeper insight into the binding of the guest molecules and the role of dispersion forces in the encapsulation process. The parent cage containing only BF_4^- counter anions as well as two host-guest systems were considered, namely $[\mathbf{G}^4@Pd_2L_4]$ and $[\mathbf{G}^5@Pd_2L_4]$. Initially, the influence of dispersion interaction on the stability of the coordination cage was computed. Calculations at the SCS-LMP2/aug'-cc-pVTZ level of theory^[95–97,135,136] gave a dispersion contribution of $14.3 \text{ kJ}\cdot\text{mol}^{-1}$ for the $[Pd_2L_4]$ system. Furthermore, the dispersion contribution in the $[\mathbf{G}^4@Pd_2L_4]$ host-guest complex was calculated to be $9.3 \text{ kJ}\cdot\text{mol}^{-1}$. Consequently, the contribution in the host-guest complex $[\mathbf{G}^4@Pd_2L_4]$ is $5 \text{ kJ}\cdot\text{mol}^{-1}$ smaller than in the $[Pd_2L_4]$ cage. Due to the guest-induced expansion of the cage, the four ligands are pushed further apart in the host-guest complex and the dispersion contribution declines. Since this effect is rather small and it

will counterbalance the steric repulsion of the adamantyl group, it will not be a major factor in the cage formation itself.

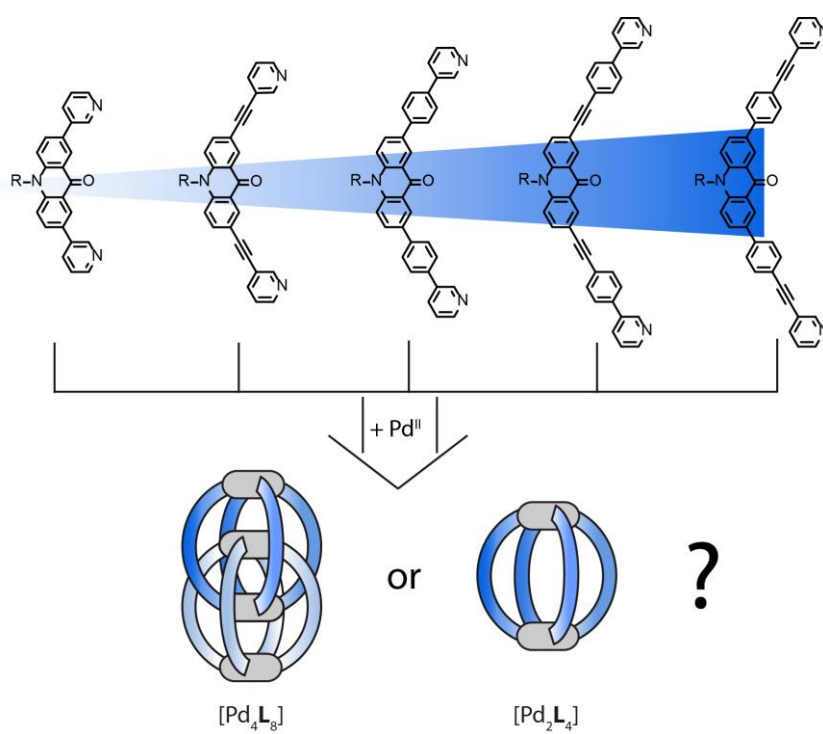
Furthermore, the influence of dispersion forces on the host-guest binding was studied. For the host-guest systems [\mathbf{G}^4 @Pd₂L₂⁴] and [\mathbf{G}^5 @Pd₂L₂⁴] the overall interaction energies between the adamantyl residues and the guest were calculated to be 52.8 kJ·mol⁻¹ and 67.2 kJ·mol⁻¹ (cation-anion interactions were not considered in this calculation). The dispersion energy contributions obtained are 86.3 kJ·mol⁻¹ and 64.0 kJ·mol⁻¹ for [\mathbf{G}^4 @Pd₂L₂⁴] and [\mathbf{G}^5 @Pd₂L₂⁴], respectively. These correspond to a strong contribution in binding, even exceeding the total interaction in the case of [\mathbf{G}^4 @Pd₂L₂⁴]. In the \mathbf{G}^5 incorporated host-guest system [\mathbf{G}^5 @Pd₂L₂⁴], the adamantyl groups are pushed stronger outside and so the relative weight of the van-der Waals forces is reduced. Therefore, it is expected, that the main contributions for the adamantyls' interaction with the guests are *Pauli* repulsion and dispersion, the two of opposite sign. The conducted calculations demonstrate that dispersion forces can easily add up to large values in such a supramolecular assembly.

For a better visualization of this effect, a plot of the Dispersion Interaction Densities (DIDs), calculated between the guest and the four adamantyl units, was prepared (see Figure 4.15c/d and section 7.5.7.3 for a definition of the Dispersion Interaction Density plots). The DID images show the interaction between the π -systems of the guest molecules and the surface of the pocket. This is in accordance with the *Hirshfeld* analysis (see page 62). In particular, some hot spots are identifiable where the adamantyl groups are in close contact with the encapsulated guests.

4.8 Conclusion

This Chapter described the synthesis of the bis-monodentate pyridyl ligand L², which possesses a bulky adamantyl group protruding sideways from its concave face. Addition of square planar metal cations (Pd²⁺, Pt²⁺) leads to the clean formation of the discrete coordination cages [Pd₂L₂⁴] or [Pt₂L₂⁴]. The adamantyl residues occupy the four entries of the cage and part of the internal cavity. In the free ligand fast flipping dynamics of the adamantyl substituent was observed. Surprisingly, the flipping mechanism occurs in the supramolecular coordination cage as well, but at a much lower velocity. The latter process did not require a ligand detachment and a sequential flipping mechanism of all adamantyl groups was postulated. The coordination cage was found to encapsulate different (bis)anionic guest molecules \mathbf{G}^1 - \mathbf{G}^9 inside the center of the supramolecular structure. Guest uptake further decreased the rate constant of the flipping dynamics in the host-guest complexes. Single crystal X-ray structure analyses of the free cage and three host-guest complexes showed that the size of the encapsulated guest influences the overall structure of the supramolecular assembly. The bigger the guest, the further the adamantyl groups are pushed aside and thereby they reduce the Pd-Pd distance (compression of the cage). Furthermore non-covalent contacts between the guest molecules and the host were investigated and substantial contribution of attractive dispersion interactions conveyed by the adamantyl groups was identified.

5 INFLUENCE OF LIGAND LENGTH ON CAGE FORMATION



5.1 Introduction

The outcome of a self-assembly process between organic ligands and metal cations depends on several factors. Most important influence factors are the type of ligand (e.g. geometry, size, flexibility, coordination site) and metal cations. In addition, choice of solvents, kind and concentration of counter anions and temperature influence the topology of the self-assembled coordination structure (see Chapter 1.3). Thus, small variations can make a significant impact on the resulting supramolecular structure.

In the previously described example, an interpenetrated coordination cage is formed as the thermodynamic product after mixing eight banana-shaped ligands **L**¹ with four square planar palladium(II) cations. The coordination cage is activated by halide anions to encapsulate neutral guest molecules inside its central pocket. Ligand **L**¹ contains an acridone backbone, which is connected *via* an ethynyl bridge to the coordinating pyridine residues. In the following Chapter, the influence of the size of the organic ligand the cage formation will be studied. A series of new ligands containing different bridging groups (e.g. aryl) will be synthesized and the self-assembly towards supramolecular cage structures investigated. Furthermore, the resulting structures will be tested for their ability to form host-guest complexes with anionic and neutral guests.

5.2 Results and Discussion

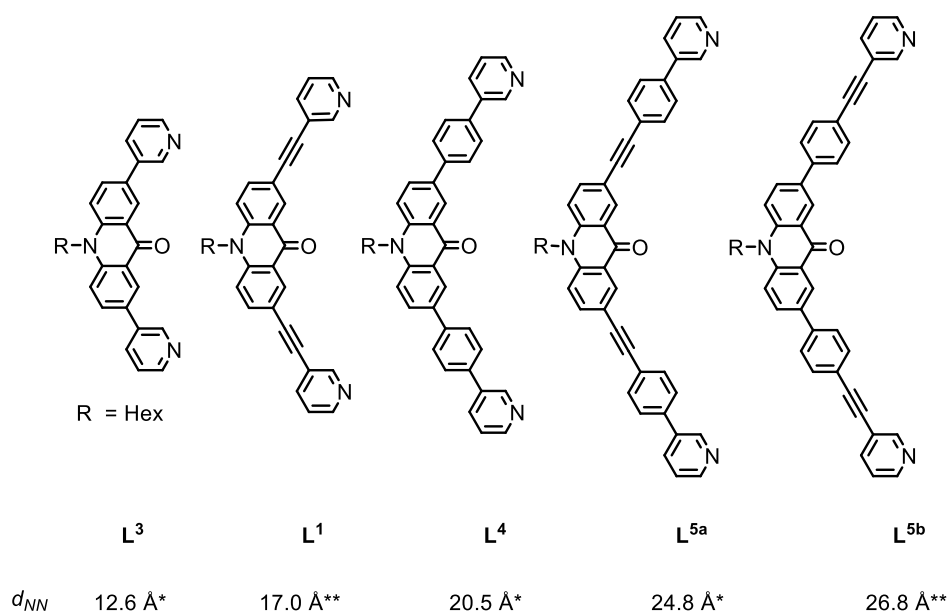


Figure 5.1 Schematic representation of different synthesized ligands **L**¹, **L**³, **L**⁴ and **L**^{5a/b} with nitrogen-nitrogen distances d_{NN} . * Values obtained from a molecular model (DFT B3LYP/6-31g(d)); ** values obtained from X-ray structure analysis.^[137]

Ligand **L**³ with a N-N distance of 12.6 Å was synthesized *via* a Suzuki coupling reaction from 2,7-dibromo-10-hexylacridone with 3-pyridineboronic acid 1,3-propanediol ester in 62 % yield (for the synthetic protocol and characterization data see Chapter 7.6). To a solution of ligand **L**³ (1.0 eq.) in deuterated acetonitrile, a solution of tetrakis(acetonitrile)palladium(II) tetrafluoroborate (0.5 eq.)

was added. The reaction mixture was heated in a closed vial for 1 h at 70 °C. Subsequent ^1H NMR analysis shows one set of sharp signals, which are shifted downfield compared to the signals of free ligand, indicating the formation of a single new symmetric species (see Figure 5.2a and b). Especially, signals assigned to the pyridine protons are shifted downfield, which indicated the coordination of the nitrogen donors to the positively charged palladium(II) cations ($\Delta\delta = 0.77$ ppm for H_g , $\Delta\delta = 0.62$ ppm for H_i). Prolonged heating at 70 °C over night did not change the outcome of the reaction, verifying that the resulting species is the thermodynamically stable product. HR-ESI mass spectrometric analysis clearly showed the formation of the self-assembled $[\text{Pd}_2\text{L}^3_4]^{4+}$ coordination cage by exhibition a series of species $[\text{Pd}_2\text{L}^3_4+n\text{BF}_4]^{(4-n)+}$ ($n = 0-2$) containing a variable number of tetrafluoroborate counter anions (see Figure 5.4a).

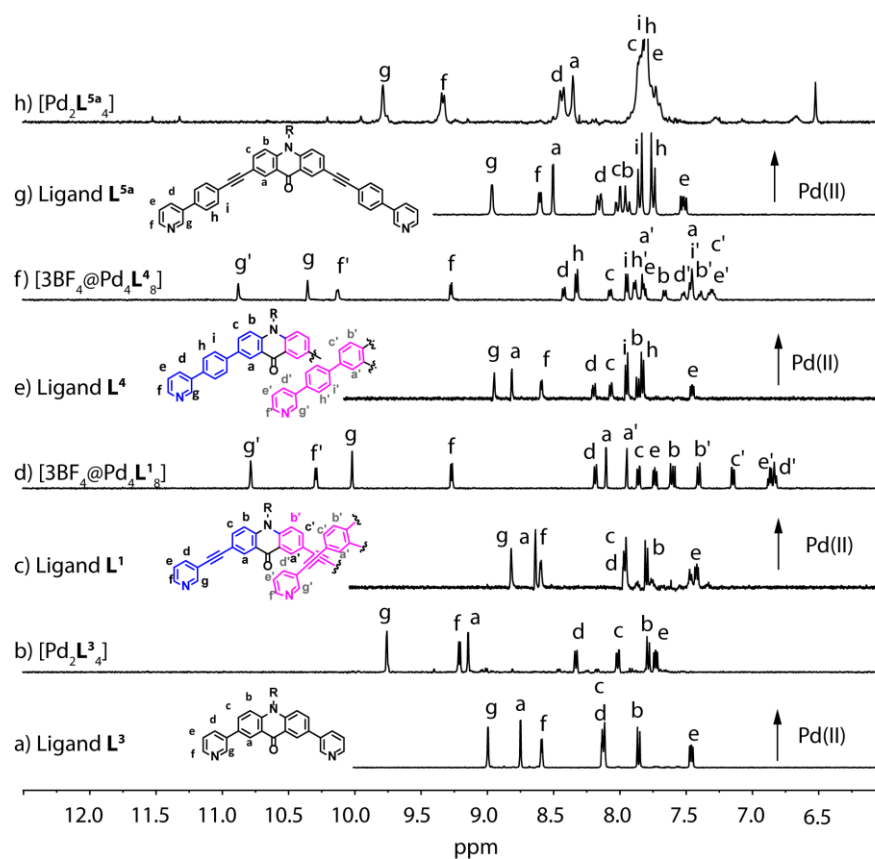


Figure 5.2 ^1H NMR spectra of a) ligand L^1 , b) monomeric $[\text{Pd}_2\text{L}^3_4]$ cage, c) ligand L^1 , d) interpenetrated coordination cage $[\text{3BF}_4@\text{Pd}_4\text{L}^1_8]$, e) ligand L^4 , f) interpenetrated cage $[\text{3BF}_4@\text{Pd}_4\text{L}^4_8]$, g) ligand L^{5a} and monomeric cage $[\text{Pd}_2\text{L}^{5a}_4]$. (500 MHz, CD_3CN , 323 K for a-f and 300 MHz, DMSO-d_6 , 298 K for g and h).

Since no crystals suitable for crystallographic analysis could be obtained, the structure of the monomeric $[\text{Pd}_2\text{L}^3_4]$ cage was calculated by geometry optimization *via* a gas-phase DFT calculation (B3LYP/ C, H, N, O = 6-31g(d)/Pd LANL2DZ) using Gaussian 09^[138] (see Figure 5.3). The model showed a Pd-Pd distance of 12.48 Å, which is too short to form the interpenetrated $[\text{Pd}_4\text{L}^3_8]$ analogue under the applied conditions (CD_3CN , BF_4^- counteranions). These results are in accordance with findings for the dibenzosuberone-^[75] and phenothiazine-^[78] based systems, where similar short ligands also formed an $[\text{Pd}_2\text{L}_4]$ cage as the thermodynamic product.

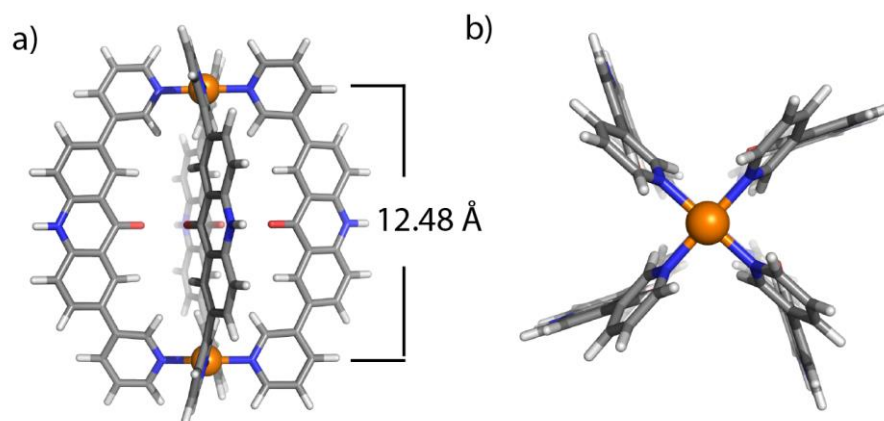


Figure 5.3 a) Side view and b) top view along the Pd-Pd axis of the DFT model of the monomeric cage $[\text{Pd}_2\text{L}^3]_4^{4+}$. *Color scheme*: C: light/dark gray; N: blue; O: red; Pd: orange, H: white. Anions and solvents were omitted and the hexyl chain was substituted by a hydrogen atom.

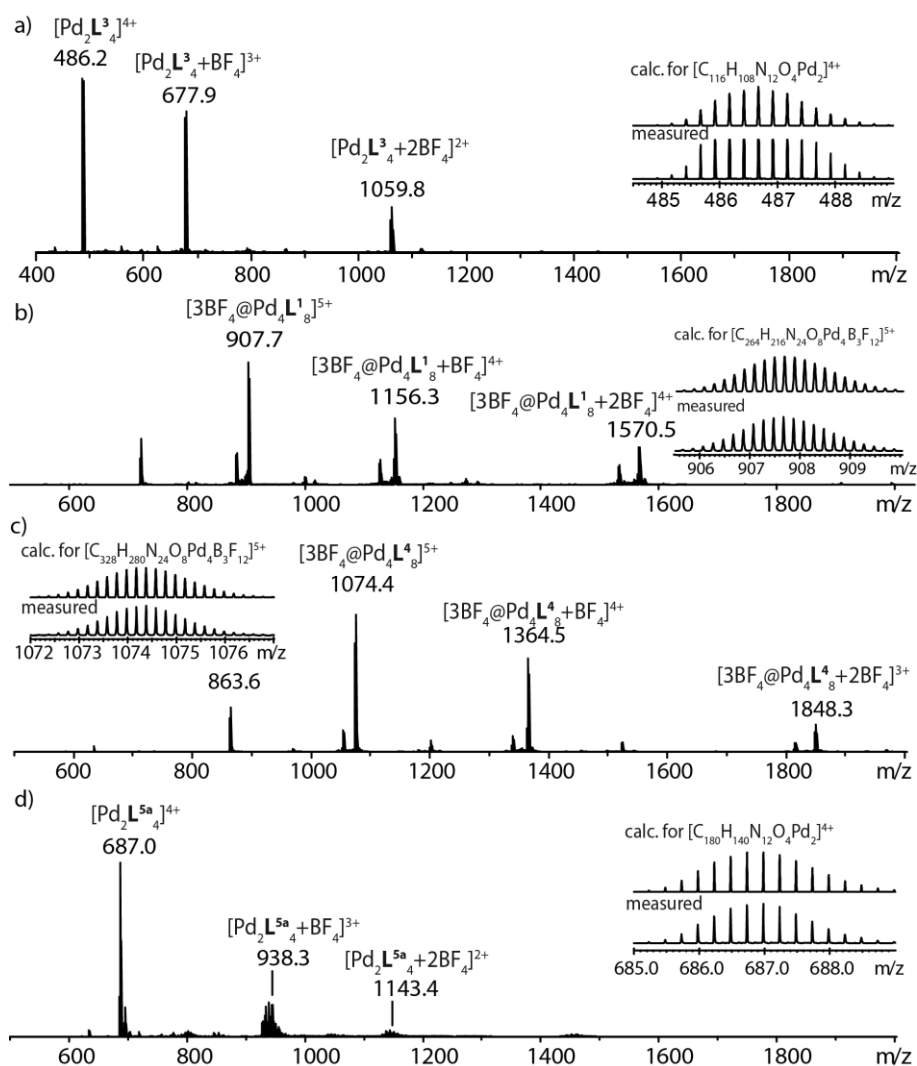


Figure 5.4 HR-ESI-MS of a) $[\text{Pd}_2\text{L}^3]_4$, b) $[3\text{BF}_4@\text{Pd}_4\text{L}^1]_5$, c) $[3\text{BF}_4@\text{Pd}_4\text{L}^4]_5$ and d) $[\text{Pd}_2\text{L}^{5a}]_4$.

Ligand L^1 contains an ethynyl bridge between the acridone backbone and the pyridine moieties and shows a nitrogen-nitrogen distance of 17.0 Å. In presence of tetrakis(acetonitrile)palladium(II)

tetrafluoroborate and prolonged heating for 24 h at 70 °C ligand **L**¹ forms the interpenetrated coordination cage [3BF₄@Pd₄**L**¹₈] as the thermodynamic product. The formation of this supramolecular assembly was verified *via* NMR spectroscopy, ESI-mass spectrometry and X-ray structure determination. The interpenetrated coordination cage [3BF₄@Pd₄**L**¹₈] is able to encapsulate a variety of small neutral molecules in the central cavity of the cage, after being activated by addition of halide anions (Cl⁻, Br⁻) (see Chapter 2). The central cavity of the [2Cl@Pd₄**L**¹₈] interpenetrated cage has a volume of ~201.3 Å³ (see Figure 7.90), consequently only a small number of neutral guest molecules were able to be encapsulated in this supramolecular structure (see Chapter 2 for detailed explanations).

To broaden the scope of encapsulated neutral guest molecules, a series of larger ligands **L**⁴, **L**^{5a} and **L**^{5b} were synthesized (Figure 5.1). It was assumed, that these novel ligands with larger nitrogen-nitrogen distances of ~20.5–26.8 Å assemble to interpenetrated cages with a larger central pocket and are able to encapsulate a greater variety of neutral guest molecules.

First, the bridging ethynyl group between the acridone backbone and the pyridine residue was exchanged for a phenyl group, generating new ligand **L**⁴. This ligand was synthesized *via* a Suzuki coupling from 2,7-dibromo-10-hexylacridone with 3-(4-(4,4,5,5-tetramethyl-1,3,2-dioxaborolan-2-yl)phenyl)pyridine in 97 % yield. The nitrogen-nitrogen distance of ligand **L**⁴, extracted from the DFT model, is ~20.5 Å (see Figure 5.1 and experimental section). To prepare the coordination cage, ligand **L**⁴ was suspended in deuterated acetonitrile and 0.5 equivalents of [Pd(CH₃CN)]₄(BF₄)₂ were added. Heating the reaction mixture at 70 °C for 24 h yielded the interpenetrated coordination cage [3BF₄@Pd₄**L**⁴₈]. ¹H NMR analysis showed a splitting of all aromatic signals into two sets of equal intensity, which indicates a different environment of the two halves of the ligand within the supramolecular cage assembly. Due to the coordination with the positively charged palladium(II) cations, the nitrogen protons H_g and H_f show a very strong downfield shift (see Figure 5.2e and f). The overall ¹H NMR spectrum looks similar to the already discussed spectrum of [3BF₄@Pd₄**L**¹₈] (see Figure 5.2d and Chapter 2). Surprisingly, the ¹H NMR spectrum of [3BF₄@Pd₄**L**⁴₈] at 298 K shows very broad signals, which sharpen at elevated temperatures (see Figure 7.154). This effect might be due to a hindered rotation of the benzene ring around the single bonds at ambient temperature. The central pocket of the interpenetrated cage is surrounded by eight ligands. Short inter ligand distances of 1.5 – 2.9 Å between the benzene ring and the acridone backbone of the neighboring ligand were found in the PM6 model of the cage structure (see Figure 5.5). This close proximity hinders a free rotation at lower temperatures. However, at elevated temperatures, the free rotation is fast in respect to the NMR time scale and all signals appeared sharp. The ¹⁹F NMR spectrum of [3BF₄@Pd₄**L**⁴₈] at ambient temperature shows three signals, which could be assigned to free BF₄⁻ (δ = -151.70 ppm) and encapsulated BF₄⁻ in the inner (δ = -147.24 ppm) and outer pockets (δ = -142.14 ppm) of the coordination cage (see Figure 7.155). Furthermore, the presence of the new interpenetrated coordination cage [3BF₄@Pd₄**L**⁴₈] was supported by HR-ESI mass spectrometry data. The spectrum of the cage solution showed a series of species with

varying number of counter anions, which was identified as $[3\text{BF}_4@Pd_4L^4_8+n\text{BF}_4]^{(5-n)+}$ ($n=0-2$) (Figure 5.4c).

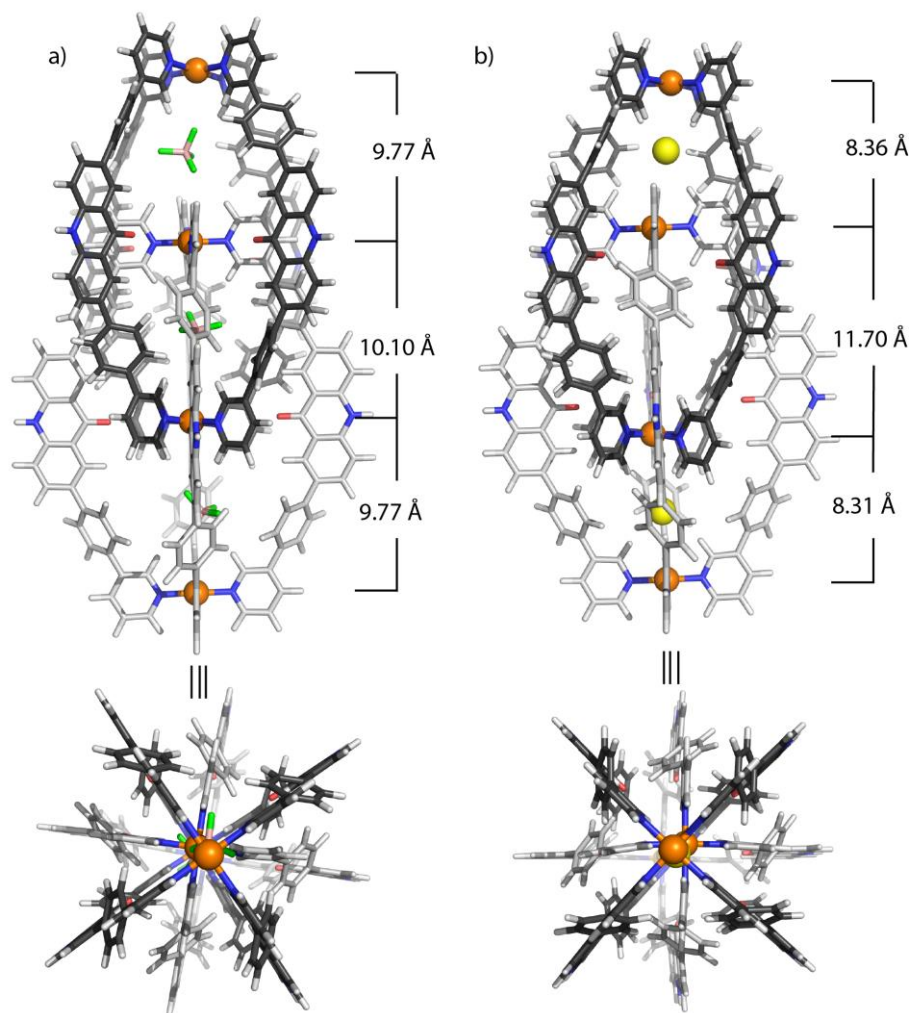


Figure 5.5 Side view and top view along the Pd-Pd axis of the PM6 model of the interpenetrated cages a) $[3\text{BF}_4@Pd_4L^4_8]$ and b) $[2\text{Cl}@Pd_4L^4_8]$. *Color scheme:* C: light/dark gray; N: blue; O: red; Pd: orange, H: white; B: tan, F: green. Non-coordinating anions and solvents were omitted and the hexyl chain was substituted by a hydrogen atom.

Since no suitable crystals for X-ray structure analysis could be obtained up to this point, the structure of the interpenetrated coordination cage $[3\text{BF}_4@Pd_4L^4_8]$ was calculated by a geometry optimization in Gaussian 09.^[138] For this, an unstrained geometry optimization on the PM6 semiempirical level of theory implemented in Gaussian 09^[138] (charge: +5, spin-multiplicity: 1) was performed. The calculated model reveals palladium-palladium distances of 9.77 Å for both outer and 10.10 Å for the inner cavity (see Figure 5.5a). The overall size of the cage is with a distance (measured between the outer Pd centers) of 29.6 Å larger than of the previously discussed $[3\text{BF}_4@Pd_4L^1_8]$ cage (see Figure 2.7a; overall size of $[3\text{BF}_4@Pd_4L^1_8]$: 24.9 Å). Furthermore, the influence of the counter anion on the formation of the cage assembly was tested. While the shorter ligand L^1 only forms the interpenetrated dimer $[3\text{BF}_4@Pd_4L^1_8]$ exclusively in the presence of $[\text{Pd}(\text{CH}_3\text{CN})_4(\text{BF}_4)_2]$, the new ligand L^4 is longer and might therefore tolerate larger anions. Indeed, the addition of

0.5 equivalents of $[\text{Pd}(\text{CH}_3\text{CN})_4(\text{PF}_6)_2]$ to a suspension of ligand L^4 and subsequent heating to 70 °C for 24 h led to the formation of the hexafluorophosphate-containing coordination cage $[\text{3PF}_6@\text{Pd}_4\text{L}^4_8]$, which was evident by NMR spectroscopy and HR-ESI mass spectrometry (see Chapter 7.6.3.3 for experimental description and analytical data).

In the next step, the tetrafluoroborate-containing interpenetrated cage was tested for the uptake of different anionic guests. Addition of two equivalents of halide anions ($X = \text{Cl}^-$, Br^- , I^-) to $[\text{3BF}_4@\text{Pd}_4\text{L}^4_8]$ results in an exchange of the loosely bound tetrafluoroborate anions in the outer two pockets of the interpenetrated cage and incorporation of the added halide with a strong positive cooperativity. The formation of the halide encapsulated coordination cages $[\text{2X}@\text{Pd}_4\text{L}^4_8]$ ($X = \text{Cl}^-$, Br^- , I^-) were supported by NMR spectroscopy and high-resolution mass spectrometry (for experimental data see Chapter 7.6.3.4). Adding excess of halide anions to the interpenetrated coordination cage leads to the disassembly of the cage and release of free ligand. Furthermore, larger anions were tested for their capability to replace the tetrafluoroborate anion. Addition of NO_3^- leads to the appearance of a series of new species in the ^1H NMR spectrum, which results in only one species after addition of up to 4.0 equivalents of nitrate (see Figure 7.171). The appearance of several species indicates the formation of mixed species with different anions encapsulated inside the three pockets of the coordination cage, namely: $[\text{NO}_3+\text{2BF}_4@\text{Pd}_4\text{L}^4_8]$ or $[\text{2NO}_3+\text{BF}_4@\text{Pd}_4\text{L}^4_8]$. This excludes that the exchange of the counter anions occurs following a positive cooperative mechanism. In contrast, addition of azide (N_3^-), hexafluorophosphate (PF_6^-), and perchlorate (ClO_4^-) does not result in any spectroscopic change in the ^1H NMR spectrum, indicating no interaction between the cationic coordination cage and these anionic guests (see Figure 7.168 – Figure 7.170).

The ^{19}F NMR spectra of the halide-containing coordination cages $[\text{2X}@\text{Pd}_4\text{L}^4_8]$ ($X = \text{Cl}^-$, Br^- , I^-) showed only one signal with a chemical shift of $\delta = -151.75$ ppm. This corresponds to free tetrafluoroborate anion in solution. Hence, no BF_4^- anions are incorporated inside the central pocket of these halide-filled cages. This observation is in accordance with the chloride-containing interpenetrated cage of ligand L^1 ($[\text{2Cl}@\text{Pd}_4\text{L}^1_8]$, see Chapter 2).

Furthermore, the binding ability of the halide anion inside the outer pockets of the interpenetrated coordination cage was tested by a silver(I) back-titration. After the addition of up to 5.0 equivalents of silver(I) cations to $[\text{2I}+\text{BF}_4@\text{Pd}_4\text{L}^4_8]$ the tetrafluoroborate-containing coordination cage $[\text{2BF}_4@\text{Pd}_4\text{L}^4_8]$ was regenerated, while AgI precipitated. In contrast, chloride or bromide anions could not be removed from the interpenetrated cages. Even addition of up to 50 equivalents of the silver salt, no change in the NMR spectra was observed.

Finally, the ability of the halide-containing cages $[\text{2X}@\text{Pd}_4\text{L}^4_8]$ ($X = \text{Cl}^-$, Br^-) to encapsulate neutral guest molecules was investigated. Addition of different neutral guest molecules (e.g. benzene, DABCO, paracyclophane or ferrocene; 9–19 eq.) and an equilibration time of several days at ambient temperature did not result in any changes in the ^1H NMR spectrum (see Figure 7.177 and Figure 7.178). Additionally, no new species were detected with high-resolution mass spectrometry.

Consequently, uptake of the neutral molecules inside the central pocket of the interpenetrated coordination cages is excluded (see Figure 5.6). The reason for this exclusion may arise from the alteration of the ligand size. While ligand **L**¹ contains an ethynyl group between the acridone and the pyridine residue, ligand **L**⁴ bridges these groups by a phenyl unit (see Figure 5.1). The PM6 model of the [2Cl@Pd₄L⁴₈] cage reveals short distances from ~1.5 – 3.2 Å between the phenyl groups of one ligand to the neighboring ligands (see Figure 5.5b). Although these moieties were initially introduced to enlarge the overall cage structure, the phenyl groups block the portals to the central cavity and may therefore hinder the entry of a neutral guest molecule (see Figure 5.5b for the PM6 model of [2Cl@Pd₄L⁴₈]). Interestingly, HR-MS spectrometry and ¹⁹F-NMR experiments showed no presence of an encapsulated BF₄ anion in the central pocket of the chloride-filled coordination cage (see *Experimental Section* chapter 7.6.3).

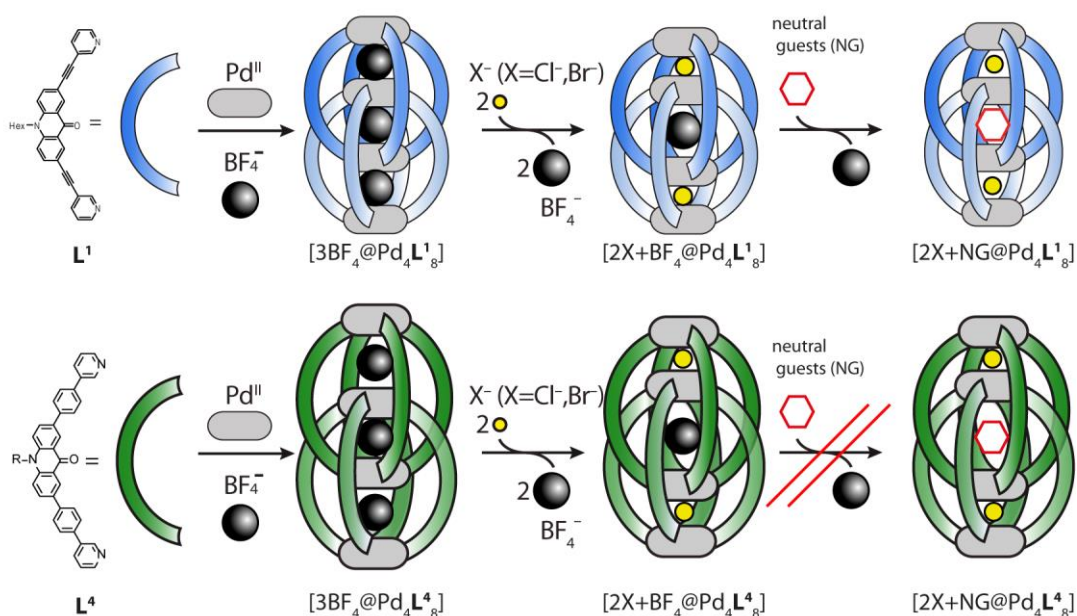


Figure 5.6 Schematic representation of the formation of interpenetrated coordination cages from ligands **L**¹ and **L**⁴. While coordination cage [3BF₄@Pd₄L¹₈] is activated by halide addition to encapsulate neutral guest molecules inside the central void of the cage, coordination cage [3BF₄@Pd₄L⁴₈] is not able to incorporate neutral guests molecules.

Since the encapsulation of neutral guests in the central pocket of the interpenetrated coordination cage assembled from ligand **L**⁴ was unsuccessful, a set of even longer ligands such as **L**^{5a} and **L**^{5b} was synthesized (For experimental explanation and analytical details see Chapter 7.6.4). These ligands both contain an ethyl and a phenyl bridge between the acridone core and the pyridine groups (see Figure 5.1). The ligand structures were calculated *via* a gas-phase DFT calculation (B3LYP/6-31g(d)) and revealed nitrogen-nitrogen distances of ~25 Å (see Figure 7.190).

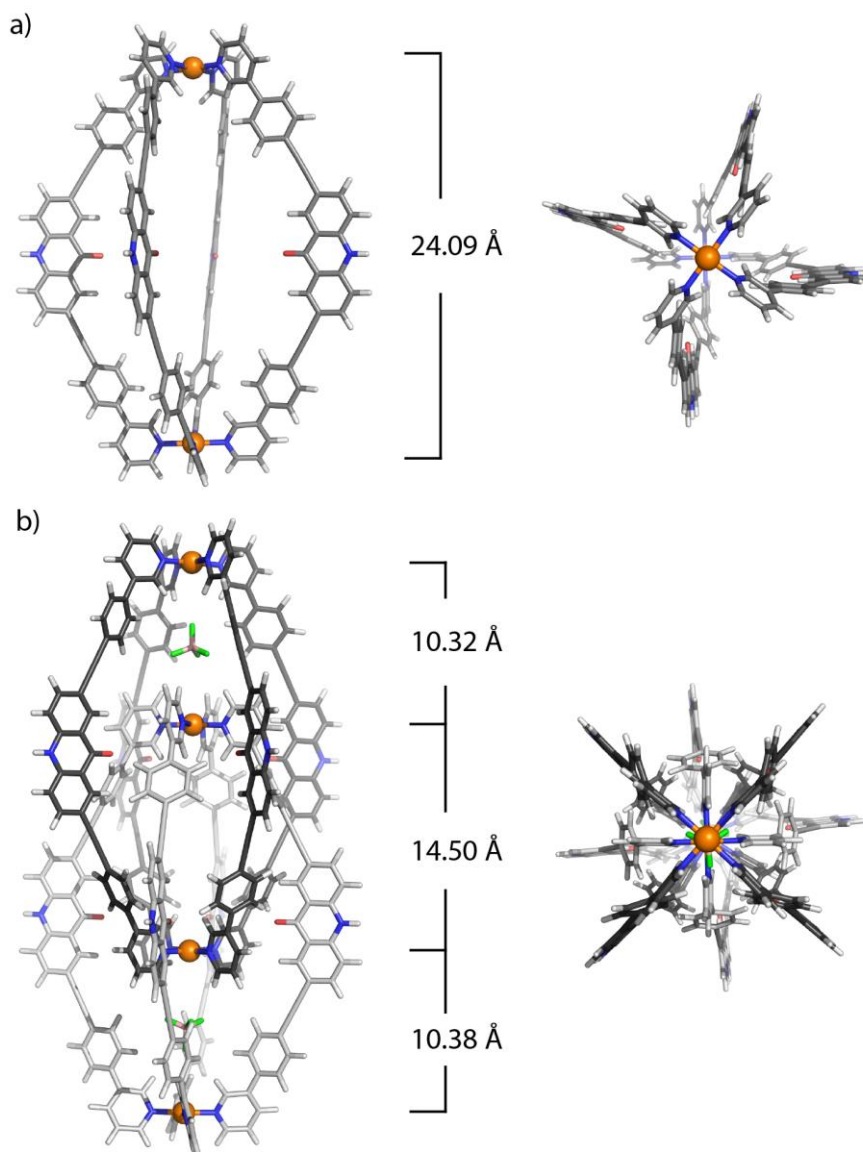


Figure 5.7 Side view and top view along the Pd-Pd axis of the PM6 models of a) the monomeric cage $[\text{Pd}_2\text{L}^{5a}_4]$ and b) the interpenetrated dimer $[2\text{BF}_4@\text{Pd}_4\text{L}^{5a}_8]$. *Color scheme:* C: light/dark gray; N: blue; O: red; Pd: orange, H: white B: tan, F: green. Anions and solvents were omitted and the hexyl chain was substituted by a hydrogen atom.

Initially, the structures for the monomeric cage and the interpenetrated dimer based on ligand L^{5a} were calculated by geometry optimization on the PM6 semiempirical level of theory without constraints (charge: +4 ($[\text{Pd}_2\text{L}^{5a}_4]$), +6 ($[2\text{BF}_4@\text{Pd}_4\text{L}^{5a}_8]$), spin-multiplicity: 1) implemented in Gaussian 09^[138,138] (see Figure 5.7). The calculated model of the $[\text{Pd}_2\text{L}^{5a}_4]$ cage revealed that the palladium-palladium distance of 24.09 Å is nearly twice as large as for the discussed $[\text{Pd}_2\text{L}^{3a}_4]$ cage (see Figure 5.3, Pd-Pd distance: 12.48 Å). The calculated model of the interpenetrated coordination cage $[2\text{BF}_4@\text{Pd}_4\text{L}^{5a}_8]$ indicates the presence of three pockets with palladium-palladium distances of 10.32 Å and 10.38 Å for the outer and 14.50 Å for the inner cavities. Compared with the previously discussed interpenetrated coordination cages based on ligand L^1 and L^4 , the calculated model of $[2\text{BF}_4@\text{Pd}_4\text{L}^{5a}_8]$ has the largest central pocket, which could encapsulate a greater diversity of neutral guest molecules, possible even before the addition of halide anions. Furthermore, the bridging

phenyl groups do not block the entire portals of the cavity and an entry of guest molecules seems possible.

To form the cage, the ligand (**L**^{5a} or **L**^{5b}) and the palladium(II) cations were heated in a closed vial at 70 °C for 24 h under various conditions (see Table 5.1). Several palladium counter anions (BF₄⁻, PF₆⁻) and deuterated solvents (acetonitrile, DMSO or acetone) were tested. After heating, the reaction mixture was analyzed by ¹H NMR spectroscopy. No signals in the aromatic region of the ¹H NMR spectra were observed for samples in acetonitrile; despite a clear solution of the reaction mixture in the NMR tubes (see entry 1–4 in Table 5.1 and Figure 7.185). This indicates the formation of a more complex product, (e.g. a polymer), which was not detectable *via* NMR spectroscopy.

Table 5.1 Conditions for cage formation reactions. *General procedure:* To a solution or suspension of the ligand; a solution of the palladium salt (0.5 eq.) was added. The resulting mixture was heated at 70 °C for 24 h. *: No signals in the aromatic region of the ¹H NMR spectrum.

Entry	Ligand	[Pd(CH ₃ CN) ₄](X) ₂	Solvent	Observation	¹ H NMR spectroscopy
1	L ^{5a}	X = BF ₄ ⁻	CD ₃ CN	clear solution	*
2	L ^{5a}	X = PF ₆ ⁻	CD ₃ CN	clear solution	*
3	L ^{5b}	X = BF ₄ ⁻	CD ₃ CN	clear solution	*
4	L ^{5b}	X = PF ₆ ⁻	CD ₃ CN	clear solution	*
5	L ^{5a}	X = BF ₄ ⁻	DMSO-d ⁶	clear solution	shifting of all signals compared to free ligand
6	L ^{5a}	X = PF ₆ ⁻	DMSO-d ⁶	clear solution	shifting of all signals compared to free ligand
7	L ^{5b}	X = BF ₄ ⁻	DMSO-d ⁶	precipitation	shifting of signals, several species
8	L ^{5b}	X = PF ₆ ⁻	DMSO-d ⁶	precipitation	shifting of signals, several species
9	L ^{5b}	X = BF ₄ ⁻	acetone-d ⁶	precipitation	*
10	L ^{5a}	X = PF ₆ ⁻	acetone-d ⁶	precipitation	*
11	L ^{5a}	X = BF ₄ ⁻	acetone-d ⁶	precipitation	signals of free ligand L ^{5b}
12	L ^{5b}	X = PF ₆ ⁻	acetone-d ⁶	precipitation	*

Cage formation in deuterated acetone led to a visible yellow precipitate in the NMR tubes. Additionally, no signals were observed in the ¹H NMR spectra (see entry 9–12 in Table 5.1 and Figure 7.187). Thus, no successful formation of the interpenetrated dimer from ligands **L**^{5a} and **L**^{5b} was achieved. This is surprising, since cage formation in acetone was observed in previously reported systems based on dibenzosuberone.^[75] In conclusion, assembly of a monomeric [Pd₂**L**^{5a/b}₄] or dimeric [Pd₄**L**^{5a/b}₈] coordination cage in acetonitrile or acetone were not successful under the tested conditions. Addition of palladium(II) cations to a solution of ligand **L**^{5a} in deuterated DMSO and prolonged heating (70 °C, 24 h) resulted in one set of signals in the ¹H NMR spectrum. Compared to the NMR signals of the free ligand **L**^{5a}, pyridine protons H_g and H_f were shifted downfield. This indicates the coordination of the palladium(II) cations with the nitrogen donor of the pyridine. Since

no splitting of all signals into two sets of equal intensity was observed, the formation of the interpenetrated $[\text{Pd}_4\text{L}^{5a}_8]$ cage can be ruled out (see Figure 5.2g and h) and indicates formation of the monomeric $[\text{Pd}_2\text{L}^{5a}_4]$ cage. Indeed, the high-resolution ESI mass spectrum showed the formation of the monomeric cage $[\text{Pd}_2\text{L}^{5a}_4]^{4+}$ at $m/z = 697.0$ (see Figure 5.4d). Previously conducted studies^[47] on ligand length variation and solvent effect, showed that cage formation carried out in DMSO resulted in the formation of monomeric cages and dimerization is ruled out. In contrast, no formation of a discrete species was observed with ligand L^{5b} in DMSO (see Figure 7.187 and entry 7 and 8 in Table 5.1).

Under all tested conditions, the formation of the desired interpenetrated coordination cages $[\text{Pd}_4\text{L}^{5a}_8]$ and $[\text{Pd}_4\text{L}^{5b}_8]$ was not successful. Thus, further investigation about halide binding and neutral guest uptake were obsolete.

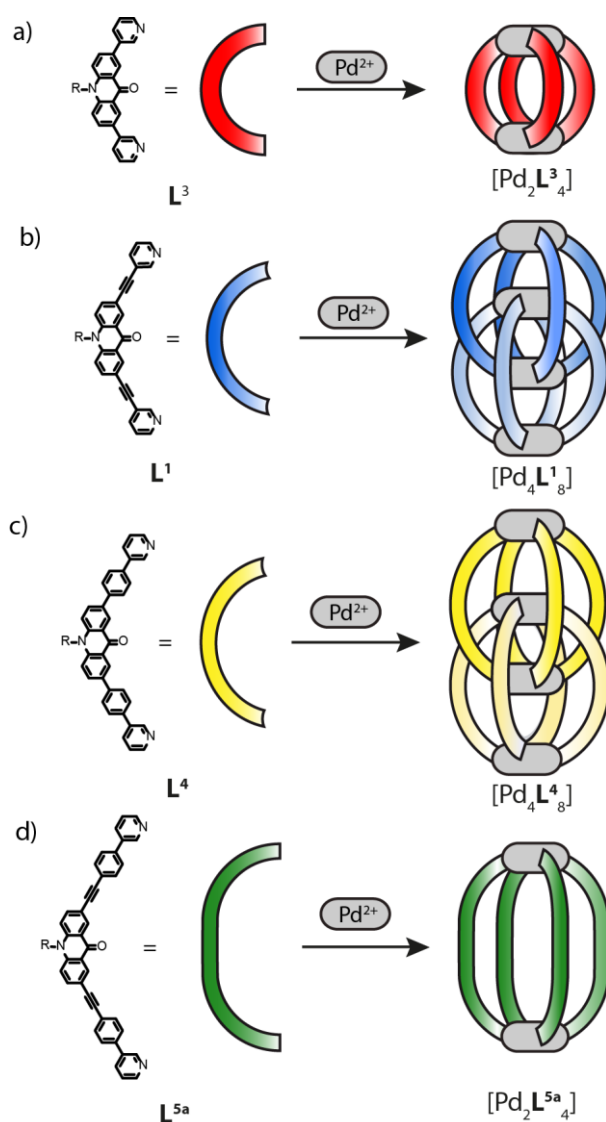


Figure 5.8 Schematic representation of cage formation from different ligands L and palladium(II) cations: a) ligand L^3 and monomeric cage $[\text{Pd}_2\text{L}^3_4]$ b) ligand L^1 and interpenetrated coordination cage $[3\text{BF}_4@[\text{Pd}_4\text{L}^1_8]]$; c) ligand L^4 and $[3\text{BF}_4@[\text{Pd}_4\text{L}^4_8]]$ cage; d) ligand L^{5a} and monomeric $[\text{Pd}_2\text{L}^{5a}_4]$ cage.

5.3 Conclusion and Prospects

This chapter describes the influence of the ligand length on the cage formation in presence of palladium(II) cations. Depending on the size, either monomeric $[\text{Pd}_2\text{L}_4]$ cages or interpenetrated coordination cages $[\text{Pd}_4\text{L}_8]$ were formed (see Figure 5.8). Ligand L^3 prefers assembling to a monomeric $[\text{Pd}_2\text{L}^3_4]$ cage, due to the very short nitrogen-nitrogen distance. Extended ligands L^1 and L^4 with similar N-N distances, showed both formation of interpenetrated dimers $[\text{Pd}_4\text{L}^1_8]$ and $[\text{Pd}_4\text{L}^4_8]$. A further extension of the ligand structure (L^{5a} and L^{5b}) was not leading to interpenetrated cages, instead the formation of the monomeric cage $[\text{Pd}_2\text{L}^{5a}_4]$ could be verified (see Figure 5.8 for an overview). It was shown, that the length of the ligand plays a significant role in the cage formation. Due to variation in the length, the thermodynamic product was either a monomeric or a dimeric cage. In future studies, the behavior of asymmetric-bridged ligands on the self-assembly and the formation of host-guest complexes will be investigated (see Figure 5.9).

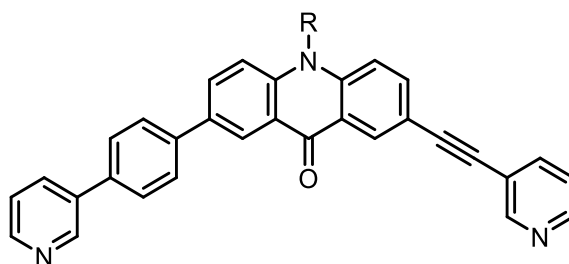
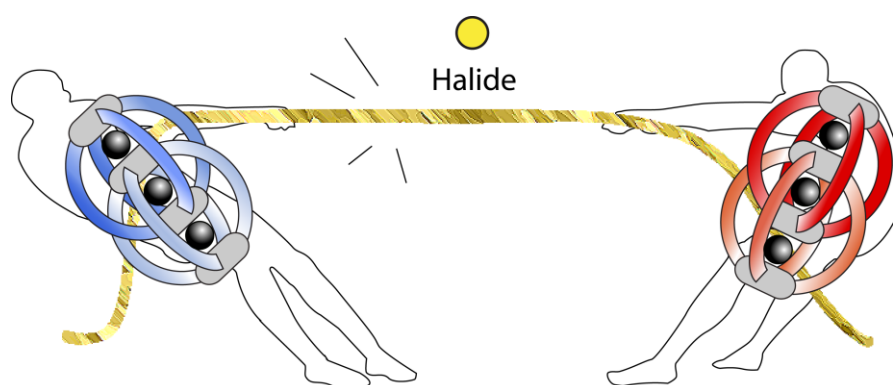


Figure 5.9 Possible scheme of an asymmetric ligand for future studies on self-assembly.

6 ANION BINDING COMPETITION EXPERIMENTS



6.1 Introduction and Objectives

Interpenetrated coordination cages $[3\text{BF}_4@Pd_4L_8]$ based on banana-shaped ligands **L** containing dibenzosuberone^[75] (ligand **L**⁸), phenothiazine^[78] (ligand **L**^{6a-c}), anthraquinone^[69] (ligand **L**⁷) or acridone^[87] (ligand **L**¹) as a backbone, are known to exchange the loosely bound tetrafluoroborate anions in the outer pockets for halide anions (Cl^- ; Br^-). This anion exchange follows an allosteric binding mechanism with positive cooperativity and results in a compression of the structures along the Pd-Pd axis (see Figure 6.1).

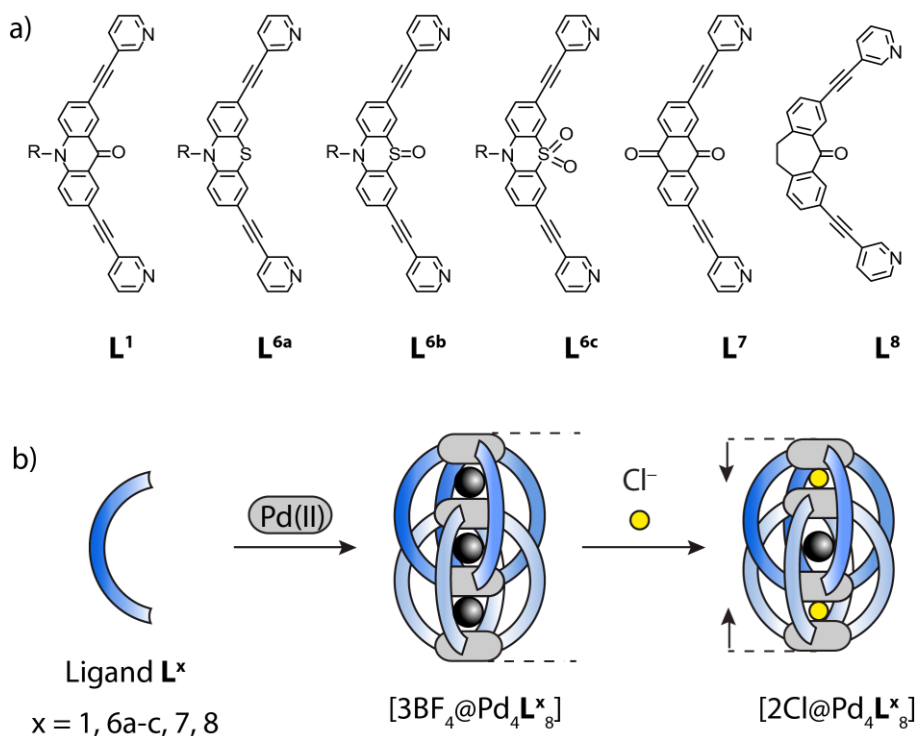
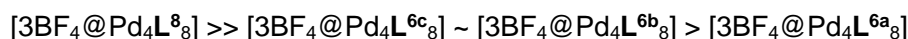


Figure 6.1 a) Chemical structures of banana-shaped ligands based on acridone (**L**¹), phenothiazine (**L**^{6a-c}), anthraquinone (**L**⁷) and dibenzosuberone (**L**⁸) backbones; b) schematic representation of the self-assembly of the interpenetrated coordination cage $[3\text{BF}_4@Pd_4L_8]$ from ligands **L**^x (x = 1, 6a-c, 7, 8) and palladium(II) cations. Two halide anions (e.g. chloride) were bound in the outer two pockets of the cage in an allosteric fashion with positive cooperativity. The anion exchange is accompanied by a compression of the supramolecular structure.

Previous studies with the interpenetrated cage $[3\text{BF}_4@Pd_4L_8]$ based on dibenzosuberone ligand **L**⁸ indicated an influence of the size on the relative binding strength of the incorporated halide anions. NMR experiments showed that the binding strength decreased in the following order: chloride > bromide > fluoride.^[75] The binding affinity towards chloride anions is so strong, that even solid silver chloride (AgCl) could be dissolved by the interpenetrated coordination cage in acetonitrile. The net binding constant for two chloride anions inside the interpenetrated coordination cage $[3\text{BF}_4@Pd_4L_8]$ was estimated to be $K \sim (1.0 \pm 0.1) \times 10^{20} \text{ M}^{-2}$.^[76]

Additional anion binding competition experiments between the phenothiazine (**L**^{6a-c}) and dibenzosuberone (**L**⁸) containing interpenetrated coordination cages allowed the determination of a relative binding strength for halide anions (bromide/chloride) in these supramolecular assemblies. The following trend was observed:



The dibenzosuberone-containing $[3\text{BF}_4@Pd_4L^8]$ coordination cage showed the strongest binding affinity, while the three phenothiazine-based interpenetrated coordination cages presented much lower affinity towards halide anions. It was found, that structural differences in the investigated ligands (L^{6a-c}), resulting from the different oxidation states of the sulfur atom carrying no (L^{6a}), one (L^{6b}) or two (L^{6c}) oxygen substituents, influences the size of the cavity of the interpenetrated coordination cages and due to that affect the binding strength. Further NMR experiments as well as theoretical calculations, demonstrated that the binding affinity towards halide anions decrease with increasing cage size.^[79]

This Chapter focusses on the binding ability of chloride anions in the acridone-based coordination cages $[3\text{BF}_4@Pd_4L^1]$ in comparison to the already described $[3\text{BF}_4@Pd_4L^x]$ cages ($x = 6a-c, 7, 8$). Anion binding competition experiments will allow determining the relative binding strength of the $[3\text{BF}_4@Pd_4L^1]$ coordination cage.

6.2 Anion Exchange between Interpenetrated Coordination Cages

All ligands L^x form interpenetrated coordination cages $[3\text{BF}_4@Pd_4L^x]$ ($x = 1, 6a-c, 7, 8$) in the presence of 0.5 equivalents of tetrakis(acetonitrile)palladium(II) tetrafluoroborate after prolonged heating at 70 °C for 24 h. Addition of chloride leads to an exchange of the outer tetrafluoroborate anions by the halide and the formation of $[2\text{Cl}@Pd_4L^x]$ ($x = 6a-c, 7, 8$).

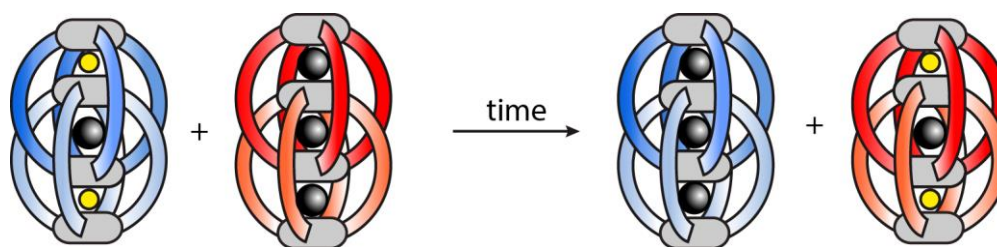


Figure 6.2 Schematic representation of an anion exchange between a chloride-containing interpenetrated coordination cage $[2\text{Cl}+BF_4@Pd_4L^x]$ (blue) and a tetrafluoroborate-containing cage $[3BF_4@Pd_4L^x]$ (red).

First, it was investigated if the chloride anion from the acridone based $[3\text{BF}_4@Pd_4L^1]$ cage could be removed by another tetrafluoroborate anion-containing cage $[3\text{BF}_4@Pd_4L^x]$ ($x = 6a-c, 7, 8$). Previous experiments showed that addition of silver(I) cations could not remove the halides from the coordination cage (see Figure 7.22), which indicates an exceptionally strong binding affinity towards chloride anions of the acridone derived coordination cage. Hence, to a $[2\text{Cl}@Pd_4L^1]$ solution (CD_3CN , 250 μL , 0.35 mM, 1.0 eq.) a solution of the tetrafluoroborate-containing cage $[3\text{BF}_4@Pd_4L^x]$ (CD_3CN , 250 μL , 0.35 mM, 1.0 eq.) was added and the sample was monitored by ^1H NMR spectroscopy over several days. No apparent changes in the spectrum were observed (see Figure 7.191 – Figure 7.195). Even after 3 weeks at room temperature, only the originally added cages $[2\text{Cl}@Pd_4L^1]$ and $[3\text{BF}_4@Pd_4L^x]$ were present in the mixture ($x = 6a-c, 7, 8$).

In contrast, the addition of tetrafluoroborate-containing $[3\text{BF}_4@\text{Pd}_4\text{L}^1_8]$ cage to a solution of $[2\text{Cl}@\text{Pd}_4\text{L}^x_8]$ (1:1) resulted in anion exchange between the acridone-derived cage and the interpenetrated cages containing ligand L^{6a-c} or L^7 (Figure 6.2a). The ^1H NMR spectra of these mixtures showed, that the intensity of the signals assigned to the starting cages $\{[3\text{BF}_4@\text{Pd}_4\text{L}^1_8]$ and $[2\text{Cl}@\text{Pd}_4\text{L}^x_8]$ ($x = 6a-c, 7\}$ are decreased over time, while the intensity of new signals corresponding to $[2\text{Cl}@\text{Pd}_4\text{L}^1_8]$ and $[3\text{BF}_4@\text{Pd}_4\text{L}^x_8]$ is increasing (see Figure 7.196 to Figure 7.199). No starting cage compounds were found in experiments containing phenothiazine-based coordination cages with ligands L^{6a-c} after 4 days, indicating complete exchange. Kinetic measurements (5 min intervals at 298 K) revealed that the kinetic rate of the halide exchange is highly dependent on the chloride-containing cage. It was found, that the chloride replacement from the coordination cage containing the non-oxidized phenothiazine ligand L^{6a} is completed after ~ 1 h (see Figure 6.3a). In contrast, the chloride anion encapsulated inside the interpenetrated coordination cage assembled from the doubly-oxidized phenothiazine ligand L^{6c} shows a significantly slower exchange rate (see Figure 6.3b). Thus, the release of the chloride anion from $[2\text{Cl}@\text{Pd}_4\text{L}^{6c}_8]$ is kinetically slowed down, in comparison to the $[2\text{Cl}@\text{Pd}_4\text{L}^{6a}_8]$ cage. Reason for this, might be the additional oxygen atoms of ligand L^{6c} . DFT calculation (B3LYP/LANL2DZ) showed, that the oxidized organic ligand L^{6c} is slightly bent (in comparison to ligand L^{6a}), which results in an overall shortening of the ligand and consequently the corresponding interpenetrated cage structure $[\text{X}@\text{Pd}_4\text{L}^{6c}_8]$ ($\text{X}=\text{Cl}, \text{BF}_4$).^[78] One can assume, that this structural change influences (and somehow hinders) the release of the halide from the outer pocket of the interpenetrated coordination cage $[2\text{Cl}@\text{Pd}_4\text{L}^{6c}_8]$ and reduces the rate of anion exchange.

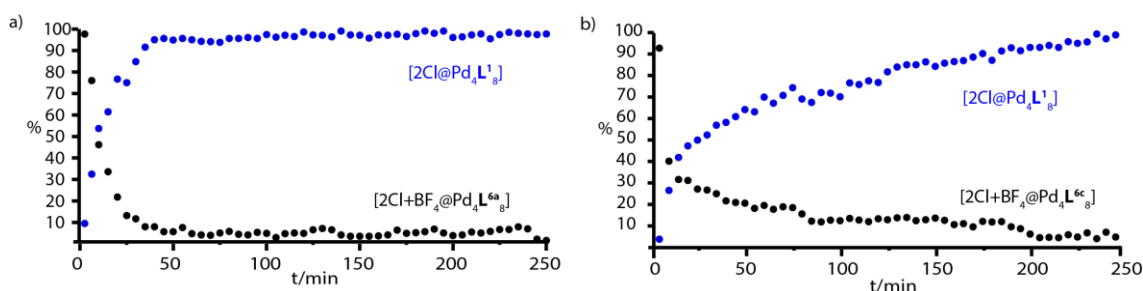


Figure 6.3 Kinetic measurements (400 MHz, CD_3CN , 298 K) of a) $[2\text{Cl}+\text{BF}_4@\text{Pd}_4\text{L}^{6a}_8]$ and $[3\text{BF}_4@\text{Pd}_4\text{L}^1_8]$ and b) $[2\text{Cl}+\text{BF}_4@\text{Pd}_4\text{L}^{6c}_8]$ and $[3\text{BF}_4@\text{Pd}_4\text{L}^1_8]$. The chloride exchange from $[2\text{Cl}+\text{BF}_4@\text{Pd}_4\text{L}^{6a}_8]$ is faster than from $[2\text{Cl}+\text{BF}_4@\text{Pd}_4\text{L}^{6c}_8]$.

Surprisingly, no change in the ^1H NMR spectra could be observed in a mixture containing $[2\text{Cl}@\text{Pd}_4\text{L}^8_8]$ and $[3\text{BF}_4@\text{Pd}_4\text{L}^1_8]$, thus no anion exchange occurs between these two interpenetrated coordination cages (see Figure 7.200).

6.3 Chloride Competition Experiments

Furthermore, ^1H NMR based competition experiments were performed to investigate the relative anion binding affinity of chloride in the interpenetrated coordination cages.^[139] Thus, a 1:1 mixture of $[3\text{BF}_4@\text{Pd}_4\text{L}^1_8]$ and $[3\text{BF}_4@\text{Pd}_4\text{L}^x_8]$ with $x = 6a-c, 7$, were prepared in an NMR tube and

1.0 equivalent of chloride anion was added. After briefly shaking the NMR tube a ^1H NMR spectrum was recorded. The sample was stored at ambient temperature and ^1H NMR spectra were recorded until no further changes were observed.

Addition of 1.0 equivalent of chloride anions to a mixture of $[\text{3BF}_4@\text{Pd}_4\text{L}^1_8]$ and $[\text{3BF}_4@\text{Pd}_4\text{L}^{6a}_8]$ cages, results in the immediate formation of $[\text{2Cl}@\text{Pd}_4\text{L}^1_8]$. No traces of the chloride-containing cage based on ligand L^{6a} were observed, indicating a selective halide binding (see Figure 6.4a). Over time, no changes in the ^1H NMR signals were observed (see Figure 7.201).

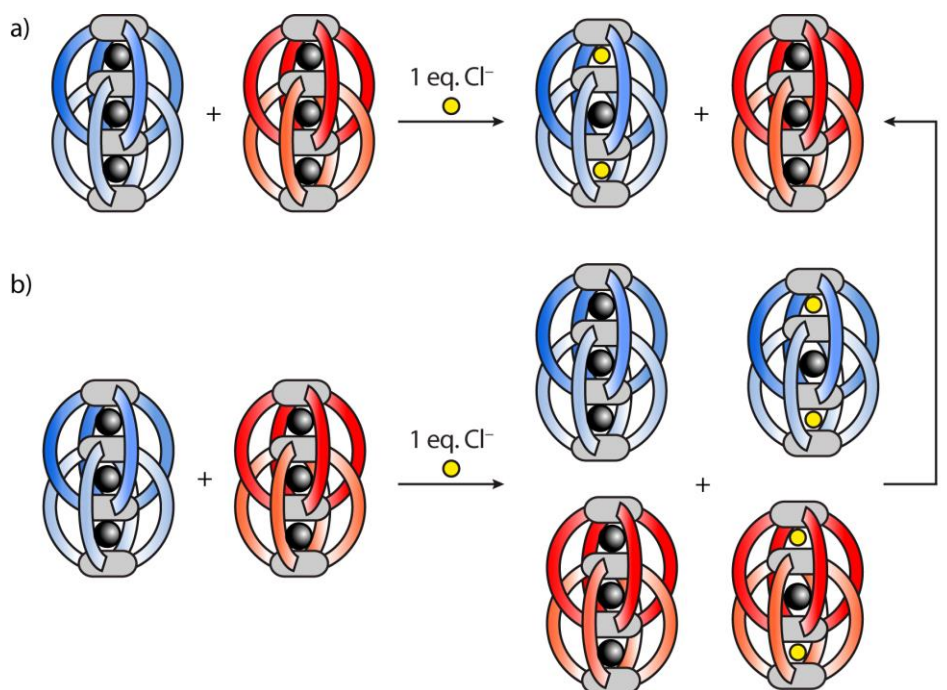


Figure 6.4 Schematic representation of chloride binding competition experiments a) selective halide binding b) statistic halide binding.

In contrast, addition of a solution of chloride anions to a 1:1 mixture of $[\text{3BF}_4@\text{Pd}_4\text{L}^1_8]$ and $[\text{3BF}_4@\text{Pd}_4\text{L}^x_8]$ with $x = 6b, 6c$ and 7 leads to a statistical mixture of all possible cage structures (see Figure 6.4b). Over time, the composition of the sample changes, indicated by an increase in intensity of signals corresponding to $[\text{2Cl}@\text{Pd}_4\text{L}^1_8]$ and decrease of $[\text{2Cl}@\text{Pd}_4\text{L}^x_8]$ ($x = 6b, 6c, 7$), until equilibrium is reached and only two cage structures are present; namely $[\text{2Cl}@\text{Pd}_4\text{L}^1_8]$ and $[\text{3BF}_4@\text{Pd}_4\text{L}^x_8]$ (see Figure 7.202 – Figure 7.204). In Chapter 6.2, it was shown, that the tetrafluoroborate-containing coordination cage $[\text{3BF}_4@\text{Pd}_4\text{L}^1_8]$, can “steal” the chloride anion from the $[\text{2Cl}@\text{Pd}_4\text{L}^x_8]$ cages ($x = 6a-c, 7$) and form $[\text{2Cl}@\text{Pd}_4\text{L}^1_8]$. The halide competition experiments confirm the latter results.

Addition of 1.0 equivalent of chloride to a 1:1 mixture of $[\text{3BF}_4@\text{Pd}_4\text{L}^1_8]$ and $[\text{3BF}_4@\text{Pd}_4\text{L}^8_8]$ lead to a statistical mixture containing four species ($[\text{3BF}_4@\text{Pd}_4\text{L}^1_8]$, $[\text{3BF}_4@\text{Pd}_4\text{L}^8_8]$, $[\text{2Cl}@\text{Pd}_4\text{L}^1_8]$ and $[\text{2Cl}+\text{BF}_4@\text{Pd}_4\text{L}^8_8]$), as observed in the ^1H NMR spectrum. The composition of the sample did not change over time, indicating a similar binding affinity towards chloride of these two interpenetrated coordination cages.

Based on the conducted experiments, the interpenetrated coordination cage $[3\text{BF}_4@Pd_4L^1_8]$ consisting of the acridone derived ligand L^1 and palladium(II) cations showed a binding affinity towards chloride anions similar to the dibenzosuberone-containing cage $[3\text{BF}_4@Pd_4L^8_8]$. Therefore, following order of relative binding affinity was obtained:



Previous experiments revealed, that the binding strength of halide anions correlates to the size of the cage, where smaller cages bind much stronger than larger ones.^[79] A comparison of the acridone-based interpenetrated coordination cage $[3\text{BF}_4@Pd_4L^1_8]$ shows a Pd-Pd distance of 16.68 Å in one $[Pd_2L_4]$ subunit, which is similar to the dibenzosuberone-containing cage $[3\text{BF}_4@Pd_4L^8_8]$ with 16.34 Å. In contrast, the phenothiazine-based cage $[3\text{BF}_4@Pd_4L^{6a}_8]$ shows a palladium-palladium distance of 17.62 Å. Based on this observation and the experimental result, it can be said, that the obtained results are in good agreement with previously reported data.

6.4 Conclusion and Prospects

This Chapter showed the binding affinity of chloride anions towards the interpenetrated coordination cage $[3\text{BF}_4@Pd_4L^1_8]$ in comparison to previously investigated similar coordination cages based on dibenzosuberone, phenothiazine and anthracene $[3\text{BF}_4@Pd_4L^x_8]$ ($x = 6a-c, 7, 8$). Anion binding competition experiments showed that the acridone-based system $[3\text{BF}_4@Pd_4L^1_8]$ binds chloride with a similar affinity as the dibenzosuberone-based coordination cage $[3\text{BF}_4@Pd_4L^8_8]$. Anion exchange experiments exhibited, that the $[3\text{BF}_4@Pd_4L^1_8]$ cage could remove chloride anions from other interpenetrated coordination cages $[2\text{Cl}+\text{BF}_4@Pd_4L^x_8]$ ($x = 6a-c, 7$) under formation of $[2\text{Cl}@Pd_4L^1_8]$.

The discussed experiments were performed in deuterated acetonitrile at ambient temperature. In further studies the conditions could be extended and optimized. Variation of solvents (e.g. usage of acetone, nitromethane or chloroform) and a change in temperature could have tremendous influence on the halide binding behavior. In addition, variation of the counter anions and the investigation of other anions (fluorine, bromine or iodine) could give interesting results and a better insight in understanding halide binding in coordination cages. Furthermore, this halide exchange competition experiments can be combined with the neutral guest uptake discussed in Chapter 2.

7 EXPERIMENTAL SECTION

7.1 Instrumentation

7.1.1 Nuclear Magnetic Resonance Spectroscopy

NMR spectra were measured on a Bruker Avance III 300 MHz, Bruker Avance III 400 MHz, Bruker Avance III HD 400 MHz, Bruker Avance III HD 500 MHz, Bruker Avance I 900 MHz, Agilent DD2-500, Varian UnityNova-500 or Bruker Avance III HD 600 MHz. ^1H and ^{13}C NMR chemical shifts are given in ppm with the residual solvent as an internal standard (CDCl_3 : $\delta_{\text{H}} = 7.25$ ppm, $\delta_{\text{C}} = 77.16$ ppm; CD_3CN : $\delta_{\text{H}} = 1.94$ ppm, $\delta_{\text{C}} = 118.26$ ppm; Dimethylsulfoxide- d_6 : $\delta_{\text{H}} = 2.50$ ppm, $\delta_{\text{C}} = 39.52$ ppm, Acetone- d_6 : $\delta_{\text{H}} = 2.05$ ppm, $\delta_{\text{C}} = 29.84$ ppm). ^{31}P NMR chemical shifts are given in ppm relative to 85 % of H_3PO_4 (0.00 ppm, external reference). Coupling constants J are given in Hz and signal multiplicities are assigned with the following abbreviations: s (singlet), s_{br} (broad singlet), d (doublet), dd (doublet of doublets), t (triplet), q (quartet), m (multiplet). The NMR data were analyzed with the *MNova* (MestReNova Version 10.0.2-15465) software.

7.1.2 Mass Spectrometry

Mass spectra were recorded on *Bruker FTICR-MS APEX IV* (ESI-HR-MS), *Bruker maXis* (ESI-HR-MS), *Bruker micrOTOF* (HR-ESI-MS), *Bruker HTC Ultra* (ESI-MS) and LQT Orbitrap FT-MS from *Thermo Electron*. The isotopic distribution and the exact masses were calculated using either the Software *Bruker Compass Data Analysis* or *XCalibur Thermo Scientific 2.2*.

7.1.3 IR Spectroscopy

Infrared measurements were carried out on a *JASCO FT-IR 4100*. While coordination cages were measured in acetonitrile solution, the organic compounds were measured as solids.

7.1.4 Cyclic Voltammetry

CV measurements were carried out at room temperature *via* application of a Potentiostat PGSTAT101. The data were recorded with the NOVA electrochemistry software (Version 1.9), which was included in Metrohm Autolabs. The sample and the electrolyte salt were dissolved in dry and degassed acetonitrile in a 1 mL sample cell. During the measurement, this cell was kept under nitrogen atmosphere. After each measurement, the glassy carbon electrode and the platinum wire

(used as a counter electrode) were carefully polished with a polishing powder and rinsed with acetone and acetonitrile. Non-aqueous Ag/AgNO₃ was used as a reference electrode. Between the measurements the reference electrode was kept in acetonitrile/tetrabutylammonium perchlorate (0.1 M) solution and rinsed with acetonitrile prior to every measurement.

7.2 General Procedures

7.2.1 Syntheses

Sensitive reactions were carried out under an inert nitrogen atmosphere using standard Schlenk techniques. Chemicals and standard solvents were purchased from ABCR, Sigma Aldrich, VWR, TCI or Acros Organics and used for syntheses without further purification. Dry solvents over molecular sieves were purchased from Acros Organics. Thin-layer chromatography was performed on Merck aluminum-based plates with silica gel (silica 60, fluorescence indicator F254 nm, thickness 0.25 mm). Column chromatography was performed with silica (Merck, silica 60, 0.02-0.063 mesh ASTM) as the stationary phase. Recycling gel permeation chromatography was performed on a JAI LC-9210 II NEXT GPC system equipped with Jaigel 1H and 2H columns in series using chloroform as the eluent.

7.2.2 Formation of Cage Compounds

To a suspension or solution of the ligand (2.8 mM, 1.0 eq.) a solution of [Pd(CH₃CN)₄](X)₂ (X= BF₄, PF₆; 15 mM, 0.55 eq.) was added and the resulting mixture was heated to 70 °C. Monomeric [Pd₂L₄] cages were formed after heating between 15 min - 1 h, while the formation of the interpenetrated cage dimers [Pt₄L₈] were only completed after 24 h at 70 °C. The self-assembly with platinum (II) cations and the ligands to [Pt₂L₄] cages required a prolonged heating period of up to 3 days. Most common used solvent were deuterated acetonitrile, acetone or DMSO.

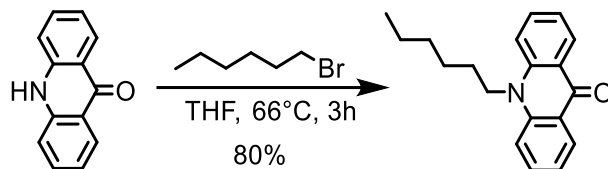
7.2.3 Titration Experiments

To a solution of the coordination cage in an NMR tube (500 μL, 0.7 mM for monomeric cages, 0.35 mM for dimeric cages) was a solution of the investigated guest (halides, other anionic guest, 17.5 mM) added *via* a microliter pipettes. The ¹H NMR spectrum was recorded after briefly shaken the NMR tube.

7.3 Part A – Neutral Guest Uptake in Interpenetrated Coordination Cages

7.3.1 Synthesis and Characterization of ligand L¹ and [BF₄@Pd₄L¹₈]

7.3.1.1 Synthesis of *N*-hexylacridone



Acridone (5.00 g, 25.0 mmol, 1.0 eq.) and potassium-*tert*-butanoxide (3.10 g, 28.8 mmol, 1.1 eq.) were dissolved in dry THF (50 mL) and stirred for 90 min. at room temperature. 1-Bromohexane (8.25 g, 50.0 mmol, 2.0 eq.) was added slowly and the mixture was stirred for 3 h at 66 °C. After cooling to room temperature the mixture was filtered over silicagel, washed with ethyl acetate and the solvent was removed under reduced pressure. The crude product was purified by column chromatography (SiO₂, dichloromethane = 100 % → dichloromethane/methanol: 10:1) and the desired product was obtained as a yellow solid (5.66 g, 20.1 mmol, 80%).

¹H NMR (300 MHz, 298 K, CDCl₃): δ (ppm) = 8.59 (dd, ³J = 8.0 Hz, ⁴J = 1.8 Hz, 2H), 7.73 (ddd, ³J = 8.7 Hz, ³J = 6.9 Hz, ⁴J = 1.8 Hz, 2H), 7.50 (d, ³J = 8.7 Hz, 2H), 7.29 (ddd, ³J = 7.9 Hz, 3J = 7.0 Hz, ⁴J = 0.9 Hz, 2H), 4.40–4.28 (m, 2H), 2.00–1.86 (m, 2H), 1.60–1.52 (m, 2H), 1.47–1.36 (m, 4H), 1.00–0.89 (t, ³J = 7.26 Hz, 3H).

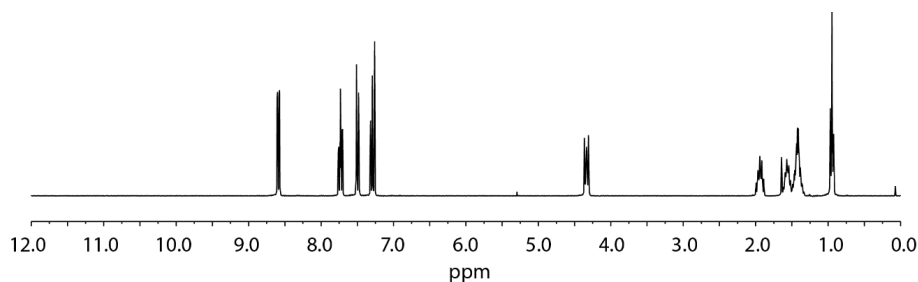


Figure 7.1 ¹H NMR spectrum of *N*-hexylacridone (300 MHz, 298 K, CDCl₃).

¹³C NMR (75 MHz, 298 K, CDCl₃): δ (ppm) = 178.15, 141.95, 134.00, 128.18, 122.67, 121.32, 114.67, 46.40, 31.67, 27.30, 26.76, 22.80, 14.14.

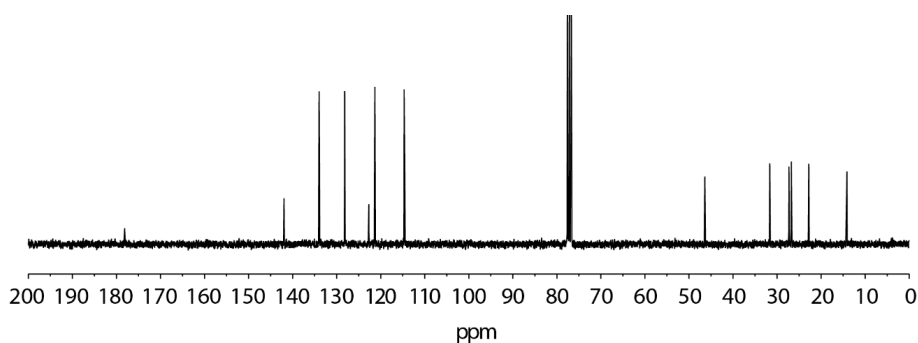
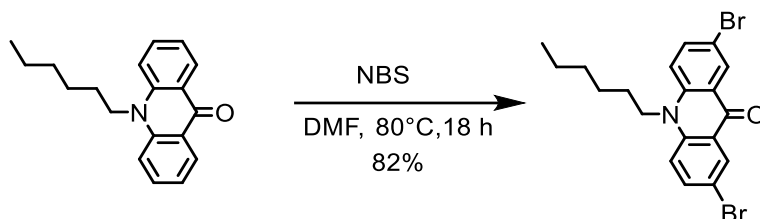


Figure 7.2 ^{13}C NMR spectrum of *N*-hexylacridone (75 MHz, 298 K, CDCl_3).

MS-EI: m/z (%) = 279.1 (30) $[\text{M}]^+$, 208.0 (100) $[\text{C}_{14}\text{H}_{10}\text{NO}]^+$.

IR (ATR): $\tilde{\nu}$ (cm^{-1}) = 2957, 2925, 1628, 1590, 1484, 1456, 1375, 1287, 1261, 1174, 1045, 936, 765, 750, 670.

7.3.1.2 Synthesis of dibromo-*N*-hexylacridone



N-hexylacridone (5.03 g, 18.1 mmol, 1.0 eq.v.) was dissolved in DMF (20 mL). A solution of *N*-bromosuccinimide (9.05 g, 50.80 mmol, 2.82 eq.) in DMF was added dropwise at 0 °C under a nitrogen atmosphere. The reaction mixture was stirred at 80 °C for 18 h. After cooling to room temperature, the mixture was quenched with water (60 mL) and filtered to collect the precipitate. The residue was washed with hexane (50 mL) to yield the product (6.45 g, 14.8 mmol, 82%) as a yellow solid.

^1H NMR (300 MHz, 298 K, CDCl_3): δ (ppm) = 8.64 (d, $^4J = 2.5$ Hz, 2H), 7.78 (dd, $^3J = 9.2$ Hz, $^4J = 2.5$ Hz, 2H), 7.36 (d, $^3J = 9.2$ Hz, 2H), 4.28 (t, $^3J = 8.3$ Hz, 2H), 1.93–1.83 (m, 2H), 1.56–1.49 (m, 2H), 1.47–1.33 (m, 4H), 0.95 (t, $^3J = 6.3$ Hz, 3H).

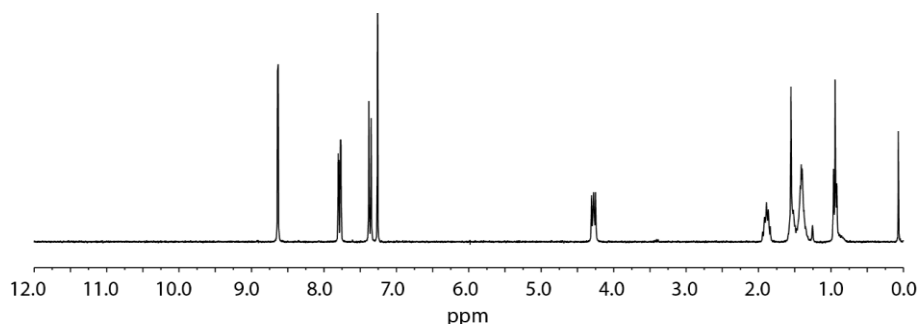


Figure 7.3 ^1H NMR spectrum of dibromo-*N*-hexylacridone (300 MHz, 298 K, CDCl_3).

^{13}C NMR (75 MHz, 298 K, CDCl_3): δ (ppm) = 175.69, 140.52, 137.08, 130.52, 123.80, 116.88, 115.13, 46.75, 31.59, 27.28, 26.69, 22.77, 14.13.

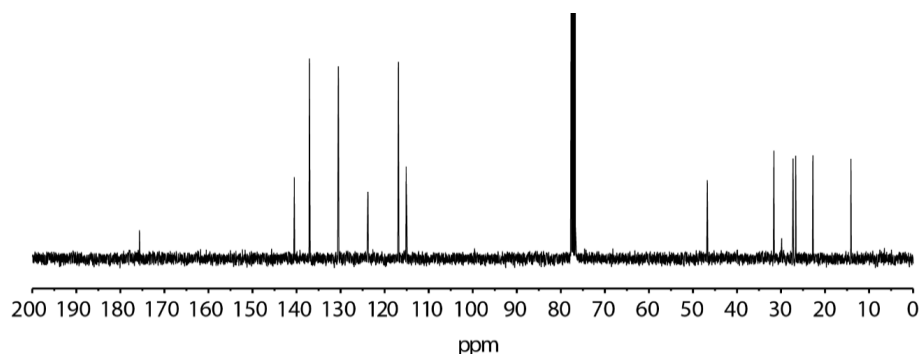
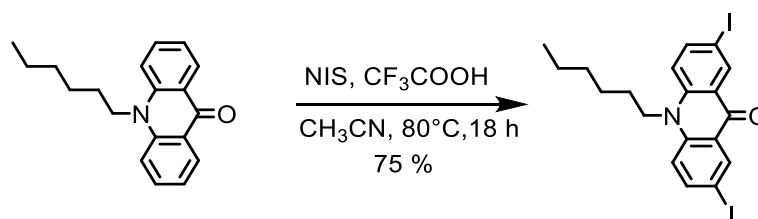


Figure 7.4 ^{13}C NMR spectrum of dibromo-*N*-hexylacridone (75 MHz, 298 K, CDCl_3).

MS-EI: m/z (%) = 437.0 (90) $[\text{M}]^+$, 365.9 (100) $[\text{C}_{14}\text{H}_{10}\text{Br}_2\text{NO}]^+$.

IR (ATR): $\tilde{\nu}$ (cm^{-1}) = 2924, 1626, 1586, 1474, 1257, 1173, 1145, 969, 816, 802, 662.

7.3.1.3 Synthesis of diiodo-*N*-hexylacridone



Under a nitrogen atmosphere, 10-hexylacridone (5.00 g, 17.9 mmol, 1.00 eq.) was dissolved in acetonitrile (120 mL). A solution of NIS (11.27 g, 50.1 mmol, 2.80 eq.) in acetonitrile (30 mL) and trifluoroacetic acid (1.8 mL, 0.83 g, 7.21 mmol, 0.40 eq.) were added dropwise at 0 °C. The reaction mixture was stirred for 18 h at 80 °C. After cooling down to room temperature, a saturated solution of sodium thiosulfate (150 mL) was added. The precipitate was filtered and washed with hexane (50 mL). The desired product could be obtained without further purification as a yellow solid (7.12 g, 13.4 mmol, 75%).

^1H -NMR (300 MHz, 298 K, CDCl_3): δ (ppm) = 8.81 (d, $^4J = 2.5$ Hz, 2H, 1-H, 8-H), 7.95 (dd, $^3J = 9.2$ Hz, $^4J = 2.5$ Hz, 2H, 3-H, 6-H), 7.23 (d, $^3J = 9.2$ Hz, 2H, 4-H, 5-H), 4.25 (t, $^3J = 8.4$ Hz, 2H, NCH_2), 1.94–1.82 (m, 2H, CH_2), 1.59–1.51 (m, 2H, CH_2), 1.46–1.36 (m, 4H, $2 \times \text{CH}_2$), 0.96 (t, $^3J = 6.3$ Hz, 3H, CH_3).

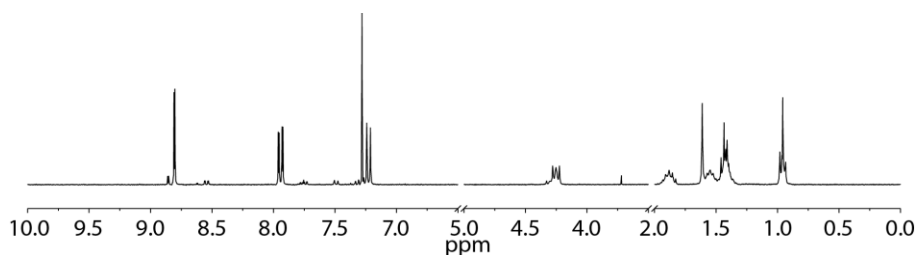


Figure 7.5 ^1H NMR spectrum of diiodo-*N*-hexylacridone (300 MHz, 298 K, CDCl_3).

^{13}C -NMR (75 MHz, 298 K, CDCl_3): δ (ppm) = 175.18, 142.41, 140.92, 136.69, 124.11, 117.03, 117.03, 85.01, 46.49, 31.59, 27.16, 26.64, 22.75, 14.14.

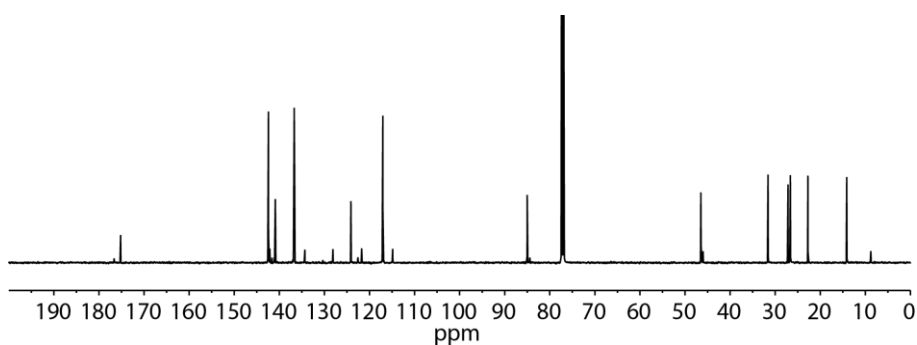
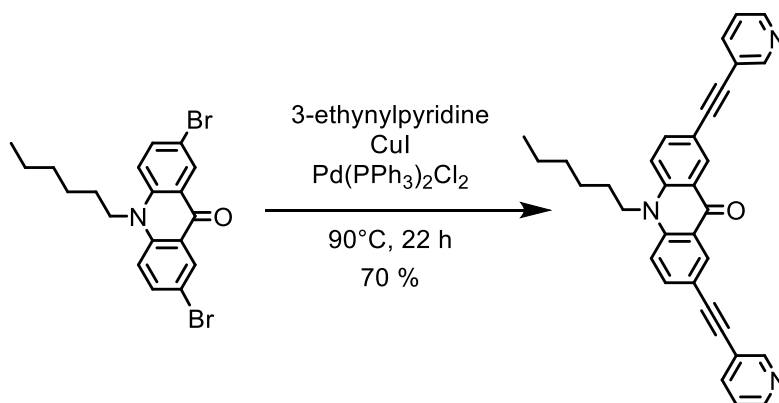


Figure 7.6 ^{13}C NMR spectrum of diiodo-*N*-hexylacridone (75 MHz, 298 K, CDCl_3).

MS-EI: m/z (%) = 532.0 (34) $[\text{M}]^+$, 406.1 (100) $[\text{C}_{19}\text{H}_{21}\text{NOI}]^+$.

IR (ATR): $\tilde{\nu}$ (cm^{-1}) = 3066, 2925, 2853, 1627, 1583, 1473, 1277, 1257, 1176, 1145, 962, 801, 753, 654, 543.

7.3.1.4 Synthesis of *N*-hexyl-2,7-bis(pyridyl-3ethynyl)acridone (ligand L^1)



A mixture of dibromo-*N*-hexylacridone (453 mg, 1.04 mmol, 1.00 equiv.), 3-ethynylpyridine (320 mg, 3.11 mmol, 3.00 equiv.) and copper(I)-iodide (23.7 mg, 0.12 mmol, 0.12 equiv.) in triethylamine (6 mL) was thoroughly degassed and bis(triphenylphosphine)palladium(II)-dichloride (36.3 mg, 0.52 mmol, 0.05 equiv.) was added. The mixture was heated under a nitrogen atmosphere at 90 °C for 20 h. After cooling to room temperature, the solvent was removed *in vacuo*.

Purification by column chromatography (SiO₂, pentane/ethyl acetate = 3:1 → 1.1 → 100 % ethyl acetate) and subsequent gel permeation chromatography (CHCl₃) gave the product as a yellow solid (345 mg, 71.7 μmol, 70%).

Using diiodo-*N*-hexylacridone as a starting material improved the yield to ~90 %.

¹H NMR (300 MHz, 298 K, CDCl₃): δ (ppm) = 8.80 (dd, ⁴*J* = 2.1 Hz, ⁵*J* = 0.9 Hz, 2H, H_g), 8.75 (d, ³*J* = 2.1 Hz, 2H, H_f), 8.57 (dd, ⁴*J* = 4.8 Hz, ⁵*J* = 1.7 Hz 2H, H_a), 7.91–7.80 (m, 4H, H_c, H_d), 7.50 (d, ³*J* = 8.9 Hz, 2H, H_b), 7.31 (ddd, ³*J* = 8.9 Hz, ⁴*J* = 4.9 Hz, ⁵*J* = 0.9 Hz, 2H, H_e), 4.36 (t, ³*J* = 8.3 Hz, 2H, NCH₂), 1.89 (p, ³*J* = 9.0 Hz, 2H, CH₂), 1.90–1.96 (m, 2 H, CH₂), 1.53–1.35 (m, 4H, CH₂), 0.96 (t, ³*J* = 9.0 Hz, 3H, CH₃).

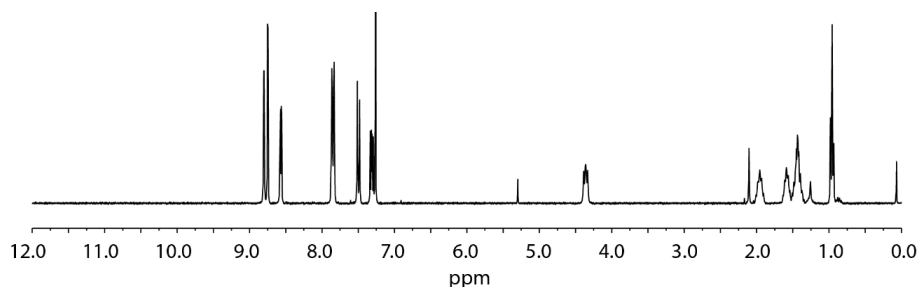


Figure 7.7 ¹H NMR spectrum of Ligand L¹ (300 MHz, 298 K, CDCl₃).

¹³C NMR (125 MHz, 298 K, CDCl₃): δ (ppm) = 176.56, 152.37, 148.75, 141.44, 138.57, 136.67, 131.95, 123.23, 122.57, 120.53, 116.12, 115.35, 100.14, 86.64, 46.73, 31.63, 27.38, 26.71, 22.78, 14.14.

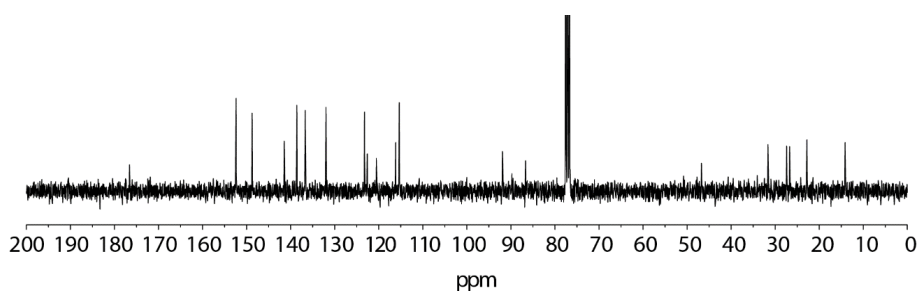
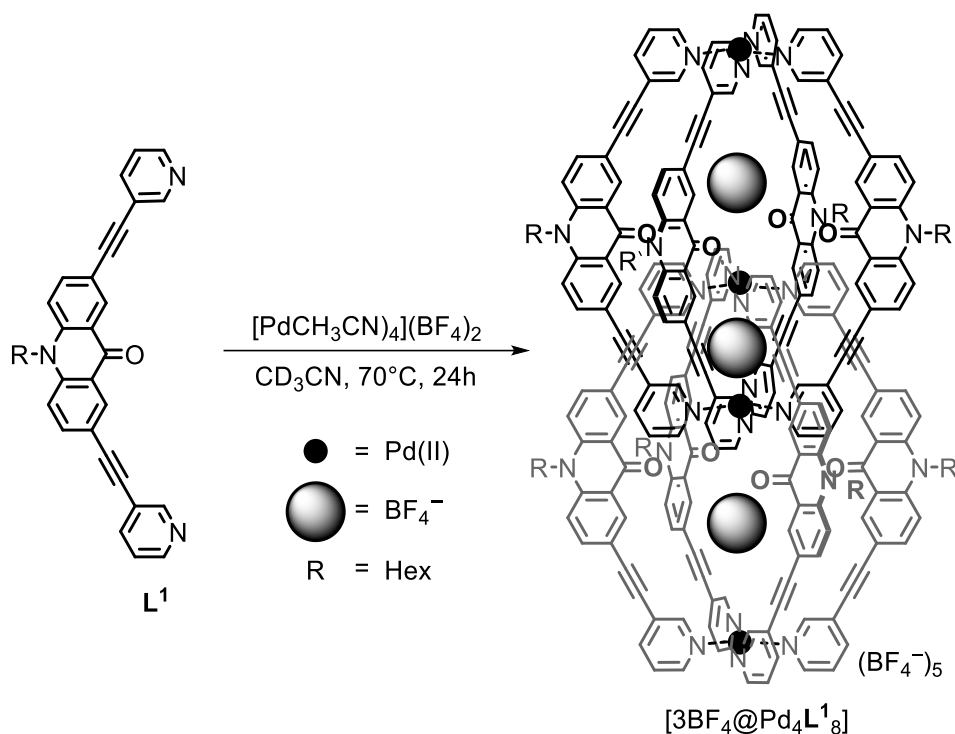


Figure 7.8 ¹³C NMR spectrum of Ligand L¹ (125 MHz, 298 K, CDCl₃).

MS-EI: *m/z* (%) = 481.2 (100) [M]⁺, 410.1 (60) [C₂₉H₁₆N₃O]⁺.

IR (ATR): $\tilde{\nu}$ (cm⁻¹) = 2953, 2921, 2858, 1735, 1639, 1602, 1488, 1401, 1365, 1260, 1180, 1114, 1094, 1022, 918, 807, 700.

7.3.1.5 Synthesis of Interpenetrated Coordination Cage $[\text{BF}_4@\text{Pd}_4\text{L}^1_8]$ 

The coordination cage was formed in quantitative yields by heating a mixture of ligand L^1 (5.79 mg, 12.0 μmol , 1.0 equiv.) in CD_3CN (4.29 mL) and a solution of $[\text{Pd}(\text{CH}_3\text{CN})_4](\text{BF}_4)_2$ (6 μmol , 429 μL of a 15 mM solution in CD_3CN) at 70 $^\circ\text{C}$ for 24 h to give the double cage.

$^1\text{H NMR}$ (500 MHz, 298 K, CD_3CN): δ (ppm) = 10.78 (d, $^4J = 0.9$ Hz, 8H, g'-H), 10.28 (dd, $^3J = 5.70$ Hz, $^4J = 1.35$ Hz, 8H, f'-H), 10.01 (d, $^4J = 1.4$ Hz, 8H, g-H), 9.26 (dd, $^3J = 6.0$ Hz, $^4J = 1.4$ Hz, 8H, f-H), 8.17 (dt, $^3J = 8.0$ Hz, $^4J = 1.6$ Hz, 8H, d-H), 8.07 (d, $^4J = 2.2$ Hz, 8H, a'-H), 7.93 (d, $^4J = 2.3$ Hz, 8H, a-H), 7.85 (dd, $^3J = 8.7$ Hz, $^4J = 2.3$ Hz, 8H, c-H), 7.74 (dd, $^3J = 8.7$ Hz, $^4J = 2.3$ Hz, 8H, e-H), 7.60 (d, $^3J = 8.9$ Hz, 8H, b-H), 7.39 (d, $^3J = 8.9$ Hz, 8H, b'-H), 7.14 (dd, $^3J = 8.7$ Hz, $^4J = 2.3$ Hz, 8H, c'-H), 6.75–6.51 (m, 16H, e'-H, d'-H), 4.21 (t, $^3J = 8.3$ Hz, 16H, NCH_2), 1.82–1.69 (m, 16H, CH_2), 1.48–1.39 (m, 16H, CH_2), 1.33–1.13 (m, 32H, CH_2), 0.86–0.81 (m, 24H, CH_3).

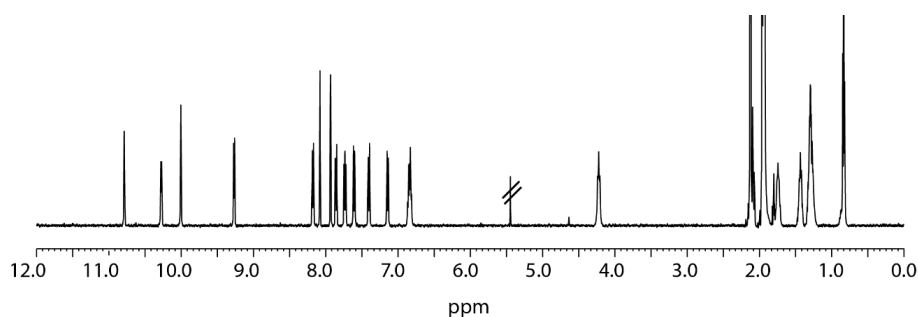


Figure 7.9 $^1\text{H NMR}$ spectrum of interpenetrated coordination cage $[\text{3BF}_4@\text{Pd}_4\text{L}^1_8]$ (500 MHz, 298 K, CD_3CN).

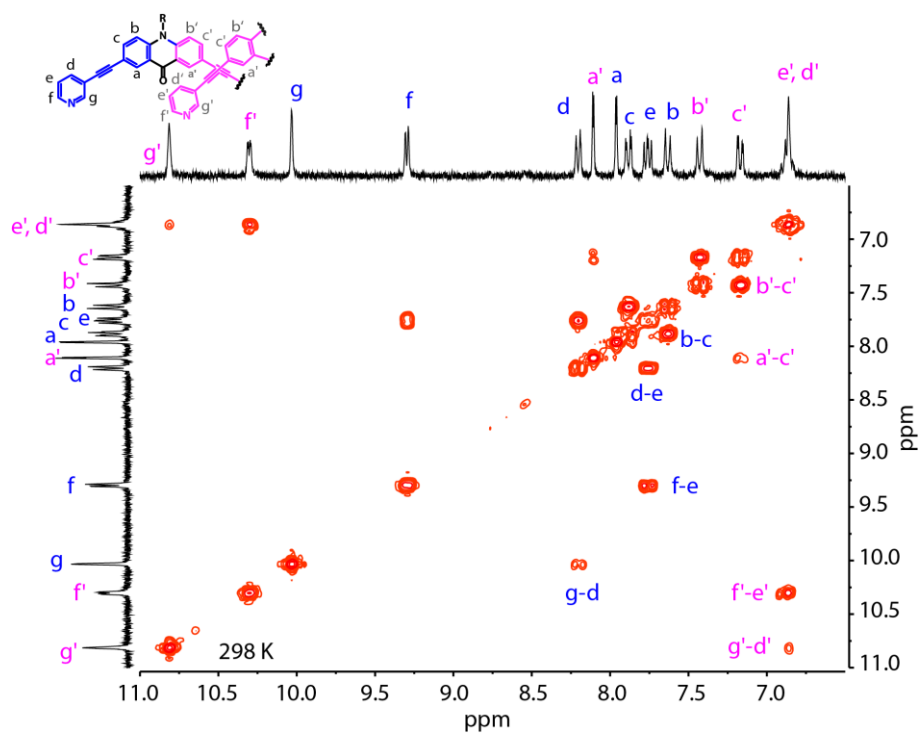


Figure 7.10 ^1H , ^1H COSY spectrum of $[3\text{BF}_4@Pd_4L^1_8]$ (400 MHz, 298 K, CD_3CN). Correlation are highlighted.

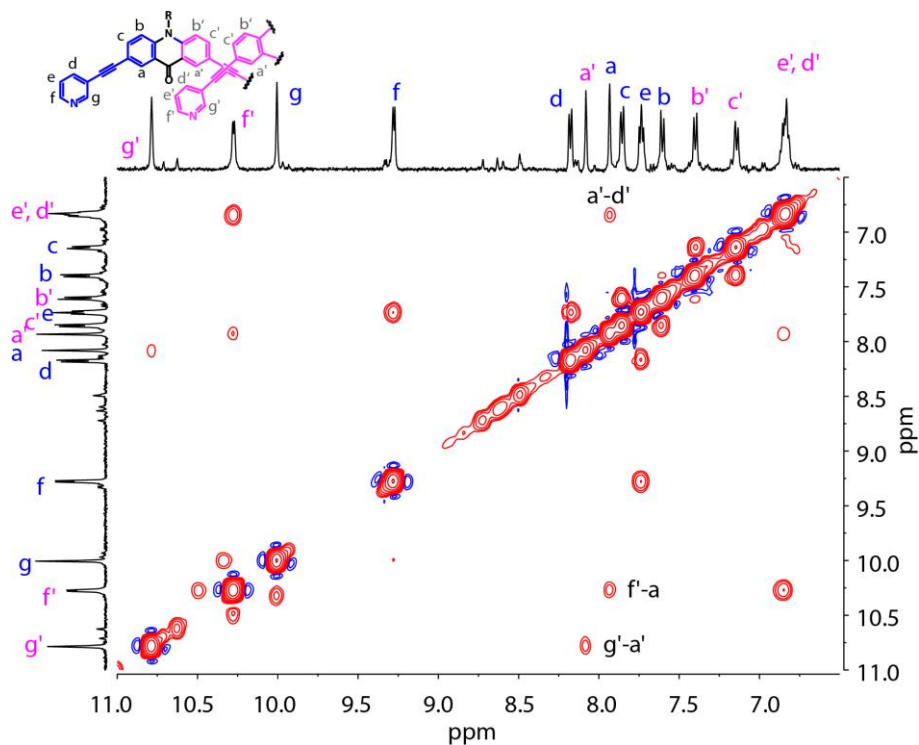


Figure 7.11 ^1H , ^1H NOESY spectrum of $[3\text{BF}_4@Pd_4L^1_8]$ (400 MHz, 298 K, CD_3CN). Correlation signals between different ligands were found between protons $g'-a'$, $f'-a$ and $a'-d'$. Non-assigned signals are COSY contacts.

^{13}C NMR (125 MHz, 298 K, CD_3CN): δ (ppm) = 174.21, 143.56, 142.90, 142.35, 140.71, 137.21, 132.33, 128.44, 126.54, 125.39, 124.18, 122.29, 122.02, 118.26, 116.95, 116.55, 114.93, 95.93,

93.80, 85.22, 84.29, 46.85, 32.13, 27.80, 26.81, 23.22, 14.19 (not all carbon signals could be identified).

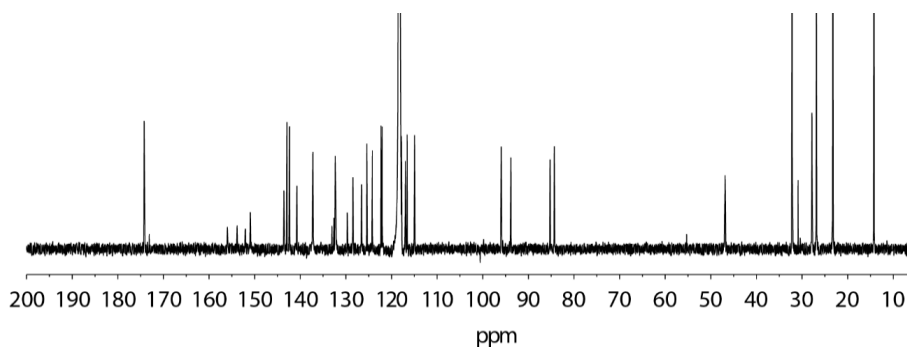


Figure 7.12 ¹³C NMR spectrum of interpenetrated coordination cage [3BF₄@Pd₄L₁₈] (125 MHz, 298 K, CD₃CN).

¹⁹F NMR (470 MHz, 298 K, CD₃CN): δ (ppm) = -143.32 (4F, encapsulated BF₄⁻), -144.85 (8F, broad signal, encapsulated BF₄⁻), -151.70 (20F, broad signal, free BF₄⁻).

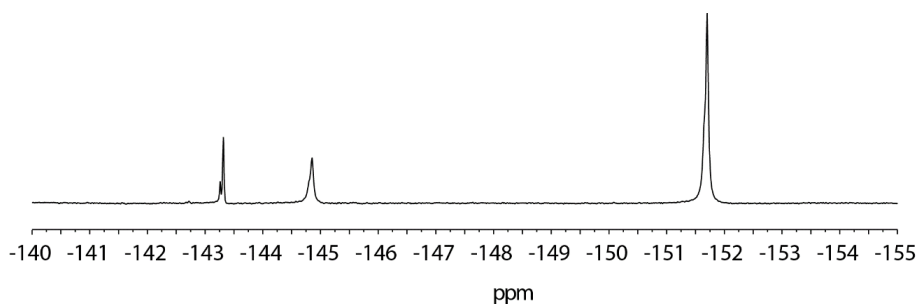


Figure 7.13 ¹⁹F NMR spectrum of interpenetrated coordination cage [Pd₄L₁₈] (470 MHz, 298 K, CD₃CN).

ESI-HR-MS ([C₂₆₄H₂₁₆N₂₄O₈Pd₄(BF₄)₃]⁵⁺): exp.: 907.6704 (calc.: 907.6715) (for detailed mass see main text).

IR (ATR): $\tilde{\nu}$ (cm⁻¹) = 2228, 2858, 2266, 2213, 1648, 1596, 1490, 1065, 814, 692.

7.3.2 Titration Experiments

7.3.2.1 Titration with Anions

General Procedure

The host-guest complexes were formed by titrating a solution of the halide (as their tetrabutylammonium salts in CD₃CN, 17.5 mM) in steps of 0.5 eq. (5 μL) to 500 μL of a 0.35 mM solution of the cage [3BF₄@Pd₄L¹₈] in CD₃CN in an NMR-tube. The NMR spectra were recorded immediately after briefly shaking the solution.

Titration of [3BF₄@Pd₄L¹₈] with NBu₄F

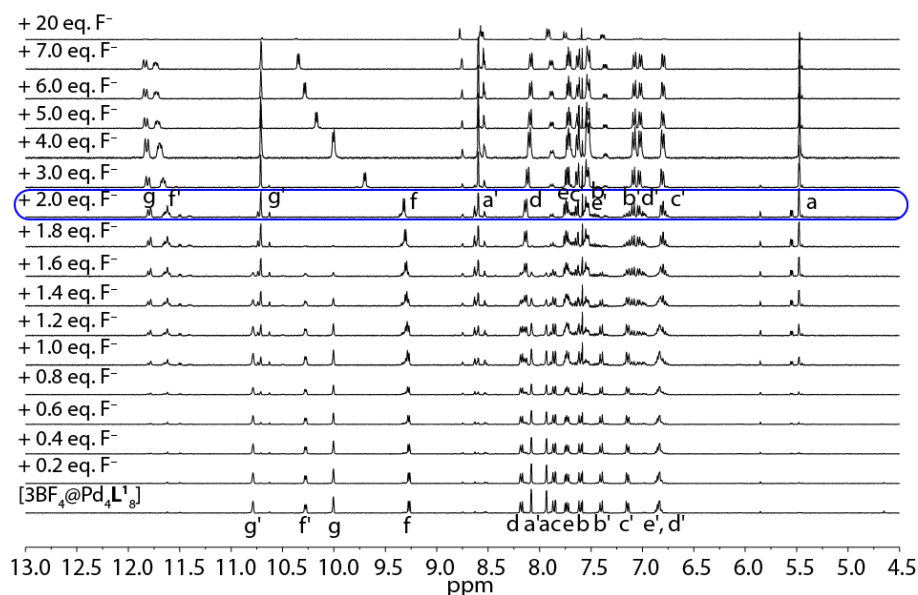


Figure 7.14 ¹H NMR titration (400 MHz, 298 K, CD₃CN) of [3BF₄@Pd₄L¹₈] with NBu₄F. Upon addition of two equivalents of fluoride anions; [3BF₄@Pd₄L¹₈] transforms into [2F@Pd₄L¹₈], indicated by strong downfield shifts of the protons pointing inside the outer two cavities. Further addition of halide results in a strong downfield shift of protons f, caused by the interaction of chloride anions with the outside of the cage. Addition of further amounts of NBu₄F leads decomposition of the cage and release of free ligand L¹.

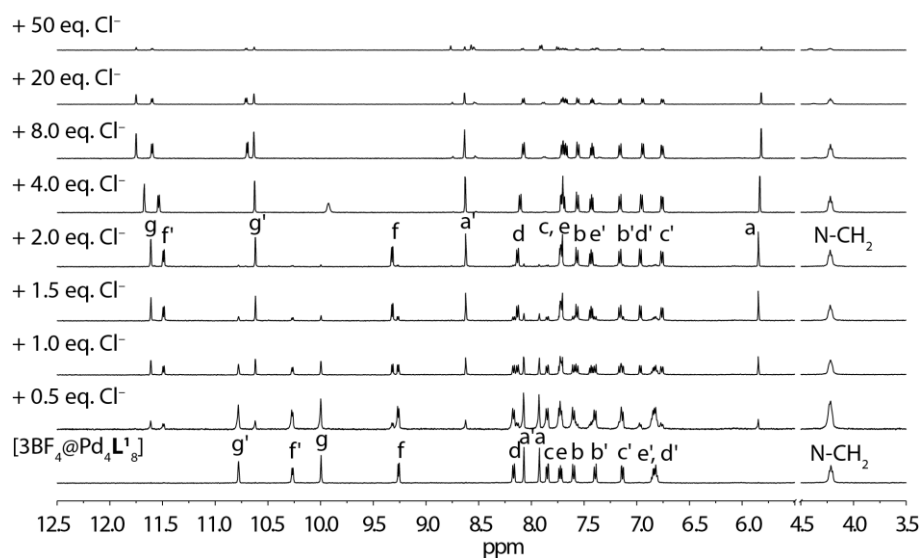
Titration of $[3\text{BF}_4@Pd_4L^1_8]$ with NBu_4Cl 

Figure 7.15 ^1H NMR titration (500 MHz, 298 K, CD_3CN) of $[3\text{BF}_4@Pd_4L^1_8]$ with NBu_4Cl . Upon addition of two equiv. of chloride ions; $[3\text{BF}_4@Pd_4L^1_8]$ transforms into $[2\text{Cl}@Pd_4L^1_8]$, indicated by strong downfield shifts of the protons pointing inside the outer two cavities. Further addition of halide results in a strong downfield shift of protons f, caused by the interaction of chloride anions with the periphery of the cage. Addition of further amounts of NBu_4Cl leads to a partial decomposition of the double cage.

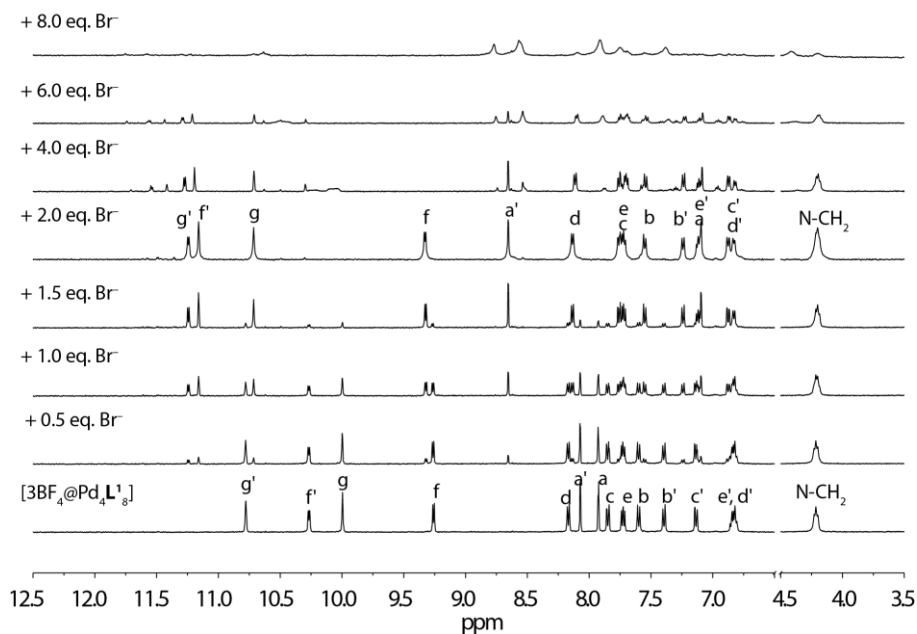
Titration of $[3\text{BF}_4@Pd_4L^1_8]$ with NBu_4Br 

Figure 7.16 ^1H NMR titration (500 MHz, 298 K, CD_3CN) of $[3\text{BF}_4@Pd_4L^1_8]$ with NBu_4Br (17.5 mM). Upon addition of two equivalents of Br^- , $[3\text{BF}_4@Pd_4L^1_8]$ transforms into $[2\text{Br}+\text{BF}_4@Pd_4L^1_8]$. Excess addition leads to complete disaggregation of the double cage under release of free ligand L^1 .

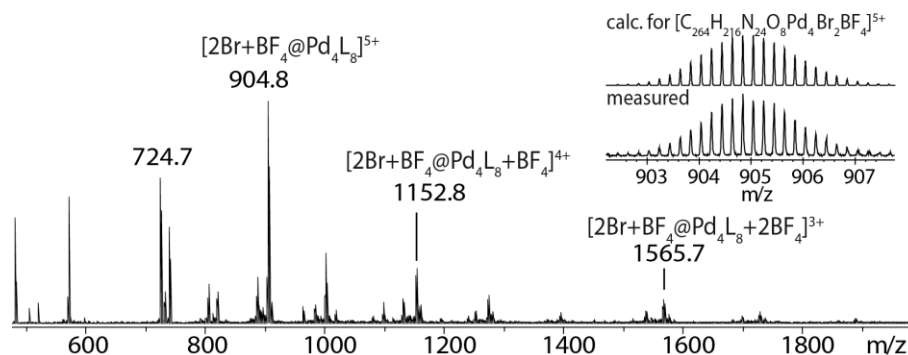


Figure 7.17 ESI-MS of $[2\text{Br}+\text{BF}_4@Pd_4L_8]$. The peak at $m/z = 724.71$ corresponds to the hexacationic coordination cage containing chloride anions $[2\text{Cl}@Pd_4L_8]^{6+}$.

Titration of $[3\text{BF}_4@Pd_4L_8]$ with NBu_4I

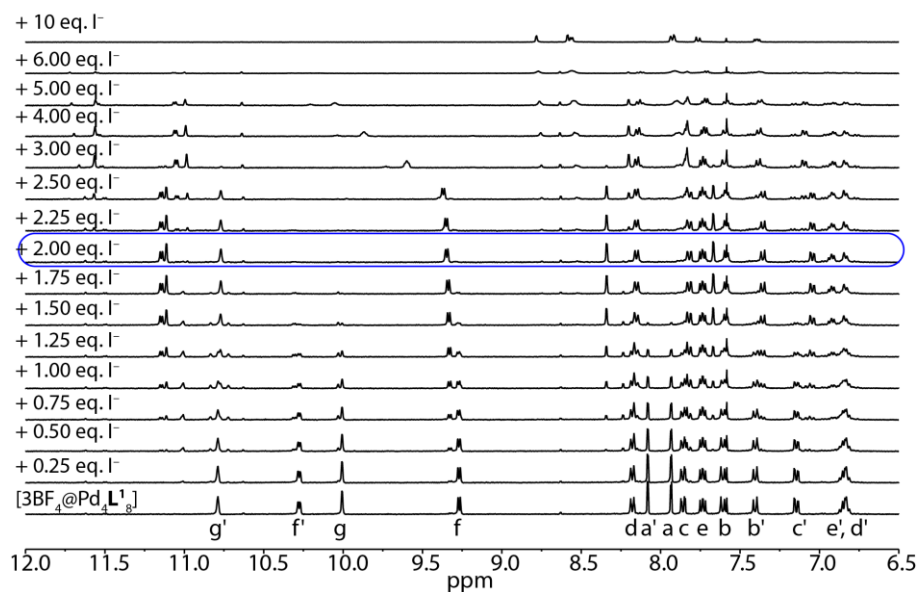


Figure 7.18 ^1H NMR titration (400 MHz, 298 K, CD_3CN) of $[3\text{BF}_4@Pd_4L_8]$ with NBu_4I (17.5 mM). Upon addition of two equivalents of iodine, $[3\text{BF}_4@Pd_4L_8]$ transforms into $[2\text{I}+\text{BF}_4@Pd_4L_8]$. Excess addition leads to complete disaggregation of the double cage under release of free ligand L^1 .

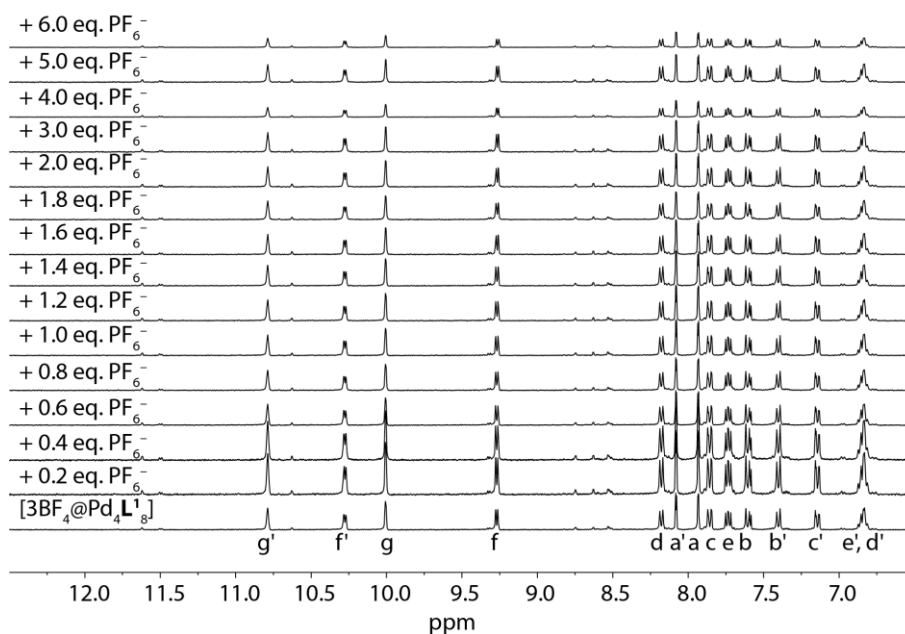


Figure 7.19 ^1H NMR titration (400 MHz, 298 K, CD_3CN) of $[\text{3BF}_4@\text{Pd}_4\text{L}^1_8]$ with NBu_4PF_6 (17.5 mM). No change in chemical shifts could be observed upon addition of NBu_4PF_6 . Hence, no anion exchange between tetrafluoroborate and hexafluorophosphate occurs.

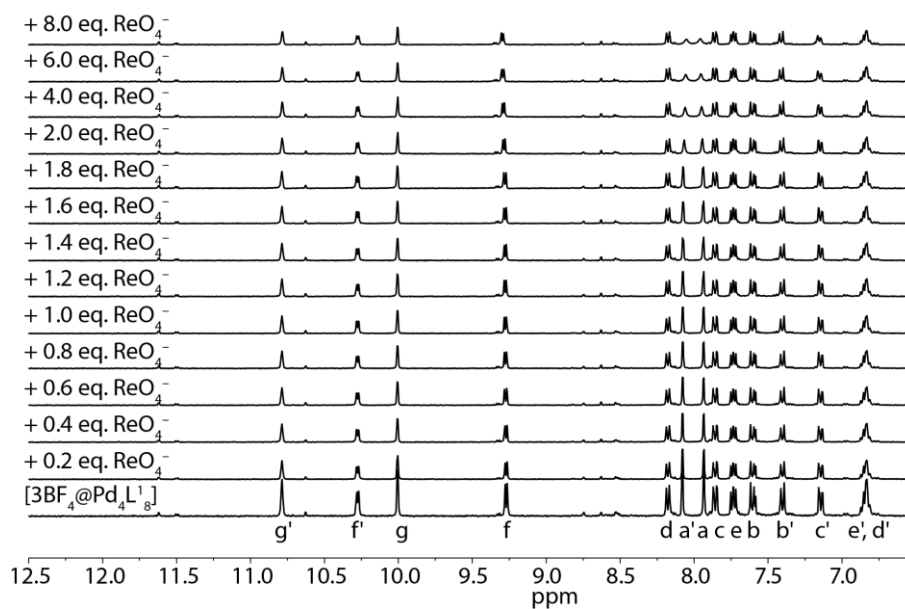


Figure 7.20 ^1H NMR titration (500 MHz, 298 K, CD_3CN) of $[\text{3BF}_4@\text{Pd}_4\text{L}^1_8]$ with NBu_4ReO_4 (17.5 mM). No change in chemical shifts was observed upon addition of tetrabutylammonium perrhenate.

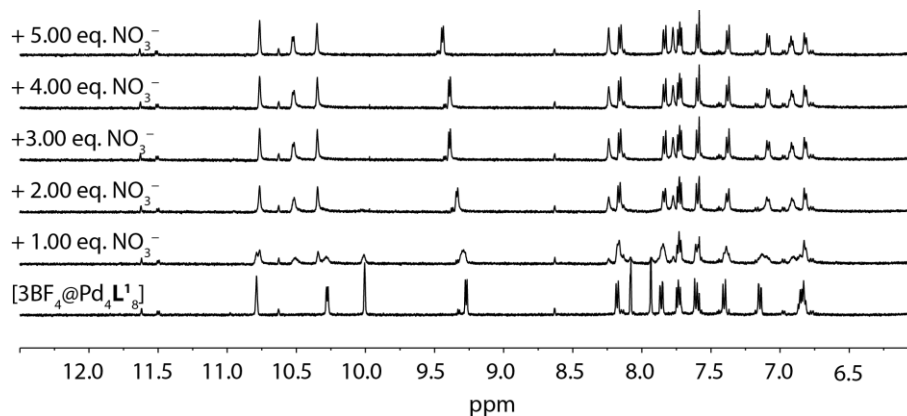


Figure 7.21 ^1H NMR titration (500 MHz, 298 K, CD_3CN) of $[\text{3BF}_4@Pd_4L^1_8]$ with NBu_4NO_3 (17.5 mM). After addition of 2 equivalents of nitrate, the $[\text{3BF}_4@Pd_4L^1_8]$ transforms into $[\text{3BF}_4+\text{NO}_3@Pd_4L^1_8]$.

7.3.2.2 Titration of the Halide-filled cages with silver(I)-tetrafluoroborate

General Procedure

To a solution of the halide-filled cage (500 μL , 0.35 mM, CD_3CN) a silver(I)-tetrafluoroborate solution (CD_3CN , 17.5 mM) was added in steps of 1.0 equiv. (10 μL). The ^1H NMR spectra were recorded immediately after briefly shaking the solution.

7.3.2.2.1 Titration of $[\text{2Cl}@Pd_4L^1_8]$ with AgBF_4

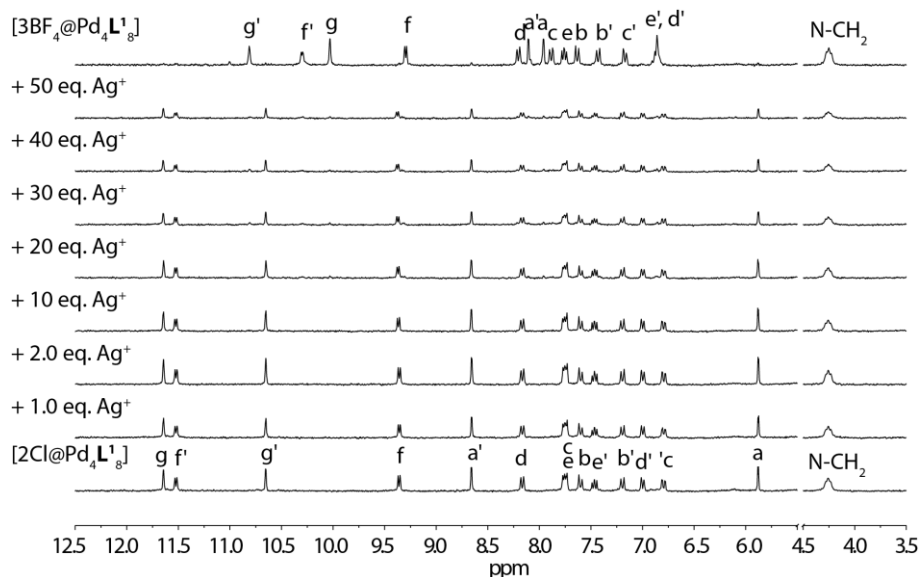


Figure 7.22 ^1H NMR titration (300 MHz, 298 K, CD_3CN) of $[\text{2Cl}@Pd_4L^1_8]$ with AgBF_4 (17.5 mM). No spectral change or precipitation is observable. Even after the addition of 50 equiv. of silver(I) ions, only signals of the $[\text{2Cl}@Pd_4L^1_8]$ species are visible. The decrease in intensity is due to dilution.

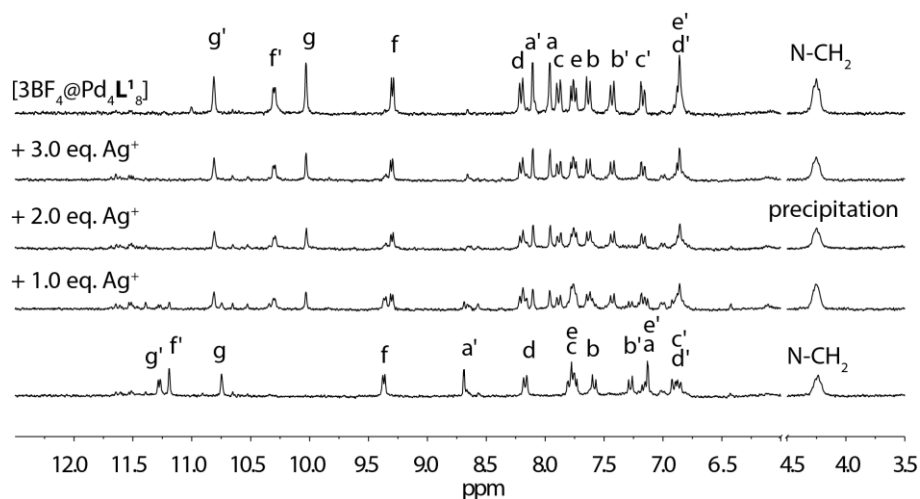
7.3.2.2 Titration of $[2\text{Br}+\text{BF}_4@\text{Pd}_4\text{L}^1_8]$ with AgBF_4 

Figure 7.23 ^1H NMR titration (300 MHz, 298 K, CD_3CN) of $[2\text{Br}+\text{BF}_4@\text{Pd}_4\text{L}^1_8]$ with AgBF_4 (17.5 mM). Precipitation of encapsulated bromide from $[2\text{Br}+\text{BF}_4@\text{Pd}_4\text{L}^1_8]$ after the addition of two equivalents of AgBF_4 under full recovery of $[3\text{BF}_4@\text{Pd}_4\text{L}^1_8]$.

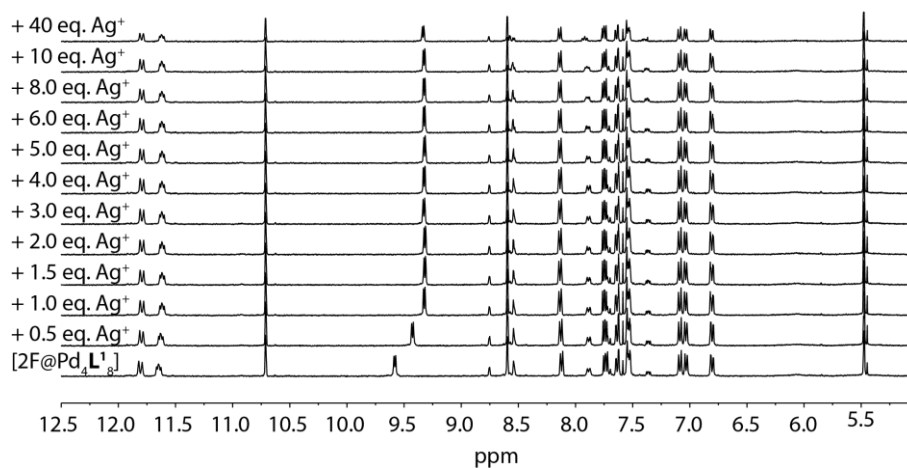
7.3.2.2.3 Titration of $[2\text{F}+\text{BF}_4@\text{Pd}_4\text{L}^1_8]$ with AgBF_4 

Figure 7.24 ^1H NMR titration (400 MHz, 298 K, CD_3CN) of $[2\text{F}+\text{BF}_4@\text{Pd}_4\text{L}^1_8]$ with AgBF_4 (17.5 mM). formation of $[3\text{BF}_4@\text{Pd}_4\text{L}^1_8]$ was observed.

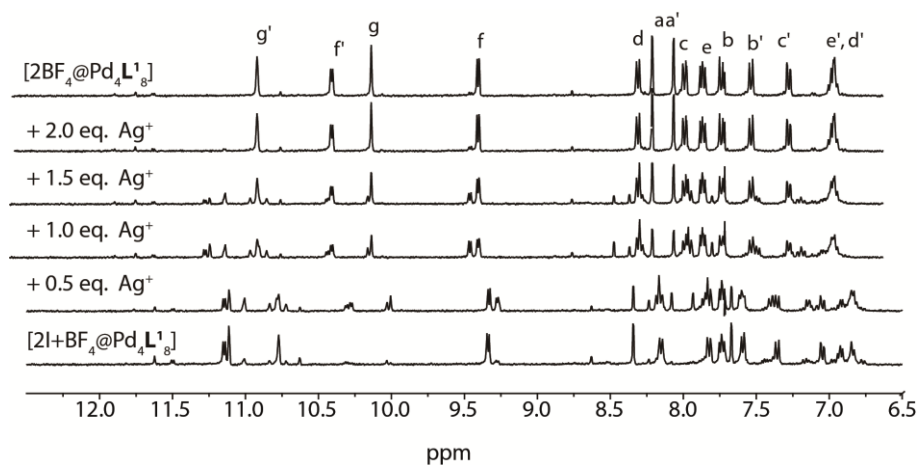
7.3.2.2.4 Titration of $[2\text{I}+\text{BF}_4@\text{Pd}_4\text{L}^1_8]$ with AgBF_4 

Figure 7.25 ^1H NMR titration (400 MHz, 298 K, CD_3CN) of $[2\text{I}+\text{BF}_4@\text{Pd}_4\text{L}^1_8]$ with AgBF_4 (17.5 mM). Precipitation of AgI from $[2\text{Br}+\text{BF}_4@\text{Pd}_4\text{L}^1_8]$ after the addition of two equivalents of AgBF_4 under full recovery of $[3\text{BF}_4@\text{Pd}_4\text{L}^1_8]$.

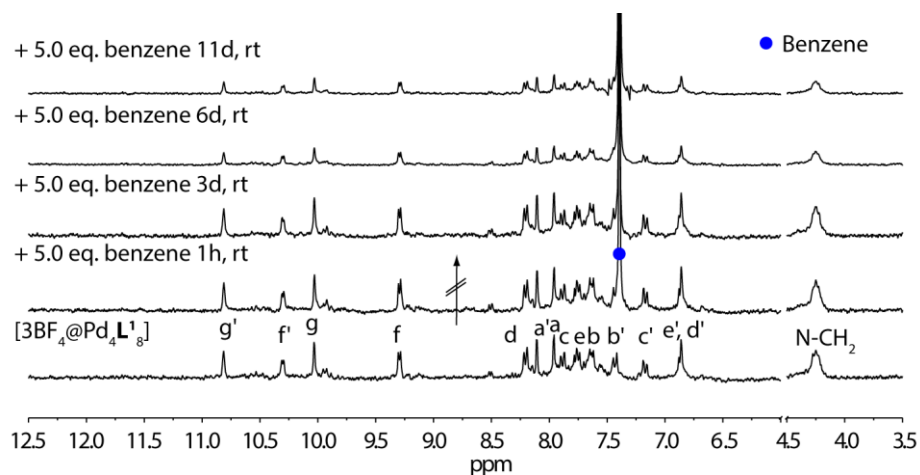
7.3.2.3 Addition of Neutral Guest Molecules to $[3\text{BF}_4@\text{Pd}_4\text{L}^1_8]$ 

Figure 7.26 ^1H NMR spectra (300 MHz, 298 K, CD_3CN) of $[3\text{BF}_4@\text{Pd}_4\text{L}^1_8]$. Addition of benzene (17.5 mM) does not result in any visible spectral changes. Same results were obtained with other neutral guest molecules.

7.3.3 Addition of Neutral Guest Molecules

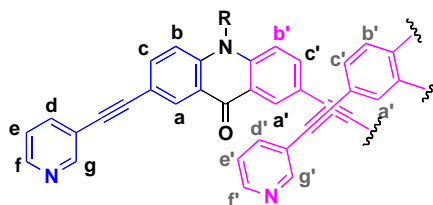
General Procedure

To a solution of the halide-filled cage (500 μL , 0.34 mM, CD_3CN) a solution of the dissolved neutral guest compound (CD_3CN , 70 mM, 2-100 eq.) was added. The ^1H NMR spectra were recorded after several days at 23 $^\circ\text{C}$ (fixed temperature in an air conditioned room) to allow full equilibration of the reaction mixture.

Data Interpretation and Determination of Binding Constant K

All spectra were referenced to the solvent signal, phase- and baseline-corrected in the usual way. All host-guest systems were found to exhibit slow exchange on the NMR timescale and the association constants could be directly determined from the integral intensities of the free/filled host species in the equilibrated mixture, given the starting concentrations of host and added guest.

The NCH_2 -signal of the hexyl chain at 4.21 ppm was used as an internal reference for signal integration since no other signals are in its vicinity and it did not show any reaction to the presence and encapsulation of the guest.



For determining the association constant, integral intensities of several protons that point inside the central cavity of the interpenetrated coordination cage, in particular proton $\text{H}_{g'}$ and $\text{H}_{a'}$, were considered. Depending on the guest, these signals were found to undergo characteristic up- or down-field shifts. In cases where signals of encapsulated guests came close to signals of the host-guest complex, COSY and NOESY NMR experiments were employed for an unambiguous signal assignment.

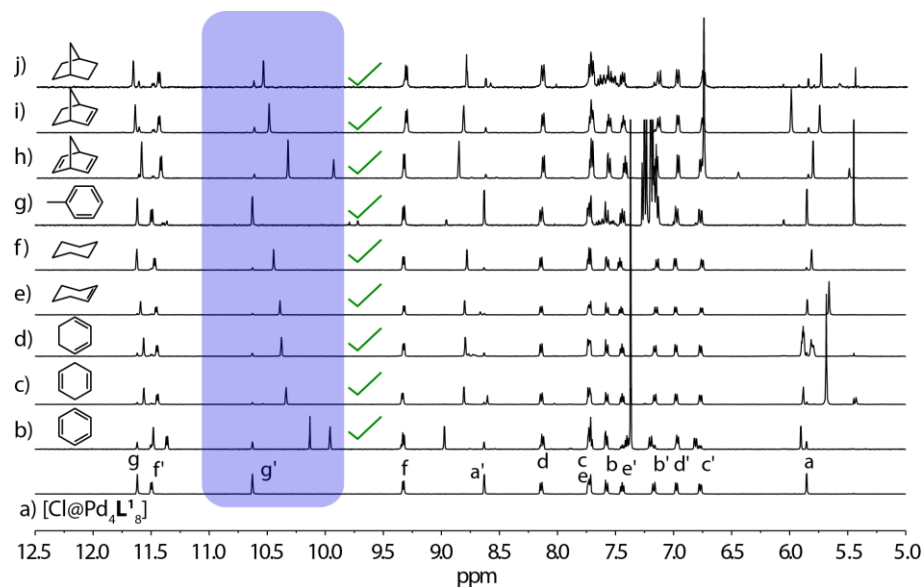
7.3.3.1 Addition of Neutral Guests to $[2\text{Cl}@Pd_4L^1_8]$ 7.3.3.1.1 ^1H NMR Spectroscopy

Figure 7.27 ^1H NMR spectra (500 MHz, 296 K, CD_3CN) of $[2\text{Cl}@Pd_4L^1_8]$ and after the addition of various neutral guest molecules: b) benzene (8.7 eq.), c) 1,4-cyclohexadiene (8.7 eq.), d) 1,3-cyclohexadiene (8.7 eq.), e) cyclohexene (8.7 eq.), f) cyclohexane (8.7 eq.), g) toluene (8.7 eq.), h) norbornadiene (8.7 eq.), i) norbornene (8.7 eq.) and j) norbornene (8.7 eq.). Upon addition of an excess of neutral guest molecule, a new set of signals can be found in the ^1H NMR spectra. The NMR spectra were recorded after 14 d at 23 °C.

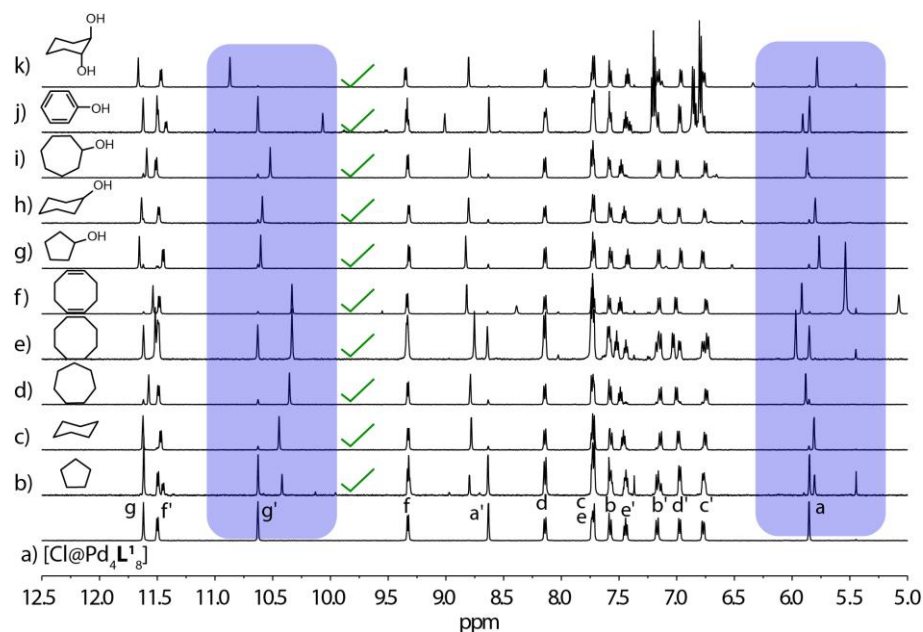


Figure 7.28 ^1H NMR spectra (500 MHz, 296 K, CD_3CN) of a) empty host $[2\text{Cl}@Pd_4L^1_8]$ and different host-guest complexes: $[X+Cl@Pd_4L_8]$ with X= b) cyclopentane (8.7 eq.), c) cyclohexane (8.7 eq.), d) cycloheptane (8.7 eq.), e) cyclooctane (8.7 eq.), f) cyclooctadiene (8.7 eq.) g) cyclopentanol (8.7 eq.), h) cyclohexanol (8.7 eq.), i) cycloheptanol (8.7 eq.), j) phenol (8.7 eq.) k) trans-1,2 cyclohexanediol (8.7 eq.).

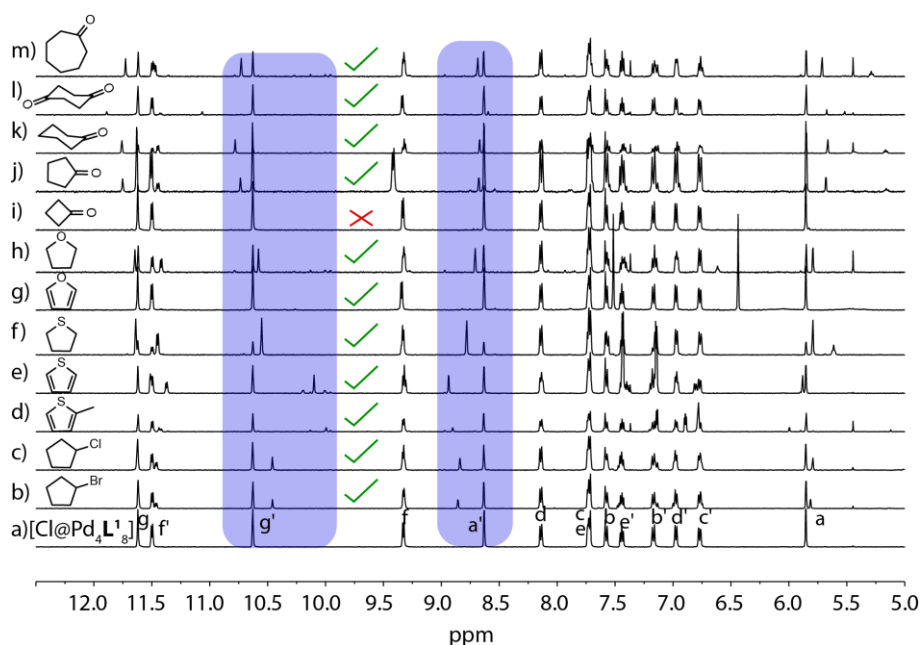


Figure 7.29 ^1H NMR spectra (500 MHz, 296 K, CD_3CN) of a) empty host $[\text{2Cl@Pd}_4\text{L}^1_8]$ and different host-guest complexes: $[\text{X+Cl@Pd}_4\text{L}_8]$ with X= b) bromocyclopentane (8.7 eq.), c) chlorocyclopentane (8.7 eq.), d) 2-methylthiophene (8.7 eq.), e) thiophene (8.7 eq.), f) tetrahydrothiophene (8.7 eq.), g) furan (8.7 eq.), h) tetrahydrofuran (8.7 eq.), i) cyclobutanone (8.7 eq.), j) cyclopentanone (8.7 eq.), k) cyclohexanone (8.7 eq.) l) 1,4 cyclohexadione (8.7 eq.) and m) cycloheptanone (8.7 eq.). Cyclobutanone does not bind.

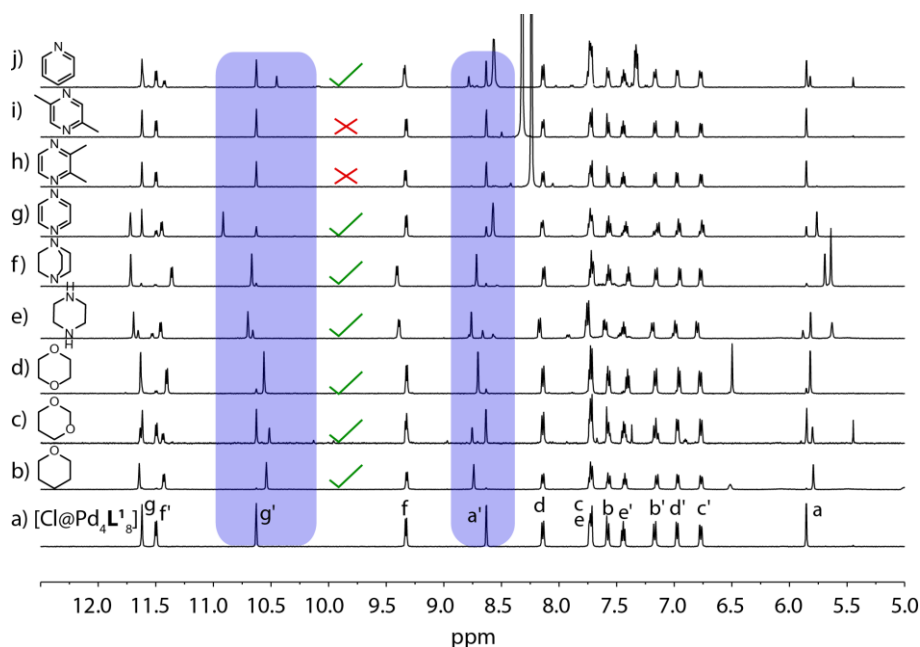


Figure 7.30 ^1H NMR spectra (500 MHz, 296 K, CD_3CN) of a) empty host $[\text{2Cl@Pd}_4\text{L}^1_8]$ and different host-guest complexes: $[\text{X+Cl@Pd}_4\text{L}_8]$ with X= b) tetrahydropyrene (18.9 eq.), c) 1,3 dioxane (8.7 eq.), d) 1,4 dioxane (1.8 eq.), e) piperazine (1.8 eq.), f) DABCO (1.8 eq.), g) pyrazine (1.8 eq.), h) 2,3 dimethylpyrazine (87 eq.), i) 2,5 dimethylpyrazine (87 eq.) and j) pyridine (8.7 eq.). Addition of guest molecules a-g and j results in the formation of the host guest complex $[\text{X+Cl@Pd}_4\text{L}^1_8]$. In contrast, the neutral guest molecules 2,5-dimethylpyrazine and 2,3-dimethylpyrazine are not encapsulated inside the interpenetrated coordination cage, due to the steric bulk of the methyl groups.

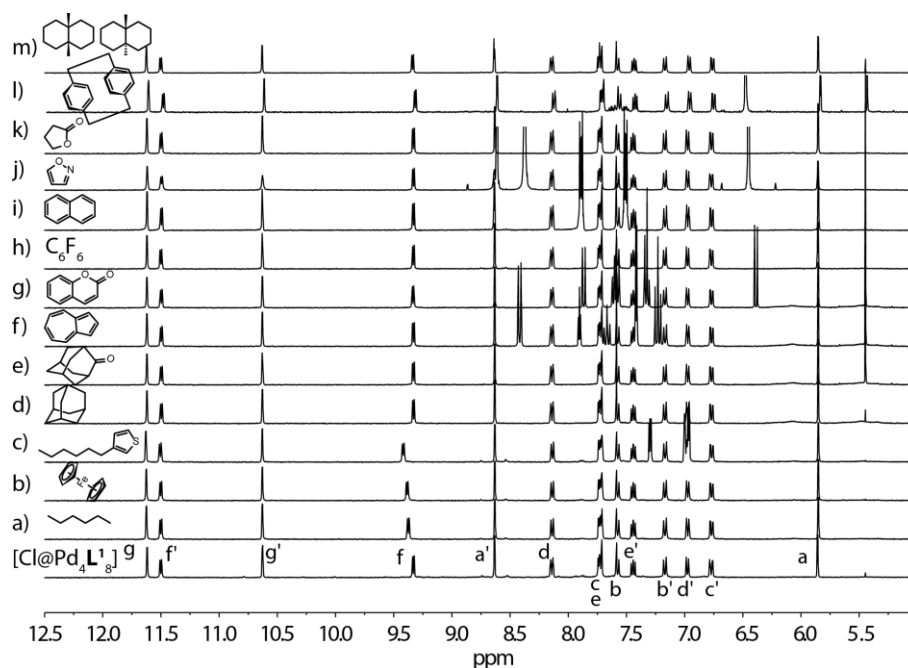


Figure 7.31 ^1H NMR spectra (400 MHz, 296 K, CD_3CN) of $[\text{Cl}@\text{Pd}_4\text{L}^1_8]$ and after the addition of various neutral guest molecules: a) hexane (18.9 eq.), b) ferrocene (18.9 eq.), c) 3-hexylthiophene (18.9 eq.), d) adamantane (18.9 eq.), e) adamantone (18.9 eq.), f) azulene (18.9 eq.), g) coumarine (18.9 eq.), h) hexafluorobenzene (18.9 eq.), i) naphthalene (18.9 eq.), j) isooxazol (18.9 eq.), k) butyrolactone (100 eq.), l) [2.2]paracyclophane (8.9 eq.) and l) decalin (18.9 eq.), (mixture of cis and trans isomer, 20 eq.). No change in chemical shift could be observed after the addition of the neutral guest molecules and an equilibration time of 7-14 days. The shifting of proton signal f, is due to association of the guest molecule to the interpenetrated coordination cage from the outside.

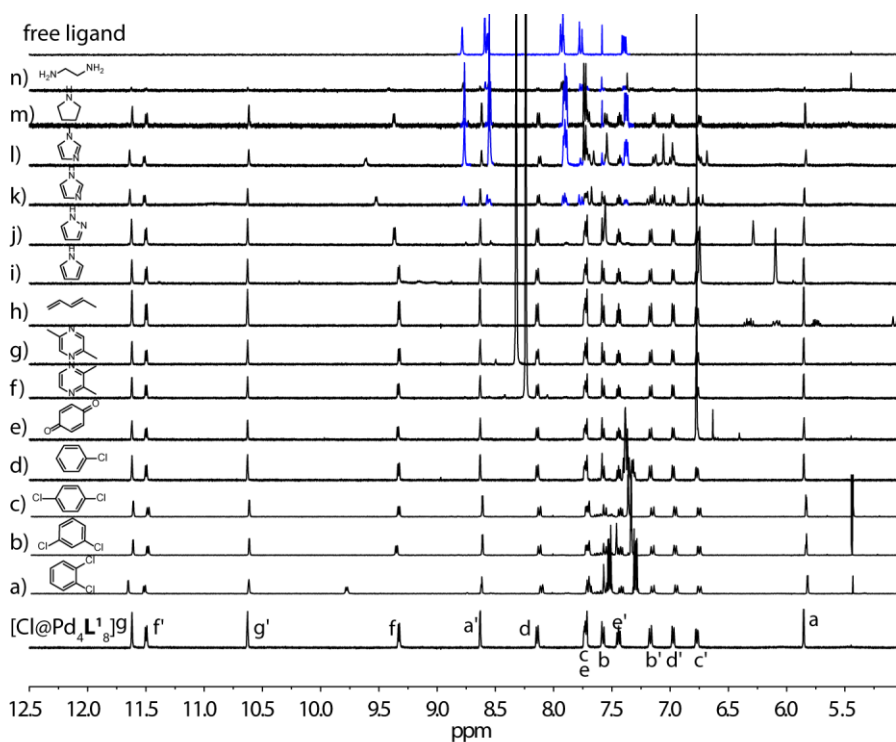


Figure 7.32 ^1H NMR spectra (500 MHz, 296 K, CD_3CN) of $[\text{Cl}@\text{Pd}_4\text{L}^1_8]$ and after the addition of various neutral guest molecules: a) 1,2 dichlorobenzene (8.7 eq.), b) 1,3 dichlorobenzene (8.7 eq.), c) 1,4 dichlorobenzene (8.7 eq.), d) chlorobenzene (8.7 eq.), e) benzoquinone (8.7 eq.), f) 2,3-dimethylpyrazine (8.7 eq.), g) 2,5-dimethylpyrazine (18.9 eq.), h) trans 1,3 pentadiene (8.7 eq.), i) pyrrole (8.7 eq.), j) pyrazole (8.7 eq.), k) imidazole (8.7 eq.), l) 1-methylimidazole (8.7 eq.), m) pyrrolidine (8.7 eq.) and n) ethylenediamine (8.7 eq.). No evidence of encapsulation of the neutral guests a-j was found after the equilibration time of 14 days, confirmed by no change in chemical shift in the ^1H NMR spectrum. In contrast, addition of neutral guest k-n resulted in the partial decomplexation of the interpenetrated coordination cage $[\text{Cl}@\text{Pd}_4\text{L}^1_8]$.

and the release of free ligand L^1 (illustrated in the 1H NMR spectra in blue). The change in chemical shift of proton signal f , is due to association of the guest molecule from the outside of the interpenetrated coordination cage.

7.3.3.1.2 ESI HR mass Spectrometry

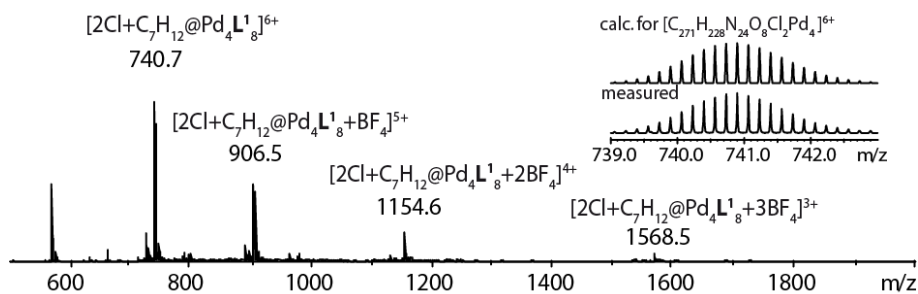


Figure 7.33 ESI mass spectrum of $[2Cl+norbornane@Pd_4L^1_8]$.

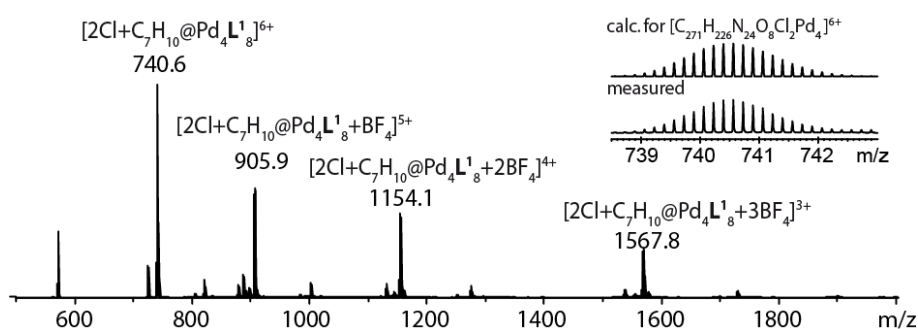


Figure 7.34 ESI mass spectrum of $[2Cl+norbornene@Pd_4L^1_8]$.

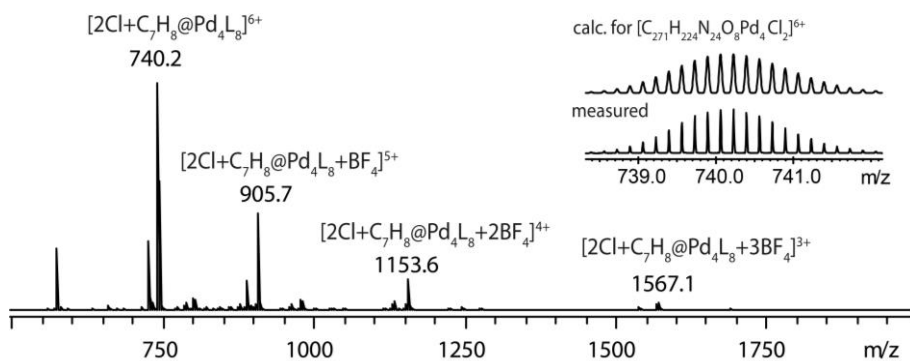


Figure 7.35 ESI mass spectrum of $[2Cl+norboradiene@Pd_4L^1_8]$.

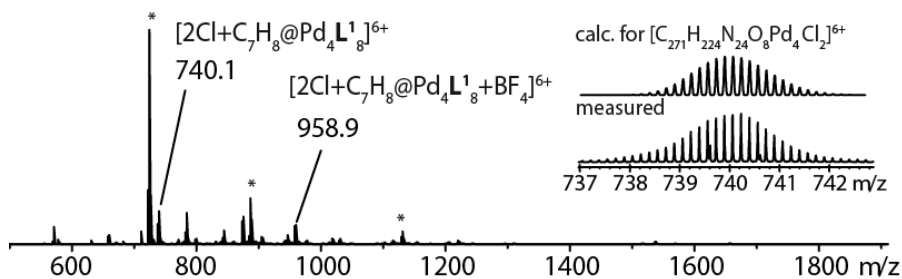
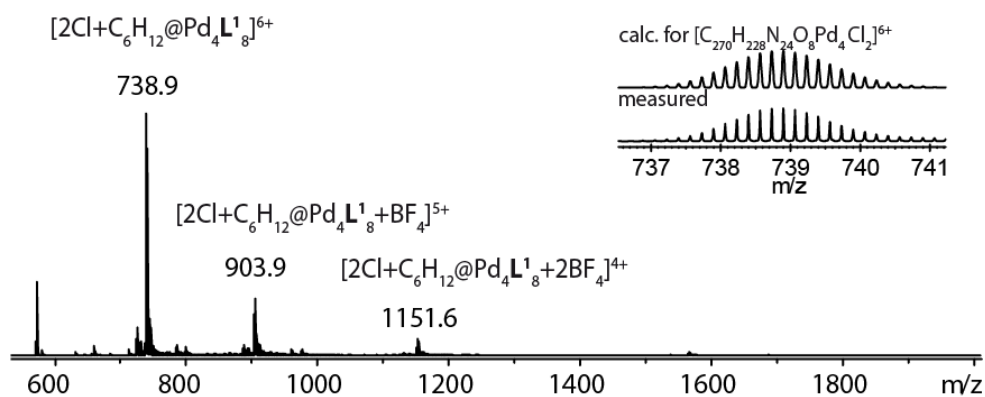
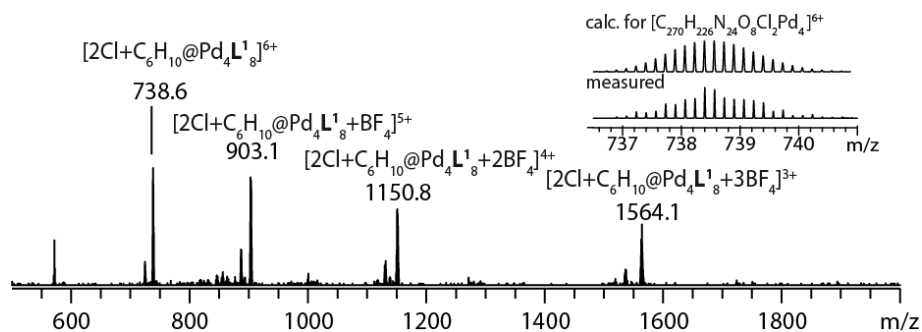
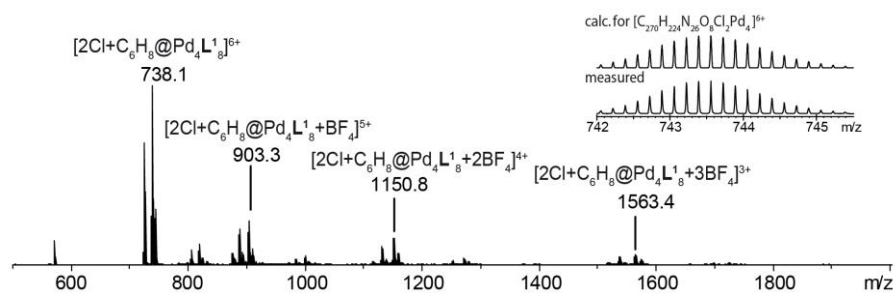
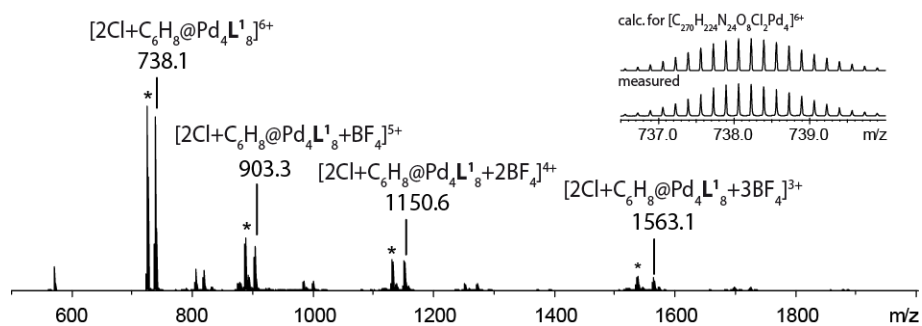


Figure 7.36 ESI mass spectrum of $[2Cl+toluene@Pd_4L^1_8]$.

Figure 7.37 ESI mass spectrum of [2Cl+cyclohexane@Pd₄L₁₈].Figure 7.38 ESI mass spectrum of [2Cl+cyclohexene@Pd₄L₁₈].Figure 7.39 ESI mass spectrum of [2Cl+1,3-cyclohexadiene@Pd₄L₁₈].Figure 7.40 ESI mass spectrum of [2Cl+1,4-cyclohexadiene@Pd₄L₁₈]. * : [2Cl@Pd₄L₁₈].

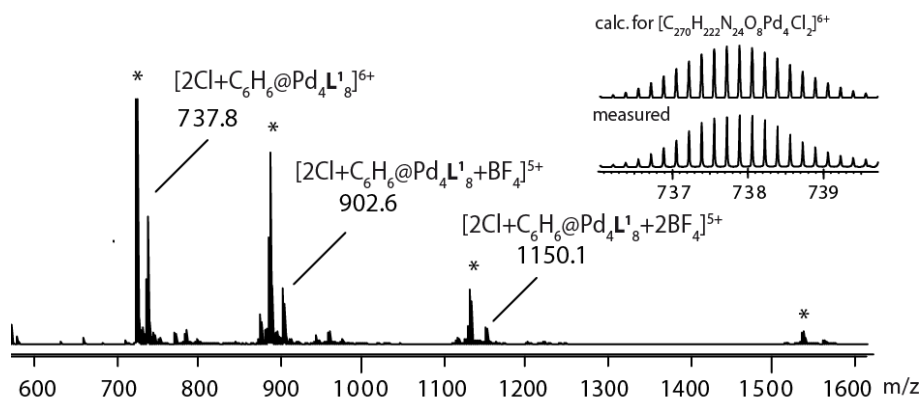


Figure 7.41 ESI mass spectrum of $[2\text{Cl}+\text{benzene}@\text{Pd}_4\text{L}^1_8]$.

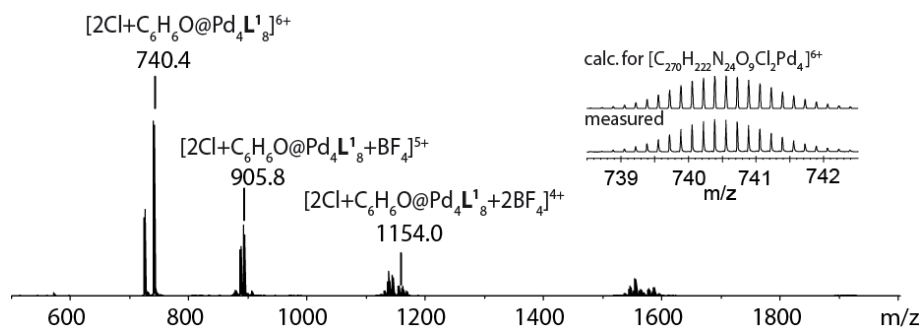


Figure 7.42 ESI mass spectrum of $[2\text{Cl}+\text{phenol}@\text{Pd}_4\text{L}^1_8]$.

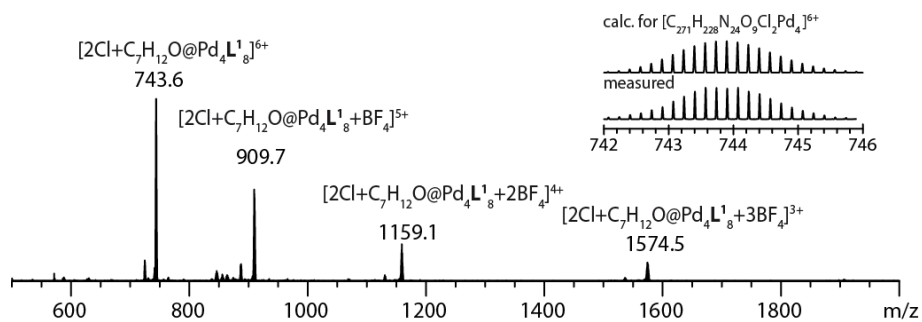


Figure 7.43 ESI mass spectrum of $[2\text{Cl}+\text{cycloheptanol}@\text{Pd}_4\text{L}^1_8]$.

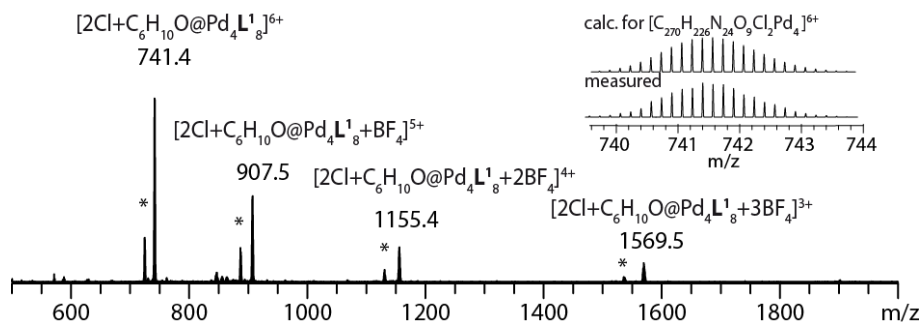
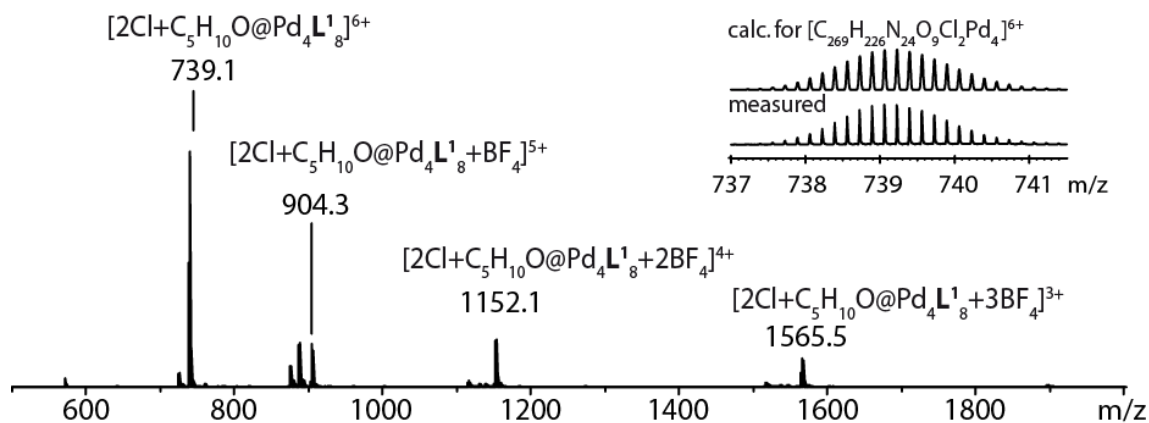
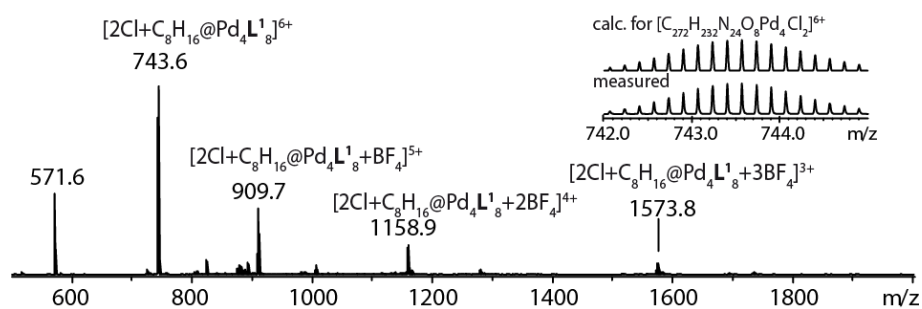
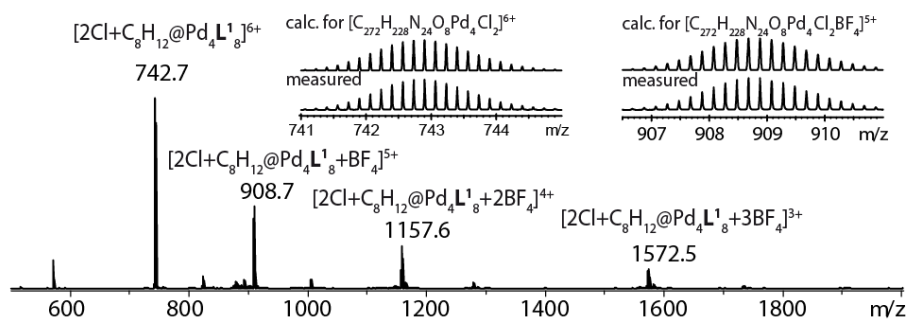
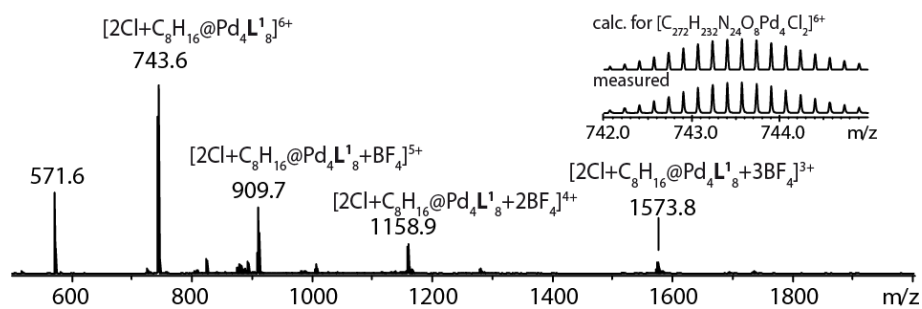


Figure 7.44 ESI mass spectrum of $[2\text{Cl}+\text{cyclohexanol}@\text{Pd}_4\text{L}^1_8]$. * = $[2\text{Cl}@\text{Pd}_4\text{L}^1_8]$.

Figure 7.45 ESI mass spectrum of $[2\text{Cl}+\text{cyclopentanol}@\text{Pd}_4\text{L}^1_8]$.Figure 7.46 ESI mass spectrum of $[2\text{Cl}+\text{cyclooctane}@\text{Pd}_4\text{L}^1_8]$.Figure 7.47 ESI mass spectrum of $[2\text{Cl}+1,4\text{ cyclooctadiene}@\text{Pd}_4\text{L}^1_8]$.Figure 7.48 ESI mass spectrum of $[2\text{Cl}+\text{cyclooctane}@\text{Pd}_4\text{L}^1_8]$.

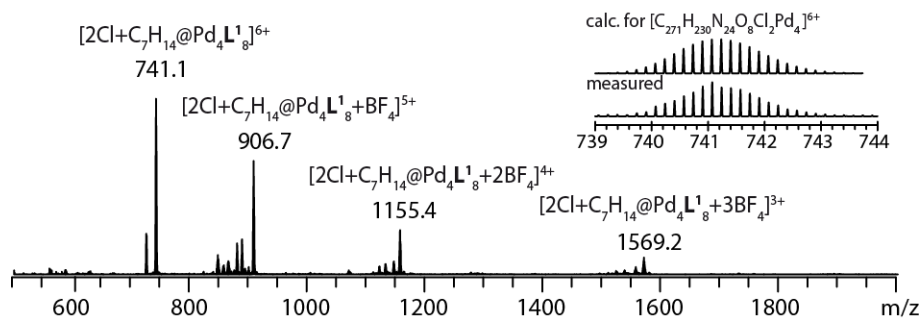


Figure 7.49 ESI mass spectrum of $[2\text{Cl}+\text{cycloheptane}@\text{Pd}_4\text{L}^1_8]$.

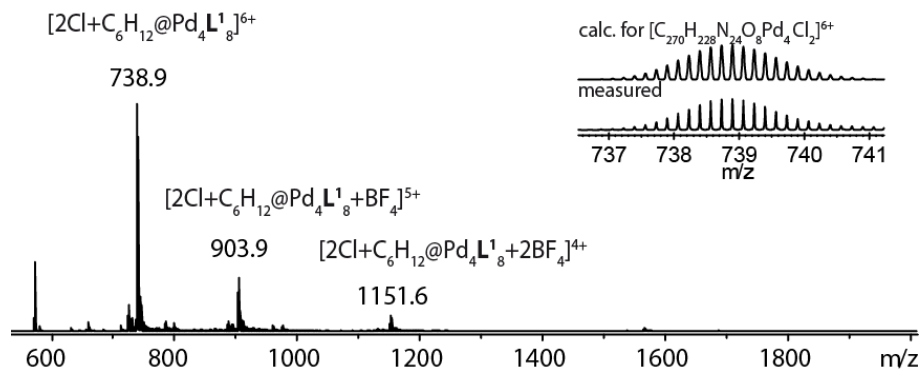


Figure 7.50 ESI mass spectrum of $[2\text{Cl}+\text{cyclohexane}@\text{Pd}_4\text{L}^1_8]$.

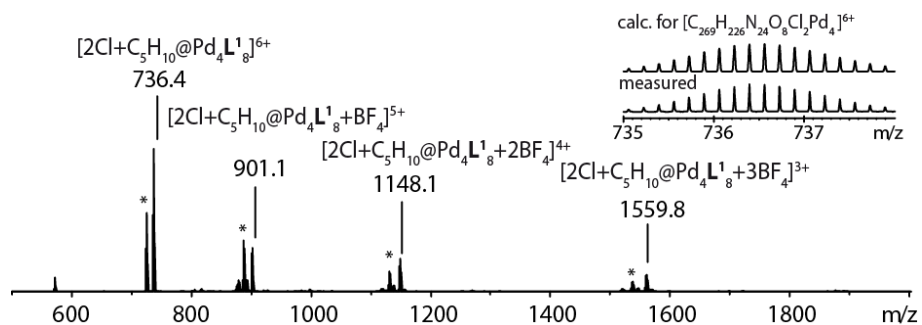


Figure 7.51 ESI mass spectrum of $[2\text{Cl}+\text{cyclopentane}@\text{Pd}_4\text{L}^1_8]$. Signals highlighted with * could be assigned to $[2\text{Cl}@\text{Pd}_4\text{L}^1_8]$.

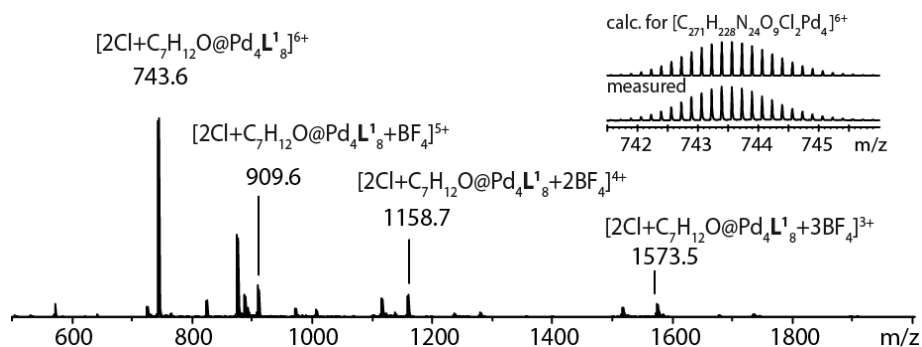


Figure 7.52 ESI mass spectrum of $[2\text{Cl}+\text{cycloheptanone}@\text{Pd}_4\text{L}^1_8]$. Signals highlighted with * could be assigned to $[2\text{Cl}@\text{Pd}_4\text{L}^1_8]$.

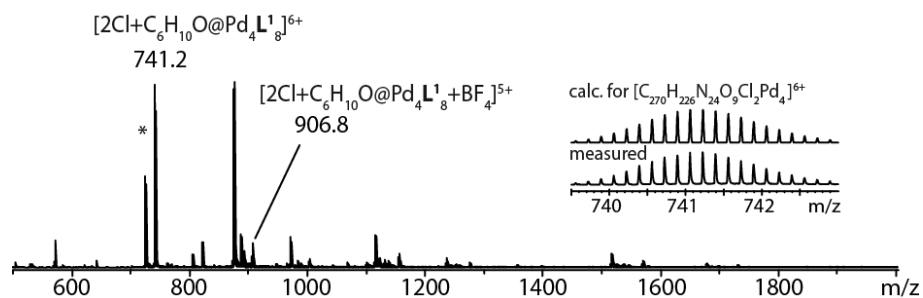


Figure 7.53 ESI mass spectrum of $[2\text{Cl}+\text{cyclohexanone}@Pd_4L^1_8]$. Signals highlighted with * could be assigned to $[2\text{Cl}@Pd_4L^1_8]$.

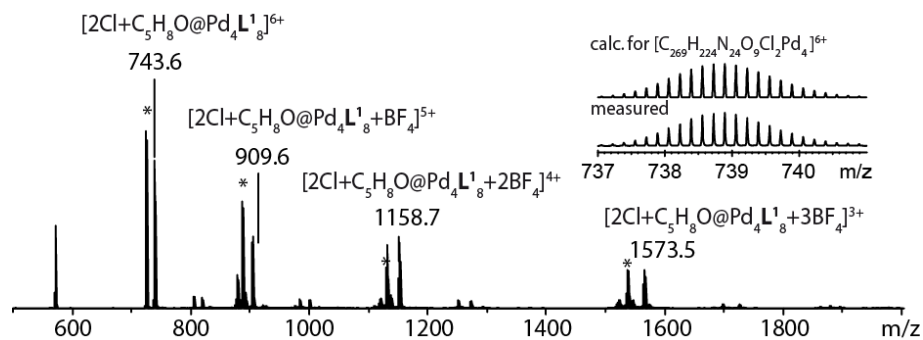


Figure 7.54 ESI mass spectrum of $[2\text{Cl}+\text{cyclopentanone}@Pd_4L^1_8]$. Signals highlighted with * could be assigned to $[2\text{Cl}@Pd_4L^1_8]$.

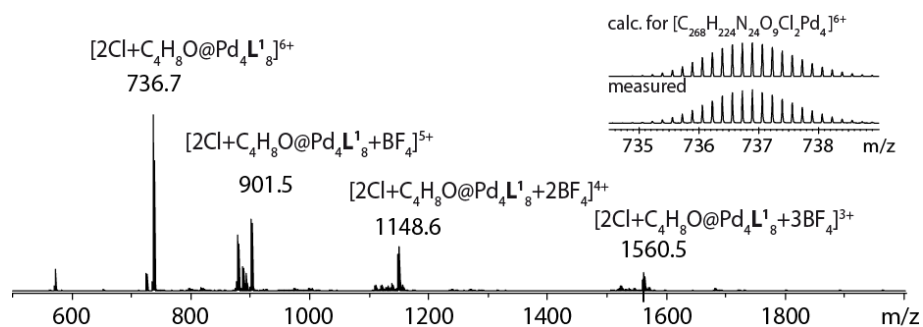


Figure 7.55 ESI mass spectrum of $[2\text{Cl}+\text{tetrahydrofuran}@Pd_4L^1_8]$.

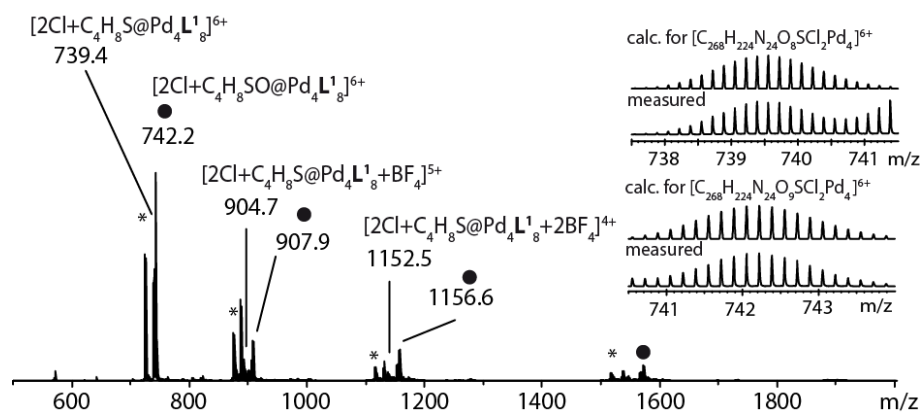


Figure 7.56 ESI mass spectrum of $[2\text{Cl}+\text{tetrahydrothiophene}@Pd_4L^1_8]$. *: $[Pd_4L^1_8]$ cage; • Encapsulation of the oxidation product of tetrahydrothiophene C_4H_8SO .

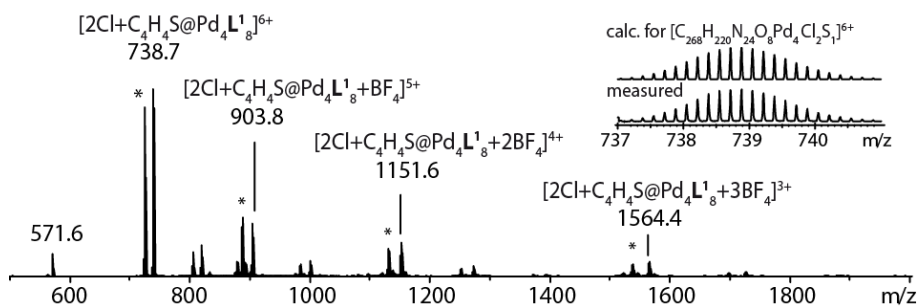


Figure 7.57 ESI mass spectrum of [2Cl+thiophene@Pd₄L₁₈]. Signals highlighted with * correspond to the interpenetrated coordination cage without any encapsulated neutral guest ([2Cl@Pd₄L₁₈]).

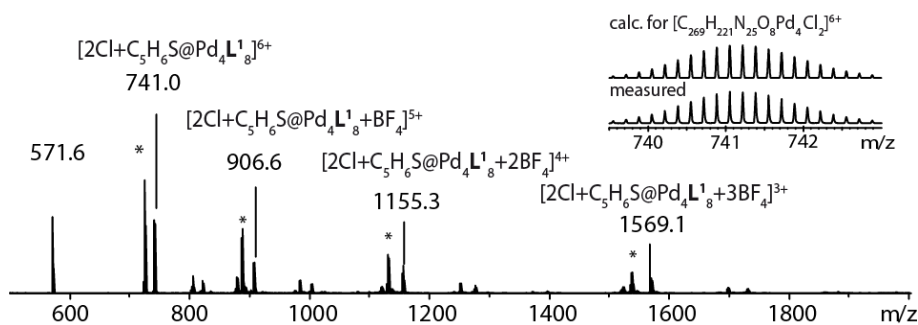


Figure 7.58 ESI mass spectrum of [2Cl+2-methylthiophene@Pd₄L₁₈]. Signals highlighted with * correspond to the host ([2Cl@Pd₄L₁₈]).

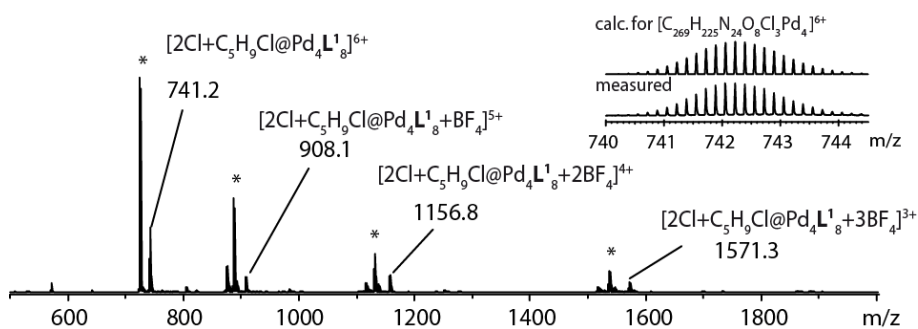


Figure 7.59 ESI mass spectrum of [2Cl+chlorocyclopentane@Pd₄L₁₈]. Signals highlighted with * could be assigned to [2Cl@Pd₄L₁₈].

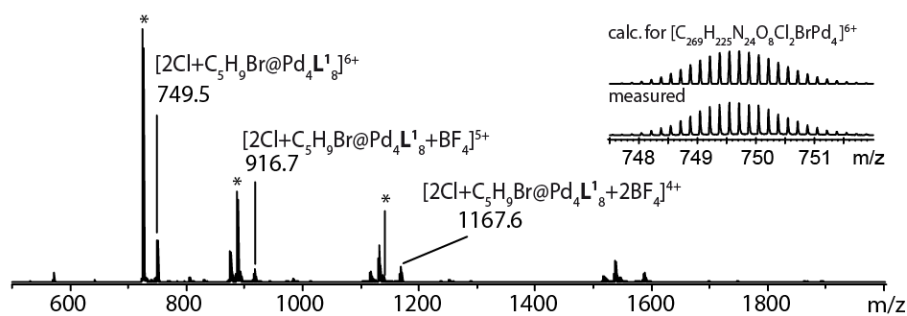


Figure 7.60 ESI mass spectrum of [2Cl+bromocyclopentane@Pd₄L₁₈]. Signals highlighted with * could be assigned to [2Cl@Pd₄L₁₈].

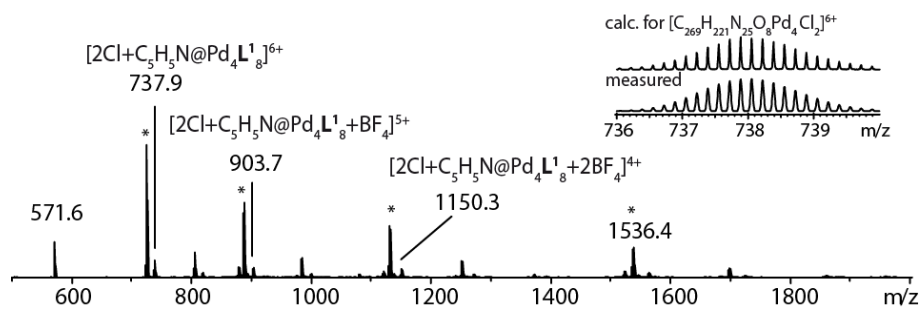


Figure 7.61 ESI mass spectrum of [2Cl+pyridine@Pd₄L¹₈]. Signals highlighted with * could be assigned to [2Cl@Pd₄L¹₈].

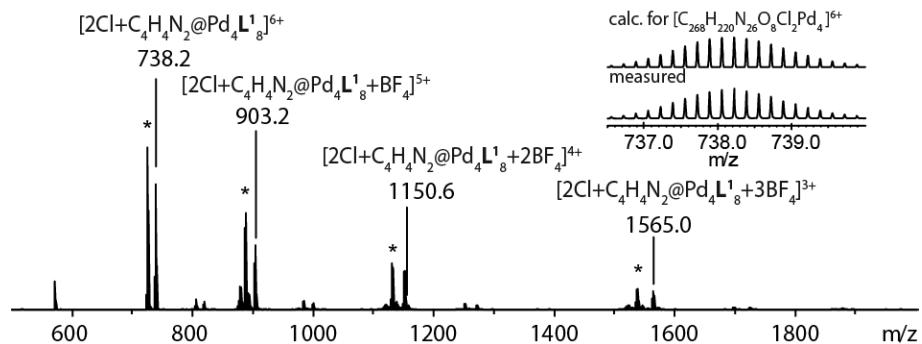


Figure 7.62 ESI mass spectrum of [2Cl+pyrazine@Pd₄L¹₈]. Signals highlighted with * could be assigned to [2Cl@Pd₄L¹₈].

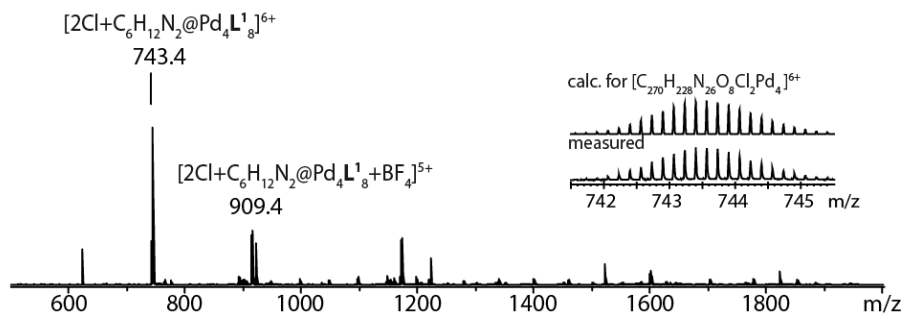


Figure 7.63 ESI mass spectrum of [2Cl+DABCO@Pd₄L¹₈].

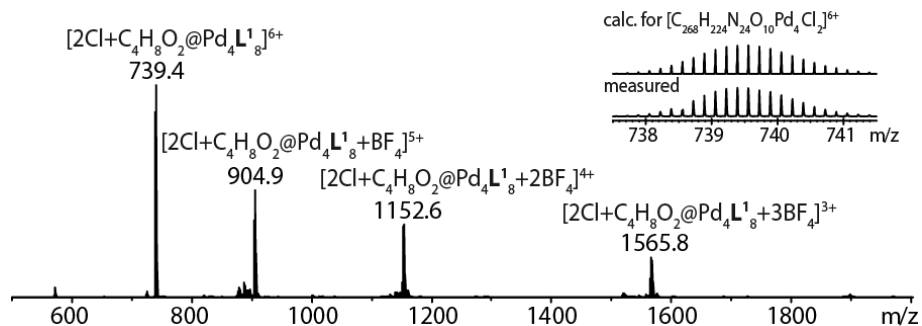


Figure 7.64 ESI mass spectrum of [2Cl+1,3-dioxane@Pd₄L¹₈].

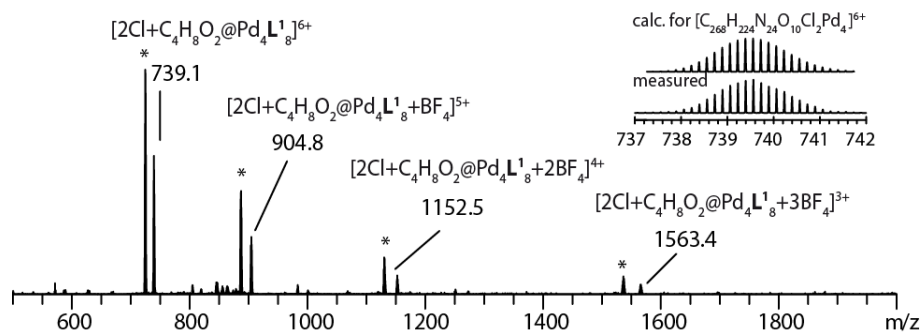


Figure 7.65 ESI mass spectrum of $[2\text{Cl}+1,3\text{-dioxane}@\text{Pd}_4\text{L}^1_8]$.

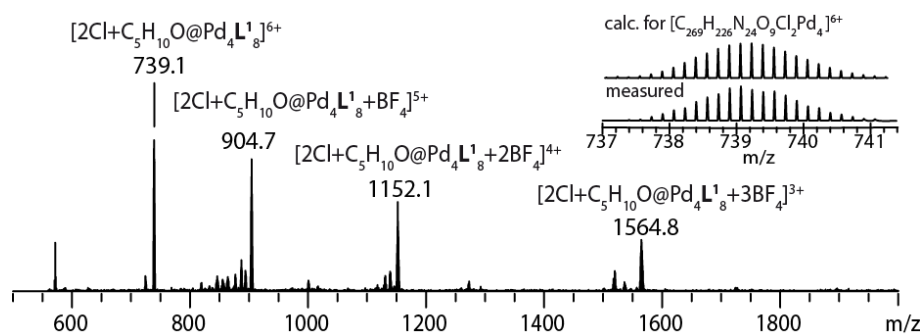


Figure 7.66 ESI mass spectrum of $[2\text{Cl}+\text{tetrahydropyran}@\text{Pd}_4\text{L}^1_8]$.

7.3.3.2 Solvent Variation

Procedure

After preparation of the interpenetrated coordination cage $[2\text{Cl}@Pd_4L^1_8]$ in deuterated acetonitrile, the solvent was removed in vacuum. After drying in high vacuum for ~2 h another deuterated solvent was added and an ^1H NMR spectrum was recorded.

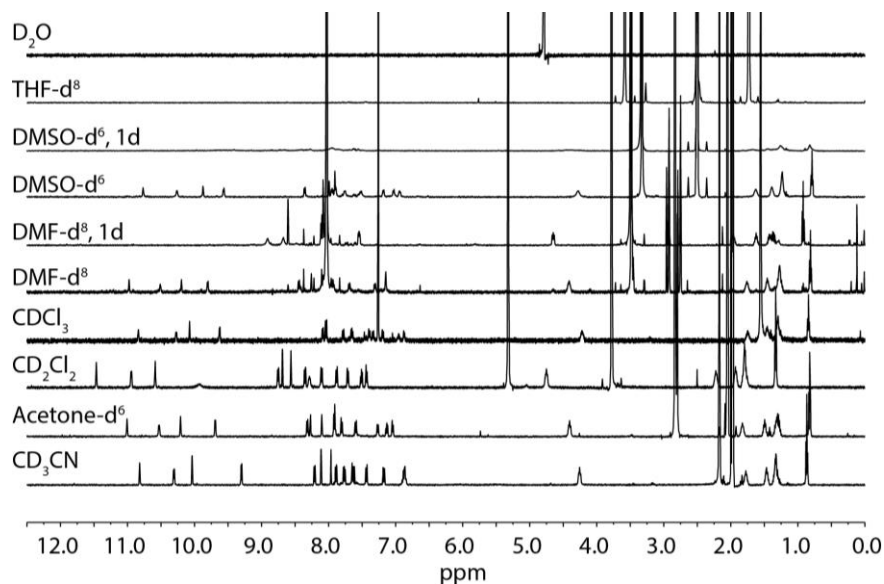


Figure 7.67 ^1H NMR spectra (500 MHz, 298 K) of $[2\text{Cl}@Pd_4L^1_8]$ in different solvents: CD_3CN , acetone- d_6 , CD_2Cl_2 , CDCl_3 , DMF- d_8 , DMSO- d_6 , THF- d_8 and D_2O . The interpenetrated coordination cage is soluble in acetone and methylene chloride and does not decompose even after several days in these solvents. In DMF and DMSO the coordination cage decomposed over a period of 24 h. Furthermore no or only low intensity signals could be found in the ^1H NMR spectrum of the coordination cage in THF, D_2O and CDCl_3 , accompanied by a dull appearance of the sample.

7.3.3.3 Addition of Neutral Guests to $[2\text{Br}+\text{BF}_4@Pd_4L^1_8]$

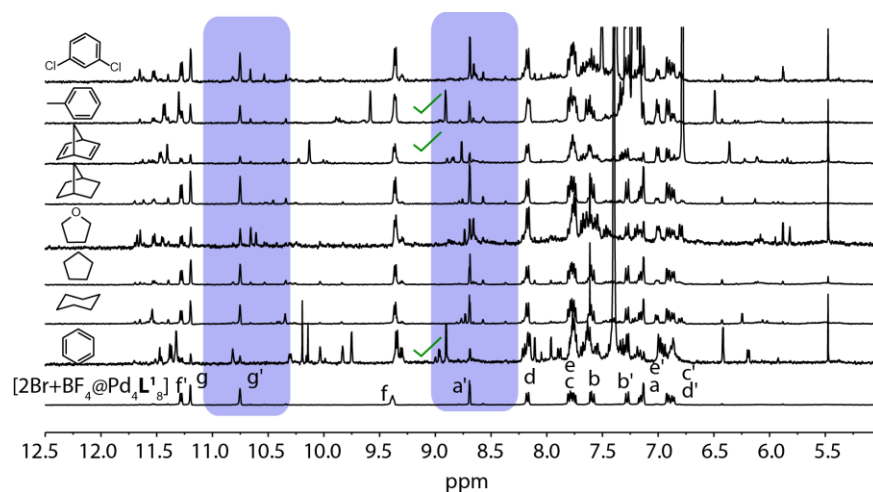


Figure 7.68 ^1H NMR spectra (400 MHz, 298 K, CD_3CN) of $[2\text{Br}+\text{BF}_4@Pd_4L^1_8]$ and after the addition of various neutral guest molecules: benzene (8.7 eq.), cyclohexane (8.7 eq.), cyclopentane (8.7 eq.), norbornene (8.7 eq.), norbornadiene (8.7 eq.), toluene (87 eq.), and 1,3 dichlorobenzene (8.7 eq.). Benzene, norbornadiene and toluene could be found to be encapsulated inside the central pocket of the interpenetrated coordination cage. No clear indication of host-guest formation could be found for the other neutral guest, due to the appearance of signals from other not-identified species.

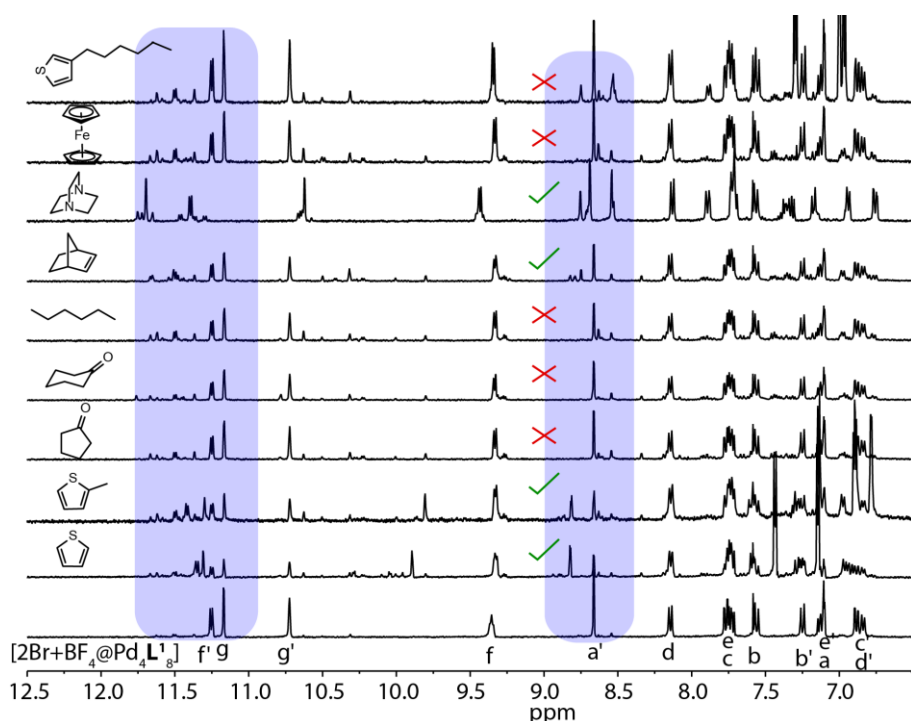


Figure 7.69 ^1H NMR spectra (400 MHz, 298 K, CD_3CN) of $[2\text{Br}+\text{BF}_4@\text{Pd}_4\text{L}_1^8]$ before and after the addition of various neutral guest molecules: thiophene (8.7 eq.), 2-methylthiophene (8.7 eq.), cyclopentanone (8.7 eq.), hexane (8.7 eq.), norbornene (8.7 eq.), DABCO (87 eq.), ferrocene (8.7 eq.) and 3-hexylthiophene. Under the tested conditions, only thiophene, 2-methylthiophene, DABCO and norbornene seemed to be encapsulated in the coordination cage. Due to the large amount of undefined side products, a clear assignment is with not possible.

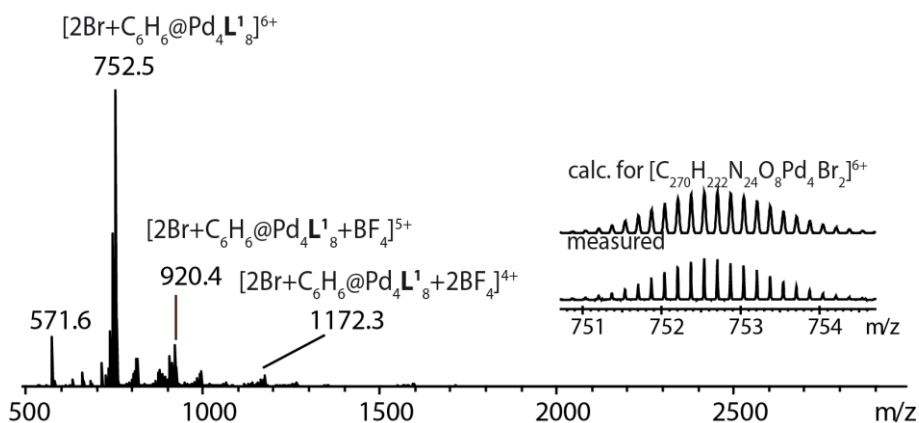


Figure 7.70 ESI-MS of $[2\text{Br}+\text{benzene}@\text{Pd}_4\text{L}_1^8]$.

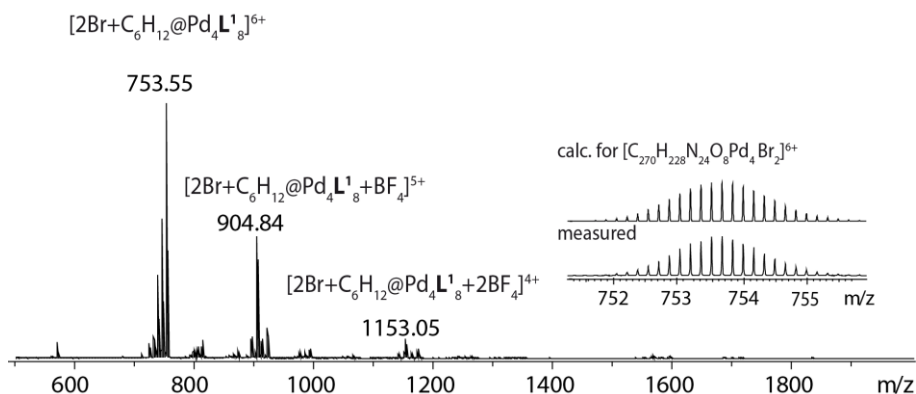


Figure 7.71 ESI-MS of $[2\text{Br}+\text{cyclohexane}@\text{Pd}_4\text{L}_1^8]$

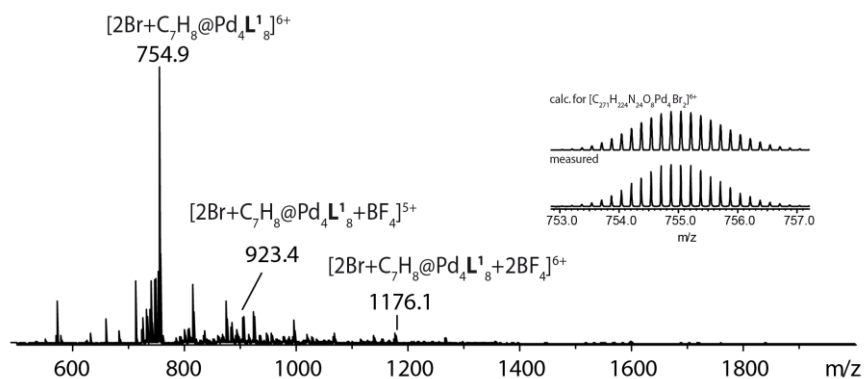


Figure 7.72 ESI-MS of $[2\text{Br} + \text{toluene} @ \text{Pd}_4\text{L}^1_8]$

7.3.3.4 Addition of Neutral Guests to $[2\text{F} + \text{BF}_4 @ \text{Pd}_4\text{L}^1_8]$

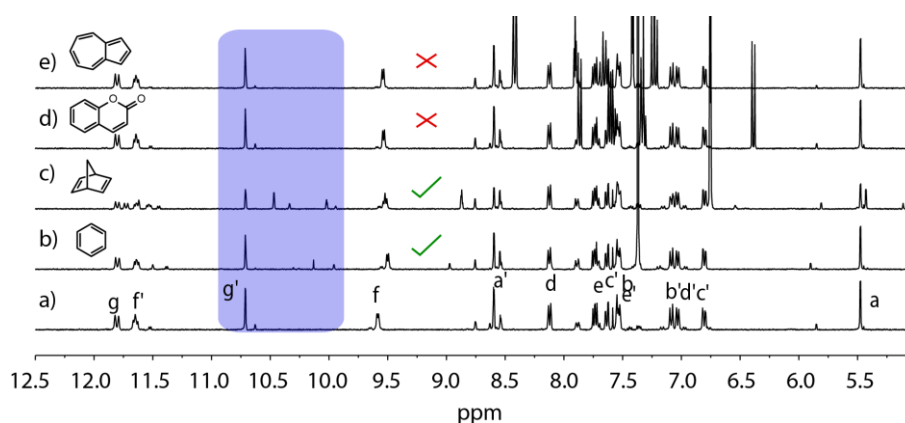


Figure 7.73 ^1H NMR spectra (400 MHz, 298 K, CD_3CN) of $[2\text{F} @ \text{Pd}_4\text{L}^1_8]$ before and after the addition of various neutral guest molecules: b) benzene (8.7 eq.), c) norbornadiene (8.7 eq.), d) coumarin (8.7 eq.) and e) azulene (8.7 eq.). While benzene and norbornadiene can be encapsulated inside the central cavity of the coordination cage, azulene and coumarin do not bind.

7.3.3.5 Addition of Neutral Guests to $[2\text{I} @ \text{Pd}_4\text{L}^1_8]$

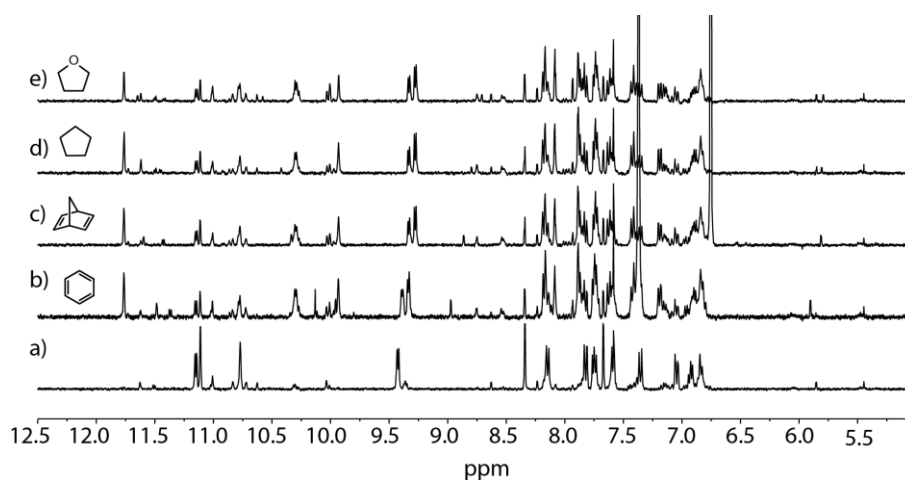


Figure 7.74 ^1H NMR spectra (400 MHz, 298 K, CD_3CN) of $[2\text{I} @ \text{Pd}_4\text{L}^1_8]$ before and after the addition of various neutral guest molecules: b) benzene (8.7 eq.), c) norbornadiene (8.7 eq.), d) cyclopentane (8.7 eq.) and e) tetrahydrofuran (8.7 eq.). After addition of neutral guest new sets of signal appear, indicating a change of the system. However, no clear indication of neutral guest uptake could be drawn from the NMR spectrum.

7.3.3.6 Competition Experiments

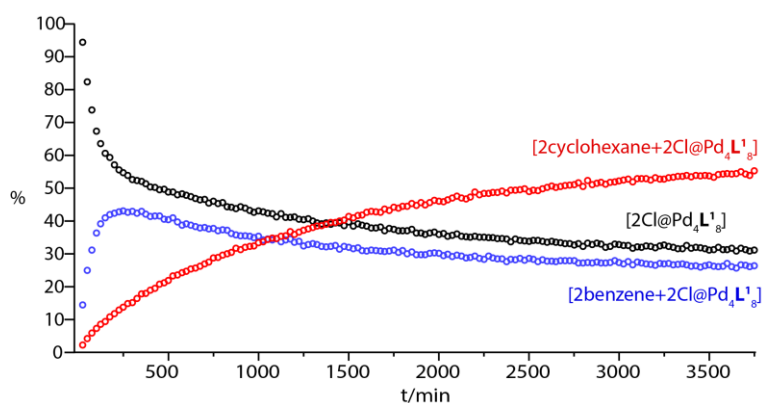


Figure 7.75 Kinetic measurement of $[2\text{Cl}@Pd_4L_1^8]$ with benzene (10 eq.) and cyclohexane (10 eq.). Color Scheme: **Red:** [cyclohexane+2Cl@Pd₄L₁⁸], **black:** [2Cl@Pd₄L₁⁸] and **blue:** [benzene+2Cl@Pd₄L₁⁸].

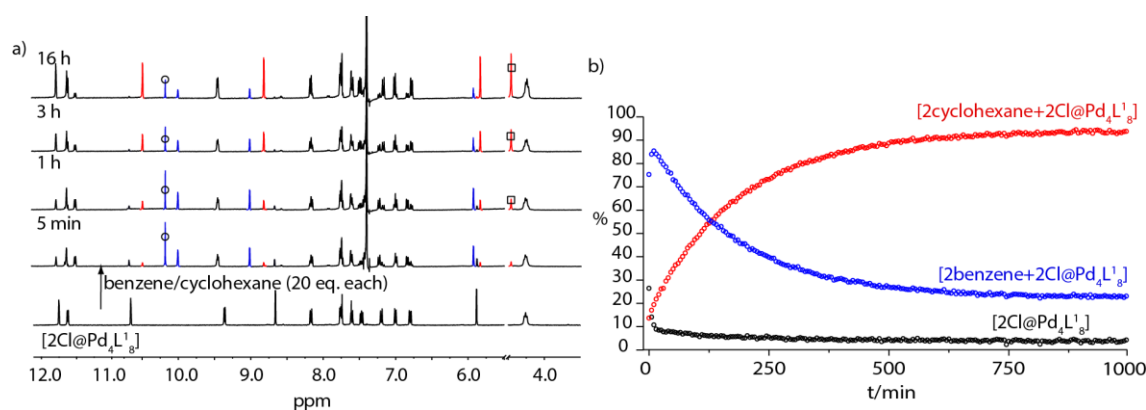


Figure 7.76 Addition of benzene (20 eq.) and cyclohexane (20 eq.) to $[2\text{Cl}@Pd_4L_1^8]$: a) ^1H NMR spectra (400 MHz, CD_3CN , 298 K) of $[2\text{Cl}@Pd_4L_1^8]$ and upon addition of the neutral guest after 5 min, 1 h, 3 h and 6 h. b) Kinetic plot (% vs. t) of encapsulation process. Color Scheme: **red:** [cyclohexane+2Cl@Pd₄L₁⁸], **black:** [2Cl@Pd₄L₁⁸], **blue:** [benzene+2Cl@Pd₄L₁⁸], **black circle:** encapsulated benzene, **black square:** encapsulated cyclohexane.

Kinetic Measurement

For kinetic measurements a sample of $[2\text{Cl}@Pd_4L_1^8]$ (CD_3CN , 500 μL , 0.35 mM, 1.0 eq.) was prepared and a solution of the neutral guest molecule in acetonitrile was added (25 μL , 70 mM, 10 eq.). The progress of the encapsulation was monitored by ^1H NMR spectroscopy at 298 K. The concentrations of $[2\text{Cl}@Pd_4L_1^8]$ and $[2\text{Cl}+\text{guest}@Pd_4L_1^8]$ were determined by relative integration of the peaks at $\delta = 10.63$ ppm (d, $J = 1.75$ Hz 2H, $[2\text{Cl}@Pd_4L_1^8]$), $\delta = 9.96$ ppm (d, $J = 1.75$ Hz, 2H, $[2\text{Cl}+\text{benzene}@Pd_4L_1^8]$) or $\delta = 10.45$ ppm (d, $J = 1.75$ Hz, 2H, $[2\text{Cl}+\text{cyclohexane}@Pd_4L_1^8]$) as a function of time.

To calculate the rate constant, the following assumptions were made:

- The concentration of the neutral guest (which was used in excess) remains nearly constant $[\text{Guest}] = \text{const.}$ (isolation method)
- $[\text{HG}]_t = [\text{H}]_0 - [\text{H}]_t$

- The concentration of the host-guest complex at any given time $[HG]_t$ is equal to the starting concentration of the empty host $[H]_0$ subtracted by the concentration of the host at time t $[H]_t$.
- The reaction is pseudo first order related to the concentration of the host $[H]$; the reaction is zero order in $[HG]$.

With this assumption and the data extracted from experiment, the rate constants at 298 K were determined as follows:

$[2Cl@Pd_4L^1_8]$	$[2Br+BF_4@Pd_4L^1_8]$
$k_{up}(\text{norbornadiene}) = (2.15 \pm 0.04) \cdot 10^{-4} \text{ s}^{-1}$	$k_{up}(\text{norbornadiene}) = (1.73 \pm 0.14) \cdot 10^{-5} \text{ s}^{-1}$
$k_{up}(\text{benzene}) = (1.07 \pm 0.02) \cdot 10^{-3} \text{ s}^{-1}$	
$k_{up}(\text{cyclohexane}) = (1.87 \pm 0.04) \cdot 10^{-4} \text{ s}^{-1}$	

7.3.4 Further NMR Experiments

7.3.4.1 ^{19}F NMR Measurements

7.3.4.1.1 ^{19}F NMR of $[\text{3BF}_4@\text{Pd}_4\text{L}^1_8]$

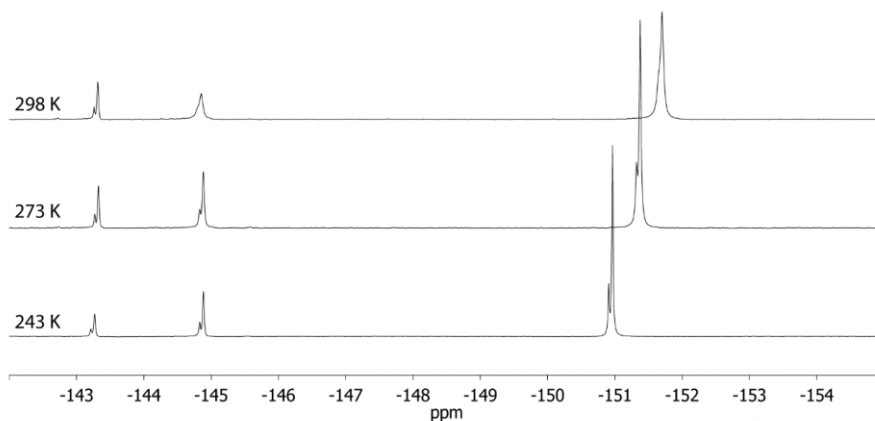


Figure 7.77 Temperature dependence of the ^{19}F NMR-signals of $[\text{3BF}_4@\text{Pd}_4\text{L}^1_8]$ (470 MHz, CD_3CN). Shoulders are due to the $^{10}\text{BF}_4^-$ isotope.

7.3.4.1.2 ^{19}F NMR of $[\text{2Cl}@\text{Pd}_4\text{L}^1_8]$

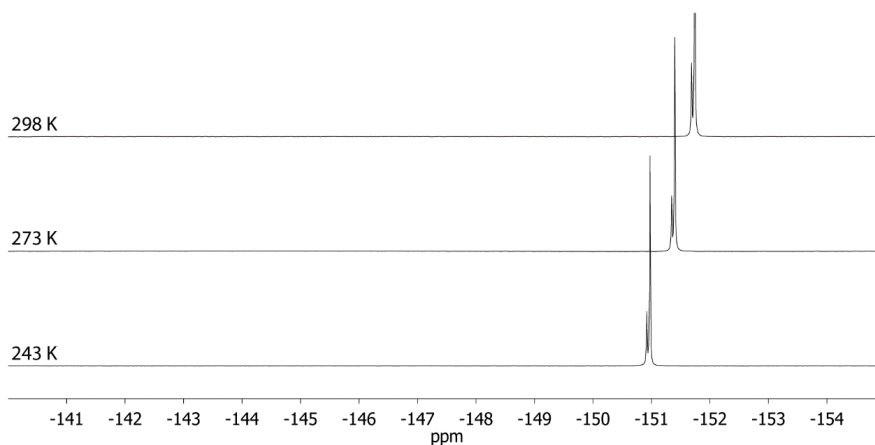


Figure 7.78 Temperature dependence of the ^{19}F NMR-signal of the $[\text{2Cl}@\text{Pd}_4\text{L}^1_8]$ sample (470 MHz, CD_3CN). The only detectable signal represents the free BF_4^- anion. No signals for encapsulated BF_4^- were observed. Shoulders are due to the $^{10}\text{BF}_4^-$ isotope.

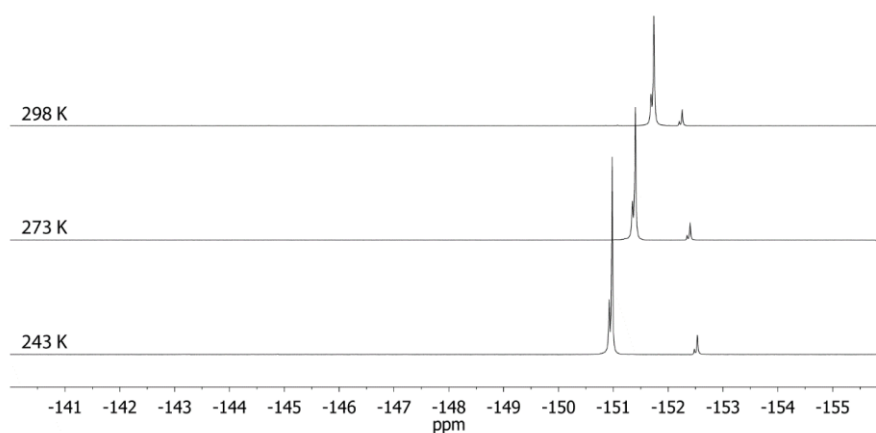
7.3.4.1.3 ^{19}F NMR of $[\text{2Br}+\text{BF}_4@\text{Pd}_4\text{L}^1_8]$ 

Figure 7.79 Temperature dependence of the ^{19}F NMR-signals of $[\text{2Br}+\text{BF}_4@\text{Pd}_4\text{L}^1_8]$ (470 MHz, CD_3CN). Besides the signal of the free BF_4^- anion, one signal representing the BF_4^- anion encapsulated in the central pocket was detected.

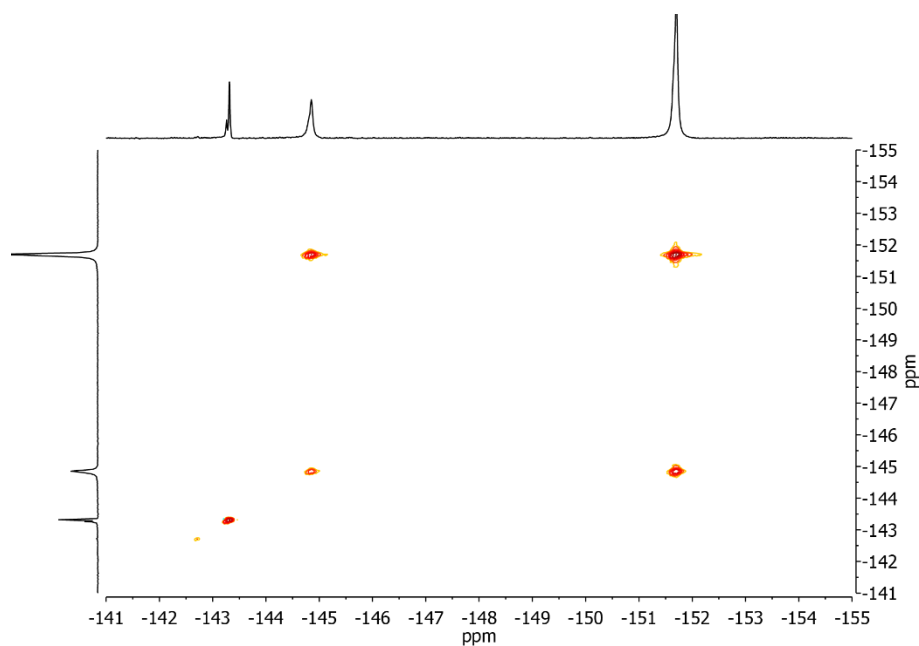
7.3.4.1.4 ^{19}F , ^{19}F EXSY NMR of $[\text{3BF}_4@\text{Pd}_4\text{L}^1_8]$ 

Figure 7.80 ^{19}F , ^{19}F EXSY spectrum (470 MHz, CD_3CN , 0.5 s mixing period) of $[\text{3BF}_4@\text{Pd}_4\text{L}^1_8]$ at room temperature. Exchange is observed between the peaks assigned to the two BF_4^- ions occupying the outer cavities of the double cage and free BF_4^- . No exchange is observed between the BF_4^- encapsulated in the inner pocket of the double cage and free BF_4^- .

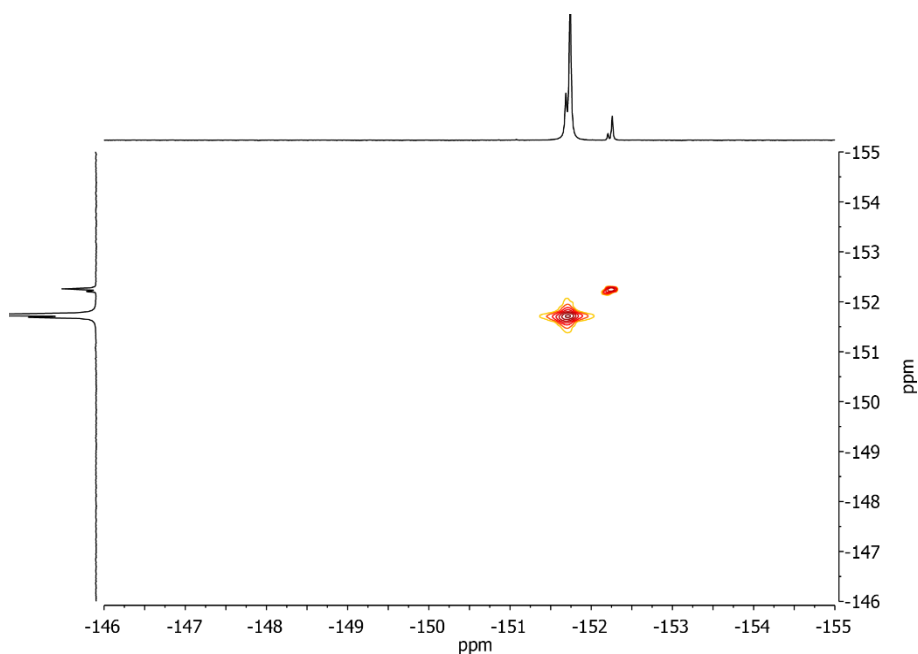
7.3.4.1.5 ^{19}F , ^{19}F EXSY NMR of $[\text{2Br}+\text{BF}_4@ \text{Pd}_4\text{L}^1_8]$ 

Figure 7.81 ^{19}F , ^{19}F -EXSY spectrum (470 MHz, CD_3CN , 0,5 s mixing period) of $[\text{2Br}+\text{BF}_4@ \text{Pd}_4\text{L}^1_8]$ at room temperature illustrating, that there is no exchange between free BF_4^- and the one encapsulated inside the central pocket of the double cage.

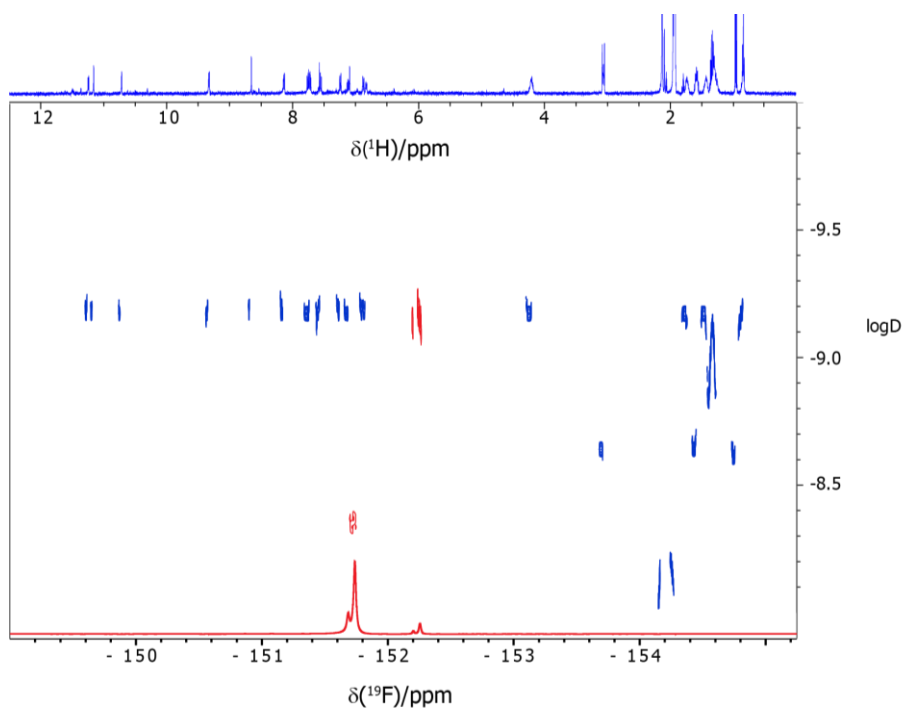
7.3.4.2 Superposition of ^{19}F and ^1H DOSY NMR spectra of $[\text{2Br}+\text{BF}_4@ \text{Pd}_4\text{L}^1_8]$ 

Figure 7.82 Superposition of ^{19}F (red) and ^1H (blue) DOSY NMR spectra of $[\text{2Br}+\text{BF}_4@ \text{Pd}_4\text{L}^1_8]$ shows encapsulation of one BF_4^- ion inside the double cage ($\log D = \text{logarithm of diffusion coefficient}$).

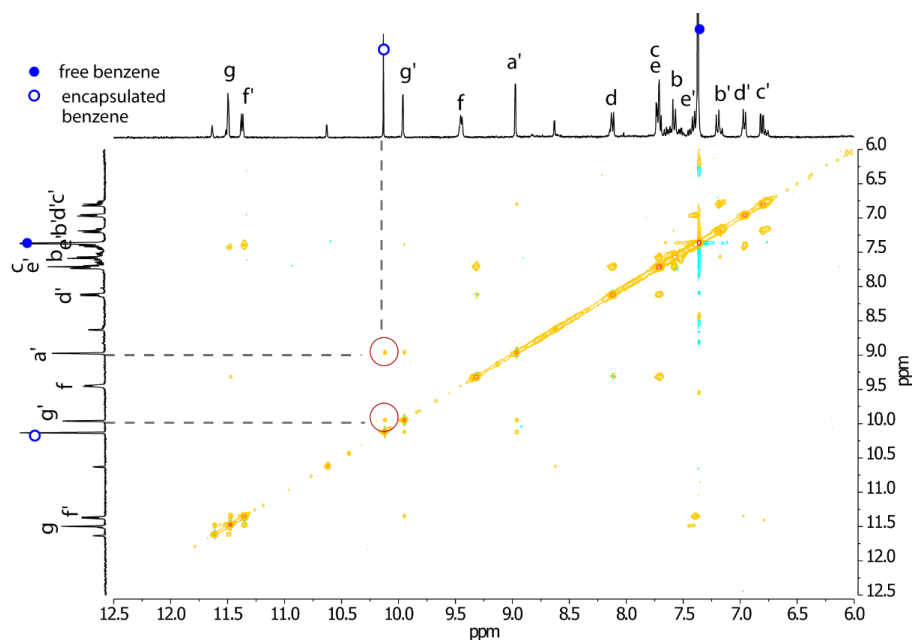
7.3.4.3 NOESY-Measurement of [2Cl+benzene@Pd₄L₈]

Figure 7.83 ¹H, ¹H NOESY spectrum of [2Cl+benzene@Pd₄L₈] (500 MHz, CD₃CN, 298 K). Contacts between encapsulated benzene and the double cage are highlighted with red circles.

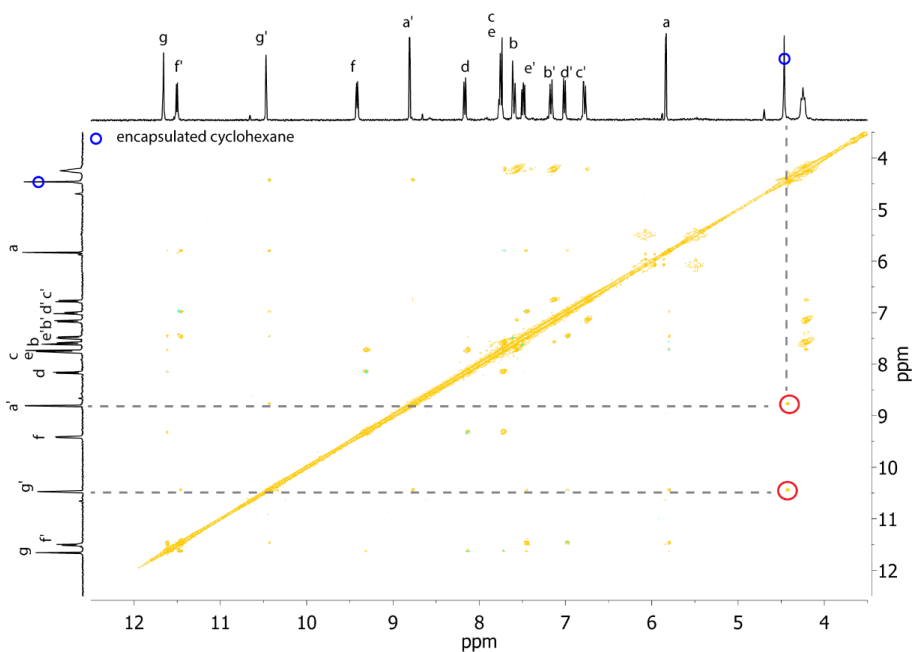
7.3.4.4 NOESY-Measurement of [2Cl+cyclohexane@Pd₄L₈]

Figure 7.84 ¹H, ¹H NOESY spectrum of [2Cl+cyclohexane@Pd₄L₈] (500 MHz, CD₃CN, 298 K). Contacts between encapsulated guest and host are highlighted with red circles.

7.3.5 X-ray Data

7.3.5.1 Ligand L¹

Crystals suitable for single crystal X-ray diffraction were obtained by slow diffusion of ethanol into a 0.3 mM solution of the interpenetrated coordination [Cl+cyclopentadiene@Pd₄L¹]₈ cage in acetonitrile. Surprisingly, no interpenetrated cage could be found, instead the free Ligand L¹ could be crystallized under the applied conditions.

X-ray data were collected at 80(2) K from *Dr. J. J. Holstein* at the DESY, Petra 3 beamline P11^[140] using a radiation wavelength of 0.5636 Å. Data processing, structure solution and refinement were conducted by *Dr. J. J. Holstein*. Data integration and reduction were undertaken using the XDS.^[141] The structure was solved by intrinsic phasing/direct methods using SHELXT^[142] and refined with SHELXL^[143] for full-matrix least-squares routines on F² and ShelXle^[144] as a graphical user interface.

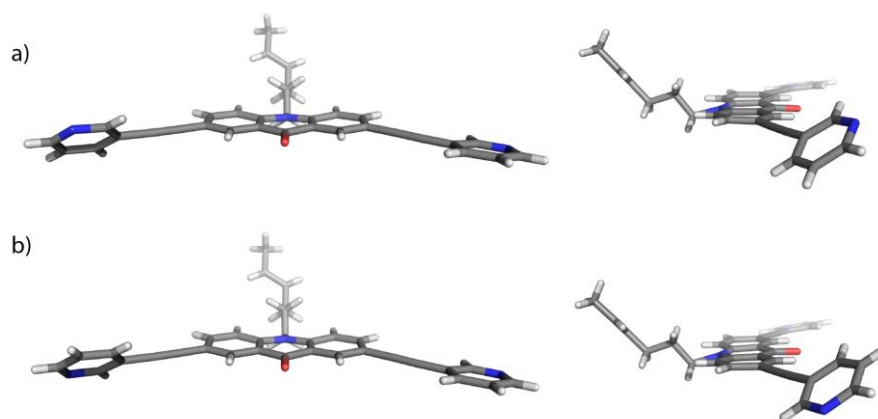


Figure 7.85 Preliminary X-ray structures of Ligand L¹. Position of the pyridine residues are disorderd, resulting in two possible confromations a) and b). *Color scheme: C: grey; N: blue; O: red.*

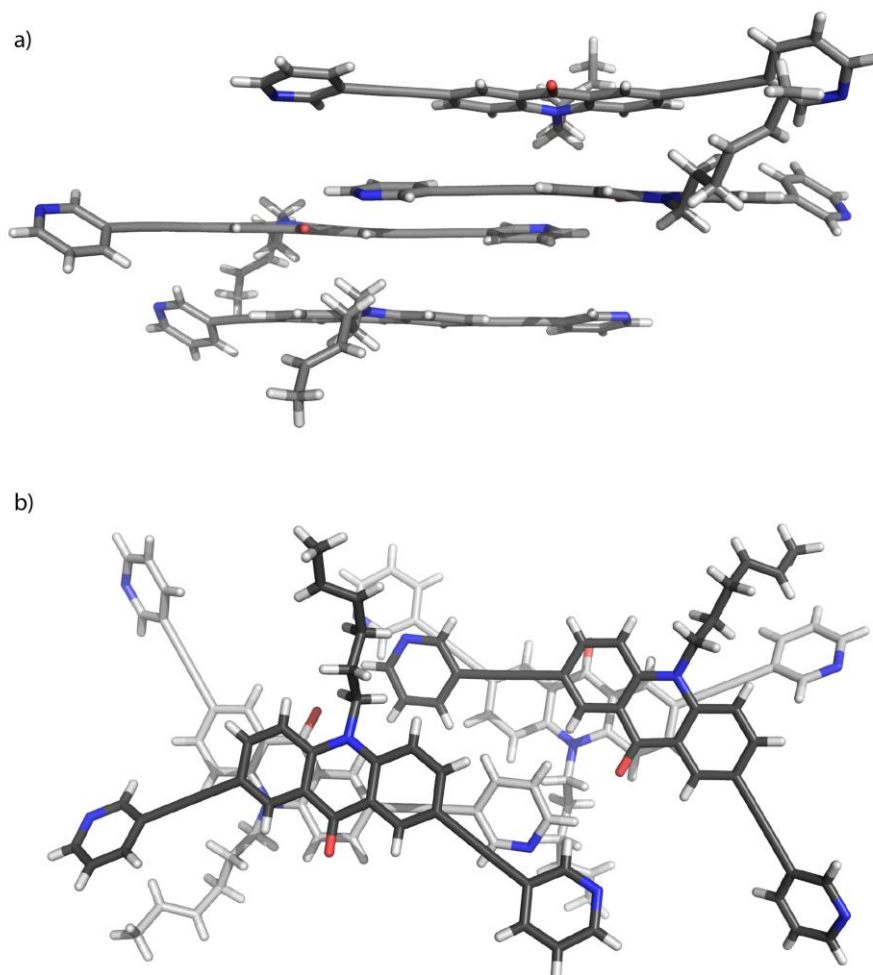


Figure 7.86 Packing of ligand L^1 in the crystal structure. Close π - π interaction between different ligands can be found. Color scheme: C: grey; N: blue; O: red.

7.3.5.2 [3BF₄@Pd₄L₈]

Single-crystal measurement was performed from *Dr. L. Krause* on Bruker SMART APEX II systems based on D8 three-circle goniometers with Incoatec microfocus X-ray sources (μ S) and Incoatec QUAZAR mirror optics. Suitable single crystals of [3BF₄@Pd₄L₈] were mounted at low temperature in inert oil under argon atmosphere by applying the X-Temp2 device^[145] The data were collected at 100 K crystal temperature (Oxford Cryosystems CRYOSTREAM 700), 50 kV and 600 μ A and an appropriate 0.5° omega scan strategy. Data reduction was performed with SAINT v8.30C (Bruker, 2009a) out of the APEX II v2.2012.2 0 (Bruker, 2009b) program package.^[146] SADABS (version 2014/4) was employed for the incident beam scaling, determination of the spherical harmonic coefficients, outlier rejection and determination of the error model parameters. All the structures were solved by direct methods with SHELXS.^[147–149]^[147–149] They were refined by full-matrix least-squares against F^2 using SHELXL-2014/3 with the help of the SHELXle graphical user interface.^[144] All non-hydrogen atoms were refined with anisotropic displacement parameters. The hydrogen atoms were set to idealized positions and refined using a riding model with their isotropic

displacement parameters constrained to be 1.5 times the equivalent isotropic displacements of the atoms to which they were attached for methyl hydrogens and 1.2 times for all other hydrogens.

Table 7.1 Crystal data and structure refinement for [2Cl+benzene@Pd₄L₈].

CCDC number	1035264
Empirical formula	C ₃₅₄ H ₃₀₆ B ₈ F ₃₂ N ₂₄ O ₈ Pd ₄
Formula weight	6144.29 g mol ⁻¹
Temperature	100(2) K
Wavelength	0.56086 Å
Crystal system	Tetragonal
Space group	P4/n
Unit cell dimensions	$a = b = 22.065(4)$ Å $c = 33.491(5)$ Å
Volume	16306(6) Å ³
Z	2
Density (calculated)	1.251 Mg/m ³
Absorption coefficient	0.164 mm ⁻¹
F(000)	6348
Crystal size	0.120 x 0.100 x 0.090 mm ³
Theta range for data collection	1.136 to 18.161°
Index ranges	-24 ≤ h ≤ 24, -24 ≤ k ≤ 24, -37 ≤ l ≤ 37
Reflections collected	143666
Independent reflections	11745 [R(int) = 0.0932]
Completeness to theta = 18.161°	99.9 %
Refinement method	Full-matrix least-squares on F ²
Data / restraints / parameters	11745 / 2105 / 1042
Goodness-of-fit on F ²	1.052
Final R indices [I > 2σ(I)]	R1 = 0.0857, wR2 = 0.2267
R indices (all data)	R1 = 0.1559, wR2 = 0.3066
Largest diff. peak and hole	3.220 and -1.070 e.Å ⁻³

All necessary BF₄⁻ anions could be found in the Fourier difference map. Some of the BF₄⁻ ions are located on special positions, exhibiting disorder but not obeying the crystallographic symmetry. They were modeled using distance and displacement restraints. Heavily disordered lattice solvent (benzene) was successfully modeled into the crystal voids.

7.3.5.3 [2Cl+C₆H₆@Pd₄L₈]

Single-crystal X-ray measurements, data processing, structure solution and refinement was conducted by *PD Dr. B. Dittrich*. Suitable single crystals for X-ray structural analysis of [2Cl+benzene@Pd₄L₈] were mounted at room temperature in Paratone N inert oil. Single crystal X-ray diffraction data were collected at the Swiss Light Source at beamline PXII. The data were integrated with XDS^[141] and converted with the utility program xds2sad by G. M. Sheldrick. An empirical absorption correction with SADABS^[150] was applied. The structure was solved by direct methods.^[151] The structure model was refined against all data by full-matrix least-squares methods on F² with the program shelxl2014.^[143] All non-hydrogen-atoms were refined with anisotropic displacement parameters. The hydrogen atoms were refined isotropically on calculated positions using a riding model with U_{iso} values constrained to 1.2/1.5 U_{eq} of their parent atoms. The SQUEEZE method provided by the program Platon was used to improve the contrast of the electron density map the structure.

Table 7.2 Crystal data and structure refinement for [2Cl+benzene@Pd₄L₈].

CCDC number	1035009
Empirical formula	C ₇₀₈ H ₆₁₂ B ₁₆ F ₆₄ N ₄₈ O ₁₆ Pd ₈
Formula weight	5042.17 g mol ⁻¹
Temperature	100(2) K
Wavelength	1.000 Å
Crystal system	Monoclinic
Space group	<i>P2₁/n</i>
Unit cell dimensions	<i>a</i> = <i>b</i> = 22.065(4) Å <i>c</i> = 33.491(5) Å
Volume	24090(9) Å ³
Z	4
Density (calculated)	1.390 Mg/m ³
Absorption coefficient	2.739 mm ⁻¹
F(000)	10352
Crystal size	0.050 x 0.050 x 0.030 mm ³
Theta range for data collection	1.235 to 22.663°
Index range	-15 ≤ <i>h</i> ≤ 14, -20 ≤ <i>k</i> ≤ 33, -21 ≤ <i>l</i> ≤ 22
Reflections collected	18081
Independent reflections	8741 [R(int) = 0.0919]
Completeness to theta = 18.161°	20.1 %
Refinement method	Full-matrix least-squares on F ²
Data / restraints / parameters	8741 / 11133 / 3106
Goodness-of-fit on F ²	1.007
Final R indices [I > 2σ(I)]	R1 = 0.0726, wR2 = 0.1878
R indices (all data)	R1 = 0.1458, wR2 = 0.2417
Largest diff. peak and hole	0.367 and -0.249 e.Å ⁻³

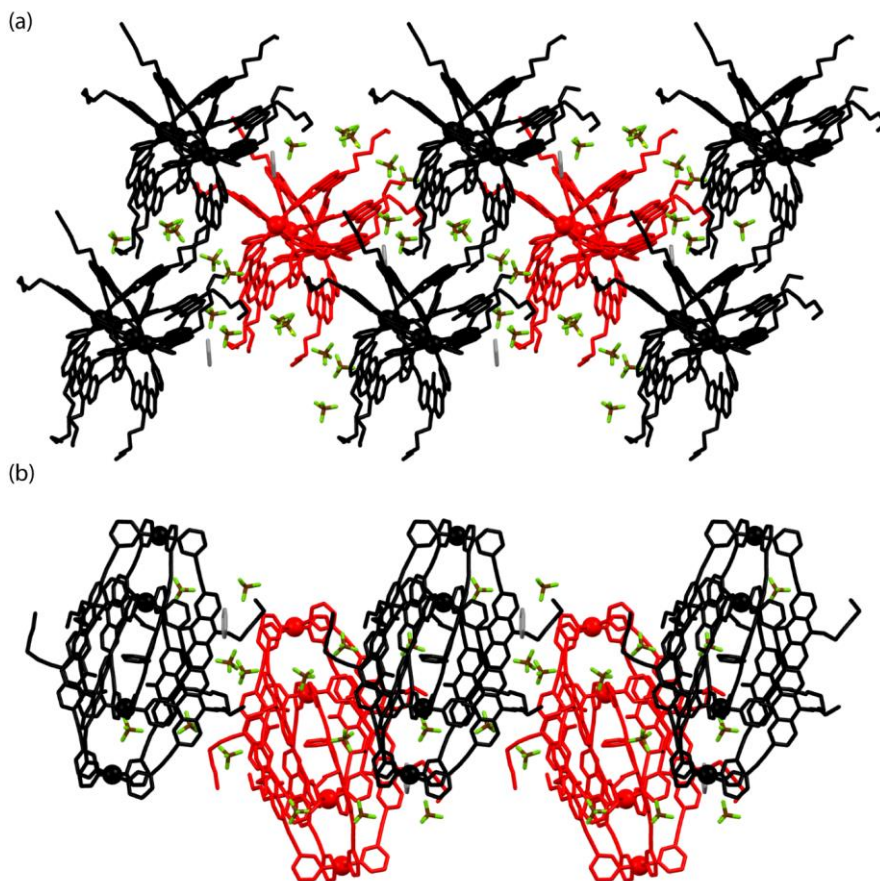


Figure 7.87 Packing of $[2\text{Cl}+\text{C}_6\text{H}_6@\text{Pd}_4\text{L}^{18}]$ (a) view along the b-axis, (b) view along the c-axis.

7.3.5.4 $[2\text{Cl}+\text{DABCO}@\text{Pd}_4\text{L}^{18}]$

Crystals suitable for single crystal X-ray diffraction were obtained by slow diffusion of ethanol into a 0.3 mM solution of the interpenetrated coordination cage in acetonitrile. Single-crystal X-ray measurements, data processing, structure solution and refinement was conducted by *Dr. J. J. Holstein*. X-ray data were collected at 80(2) K at the DESY beamline P11^[140] using a radiation wavelength of 0.5636 Å. Data integration and reduction were undertaken using the XDS.^[141] The structure was solved by intrinsic phasing/direct methods using SHELXT^[142] and refined with SHELXL^[143] using 24 cpu cores for full-matrix least-squares routines on F^2 and ShelXle^[144] as a graphical user interface. Hydrogen atoms were included as invariants at geometrically estimated positions. Techniques commonly applied for macromolecular structures were employed to generate a molecular model and increase robustness of the refinement. Stereochemical restraints for the acridone (residue class ACR) ligands and DABCO (residue class DAB) guest of the structure were generated by the GRADE program using the GRADE Web Server (<http://grade.globalphasing.org>) and applied in the refinement. A GRADE dictionary for SHELXL contains target values and standard deviations for 1.2-distances (DFIX) and 1.3-distances (DANG), as well as restraints for planar groups (FLAT). Both BF_4^- counter ions sit on a special position and were treated with similarity restraints (SADI) for 1.2 and 1.3 distances. All non-hydrogen atoms other than Boron atoms (of the BF_4^- counter ions) were refined anisotropically. The refinement of ADP's for non-hydrogen atoms was enabled by

using the rigid bond restraint (RIGU) in the SHELXL^[143] program. SIMU restraints were additionally employed. Due to high flexibility of terminal hexyl chains, non-crystallographic symmetry (NCS) restraints for similarity of 1.4 distances in between both acridone (ACR) ligands were employed. SADI restraints were employed for to ensure similarity in between 1.2 distances of hexyl chain carbon atoms.

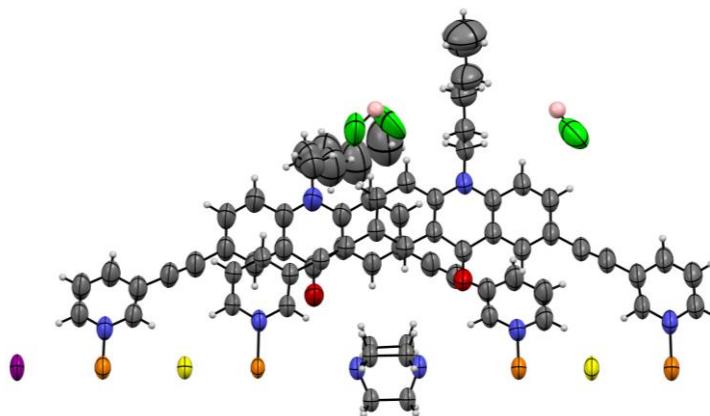


Figure 7.88 The asymmetric unit of the $[2\text{Cl}+\text{DABCO}@\text{Pd}_4\text{L}^{18}]^{6+}$, with all non-hydrogen atoms shown as ellipsoids at the 50% probability level. *Color scheme:* C: gray; N: blue; O: red; Cl: yellow; Pd: orange, H: white, F: green, B: salmon.

Table 7.3 Crystal data and structure refinement for $[2\text{Cl}+\text{DABCO}@\text{Pd}_4\text{L}^{18}]^{6+}$.

CCDC number	1557039
Identification code	sl324a_sq
Empirical formula	$\text{C}_{270}\text{H}_{228}\text{B}_3\text{Cl}_2\text{F}_{12}\text{N}_{26}\text{O}_8\text{Pd}_4$
Formula weight	4848.60
Temperature	80(2) K
Wavelength	0.5636 Å
Crystal system	tetragonal
Space group	$P4/ncc$
Unit cell dimensions	$a = 22.064(3)$ Å; $\alpha = 90^\circ$. $b = 22.064(3)$ Å; $\beta = 90^\circ$. $c = 62.075(12)$ Å; $\gamma = 90^\circ$.
Volume	$30219(10)$ Å ³
Z	4
Density (calculated)	1.066 Mg/m ³
Absorption coefficient	0.224 mm ⁻¹
F(000)	9952
Crystal size	$0.200 \times 0.200 \times 0.020$ mm ³
Theta range for data collection	0.520 to 17.631° .
Index ranges	$-23 \leq h \leq 23$, $-23 \leq k \leq 23$, $-66 \leq l \leq 66$
Reflections collected	249159
Independent reflections	9732 [R(int) = 0.0622]
Completeness to theta = 17.631°	98.7 %

7 Experimental Section

Absorption correction	None
Refinement method	Full-matrix least-squares on F ²
Data / restraints / parameters	9732 / 1644 / 790
Goodness-of-fit on F ²	1.632
Final R indices [$I > 2\sigma(I)$]	R1 = 0.0950, wR2 = 0.3564
R indices (all data)	R1 = 0.1132, wR2 = 0.3840
Largest diff. peak and hole	1.664 and -0.790 e.Å ⁻³

7.3.6 Cyclic voltammetry (CV)

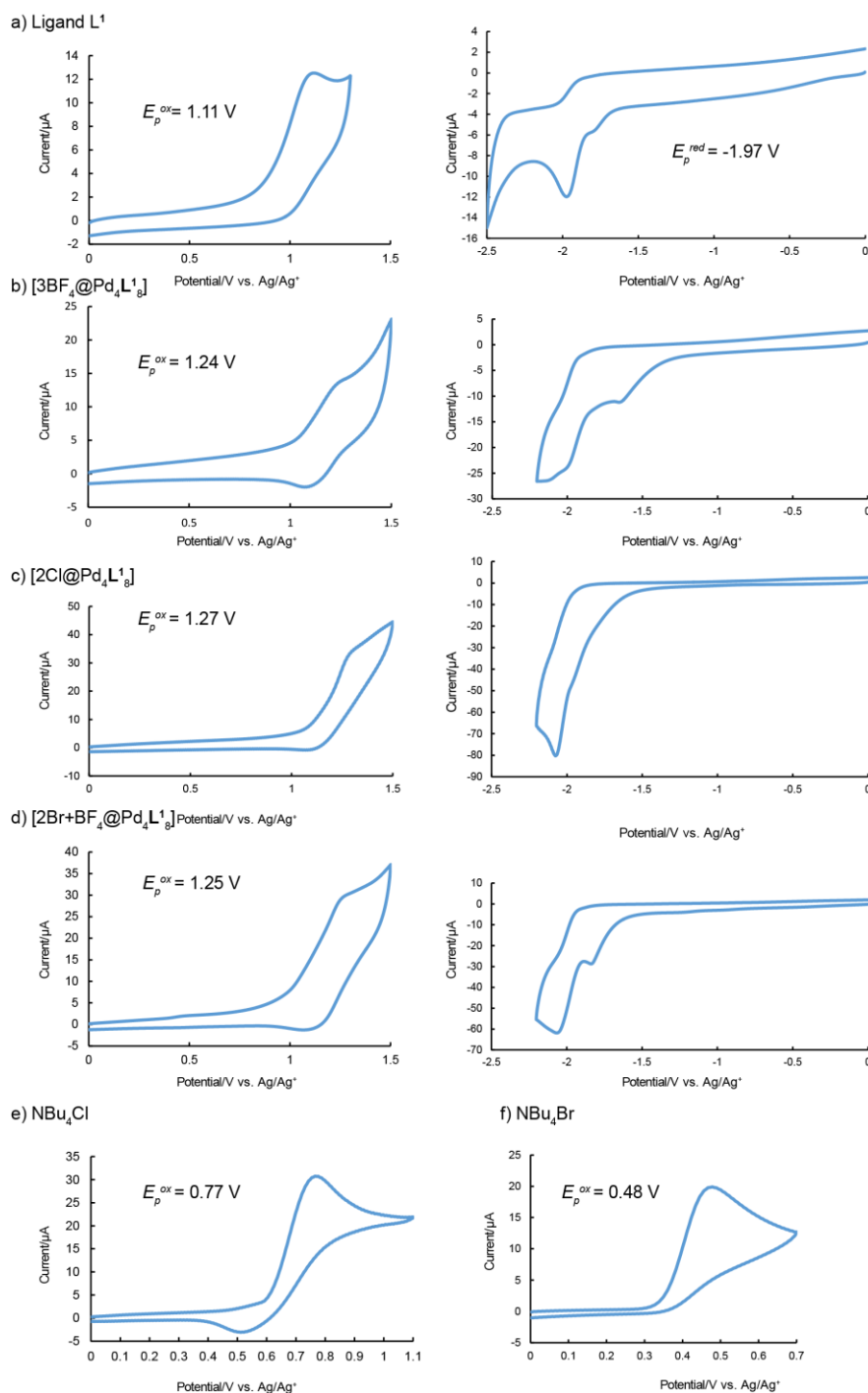


Figure 7.89 Cyclic voltammograms of the a) free ligand L^1 (0.5 mM) b) $[3BF_4@Pd_4L^1_8]$ cage (0.125 mM) c) $[2Cl@Pd_4L^1_8]$ (0.25 mM) d) $[2Br+BF_4@Pd_4L^1_8]$ (0.25 mM) e) NBu_4Cl (1.0 mM) and f) NBu_4Br (1.0 mM) at 298 K, in 0.1 M nBu_4NBF_4/CH_3CN solution, scan rate 0.1 Vs $^{-1}$. Potentials given against an $Ag/AgNO_3$ reference electrode; $[AgNO_3] = 0.001$ M.

Table 7.4 Redox potentials $E_p^{(\text{red/ox})}$ vs. Ag/Ag^+ of cyclic voltammetry measurements. a) Oxidation of halide (chloride/bromide) was not observed.

	$E_p^{(\text{red})}$ vs. Ag/Ag^+	$E_p^{(\text{ox})}$ vs. Ag/Ag^+
free ligand L^1	1.11 V	-1.97 V
$[\text{3BF}_4@\text{Pd}_4\text{L}_8^1]$	1.24 V	-
$[\text{2Cl}@\text{Pd}_4\text{L}_8^1]$	1.27 V ^a	-
$[\text{2Br}+\text{BF}_4@\text{Pd}_4\text{L}_8^1]$	1.25 V ^a	-
NBu_4Cl	0.77 V	-
NBu_4Br	0.48 V	-

The CV measurements and the resulting redox potentials are illustrated in Figure 7.89 and Table 7.4. Interestingly, no redox potentials of the halides anions (bromide/chloride) are anodically shifted in the halide-containing coordination cages $[\text{Br}/\text{Cl}@\text{Pd}_4\text{L}_8]$. While the free ligand shows a redox reaction at 1.11 V, the corresponding coordination cages $[\text{X}@\text{Pd}_4\text{L}_8^1]$ ($\text{X} = \text{BF}_4, \text{Br}, \text{Cl}$) show an anodic shift of 130-160 mV. Incorporated inside the interpenetrated cage the ligand as well as the halide anion are more difficult to oxidize than in its free form.

7.3.7 Cavity volumes and calculation of packing coefficients (PC)

Crystallographically determined structures of $[\text{2Cl}+\text{NG}@\text{Pd}_4\text{L}_8]^{6+}$ (NG = neutral guests (benzene, DABCO)) and $[\text{3BF}_4@\text{Pd}_4\text{L}_8]^{5+}$ were symmetry expanded and the encapsulated guest molecules (DABCO, chloride and tetrafluoroborate) in the cavities of the interpenetrated structures were removed. Resulting cavities were calculated with VOIDOO,^[92] using a primary grid and plot grid spacing of 0.1 Å and 40 cycles of volume refinement with the default water size probe radius of 1.4 Å. Molecular visualization were done using PyMol.^[130]

The $[\text{3BF}_4@\text{Pd}_4\text{L}_8]^{5+}$ cage cavities of all three pockets show very similar volumes. For the outer two pockets, 58.62 Å³ and 54.90 Å³ and for the central cavity a volume of 67.16 Å³ was calculated. In the halide-containing cages $[\text{2Cl}+\text{NG}@\text{Pd}_4\text{L}_8]^{6+}$ volumes of inner and outer pockets show significant different cavity volumes. While the volume for outside pointing void were around 11.68–14.68 Å³, the central cavity is ~ 200 Å³. For the benzene-containing cage, a volume of 201.66 Å³ was calculated for the central pocket, while for the DABCO structure a volume of 200.84 Å³ was obtained. Thus, the average volume of the central cavity is 201.25 Å³. This value was used to calculate the packing coefficient in Table 2.1).

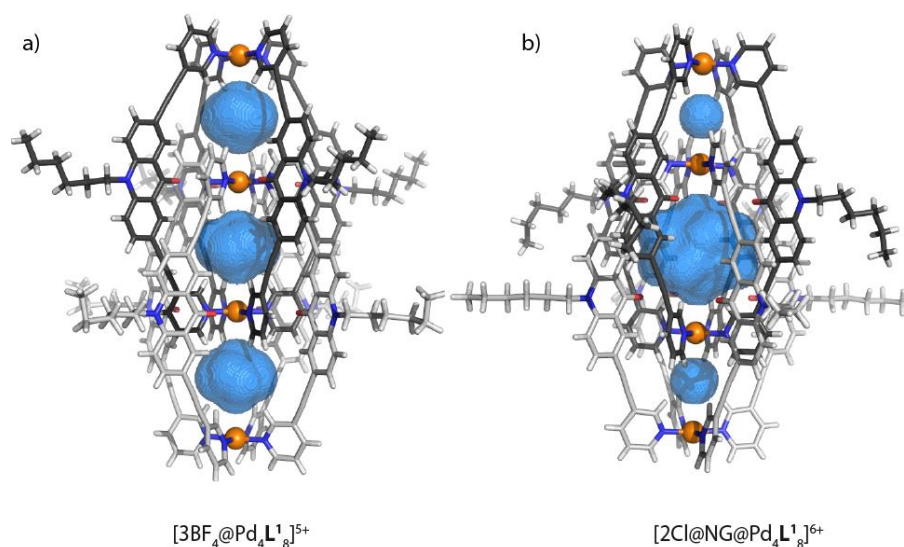


Figure 7.90 Visualization of the cavities of the interpenetrated coordination cages: a) $[3\text{BF}_4@\text{Pd}_4\text{L}_1]^{5+}$ and b) $[2\text{Cl}@\text{NG}@\text{Pd}_4\text{L}_1]^{6+}$ (the encapsulated neutral guest (NG) is DABDO). The cavity boundaries of the central pocket of the interpenetrated coordination structure are depicted as blue solids. *Color scheme*: C: gray; N: blue; O: red; Pd: orange, H: white.

7.3.8 Computational Details

The host, guest and combined host-guest geometries were optimized with RI-BP86,^[152,153] the def2-SVP^[154,155] orbital basis and the corresponding J-basis^[156] using the TURBOMOLE package^[157] For the Pd atoms the ECP-28MWB pseudopotential^[158] was used. The host structure was taken from X-ray crystallography results at a distance of 10.16 Å between the palladium atoms. To lower the number of atoms and make the system computationally more feasible the host was reduced to the pocket region. This was done by cutting out the top and bottom palladium-pyridine planes and saturating with hydrogens as shown in Figure 7.91. Only the hydrogens were optimized. The guest molecules were manually inserted into the pocket. Different conformations were used as starting structures for optimizations whereby the host was kept fixed. Out of this conformational sampling, the most stable structures were selected.

For the obtained minimum structures single point DF^[95]-SCS^[96]-LMP2^[159,160,160] calculations were performed. The Dunning cc-pVTZ^[97] orbital basis set was used in combination with the cc-pVTZ-PP^[98] basis and ECP28MDF^[98] pseudopotential for Pd (this basis will be referred to as VTZ). The density fitting basis used were the corresponding defaults (for the cc-pVTZ^[161]) except for calculations with Pd where the JKFIT and MP2FIT def2-TZVPP^[162] basis set was used. The orbitals were localized by the Pipek-Mezey scheme.^[163] The corresponding orbital domains were determined with a Boughton-Pulay criterion^[164] at a threshold of 0.985. To speed up the calculations we made use of the multipole-approximation^[165] for very-distant pairs ($r=10$ Bohr) and local fitting.^[95] The parameters were chosen by taking test calculations of the host pocket and increasing the distance parameter between 8 and 12 Bohr. All calculations were carried out with a development version of Molpro2015.1.^[136]

According to the locality of the orbitals we were able to build fragments (guest plus host) to determine the dispersion contributions^[166] at the SCS-LMP2/VTZ level of theory, stabilizing the guest molecules.

To build a bridge between theory and experiment we computed the binding affinities. A computational protocol was devised, making use of the aforementioned geometries. Solvent effects (acetonitrile) were included by D-COSMO-RS^[167] at the RI-BP86/def2-TZVP^[155,156,168] level in a supramolecular approach (Turbomole) - ΔE_{solv} . Ambient pressure (1bar) and temperature (298.15 K) were used in all solvent corrections and thermodynamic corrections. Thermochemistry corrections were computed with the RRHO-approach.^[122] The frequencies were computed at the RI-BP86/def2-SVP level for guests@host and a truncated Hessian containing only the guest molecules' 2nd derivatives was weighted and diagonalized. Those values are compared to the free guest-molecule, building ΔE_{ZPVE} , $\Delta H(0 \rightarrow T)$ and ΔS . Furthermore, a correction to the solvation energies was added, accounting for the missing translational degrees of freedom in solution, based on the Ardura *et al.* equation for bimolecular reactions^[169] (ΔG_{trans}). Final electronic energies were calculated at the SCS-LMP2/cc-pVTZ level of theory.

The total free energy of binding was then calculated as:

$$\Delta G = \Delta E(\text{SCS-LMP2/VTZ}) + \Delta E_{\text{solv}} + \Delta E_{\text{ZPVE}} + \Delta H(0 \rightarrow T) - T\Delta S + \Delta G_{\text{trans}}$$

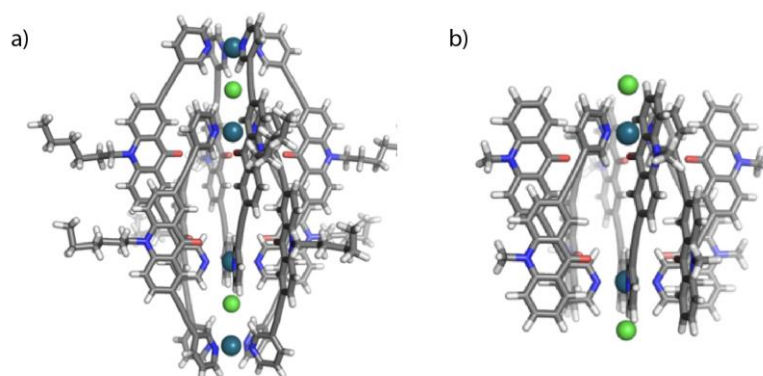


Figure 7.91 a) double cage structure, b) model used for the cage system in the calculations. The ligands were truncated (C-C bonds replaced by C-H) and the bottom and lower planes were removed. The chlorides in the inner pockets were kept in order to neutralize part of the charge.

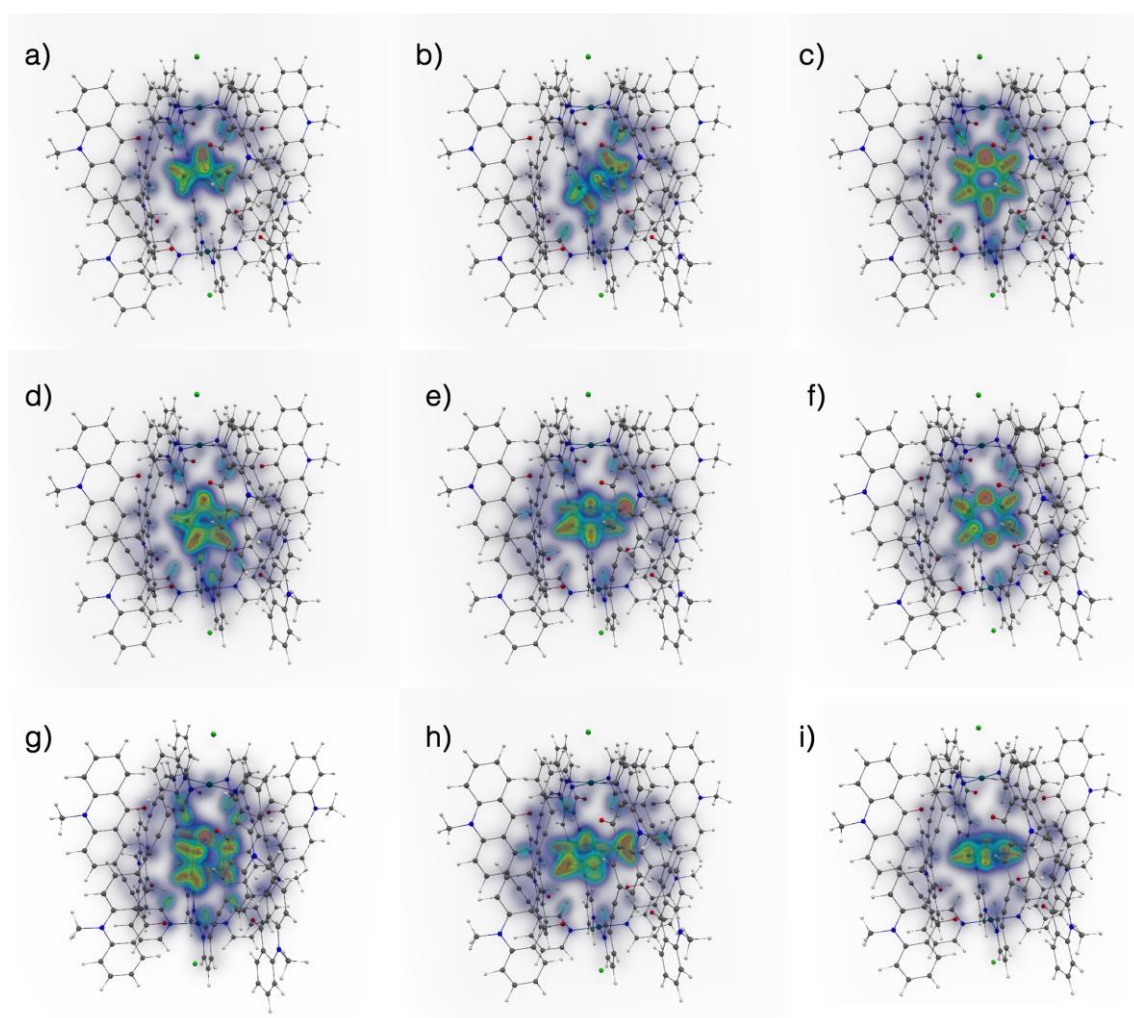


Figure 7.92 DID (Dispersion Interaction Density) plots of some selected guests inside the cavity, *color coding*: **red** = strong; **blue** = weak interacting regions): a) cyclopentane, b) cyclohexane, c) pyridine, d) norbornadiene, e) phenol, f) 1,4-dioxane, g) DABCO, h) 2-methylthiophene, i) benzene.

7.4 Part B – Coordination Cage as Photosensitizer

7.4.1 Guest Addition in the Presence of Atmospheric Oxygen and Ambient Light

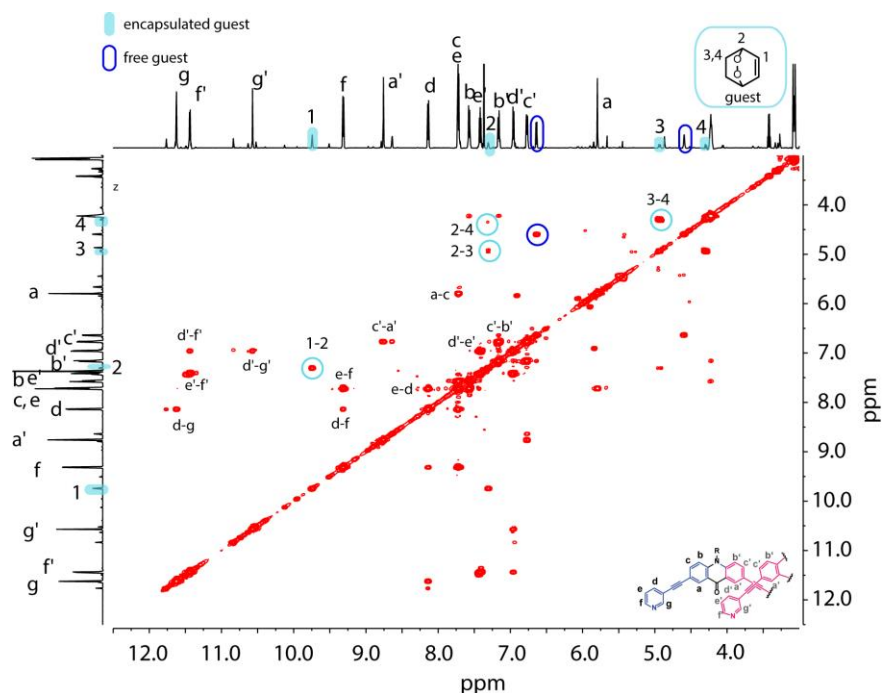


Figure 7.93 ^1H - ^1H COSY NMR spectrum of $[2\text{Cl}+\text{C}_6\text{H}_8\text{O}_2@\text{Pd}_4\text{L}^1_8]$. (600 MHz, CD_3CN , 298 K) in the aromatic region. Cross peaks are assigned and highlighted for the encapsulated guest (light blue) and free guest (dark blue).

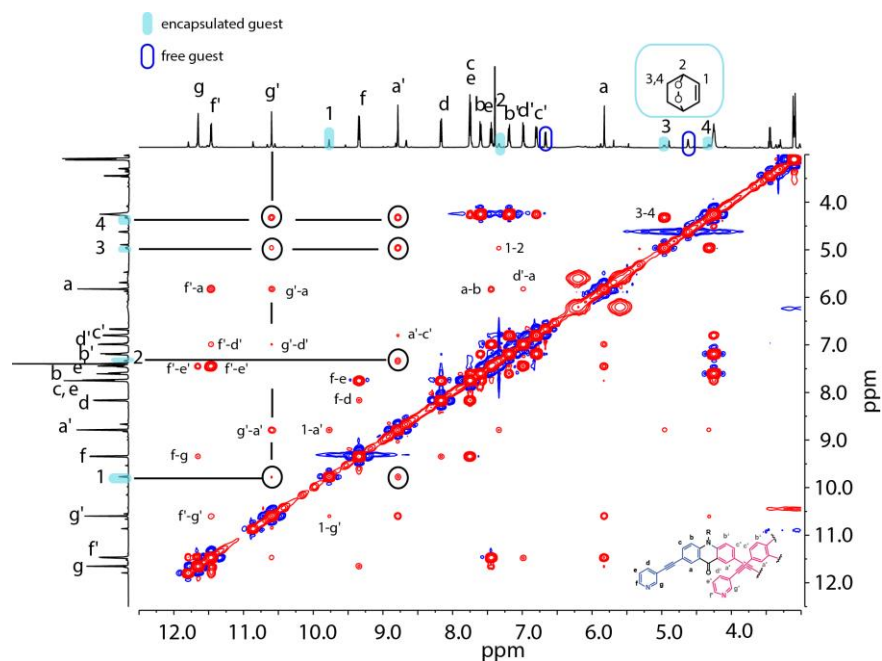


Figure 7.94 ^1H - ^1H NOESY spectrum of $[2\text{Cl}+\text{C}_6\text{H}_8\text{O}_2@\text{Pd}_4\text{L}^1_8]$. (600 MHz, CD_3CN , 298 K). Cross peaks between the encapsulated guest molecule ($\text{C}_6\text{H}_8\text{O}_2$) and the proton signals pointing towards the inner pocket of the coordination cage (H_a , H_g) are highlighted with a black circle.

7.4.2 Guest Addition in Absence of Oxygen

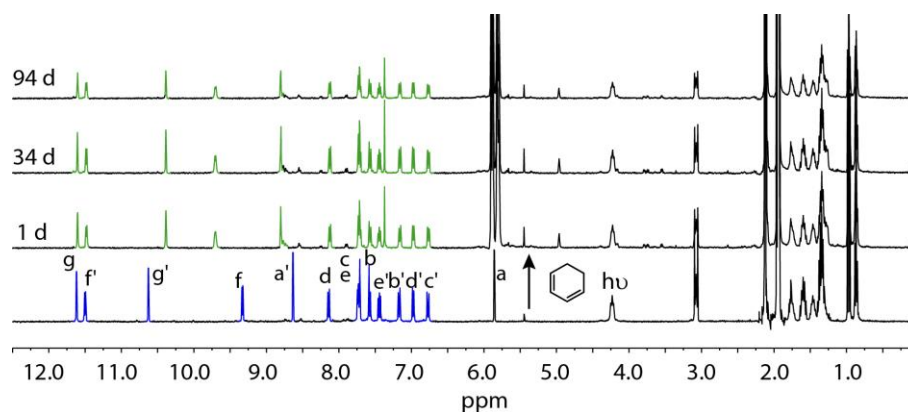


Figure 7.95 ^1H NMR spectra (400 MHz, 298 K, CD_3CN) of $[2\text{Cl}@Pd_4L^1_8]$ before and after the addition of 1,3-cyclohexadiene (20 eq.) and incubation time of 1 day, 34 days and 94 days in the absence of oxygen (sample stored in a nitrogen glove box). After 1 day the host-guest complex $[\text{Cl}+\text{C}_6\text{H}_8@Pd_4L^1_8]$ is formed (marked in green). In the absence of oxygen, no formation of the host-guest complex $[\text{Cl}+\text{C}_6\text{H}_8\text{O}_2@Pd_4L^1_8]$ was observed.

7.4.3 Guest Addition in the Dark (Absence of Ambient Light)

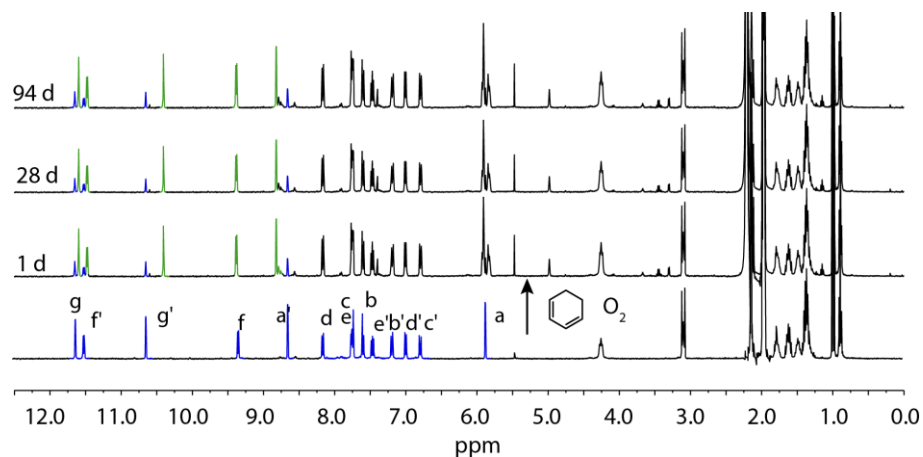


Figure 7.96 ^1H NMR spectra (400 MHz, 298 K, CD_3CN) of $[2\text{Cl}@Pd_4L^1_8]$ and after the addition of 1,3-cyclohexadiene (10 eq.) after an incubation time of 1 day, 34 days and 94 days in the absence of ambient light (sample wrapped in aluminum foil and stored in a light-tight cupboard). After 1 day the host-guest complex $[\text{Cl}+\text{C}_6\text{H}_8@Pd_4L^1_8]$ is formed (marked in green) and a transformation in the $[\text{Cl}+\text{C}_6\text{H}_8\text{O}_2@Pd_4L^1_8]$ complex is not observed under exclusion of ambient light.

7.4.4 Addition of 1,4-cyclohexadiene to $[2\text{Cl}@Pd_4L^1_8]$ in the Presence of Atmospheric Oxygen and Ambient Light

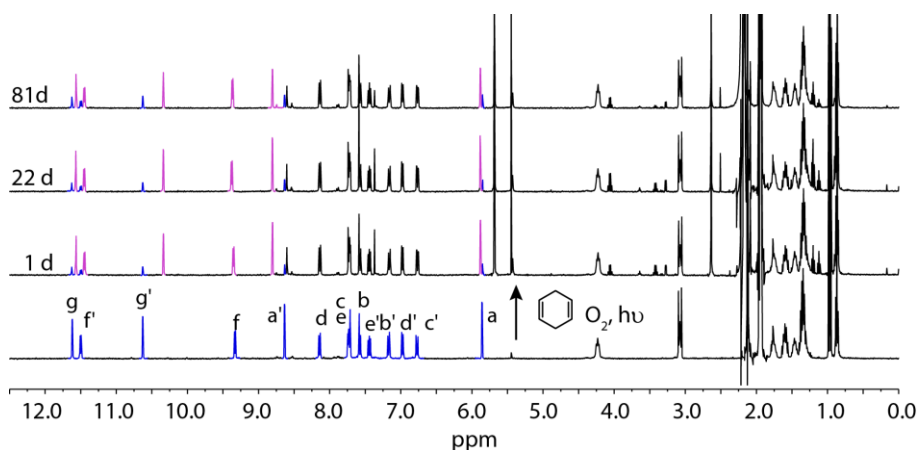


Figure 7.97 ^1H NMR spectra (400 MHz, 298 K, CD_3CN) of $[2\text{Cl}@Pd_4L^1_8]$ and after the addition of 1,4-cyclohexadiene (10 eq.) at different time intervals after the addition (1 day, 22 days and 81 days.). After 1 day the host-guest complex $[\text{Cl}+\text{C}_6\text{H}_8@Pd_4L^1_8]$ is formed. No further change could be observed after an extended period of time.

7.4.5 1,3-cyclohexadiene in CD_3CN

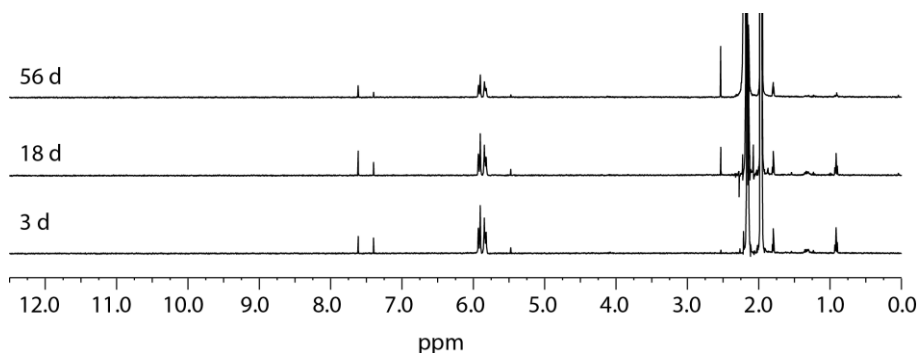


Figure 7.98 ^1H NMR spectra (400 MHz, 298 K, CD_3CN) of 1,3-cyclohexadiene in CD_3CN in the presence of atmospheric oxygen and ambient light. No significant changes could be observed in the ^1H NMR spectra after 56 days.

7.4.6 1,3-cyclohexadiene in presence of NBu_4Cl

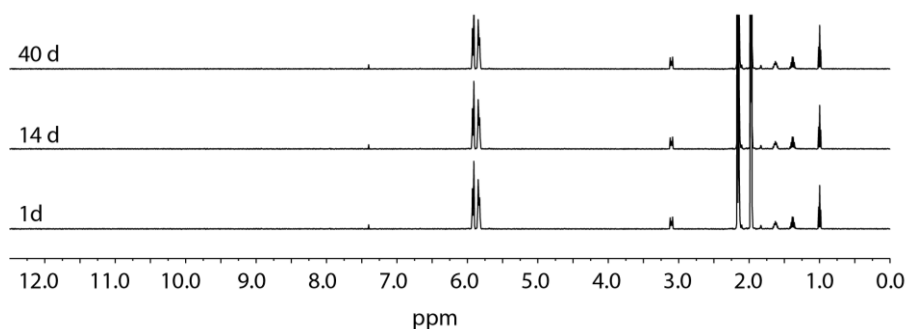


Figure 7.99 ^1H NMR spectra (500 MHz, 298 K, CD_3CN) of 1,3-cyclohexadiene (50 eq.) and tetrabutylammonium chloride in the presence of atmospheric oxygen and ambient light. No significant changes could be observed in the ^1H NMR spectra after 40 days.

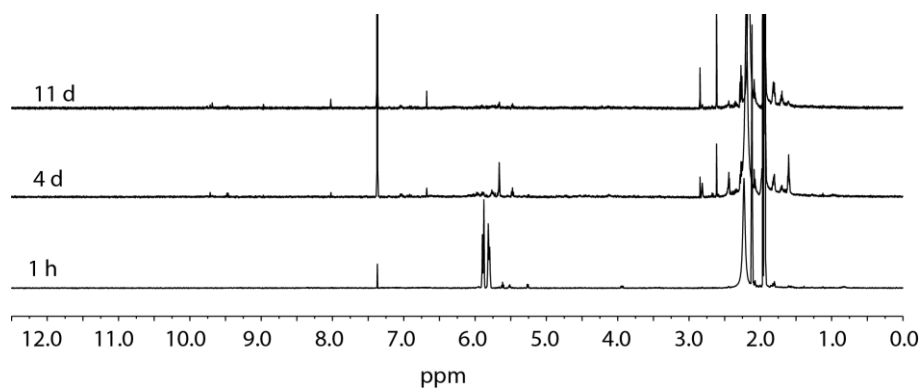
7.4.7 1,3-cyclohexadiene in presence of $[\text{Pd}(\text{CH}_3\text{CN})_4](\text{BF}_4)_2$ 

Figure 7.100 ^1H NMR spectra (500 MHz, 298 K, CD_3CN) of 1,3-cyclohexadiene (50 eq.) and $[\text{Pd}(\text{CH}_3\text{CN})_4](\text{BF}_4)_2$ in the presence of atmospheric oxygen and ambient light. The presence of the palladium source seems to lead to a decomposition of the cyclohexadiene.

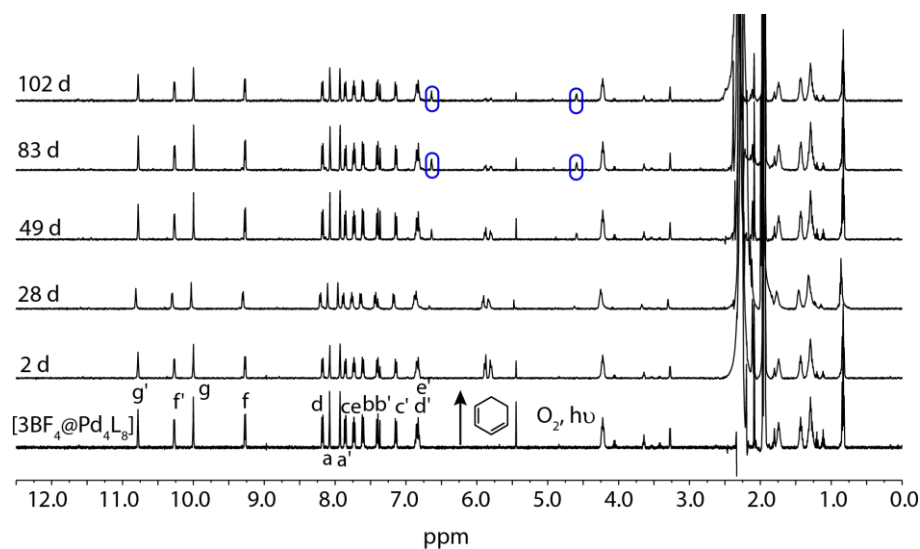
7.4.8 Addition of 1,3-cyclohexadiene to $[\text{BF}_4@[\text{Pd}_4\text{L}^1]_8]$ in the Presence of Atmospheric Oxygen and Ambient Light

Figure 7.101 ^1H NMR spectra (500 MHz, 298 K, CD_3CN) of $[\text{3BF}_4@[\text{Pd}_4\text{L}^1]_8]$ before and after the addition of 1,3-cyclohexadiene in the presence of atmospheric oxygen and ambient light. After several days, new signals could be observed which corresponds to the oxidation product $\text{C}_6\text{H}_8\text{O}_2$.

7.4.9 Addition of 1,3-cyclohexadiene to $[2\text{Cl}+\text{C}_6\text{H}_8\text{O}_2@\text{Pd}_4\text{L}^1_8]$ in the Presence of Atmospheric Oxygen and Ambient Light

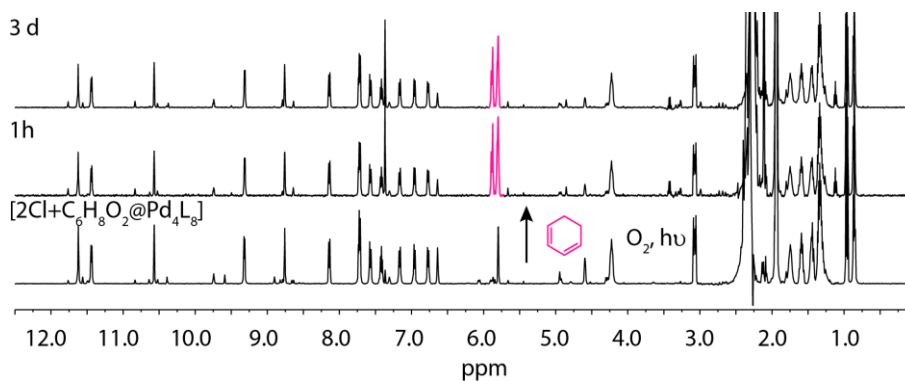
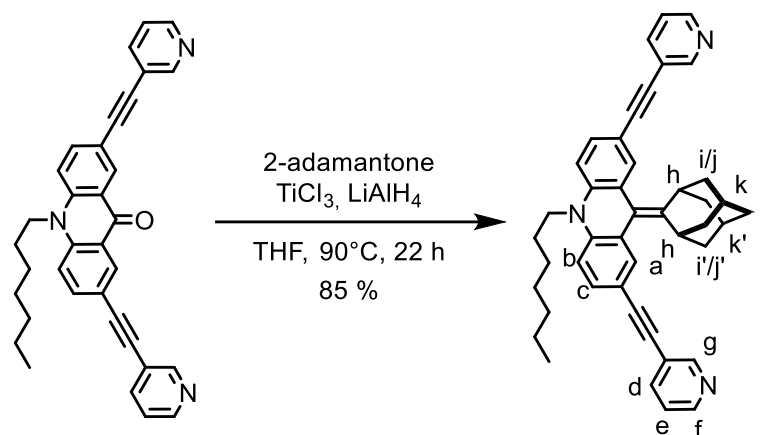


Figure 7.102 ^1H NMR spectra (500 MHz, 298 K, CD_3CN) of $[2\text{Cl}+\text{C}_6\text{H}_8\text{O}_2@\text{Pd}_4\text{L}^1_8]$ before and after the addition of 1,3-cyclohexadiene in the presence of atmospheric oxygen and ambient light. No exchange of the peroxide $\text{C}_6\text{H}_8\text{O}_2$ and 1,3-cyclohexadiene in the central pocket of the coordination cage was observed after 3 days.

7.5 Part C – Endohedral Functionalization and Dynamics

7.5.1 Synthesis

7.5.1.1 Synthesis of Ligand L²



Under a nitrogen atmosphere, titanium(III)-chloride (286.0 mg, 2.66 mmol, 17 eq.) in THF (8 mL) was cooled to 0 °C, lithium aluminium hydride (50.4 mg, 1.33 mmol, 9 eq.) added and stirred for 10 min at 0 °C. Triethylamine (135.5 mg, 1.33 μ mol, 9 eq.) was added dropwise at room temperature and the mixture was stirred for 1 h at 90 °C. 10-hexyl-2,7-bis(pyridine-3-ylethynyl)lacrid-9(10*H*)-one (ligand L¹) (74.4 mg, 155 μ mol, 1.0 eq.) and 2-adamantone (23.2 mg, 155 μ mol, 1.0 eq.) in THF (5 mL) were added dropwise and the mixture was stirred at 90 °C. After 18 h, the mixture was cooled to room temperature and filtered over Celite®. The solvent was removed *in vacuo* and the residue was purified using flash column chromatography on silica gel (0–2.5% MeOH in CHCl₃) to give the product as a yellow solid (79.4 mg, 132 μ mol, 85%).

¹H NMR (500 MHz, 273 K, CD₃CN): δ (ppm) = 8.72 (dd, ⁴*J* = 2.1 Hz, ⁴*J* = 0.9 Hz, 2H), 8.53 (dd, ³*J* = 4.9 Hz, ⁴*J* = 1.7 Hz, 2H), 7.86 (ddd, ³*J* = 7.9 Hz, ⁴*J* = 2.2 Hz, ⁴*J* = 1.7 Hz, 2H), 7.42 (dd, ³*J* = 8.5 Hz, ⁴*J* = 2.0 Hz, 2H), 7.36 (ddd, ³*J* = 7.9 Hz, ⁴*J* = 4.9 Hz, ⁵*J* = 0.8 Hz), 7.34 (d, ³*J* = 1.9 Hz, 2H), 7.17 (d, ³*J* = 8.6 Hz, 2H), 4.04 (t, ³*J* = 6.9 Hz, 2H, N-CH₂), 3.32 (s, 2H), 2.10–2.02 (m, 5H), 1.90 (s, 2H), 1.85–1.81 (m, 1H) 1.80–1.75 (m, 4H, hexyl-CH₂, adamantyl-*H*), 1.50–1.42 (m, 2H), 1.38–1.30 (m, 2H, hexyl-CH₂), 1.29–1.22 (m, 4H, hexyl-CH₂), 0.84 (t, ³*J* = 6.9 Hz, 3H, hexyl-CH₃).

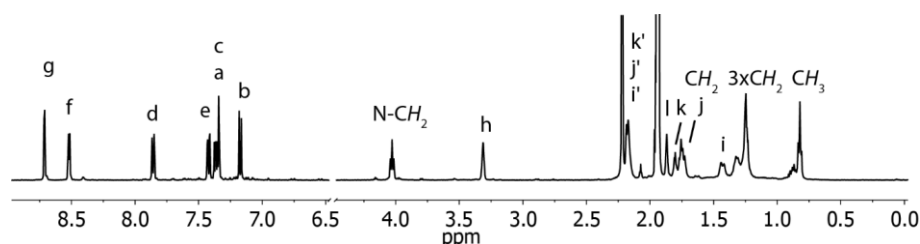


Figure 7.103 ¹H NMR spectrum of Ligand L² (500 MHz, 298 K, CD₃CN).

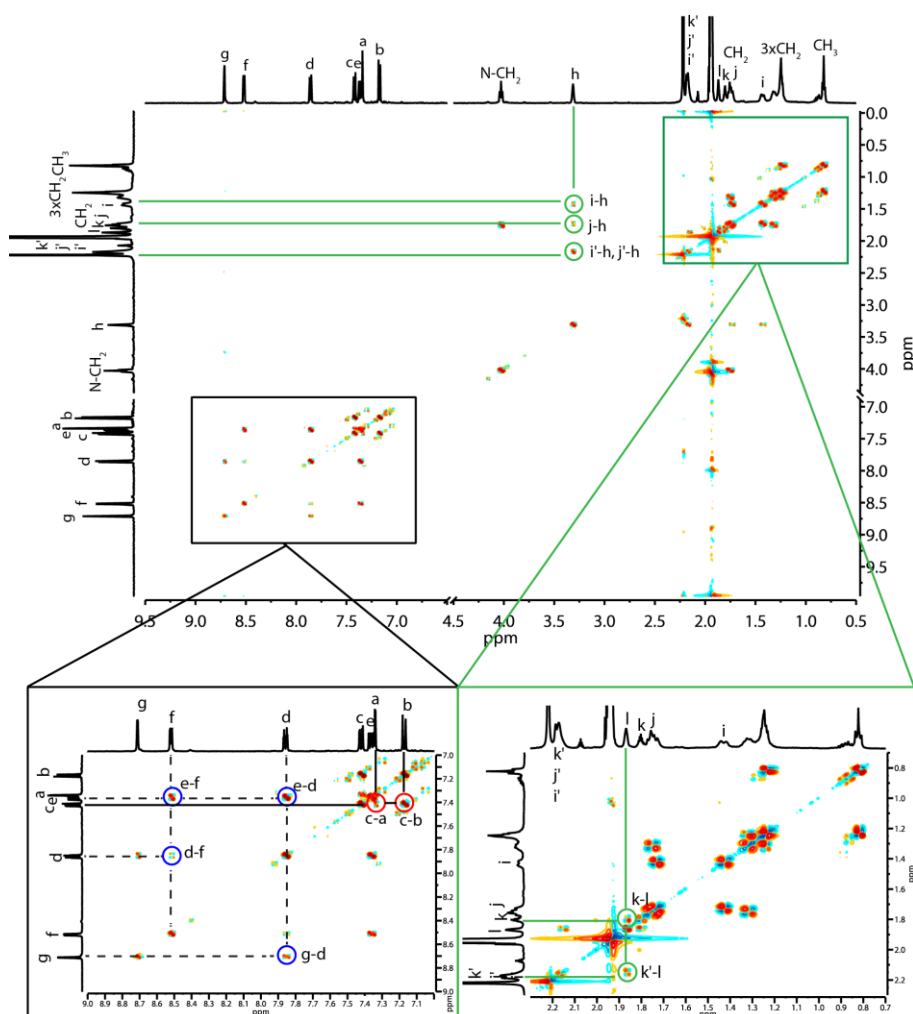


Figure 7.104 ^1H - ^1H COSY spectrum of ligand L^2 (500 MHz, CD_3CN , 273 K). Cross Peaks are highlighted: Blue: pyridine hydrogen, red: acridone protons, green: adamantyl hydrogen atoms.

^{13}C NMR (75 MHz, 273 K, CD_3CN): δ (ppm) = 151.66, 148.51, 146.32, 143.45, 138.08, 130.32, 130.06, 125.84, 123.45, 120.41, 114.10, 113.87, 92.72, 85.17, 45.11, 39.41, 38.61, 36.37, 32.19, 31.19, 28.20, 27.49, 25.97, 22.49, 13.40.

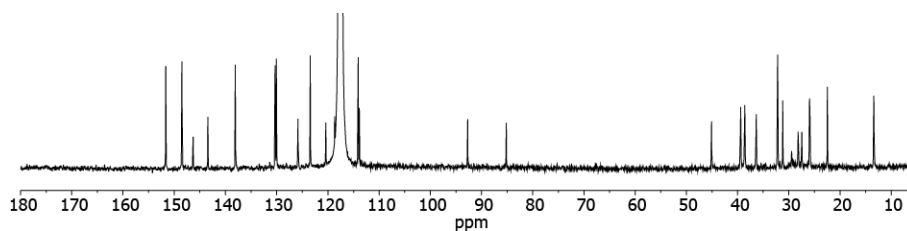
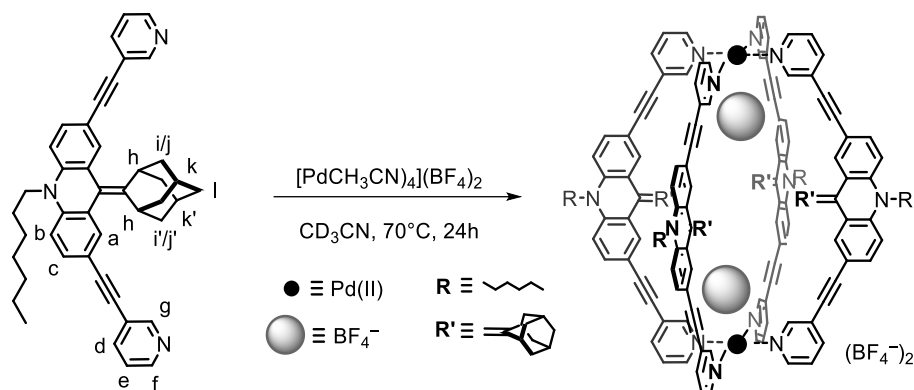


Figure 7.105 ^{13}C NMR spectrum of Ligand L^2 (75 MHz, 273 K, CD_3CN).

ESI HR-MS ($\text{C}_{43}\text{H}_{41}\text{N}_3$): exp.: 600.3375 (calc.: 600.3373).

IR (ATR): $\tilde{\nu}$ (cm^{-1}) = 2954, 2920, 2849, 2206, 1733, 1577, 1462, 1373, 1259, 1019, 799, 702.

7.5.1.2 Formation of Cage $[\text{Pd}_2\text{L}^2_4]$ 

The cage compound was formed in quantitative yields by heating a mixture of the ligand L^2 (804 μL , 1.35 mg, 2.3 μmol , 1.0 eq.) in CD_3CN (804 μL) and $[\text{Pd}(\text{CH}_3\text{CN})_4](\text{BF}_4)_2$ (1.13 μmol , 0.5 eq, 80.4 μL of a 15 mM solution in CD_3CN) at 70 °C for 15 min to give a 0.70 mM solution of the $[\text{Pd}_2\text{L}^2_4]$ cage.

^1H NMR (500 MHz, 298 K, CD_3CN): δ (ppm) = 9.12 (s, 8H), 8.86 (d, $^3J = 5.8$ Hz, 8H), 8.07 (dt, $^3J = 8.1$ Hz, $^4J = 1.6$ Hz, 8H), 7.58 (dd, $^3J = 8.0$ Hz, $^3J = 5.7$ Hz, 8H), 7.48 (dd, $^3J = 8.5$ Hz, $^4J = 1.8$ Hz, 8H), 7.35 (d, $^4J = 2.0$ Hz, 8H), 7.19 (d, $^3J = 8.5$ Hz, 8H), 4.01 (t, $^3J = 6.9$ Hz, 8H, NCH_2), 3.17 (s, 8H), 2.00 (8 H), 1.75–1.66 (m, 16 H, CH_2), 1.47–1.43 (m, 8H), 1.35–1.32 (m, 8H), 1.20–1.15 (m, 40H, CH_2), 0.75 (t, $^3J = 6.9$ Hz, 12H, CH_3), 0.59 (s, 8H).

Overlapping signals in the aliphatic region could be assigned *via* 2D NMR spectroscopy.

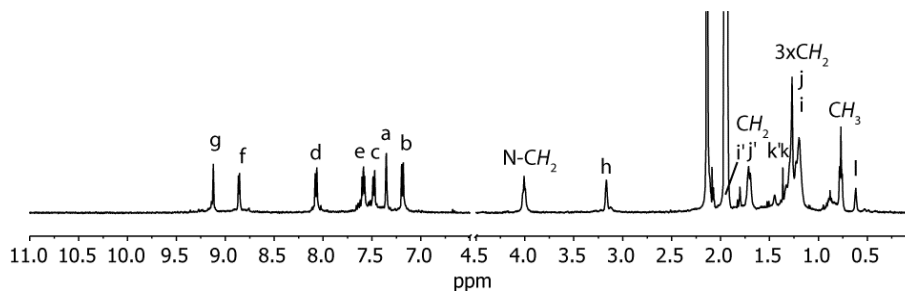
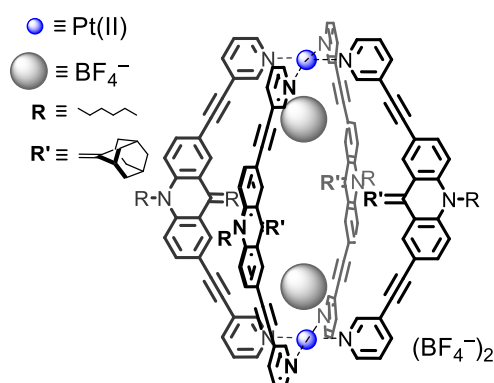


Figure 7.106 ^1H NMR spectrum of coordination cage $[\text{Pd}_2\text{L}^2_4]$ (500 MHz, 298 K, CD_3CN).

^{19}F NMR (282 MHz, 298 K, CD_3CN): δ (ppm) = -151.56 (sharp, BF_4^-).

ESI HR-MS $[\text{C}_{172}\text{H}_{164}\text{N}_{12}\text{Pd}_2(\text{BF}_4)_2]^{2+}$: exp.: 1392.6103 (calc.: 1392.6100).

IR (ATR): $\tilde{\nu}$ (cm^{-1}) = 3620, 2921, 2858, 2261, 2211, 1588, 1469, 1104, 1038, 832, 690.

7.5.1.3 Formation of Cage $[\text{Pt}_2\text{L}_2^4]$ 

Ligand L^2 (1.68 mg, 2.8 mmol, 1.0 eq.), $[\text{PtCl}_2(\text{CH}_3\text{CN})_2]$ (0.58 mg, 1.4 mmol, 0.5 eq.) and AgClO_4 (0.58 mg, 2.8 mmol, 1.0 eq.) were heated to 80 °C in acetonitrile (1 mL) for 3 days and the precipitated silver chloride was removed by filtration. The $[\text{Pt}_2\text{L}_2^4]$ cage was formed quantitatively as a 0.70 mM solution.

$^1\text{H NMR}$ (500 MHz, 298 K, CD_3CN): δ (ppm) = 9.23 (s, 8H), 8.86 (d, $^3J = 5.8$ Hz, 8H), 8.06 (dt, $^3J = 8.1$ Hz, $^4J = 1.6$ Hz, 8H), 7.58 (dd, $^3J = 8.0$ Hz, $^3J = 5.7$ Hz, 8H), 7.48 (dd, $^3J = 8.5$ Hz, $^4J = 1.8$ Hz, 8H), 7.39 (d, $^4J = 2.0$ Hz, 8H), 7.18 (d, $^3J = 8.5$ Hz, 8H), 4.01 (t, $^3J = 6.9$ Hz, 8H, NCH_2), 3.17 (s, 8H), 2.04 (8H), 1.75–1.66 (m, 16H, CH_2), 1.59–1.52 (m, 8H), 1.35–1.15 (m, 44H, CH_2), 0.77 (t, $^3J = 6.9$ Hz, 12H, CH_3), 0.49 (s, 8H).

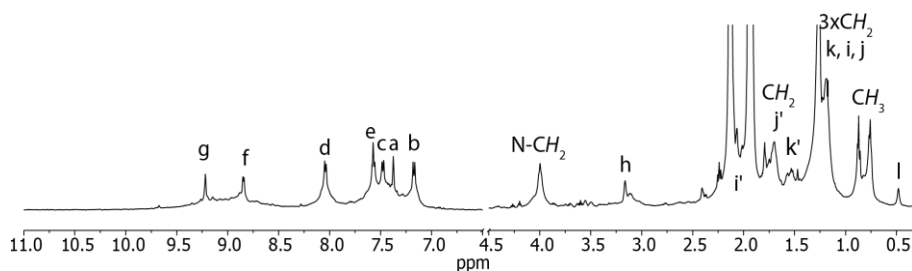


Figure 7.107 $^1\text{H NMR}$ spectrum of coordination cage $[\text{Pt}_2\text{L}_2^4]$ (500 MHz, 298 K, CD_3CN).

ESI HR-MS ($[\text{C}_{172}\text{H}_{164}\text{N}_{12}\text{Pd}_2(\text{ClO}_4)_2]^{2+}$): exp.: 1494.0765 (calc: 1494.0746).

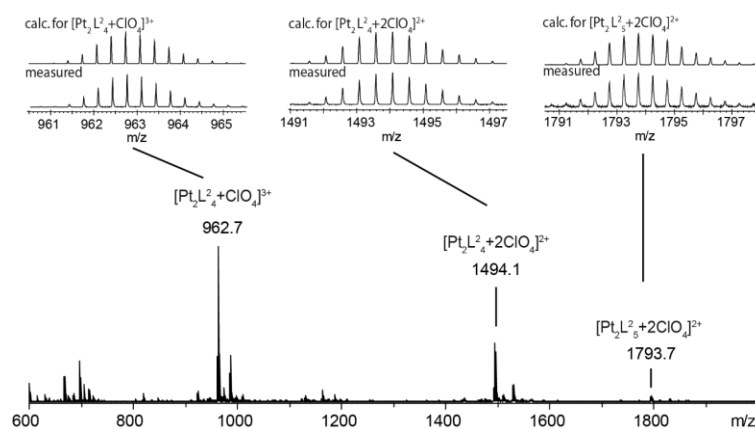


Figure 7.108 HR-ESI MS of $[\text{Pt}_2\text{L}_2^4]$.

7.5.1.4 Synthesis of Guest Molecules

The tetrabutylammonium salts of the guests were obtained according to a previously reported procedure.^[62,139,170] All starting materials were obtained commercially as sodium salts or free acids in the highest available purity. The ferrocene 1,1'-disulfonic acid was prepared following the procedure reported by Jones and coworkers.^[171]

The sodium salts (1.0 eq.) were dissolved in methanol and an acidic cation exchange resin (DOWEX®50WX8) was added and stirred for 1–2 h, filtered and the solvent evaporated to obtain the free acids. To a solution of the disulfonic acids in methanol, tetrabutylammonium hydroxide (10 % in MeOH, 2.0 eq.) was added and the pH was adjusted to 7. After evaporation of the solvent, the crude residue was mixed with CHCl₃ and then filtered to remove any remaining solids. Finally, the solvent was removed *in vacuo* to yield the tetrabutylammonium salts. The purity of the compounds and the correct cation : anion ratio was verified by ¹H NMR spectroscopy.

The preparation of the potassium@18-crown-6 salts was carried out as follows: To a solution of the bis-sulfonic acid (1.0 eq.) in methanol, a solution of potassium hydroxide (1 M in MeOH, 2.0 eq.) was added until the pH was adjusted to 7. Then, a stoichiometric solution of 18-crown-6 (1 M in MeOH, 2.0 eq.) was added and the solvent was removed *in vacuo*. The potassium 18-crown-6 salts were obtained in good yields (83–95 %) after recrystallization from methanol.

7.5.2 Titration of (bis)-anionic Guests to [Pd₂L₂]₄ cage

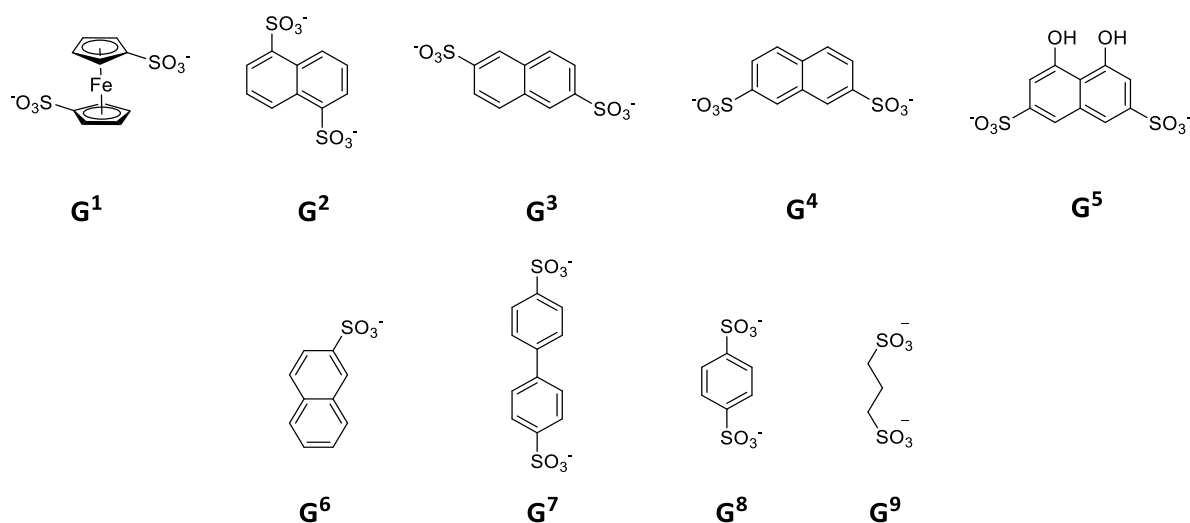


Figure 7.109 Structure of used (bis)-anionic guest molecules G^{1-9} .

General Procedure

The host-guest complexes were formed by titrating a solution of the bis-sulfonate guests (as their tetrabutylammonium or potassium@18-crown-6 salts in CD_3CN , 17.5 mM) into a solution of the cage $[\text{Pd}_2\text{L}_2^4]$ (0.70 mM, 500 μL , CD_3CN) in an NMR tube. The NMR spectra were recorded immediately after briefly shaking the solution.

7.5.2.1 Addition of \mathbf{G}^1

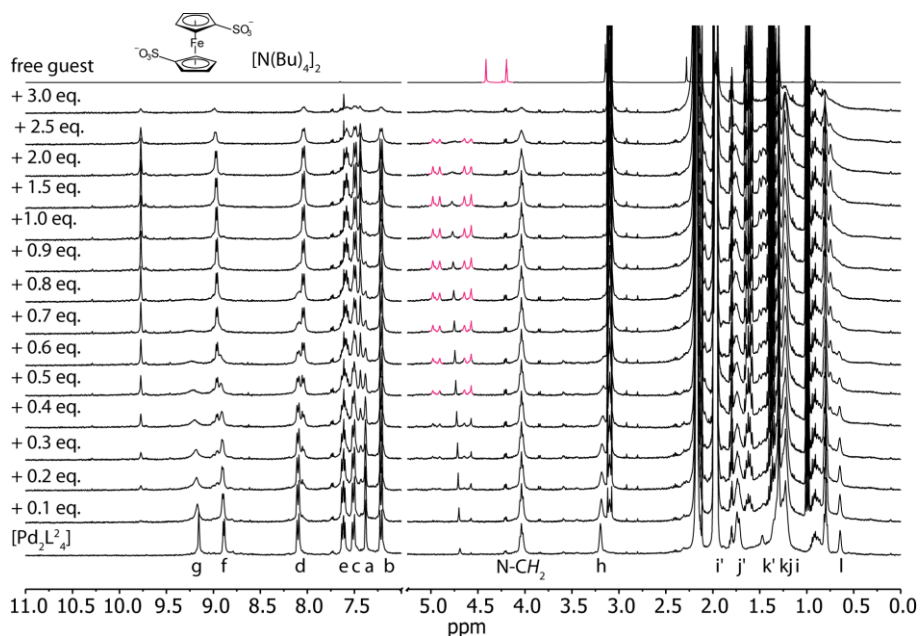


Figure 7.110 ^1H NMR titration (400 MHz, 298 K, CD_3CN) of $[\text{Pd}_2\text{L}_2^4]$ with $(\text{NBu}_4)_2\mathbf{G}^1$. Upon addition of one equivalent of guest \mathbf{G}^1 the $[\text{Pd}_2\text{L}_2^4]$ cage transforms into $[\mathbf{G}^1@[\text{Pd}_2\text{L}_2^4]]$. Excess addition of \mathbf{G}^1 leads to disaggregation of the cage.

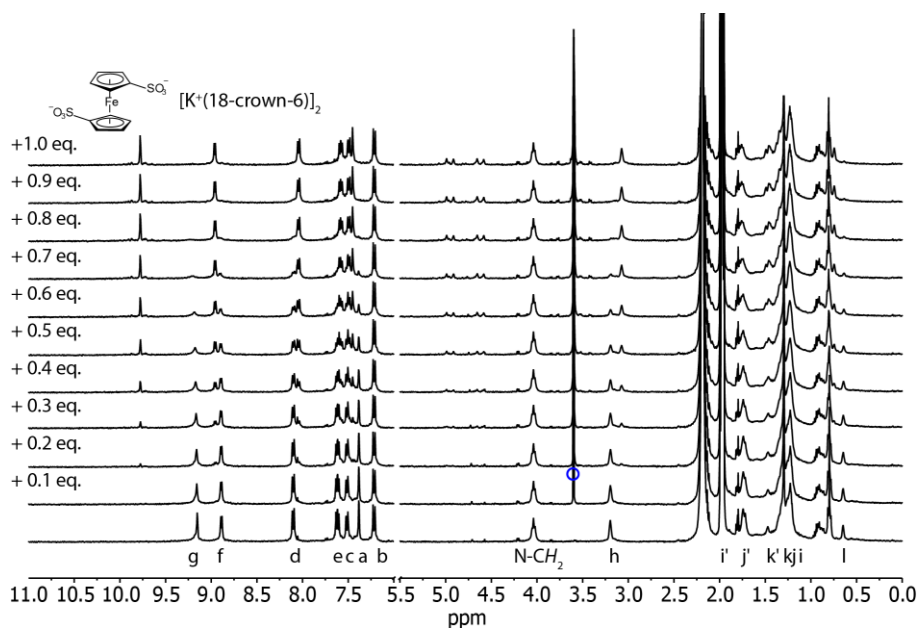


Figure 7.111 ^1H NMR titration (400 MHz, 298 K, CD_3CN) of $[\text{Pd}_2\text{L}_2^4]$ with $[\text{K}^+(18\text{-crown-6})]_2\mathbf{G}^1$. Upon addition of one equivalent of guest \mathbf{G}^1 the $[\text{Pd}_2\text{L}_2^4]$ cage transforms into $[\mathbf{G}^1@[\text{Pd}_2\text{L}_2^4]]$. The blue circle indicates the crown ether signal.

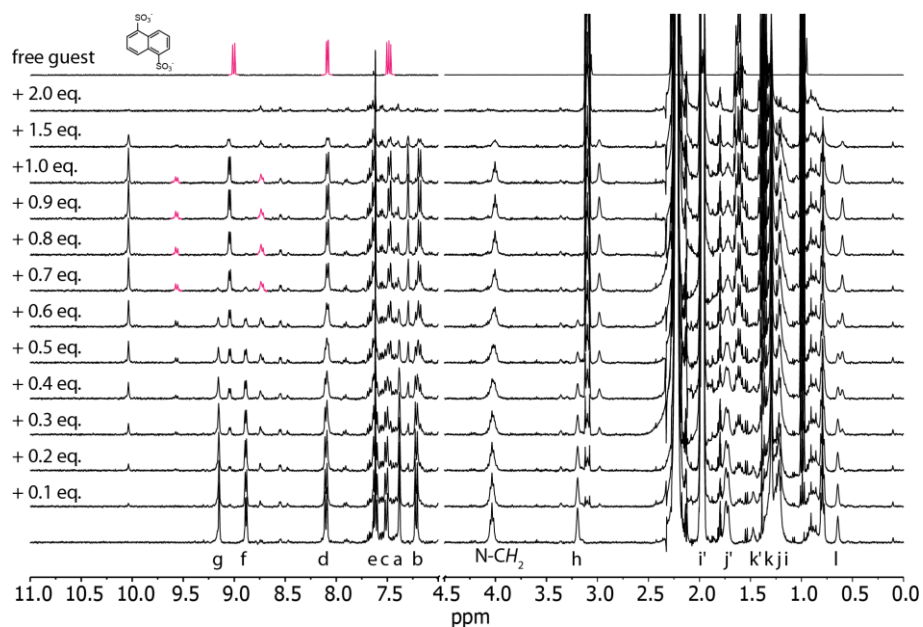
7.5.2.2 Addition of Guest G^2 

Figure 7.112 ^1H NMR titration (400 MHz, 298 K, CD_3CN) of $[\text{Pd}_2\text{L}_2^4]$ with $(\text{NBu}_4)_2\text{G}^2$. Upon addition of 1.0 eq. of guest G^2 the $[\text{Pd}_2\text{L}_2^4]$ cage transforms into the host-guest complex $[\text{G}^2@[\text{Pd}_2\text{L}_2^4]]$. Excess addition of G^2 leads to precipitation and disassembly of the cage. Signals of encapsulated guest G^2 are highlighted in magenta.

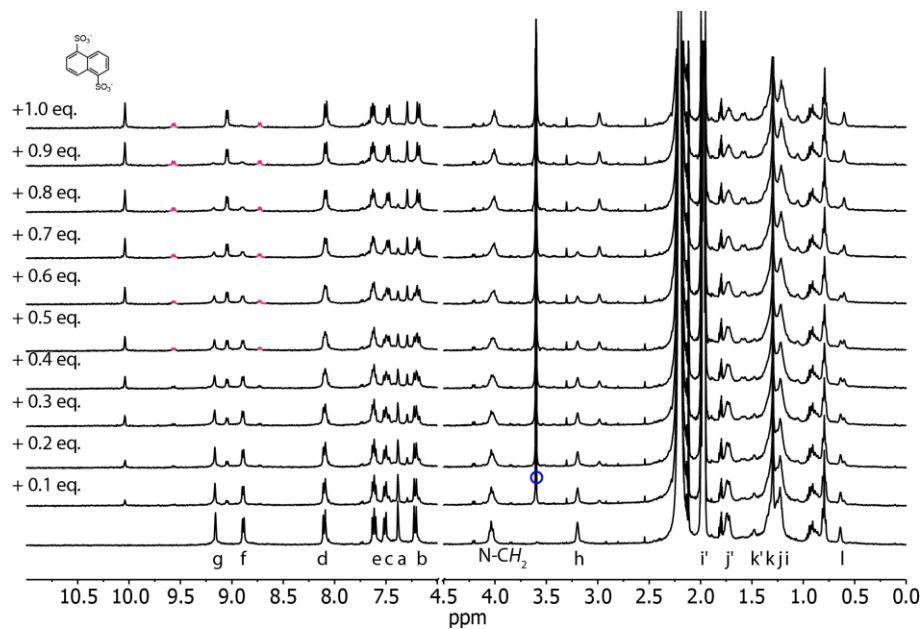


Figure 7.113 ^1H NMR titration (400 MHz, 298 K, CD_3CN) of $[\text{Pd}_2\text{L}_2^4]$ with $[\text{K}^+@(\text{18-crown-6})_2\text{G}^2]$. Upon addition of 1.0 eq. of guest G^2 to the $[\text{Pd}_2\text{L}_2^4]$ cage the new host-guest complex $[\text{G}^2@[\text{Pd}_2\text{L}_2^4]]$ is formed. The blue circle indicates the crown ether signal.

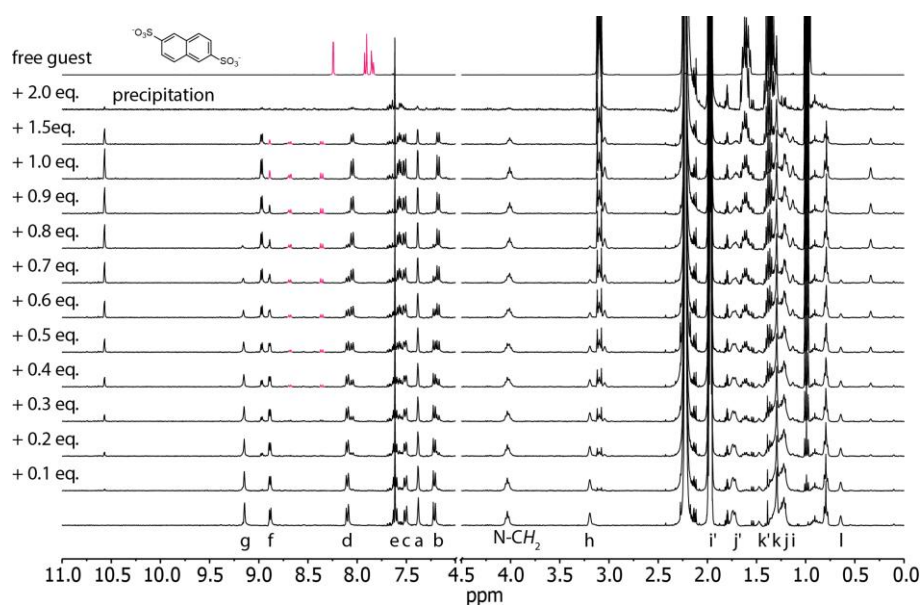
7.5.2.3 Addition of Guest G^3 

Figure 7.114 ^1H NMR titration (400 MHz, 298 K, CD_3CN) of $[\text{Pd}_2\text{L}_2^2_4]$ with $(\text{NBu}_4)_3\text{G}^3$. Excess addition of guest molecules leads to decomposition of the host guest complex.

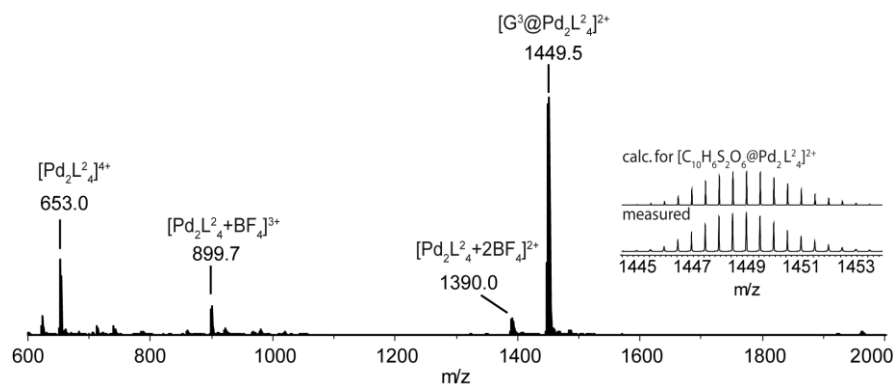


Figure 7.115 ESI-MS of $[\text{G}^3@\text{Pd}_2\text{L}_2^2_4]$.

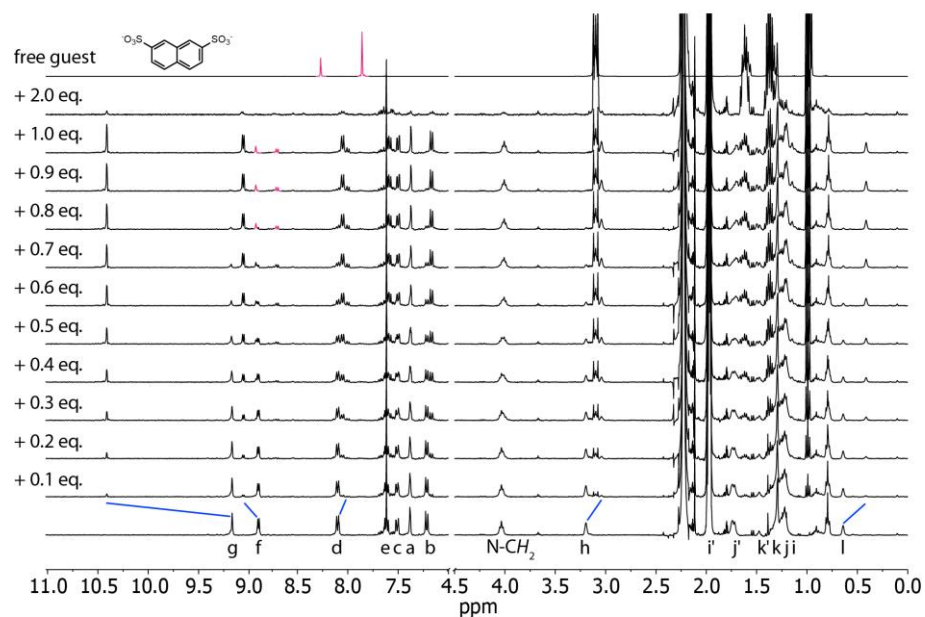
7.5.2.4 Addition of Guest G^4 

Figure 7.116 ^1H NMR titration (400 MHz, 298 K, CD_3CN) of $[\text{Pd}_2\text{L}_4]$ with $(\text{NBu}_4)_2\text{G}^4$. Upon addition of 1.0 eq. of guest G^4 to the $[\text{Pd}_2\text{L}_4]$ cage the new species $[\text{G}^4@[\text{Pd}_2\text{L}_4]]$ is formed.

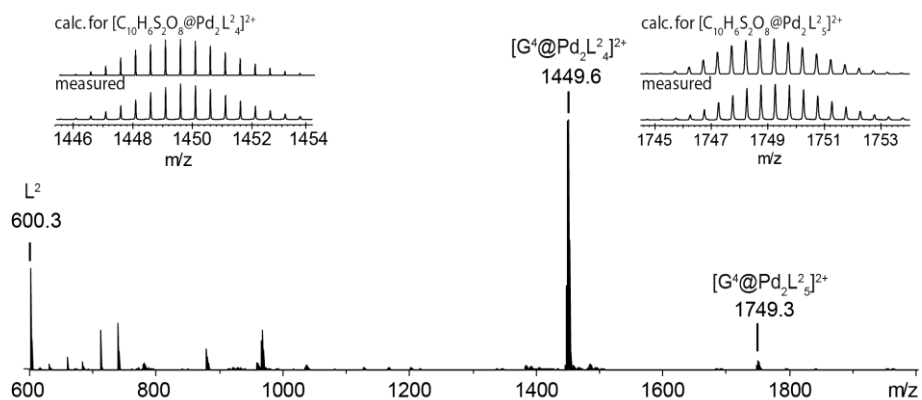


Figure 7.117 ESI-MS of $[\text{G}^4@[\text{Pd}_2\text{L}_4]]$.

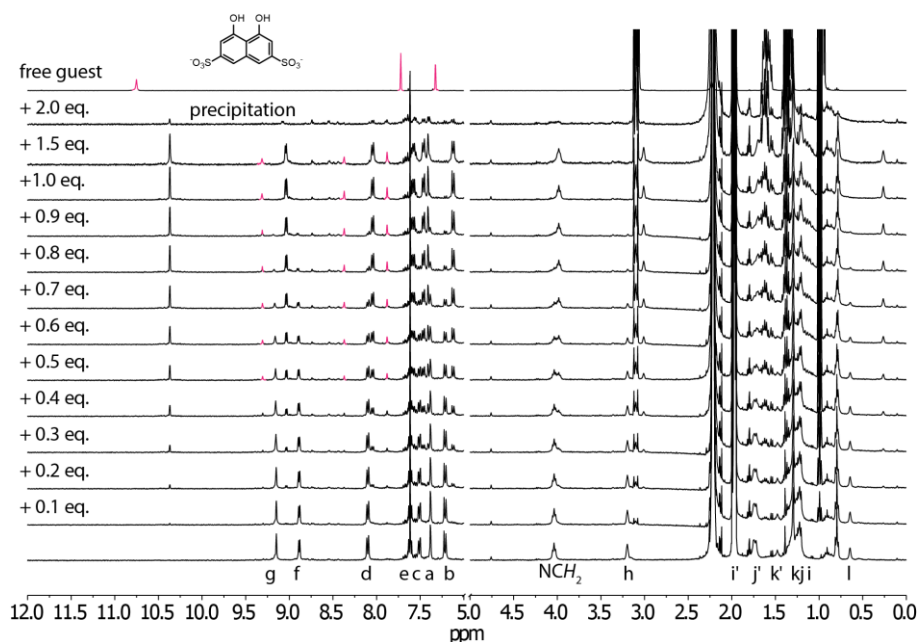
7.5.2.5 Addition of Guest G^5 

Figure 7.118 ^1H NMR titration (400 MHz, 298 K, CD_3CN) of $[\text{Pd}_2\text{L}_2^4]$ with $(\text{NBu}_4)_2\text{G}^5$. Upon addition of one equivalent of guest G^5 to the $[\text{Pd}_2\text{L}_2^4]$ cage the new species $[\text{G}^5@ \text{Pd}_2\text{L}_2^4]$ is formed. Excess addition of G^5 leads to complete disaggregation of the cage and precipitation was observed in the NMR tube.

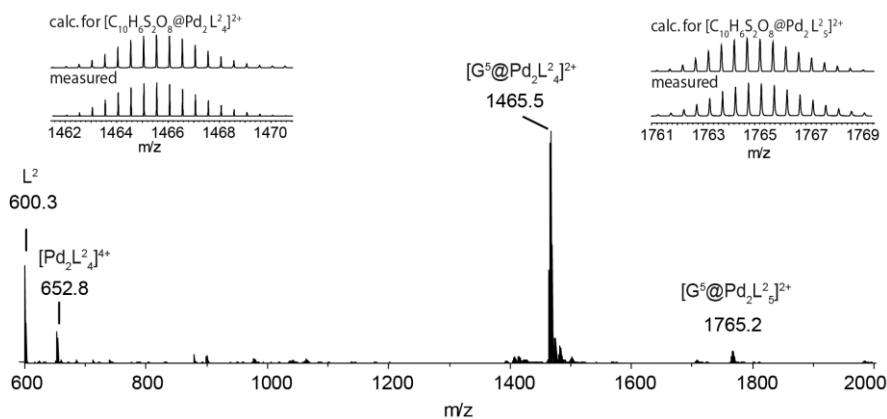


Figure 7.119 ESI-MS of $[\text{G}^5@ \text{Pd}_2\text{L}_2^4]$.

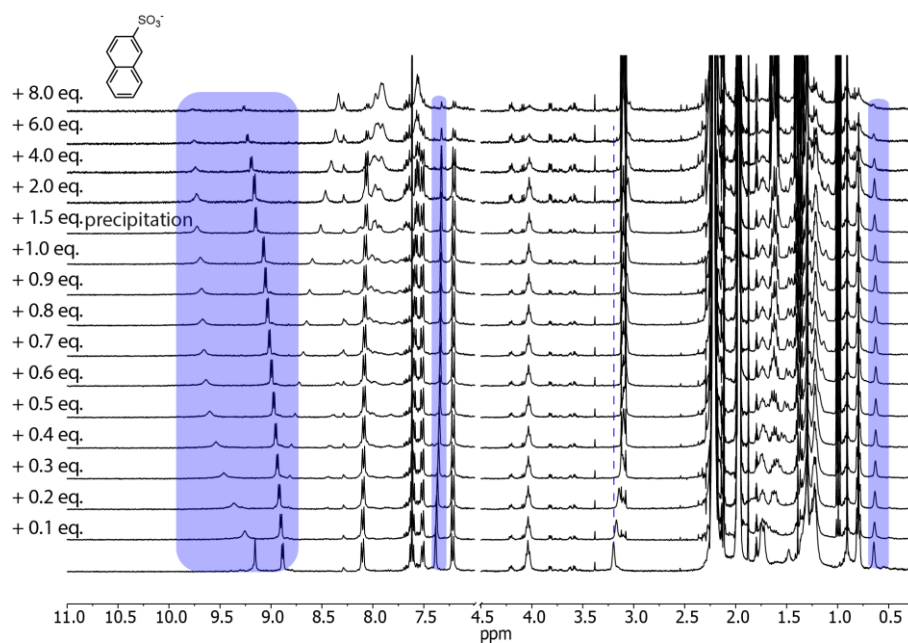
7.5.2.6 Addition of G^6 

Figure 7.120 ^1H NMR titration (400 MHz, 298 K, CD_3CN) of $[\text{Pd}_2\text{L}^2_4]$ with $(\text{NBu}_4)_2\text{G}^6$.

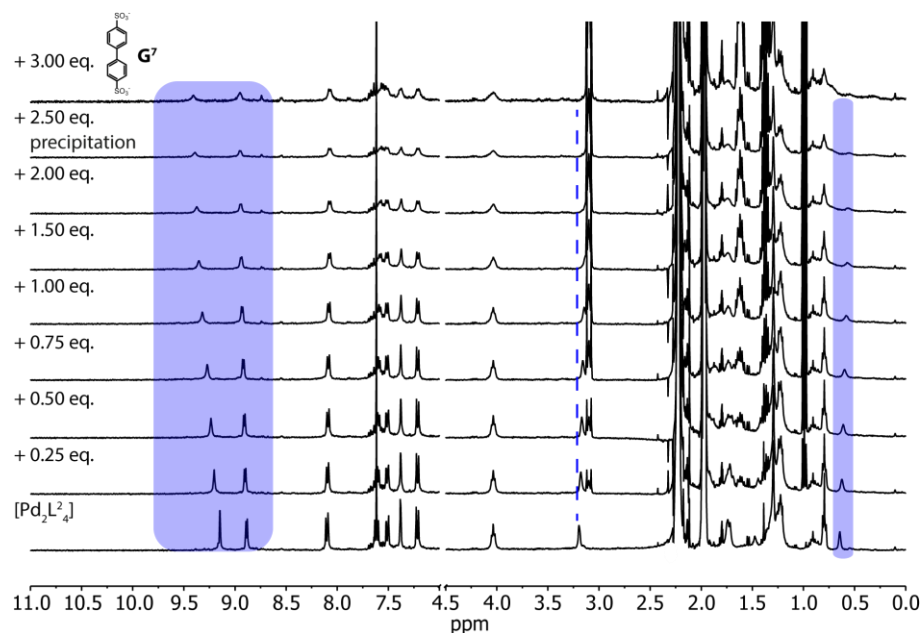
7.5.2.7 Addition of G^7 

Figure 7.121 ^1H NMR titration (400 MHz, 298 K, CD_3CN) of $[\text{Pd}_2\text{L}^2_4]$ with $(\text{NBu}_4)_2\text{G}^7$. The chemical shifts of the inward pointing protons changed gradually, due to fast exchange of the guest.

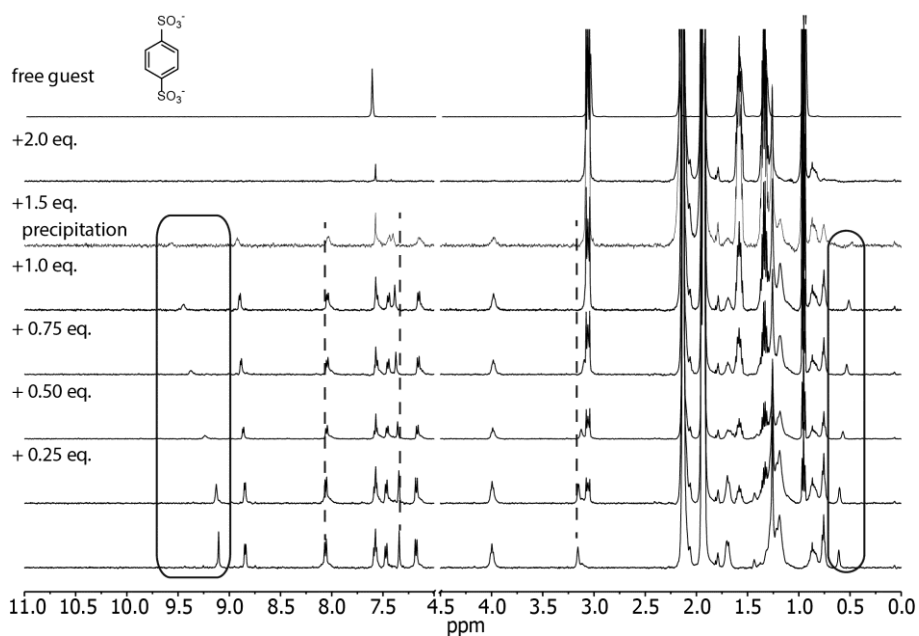
7.5.2.8 Addition of G^8 

Figure 7.122 ^1H NMR titration (400 MHz, 298 K, CD_3CN) of $[\text{Pd}_2\text{L}^{24}]$ with $(\text{NBu}_4)_2\text{G}^8$. The chemical shifts of the inward pointing protons changed gradually, due to fast exchange of the guest.

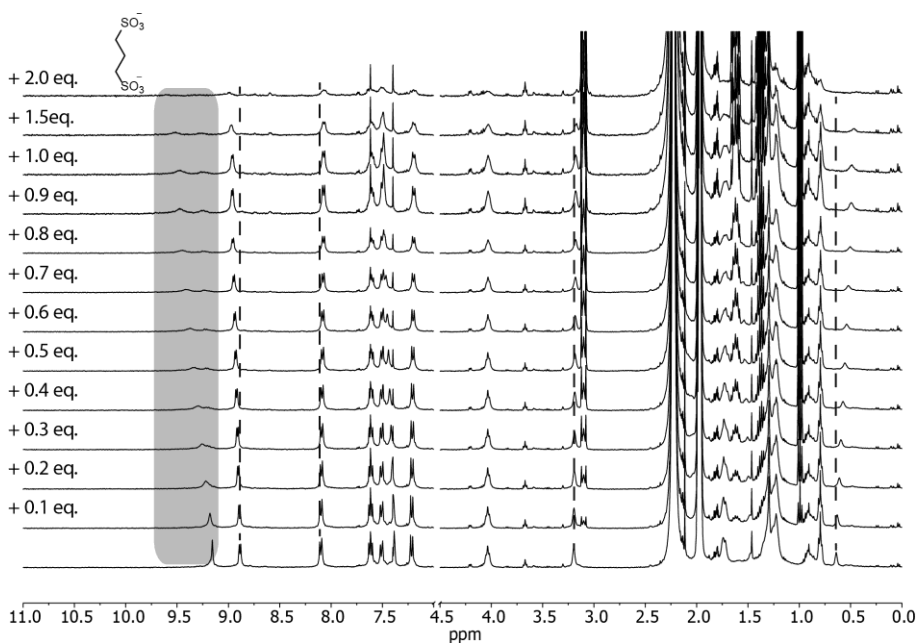
7.5.2.9 Addition of G^9 

Figure 7.123 ^1H NMR titration (400 MHz, 298 K, CD_3CN) of $[\text{Pd}_2\text{L}^{24}]$ with $(\text{NBu}_4)_2\text{G}^9$. The chemical shifts of the inward pointing protons changed gradually, due to fast exchange of the guest.

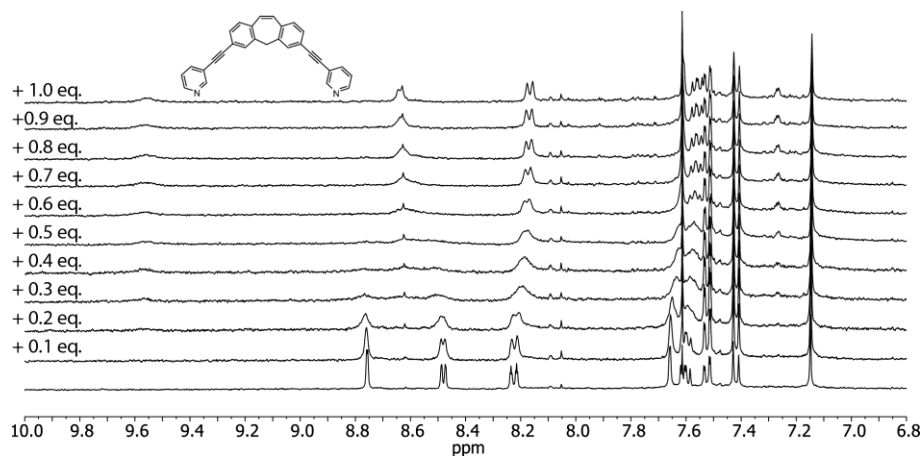
7.5.3 Titration of Cage $[\text{Pd}_2\text{L}^{2*}_4]$ and G^1 

Figure 7.124 ^1H NMR titration (400 MHz, 298 K, CD_3CN) of $[\text{Pd}_2\text{L}^{3*}_4]$ with $[\text{K}^+(\text{18-crown-6})]_2\text{G}^1$. Gradual shifting of the signals indicates fast exchange. The exchange rate of a 1:1 sample of $[\text{Pd}_2\text{L}^{2*}_4]$ and $[\text{G}^1@[\text{Pd}_2\text{L}^{2*}_4]]$ could be given through line shape fitting to $k \sim 90\text{s}^{-1}$.

7.5.4 2D NMR Experiments

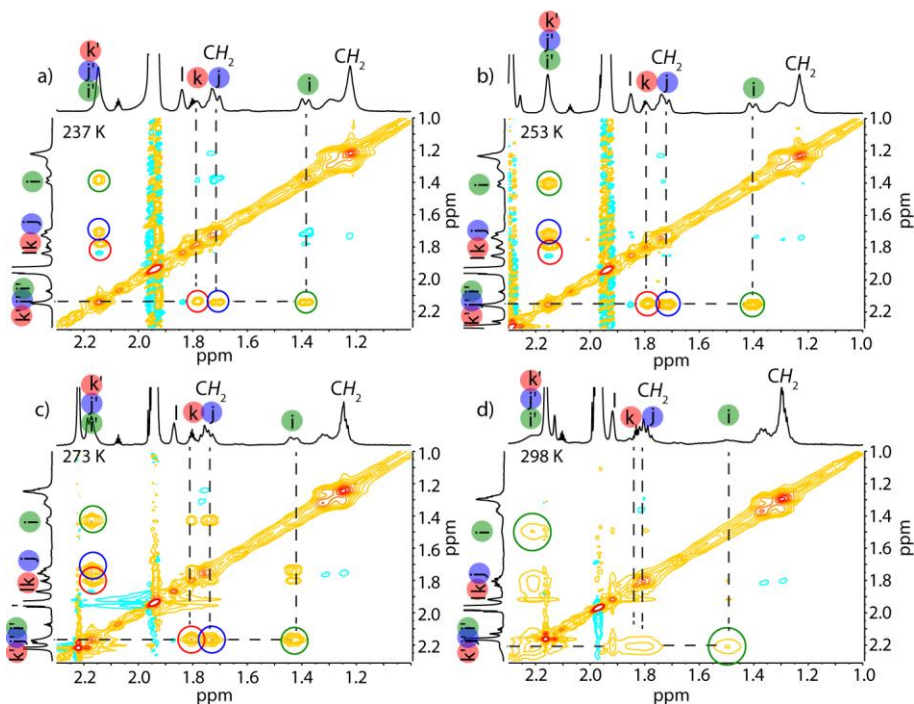
7.5.4.1 NOESY Measurements of Ligand L² at different Temperatures

Figure 7.125 ¹H-¹H NOESY spectrum of ligand L² (500 MHz, CD₃CN) at different temperatures: a) 237 K, b) 253 K, c) 273 K and d) 298 K. The cross-peaks indicate the exchange between the inward (i', j' and k') and outward (i, j, k) pointing hydrogen atoms and are increasing with rising temperature. This indicates the adamantyl group is undergoing a rapid flipping motion.

Integration of the signals yielded the exchange or “flipping rate” of the adamantyl group within the ligand at different temperatures (Eyring plot analysis see below):

T (K)	k (s ⁻¹)
237	0.18
253	0.90
273	14
298	150

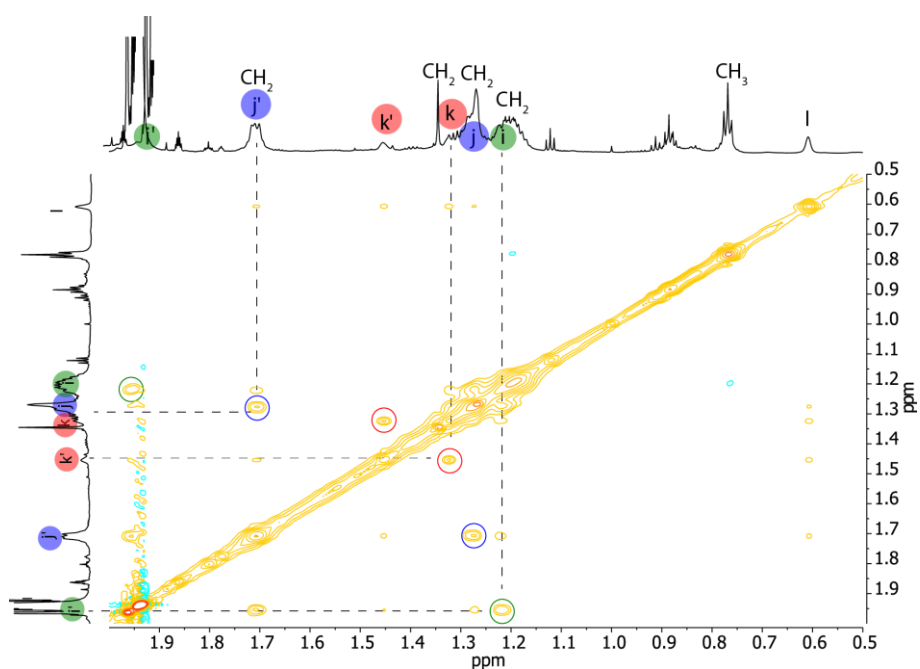
7.5.4.2 NOESY Measurements of $[\text{Pd}_2\text{L}^2_4]$ 

Figure 7.126 ^1H - ^1H NOESY spectrum of $[\text{Pd}_2\text{L}^2_4]$ (900 MHz, 298 K, mixing time 0.5 s, CD_3CN). Exchange signals between related protons are highlighted as followed: i/i' (green), j/j' (blue), k/k' (red). Integration of the inner and outer adamantyl signals determined the exchange rate as 0.32 s^{-1} .

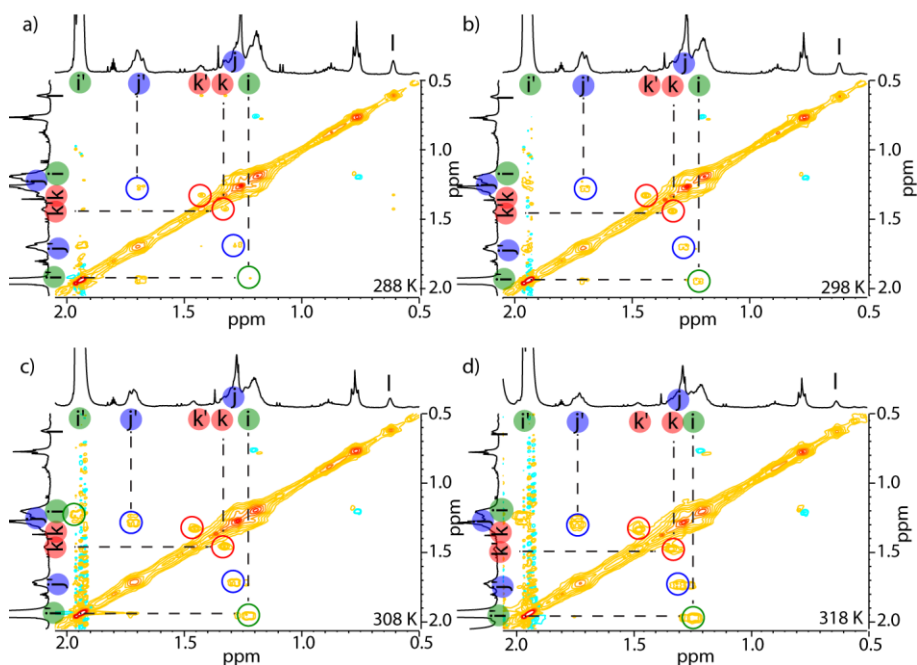
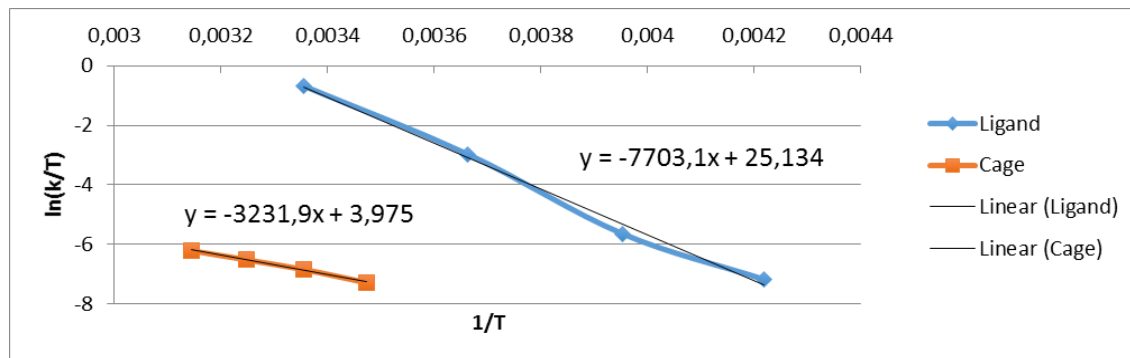


Figure 7.127 ^1H - ^1H NOESY spectra of cage $[\text{Pd}_2\text{L}^2_4]$ (500 MHz, CD_3CN , 0.5 s mixing time) at different temperatures: a) 288 K, b) 298 K, c) 308 K and d) 318 K. The intensities of the highlighted exchange signals between inward (i' , j' and k') and outward (i , j , k) pointing protons are increasing with rising temperature.

Integration of the signals yielded the exchange or “flipping rate” of the adamantyl groups within the cage at different temperatures:

T/K	k/s ⁻¹
288	0.20
298	0.32
308	0.46
318	0.64

Eyring plot analysis for the flipping processes observed for ligand **L²** and cage [Pd₂L₂⁴]:



Activation Parameters (298 K):

	Ligand	Cage
ΔH^\ddagger (kJ·mol ⁻¹)	64.0	26.9
ΔS^\ddagger (J·K ⁻¹ ·mol ⁻¹)	11.4	-164.5
ΔG^\ddagger (kJ·mol ⁻¹)	60.6	75.9

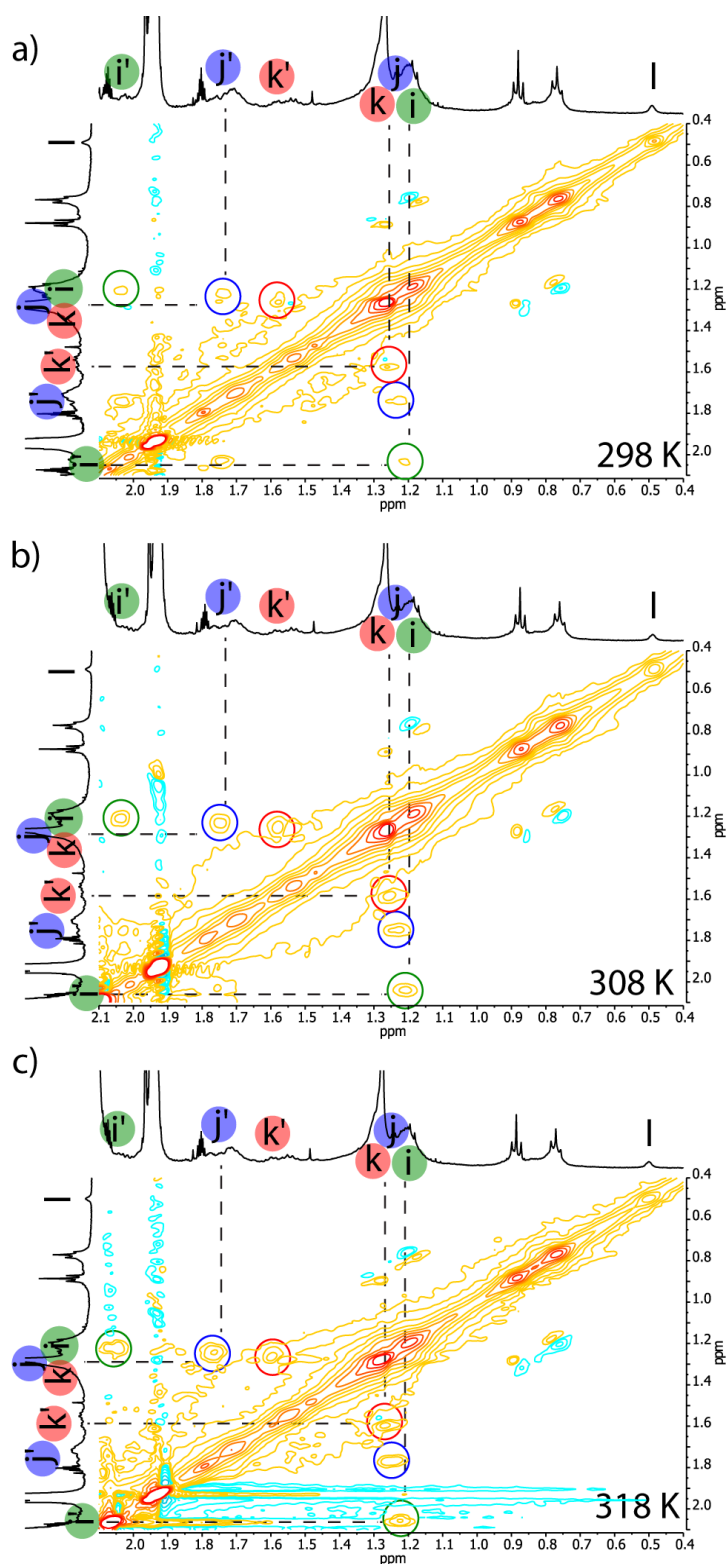
7.5.4.3 NOESY Measurements of [Pt₂L₄]

Figure 7.128 ^1H - ^1H NOESY spectra of cage [Pt₂L₂₄] (500 MHz, CD₃CN, 0.5 s mixing time) at different temperatures: a) 298 K, b) 308 K, and c) 318 K. The intensities of the highlighted exchange signals between inward (i', j' and k') and outward (i, j, k) pointing protons are increasing with rising temperature. The rate constants could be determined through integration: 298 K: $k = 0.13 \text{ s}^{-1}$, 308 K: $k = 0.22 \text{ s}^{-1}$ and 318 K: $k = 0.35 \text{ s}^{-1}$.

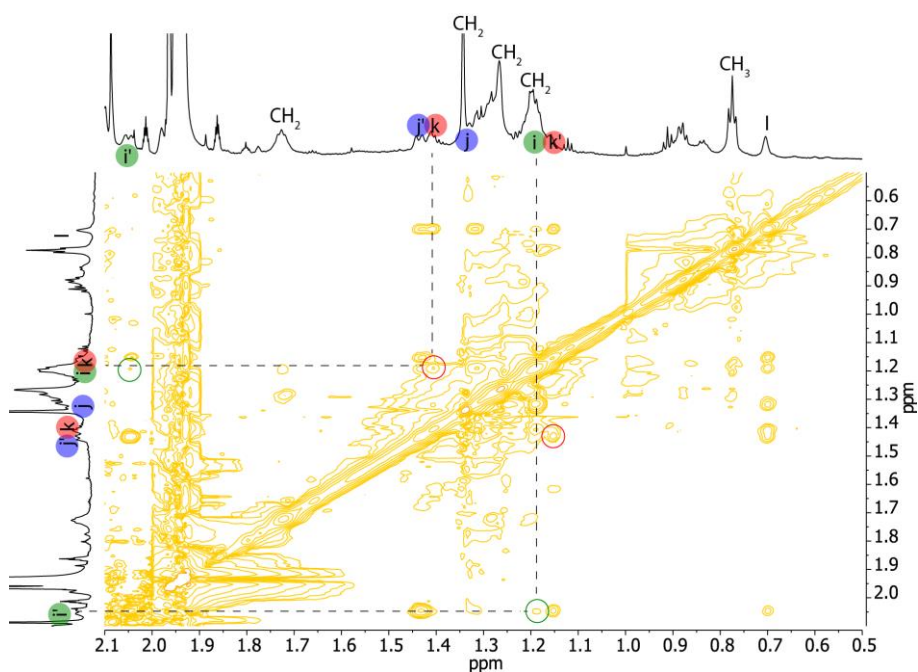
7.5.4.4 NOESY Measurements of $[G^1@Pd_2L^2_4]$ 

Figure 7.129 ^1H - ^1H NOESY spectrum of host-guest compound $[G^1@Pd_2L^2_4]$ (900 MHz, 298 K, CD_3CN , 0.5 s mixing time). The exchange signals between inside and outside pointing protons are highlighted: green = i/i' (2.05 ppm/1.19 ppm) and red = k/k' (1.42 ppm/1.17 ppm). Integration gave the exchange rate as: $k < 0.03\text{ s}^{-1}$. The exchange signals between j/j' (1.44 ppm/1.32 ppm) overlap with the diagonal baseline.

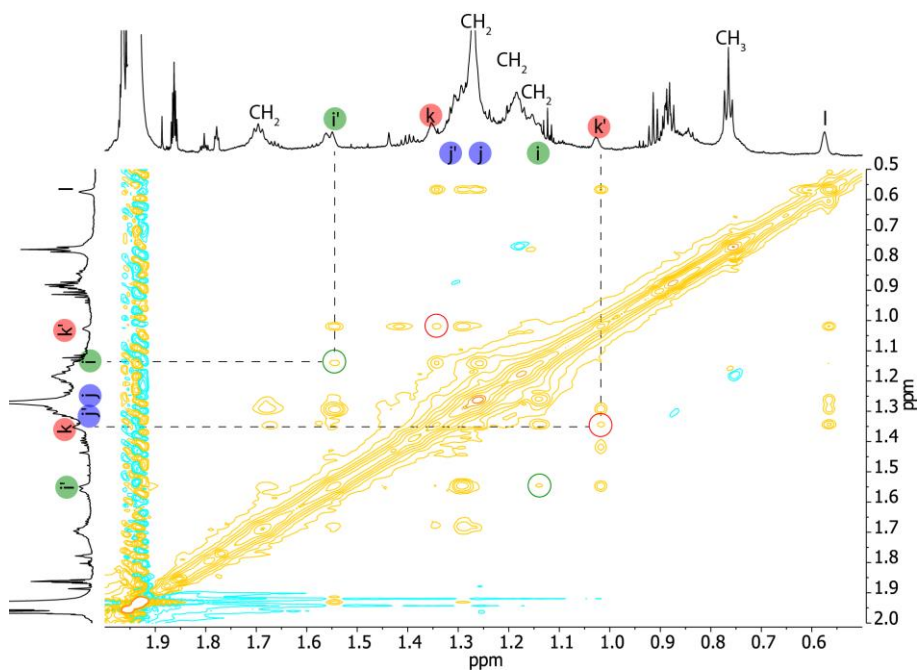
7.5.4.5 NOESY Measurements of $[G^2@Pd_2L^2_4]$ 

Figure 7.130 ^1H - ^1H NOESY spectrum of host-guest compound $[G^2@Pd_2L^2_4]$ (900 MHz, 298 K, CD_3CN , 0.5 s mixing time). Exchange signals between inside and outside pointing protons are highlighted: green = i/i' (1.54 ppm/1.14 ppm) and red = k/k' (1.35 ppm/1.02 ppm). Integration gave the exchange rate as: $k < 0.02\text{ s}^{-1}$. The exchange signals between j/j' (1.33 ppm/1.25 ppm) are hidden in the diagonal base line.

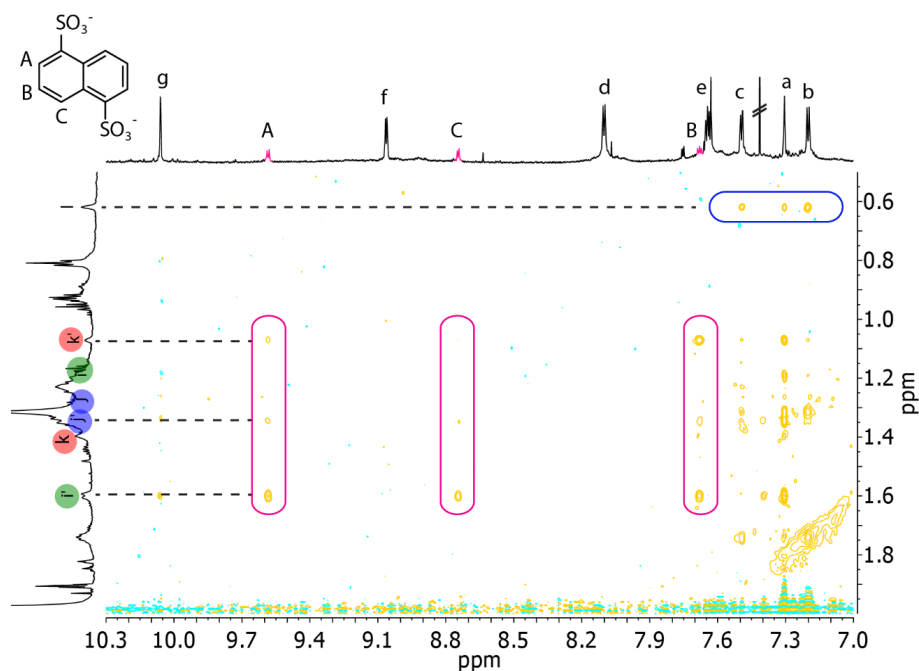


Figure 7.131 ^1H - ^1H NOESY spectrum of host-guest compound $[\text{G}^2@Pd_2\text{L}^2_4]$ (900 MHz, 298 K, CD_3CN). Highlighted are NOE contacts between guest G^2 and inside pointing adamantyl protons i' , j' and k' (pink) and intramolecular contacts between the ligands (blue).

7.5.4.6 EXSY Measurements

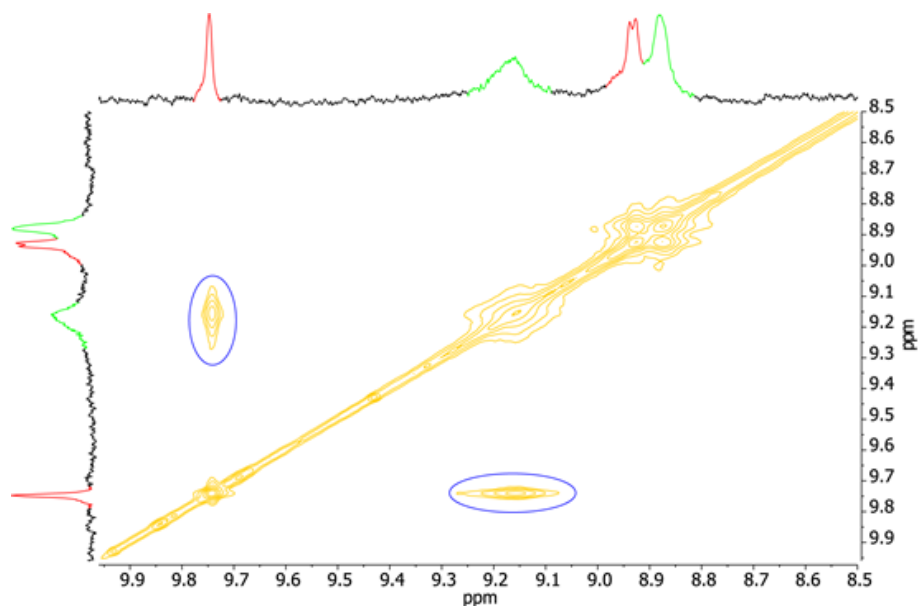


Figure 7.132 ^1H - ^1H EXSY spectrum (500 MHz, 298 K, CD_3CN , 0.1 s mixing period) of a 1:1 mixture of cage $[\text{Pd}_2\text{L}^2_4]$ (green) and host-guest compound $[\text{G}^1@Pd_2\text{L}^2_4]$ (red). Exchange is observed between the empty cage and the host-guest complex (highlighted in blue). The rate constant could be determined *via* integration to $k_{in} = k_{out} \sim 7 \text{ s}^{-1}$ (due to signal broadening this value has an error of $\sim 20\%$).

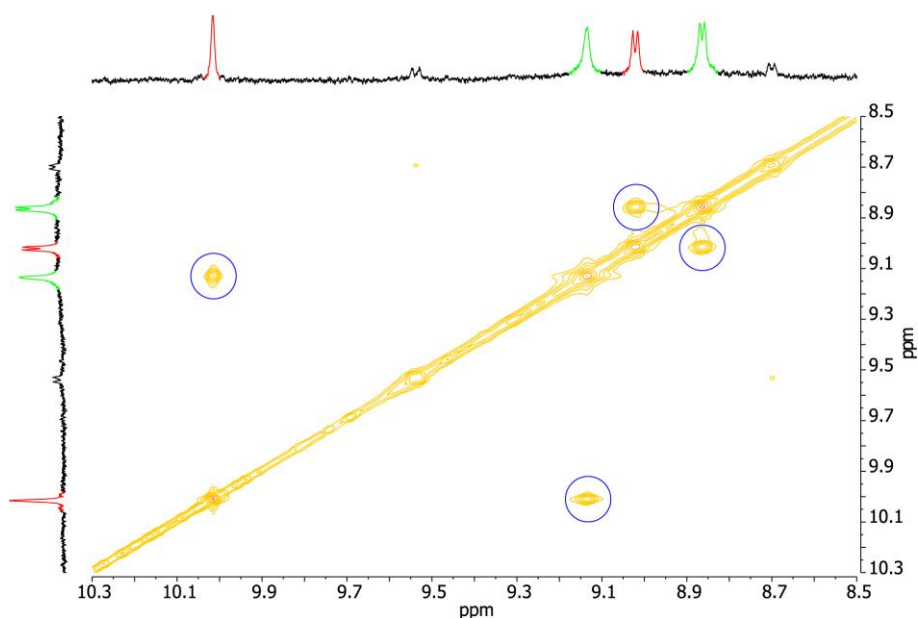


Figure 7.133 ^1H - ^1H EXSY spectrum (500 MHz, 298 K, CD_3CN , 0.1 s mixing period) of a 1:1 mixture of cage $[\text{Pd}_2\text{L}^2_4]$ (green) and host-guest compound $[\text{G}^2@\text{Pd}_2\text{L}^2_4]$ (red). Exchange is observed between the empty cage and the host-guest complex (highlighted in blue). The rate constant could be determined *via* integration to $k_{\text{in}} = k_{\text{out}} \sim 4 \text{ s}^{-1}$.

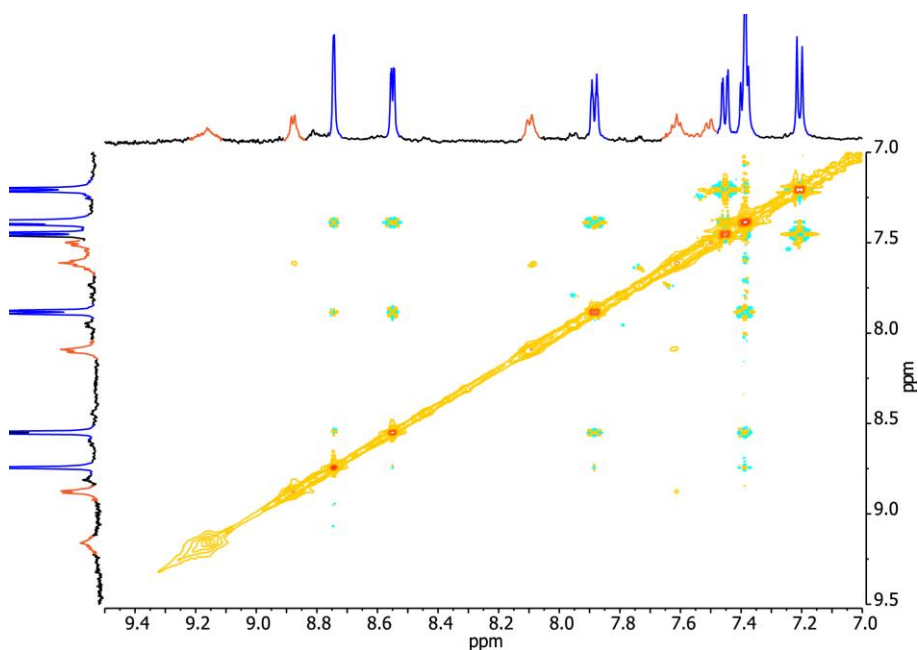


Figure 7.134 ^1H - ^1H EXSY spectrum (500 MHz, 298 K, CD_3CN , 0.1 s mixing period) of a 3:1 mixture of ligand L^2 (blue) and cage $[\text{Pd}_2\text{L}^2_4]$ (orange) at room temperature, illustrating that there is no exchange between free ligand and the cage within the mixing time.

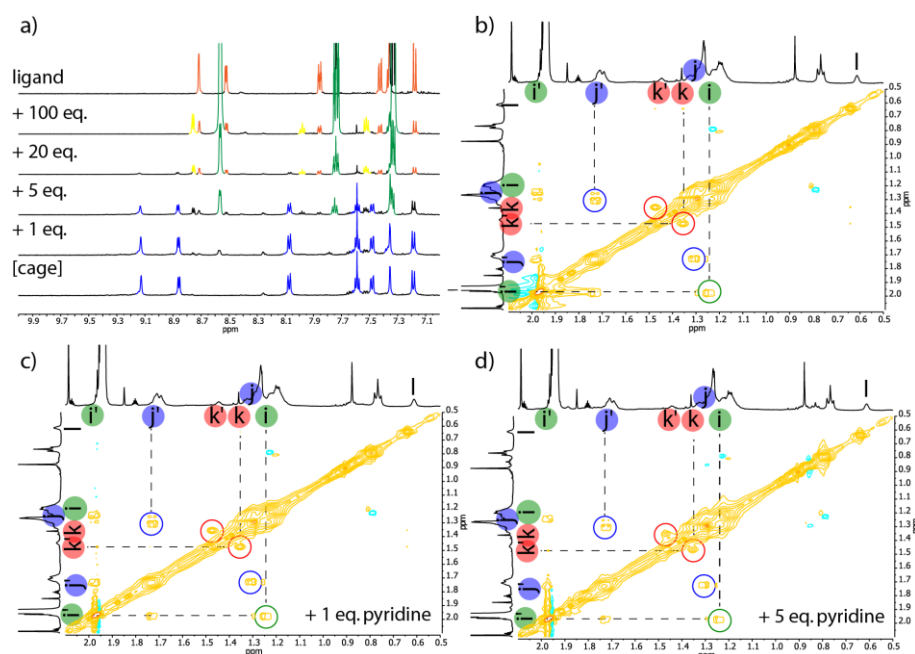
7.5.4.7 Addition of Pyridine to $[\text{Pd}_2\text{L}^2_4]$ 

Figure 7.135 a) ^1H NMR titration (500 MHz, 298 K, CD_3CN) with 1 eq., 5 eq., 20 eq. and 100 eq. of pyridine to the $[\text{Pd}_2\text{L}^2_4]$ cage. After the addition of 20 eq. of pyridine the cage is disassembled to free ligand and $\text{Pd}(\text{pyridine})_4$. Color code = blue: $[\text{Pd}_2\text{L}^2_4]$, green: free pyridine, orange: free ligand L^2 , yellow: $\text{Pd}(\text{pyridine})_4$. b–d) ^1H - ^1H NOESY spectra (500 MHz, 298 K, CD_3CN , 0.5 s mixing period) of the $[\text{Pd}_2\text{L}^2_4]$ cage (b), with 1 eq. (c), or 5 eq. pyridine (d). The intensity of the highlighted exchange signals between inward (i', j' and k') and outward (i, j, k) pointing protons do not change with increasing pyridine concentration, indicating pyridine is not acting as a competitive ligand and has no influence on the exchange rate of the adamantyl group. The exchange rate could be determined as $k = 0.32 \text{ s}^{-1}$ for $[\text{Pd}_2\text{L}^2_4]$, and 0.25 s^{-1} for $[\text{Pd}_2\text{L}^2_4] + 1 \text{ eq. pyridine}$ and $[\text{Pd}_2\text{L}^2_4] + 5.0 \text{ eq. pyridine}$.

7.5.5 X-ray Data

Single-crystal X-ray measurements, data processing, structure solution and refinement was conducted by *PD Dr. B. Dittrich* and coworker. Crystals suitable for X-ray structural analysis were mounted at room temperature in Paratone N inert oil. Single crystal X-ray diffraction data were collected at the Swiss Light Source at beamline PXII. The data were integrated with XDS^[141] and converted with the utility program xds2sad by *G. M. Sheldrick*. An empirical absorption correction with SADABS^[150] was applied and the structures were solved by direct methods.^[151] The structure models were refined against all data by full-matrix least-squares methods on F^2 with the program shelxl2014.^[143] Non-hydrogen-atoms (with the exception of a disordered ligand on an inversion center in structure $[\text{G}^5@[\text{Pd}_2\text{L}^2_4]]$ and several atoms in highly disordered hexyl groups) were refined with anisotropic displacement parameters. The hydrogen atoms were refined isotropically on calculated positions using a riding model with U_{iso} values constrained to 1.2/1.5 U_{eq} of their parent atoms. The SQUEEZE method provided by the program Platon was used to improve the contrast of the electron density map of the structures $[\text{Pd}_2\text{L}^2_4]$, $[\text{G}^4@[\text{Pd}_2\text{L}^2_4]]$ and $[\text{G}^5@[\text{Pd}_2\text{L}^2_4]]$.

Table 7.5 Crystal data and structure refinement.

Structure	[G ¹ @Pd ₂ L ₂ ² ₄]	[Pd ₂ L ₂ ² ₄]	[G ⁴ @Pd ₂ L ₂ ² ₄]	[G ⁵ @Pd ₂ L ₂ ² ₄]
CCDC number	1053082	1053083	1053081	1053080
Empirical formula	C ₁₉₂ H ₁₇₇ Fe ₂ N ₁₂ O ₁₅ Pd ₂ S ₄	C ₁₇₂ H ₁₆₄ B ₄ F ₁₆ N ₁₂ Pd ₂	C ₁₈₅ H ₁₇₃ B ₂ F ₈ N ₁₄ O ₆ Pd ₂ S ₂	C ₁₇₇ H ₁₅₃ B ₂ F ₈ N ₁₂ O ₈ Pd ₂ S ₂
Formula weight	3345.19 g mol ⁻¹	2959.18 g mol ⁻¹	3138.90 g mol ⁻¹	3021.04 g mol ⁻¹
Temperature	100(2) K	100(2) K	100(2) K	100(2) K
Wavelength	1.000 Å	1.000 Å	0.97896 Å	0.97896 Å
Crystal system	Triclinic	Triclinic	Triclinic	Triclinic
Space group	<i>P</i> $\bar{1}$	<i>P</i> $\bar{1}$	<i>P</i> $\bar{1}$	<i>P</i> $\bar{1}$
Unit cell dimensions	<i>a</i> = 18.000(4) Å <i>b</i> = 24.665(5) Å <i>c</i> = 25.221(5) Å α = 109.16° β = 97.62° γ = 100.30°	<i>a</i> = 16.196(3) Å <i>b</i> = 16.375(3) Å <i>c</i> = 17.065(3) Å α = 74.20° β = 62.65° γ = 71.79°	<i>a</i> = 15.190(3) Å <i>b</i> = 18.168(4) Å <i>c</i> = 18.770(4) Å α = 64.90° β = 79.12° γ = 76.17°	<i>a</i> = 19.202(4) Å <i>b</i> = 20.734(4) Å <i>c</i> = 23.321(5) Å α = 93.96° β = 108.19° γ = 92.25°
Volume	10184(4) Å ³	3774.0(18) Å ³	4532(2) Å ³	9090(4) Å ³
Z	2	1	1	2
Density (calculated)	1.091 Mg/m ³	1.302 Mg/m ³	1.150 Mg/m ³	1.104 Mg/m ³
Absorption coefficient	1.018 mm ⁻¹	0.766 mm ⁻¹	0.657 mm ⁻¹	0.652 mm ⁻¹
F(000)	3482	1536	1635	3133
Crystal size	0.011 x 0.011 x 0.005 mm ³	0.010 x 0.010 x 0.005 mm ³	0.011 x 0.011 x 0.005 mm ³	0.011 x 0.011 x 0.005 mm ³
Theta range for data collection	1.229 to 27.136°	1.864 to 27.274°	1.658 to 29.356°	1.221 to 24.196°
Index range	-14 ≤ <i>h</i> ≤ 13, - 21 ≤ <i>k</i> ≤ 21, - 22 ≤ <i>l</i> ≤ 22	-14 ≤ <i>h</i> ≤ 13, - 13 ≤ <i>k</i> ≤ 13, - 14 ≤ <i>l</i> ≤ 14	-14 ≤ <i>h</i> ≤ 14, - 18 ≤ <i>k</i> ≤ 18, - 18 ≤ <i>l</i> ≤ 18	-15 ≤ <i>h</i> ≤ 15, - 17 ≤ <i>k</i> ≤ 76, - 18 ≤ <i>l</i> ≤ 17
Reflections collected	44258	14035	36786	32793
Independent reflections	13349 [R(int) = 0.0927]	4035 [R(int) = 0.1575]	8052 [R(int) = 0.0908]	9379 [R(int) = 0.0483]
Completeness to theta	82.2 % [27.163°]	67.1 % [27.274°]	84.4 % [29.356°]	83.9 % [24.196°]
Refinement method	Full-matrix least-squares on F ²	Full-matrix least-squares on F ²	Full-matrix least-squares on F ²	Full-matrix least-squares on F ²
Data / restraints / parameters	13349 / 5905 / 2050	4082 / 1894 / 928	8052 / 3335 / 1389	9379 / 5839 / 1906

Goodness-of-fit on F2	1.162	1.280	1.086	1.388
Final R indices [I>2sigma(I)]	R1 = 0.1178 wR2 = 0.2941	R1 = 0.1421 wR2 = 0.3421	R1 = 0.0798 wR2 = 0.2269	R1 = 0.1071 wR2 = 0.3096
R indices (all data)	R1 = 0.1380 wR2 = 0.3132	R1 = 0.1830 wR2 = 0.3767	R1 = 0.0947 wR2 = 0.2374	R1 = 0.1254 wR2 = 0.3285
Largest diff. peak and hole	1.632 and -0.532 e.Å ⁻³	0.996 and -0.485 e.Å ⁻³	0.576 and -0.517 e.Å ⁻³	0.677 and -0.431 e.Å ⁻³

Further X-ray views:

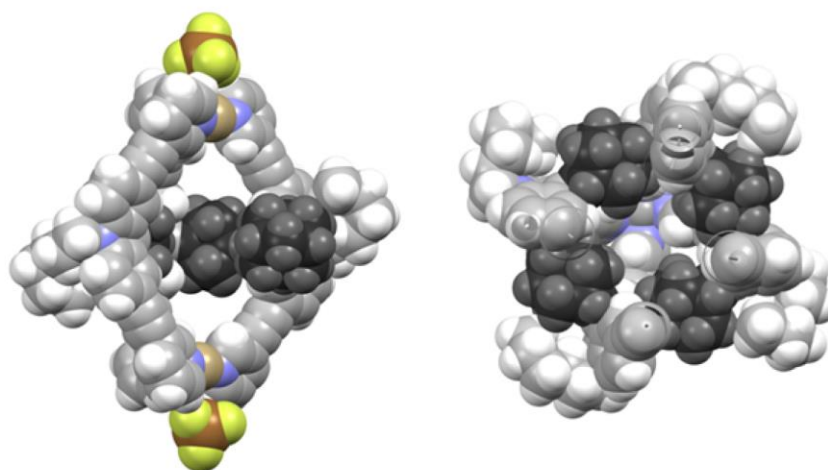


Figure 7.136 Partially clipped space-filling representations of $[\text{Pd}_2\text{L}_{24}]$ from the side (left; one ligand removed) and the top (right). The adamantyl groups are highlighted in dark grey and the internal counter anions have been removed.

7.5.6 Hirshfeld Surface Analysis

A Hirshfeld surface analysis was performed for the host-guest complexes $[\mathbf{G}^1@Pd_2L_2^4]$ and $[\mathbf{G}^5@Pd_2L_2^4]$ using the software Crystal Explorer 3.1.^[134] Since a few disordered solvent molecules could not be refined in the X-ray structures and the corresponding areas of residual electron density were treated by the SQUEEZE method (see above), small parts of the calculated Hirshfeld surfaces ‘bleed’ into void spaces that appear to be empty but should be filled by solvent. Nevertheless, we anticipate that the errors in the interpretations of the Hirshfeld surfaces caused by this effect are negligible since the guest molecules’ surroundings are by far dominated by the closely packed cage structure.

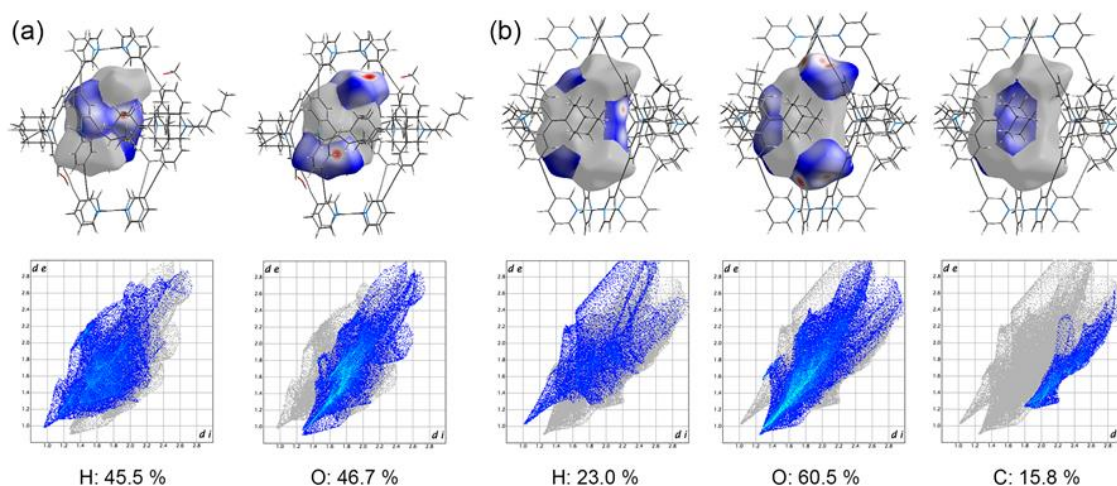


Figure 7.137 Element-mapped Hirshfeld surfaces and fingerprints of (a) $[\mathbf{G}^1@Pd_2L_2^4]$ and (b) $[\mathbf{G}^5@Pd_2L_2^4]$.

7.5.7 Computational Details (provided by Prof. Mata and Coworkers)

7.5.7.1 Ligand Flipping

The flipping barrier for the free ligand was computed by optimizing a connected reaction path from one orientation towards its reflection at the BP86-D3/def2-SVP (BJ damping) level of theory.^{[99,152,153,172][155]} The computations show that the flipping occurs by traversing an extremely shallow plateau, built from two symmetric transition states. Due to the flatness of the potential energy surface in this region, we were unable to localize a minimum in between. Hence, the structure of the transition state depicted in Figure 4.9 is not as highly symmetric as one might expect. Nevertheless, the barrier should be defined by the energy difference between the found transition states and the starting structure. Free energies were computed for 298.15 K at the B3LYP-D3/def2-TZVP (BJ damping) level of theory^{[155][133]}, including solvent corrections through the COSMO model (for acetonitrile).^[173] The value obtained was $56.6 \text{ kJ}\cdot\text{mol}^{-1}$, in close agreement with the NMR derived flipping rate constant. All calculations were carried out with the ORCA 3.0 program package.^[174]

7.5.7.2 Guest Binding

In order to obtain further insight into the binding of the guest molecules, in particular the role of dispersion forces, electronic structure calculations were carried out for $[\text{Pd}_2\text{L}^2_4]$, $[\text{G}^4@\text{Pd}_2\text{L}^2_4]$ and $[\text{G}^5@\text{Pd}_2\text{L}^2_4]$. Due to the large size of these system, the calculations involving the binding pocket were limited to the four adamantane moieties (with the covalent double bond to the ligand backbone cut and capped with two hydrogen atoms). The adamantane fragments and guest compounds were optimized at the B3LYP-D3/def2-TZVP level of theory (with Becke-Johnson type damping), and then overlapped with the crystal structure positions. These should correspond to a suitable average conformation of the ligands and guest molecules. Also, given the small space available in the pocket, dynamic fluctuations in the structure should not affect our results severely. On the basis of the structures obtained, spin-component-scaled local second-order Møller-Plesset perturbation theory SCS-LMP2^{[96][95]} calculations were performed, together with the aug'-cc-pVTZ basis set (diffuse functions on all atoms, except hydrogens).^[97,135] Density fitting approximations were used throughout, with the default fitting basis for aug-cc-pVTZ. The latter calculations were used to investigate the interaction between the guests and the adamantane moieties. The reasons behind the choice of SCS-LMP2 are manifold. The use of local correlation reduces basis set superposition effects, which are quite significant in such host-guest binding studies. Through the use of SCS, the known overestimation of dispersion forces in MP2 theory is avoided. Finally, local correlation allows for an intuitive and direct separation of the different components of the correlation energy,^[166] including dispersion, which is expected to play a major role in the stabilization of these systems. All interaction energies are solely electronic. The total energies are given according to the supermolecular (not 'supramolecular') approach, with fixed host and guest structures. The dispersion energies were obtained through the decomposition of the scaled LMP2 pair energies. Calculations in the system $[\text{Pd}_2\text{L}^2_4]$ were primarily intended to estimate the stabilization of the cage brought forth by dispersion interactions between the adamantane moieties in the pocket. This system was chosen since it contains the smallest guest (BF_4^-), allowing for the adamantane moieties to come closest. In the calculations of the host-guest complexes, only the interactions of the guests with the adamantanes were considered, disregarding the interaction with the remaining parts of the ligands and the Pd ions. The latter would be particularly difficult to estimate given that the electrostatics will be strongly influenced by the solvent model used. The remaining parts of the ligands should have no strong interaction with the guests considered. All local correlation calculations were carried out with the Molpro2012.1 program package.^[136]

7.5.7.3 Dispersion Interaction Density plots

In order to obtain a visual description of dispersion forces, a decomposition of the SCS-LMP2 pair energies has been carried out. The energy terms associated with a double excitation $i \rightarrow a$ and $j \rightarrow b$, with i/a being occupied/virtual orbitals located in monomer A, j/b occupied/virtual orbitals in monomer B, were summed together into $\epsilon^d_{(ij)}$ dispersion energy contributions. These are used to compute the dispersion interaction density matrix D for an arbitrary monomer A as:

$$D_{\mu\nu}^A = \sum_{i \in A} \left(\sum_B \sum_{j \in B} \varepsilon_{(ij)}^d \right) P_{\mu\nu}^i$$

Whereby P^i is the density matrix for the occupied orbital i . A numerical grid can then be generated and the DID value at a given point in space computed as

$$T(r) = \sum_{\mu\nu} D_{\mu\nu}^A \chi_{\mu}(r) \chi_{\nu}(r)$$

In the end, one obtains a tensor in cartesian space, with a value proportional to the dispersion interaction of each orbital and its density.

7.5.7.4 Cavity volume of [Pd₂L₂]₄ by VOIDOO

The crystallographically determined structure of [Pd₂L₂]₄⁴⁺ were symmetry expanded and the encapsulated tetrafluoroborate guest molecules in the central cavities of the cage structures were removed. The resulting cavity was calculated with VOIDOO,^[92] using a primary grid and plot grid spacing of 0.1 Å and 20 cycles of volume refinement with the water size probe radius of 2.0 Å. Molecular visualization were done using PyMol.^[130]

7.6 Part D – Influence of Ligand Length on Cage Formation

7.6.1 Overview of Ligands

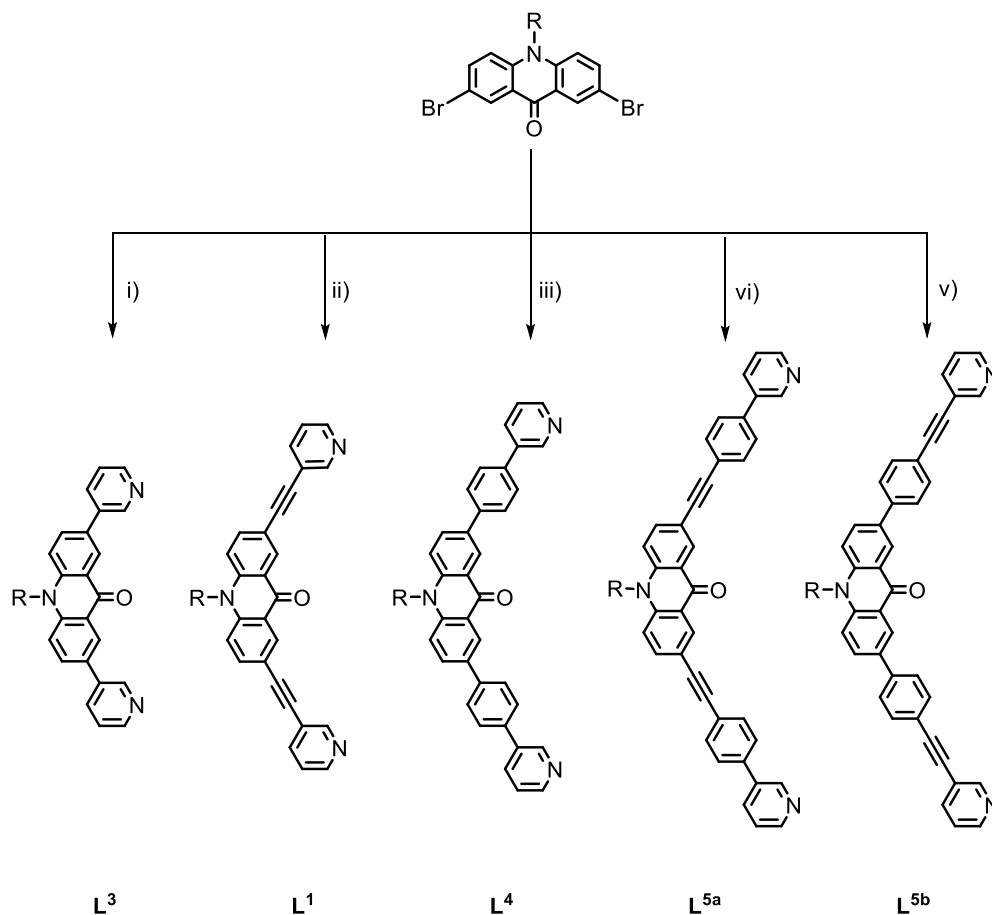
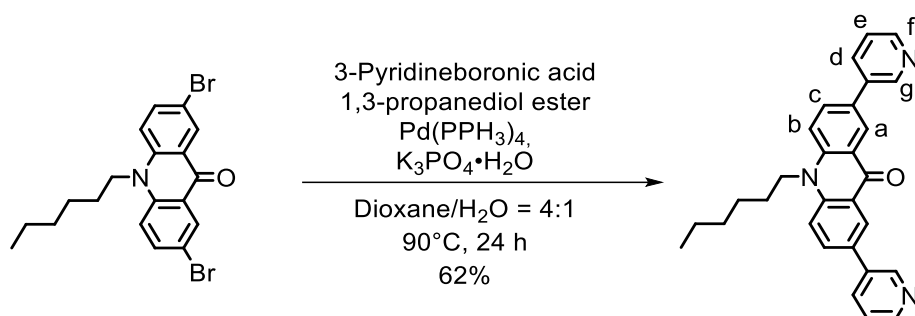


Figure 7.138 Schematic synthetic route leading to acridone based ligands **L¹**, **L³**, **L⁴**, **L^{5a}** and **L^{5b}**. i) 3-pyridineboronic acid 1,3-propanediol ester, K₃PO₄·H₂O, Pd(PPh₃)₄, dioxane/H₂O; ii) 3-ethynylpyridine, CuI, [Pd(PPh₃)₂Cl₂], NEt₃; iii) 3-(4-pinacolboronic acid-phenyl)pyridine, K₃PO₄·H₂O, Pd(PPh₃)₄, dioxane/H₂O; iv) 3-((4-ethynyl)phenyl)pyridine, CuI, [Pd(PPh₃)₂Cl₂], NEt₃; v) 3-((4-phenylboronic acid pinacol ester)ethynyl)pyridine, K₃PO₄·H₂O, Pd(PPh₃)₄, dioxane/H₂O.

7.6.2 Ligand L³ and Coordination Cage [Pd₂L³]₄7.6.2.1 Synthesis of Ligand L³

3-Pyridineboronic acid 1,3-propanediol ester (187 mg, 1.15 mmol, 2.00 eq.), 2,7-dibromo-10-hexylacridin-9(10*H*)-one (252 mg, 0.58 mmol, 1.00 eq.), and K₃PO₄·H₂O (3.78 g, 16.4 mmol, 28.60 eq.) were suspended in a mixture of 1,4-dioxane/H₂O (4:1, 10 mL). This mixture was degassed using the *Freeze-Pump-Thaw*-method. Pd(PPh₃)₄ (40.1 mg, 0.035 mmol, 0.06 eq.) was added and it was stirred for 24 h at 90 °C. After cooling down to room temperature, dichloromethane (100 mL) was added and the organic phase was washed with water (3 x 20 mL), dried over MgSO₄ and the solvent was removed under reduced pressure. The crude product was purified by column chromatography (petroleum ether : ethyl acetate = 1:1; → CHCl₃:MeOH = 25:1) to give the product as a yellow solid (172 mg, 0.36 mmol, 62%).

¹H NMR (500 MHz, CDCl₃, 298 K): δ (ppm) = 9.00 (dd, ⁴J = 1.4 Hz, ⁵J = 0.5 Hz, 2H, g-H), 8.86 (d, ³J = 2.4 Hz, 2H, a-H), 8.64 (d, ³J = 4.7 Hz, ⁴J = 1.4 Hz, 2H, f-H), 8.11 (dt, ³J = 8.0 Hz, ⁴J = 1.9 Hz, 2H, c-H), 8.04 (dd, ³J = 9.0 Hz, 2H, d-H), 7.68 (d, ⁴J = 8.8 Hz, 2H, b-H), 7.40–7.43 (m, 2H, e-H), 4.45 (t, ³J = 5.0 Hz, 2H, NCH₂), 2.00 (qi, ³J = 3.6 Hz, 2H, CH₂), 1.63 (qi, ³J = 1.5 Hz, 2H, CH₂), 1.54–1.37 (m, 4H, CH₂-CH₂), 0.97 (t, ³J = 4.2 Hz, 3H, CH₃).

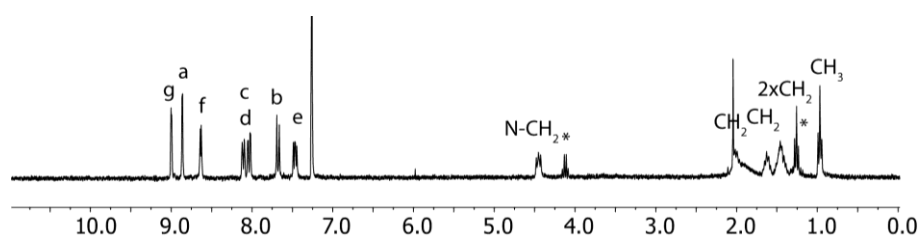


Figure 7.139 ¹H NMR spectrum of ligand L³ (500 MHz, 298 K, CDCl₃).

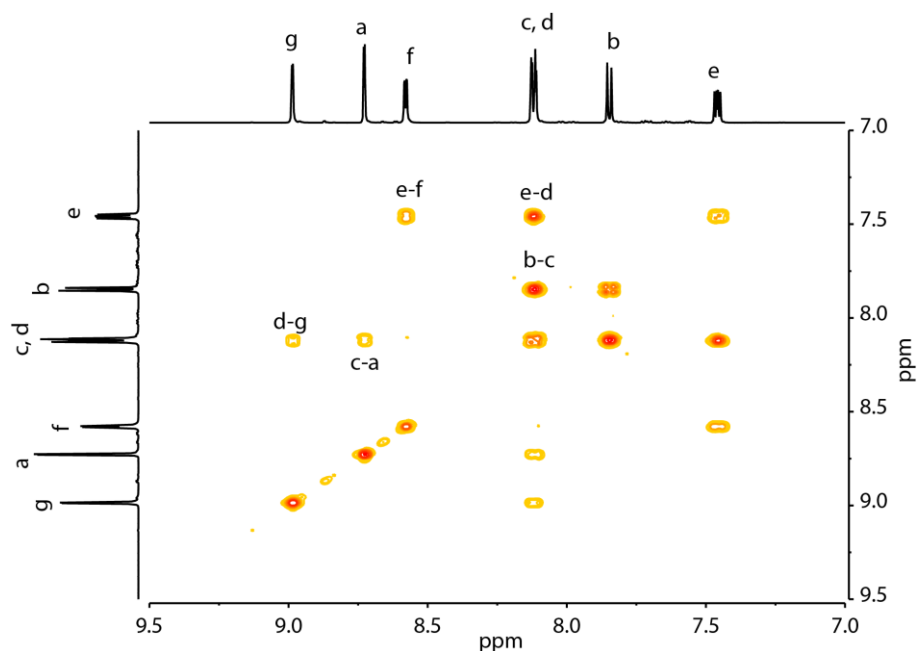


Figure 7.140 ^1H - ^1H COSY spectrum of ligand L^3 (600 MHz, CD_3CN , 298 K). Cross Peaks are highlighted.

^{13}C -NMR (125 MHz, CD_3CN , 298 K): δ (ppm) = 177.96, 149.37, 148.74, 142.56, 135.93, 135.02, 133.46, 131.49, 125.94, 124.78, 123.54, 117.83, 47.14, 32.27, 27.97, 27.01, 23.36, 14.30.

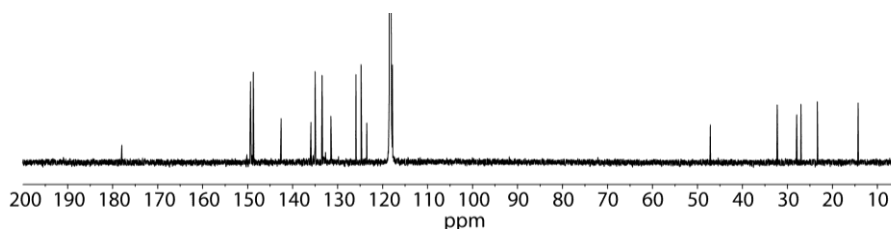
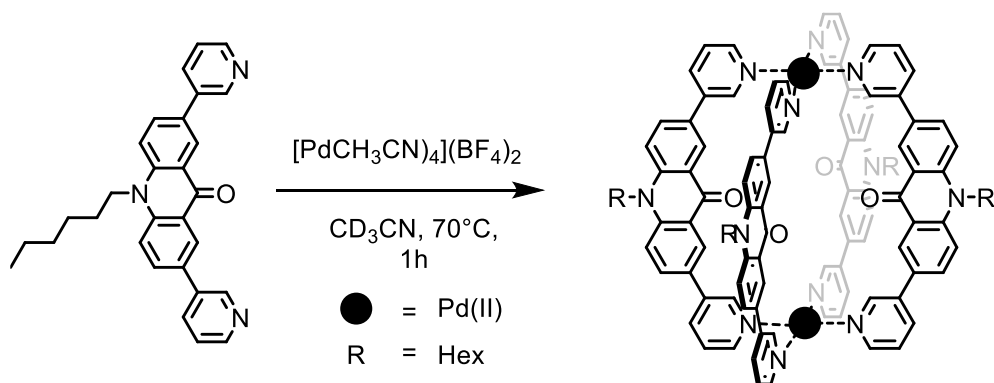


Figure 7.141 ^{13}C NMR spectrum of ligand L^3 (125 MHz, 298 K, CD_3CN).

MS-ESI: m/z (%) = 456.2 (35) $[\text{M}+\text{Na}]^+$, 434.3 (100) $[\text{M}+\text{H}]^+$, 251.2 (60) $[\text{C}_{17}\text{H}_{17}\text{NO}]^+$, 157.1 $[\text{C}_{21}\text{H}_{18}\text{N}_2\text{O}]^{2+}$.

7.6.2.2 Formation of $[\text{Pd}_2\text{L}^3_4]$



Ligand **L**³ (5.94 mg, 12.3 μmol, 1.0 eq.) in CD₃CN (4.89 mL) and [Pd(CH₃CN)₄](BF₄)₂ (489 μmol, 0.5 eq, 80.4 μL of a 15 mM solution in CD₃CN) were heated at 70 °C for 1 h to give a 0.70 mM solution of the [Pd₂L₂]₄ cage. The formation of the supramolecular complex was quantitative.

¹H NMR (500 MHz, CD₃CN, 298 K): δ (ppm) = 9.75 (d, ⁴J = 0.9 Hz, 2H, g-H), 9.20 (dd, ³J = 3.6 Hz, ⁴J = 0.6 Hz, 2H, d-H), 9.11 (d, ³J = 1.5 Hz, 2H, a-H), 8.31 (dt, ³J = 4.8 Hz, ⁴J = 1.0 Hz, 2H, f-H), 8.00 (dd, ³J = 5.4 Hz, ⁴J = 1.5 Hz, 2H, c-H), 7.78 (d, ³J = 5.4 Hz, 2H, b-H), 7.71 (dd, ³J = 4.8 Hz, ³J = 3.6 Hz, 2H, e-H), 4.36 (t, ³J = 4.8 Hz, 2H, NCH₂), 1.76 (qi, ³J = 4.7 Hz, 2H, CH₂), 1.47 (qi, ³J = 4.5 Hz, 2H, CH₂), 1.25–1.31 (m, 4H, CH₂-CH₂), 0.83 (t, ³J = 4.2 Hz, 3H, CH₃).

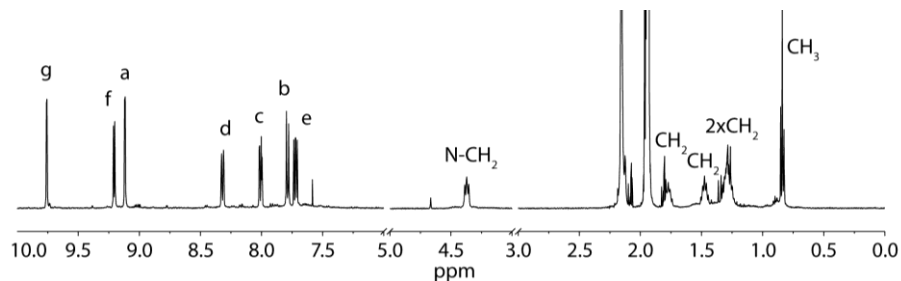


Figure 7.142 ¹H NMR spectrum of coordination cage [Pd₂L₃]₄ (500 MHz, 298 K, CD₃CN).

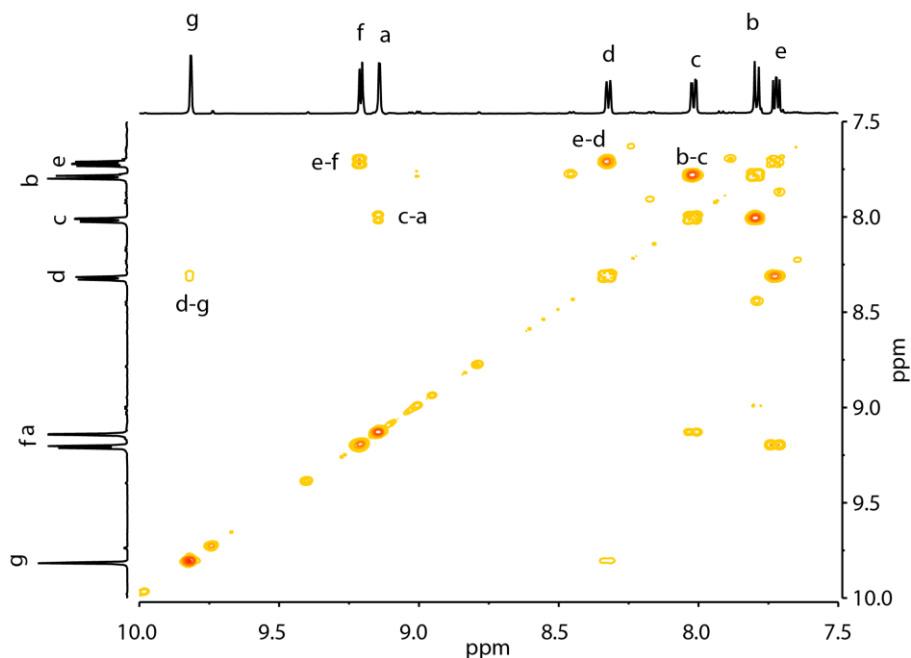


Figure 7.143 ¹H-¹H COSY spectrum of [Pd₂L₃]₄ cage (600 MHz, CD₃CN, 298 K). Cross Peaks are assigned.

¹³C NMR (125 MHz, CD₃CN, 298 K): δ (ppm) = 177.81, 149.93, 143.28, 139.74, 138.88, 133.57, 128.88, 128.38, 126.28, 123.63, 118.48, 118.26, 47.20, 32.08, 27.83, 26.80, 23.20, 14.16.

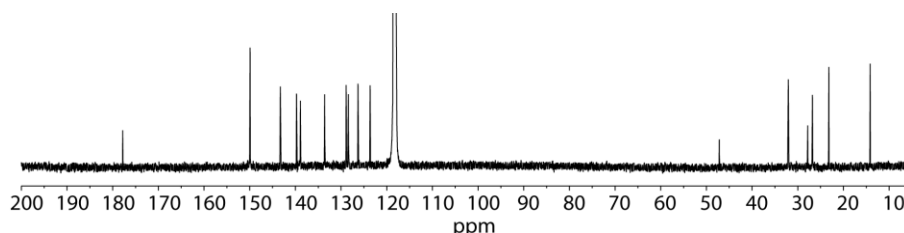


Figure 7.144 ¹³C NMR spectrum of coordination cage [Pd₂L₃]₄ (125 MHz, 298 K, CD₃CN).

MS-ESI: m/z (%) = 486.2 (100) ($[\text{Pd}_2\text{L}^3_4]^{4+}$), 677.9 (82) ($[[\text{Pd}_2\text{L}^3_4]+\text{BF}_4]^{3+}$), 1059.8 (60) ($[\text{Pd}_2\text{L}^3_4]+2\text{BF}_4]^{2+}$).

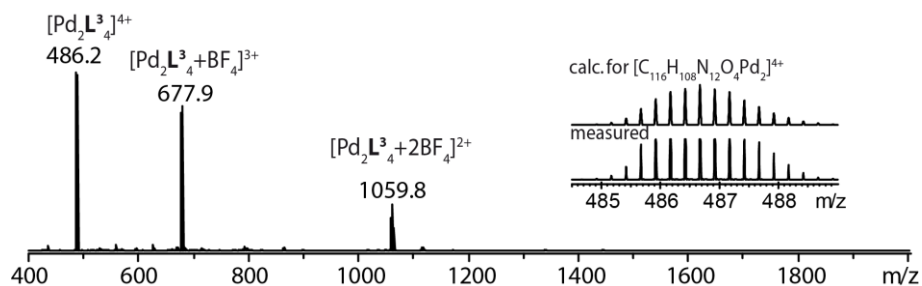


Figure 7.145 HR-MS of $[\text{Pd}_2\text{L}^3_8]$ in CD_3CN with a variable number of tetrafluoroborate counter anions. The isotopic pattern of the measured peaks match perfectly with the calculation.

7.6.2.3 Titration Experiments

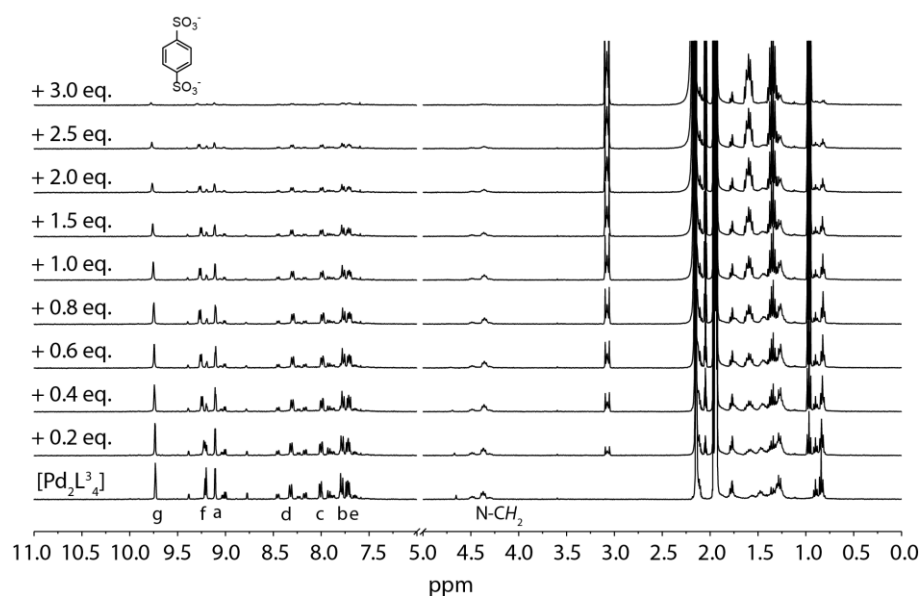


Figure 7.146 ^1H NMR titration (400 MHz, 298 K, CD_3CN) of $[\text{Pd}_2\text{L}^3_4]$ with $(\text{NBu}_4)_2\text{G}^8$. Upon addition of one equivalent of guest G^8 the $[\text{Pd}_2\text{L}^3_4]$ no significant changes could be observed in the ^1H NMR spectra, indicating no encapsulation inside the monomeric coordination cage. Excess addition of G^8 leads to disassembly of the cage.

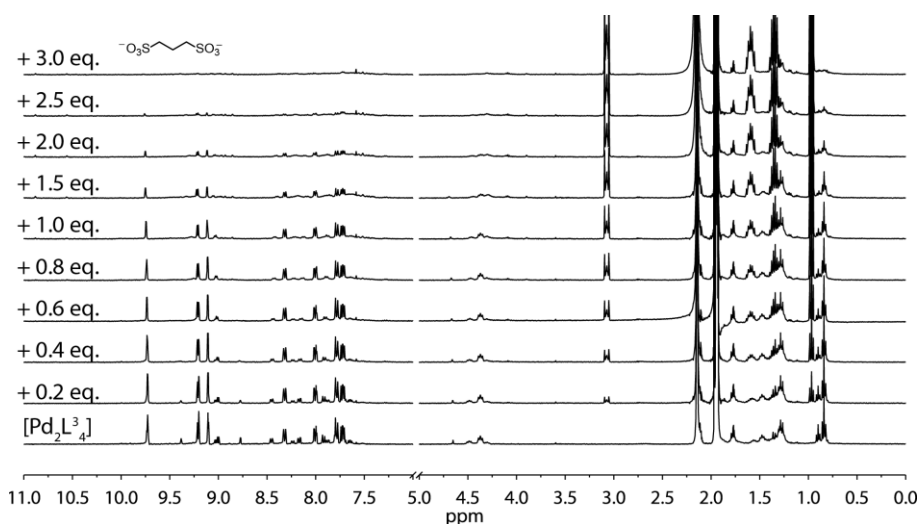
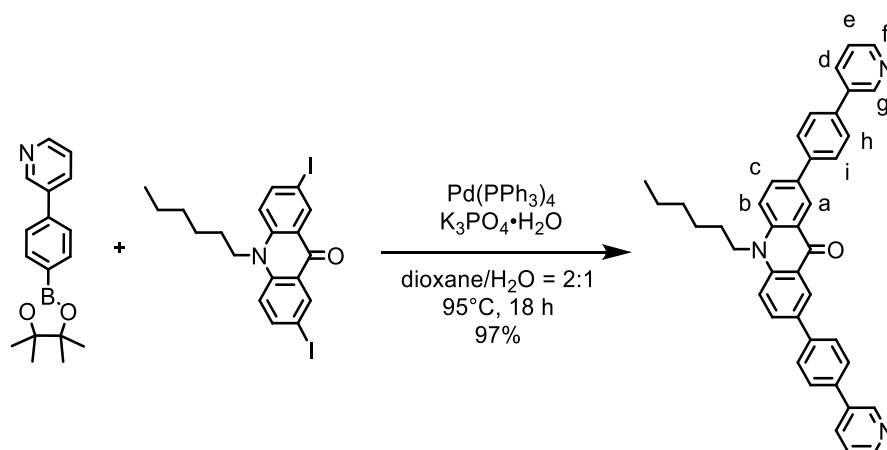


Figure 7.147 ^1H NMR titration (400 MHz, 298 K, CD_3CN) of $[\text{Pd}_2\text{L}^3_4]$ with $(\text{NBu}_4)_2\text{G}^9$. Upon addition of one equivalent of guest G^9 to the $[\text{Pd}_2\text{L}^3_4]$ no significant changes could be observed in the ^1H NMR spectra, indicating no encapsulation inside the monomeric coordination cage. Excess addition of G^9 leads to disassembly of the cage.

7.6.3 Ligand L^4 and Interpenetrated $[\text{Pd}_4\text{L}^4_8]$ cage

7.6.3.1 Synthesis of Ligand L^4



3-(4-(4,4,5,5-tetramethyl-1,3,2-dioxaborolan-2-yl)phenyl)pyridine (180 mg, 640 μmol 2.10 eq.), 10-hexyl-2,7-diiodo-10H-acridone (166 mg, 305 μmol , 1.00 eq), tetrakis(triphenylphosphine) palladium(0) (21.14 mg, 15 μmol , 0.06 eq) and potassium phosphate (250 mg, 1.09 mmol, 3.60 eq) were suspended in a mixture of dioxane (8 mL) and water (4 mL) and stirred for 42 h at 95 $^\circ\text{C}$ under nitrogen atmosphere. After heating, the solvent was removed *in vacuo* and column chromatography (SiO_2 , pentane/ethyl acetate = 1:1 \rightarrow Chloroform (0-2% Methanol)) and subsequent GPC chromatography (CHCl_3) yielded the product as a yellow solid (174 mg, 298 μmol , 97%).

^1H NMR (500 MHz, 298 K, CDCl_3): δ (ppm) = 8.96 (s, 2H, g-H), 8.92 (d, $^4J = 2.3$ Hz, 2H, a-H), 8.64 (s, 2H, g-H), 8.12–8.02 (m, 2H, c-H, d-H), 7.89 (d, $^3J = 8.3$ Hz, 2H, i-H), 7.73 (d, $^3J = 8.3$ Hz, 2H, h-H), 7.65 (d, $^3J = 9.0$ Hz, 2H, b-H), 7.50 (dd, $^3J = 7.4$ Hz, $^4J = 5.2$ Hz 2H, e-H), 4.44 (t, $^3J = 8.4$ Hz, 2H, NCH_2), 2.02 (p, $^3J = 8.6$ Hz, 2H, CH_2), 1.63 (p, $^3J = 7.4$ Hz, 2H, CH_2), 1.54–1.37 (m, 4H, 2 x CH_2), 0.97 (t, $^3J = 7.4$ Hz, CH_3).

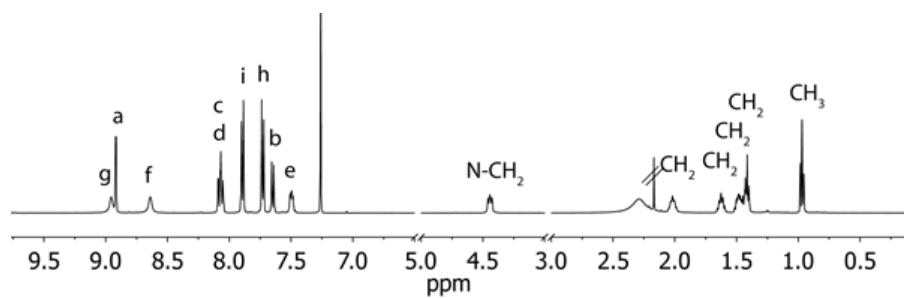


Figure 7.148 ^1H NMR spectrum of ligand L^4 (500 MHz, 298 K, CDCl_3).

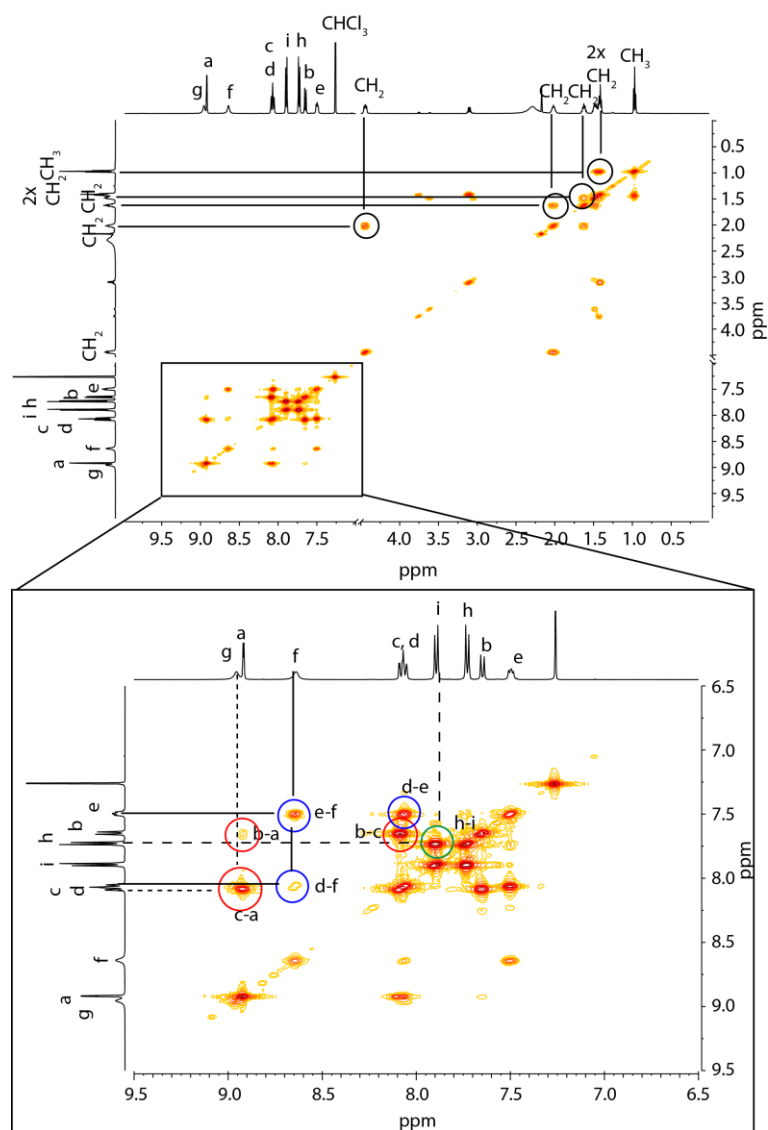


Figure 7.149 ^1H - ^1H COSY spectrum of ligand L^4 (500 MHz, 298 K, CD_3CN). Cross Peaks are indicated.

^{13}C NMR (125 MHz, 298 K, CD_3CN): δ (ppm) = 177.96, 147.04, 146.80, 141.12, 139.82, 135.98, 135.45, 136.06, 132.56, 125.83, 122.76, 115.54, 46.46, 31.54, 27.33, 26, 64, 22.67, 14.02.

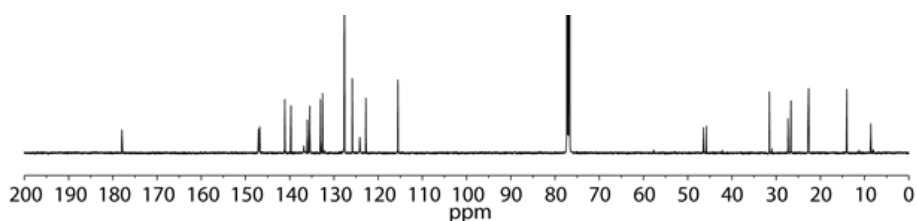
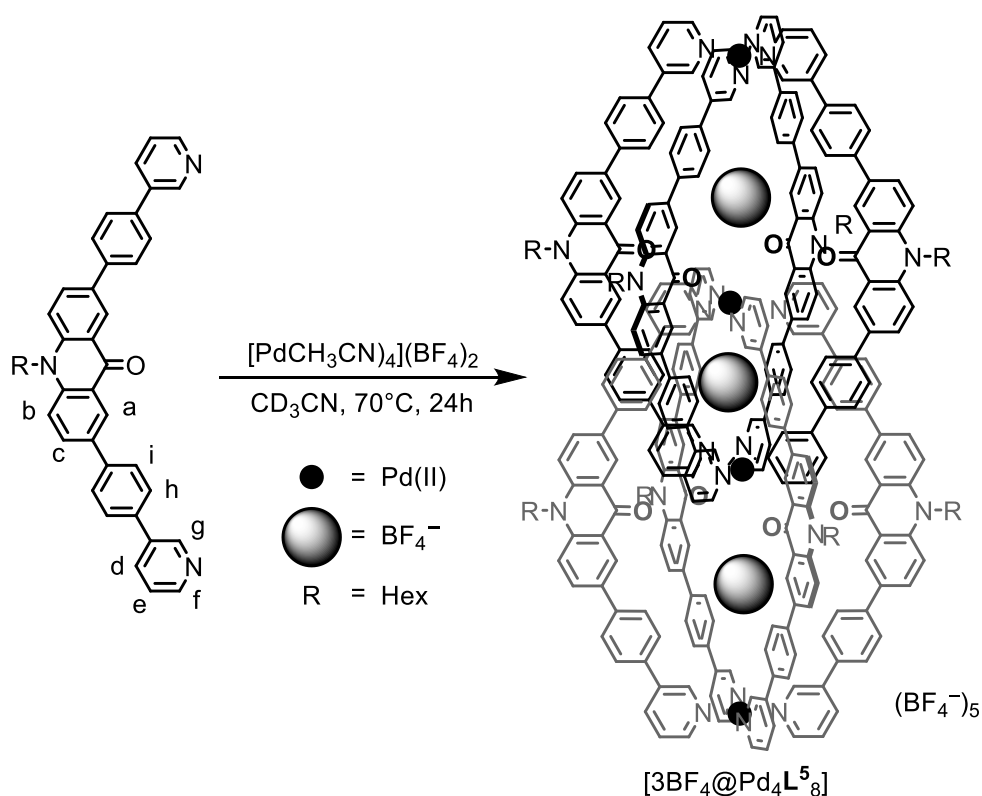


Figure 7.150 ^{13}C NMR spectrum of ligand L^4 (125 MHz, 298 K, CD_3CN).

ESI HR-MS ($\text{C}_{41}\text{H}_{36}\text{N}_3\text{O}$): 586.2842 (M^+).

IR (ATR): $\tilde{\nu}$ (cm^{-1}) = 3031, 2925, 2853, 1638, 1598, 1487, 1470, 1361, 1252, 1183, 1023, 1000, 843, 792, 750, 703, 650, 459, 403.

7.6.3.2 Formation of Interpenetrated Coordination Cage [$3\text{BF}_4@[\text{Pd}_4\text{L}^4]_8$]



To a suspension of ligand L^4 (1.65 mg, 2.8 μmol , 1.00 eq.) in CD_3CN , a solution of $\text{Pd}(\text{CH}_3\text{CN})_4(\text{BF}_4)_2$ (15 mM, 0.55 eq.) was added. The reaction mixture was heated to 70 $^\circ\text{C}$ for 24 h. The resulting supramolecular structure was formed quantitative and no further purification was necessary.

$^1\text{H-NMR}$ (400 MHz, 345 K, CD_3CN): δ (ppm) = 10.98 (s, 8H, H_g), 10.47 (s, 8H, H_g), 10.25 (d, $^3J = 6.2$ Hz, 8H, H_f), 9.40 (d, $^3J = 6.0$ Hz, 8H, H_f), 8.54 (dd, $^3J = 8.0$ Hz, $^4J = 1.2$ Hz, 8H, H_d), 8.45 (d, $^3J = 8.1$ Hz, 16H, H_h), 8.19 (d, $^3J = 8.7$ Hz, 8H, H_c), 8.07 (d, $^3J = 8.2$ Hz, 16H, H_i), 8.01 (d, $^3J = 7.8$ Hz, 16H, H_h), 7.98–7.88 (m, 16H, H_e/H_a), 7.77 (d, $^3J = 8.9$ Hz, 8H, H_b), 7.64 (d, $^3J = 7.9$ Hz, 8H, H_d), 7.64–7.45 (m, 16H, H_a/H_i), 7.51 (d, $^3J = 9.3$ Hz, 16H, H_b), 7.47–7.37 (m, 16H, H_c/H_e),

4.43 (d, $^3J = 6.3$ Hz, 16H, NCH_2), 1.99–1.84 (m, 16H, CH_2), 1.67–1.55 (m, 16H, CH_2), 1.55–1.35 (m, 32H, CH_2), 0.99 (t, $^3J = 7.0$ Hz, 24H, CH_3).

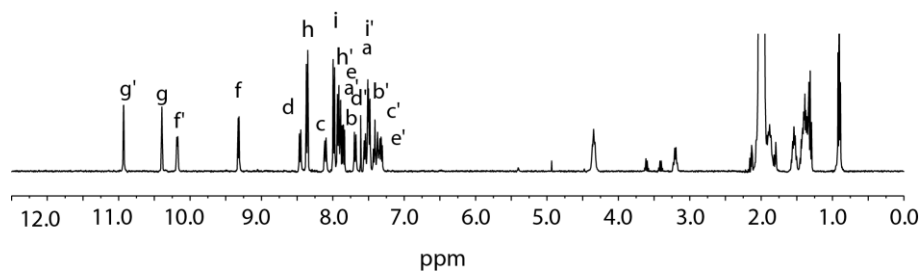


Figure 7.151 ^1H NMR spectrum of interpenetrated coordination cage $[\text{Pd}_4\text{L}_4_8]$ (500 MHz, 298 K, CD_3CN).

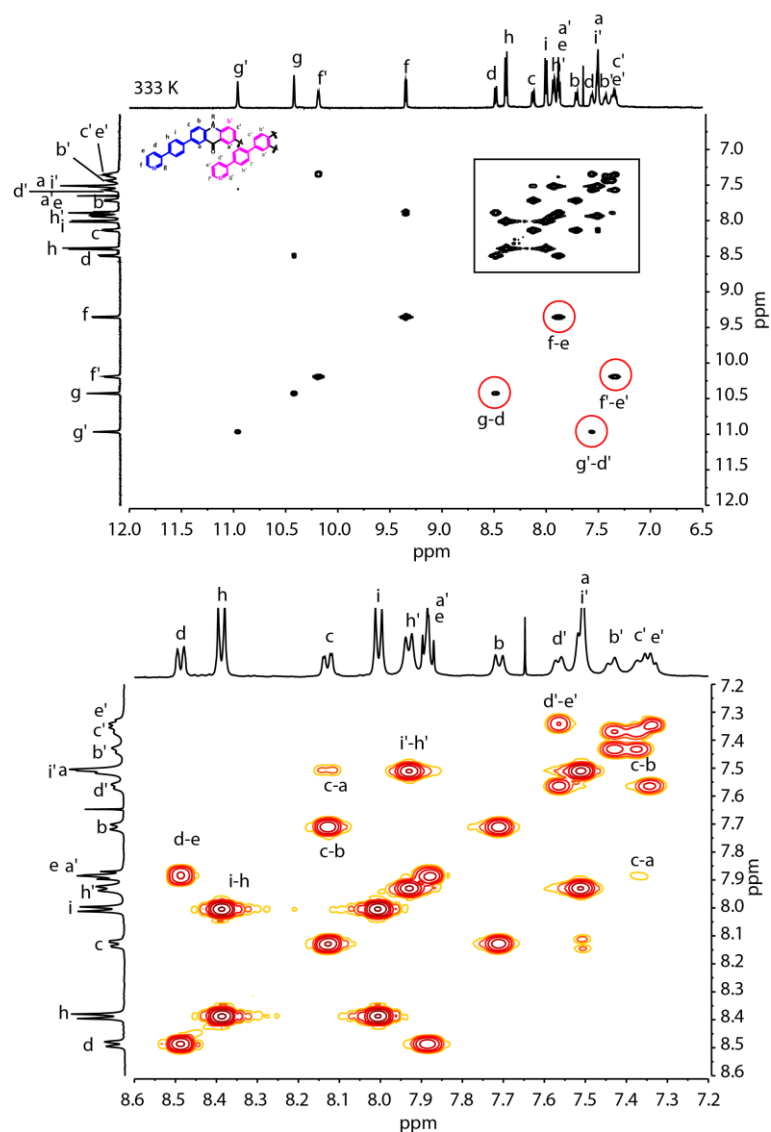


Figure 7.152 ^1H - ^1H COSY spectrum of interpenetrated coordination cage $[\text{3BF}_4@[\text{Pd}_4\text{L}_4_8]]$ (500 MHz, 333 K, CD_3CN). Cross Peaks are indicated.

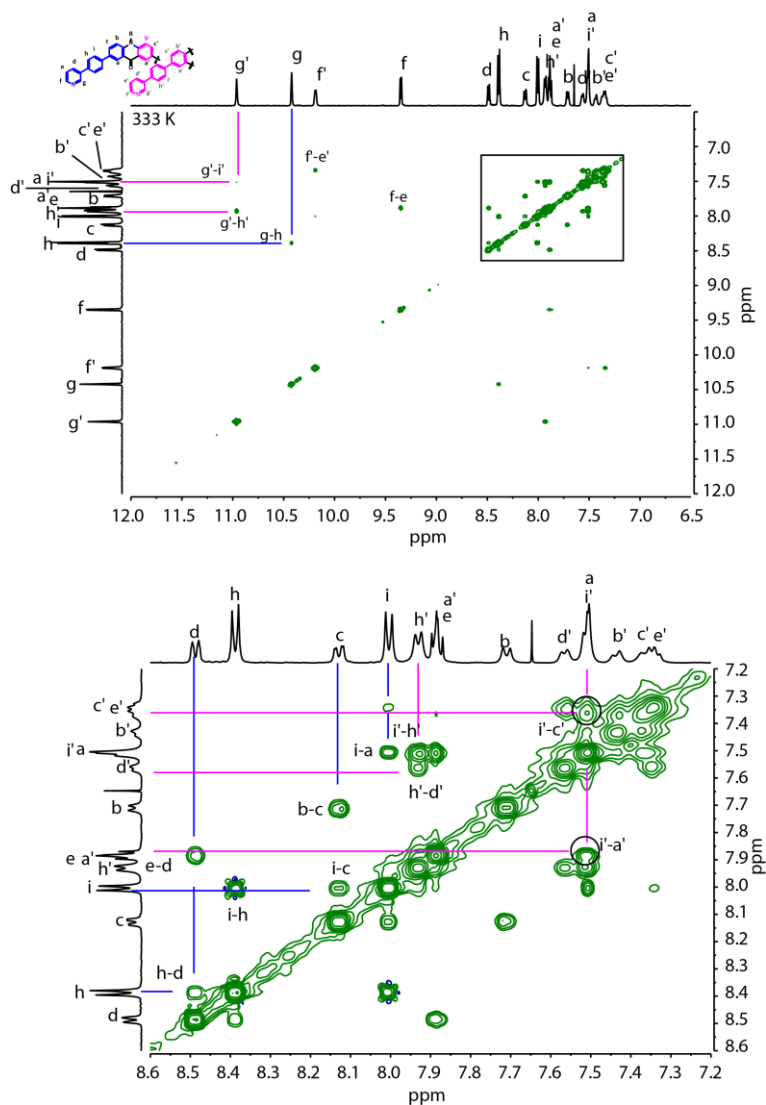


Figure 7.153 ^1H - ^1H NOESY spectrum of $[\text{Pd}_4\text{L}_8]$ cage (500 MHz, 333 K, CD_3CN). Cross Peaks are indicated.

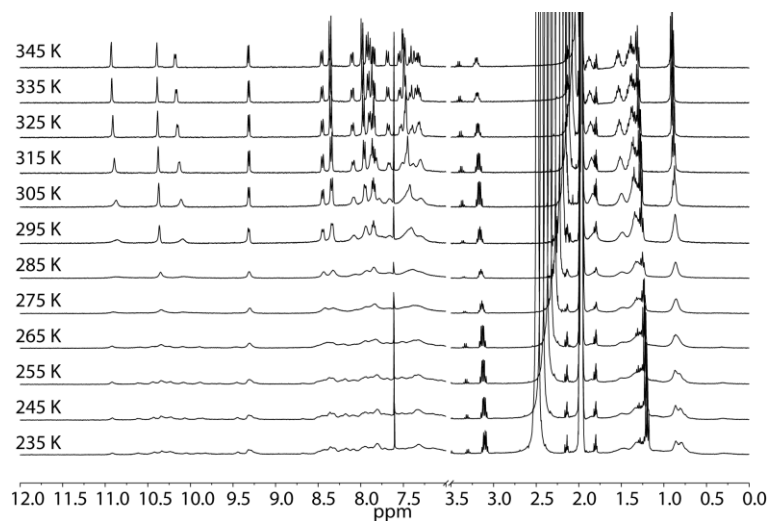


Figure 7.154 Temperature dependence of the ^1H NMR-signals of $[\text{3BF}_4@ \text{Pd}_4\text{L}_8]$ (400 MHz, CD_3CN). Increase in temperature leads to a sharpening of the signals, due to free rotation of the benzyl group.

^{19}F NMR (470 MHz, CD_3CN , 273 K): δ (ppm) = -143.17 (4F, encapsulated BF_4^-), -147.05 (8F, broad signal, encapsulated BF_4^-), -151.30 (20F, broad signal, free BF_4^-).

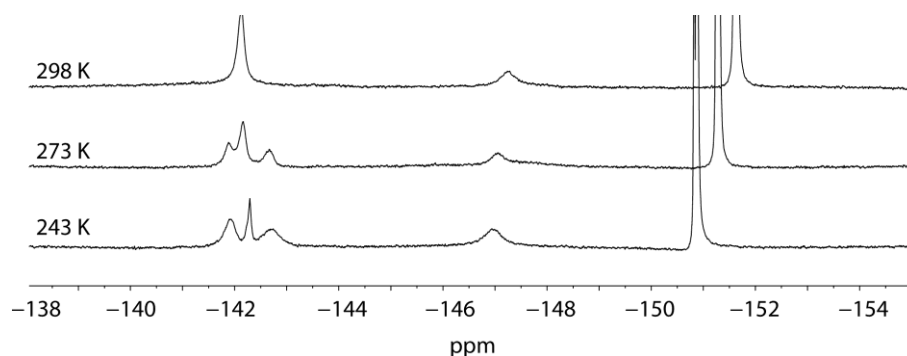


Figure 7.155 Temperature dependence of the ^{19}F -NMR-signals of $[\text{3BF}_4@Pd_4L_4^8]$ (470 MHz, CD_3CN). Shoulders are due to the $^{10}\text{BF}_4^-$ isotope.

ESI HR-MS: 1074.4 ($[\text{3BF}_4@Pd_4L_4^8]^{5+}$), 1364.5 ($[\text{3BF}_4@Pd_4L_4^8+\text{BF}_4]^{4+}$), 1848.3 ($[\text{3BF}_4@Pd_4L_4^8+2\text{BF}_4]^{3+}$).

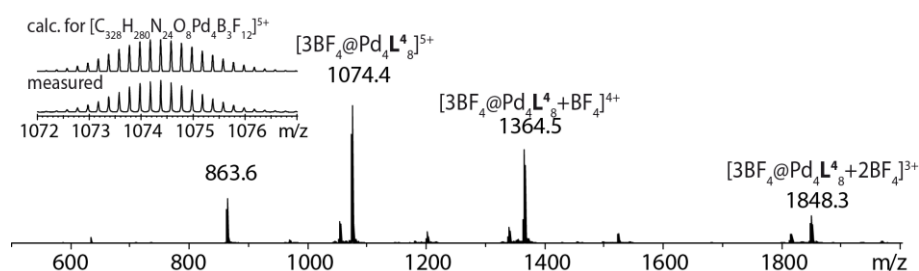


Figure 7.156 HR-MS of $[\text{3BF}_4@Pd_4L_4^8]$ with a variable number of tetrafluoroborate counter anions. The isotopic pattern of the measured peaks matches the calculation.

7.6.3.3 Formation of Interpenetrated Coordination Cage $[\text{3PF}_6@Pd_4L_4^8]$

To a suspension of ligand L^4 (1.65 mg, 2.8 μmol , 1.0 eq.) in CD_3CN , a solution of $[\text{Pd}(\text{CH}_3\text{CN})_4](\text{PF}_6)_2$ (15 mM, 0.5 eq.) was added. The reaction mixture was heated to 70 $^\circ\text{C}$ for 24 h. The resulting interpenetrated complex was formed quantitative and no further purification was necessary.

$^1\text{H-NMR}$ (400 MHz, CD_3CN , 298K): δ (ppm) = 10.73 (s, 8H, H_g), 10.67 (dd, $^3J = 8.1$ Hz, $^4J = 1.5$ Hz, 8H, H_g), 10.28 (d, $^3J = 6.0$ Hz, 8H, H_f), 9.26 (d, $^3J = 5.8$ Hz, 8H, H_f), 8.40 (d, $^3J = 8.0$ Hz, 8H, H_d), 8.28 (d, $^3J = 8.0$ Hz, 16H, H_h), 8.04 (d, $^3J = 8.0$ Hz, 16H, H_i), 7.84 (s, 8H, H_g), 7.82 (s, 8H, H_a'), 7.79 (d, $^3J = 6.2$ Hz, 16H, H_e), 7.66 (d, $^3J = 10.0$ Hz, 16H, H_a/H_d), 7.58 (s, 8H, H_b), 7.49 (d, $^3J = 8.1$ Hz, 8H, H_f), 7.40 (s, 16H, H_b/H_c), 7.13 (d, $^3J = 7.8$ Hz, 8H, H_g), 4.26 (d, $^3J = 6.3$ Hz, 16H, NCH_2), 1.83–1.70 (m, 16H, CH_2), 1.51–1.39 (m, 16H, CH_2), 1.38–1.20 (m, 32H, CH_2), 0.84 (t, $^3J = 7.0$ Hz, 24H, CH_3).

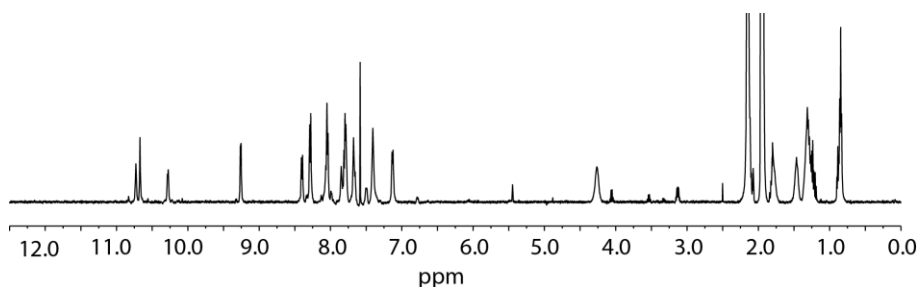


Figure 7.157 ^1H NMR spectrum of interpenetrated coordination cage $[3\text{PF}_6@Pd_4L^4]$ (500 MHz, 298 K, CD_3CN).

ESI HR-MS: 1109.2 ($[3\text{PF}_6@Pd_4L^4]^{5+}$), 1422.9 ($[3\text{PF}_6@Pd_4L^4+\text{PF}_6]^{4+}$), 1848.3 ($[3\text{PF}_6@Pd_4L^4+2\text{PF}_6]^{3+}$).

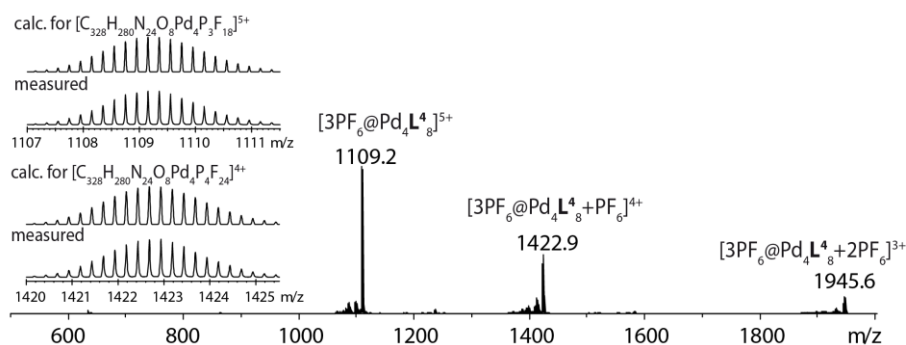


Figure 7.158 HR-MS of $[3\text{PF}_6@Pd_4L^4]$ with a variable number of tetrafluoroborate counter anions.

7.6.3.4 Addition of anions to the Interpenetrated Coordinating Cage $[Pd_4L^4]$

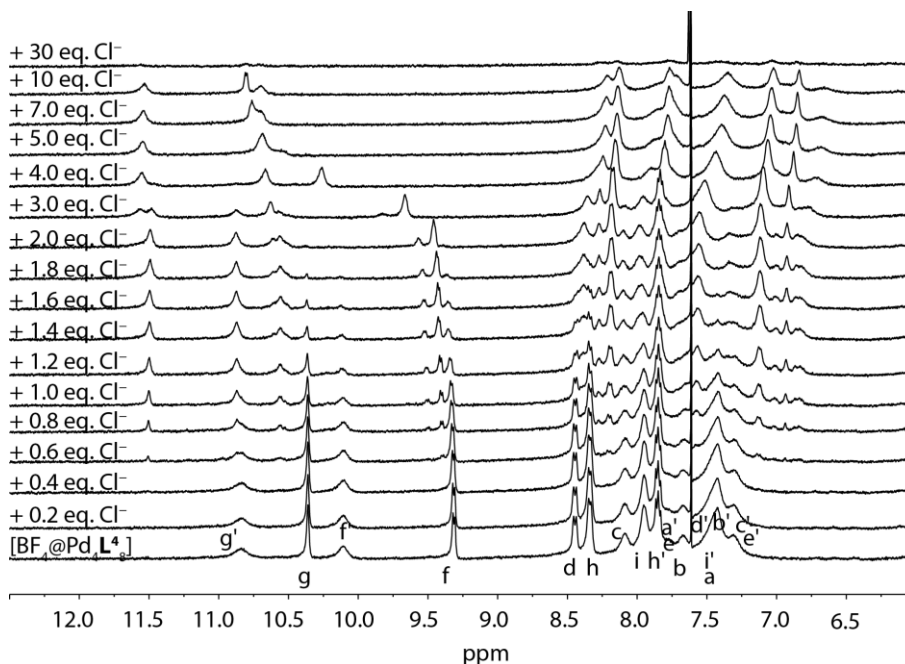


Figure 7.159 ^1H NMR titration (400 MHz, 298 K, CD_3CN) of $[3\text{BF}_4@Pd_4L^4]$ with NBu_4Cl . Upon addition of two equiv. of chloride ions; $[3\text{BF}_4@Pd_4L^4]$ transforms into $[2\text{Cl}@Pd_4L^4]$, as indicated by strong downfield shifts of the protons pointing inside the outer two cavities. Further addition of halide results in a strong downfield shift of protons f, caused by the interaction of chloride anions with the periphery of the cage. Addition of up to 30 equivalents of NBu_4Cl leads to disassembly of the cage and the release of free ligand. This could be observed by eye due to the formation of a yellow precipitate inside the NMR tube (the solubility of the ligand in CD_3CN is low).

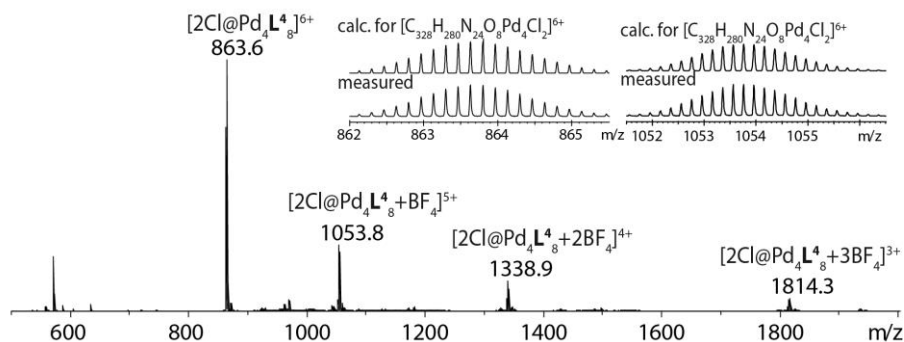


Figure 7.160 HR-MS of $[2\text{Cl}@Pd_4L_8]$ with a variable number of tetrafluoroborate counter anions.

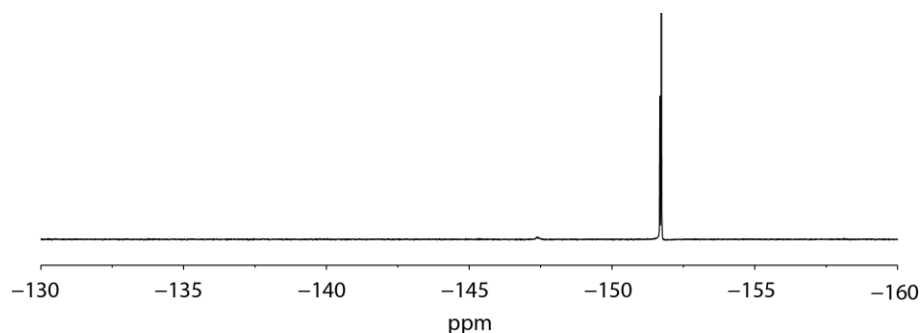


Figure 7.161 ^{19}F NMR of $[2\text{Cl}@Pd_4L_8]$ (540 MHz, 298 K, CD_3CN). The signal at -151.70 ppm represents free BF_4 in solution.

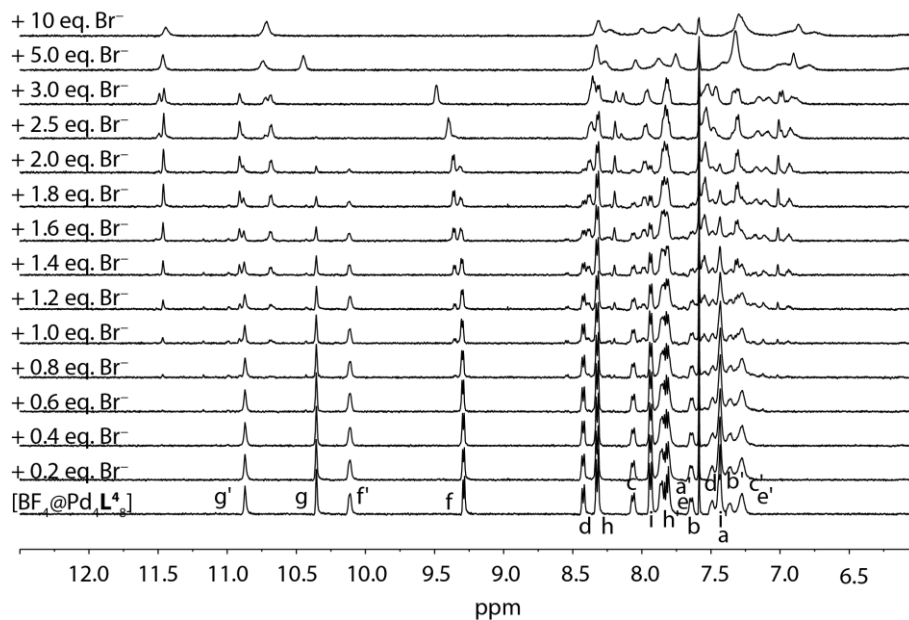


Figure 7.162 ^1H NMR titration (500 MHz, 323 K, CD_3CN) of $[3\text{BF}_4@Pd_4L_8]$ with NBu_4Br . Upon addition of two equivalents of bromide ions $[3\text{BF}_4@Pd_4L_8]$ transforms into $[2\text{Br}@Pd_4L_8]$, indicated by the appearance of a new set of signals at a downfield shift. Further addition of halide anions results in a strong downfield shift of protons f, caused by the interaction of bromide anions with the periphery of the cage. Disassembly of the cage and precipitation of the free ligand was observed after the addition of 25 eq. of halide anion.

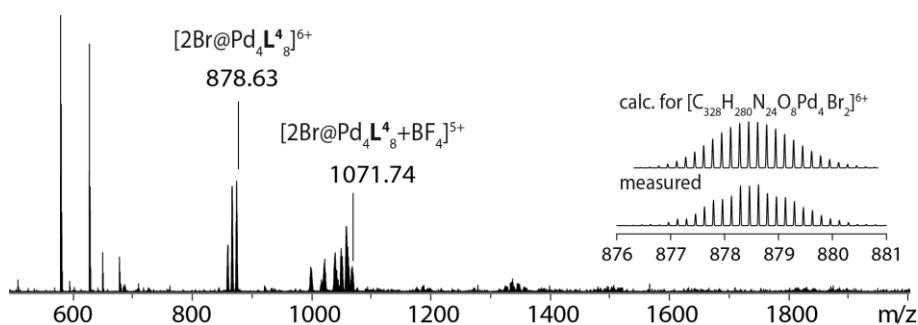


Figure 7.163 HR-MS of $[2\text{Br}@Pd_4L_8]$ with a variable number of tetrafluoroborate counter anions.

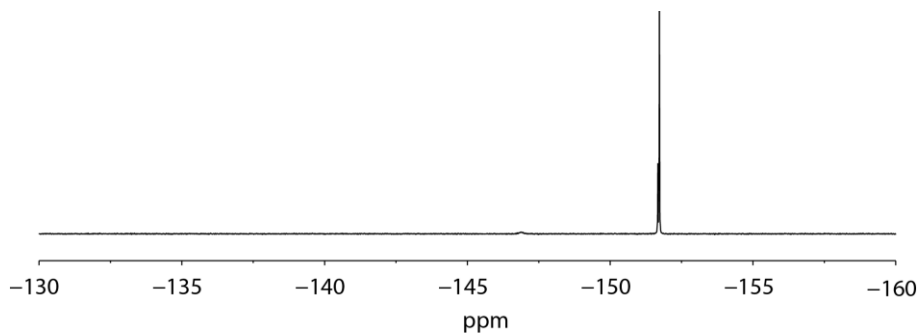


Figure 7.164 ^{19}F NMR of $[2\text{Br}@Pd_4L_8]$ (540 MHz, CD_3CN , 298 K). The signal at -151.70 ppm represents free BF_4 in solution.

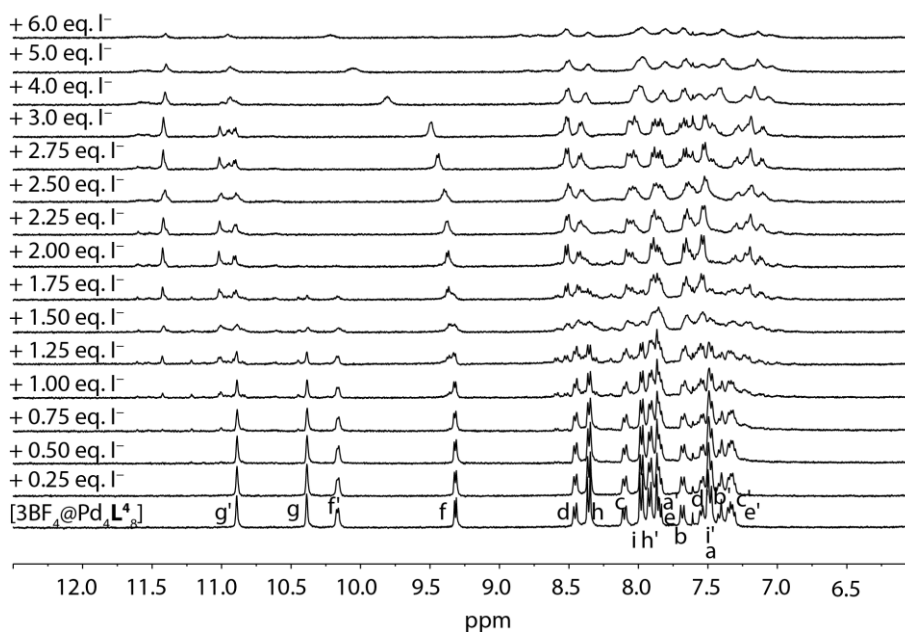


Figure 7.165 ^1H NMR titration (400 MHz, 335 K, CD_3CN) of $[3\text{BF}_4@Pd_4L_8]$ with NBu_4I . Upon addition of two equivalents of iodine anions the $[3\text{BF}_4@Pd_4L_8]$ cage transforms into $[2\text{I}@Pd_4L_8]$, indicated by strong downfield shifts of the protons pointing inside the outer two cavities. Further addition of halide results in a strong downfield shift of protons f, caused by the interaction of chloride anions with the periphery of the cage.

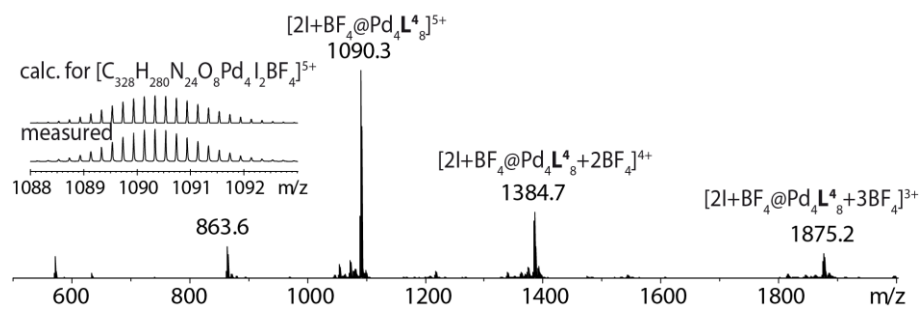


Figure 7.166 HR-MS of $[2I+BF_4@Pd_4L_8]$ with a variable number of tetrafluoroborate counter anions.

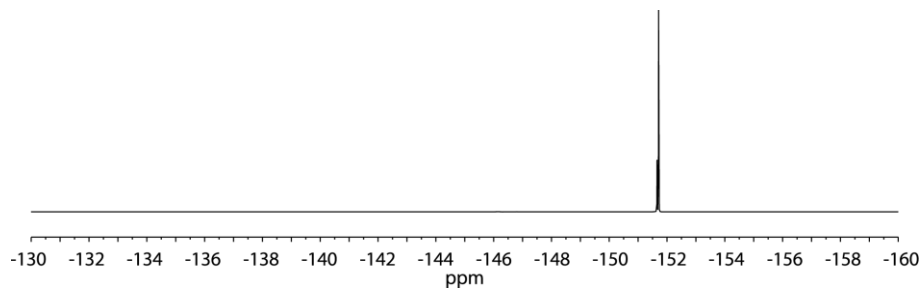


Figure 7.167 ^{19}F NMR of $[2I+BF_4@Pd_4L_8]$ (564 MHz, CD_3CN , 298 K). The signal at -151.70 ppm represents free BF_4^- in solution.

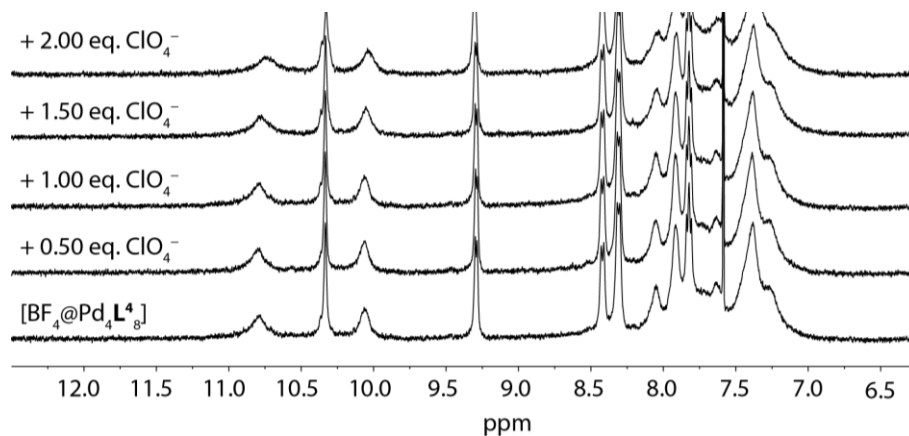


Figure 7.168 1H NMR titration (400 MHz, 298 K, CD_3CN) of $[3BF_4@Pd_4L_8]$ with NBU_4ClO_4 . No change in chemical shift could be observed in the 1H NMR spectra.

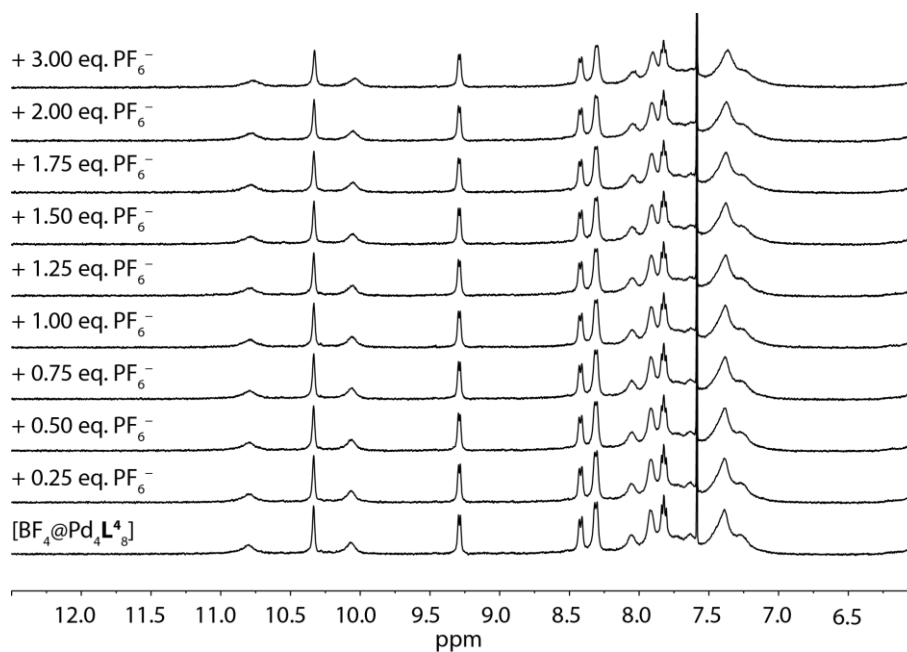


Figure 7.169 ¹H NMR titration (400 MHz, 298 K, CD₃CN) of [3BF₄@Pd₄L₈] with NBU₄PF₆. No change in chemical shift occur. Thus, tetrafluoroborate is not exchanged by hexafluorophosphate anions.

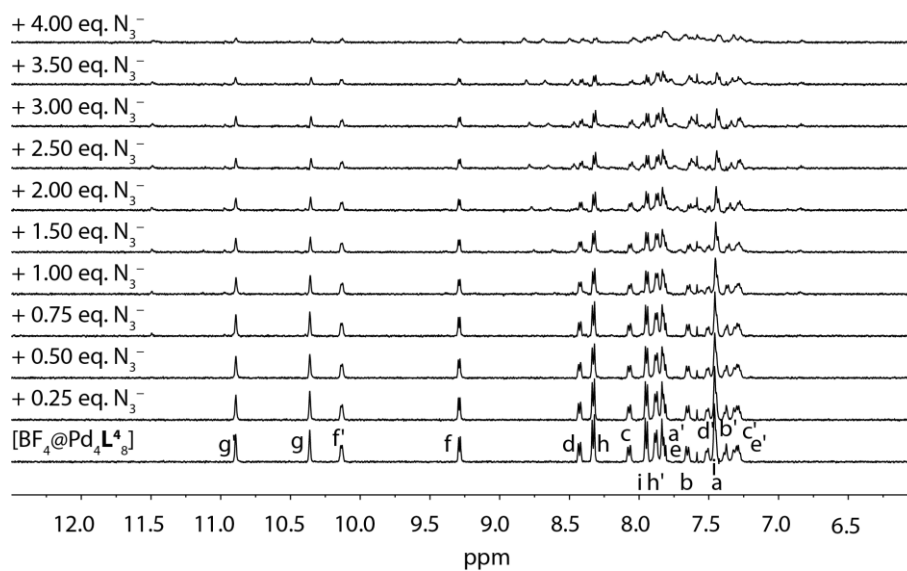


Figure 7.170 ¹H NMR titration (500 MHz, 335 K, CD₃CN) of [3BF₄@Pd₄L₈] with NBU₄N₃.

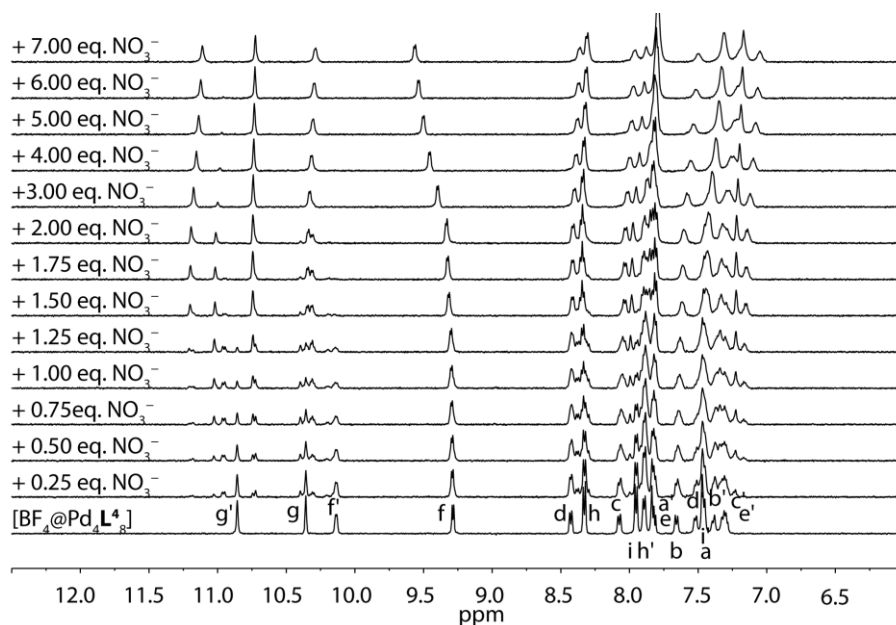


Figure 7.171 ^1H NMR titration (500 MHz, 335 K, CD_3CN) of $[\text{3BF}_4@Pd_4L_8]$ with NBu_4NO_3 .

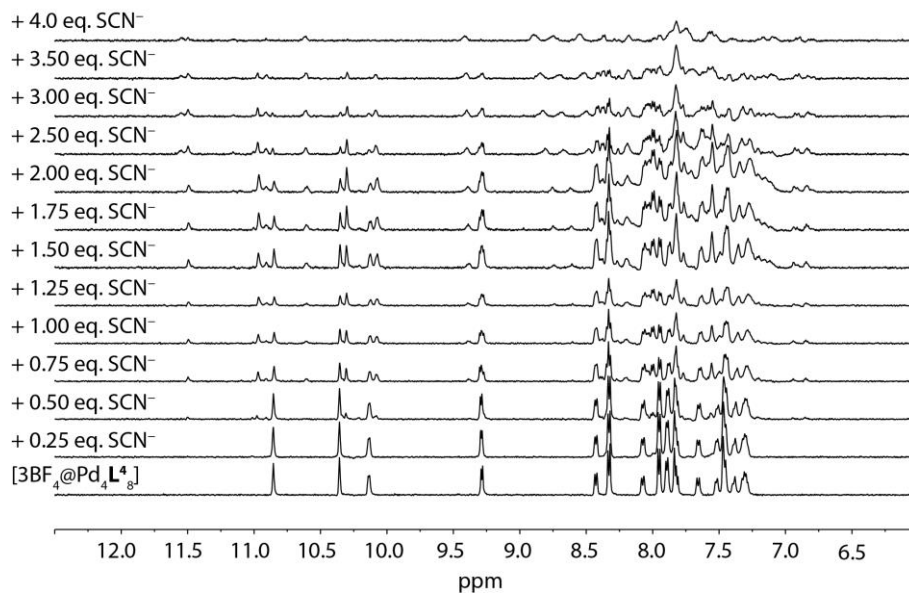


Figure 7.172 ^1H NMR titration (500 MHz, 335 K, CD_3CN) of $[\text{3BF}_4@Pd_4L_8]$ with NBu_4SCN .

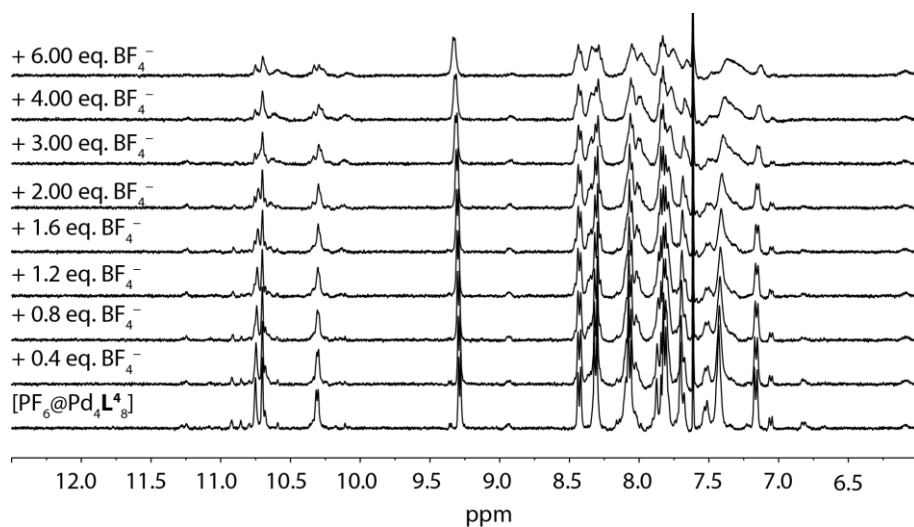


Figure 7.173 ^1H NMR titration (400 MHz, 335 K, CD_3CN) of $[\text{3PF}_6@Pd_4L_4^8]$ with NBu_4BF_4 .

7.6.3.5 Addition of Silver(I)-cations to the Halide-filled Coordination Cages containing Ligand L^4

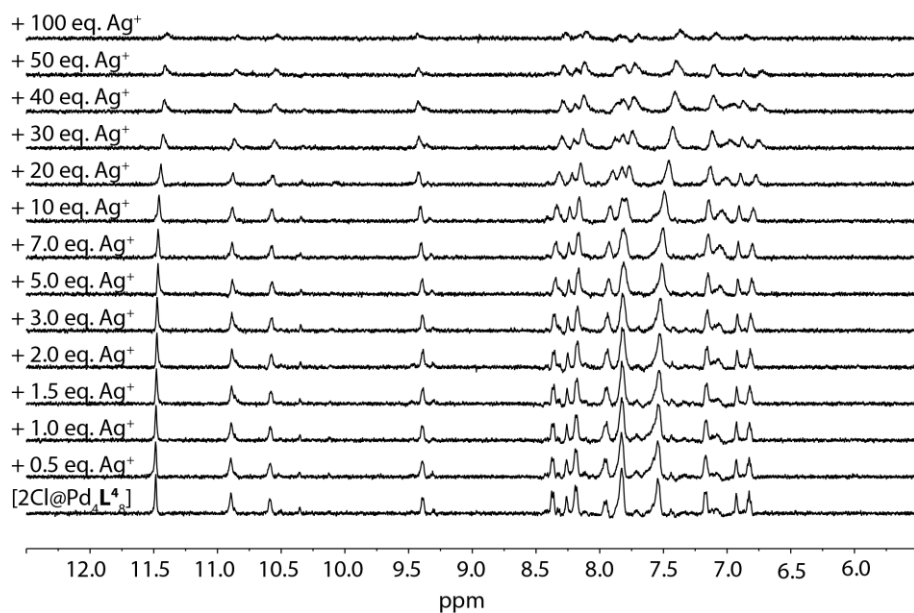


Figure 7.174 ^1H NMR titration (500 MHz, 323 K, CD_3CN) of $[\text{2Cl}@Pd_4L_4^8]$ with AgBF_4 (17.5 mM). No change in chemical shift could be observed. Even after the addition of 100 equiv. of silver(I) ions, only signals of the $[\text{2Cl}@Pd_4L_4^8]$ species are visible. The decrease in intensity is due to dilution.

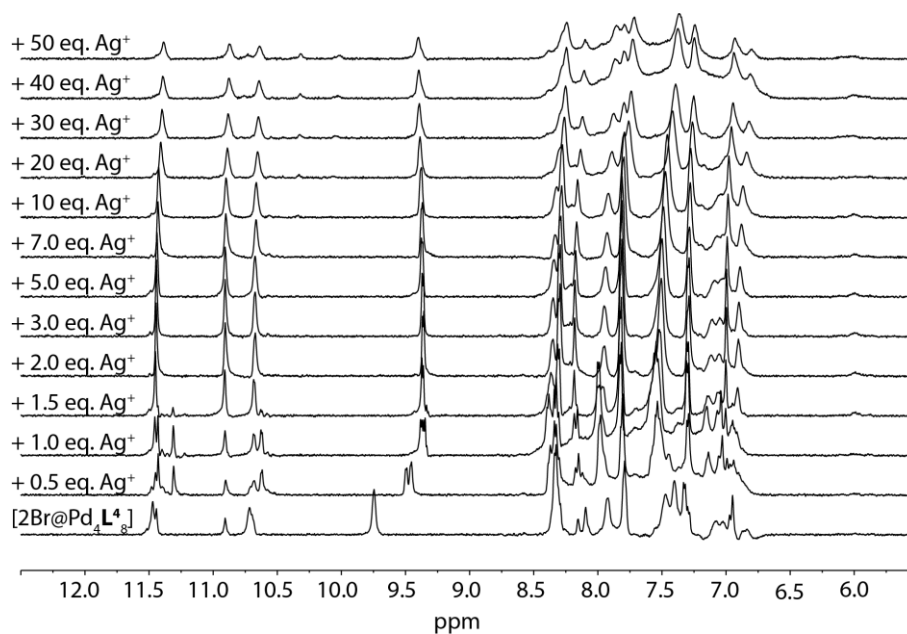


Figure 7.175 ^1H NMR titration (500 MHz, 323 K, CD_3CN) of $[\text{2Br@Pd}_4\text{L}_8]$ with AgBF_4 (17.5 mM). No formation of the tetrafluoroborate anion-containing cage $[\text{2BF}_4\text{@Pd}_4\text{L}_8]$ was observed.

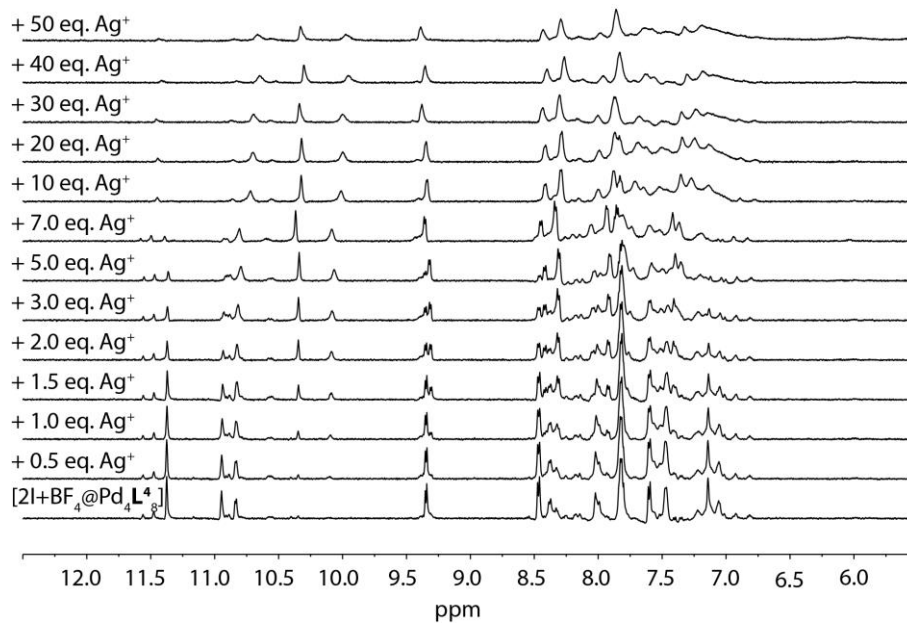


Figure 7.176 ^1H NMR titration (500 MHz, 323 K, CD_3CN) of $[\text{2I+BF}_4\text{@Pd}_4\text{L}_8]$ with AgBF_4 (17.5 mM). Excess addition of silver(I) cations lead to precipitation of AgI under full recovery of $[\text{3BF}_4\text{@Pd}_4\text{L}_8]$.

7.6.3.6 Addition of Neutral Guest Molecules to Halide-filled Coordination Cages of ligand L⁴

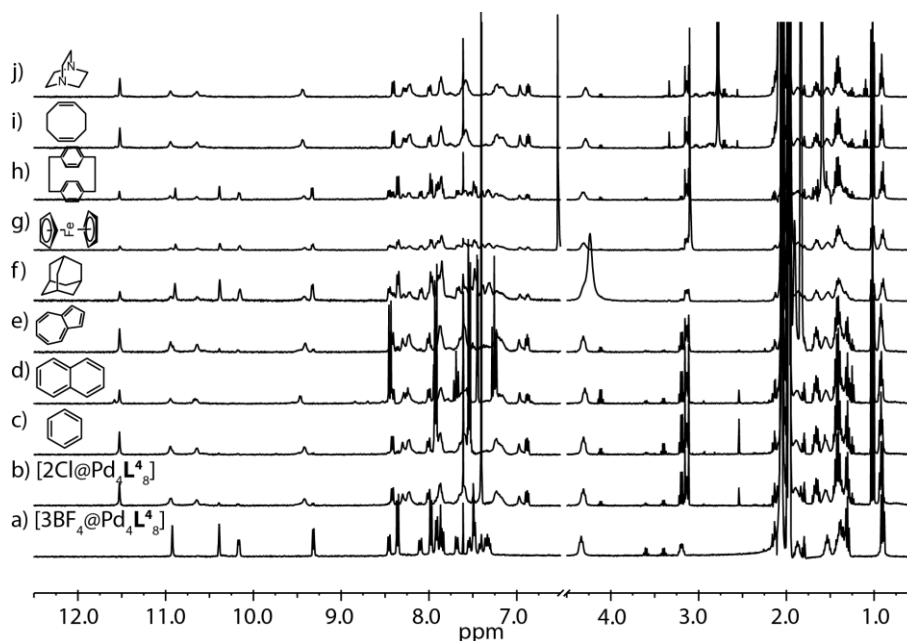


Figure 7.177 ¹H NMR spectra (400 MHz, 335 K, CD₃CN) of a) [3BF₄@Pd₄L₄⁸], b) [2Cl@Pd₄L₄⁸], and addition of different neutral guest molecules to the chloride-containing interpenetrated coordination cage [2Cl@Pd₄L₄⁸]: c) benzene (20 eq.) d) naphthalene (10 eq.) e) azulene (10 eq.), f) adamantane (10 eq.), g) ferrocene (10 eq.), h) [2.2]paracyclophane (10 eq.), i) 1,5-cyclooctadiene (10 eq.), j) DABCO (10 eq.) and an equilibration time of 3 weeks. No change in chemical shift could be observed after the addition of the neutral guest molecules to the [2Cl@Pd₄L₄⁸] cage, indicating no incorporation inside the interpenetrated coordination cage.

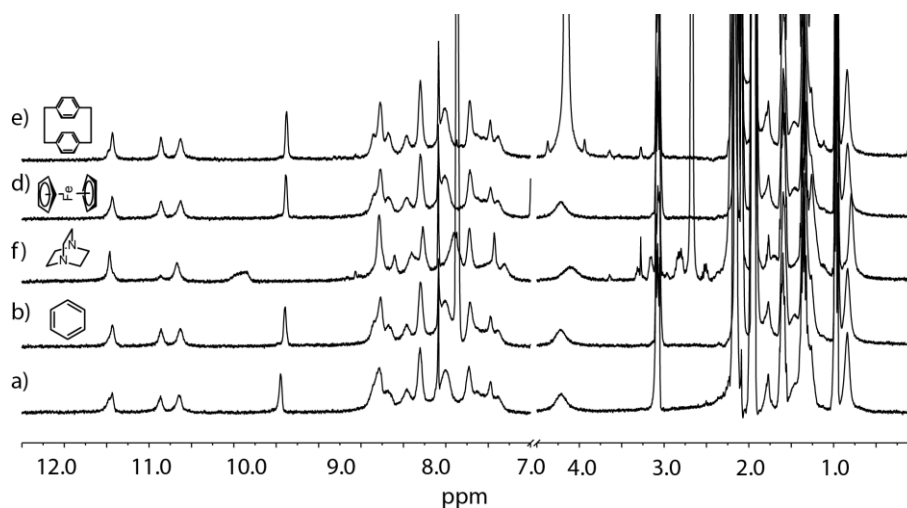
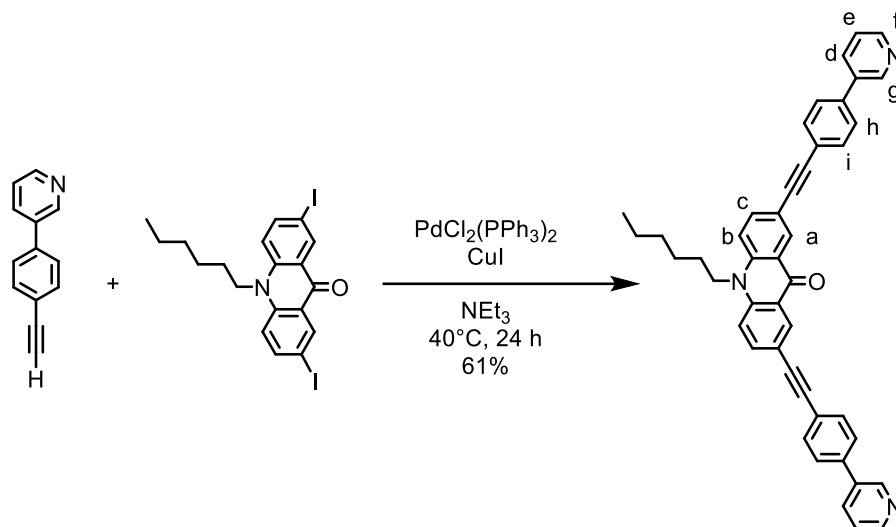


Figure 7.178 ¹H NMR spectra (400 MHz, 298 K, CD₃CN) of a) [2Br@Pd₄L₄⁸] before and after the addition of different neutral guest molecules: b) benzene (20 eq.), d) DABCO (20 eq.), d) ferrocene (20 eq.), and e) [2.2] paracyclophane (20 eq.). No significant change in the NMR spectra could be observed after several days at room temperature.

7.6.4 Ligand L^{5a/b} and Corresponding Coordination Cages

7.6.4.1 Ligand Synthesis

7.6.4.1.1 Ligand L^{5a}



2,7-diiodo-*N*-hexylacridone (164.3 mg, 0.31 mmol, 1.00 eq.) and 3-((4-ethynyl)phenyl)pyridine (114.8 mg, 0.64 mmol, 2.06 eq.) were dissolved in triethylamine (15 mL) and degassed by freeze-pump-thaw cycles (3x). Under a nitrogen atmosphere [PdCl₂(PPh₃)₂] (25.4 mg, 0.04 mmol, 0.12 eq.) and copper(I) iodide (17.3 mg, 0.09 mmol, 0.29 eq.) were added. After short degassing, the reaction mixture was stirred at 40 °C for 24 h. After cooling to ambient temperature the mixture was filtered through Celite® and the solvent was removed under reduced pressure. The crude product was purified by column chromatography (SiO₂, CHCl₃:MeOH = 49:1 → CHCl₃:MeOH = 9:1) and subsequent gel permeation chromatography (CHCl₃). The product could be obtained as a yellow solid (120 mg, 0.19 mmol, 61%).

¹H NMR (500 MHz, 298 K, CDCl₃): δ (ppm) = 8.90 (s, 2H, H_g), 8.72 (d, ⁴*J* = 2.1 Hz, 2H, H_a), 8.69–6.54 (m, 2H, H_i), 7.90 (d, ³*J* = 7.9 Hz, 2H, H_d), 7.82 (dd, ³*J* = 8.9 Hz, ⁴*J* = 2.2 Hz, 2H, H_c), 7.66 (dt, ³*J* = 8.5 Hz, ⁴*J* = 1.9 Hz, 4H, H_i), 7.59 (dt, ³*J* = 8.5 Hz, ⁴*J* = 1.9 Hz, 4H, H_h), 7.45 (d, ³*J* = 9.1 Hz, 2H, H_b), 7.42–7.30 (m, 2H, H_e), 4.32 (t, ³*J* = 8.3 Hz, 2H, NCH₂), 1.93 (p, ³*J* = 8.0 Hz, 2H, CH₂), 1.57 (p, ³*J* = 7.3/7.7 Hz, 2H, CH₂), 1.49–1.35 (m, 4H, CH₂), 0.95 (t, ³*J* = 7.2 Hz, 3H, CH₃).

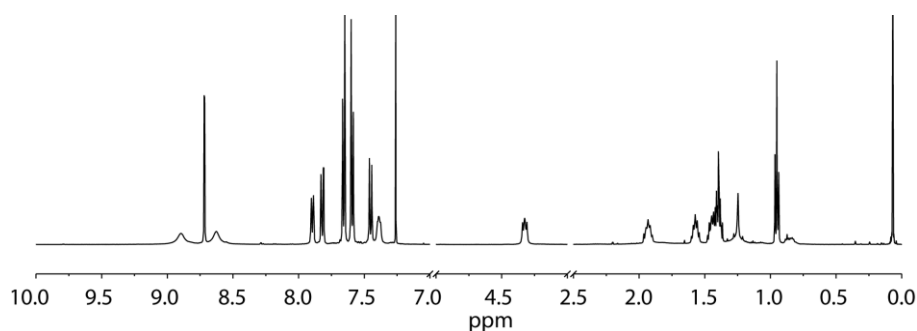


Figure 7.179 ¹H NMR spectrum of ligand L^{5a} (500 MHz, 298 K, CDCl₃).

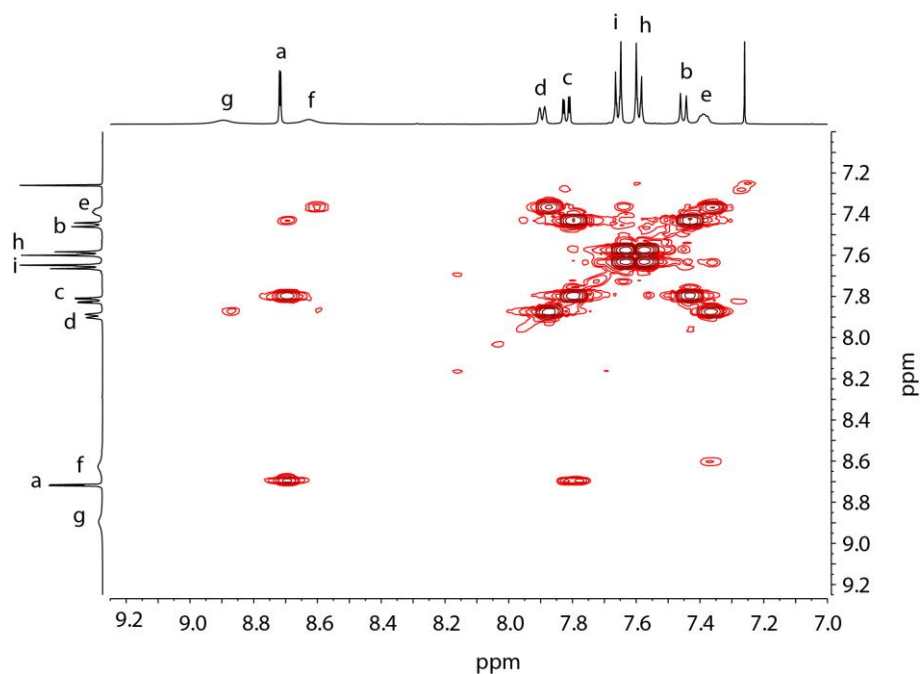


Figure 7.180 ^1H - ^1H COSY spectrum of ligand L^{5a} (500 MHz, 298 K, CD_3CN).

^{13}C NMR (75 MHz, 298 K, CDCl_3): δ (ppm) = 176.88, 149.15, 148.55, 141.42, 137.93, 136.91, 134.58, 132.67, 131.95, 127.44, 123.47, 122.75, 116.85, 115.50, 90.21, 89.84, 46.93, 46.23, 31.88, 27.61, 26.97, 23.05, 14.41, 9.04, 1.42.

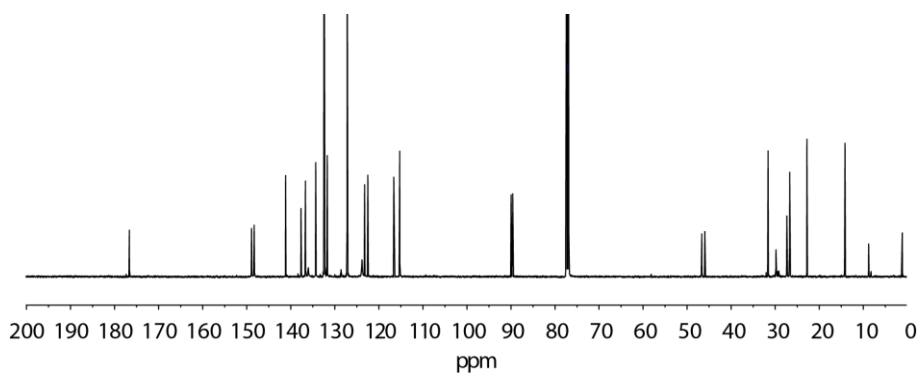
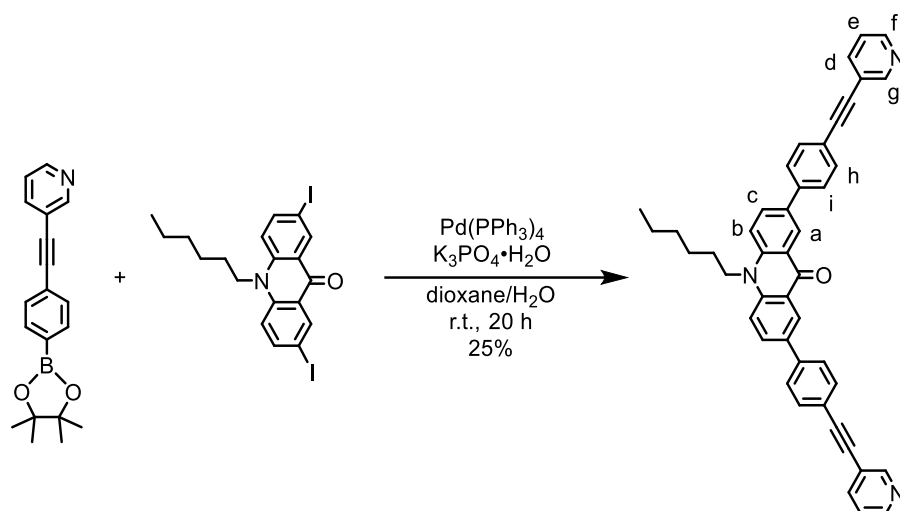


Figure 7.181 ^{13}C NMR spectrum of ligand L^{5a} (75 MHz, 298 K, CDCl_3).

ESI MS: m/z (%) = 634.1 (37) $[\text{M}+\text{H}]^+$, 381.3 (87), 317.7 (100).

7.6.4.1.2 Ligand L^{5b}

2,7-diiodo-*N*-hexylacridone (81.1 mg, 0.15 mmol, 1.00 eq.), 3-((4-phenylboronic acid pinacol ester)ethynyl)pyridine (104.6 mg, 0.34 mmol, 2.27 eq.) and $K_3PO_4 \cdot H_2O$ (182.7 mg, 0.79 mmol, 5.27 eq.) were dissolved in dioxane (8.5 mL) and H_2O (3.3 mL). The mixture was degassed by three freeze-pump-thaw cycles and under a nitrogen atmosphere $Pd(PPh_3)_4$ (16.0 mg, 0.01 mmol, 0.09 equiv.) was added. After stirring for 20 h at ambient temperature, the mixture was filtered through Celite[®], dried with Na_2SO_4 and concentrated under reduced pressure. The crude product was purified by column chromatography (SiO_2 , $CHCl_3:MeOH=49:1$) and subsequent gel permeation chromatography ($CHCl_3$). The product was yielded as a yellow solid (23.6 mg, 0.04 mmol, 25%).

¹H NMR (500 MHz, 298 K, $CDCl_3$): δ (ppm) = 8.89 (d, $^4J = 2.4$ Hz, 2H, H_a), 8.82 (s_{br}, 2H, H_g), 8.58 (s, 2H, H_f), 8.05 (dd, $^3J = 9.0$ Hz, $^4J = 2.4$ Hz, 2H, H_c), 7.85 (dt, $^3J = 7.9$ Hz, $^4J = 1.7$ Hz, 2H, H_d), 7.78 (dt, $^3J = 8.6$ Hz, $^4J = 1.9$ Hz, 4H, H_i), 7.67 (dt, $^3J = 8.6$ Hz, $^4J = 1.9$ Hz, 4H, H_h), 7.63 (d, $^3J = 9.1$ Hz, 2H, H_b), 7.32 (dd, $^3J = 7.4$ Hz, $^3J = 4.7$ Hz, 2H, H_e), 4.44 (t, $^3J = 8.4$ Hz, 2H, NCH_2), 2.01 (p, $^3J = 8.3$ Hz, 2H, CH_2), 1.62 (p, $^3J = 7.4$ Hz, 2H, CH_2), 1.52–1.38 (m, 4H, CH_2), 0.97 (t, $^3J = 7.2$ Hz, 3H, CH_3).

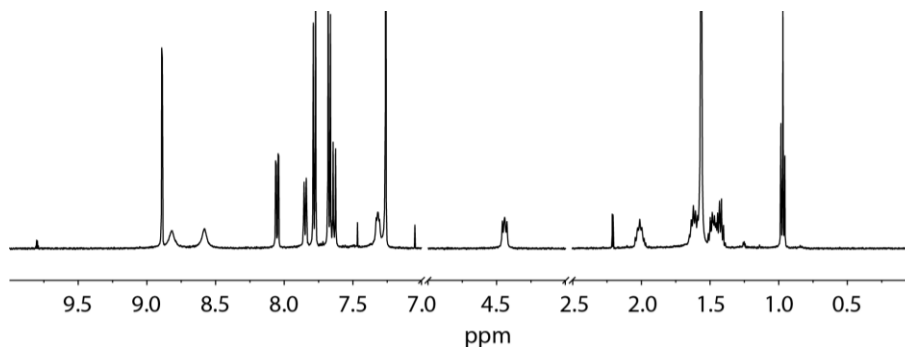


Figure 7.182 ¹H NMR spectrum of ligand L^{5b} (500 MHz, 298 K, $CDCl_3$).

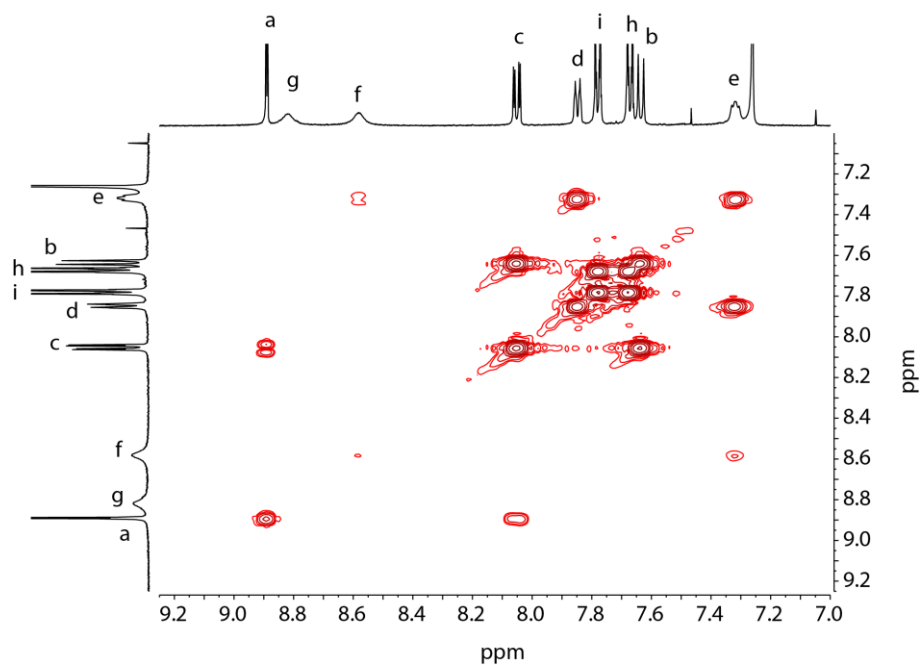


Figure 7.183 ^1H - ^1H COSY spectrum of ligand L^{5b} (500 MHz, 298 K, CD_3CN).

^{13}C NMR (75 MHz, 298 K, CDCl_3): δ (ppm) = 178.31, 152.67, 148.96, 141.55, 140.25, 138.83, 133.49, 132.91, 132.72, 127.23, 126.33, 123.55, 123.18, 121.86, 115.93, 93.00, 87.24, 46.86, 31.95, 27.74, 27.06, 23.08, 14.45. (one aromatic signal missing)

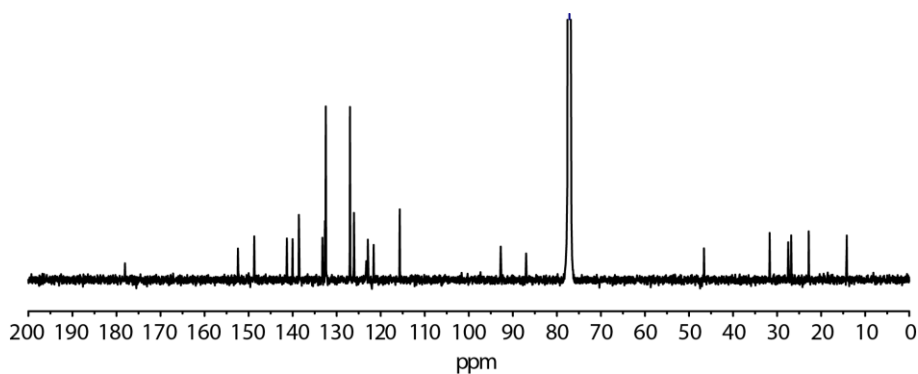


Figure 7.184 ^{13}C NMR spectrum of ligand L^{5b} (500 MHz, 298 K, CDCl_3).

ESI MS: m/z (%) = 634.3 (66) $[\text{M}+\text{H}]^+$, 389.3 (16), 180.1 (30), 118.1 (100).

7.6.4.2 Cage Formation

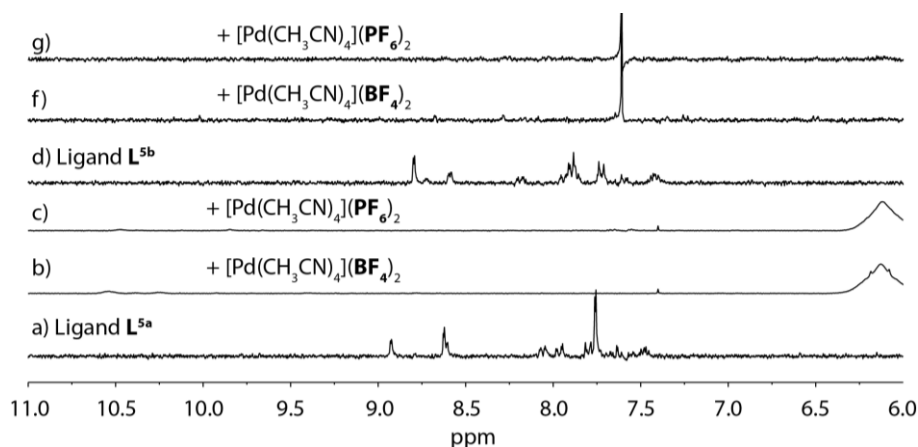


Figure 7.185 ^1H NMR spectra (300 MHz, CD_3CN , 298 K) of ligand L^{5a} and ligand L^{5b} before and after the addition of different palladium salts ($[\text{Pd}(\text{CH}_3\text{CN})_4](\text{BF}_4)_2$ or $[\text{Pd}(\text{CH}_3\text{CN})_4](\text{PF}_6)_2$) and heating at 70°C overnight. No signals in the ^1H NMR spectra were observed after the addition of palladium cations.

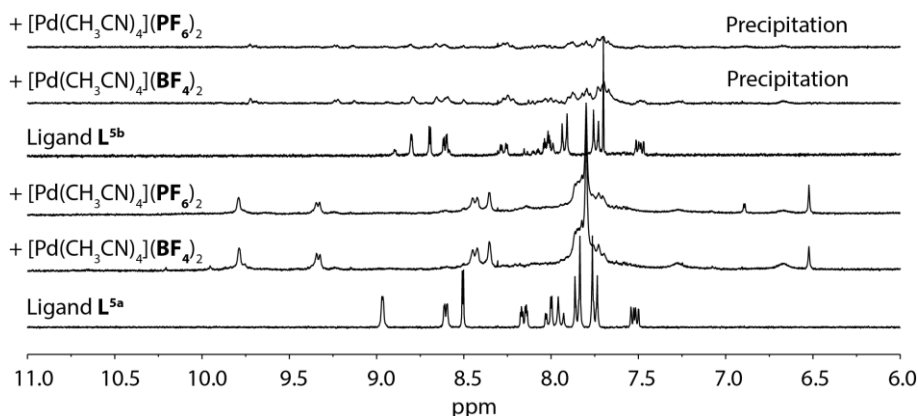


Figure 7.186 ^1H NMR spectra of ligand L^{5a} and Ligand L^{5b} (300 MHz, DMSO-d_6 , 298 K) before and after the addition of different palladium salts ($[\text{Pd}(\text{CH}_3\text{CN})_4](\text{BF}_4)_2$ or $[\text{Pd}(\text{CH}_3\text{CN})_4](\text{PF}_6)_2$). Addition of palladium(II) cations to ligand L^{5a} and heating the mixture to 70°C over night leads to a shifting of all signals, indicating the formation of a monomeric $[\text{Pd}_2\text{L}^{5a}_4]$ cage. A clean formation of a discrete species could not be observed for ligand L^{5b} in the presence of the used palladium salts.

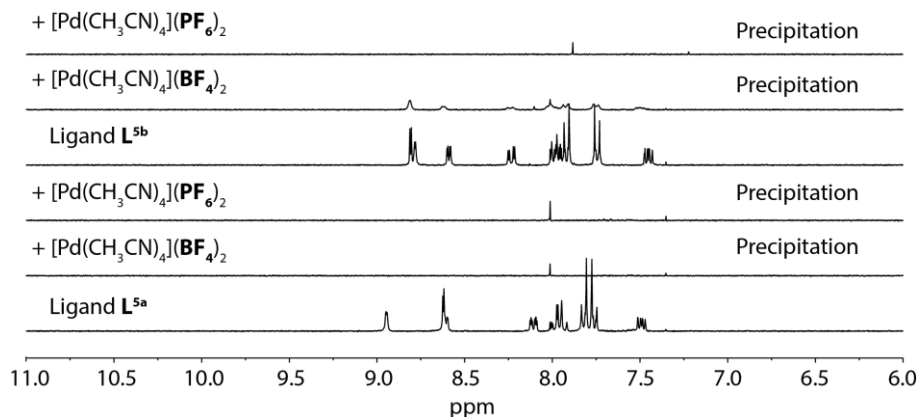


Figure 7.187 ^1H NMR spectra of ligand L^{5a} and ligand L^{5b} (300 MHz, Aceton-d_6 , 298 K) before and after the addition of different palladium salts and heating the sample at 70°C overnight. In all cases, a precipitation was visible in the NMR tube.

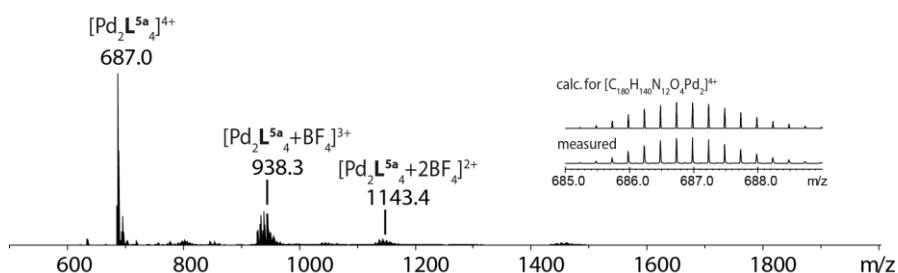


Figure 7.188 ESI MS of monomeric $[\text{Pd}_2\text{L}^{5a}_4]$ cage in DMSO. The spectra clearly shows a series of species $[\text{Pd}_2\text{L}^{5a}_4+n\text{BF}_4]^{(4-n)}$ ($n=0-2$) containing a variable number of tetrafluoroborate counter anions.

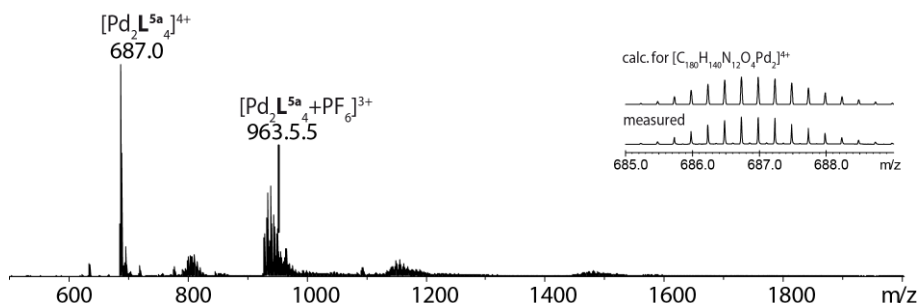


Figure 7.189 ESI MS of monomeric $[\text{Pd}_2\text{L}^{5a}_4]$ cage, assembled from ligand L^{5a} and $[\text{Pd}(\text{CH}_3\text{CN})_4](\text{PF}_6)_2$ in DMSO.

7.6.5 Computational Studies

All models were constructed using Spartan^[91] and were first optimized on a PM6 level of theory called “Ich bin die Geilste” (**charge**: 0 (ligands), 4+ ($[\text{Pd}_2\text{L}_4]$), 5+ ($[\text{3BF}_4@\text{Pd}_4\text{L}_8]$), 6+ ($[\text{2Cl}@\text{Pd}_4\text{L}_8]/[\text{2BF}_4@\text{Pd}_4\text{L}^{5a}_8]$); **multiplicity** = singlet, no counter ions were included).

Ligand and monomeric cage structures were then further refined by DFT calculations (B3LYP/ C, H, N, O = 6-31g(d)/Pd LANL2DZ) using GAUSSIAN 09.^[138] Interpenetrated coordination cages were not refined *via* DFT calculation, because of the complexity of the systems.

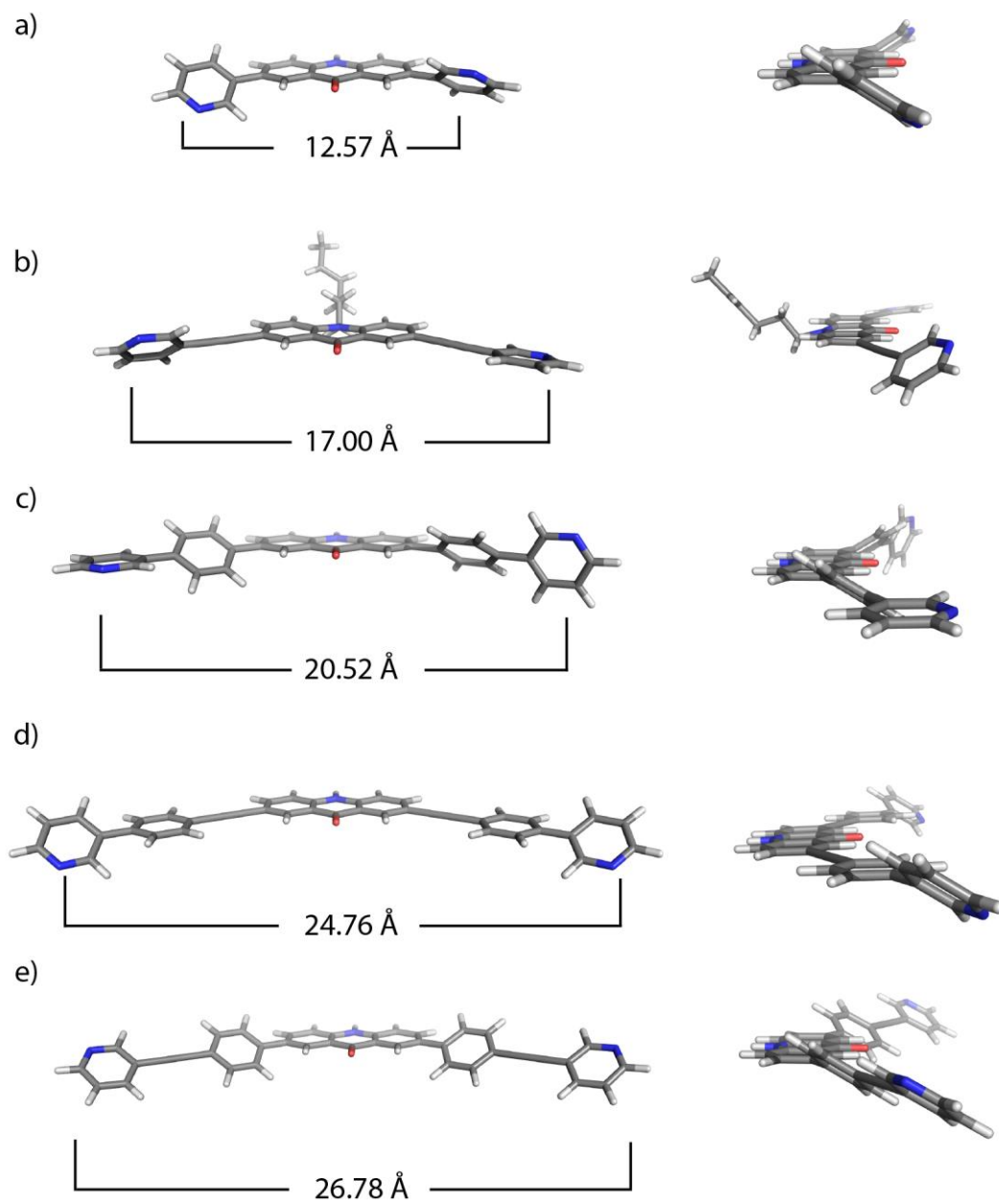
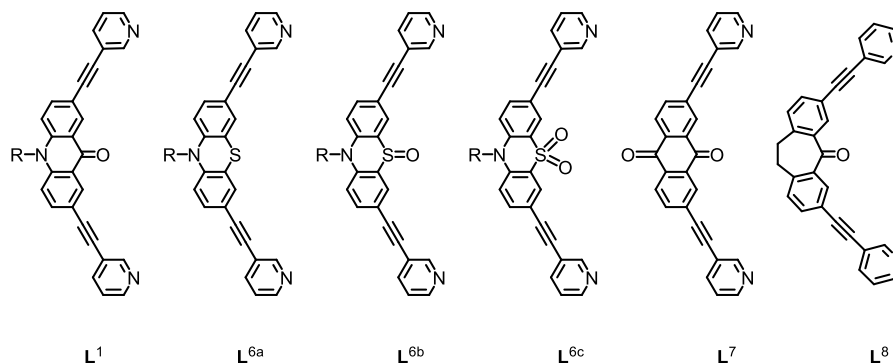


Figure 7.190 Front (left) and side (right) view with distance between nitrogen atoms for a) ligand L^3 , b) ligand L^1 , c) ligand L^4 , d) ligand L^{5a} and e) ligand L^{5b} . Values for ligand L^1 were obtained from a crystal structure, while the other values were gained from a molecular model (DFT B3LYP/6-31g(d)).

7.7 Part E – Anion Binding Competitions Experiments



Syntheses of all ligands and corresponding coordination cages were performed after previous reported procedures.^[69,75,78,87]

7.7.1 Chloride Exchange Studies in Interpenetrated Coordination Cages

General Procedure

To a chloride-containing coordination cage $[2\text{Cl}@Pd_4L^x_8]$ with $x = 1, 6a-c, 7, 8$ (250 μL , 0.35 mM, 1.0 eq.) in deuterated acetonitrile, a solution of the tetrafluoroborate double cage $[3\text{BF}_4@Pd_4L^1_8]$ was added. Immediately, after shaking the NMR tube, a ^1H NMR spectrum was recorded. The reaction mixture was kept at room temperature and ^1H NMR spectra were measured after several days.

7.7.1.1 $[2\text{Cl}@Pd_4L^1_8] + [3\text{BF}_4@Pd_4L^x_8]$ ($x = 6a-c, 7, 8$)

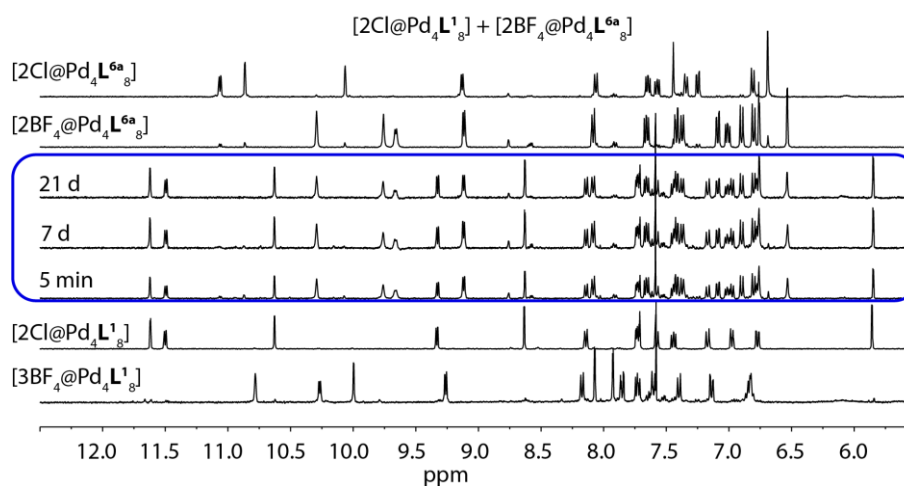


Figure 7.191 ^1H NMR spectra (400 MHz, CD_3CN , 298 K) of a mixture of $[2\text{Cl}@Pd_4L^1_8]$ and $[3\text{BF}_4@Pd_4L^{6a}_8]$ after 5 min, 7 days and 21 days after preparing the mixture (blue square). No change in the NMR spectra were observed. Hence, no exchange of the chloride anion between these interpenetrated cages occurs.

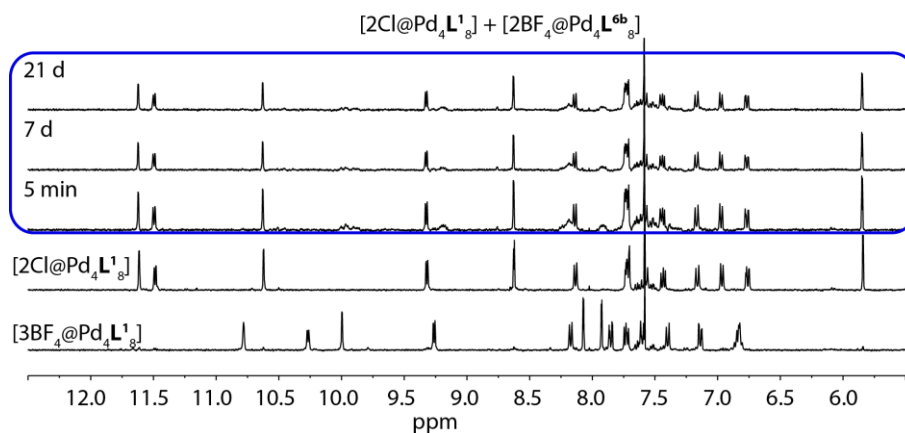


Figure 7.192 ^1H NMR spectra (400 MHz, CD_3CN , 298 K) of a mixture of $[2\text{Cl}@Pd_4L^1_8]$ and $[3\text{BF}_4@Pd_4L^{6b}_8]$ after 5 min, 7 and 21 days (blue spare). The $[3\text{BF}_4@Pd_4L^{6b}_8]$ coordination cage shows very broad signals in the NMR spectrum, due to the formation of several diastereomeric interpenetrated coordination cages (oxygen substituent in pseudo-axial or pseudo-equatorial position).^[78] Since no change in the NMR spectra was observed, a halide exchange does not take place between these two cage structures.

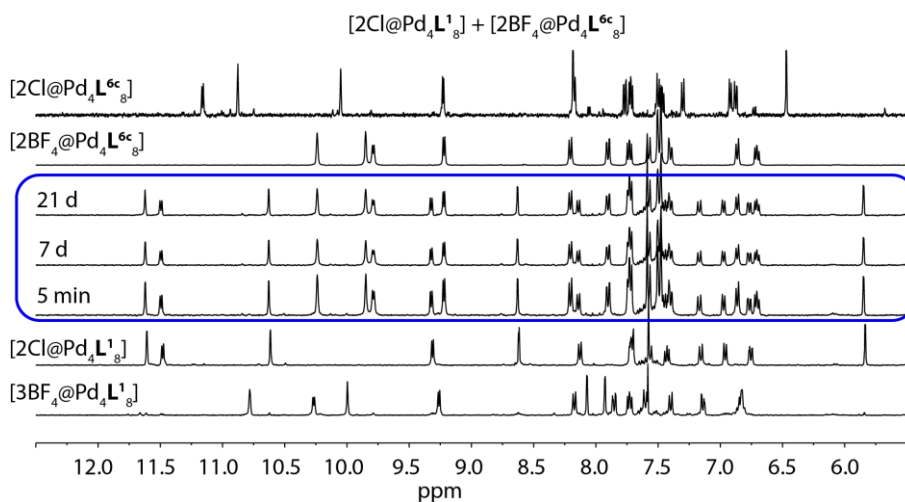


Figure 7.193 ^1H NMR spectra (400 MHz, CD_3CN , 298 K) of a mixture of $[2\text{Cl}@Pd_4L^1_8]$ and $[3\text{BF}_4@Pd_4L^{6c}_8]$ after 5 min, 7 and 21 days (blue spare). Due to no change in the ^1H NMR spectrum over time, the interpenetrated coordination cage based on an acridone ligand $[2\text{Cl}@Pd_4L^1_8]$ does not exchange the chloride anion in the outer two pockets of the cage.

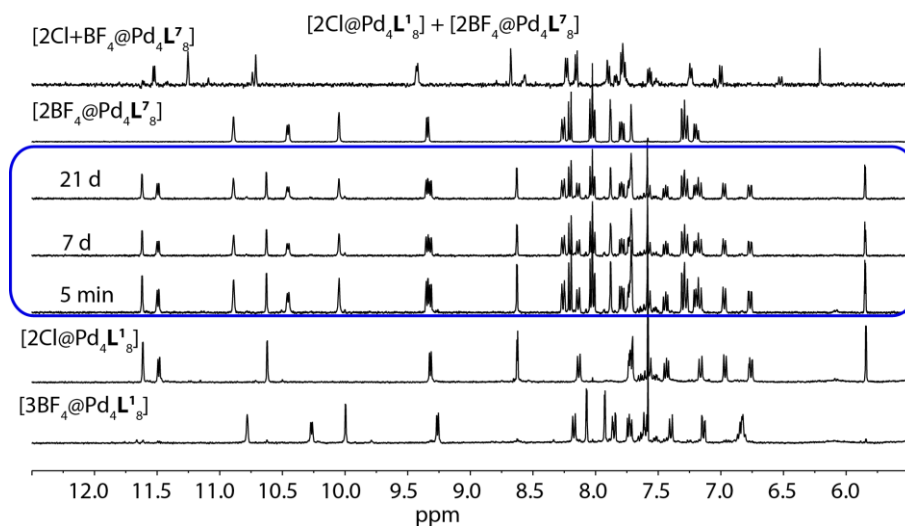


Figure 7.194 ^1H NMR spectra (400 MHz, CD_3CN , 298 K) of a mixture of $[2\text{Cl}@Pd_4L^1_8]$ and $[3\text{BF}_4@Pd_4L^7_8]$ after 5 min, 7 and 21 days (blue spare). No halide exchange between the two interpenetrated cages occurs.

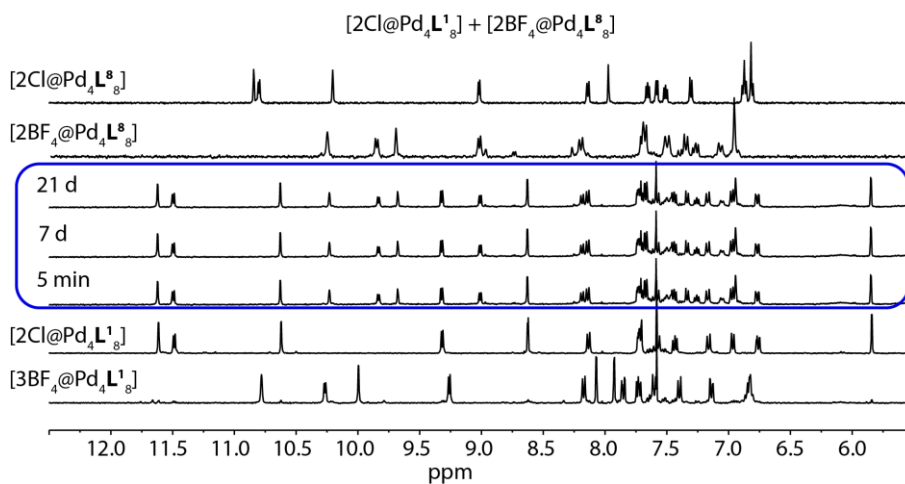


Figure 7.195 ^1H NMR spectra (400 MHz, CD_3CN , 298 K) of a mixture of $[2\text{Cl}@Pd_4L^1_8]$ and $[3\text{BF}_4@Pd_4L^8_8]$ after 5 min, 7 and 21 days (blue spare). No halide exchange between the two interpenetrated cages takes place.

7.7.1.2 $[2\text{Cl}@Pd_4L^x_8] + [3\text{BF}_4@Pd_4L^1_8]$ ($x = 6a-c, 7, 8$)

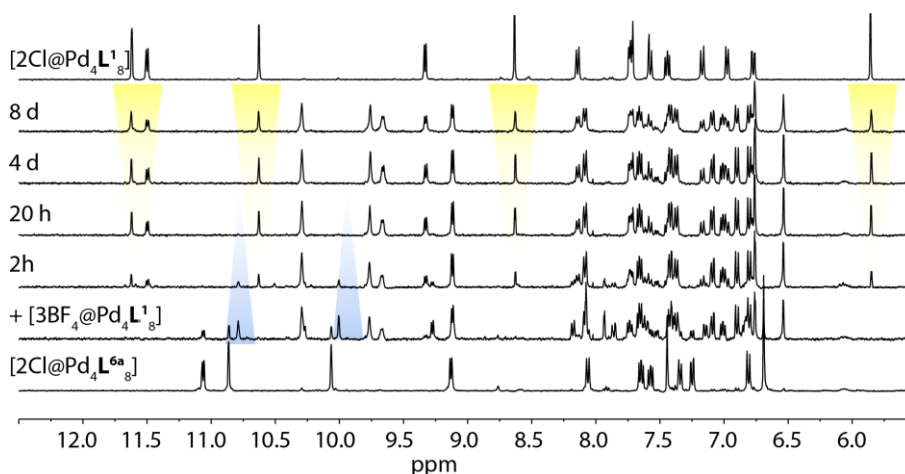


Figure 7.196 ^1H NMR spectra (400 MHz, CD_3CN , 298 K) of a mixture of $[2\text{Cl}@Pd_4L^{6a}_8]$ and $[3\text{BF}_4@Pd_4L^1_8]$ after 2 h, 20 h, 4 and 8 days. The intensity of the halide-containing $[3\text{BF}_4@Pd_4L^1_8]$ was decreased (highlighted in blue), while signals corresponding to the chloride-containing cage $[2\text{Cl}@Pd_4L^1_8]$ arise (yellow). After, 20 h only the coordination cages $[2\text{Cl}@Pd_4L^1_8]$ and $[3\text{BF}_4@Pd_4L^{6a}_8]$ are found in the mixture, indicating a halide exchange.

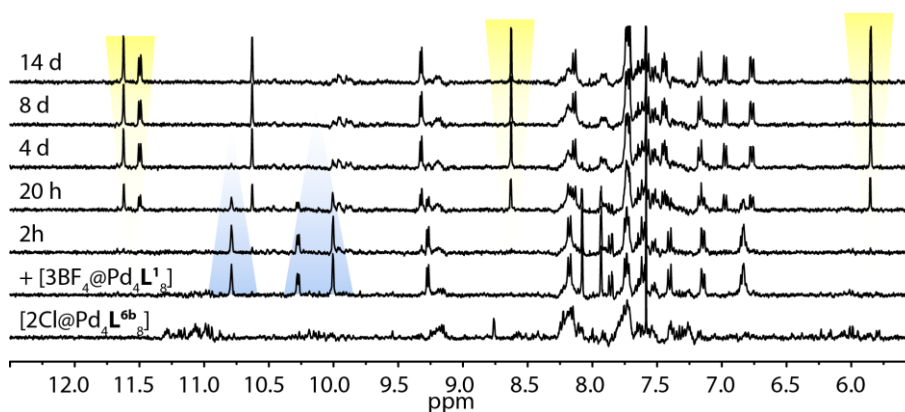


Figure 7.197 ^1H NMR spectra (400 MHz, CD_3CN , 298 K) of a mixture of $[2\text{Cl}@Pd_4L^{6b}_8]$ and $[3\text{BF}_4@Pd_4L^1_8]$ after 2 h, 20 h, 4, 8 and 14 days. After 4 days the composition of the mixture changes to $[2\text{Cl}@Pd_4L^1_8]$ and $[3\text{BF}_4@Pd_4L^{6b}_8]$, confirming a halide exchange. Highlighted: yellow: $[2\text{Cl}@Pd_4L^1_8]$, blue: $[3\text{BF}_4@Pd_4L^1_8]$.

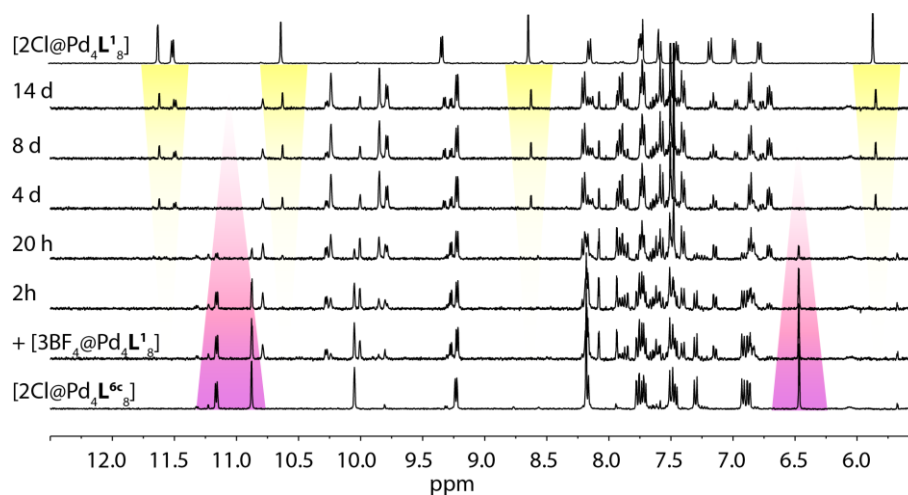


Figure 7.198 ^1H NMR spectra (400 MHz, CD_3CN , 298 K) of a mixture of $[\text{2Cl@Pd}_4\text{L}^{6\text{c}}]$ and $[\text{3BF}_4\text{@Pd}_4\text{L}^{\text{1s}}]$ after 2 h, 20 h, 4, 8 and 14 days. After 4 days the composition of the mixture completely changed to $[\text{2Cl@Pd}_4\text{L}^{\text{1s}}]$ and $[\text{3BF}_4\text{@Pd}_4\text{L}^{6\text{c}}]$, confirming a halide exchange. **Highlighted:** yellow: $[\text{2Cl@Pd}_4\text{L}^{\text{1s}}]$, purple: $[\text{2Cl@Pd}_4\text{L}^{6\text{c}}]$.

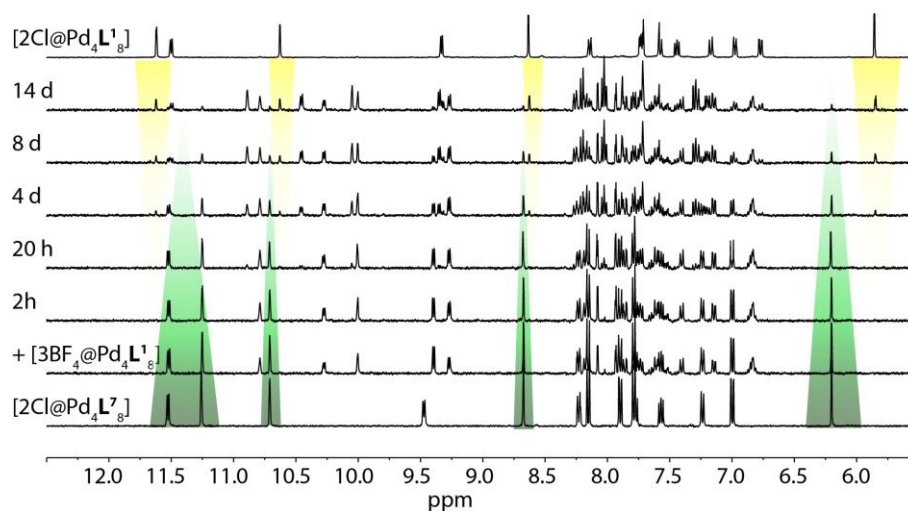


Figure 7.199 ^1H NMR spectra (400 MHz, CD_3CN , 298 K) of a mixture of $[\text{2Cl@Pd}_4\text{L}^{\text{7s}}]$ and $[\text{3BF}_4\text{@Pd}_4\text{L}^{\text{1s}}]$ after 2 h, 20 h, 4, 8 and 14 days. Slowly, the intensity of the $[\text{2Cl@Pd}_4\text{L}^{\text{7s}}]$ coordination cage was decreased (green), while the intensity of $[\text{2Cl@Pd}_4\text{L}^{\text{1s}}]$ increased. **Highlighted:** yellow: $[\text{2Cl@Pd}_4\text{L}^{\text{1s}}]$, green: $[\text{2Cl@Pd}_4\text{L}^{\text{7s}}]$.

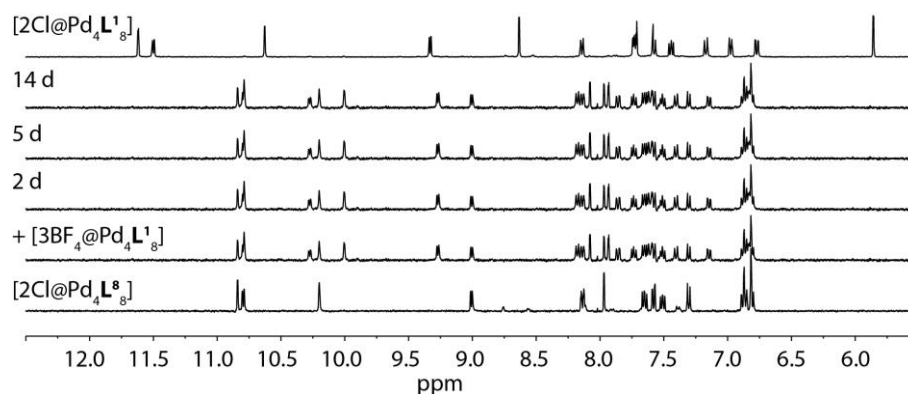


Figure 7.200 ^1H NMR spectra (400 MHz, CD_3CN , 298 K) of a mixture of $[\text{2Cl@Pd}_4\text{L}^{\text{8s}}]$ and $[\text{3BF}_4\text{@Pd}_4\text{L}^{\text{1s}}]$ after 2 h, 20 h, 4, 8 and 14 days. Since no change in the NMR spectra was observed, a halide exchange does occur between these two cage structures.

7.7.2 Chloride Competition Experiments

General Procedure

To a 1:1 mixture of two different tetrafluoroborate-containing cages $[3\text{BF}_4@Pd_4L^1_8]$ and $[3\text{BF}_4@Pd_4L^x_8]$ ($x = 6a-c, 7, 8$) (each 300 μL , 0.35 mM in CD_3CN) a solution of tetrabutylammonium chloride was added (17.5 mM, 1.0 eq.) and a ^1H NMR spectrum was recorded after briefly shaking the NMR tube. The reaction mixture was stored at room temperature and the progress of the reaction was monitored by successive NMR spectroscopy.

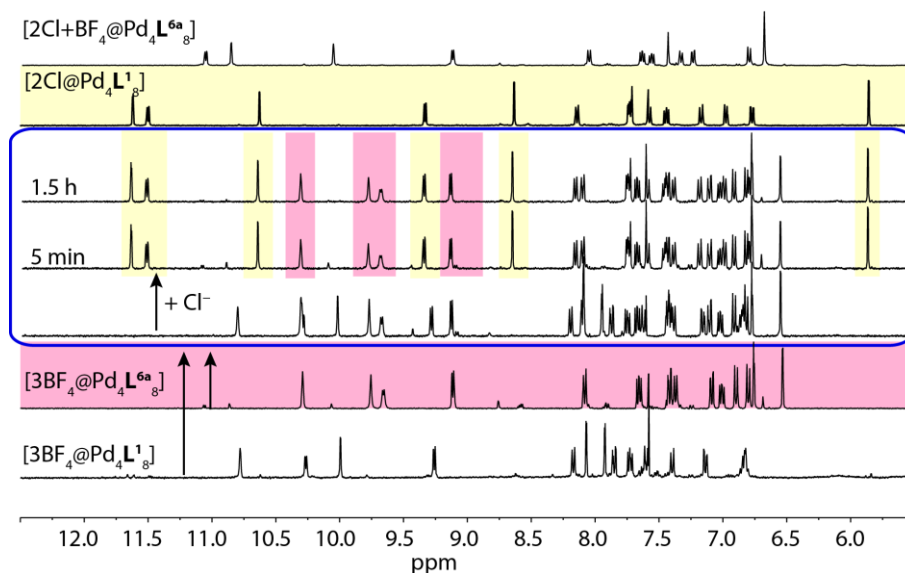


Figure 7.201 ^1H NMR spectra (400 MHz, CD_3CN , 298 K) of a mixture of $[3\text{BF}_4@Pd_4L^1_8]$ and $[3\text{BF}_4@Pd_4L^{6a}_8]$. Upon addition of chloride anions (1.0 eq.) only $[3\text{BF}_4@Pd_4L^1_8]$ transforms into $[2\text{Cl}@Pd_4L^1_8]$, while only a small amount of $[2\text{Cl}+\text{BF}_4@Pd_4L^1_8]$ is present. After 1.5 h, only two species can be observed in the NMR spectra ($[2\text{Cl}@Pd_4L^1_8]$ and $[3\text{BF}_4@Pd_4L^{6a}_8]$). Highlighted: yellow: $[2\text{Cl}@Pd_4L^1_8]$, pink: $[3\text{BF}_4@Pd_4L^{6a}_8]$.

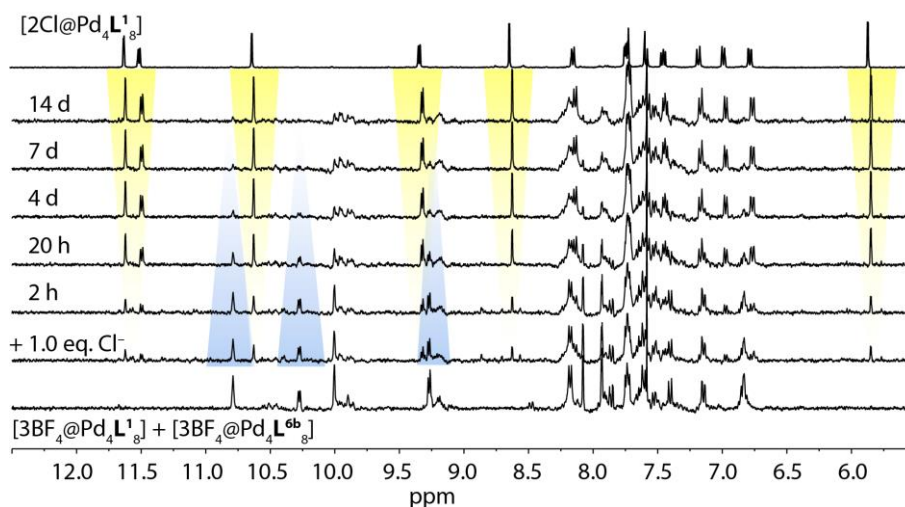


Figure 7.202 ^1H NMR spectra (400 MHz, CD_3CN , 298 K) of a mixture of $[3\text{BF}_4@Pd_4L^1_8]$ and $[3\text{BF}_4@Pd_4L^{6b}_8]$. After adding tetrabutylammonium chloride (1.0 eq.), the intensity of $[3\text{BF}_4@Pd_4L^1_8]$ over time decreases, while $[2\text{Cl}@Pd_4L^1_8]$ increases. Highlighted: yellow: $[2\text{Cl}@Pd_4L^1_8]$, blue: $[3\text{BF}_4@Pd_4L^1_8]$.

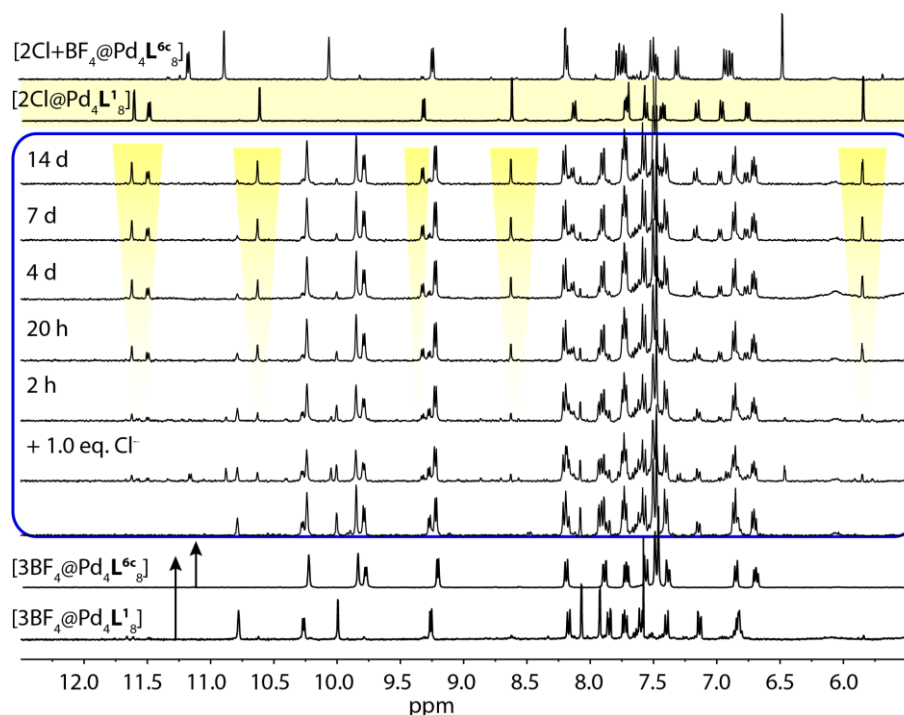


Figure 7.203 ^1H NMR spectra (400 MHz, CD_3CN , 298 K) of a mixture of $[3\text{BF}_4@Pd_4L^1_8]$ and $[3\text{BF}_4@Pd_4L^{6c}_8]$. After addition of tetrabutylammonium chloride (1.0 eq.), all possible structures were observed in the NMR spectrum. After 14 days, $[2\text{Cl}@Pd_4L^1_8]$ and $[3\text{BF}_4@Pd_4L^{6c}_8]$ were present in the solution (blue box). The affinity for halide anions in $[3\text{BF}_4@Pd_4L^1_8]$ is higher than in $[3\text{BF}_4@Pd_4L^{6c}_8]$. Highlighted: yellow: $[2\text{Cl}@Pd_4L^1_8]$.

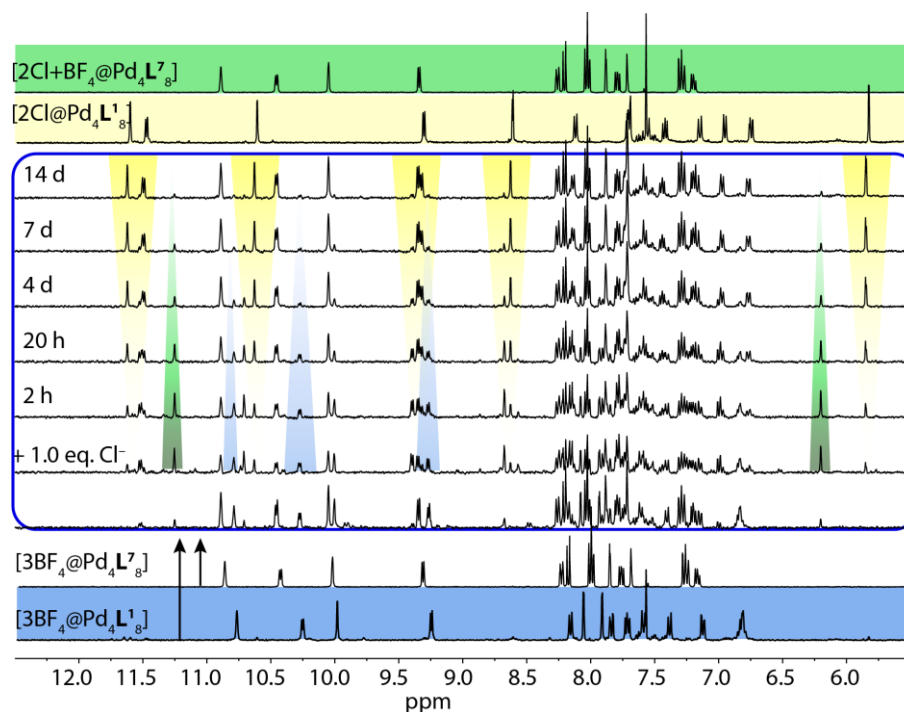


Figure 7.204 ^1H NMR spectra (400 MHz, CD_3CN , 298 K) of a mixture of $[3\text{BF}_4@Pd_4L^1_8]$ and $[3\text{BF}_4@Pd_4L^7_8]$. Upon addition of chloride anions (1.0 eq.) a mixture of all possible cage structure were observed ($[3\text{BF}_4@Pd_4L^1_8]$, $[3\text{BF}_4@Pd_4L^7_8]$, $[2\text{Cl}@Pd_4L^1_8]$ and $[2\text{Cl}+2\text{BF}_4@Pd_4L^7_8]$). Over time the intensity of $[2\text{Cl}@Pd_4L^1_8]$ increases, while the intensity of $[2\text{Cl}+2\text{BF}_4@Pd_4L^7_8]$ decreases, indicating a stronger affinity towards halide anions for the interpenetrated coordination cage containing ligand L^1 . Highlighted: yellow: $[2\text{Cl}@Pd_4L^1_8]$, blue: $[3\text{BF}_4@Pd_4L^1_8]$, green: $[2\text{Cl}+2\text{BF}_4@Pd_4L^7_8]$.

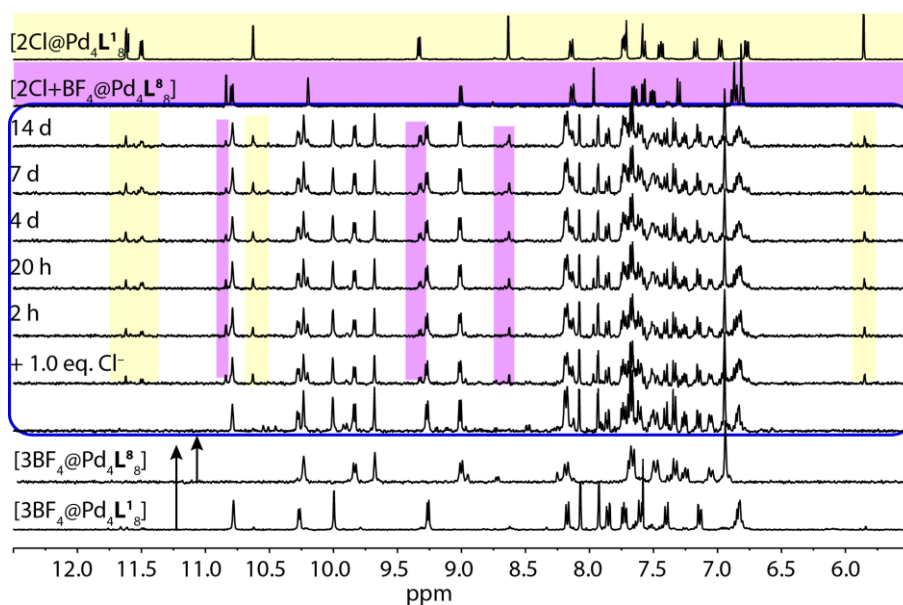


Figure 7.205 ^1H NMR spectra (400 MHz, CD_3CN , 298 K) of a mixture of $[3\text{BF}_4@Pd_4L^8_8]$ and $[3\text{BF}_4@Pd_4L^8_8]$. Upon addition of 1.0 equivalents of chloride anions, a mixture of all four possible structures were present in the mixture ($[3\text{BF}_4@Pd_4L^8_8]$, $[3\text{BF}_4@Pd_4L^1_8]$, $[2\text{Cl}@Pd_4L^8_8]$ and $[2\text{Cl}+\text{BF}_4@Pd_4L^8_8]$). No significant changes were observed over time. This indicates a similar binding affinity to the chloride anions of both interpenetrated coordination cages. Highlighted: yellow: $[2\text{Cl}@Pd_4L^1_8]$, pink: $[2\text{Cl}+\text{BF}_4@Pd_4L^8_8]$.

8 ABBREVIATIONS

Å	Ångström
°C	Celsius (centigrad)
BF ₄ ⁻	tetrafluoroborate anion
CHCl ₃	Chloroform
CD ₃ CN	Deuterated Acetonitrile
COSY	correlated spectroscopy
CV	cyclic voltammetry
d	day(s)
DABCO	1,4-Diazabicyclo[2.2.2]octan
DMSO	dimethylsulfoxid
DNA	deoxyribonucleic acid
DOSY	Diffusion-ordered spectroscopy
DTE	Dithienylethene
eq.	equivalent
ESI	electrospray ionization
EXSY	Exchange spectroscopy
h	hour
HR-MS	High resolution mass spectrometry
Hz	Hertz
IR	Infrared
<i>J</i>	coupling constant
K	Kelvin
L	Ligand
M	Metal
m/z	Mass-to-charge ratio
MeOH	Methanol
MHz	Megahertz
mM	mmol L ⁻¹
NBS	<i>N</i> -Bromosuccinimide
NIS	<i>N</i> -Iodosuccinimide
NEt ₃	triethylamine
nm	nanometer
NMR	nuclear magnetic resonance

NOESY	nuclear overhauser effect spectroscopy
PC	Packing coefficient
Pd	Palladium
PF ₆ ⁻	hexafluorophosphate anion
ppm	parts per million
Pt	Platinum
RNA	Ribonucleic acid
r.t.	room temperature
t	time
THF	tetrahydrofuran
TLC	thin layer chromatography
VT	various temperature
δ	chemical shift

9 LIST OF FIGURES

- Figure 1.1** Schematic representation of a) Dibenzo-[18]crown-6 complex by *Pederson*^[8] b) [2.2.2]cryptand complex by *Lehn*^[9] and c) spherand-6 complex by *Cram*.^[10]..... 1
- Figure 1.2** Schematic representation of different links and knots: a) Catenane, b) Borromean rings, c) trefoil knot, and d) Solomon knot..... 2
- Figure 1.3** Schematic representation of a) molecular shuttle^[22] and b) molecular muscle.^[23]..... 3
- Figure 1.4** Schematic representation of a molecular elevator.^[24] Addition of base causes the platform (red) to move to the lower level. Addition of acid results in a lift of the platform to the upper level..... 3
- Figure 1.5** Non-covalent interactions: a) ion-ion b) hydrogen bonding c) π - π and CH- π stacking. 4
- Figure 1.6** Types of self-assembly: a) strict self-assembly and b) directed (templated) self-assembly..... 6
- Figure 1.7** Schematic representation of a supramolecular host, which can encapsulate another molecule in its cavity and form a host-guest complex. 6
- Figure 1.8** Schematic representation of positive and negative allosteric effect..... 7
- Figure 1.9** Coordination geometries of metal cations including angles. *From left to right*: linear, trigonal planar, square planar, tetrahedral, trigonal bipyramidal and octahedral (M = metal cation). 8
- Figure 1.10** Schematic representation of Platonic solids: a) tetrahedron, b) octahedron c) cube, d) dodecahedron and e) icosahedron. 9
- Figure 1.11** a) Schematic representation of self-assembled architectures based on metal(II) cations (e.g. Pd^(II) or Pt^(II)) and banana-shaped bispyridyl ligands **L**. Resulting products are b) [M₃L₆] ring, c) [M₃L₆] double-trefoil knot, d) [M₄L₈] ring, e) [M₂L₃X₂] bowl (X = solvent), f) [M₂L₄] coordination cage, g) [M₄L₈] interpenetrated coordination cage, h) triple catenane {trans-[(MBr₂)₂L₂]₃ and i) rhombicuboctahedral sphere [M₂₄L₄₈]. 10
- Figure 1.12** Schematic representation of the self-assembly of interpenetrated [Pd₄L₈] coordination cages..... 11
- Figure 1.13** Schematic illustration of the formation of the monomeric [Pd₂1.1₄] coordination cage from benzophenone-based ligand **1.1** and Pd(NO₃)₂. Prolonged heating yielded the interpenetrated dimer [Pd₄1.1₈].^[72] *Color scheme*: **C**: light/dark gray; **N**: blue; **O**: red; **Pd**: orange. 12
- Figure 1.14** a) Addition of [Pd(CH₃CN)₄](BF₄)₂ to dibenzosuberone-based ligand **1.2** leads to formation of the thermodynamically unstable monomeric [Pd₂1.2₄] cage. Heating the mixture for 8 h at 70 °C gave the interpenetrated coordination cage [3BF₄@Pd₄1.2₈], which can

encapsulate chloride anions in its outer pockets in an allosteric fashion and form $[2\text{Cl}+\text{BF}_4@\text{Pd}_4\mathbf{1.2}_8]$. b) Ligand **1.3** forms the stable monomeric $[\text{Pd}_2\mathbf{1.3}_4]$ cage after addition of $[\text{Pd}(\text{CH}_3\text{CN})_4](\text{BF}_4)_2$. In presence of chloride anions (0.5 eq.) the interpenetrated dimer $[\text{Cl}@\text{Pd}_4\mathbf{1.3}_8]$ is formed, which can incorporate two perchlorate anions in the outer pockets.^[77]
Color scheme: **C**: light/dark gray; **N**: blue; **O**: red; **Cl**: yellow; **F**: green; **B**: salmon; **Pd**: orange. Hydrogens, solvent molecules and disordered counter anions were removed for clarity.**14**

Figure 1.15 Self-assembly of the carbazole-based ligand **1.4** to the monomeric $[\text{Pd}_2\mathbf{1.4}_4]$ cage. Addition of 1.5 eq. of halide (e.g. bromide or chloride) forms the dimer $[3\text{Br}@\text{Pd}_4\mathbf{1.4}_8]$ with all three pockets occupied by bromide anions. Upon addition of larger amounts of halide the triple catenane $[(\text{PdBr}_2)_6\mathbf{1.4}_6]$ is formed.^[65] *Color scheme*: **C**: light/dark gray; **N**: blue; **O**: red; **Br**: purple **F**: green; **B**: salmon; **Pd**: orange. Hydrogens, solvents and disordered counter anions have been removed for clarity.**15**

Figure 1.16 a) Self-assembly of phenothiazine-based interpenetrated coordination cages $[3\text{BF}_4@\text{Pd}_4\mathbf{1.5}_8]$, $[3\text{BF}_4@\text{Pd}_4\mathbf{1.6}_8]$ and $[3\text{BF}_4@\text{Pd}_4\mathbf{1.7}_8]$ in presence of palladium(II) cations. b) Addition of palladium(II) to anthraquinone-based ligand **1.8** results in the formation of the thermodynamic driven product $[3\text{BF}_4@\text{Pd}_4\mathbf{1.8}_8]$ cage.^[78] *Color scheme*: **C**: light/dark gray; **N**: blue; **O**: red; **F**: green; **B**: salmon; **S**: yellow; **Pd**: orange. Hydrogens, solvents molecules and disordered counter anions have been removed for clarity.**16**

Figure 2.1 Schematic representation of influencing factors of the ligand modification on the self-assembly of the interpenetrated $[\text{M}_4\text{L}_8]$ cage dimer.**18**

Figure 2.2 a) Front and b) side view of the preliminary X-ray crystal structure of ligand **L¹**. *Color scheme*: **C**: gray; **N**: blue; **O**: red.**19**

Figure 2.3 Synthesis of ligand **L¹** and assembly to cage $[3\text{BF}_4@\text{Pd}_4\mathbf{L}^1_8]$: i) 1-bromohexane, KO^tBu , THF; ii) NBS, DMF; iii) 3-ethynylpyridine, CuI , $[\text{Pd}(\text{PPh}_3)_2\text{Cl}_2]$, NEt_3 ; iv) $[\text{Pd}(\text{CH}_3\text{CN})_4](\text{BF}_4)_2$, CD_3CN , 24 h, 70 °C. Reprinted with permission from reference ^[87] Copyright © 2015 American Chemical Society.**20**

Figure 2.4 ¹H NMR spectra of (a) ligand **L¹** and b) the interpenetrated double cage $[3\text{BF}_4@\text{Pd}_4\mathbf{L}^1_8]$ (400 MHz, 298 K, CD_3CN). Reprinted with permission from reference ^[87] Copyright © 2015 American Chemical Society.**20**

Figure 2.5 ESI mass spectra of (a) $[3\text{BF}_4@\text{Pd}_4\mathbf{L}^1_8]$, (b) $[2\text{Cl}@\text{Pd}_4\mathbf{L}^1_8]$, and (c) $[2\text{Cl}+\text{C}_6\text{H}_6@\text{Pd}_4\mathbf{L}^1_8]$ (* = free host). Reprinted with permission from reference ^[87] Copyright © 2015 American Chemical Society.**21**

Figure 2.6 ¹H NMR titration (500 MHz, 298 K, CD_3CN) of $[3\text{BF}_4@\text{Pd}_4\mathbf{L}^1_8]$ with NBu_4Cl . Upon addition of two equivalents of chloride ions; $[3\text{BF}_4@\text{Pd}_4\mathbf{L}^1_8]$ transforms into $[2\text{Cl}@\text{Pd}_4\mathbf{L}^1_8]$, indicated by strong downfield shifts of the protons pointing inside the outer two cavities. Further addition of halide results in a strong downfield shift of protons f, caused by the interaction of chloride anions with the periphery of the cage. Addition of further amounts of NBu_4Cl leads to a partial decomposition of the double cage.**23**

- Figure 2.7** X-ray crystal structures of cage (a) $[3\text{BF}_4@\text{Pd}_4\text{L}^1_8]$, (b) $[2\text{Cl}+\text{benzene}@\text{Pd}_4\text{L}^1_8]$ and c) $[2\text{Cl}+\text{DABCO}@\text{Pd}_4\text{L}^1_8]$ with disordered DABCO guest. *Color scheme*: **C**: light/dark gray; **N**: blue; **O**: red; **Cl**: yellow; **F**: green; **B**: salmon; **Pd**: orange. Hydrogen atoms, some of the solvent molecules and disordered components have been removed for clarity. Benzene molecules were highlighted in red..... **25**
- Figure 2.8** Central pockets of the X-ray structure of the host-guest complexes $[2\text{Cl}+\text{NG}@\text{Pd}_4\text{L}^1_8]$ (NG = neutral guest) with a) benzene and b) one selected orientation of DACBO. While the benzene molecules is oriented perpendicular to the Pd_4 axis, the DABCO molecules stands upright in the central pocket of the interpenetrated coordination cage. Reproduced from reference ^[90] with permission from The Royal Society of Chemistry. **26**
- Figure 2.9** Schematic representation of formation of the interpenetrated coordination cage $[3\text{BF}_4@\text{Pd}_4\text{L}^1_8]$. Addition of halide anions triggers the exchange of neutral guest molecules inside the central pocket of the structure..... **28**
- Figure 2.10** ^1H NMR spectra of a) Ligand L^1 , b) double cage $[3\text{BF}_4@\text{Pd}_4\text{L}^1_8]$ (c) $[2\text{Cl}@\text{Pd}_4\text{L}^1_8]$ which forms upon addition of 2.0 eq. of *n*- NBu_4Cl , (d) $[2\text{Cl}+\text{C}_6\text{H}_6@\text{Pd}_4\text{L}^1_8]$ and e) $[2\text{Cl}+\text{C}_6\text{H}_{12}@\text{Pd}_4\text{L}^1_8]$ which form after addition of 20 eq. of neutral guest (benzene or cyclohexane; 400 MHz, 298 K, CD_3CN). Filled circle: free benzene, empty circle: encapsulated benzene (the cyclohexane signals are out of the depicted range, see Figure 7.84). Reprinted with permission from reference ^[87] Copyright © 2015 American Chemical Society. **28**
- Figure 2.11** Overview of tested neutral guest for encapsulation inside the chloride-containing coordination cages $[2\text{Cl}@\text{Pd}_4\text{L}^1_8]$. *Color Scheme*: **green**: encapsulation, **red**: no interaction between neutral guest and $[2\text{Cl}@\text{Pd}_4\text{L}^1_8]$ host, **blue**: disassembly of coordination cage under release of free ligand L^1 **29**
- Figure 2.12** Binding free enthalpies over guest volume for a) various guest families with different ring sizes, 3D structures and heteroatom content and b) selected series of cyclic alkanes and alkanones (packing coefficients are shown for the alkanes). Reprinted with permission from reference ^[90] Copyright © 2017 The Royal Society of Chemistry. **31**
- Figure 2.13** Uptake kinetics of (a) $[2\text{Cl}@\text{Pd}_4\text{L}^1_8]$ with benzene (black) and cyclohexane (red); (b) addition of norbornadiene to $[2\text{Cl}@\text{Pd}_4\text{L}^1_8]$ (green) and $[2\text{Br}+\text{BF}_4@\text{Pd}_4\text{L}^1_8]$ (blue). Reprinted with permission from reference ^[87] Copyright © 2015 American Chemical Society. **32**
- Figure 2.14** a) ^1H NMR competition experiment (400 MHz, 298 K, CD_3CN) of cyclohexane and benzene (each 20 equivalent) into the $[2\text{Cl}@\text{Pd}_4\text{L}^1_8]$ cage, b) kinetic plot of the competition experiment. *Color Scheme*: **black**: $[2\text{Cl}@\text{Pd}_4\text{L}^1_8]$, **blue**: $[\text{benzene}+2\text{Cl}@\text{Pd}_4\text{L}^1_8]$ and **red**: $[\text{cyclohexane}+2\text{Cl}@\text{Pd}_4\text{L}^1_8]$. Reproduced from Reference ^[90] with permission from The Royal Society of Chemistry. **33**
- Figure 2.15** ^1H NMR titrations (400 MHz, 298 K, CD_3CN) with silver(I) ions to a) $[2\text{Br}+\text{BF}_4@\text{Pd}_4\text{L}^1_8]$, b) $[2\text{Cl}@\text{Pd}_4\text{L}^1_8]$ and c) $[\text{norbornadiene}+2\text{Cl}@\text{Pd}_4\text{L}^1_8]$ **34**
- Figure 2.16** a) central pocket of the X-ray structure of $[\text{DABCO}+2\text{Cl}@\text{Pd}_4\text{L}^1_8]$ (top) and $[\text{benzene}+2\text{Cl}@\text{Pd}_4\text{L}^1_8]$ (bottom). b) calculated dispersion interaction density (DIDs) profile of

DABCO (top) compared to benzene (bottom; from X-ray structure [2Cl+benzene@Pd₄L¹₈]; CCDC 1035009). *Color scheme*: **red** = strong; **blue** = weak interacting regions. c) Correlation of experimental guest affinities listed in Table 2.2 with computed dispersion contributions. Reproduced from Reference ^[90] with permission from The Royal Society of Chemistry.....**36**

Figure 3.1 ¹H NMR spectra (400 MHz, 298 K, CD₃CN) of [2Cl@Pd₄L¹₈] and after the addition of 1,3-cyclohexadiene (10 eq.) and an incubation time of 1 day, 22 days and 94 days. 1 day after the addition, the neutral guest molecule is encapsulated inside the cationic cage and the host-guest complex [2Cl+C₆H₈@Pd₄L¹₈] is formed (highlighted in green). After 22 days a new set of signal arise (highlighted in orange), which is the main species after 94 days. This NMR spectrum corresponds to the host-guest complex [2Cl+C₆H₈O₂@Pd₄L¹₈].**40**

Figure 3.2 In the presence of the interpenetrated coordination cage [2Cl@Pd₄L¹₈], atmospheric oxygen and ambient light, 1,3-cyclohexadiene **3.1** transforms into 2,3-dioxabicyclo[2.2.2]oct-5-ene **3.2**.**41**

Figure 3.3 HR-MS of a) [2Cl@Pd₄L¹₈], b) [2Cl+C₆H₈@Pd₄L¹₈] and c) [2Cl+C₆H₈O₂@Pd₄L¹₈].**42**

Figure 3.4 Preliminary X-ray crystal structures of cage (a) [2Cl+C₆H₈@Pd₄L¹₈] and b) [2Cl+C₆H₈O₂@Pd₄L¹₈]. *Color scheme*: **C**: light/dark gray; **N**: blue; **O**: red; **Cl**: yellow; **F**: green; **B**: salmon; **Pd**: orange, **H**: white. For clarity, the hydrogen atoms of the coordination cage and some of the solvent molecules were removed. The depicted neutral guest molecules in the central pockets of the cavity are one of four symmetry equivalent positions.**44**

Figure 4.1 Photo-induced conformation switching of the dithienylethene-based ligands and their self-assembly to monomeric [Pd₂L₄] coordination cages. Figure redrawn and adapted from reference ^[81].**47**

Figure 4.2 a) Endohedral ligand modification, cage assembly and guest uptake, b) rotation of the endohedral functionality *via* a charge-separated transition state, c) electrostatic potential map of the endohedral functionalized ligand backbone, highlighted the partial charge separation and C=C double-bond weakening in the push-pull backbone (R=CN, COOEt, COO^tBu, COOPh). Figure redrawn and adapted from reference ^[116].**48**

Figure 4.3 Synthesis of ligand L² from ligand L¹.**49**

Figure 4.4 Self-assembly of the monomeric coordination cage [Pd₂L²₄]. Addition of a guest **G** to [Pd₂L²₄] leads to the formation of a host-guest complex [**G**@Pd₂L²₄]. Reprinted with permission from reference ^[107]. Copyright © 2016 Royal Society of Chemistry.**50**

Figure 4.5 ¹H NMR spectra of (a) free ligand L², (b) cage [Pd₂L²₄] and the corresponding host-guest complexes (c) [**G**¹@Pd₂L²₄] and (d) [**G**²@Pd₂L²₄] (400 MHz, 298 K, CD₃CN). The signals of the encapsulated guest molecules are highlighted in red. H_i, H_j and H_k represent outside (*exo*) and H_i['], H_j['] and H_k['] inside (*endo*) pointing hydrogen atoms of the adamantyl substituent with respect to the acridone backbone (compare Figure 4.9). Empty circle: [K(18-crown-6)]⁺. Reprinted with permission from reference ^[107]. Copyright © 2016 Royal Society of Chemistry.**50**

- Figure 4.6** ESI(+) mass spectra of (a) $[\text{Pd}_2\text{L}^2_4]$ coordination cage and the host-guest complexes: (b) $[\text{G}^1@ \text{Pd}_2\text{L}^2_4]$ and (c) $[\text{G}^2@ \text{Pd}_2\text{L}^2_4]$. Reprinted with permission from reference ^[107]. Copyright © 2016 Royal Society of Chemistry. 51
- Figure 4.7** ^1H - ^1H NOESY spectrum of ligand L^2 (500 MHz, CD_3CN) at different temperatures: a) 237 K, b) 253 K, c) 273 K and d) 298 K. The highlighted cross-peaks indicate the exchange between the inward (i', j' and k') and outward (i, j, k) pointing hydrogen atoms and are increasing with rising temperature. This indicates the adamantyl group is undergoing a rapid flipping motion. Reprinted with permission from reference ^[107]. Copyright © 2016 Royal Society of Chemistry. 52
- Figure 4.8** ^1H - ^1H NOESY spectra of cage $[\text{Pd}_2\text{L}^2_4]$ (500 MHz, CD_3CN , 0.5 s mixing time) at different temperatures: a) 288 K, b) 298 K, c) 308 K and d) 318 K. The intensities of the highlighted exchange signals between inward (i', j' and k') and outward (i, j, k) pointing protons are increasing with rising temperature. Reprinted with permission from reference ^[107]. Copyright © 2016 Royal Society of Chemistry. 53
- Figure 4.9** Flipping rate constants in ligand L^2 , coordination cage $[\text{Pd}_2\text{L}^2_4]$ and host-guest complexes $[\text{G}^1@ \text{Pd}_2\text{L}^2_4]$ and $[\text{G}^2@ \text{Pd}_2\text{L}^2_4]$. (a) Depiction of the degenerate minimum conformations of ligand L^2 and the calculated transition state. The flipping rate constant of the free ligand L^2 was experimentally determined to $k \approx 150 \text{ s}^{-1}$ at 298 K. (b) The flipping rate constant in the 'empty' $[\text{Pd}_2\text{L}^2_4]$ cage was determined to $k \approx 0.32 \text{ s}^{-1}$. After addition of bis-anionic guests G^1 or G^2 , the rate constant decreased to $k < 0.03 \text{ s}^{-1}$. Reprinted with permission from reference ^[107]. Copyright © 2016 Royal Society of Chemistry. 54
- Figure 4.10** Possible mechanism for flipping movement a) full decomplexation of one ligand b) one-side decomplexation c) concerted flipping and d) sequential flipping. 55
- Figure 4.11** Structures of various guest molecules encapsulated by coordination cage $[\text{Pd}_2\text{L}^2_4]$. Reprinted with permission from reference ^[107]. Copyright © 2016 Royal Society of Chemistry. 56
- Figure 4.12** Visualization of the central cavity of the $[\text{Pd}_2\text{L}^2_4]$ coordination cages: a) side and b) top view. Color scheme: C: gray; N: blue; Pd: orange, H: white. 57
- Figure 4.13** Cyclic voltammograms (CV) of the free guest G^1 (blue), the coordination cage $[\text{Pd}_2\text{L}^2_4]$ (black) and the host-guest complex $[\text{G}^1@ \text{Pd}_2\text{L}^2_4]$ (red) at 298 K, 0.07 mM, 0.1 M NBu_4PF_6 , scan rate 0.1 Vs^{-1} (potentials given against an Ag/AgNO_3 reference electrode; $[\text{AgNO}_3] = 0.001 \text{ M}$). While the cage $[\text{Pd}_2\text{L}^2_4]$ does not show a redox reaction in the examined potential range, the encapsulated guest G^1 shows an anodic shift of 123 mV for $E_{1/2}(\text{Fe}^{\text{II/III}})$ with respect to free guest G^1 . Inside the cationic coordination cage $[\text{Pd}_2\text{L}^2_4]$ it becomes more difficult to oxidize the guest. 58
- Figure 4.14** X-ray crystal structures of (a) $[\text{Pd}_2\text{L}^2_4]$, (b) $[\text{G}^1@ \text{Pd}_2\text{L}^2_4]$, (c) $[\text{G}^4@ \text{Pd}_2\text{L}^2_4]$ and (d) $[\text{G}^5@ \text{Pd}_2\text{L}^2_4]$. Color scheme: C, grey; N: blue; O: red; S: yellow; F: green; B: salmon; Pd: orange Fe: forest green. For clarity, solvent molecules and free (non encapsulated) anions are omitted. Appendix section 7.5.5 and CCDC numbers 1053080-83 contain details of the

- crystallographic data. Reprinted with permission from reference ^[107]. Copyright © 2016 Royal Society of Chemistry.....60
- Figure 4.15** Visualization of non-covalent host-guest interaction. *Hirshfeld* d_{norm} surfaces for the guest molecules in (a) $[G^1@Pd_2L^2_4]$ and (b) $[G^5@Pd_2L^2_4]$ (plotted with isovalues from -0.4 (red: short contact) to 1.4 (blue: long contact); red dotted lines and arrows indicate some close non-hydrogen bond interactions that are shorter than 3.0 Å). Below: Depiction of dispersion interaction densities (DIDs) between the guests and the surrounding adamantyl groups in (c) $[G^4@Pd_2L^2_4]$ and (d) $[G^5@Pd_2L^2_4]$ (red: high DID; blue: low DID). Reprinted with permission from reference ^[107]. Copyright © 2016 Royal Society of Chemistry.....63
- Figure 5.1** Schematic representation of different synthesized ligands L^1 , L^3 , L^4 and $L^{5a/b}$ with nitrogen-nitrogen distances d_{NN} . * Values obtained from a molecular model (DFT B3LYP/6-31g(d)); ** values obtained from X-ray structure analysis.^[137]66
- Figure 5.2** ¹H NMR spectra of a) ligand L^1 , b) monomeric $[Pd_2L^3_4]$ cage, c) ligand L^1 , d) interpenetrated coordination cage $[3BF_4@Pd_4L^1_8]$, e) ligand L^4 , f) interpenetrated cage $[3BF_4@Pd_4L^4_8]$, g) ligand L^{5a} and monomeric cage $[Pd_2L^{5a}_4]$. (500 MHz, CD₃CN, 323 K for a-f and 300 MHz, DMSO-d₆, 298 K for g and h).....67
- Figure 5.3** a) Side view and b) top view along the Pd-Pd axis of the DFT model of the monomeric cage $[Pd_2L^3_4]$. Color scheme: C: light/dark gray; N: blue; O: red; Pd: orange, H: white. Anions and solvents were omitted and the hexyl chain was substituted by a hydrogen atom.68
- Figure 5.4** HR-ESI-MS of a) $[Pd_2L^3_4]$, b) $[3BF_4@Pd_4L^1_8]$, c) $[3BF_4@Pd_4L^4_8]$ and d) $[Pd_2L^{5a}_4]$68
- Figure 5.5** Side view and top view along the Pd-Pd axis of the PM6 model of the interpenetrated cages a) $[3BF_4@Pd_4L^4_8]$ and b) $[2Cl@Pd_4L^4_8]$. Color scheme: C: light/dark gray; N: blue; O: red; Pd: orange, H: white; B: tan, F: green. Non-coordinating anions and solvents were omitted and the hexyl chain was substituted by a hydrogen atom.70
- Figure 5.6** Schematic representation of the formation of interpenetrated coordination cages from ligands L^1 and L^4 . While coordination cage $[3BF_4@Pd_4L^1_8]$ is activated by halide addition to encapsulate neutral guest molecules inside the central void of the cage, coordination cage $[3BF_4@Pd_4L^4_8]$ is not able to incorporate neutral guests molecules.72
- Figure 5.7** Side view and top view along the Pd-Pd axis of the PM6 models of a) the monomeric cage $[Pd_2L^{5a}_4]$ and b) the interpenetrated dimer $[2BF_4@Pd_4L^{5a}_8]$. Color scheme: C: light/dark gray; N: blue; O: red; Pd: orange, H: white B: tan, F: green. Anions and solvents were omitted and the hexyl chain was substituted by a hydrogen atom.73
- Figure 5.8** Schematic representation of cage formation from different ligands L and palladium(II) cations: a) ligand L^3 and monomeric cage $[Pd_2L^3_4]$ b) ligand L^1 and interpenetrated coordination cage $[3BF_4@Pd_4L^1_8]$; c) ligand L^4 and $[3BF_4@Pd_4L^4_8]$ cage; d) ligand L^{5a} and monomeric $[Pd_2L^{5a}_4]$ cage.75
- Figure 5.9** Possible scheme of an asymmetric ligand for future studies on self-assembly.76
- Figure 6.1** a) Chemical structures of banana-shaped ligands based on acridone (L^1), phenothiazine (L^{6a-c}), anthraquinone (L^7) and dibenzosuberone (L^8) backbones; b) schematic representation

- of the self-assembly of the interpenetrated coordination cage $[3\text{BF}_4@Pd_4L^x_8]$ from ligands L^x ($x = 1, 6a-c, 7, 8$) and palladium(II) cations. Two halide anions (e.g. chloride) were bound in the outer two pockets of the cage in an allosteric fashion with positive cooperativity. The anion exchange is accompanied by a compression of the supramolecular structure. **78**
- Figure 6.2** Schematic representation of an anion exchange between a chloride-containing interpenetrated coordination cage $[2\text{Cl}+\text{BF}_4@Pd_4L_8]$ (blue) and a tetrafluoroborate-containing cage $[3\text{BF}_4@Pd_4L_8]$ (red)..... **79**
- Figure 6.3** Kinetic measurements (400 MHz, CD_3CN , 298 K) of a) $[2\text{Cl}+\text{BF}_4@Pd_4L^{6a}_8]$ and $[3\text{BF}_4@Pd_4L^1_8]$ and b) $[2\text{Cl}+\text{BF}_4@Pd_4L^{6c}_8]$ and $[3\text{BF}_4@Pd_4L^1_8]$. The chloride exchange from $[2\text{Cl}+\text{BF}_4@Pd_4L^{6a}_8]$ is faster than from $[2\text{Cl}+\text{BF}_4@Pd_4L^{6c}_8]$ **80**
- Figure 6.4** Schematic representation of chloride binding competition experiments a) selective halide binding b) statistic halide binding. **81**
- Figure 7.1** ^1H NMR spectrum of *N*-hexylacridone (300 MHz, 298 K, CDCl_3). **85**
- Figure 7.2** ^{13}C NMR spectrum of *N*-hexylacridone (75 MHz, 298 K, CDCl_3). **86**
- Figure 7.3** ^1H NMR spectrum of dibromo-*N*-hexylacridone (300 MHz, 298 K, CDCl_3). **86**
- Figure 7.4** ^{13}C NMR spectrum of dibromo-*N*-hexylacridone (75 MHz, 298 K, CDCl_3). **87**
- Figure 7.5** ^1H NMR spectrum of diiodo-*N*-hexylacridone (300 MHz, 298 K, CDCl_3). **88**
- Figure 7.6** ^{13}C NMR spectrum of diiodo-*N*-hexylacridone (75 MHz, 298 K, CDCl_3). **88**
- Figure 7.7** ^1H NMR spectrum of Ligand L^1 (300 MHz, 298 K, CDCl_3). **89**
- Figure 7.8** ^{13}C NMR spectrum of Ligand L^1 (125 MHz, 298 K, CDCl_3). **89**
- Figure 7.9** ^1H NMR spectrum of interpenetrated coordination cage $[3\text{BF}_4@Pd_4L^1_8]$ (500 MHz, 298 K, CD_3CN)..... **90**
- Figure 7.10** ^1H , ^1H COSY spectrum of $[3\text{BF}_4@Pd_4L^1_8]$ (400 MHz, 298 K, CD_3CN). Correlation are highlighted..... **91**
- Figure 7.11** ^1H , ^1H NOESY spectrum of $[3\text{BF}_4@Pd_4L^1_8]$ (400 MHz, 298 K, CD_3CN). Correlation signals between different ligands were found between protons g'-a', f'-a and a'-d'. Non-assigned signals are COSY contacts. **91**
- Figure 7.12** ^{13}C NMR spectrum of interpenetrated coordination cage $[3\text{BF}_4@Pd_4L^1_8]$ (125 MHz, 298 K, CD_3CN)..... **92**
- Figure 7.13** ^{19}F NMR spectrum of interpenetrated coordination cage $[Pd_4L^1_8]$ (470 MHz, 298 K, CD_3CN). **92**
- Figure 7.14** ^1H NMR titration (400 MHz, 298 K, CD_3CN) of $[3\text{BF}_4@Pd_4L^1_8]$ with NBu_4F . Upon addition of two equivalents of fluorine anions; $[3\text{BF}_4@Pd_4L^1_8]$ transforms into $[2\text{F}@Pd_4L^1_8]$, indicated by strong downfield shifts of the protons pointing inside the outer two cavities. Further addition of halide results in a strong downfield shift of protons f, caused by the interaction of chloride anions with the outside of the cage. Addition of further amounts of NBu_4F leads decomposition of the cage and release of free ligand L^1 **93**
- Figure 7.15** ^1H NMR titration (500 MHz, 298 K, CD_3CN) of $[3\text{BF}_4@Pd_4L^1_8]$ with NBu_4Cl . Upon addition of two equiv. of chloride ions; $[3\text{BF}_4@Pd_4L^1_8]$ transforms into $[2\text{Cl}@Pd_4L^1_8]$, indicated

- by strong downfield shifts of the protons pointing inside the outer two cavities. Further addition of halide results in a strong downfield shift of protons f, caused by the interaction of chloride anions with the periphery of the cage. Addition of further amounts of NBu₄Cl leads to a partial decomposition of the double cage.....94
- Figure 7.16** ¹H NMR titration (500 MHz, 298 K, CD₃CN) of [3BF₄@Pd₄L₁₈] with NBu₄Br (17.5 mM). Upon addition of two equivalents of Br⁻, [3BF₄@Pd₄L₁₈] transforms into [2Br+BF₄@Pd₄L₁₈]. Excess addition leads to complete disaggregation of the double cage under release of free ligand L¹.....94
- Figure 7.17** ESI-MS of [2Br+BF₄@Pd₄L₁₈]. The peak at m/z = 724.71 corresponds to the hexacationic coordination cage containing chloride anions [2Cl@Pd₄L₁₈]⁶⁺.95
- Figure 7.18** ¹H NMR titration (400 MHz, 298 K, CD₃CN) of [3BF₄@Pd₄L₁₈] with NBu₄I (17.5 mM). Upon addition of two equivalents of iodine, [3BF₄@Pd₄L₁₈] transforms into [2I+BF₄@Pd₄L₁₈]. Excess addition leads to complete disaggregation of the double cage under release of free ligand L¹.....95
- Figure 7.19** ¹H NMR titration (400 MHz, 298 K, CD₃CN) of [3BF₄@Pd₄L₁₈] with NBu₄PF₆ (17.5 mM). No change in chemical shifts could be observed upon addition of NBu₄PF₆. Hence, no anion exchange between tetrafluoroborate and hexafluorophosphate occurs.96
- Figure 7.20** ¹H NMR titration (500 MHz, 298 K, CD₃CN) of [3BF₄@Pd₄L₁₈] with NBu₄ReO₄ (17.5 mM). No change in chemical shifts was observed upon addition of tetrabutylammonium perrhenate.....96
- Figure 7.21** ¹H NMR titration (500 MHz, 298 K, CD₃CN) of [3BF₄@Pd₄L₁₈] with NBu₄NO₃ (17.5 mM). After addition of 2 equivalents of nitrate, the [3BF₄@Pd₄L₁₈] transforms into [3BF₄+NO₃@Pd₄L₁₈]......97
- Figure 7.22** ¹H NMR titration (300 MHz, 298 K, CD₃CN) of [2Cl@Pd₄L₁₈] with AgBF₄ (17.5 mM). No spectral change or precipitation is observable. Even after the addition of 50 equiv. of silver(I) ions, only signals of the [2Cl@Pd₄L₁₈] species are visible. The decrease in intensity is due to dilution.....97
- Figure 7.23** ¹H NMR titration (300 MHz, 298 K, CD₃CN) of [2Br+BF₄@Pd₄L₁₈] with AgBF₄ (17.5 mM). Precipitation of encapsulated bromide from [2Br+BF₄@Pd₄L₁₈] after the addition of two equivalents of AgBF₄ under full recovery of [3BF₄@Pd₄L₁₈].98
- Figure 7.24** ¹H NMR titration (400 MHz, 298 K, CD₃CN) of [2F+BF₄@Pd₄L₁₈] with AgBF₄ (17.5 mM). formation of [3BF₄@Pd₄L₁₈] was observed.....98
- Figure 7.25** ¹H NMR titration (400 MHz, 298 K, CD₃CN) of [2I+BF₄@Pd₄L₁₈] with AgBF₄ (17.5 mM). Precipitation of AgI from [2Br+BF₄@Pd₄L₁₈] after the addition of two equivalents of AgBF₄ under full recovery of [3BF₄@Pd₄L₁₈].99
- Figure 7.26** ¹H NMR spectra (300 MHz, 298 K, CD₃CN) of [3BF₄@Pd₄L₁₈]. Addition of benzene (17.5 mM) does not result in any visible spectral changes. Same results were obtained with other neutral guest molecules.99

- Figure 7.27** ^1H NMR spectra (500 MHz, 296 K, CD_3CN) of $[\text{2Cl@Pd}_4\text{L}^1_8]$ and after the addition of various neutral guest molecules: b) benzene (8.7 eq.), c) 1,4-cyclohexadiene (8.7 eq.), d) 1,3-cyclohexadiene (8.7 eq.), e) cyclohexene (8.7 eq.), f) cyclohexane (8.7 eq.), g) toluene (8.7 eq.), h) norbornadiene (8.7 eq.), i) norbornene (8.7 eq.) and j) norbornene (8.7 eq.). Upon addition of an excess of neutral guest molecule, a new set of signals can be found in the ^1H NMR spectra. The NMR spectra were recorded after 14 d at 23 °C. 101
- Figure 7.28** ^1H NMR spectra (500 MHz, 296 K, CD_3CN) of a) empty host $[\text{2Cl@Pd}_4\text{L}^1_8]$ and different host-guest complexes: $[\text{X+Cl@Pd}_4\text{L}_8]$ with X= b) cyclopentane (8.7 eq.), c) cyclohexane (8.7 eq.), d) cycloheptane (8.7 eq.), e) cyclooctane (8.7 eq.), f) cyclooctadiene (8.7 eq.) g) cyclopentanol (8.7 eq.), h) cyclohexanol (8.7 eq.), i) cycloheptanol (8.7 eq.), j) phenol (8.7 eq.) k) trans-1,2 cyclohexanediol (8.7 eq.)..... 101
- Figure 7.29** ^1H NMR spectra (500 MHz, 296 K, CD_3CN) of a) empty host $[\text{2Cl@Pd}_4\text{L}^1_8]$ and different host-guest complexes: $[\text{X+Cl@Pd}_4\text{L}_8]$ with X= b) bromocyclopentane (8.7 eq.), c) chlorocyclopentane (8.7 eq.), d) 2-methylthiophene (8.7 eq.), e) thiophene (8.7 eq.), f) tetrahydrothiophene (8.7 eq.), g) furan (8.7 eq.), h) tetrahydrofuran (8.7 eq.), i) cyclobutanone (8.7 eq.), j) cyclopentanone (8.7 eq.), k) cyclohexanone (8.7 eq.) l) 1,4 cyclohexadione (8.7 eq.) and m) cycloheptanone (8.7 eq.). Cyclobutanone does not bind..... 102
- Figure 7.30** ^1H NMR spectra (500 MHz, 296 K, CD_3CN) of a) empty host $[\text{2Cl@Pd}_4\text{L}^1_8]$ and different host-guest complexes: $[\text{X+Cl@Pd}_4\text{L}_8]$ with X= b) tetrahydropyran (18.9 eq.), c) 1,3 dioxane (8.7 eq.), d) 1,4 dioxane (1.8 eq.), e) piperazine (1.8 eq.), f) DABCO (1.8 eq.), g) pyrazine (1.8 eq.), h) 2,3 dimethylpyrazine (8.7 eq.), i) 2,5 dimethylpyrazine (8.7 eq.) and j) pyridine (8.7 eq.). Addition of guest molecules a-g and j results in the formation of the host guest complex $[\text{X+Cl@Pd}_4\text{L}^1_8]$. In contrast, the neutral guest molecules 2,5-dimethylpyrazine and 2,3-dimethylpyrazine are not encapsulated inside the interpenetrated coordination cage, due to the steric bulk of the methyl groups..... 102
- Figure 7.31** ^1H NMR spectra (400 MHz, 296 K, CD_3CN) of $[\text{Cl@Pd}_4\text{L}^1_8]$ and after the addition of various neutral guest molecules: a) hexane (18.9 eq.), b) ferrocene (18.9 eq.), c) 3-hexylthiophene (18.9 eq.), d) adamantane (18.9 eq.), e) adamantone (18.9 eq.), f) azulene (18.9 eq.), g) coumarine (18.9 eq.), h) hexafluorobenzene (18.9 eq.), i) naphthalene (18.9 eq.), j) isooxazol (18.9 eq.), k) butyrolactone (100 eq.), l) [2.2]paracyclophane (8.9 eq.) and l) decalin(18.9 eq.), (mixture of cis and trans isomer, 20 eq.). No change in chemical shift could be observed after the addition of the neutral guest molecules and an equilibration time of 7-14 days. The shifting of proton signal f, is due to association of the guest molecule to the interpenetrated coordination cage from the outside..... 103
- Figure 7.32** ^1H NMR spectra (500 MHz, 296 K, CD_3CN) of $[\text{Cl@Pd}_4\text{L}^1_8]$ and after the addition of various neutral guest molecules: a) 1,2 dichlorobenzene (8.7 eq.), b) 1,3 dichlorobenzene (8.7 eq.), c) 1,4 dichlorobenzene (8.7 eq.), d) chlorobenzene(8.7 eq.), e) benzoquinone (8.7 eq.), f) 2,3-dimethylpyrazine (8.7 eq.), g) 2,5-dimethylpyrazine (18.9 eq.), h) trans 1,3 pentadiene (8.7 eq.), i) pyrrole (8.7 eq.), j) pyrazole (8.7 eq.), k) imidazole (8.7 eq.), l) 1-

methylimidazole (8.7 eq.), m) pyrrolidine (8.7 eq.) and n) ethylenediamine (8.7 eq.). No evidence of encapsulation of the neutral guests a-j was found after the equilibration time of 14 days, confirmed by no change in chemical shift in the ^1H NMR spectrum. In contrast, addition of neutral guest k-n resulted in the partial decomplexation of the interpenetrated coordination cage $[\text{Cl}@Pd_4L^1_8]$ and the release of free ligand L^1 (illustrated in the ^1H NMR spectra in blue).

The change in chemical shift of proton signal f, is due to association of the guest molecule from the outside of the interpenetrated coordination cage..... 103

Figure 7.33 ESI mass spectrum of $[2\text{Cl}+\text{norbornane}@Pd_4L^1_8]$	104
Figure 7.34 ESI mass spectrum of $[2\text{Cl}+\text{norbornene}@Pd_4L^1_8]$	104
Figure 7.35 ESI mass spectrum of $[2\text{Cl}+\text{norboradiene}@Pd_4L^1_8]$	104
Figure 7.36 ESI mass spectrum of $[2\text{Cl}+\text{toluene}@Pd_4L^1_8]$	104
Figure 7.37 ESI mass spectrum of $[2\text{Cl}+\text{cyclohexane}@Pd_4L^1_8]$	105
Figure 7.38 ESI mass spectrum of $[2\text{Cl}+\text{cyclohexene}@Pd_4L^1_8]$	105
Figure 7.39 ESI mass spectrum of $[2\text{Cl}+1,3\text{-cyclohexadiene}@Pd_4L^1_8]$	105
Figure 7.40 ESI mass spectrum of $[2\text{Cl}+1,4\text{-cyclohexadiene}@Pd_4L^1_8]$. * : $[2\text{Cl}@Pd_4L^1_8]$	105
Figure 7.41 ESI mass spectrum of $[2\text{Cl}+\text{benzene}@Pd_4L^1_8]$	106
Figure 7.42 ESI mass spectrum of $[2\text{Cl}+\text{phenol}@Pd_4L^1_8]$	106
Figure 7.43 ESI mass spectrum of $[2\text{Cl}+\text{cycloheptanol}@Pd_4L^1_8]$	106
Figure 7.44 ESI mass spectrum of $[2\text{Cl}+\text{cyclohexanol}@Pd_4L^1_8]$. * = $[2\text{Cl}@Pd_4L^1_8]$	106
Figure 7.45 ESI mass spectrum of $[2\text{Cl}+\text{cyclopentanol}@Pd_4L^1_8]$	107
Figure 7.46 ESI mass spectrum of $[2\text{Cl}+\text{cyclooctane}@Pd_4L^1_8]$	107
Figure 7.47 ESI mass spectrum of $[2\text{Cl}+1,4\text{ cyclooctadiene}@Pd_4L^1_8]$	107
Figure 7.48 ESI mass spectrum of $[2\text{Cl}+\text{cyclooctane}@Pd_4L^1_8]$	107
Figure 7.49 ESI mass spectrum of $[2\text{Cl}+\text{cycloheptane}@Pd_4L^1_8]$	108
Figure 7.50 ESI mass spectrum of $[2\text{Cl}+\text{cyclohexane}@Pd_4L^1_8]$	108
Figure 7.51 ESI mass spectrum of $[2\text{Cl}+\text{cyclopentane}@Pd_4L^1_8]$. Signals highlighted with * could be assigned to $[2\text{Cl}@Pd_4L^1_8]$	108
Figure 7.52 ESI mass spectrum of $[2\text{Cl}+\text{cycloheptanone}@Pd_4L^1_8]$. Signals highlighted with * could be assigned to $[2\text{Cl}@Pd_4L^1_8]$	108
Figure 7.53 ESI mass spectrum of $[2\text{Cl}+\text{cyclohexanone}@Pd_4L^1_8]$. Signals highlighted with * could be assigned to $[2\text{Cl}@Pd_4L^1_8]$	109
Figure 7.54 ESI mass spectrum of $[2\text{Cl}+\text{cyclopentanone}@Pd_4L^1_8]$. Signals highlighted with * could be assigned to $[2\text{Cl}@Pd_4L^1_8]$	109
Figure 7.55 ESI mass spectrum of $[2\text{Cl}+\text{tetrahydrofuran}@Pd_4L^1_8]$	109
Figure 7.56 ESI mass spectrum of $[2\text{Cl}+\text{tetrahydrothiophene}@Pd_4L^1_8]$. *: $[Pd_4L^1_8]$ cage; • Encapsulation of the oxidation product of tetrahydrothiophene $\text{C}_4\text{H}_8\text{SO}$	109
Figure 7.57 ESI mass spectrum of $[2\text{Cl}+\text{thiophene}@Pd_4L^1_8]$. Signals highlighted with * correspond to the interpenetrated coordination cage without any encapsulated neutral guest $([2\text{Cl}@Pd_4L^1_8])$	110

Figure 7.58 ESI mass spectrum of [2Cl+2-methylthiophene@Pd ₄ L ¹ ₈]. Signals highlighted with * correspond to the host ([2Cl@Pd ₄ L ¹ ₈]).	110
Figure 7.59 ESI mass spectrum of [2Cl+chlorocyclopentane@Pd ₄ L ¹ ₈]. Signals highlighted with * could be assigned to [2Cl@Pd ₄ L ¹ ₈].	110
Figure 7.60 ESI mass spectrum of [2Cl+bromocyclopentane@Pd ₄ L ¹ ₈]. Signals highlighted with * could be assigned to [2Cl@Pd ₄ L ¹ ₈].	110
Figure 7.61 ESI mass spectrum of [2Cl+pyridine@Pd ₄ L ¹ ₈]. Signals highlighted with * could be assigned to [2Cl@Pd ₄ L ¹ ₈].	111
Figure 7.62 ESI mass spectrum of [2Cl+pyrazine@Pd ₄ L ¹ ₈]. Signals highlighted with * could be assigned to [2Cl@Pd ₄ L ¹ ₈].	111
Figure 7.63 ESI mass spectrum of [2Cl+DABCO@Pd ₄ L ¹ ₈].	111
Figure 7.64 ESI mass spectrum of [2Cl+1,3-dioxane@Pd ₄ L ¹ ₈].	111
Figure 7.65 ESI mass spectrum of [2Cl+1,3-dioxane@Pd ₄ L ¹ ₈].	112
Figure 7.66 ESI mass spectrum of [2Cl+tetrahydropyran@Pd ₄ L ¹ ₈].	112
Figure 7.67 ¹ H NMR spectra (500 MHz, 298 K) of [2Cl@Pd ₄ L ¹ ₈] in different solvents: CD ₃ CN, acetone-d ⁶ , CD ₂ Cl ₂ , CDCl ₃ , DMF-d ⁸ , DMSO-d ⁶ , THF-d ⁸ and D ₂ O. The interpenetrated coordination cage is soluble in acetone and methylene chloride and does not decompose even after several days in these solvents. In DMF and DMSO the coordination cage decomposed over a period of 24 h. Furthermore no or only low intensity signals could be found in the ¹ H NMR spectrum of the coordination cage in THF, D ₂ O and CDCl ₃ , accompanied by a dull appearance of the sample.	113
Figure 7.68 ¹ H NMR spectra (400 MHz, 298 K, CD ₃ CN) of [2Br+BF ₄ @Pd ₄ L ¹ ₈] and after the addition of various neutral guest molecules: benzene (8.7 eq.), cyclohexane (8.7 eq.), cyclopentane (8.7 eq.), norbornene (8.7 eq.), norbornadiene (8.7 eq.), toluene (87 eq.), and 1,3 dichlorobenzene (8.7 eq.). Benzene, norbornadiene and toluene could be found to be encapsulated inside the central pocket of the interpenetrated coordination cage. No clear indication of host-guest formation could be found for the other neutral guest, due to the appearance of signals from other not-identified species.	113
Figure 7.69 ¹ H NMR spectra (400 MHz, 298 K, CD ₃ CN) of [2Br+BF ₄ @Pd ₄ L ¹ ₈] before and after the addition of various neutral guest molecules: thiophene (8.7 eq.), 2-methylthiophene (8.7 eq.), cyclopentanone (8.7 eq.), hexane (8.7 eq.), norbornene (8.7 eq.), DABCO (87 eq.) ferrocene (8.7 eq.) and 3-hexylthiophene. Under the tested conditions, only thiophene, 2-methylthiophene, DABCO and norbornene seemed to be encapsulated in the coordination cage. Due to the large amount of undefined side products, a clear assignment is with not possible.	114
Figure 7.70 ESI-MS of [2Br+benzene@Pd ₄ L ¹ ₈].	114
Figure 7.71 ESI-MS of [2Br+cyclohexane@Pd ₄ L ¹ ₈].	114
Figure 7.72 ESI-MS of [2Br+toluene@Pd ₄ L ¹ ₈].	115

- Figure 7.73** ^1H NMR spectra (400 MHz, 298 K, CD_3CN) of $[\text{2F@Pd}_4\text{L}^1_8]$ before and after the addition of various neutral guest molecules: b) benzene (8.7 eq.), c) norbornadiene (8.7 eq.), d) coumarin (8.7 eq.) and e) azulene (8.7 eq.). While benzene and norbornadiene can be encapsulated inside the central cavity of the coordination cage, azulene and coumarin do not bind. **115**
- Figure 7.74** ^1H NMR spectra (400 MHz, 298 K, CD_3CN) of $[\text{2F@Pd}_4\text{L}^1_8]$ before and after the addition of various neutral guest molecules: b) benzene (8.7 eq.), c) norbornadiene (8.7 eq.), d) cyclopentane (8.7 eq.) and e) tetrahydrofuran (8.7 eq.). After addition of neutral guest new sets of signal appear, indicating a change of the system. However, no clear indication of neutral guest uptake could be drawn from the NMR spectrum..... **115**
- Figure 7.75** Kinetic measurement of $[\text{2Cl@Pd}_4\text{L}^1_8]$ with benzene (10 eq.) and cyclohexane (10 eq.). Color Scheme: **Red**: [cyclohexane+ $2\text{Cl@Pd}_4\text{L}^1_8$], **black**: $[\text{2Cl@Pd}_4\text{L}^1_8]$ and **blue**: [benzene+ $2\text{Cl@Pd}_4\text{L}^1_8$]. **116**
- Figure 7.76** Addition of benzene (20 eq.) and cyclohexane (20 eq.) to $[\text{2Cl@Pd}_4\text{L}^1_8]$: a) ^1H NMR spectra (400 MHz, CD_3CN , 298 K) of $[\text{2Cl@Pd}_4\text{L}^1_8]$ and upon addition of the neutral guest after 5 min, 1 h, 3 h and 6 h. b) Kinetic plot (% vs. t) of encapsulation process. Color Scheme: **red**: [cyclohexane+ $2\text{Cl@Pd}_4\text{L}^1_8$], **black**: $[\text{2Cl@Pd}_4\text{L}^1_8]$, **blue**: [benzene+ $2\text{Cl@Pd}_4\text{L}^1_8$], **black circle**: encapsulated benzene, **black square**: encapsulated cyclohexane. **116**
- Figure 7.77** Temperature dependence of the ^{19}F NMR-signals of $[\text{3BF}_4\text{@Pd}_4\text{L}^1_8]$ (470 MHz, CD_3CN). Shoulders are due to the $^{10}\text{BF}_4^-$ isotope. **118**
- Figure 7.78** Temperature dependence of the ^{19}F NMR-signal of the $[\text{2Cl@Pd}_4\text{L}^1_8]$ sample (470 MHz, CD_3CN). The only detectable signal represents the free BF_4^- anion. No signals for encapsulated BF_4^- were observed. Shoulders are due to the $^{10}\text{BF}_4^-$ isotope. **118**
- Figure 7.79** Temperature dependence of the ^{19}F NMR-signals of $[\text{2Br+BF}_4\text{@Pd}_4\text{L}^1_8]$ (470 MHz, CD_3CN). Besides the signal of the free BF_4^- anion, one signal representing the BF_4^- anion encapsulated in the central pocket was detected. **119**
- Figure 7.80** ^{19}F , ^{19}F EXSY spectrum (470 MHz, CD_3CN , 0.5 s mixing period) of $[\text{3BF}_4\text{@Pd}_4\text{L}^1_8]$ at room temperature. Exchange is observed between the peaks assigned to the two BF_4^- ions occupying the outer cavities of the double cage and free BF_4^- . No exchange is observed between the BF_4^- encapsulated in the inner pocket of the double cage and free BF_4^- **119**
- Figure 7.81** ^{19}F , ^{19}F -EXSY spectrum (470 MHz, CD_3CN , 0,5 s mixing period) of $[\text{2Br+BF}_4\text{@Pd}_4\text{L}^1_8]$ at room temperature illustrating, that there is no exchange between free BF_4^- and the one encapsulated inside the central pocket of the double cage. **120**
- Figure 7.82** Superposition of ^{19}F (red) and ^1H (blue) DOSY NMR spectra of $[\text{2Br+BF}_4\text{@Pd}_4\text{L}^1_8]$ shows encapsulation of one BF_4^- ion inside the double cage (logD = logarithm of diffusion coefficient)..... **120**
- Figure 7.83** ^1H , ^1H NOESY spectrum of $[\text{2Cl+benzene@Pd}_4\text{L}^1_8]$ (500 MHz, CD_3CN , 298 K). Contacts between encapsulated benzene and the double cage are highlighted with red circles. **121**

- Figure 7.84** ^1H , ^1H NOESY spectrum of $[\text{2Cl}+\text{cyclohexane}@\text{Pd}_4\text{L}^1_8]$ (500 MHz, CD_3CN , 298 K). Contacts between encapsulated guest and host are highlighted with red circles. 121
- Figure 7.85** Preliminary X-ray structures of Ligand L^1 . Position of the pyridine residues are disorderd, resulting in two possible conformations a) and b).]. *Color scheme*: **C**: grey; **N**: blue; **O**: red. 122
- Figure 7.86** Packing of ligand L^1 in the crystal structure. Close π - π interaction between different ligands can be found. *Color scheme*: **C**: grey; **N**: blue; **O**: red. 123
- Figure 7.87** Packing of $[\text{2Cl}+\text{C}_6\text{H}_6@\text{Pd}_4\text{L}^1_8]$ (a) view along the b-axis, (b) view along the c-axis. 126
- Figure 7.88** The asymmetric unit of the $[\text{2Cl}+\text{DABCO}@\text{Pd}_4\text{L}^1_8]^{6+}$, with all non-hydrogen atoms shown as ellipsoids at the 50% probability level. *Color scheme*: **C**: gray; **N**: blue; **O**: red; **Cl**: yellow; **Pd**: orange, **H**: white, **F**: green, **B**: salmon. 127
- Figure 7.89** Cyclic voltammograms of the a) free ligand L^1 (0.5 mM) b) $[\text{3BF}_4@\text{Pd}_4\text{L}^1_8]$ cage (0.125 mM) c) $[\text{2Cl}@\text{Pd}_4\text{L}^1_8]$ (0.25 mM) d) $[\text{2Br}+\text{BF}_4@\text{Pd}_4\text{L}^1_8]$ (0.25 mM) e) NBu_4Cl (1.0 mM) and f) NBu_4Br (1.0 mM) at 298 K, in 0.1 M $n\text{Bu}_4\text{NBF}_4/\text{CH}_3\text{CN}$ solution, scan rate 0.1 Vs^{-1} . Potentials given against an Ag/AgNO_3 reference electrode; $[\text{AgNO}_3] = 0.001 \text{ M}$ 129
- Figure 7.90** Visualization of the cavities of the interpenetrated coordination cages: a) $[\text{3BF}_4@\text{Pd}_4\text{L}^1_8]$ and b) $[\text{2Cl}+\text{NG}@\text{Pd}_4\text{L}^1_8]$ (the encapsulated neutral guest (NG) is DABDO). The cavity boundaries of the central pocket of the interpenetrated coordination structure are depicted as blue solids. *Color scheme*: **C**: gray; **N**: blue; **O**: red; **Pd**: orange, **H**: white. 131
- Figure 7.91** a) double cage structure, b) model used for the cage system in the calculations. The ligands were truncated (C-C bonds replaced by C-H) and the bottom and lower planes were removed. The chlorides in the inner pockets were kept in order to neutralize part of the charge. 132
- Figure 7.92** DID (Dispersion Interaction Density) plots of some selected guests inside the cavity, *color coding*: **red** = strong; **blue** = weak interacting regions): a) cyclopentane, b) cyclohexane, c) pyridine, d) norbornadiene, e) phenol, f) 1,4-dioxane, g) DABCO, h) 2-methylthiophene, i) benzene. 133
- Figure 7.93** ^1H - ^1H COSY NMR spectrum of $[\text{2Cl}+\text{C}_6\text{H}_8\text{O}_2@\text{Pd}_4\text{L}^1_8]$. (600 MHz, CD_3CN , 298 K) in the aromatic region. Cross peaks are assigned and highlighted for the encapsulated guest (light blue) and free guest (dark blue). 134
- Figure 7.94** ^1H - ^1H NOESY spectrum of $[\text{2Cl}+\text{C}_6\text{H}_8\text{O}_2@\text{Pd}_4\text{L}^1_8]$. (600 MHz, CD_3CN , 298 K). Cross peaks between the encapsulated guest molecule ($\text{C}_6\text{H}_8\text{O}_2$) and the proton signals pointing towards the inner pocket of the coordination cage (H_a , H_g) are highlighted with a black circle. 134
- Figure 7.95** ^1H NMR spectra (400 MHz, 298 K, CD_3CN) of $[\text{2Cl}@\text{Pd}_4\text{L}^1_8]$ before and after the addition of 1,3-cyclohexadiene (20 eq.) and incubation time of 1 day, 34 days and 94 days in the absence of oxygen (sample stored in a nitrogen glove box). After 1 day the host-guest

- complex $[\text{Cl}+\text{C}_6\text{H}_8@\text{Pd}_4\text{L}^1_8]$ is formed (marked in green). In the absence of oxygen, no formation of the host-guest complex $[\text{Cl}+\text{C}_6\text{H}_8\text{O}_2@\text{Pd}_4\text{L}^1_8]$ was observed..... 135
- Figure 7.96** ^1H NMR spectra (400 MHz, 298 K, CD_3CN) of $[\text{2Cl}@\text{Pd}_4\text{L}^1_8]$ and after the addition of 1,3-cyclohexadiene (10 eq.) after an incubation time of 1 day, 34 days and 94 days in the absence of ambient light (sample wrapped in aluminum foil and stored in a light-tight cupboard). After 1 day the host-guest complex $[\text{Cl}+\text{C}_6\text{H}_8@\text{Pd}_4\text{L}^1_8]$ is formed (marked in green) and a transformation in the $[\text{Cl}+\text{C}_6\text{H}_8\text{O}_2@\text{Pd}_4\text{L}^1_8]$ complex is not observed under exclusion of ambient light..... 135
- Figure 7.97** ^1H NMR spectra (400 MHz, 298 K, CD_3CN) of $[\text{2Cl}@\text{Pd}_4\text{L}^1_8]$ and after the addition of 1,4-cyclohexadiene (10 eq.) at different time intervals after the addition (1 day, 22 days and 81 days.). After 1 day the host-guest complex $[\text{Cl}+\text{C}_6\text{H}_8@\text{Pd}_4\text{L}^1_8]$ is formed. No further change could be observed after an extended period of time. 136
- Figure 7.98** ^1H NMR spectra (400 MHz, 298 K, CD_3CN) of 1,3-cyclohexadiene in CD_3CN in the presence of atmospheric oxygen and ambient light. No significant changes could be observed in the ^1H NMR spectra after 56 days. 136
- Figure 7.99** ^1H NMR spectra (500 MHz, 298 K, CD_3CN) of 1,3-cyclohexadiene (50 eq.) and tetrabutylammonium chloride in the presence of atmospheric oxygen and ambient light. No significant changes could be observed in the ^1H NMR spectra after 40 days. 136
- Figure 7.100** ^1H NMR spectra (500 MHz, 298 K, CD_3CN) of 1,3-cyclohexadiene (50 eq.) and $[\text{Pd}(\text{CH}_3\text{CN})_4](\text{BF}_4)_2$ in the presence of atmospheric oxygen and ambient light. The presence of the palladium source seems to lead to a decomposition of the cyclohexadiene. 137
- Figure 7.101** ^1H NMR spectra (500 MHz, 298 K, CD_3CN) of $[\text{3BF}_4@\text{Pd}_4\text{L}^1_8]$ before and after the addition of 1,3-cyclohexadiene in the presence of atmospheric oxygen and ambient light. After several days, new signals could be observed which corresponds to the oxidation product $\text{C}_6\text{H}_8\text{O}_2$ 137
- Figure 7.102** ^1H NMR spectra (500 MHz, 298 K, CD_3CN) of $[\text{2Cl}+\text{C}_6\text{H}_8\text{O}_2@\text{Pd}_4\text{L}^1_8]$ before and after the addition of 1,3-cyclohexadiene in the presence of atmospheric oxygen and ambient light. No exchange of the peroxide $\text{C}_6\text{H}_8\text{O}_2$ and 1,3-cyclohexadiene in the central pocket of the coordination cage was observed after 3 days. 138
- Figure 7.103** ^1H NMR spectrum of Ligand L^2 (500 MHz, 298 K, CD_3CN). 139
- Figure 7.104** ^1H - ^1H COSY spectrum of ligand L^2 (500 MHz, CD_3CN , 273 K). Cross Peaks are highlighted: Blue: pyridine hydrogen, red: acridone protons, green: adamantyl hydrogen atoms. 140
- Figure 7.105** ^{13}C NMR spectrum of Ligand L^2 (75 MHz, 273 K, CD_3CN). 140
- Figure 7.106** ^1H NMR spectrum of coordination cage $[\text{Pd}_4\text{L}^2_4]$ (500 MHz, 298 K, CD_3CN). 141
- Figure 7.107** ^1H NMR spectrum of coordination cage $[\text{Pt}_4\text{L}^2_4]$ (500 MHz, 298 K, CD_3CN). 142
- Figure 7.108** HR-ESI MS of $[\text{Pt}_2\text{L}^2_4]$ 142
- Figure 7.109** Structure of used (bis)-anionic guest molecules G^{1-9} 143

- Figure 7.110** ^1H NMR titration (400 MHz, 298 K, CD_3CN) of $[\text{Pd}_2\text{L}^2_4]$ with $(\text{NBu}_4)_2\text{G}^1$. Upon addition of one equivalent of guest G^1 the $[\text{Pd}_2\text{L}^2_4]$ cage transforms into $[\text{G}^1@ \text{Pd}_2\text{L}^2_4]$. Excess addition of G^1 leads to disaggregation of the cage..... 144
- Figure 7.111** ^1H NMR titration (400 MHz, 298 K, CD_3CN) of $[\text{Pd}_2\text{L}^2_4]$ with $[\text{K}^+@ (18\text{-crown-6})]_2\text{G}^1$. Upon addition of one equivalent of guest G^1 the $[\text{Pd}_2\text{L}^2_4]$ cage transforms into $[\text{G}^1@ \text{Pd}_2\text{L}^2_4]$. The blue circle indicates the crown ether signal..... 144
- Figure 7.112** ^1H NMR titration (400 MHz, 298 K, CD_3CN) of $[\text{Pd}_2\text{L}^2_4]$ with $(\text{NBu}_4)_2\text{G}^2$. Upon addition of 1.0 eq. of guest G^2 the $[\text{Pd}_2\text{L}^2_4]$ cage transforms into the host-guest complex $[\text{G}^2@ \text{Pd}_2\text{L}^2_4]$. Excess addition of G^2 leads to precipitation and disassembly of the cage. Signals of encapsulated guest G^2 are highlighted in magenta..... 145
- Figure 7.113** ^1H NMR titration (400 MHz, 298 K, CD_3CN) of $[\text{Pd}_2\text{L}^2_4]$ with $[\text{K}^+@ (18\text{-crown-6})]_2\text{G}^2$. Upon addition of 1.0 eq. of guest G^2 to the $[\text{Pd}_2\text{L}^2_4]$ cage the new host guest complex $[\text{G}^2@ \text{Pd}_2\text{L}^2_4]$ is formed. The blue circle indicates the crown ether signal..... 145
- Figure 7.114** ^1H NMR titration (400 MHz, 298 K, CD_3CN) of $[\text{Pd}_2\text{L}^2_4]$ with $(\text{NBu}_4)_2\text{G}^3$. Excess addition of guest molecules leads to decomposition of the host guest complex. 146
- Figure 7.115** ESI-MS of $[\text{G}^3@ \text{Pd}_2\text{L}^2_4]$ 146
- Figure 7.116** ^1H NMR titration (400 MHz, 298 K, CD_3CN) of $[\text{Pd}_2\text{L}^2_4]$ with $(\text{NBu}_4)_2\text{G}^4$. Upon addition of 1.0 eq. of guest G^4 to the $[\text{Pd}_2\text{L}^2_4]$ cage the new species $[\text{G}^4@ \text{Pd}_2\text{L}^2_4]$ is formed. 147
- Figure 7.117** ESI-MS of $[\text{G}^4@ \text{Pd}_2\text{L}^2_4]$ 147
- Figure 7.118** ^1H NMR titration (400 MHz, 298 K, CD_3CN) of $[\text{Pd}_2\text{L}^2_4]$ with $(\text{NBu}_4)_2\text{G}^5$. Upon addition of one equivalent of guest G^5 to the $[\text{Pd}_2\text{L}^2_4]$ cage the new species $[\text{G}^5@ \text{Pd}_2\text{L}^2_4]$ is formed. Excess addition of G^5 leads to complete disaggregation of the cage and precipitation was observed in the NMR tube. 148
- Figure 7.119** ESI-MS of $[\text{G}^5@ \text{Pd}_2\text{L}^2_4]$ 148
- Figure 7.120** ^1H NMR titration (400 MHz, 298 K, CD_3CN) of $[\text{Pd}_2\text{L}^2_4]$ with $(\text{NBu}_4)_2\text{G}^6$ 149
- Figure 7.121** ^1H NMR titration (400 MHz, 298 K, CD_3CN) of $[\text{Pd}_2\text{L}^2_4]$ with $(\text{NBu}_4)_2\text{G}^7$. The chemical shifts of the inward pointing protons changed gradually, due to fast exchange of the guest. 149
- Figure 7.122** ^1H NMR titration (400 MHz, 298 K, CD_3CN) of $[\text{Pd}_2\text{L}^2_4]$ with $(\text{NBu}_4)_2\text{G}^8$. The chemical shifts of the inward pointing protons changed gradually, due to fast exchange of the guest. 150
- Figure 7.123** ^1H NMR titration (400 MHz, 298 K, CD_3CN) of $[\text{Pd}_2\text{L}^2_4]$ with $(\text{NBu}_4)_2\text{G}^9$. The chemical shifts of the inward pointing protons changed gradually, due to fast exchange of the guest. 150
- Figure 7.124** ^1H NMR titration (400 MHz, 298 K, CD_3CN) of $[\text{Pd}_2\text{L}^3_4]$ with $[\text{K}^+-(18\text{-crown-6})]_2\text{G}^1$. Gradual shifting of the signals indicates fast exchange. The exchange rate of a 1:1 sample of $[\text{Pd}_2\text{L}^2_4]$ and $[\text{G}^1@ \text{Pd}_2\text{L}^2_4]$ could be given through line shape fitting to $k \sim 90\text{s}^{-1}$ 151
- Figure 7.125** ^1H - ^1H NOESY spectrum of ligand L^2 (500 MHz, CD_3CN) at different temperatures: a) 237 K, b) 253 K, c) 273 K and d) 298 K. The cross-peaks indicate the exchange between the

inward (i', j' and k') and outward (i, j, k) pointing hydrogen atoms and are increasing with rising temperature. This indicates the adamantyl group is undergoing a rapid flipping motion. ... **152**

Figure 7.126 ^1H - ^1H NOESY spectrum of $[\text{Pd}_2\text{L}^2_4]$ (900 MHz, 298 K, mixing time 0.5 s, CD_3CN). Exchange signals between related protons are highlighted as followed: i/i' (green), j/j' (blue), k/k' (red). Integration of the inner and outer adamantyl signals determined the exchange rate as 0.32 s^{-1} **153**

Figure 7.127 ^1H - ^1H NOESY spectra of cage $[\text{Pd}_2\text{L}^2_4]$ (500 MHz, CD_3CN , 0.5 s mixing time) at different temperatures: a) 288 K, b) 298 K, c) 308 K and d) 318 K. The intensities of the highlighted exchange signals between inward (i', j' and k') and outward (i, j, k) pointing protons are increasing with rising temperature. **153**

Figure 7.128 ^1H - ^1H NOESY spectra of cage $[\text{Pt}_2\text{L}^2_4]$ (500 MHz, CD_3CN , 0.5 s mixing time) at different temperatures: a) 298 K, b) 308 K, and c) 318 K. The intensities of the highlighted exchange signals between inward (i', j' and k') and outward (i, j, k) pointing protons are increasing with rising temperature. The rate constants could be determined through integration: 298 K: $k = 0.13\text{ s}^{-1}$, 308 K: $k = 0.22\text{ s}^{-1}$ and 318 K: $k = 0.35\text{ s}^{-1}$ **155**

Figure 7.129 ^1H - ^1H NOESY spectrum of host-guest compound $[\text{G}^1@ \text{Pd}_2\text{L}^2_4]$ (900 MHz, 298 K, CD_3CN , 0.5 s mixing time). The exchange signals between inside and outside pointing protons are highlighted: green = i/i' (2.05 ppm/1.19 ppm) and red = k/k' (1.42 ppm/1.17 ppm). Integration gave the exchange rate as: $k < 0.03\text{ s}^{-1}$. The exchange signals between j/j' (1.44 ppm/1.32 ppm) overlap with the diagonal baseline. **156**

Figure 7.130 ^1H - ^1H NOESY spectrum of host-guest compound $[\text{G}^2@ \text{Pd}_2\text{L}^2_4]$ (900 MHz, 298 K, CD_3CN , 0.5 s mixing time). Exchange signals between inside and outside pointing protons are highlighted: green = i/i' (1.54 ppm/1.14 ppm) and red = k/k' (1.35 ppm/1.02 ppm). Integration gave the exchange rate as $k < 0.02\text{ s}^{-1}$. The exchange signals between j/j' (1.33 ppm/1.25 ppm) are hidden in the diagonal base line. **156**

Figure 7.131 ^1H - ^1H NOESY spectrum of host-guest compound $[\text{G}^2@ \text{Pd}_2\text{L}^2_4]$ (900 MHz, 298 K, CD_3CN). Highlighted are NOE contacts between guest G^2 and inside pointing adamantyl protons i', j' and k' (pink) and intramolecular contacts between the ligands (blue). **157**

Figure 7.132 ^1H - ^1H EXSY spectrum (500 MHz, 298 K, CD_3CN , 0.1 s mixing period) of a 1:1 mixture of cage $[\text{Pd}_2\text{L}^2_4]$ (green) and host-guest compound $[\text{G}^1@ \text{Pd}_2\text{L}^2_4]$ (red). Exchange is observed between the empty cage and the host-guest complex (highlighted in blue). The rate constant could be determined *via* integration to $k_{\text{in}} = k_{\text{out}} \sim 7\text{ s}^{-1}$ (due to signal broadening this value has an error of $\sim 20\%$). **157**

Figure 7.133 ^1H - ^1H EXSY spectrum (500 MHz, 298 K, CD_3CN , 0.1 s mixing period) of a 1:1 mixture of cage $[\text{Pd}_2\text{L}^2_4]$ (green) and host-guest compound $[\text{G}^2@ \text{Pd}_2\text{L}^2_4]$ (red). Exchange is observed between the empty cage and the host-guest complex (highlighted in blue). The rate constant could be determined *via* integration to $k_{\text{in}} = k_{\text{out}} \sim 4\text{ s}^{-1}$ **158**

- Figure 7.134** ^1H - ^1H EXSY spectrum (500 MHz, 298 K, CD_3CN , 0.1 s mixing period) of a 3:1 mixture of ligand L^2 (blue) and cage $[\text{Pd}_2\text{L}^2_4]$ (orange) at room temperature, illustrating that there is no exchange between free ligand and the cage within the mixing time..... **158**
- Figure 7.135** a) ^1H NMR titration (500 MHz, 298 K, CD_3CN) with 1 eq., 5 eq, 20 eq. and 100 eq. of pyridine to the $[\text{Pd}_2\text{L}^2_4]$ cage. After the addition of 20 eq. of pyridine the cage is disassembled to free ligand and $\text{Pd}(\text{pyridine})_4$. Color code = blue: $[\text{Pd}_2\text{L}^2_4]$, green: free pyridine, orange: free ligand L^2 , yellow: $\text{Pd}(\text{pyridine})_4$. b-d) ^1H - ^1H NOESY spectra (500 MHz, 298 K, CD_3CN , 0.5 s mixing period) of the $[\text{Pd}_2\text{L}^2_4]$ cage (b), with 1 eq. (c), or 5 eq. pyridine (d). The intensity of the highlighted exchange signals between inward (i', j' and k') and outward (i, j, k) pointing protons do not change with increasing pyridine concentration, indicating pyridine is not acting as a competitive ligand and has no influence on the exchange rate of the adamantyl group. The exchange rate could be determined as $k = 0.32 \text{ s}^{-1}$ for $[\text{Pd}_2\text{L}^2_4]$, and 0.25 s^{-1} for $[\text{Pd}_2\text{L}^2_4] + 1 \text{ eq. pyridine}$ and $[\text{Pd}_2\text{L}^2_4] + 5.0 \text{ eq. pyridine}$ **159**
- Figure 7.136** Partially clipped space-filling representations of $[\text{Pd}_2\text{L}^2_4]$ from the side (left; one ligand removed) and the top (right). The adamantyl groups are highlighted in dark grey and the internal counter anions have been removed. **161**
- Figure 7.137** Element-mapped Hirshfeld surfaces and fingerprints of (a) $[\text{G}^1@[\text{Pd}_2\text{L}^2_4]]$ and (b) $[\text{G}^5@[\text{Pd}_2\text{L}^2_4]]$ **162**
- Figure 7.138** Schematic synthetic route leading to acridone based ligands L^1 , L^3 , L^4 , L^{5a} and L^{5b} .
i) 3-pyridineboronic acid 1,3-propanediol ester, $\text{K}_3\text{PO}_4 \cdot \text{H}_2\text{O}$, $\text{Pd}(\text{PPh}_3)_4$, dioxane/ H_2O ; ii) 3-ethynylpyridine, CuI , $[\text{Pd}(\text{PPh}_3)_2\text{Cl}_2]$, NEt_3 ; iii) 3-(4-pinacolboronic acid-phenyl)pyridine, $\text{K}_3\text{PO}_4 \cdot \text{H}_2\text{O}$, $\text{Pd}(\text{PPh}_3)_4$, dioxane/ H_2O ; iv) 3-((4-ethynyl)phenyl)pyridine, CuI , $[\text{Pd}(\text{PPh}_3)_2\text{Cl}_2]$, NEt_3 ; v) 3-((4-phenylboronic acid pinacol ester)ethynyl)pyridine, $\text{K}_3\text{PO}_4 \cdot \text{H}_2\text{O}$, $\text{Pd}(\text{PPh}_3)_4$, dioxane/ H_2O **165**
- Figure 7.139** ^1H NMR spectrum of ligand L^3 (500 MHz, 298 K, CDCl_3)..... **166**
- Figure 7.140** ^1H - ^1H COSY spectrum of ligand L^3 (600 MHz, CD_3CN , 298 K). Cross Peaks are highlighted..... **167**
- Figure 7.141** ^{13}C NMR spectrum of ligand L^3 (125 MHz, 298 K, CD_3CN). **167**
- Figure 7.142** ^1H NMR spectrum of coordination cage $[\text{Pd}_2\text{L}^3_4]$ (500 MHz, 298 K, CD_3CN)..... **168**
- Figure 7.143** ^1H - ^1H COSY spectrum of $[\text{Pd}_2\text{L}^3_4]$ cage (600 MHz, CD_3CN , 298 K). Cross Peaks are assigned..... **168**
- Figure 7.144** ^{13}C NMR spectrum of coordination cage $[\text{Pd}_2\text{L}^3_4]$ (125 MHz, 298 K, CD_3CN). **168**
- Figure 7.145** HR-MS of $[\text{Pd}_4\text{L}^3_8]$ in CD_3CN with a variable number of tetrafluoroborate counter anions. The isotopic pattern of the measured peaks match perfectly with the calculation. . **169**
- Figure 7.146** ^1H NMR titration (400 MHz, 298 K, CD_3CN) of $[\text{Pd}_2\text{L}^3_4]$ with $(\text{NBu}_4)_2\text{G}^8$. Upon addition of one equivalent of guest G^8 the $[\text{Pd}_2\text{L}^3_4]$ no significant changes could be observed in the ^1H NMR spectra, indicating no encapsulation inside the monomeric coordination cage. Excess addition of G^8 leads to disassembly of the cage..... **169**

- Figure 7.147** ^1H NMR titration (400 MHz, 298 K, CD_3CN) of $[\text{Pd}_2\text{L}^3_4]$ with $(\text{NBu}_4)_2\text{G}^9$. Upon addition of one equivalent of guest G^9 to the $[\text{Pd}_2\text{L}^3_4]$ no significant changes could be observed in the ^1H NMR spectra, indicating no encapsulation inside the monomeric coordination cage. Excess addition of G^8 leads to disassembly of the cage. 170
- Figure 7.148** ^1H NMR spectrum of ligand L^4 (500 MHz, 298 K, CDCl_3). 171
- Figure 7.149** ^1H - ^1H COSY spectrum of ligand L^4 (500 MHz, 298 K, CD_3CN). Cross Peaks are indicated. 171
- Figure 7.150** ^{13}C NMR spectrum of ligand L^4 (125 MHz, 298 K, CD_3CN). 172
- Figure 7.151** ^1H NMR spectrum of interpenetrated coordination cage $[\text{Pd}_4\text{L}^4_8]$ (500 MHz, 298 K, CD_3CN). 173
- Figure 7.152** ^1H - ^1H COSY spectrum of interpenetrated coordination cage $[3\text{BF}_4@ \text{Pd}_4\text{L}^4_8]$ (500 MHz, 333 K, CD_3CN). Cross Peaks are indicated. 173
- Figure 7.153** ^1H - ^1H NOESY spectrum of $[\text{Pd}_4\text{L}^4_8]$ cage (500 MHz, 333 K, CD_3CN). Cross Peaks are indicated. 174
- Figure 7.154** Temperature dependence of the ^1H NMR-signals of $[3\text{BF}_4@ \text{Pd}_4\text{L}^4_8]$ (400 MHz, CD_3CN). Increase in temperature leads to a sharpening of the signals, due to free rotation of the benzyl group. 174
- Figure 7.155** Temperature dependence of the ^{19}F -NMR-signals of $[3\text{BF}_4@ \text{Pd}_4\text{L}^4_8]$ (470 MHz, CD_3CN). Shoulders are due to the $^{10}\text{BF}_4^-$ isotope. 175
- Figure 7.156** HR-MS of $[3\text{BF}_4@ \text{Pd}_4\text{L}^4_8]$ with a variable number of tetrafluoroborate counter anions. The isotopic pattern of the measured peaks matches the calculation. 175
- Figure 7.157** ^1H NMR spectrum of interpenetrated coordination cage $[3\text{PF}_6@ \text{Pd}_4\text{L}^4_8]$ (500 MHz, 298 K, CD_3CN). 176
- Figure 7.158** HR-MS of $[3\text{PF}_6@ \text{Pd}_4\text{L}^4_8]$ with a variable number of tetrafluoroborate counter anions. 176
- Figure 7.159** ^1H NMR titration (400 MHz, 298 K, CD_3CN) of $[3\text{BF}_4@ \text{Pd}_4\text{L}^4_8]$ with NBu_4Cl . Upon addition of two equiv. of chloride ions; $[3\text{BF}_4@ \text{Pd}_4\text{L}^4_8]$ transforms into $[2\text{Cl}@ \text{Pd}_4\text{L}^4_8]$, as indicated by strong downfield shifts of the protons pointing inside the outer two cavities. Further addition of halide results in a strong downfield shift of protons f, caused by the interaction of chloride anions with the periphery of the cage. Addition of up to 30 equivalents of NBu_4Cl leads to disassembly of the cage and the release of free ligand. This could be observed by eye due to the formation of a yellow precipitate inside the NMR tube (the solubility of the ligand in CD_3CN is low). 176
- Figure 7.160** HR-MS of $[2\text{Cl}@ \text{Pd}_4\text{L}^4_8]$ with a variable number of tetrafluoroborate counter anions. 177
- Figure 7.161** ^{19}F NMR of $[2\text{Cl}@ \text{Pd}_4\text{L}^4_8]$ (540 MHz, 298 K, CD_3CN). The signal at -151.70 ppm represents free BF_4 in solution. 177
- Figure 7.162** ^1H NMR titration (500 MHz, 323 K, CD_3CN) of $[3\text{BF}_4@ \text{Pd}_4\text{L}^5_8]$ with NBu_4Br . Upon addition of two equivalents of bromide ions $[3\text{BF}_4@ \text{Pd}_4\text{L}^4_8]$ transforms into $[2\text{Br}@ \text{Pd}_4\text{L}^4_8]$,

- indicated by the appearance of a new set of signals at a downfield shift. Further addition of halide anions results in a strong downfield shift of protons f, caused by the interaction of bromide anions with the periphery of the cage. Disassembly of the cage and precipitation of the free ligand was observed after the addition of 25 eq. of halide anion..... 177
- Figure 7.163** HR-MS of $[2\text{Br}@Pd_4L^4_8]$ with a variable number of tetrafluoroborate counter anions. 178
- Figure 7.164** ^{19}F NMR of $[2\text{Br}@Pd_4L^4_8]$ (540 MHz, CD_3CN , 298 K). The signal at -151.70 ppm represents free BF_4 in solution..... 178
- Figure 7.165** ^1H NMR titration (400 MHz, 335 K, CD_3CN) of $[3\text{BF}_4@Pd_4L^4_8]$ with NBu_4I . Upon addition of two equivalents of iodine anions the $[3\text{BF}_4@Pd_4L^4_8]$ cage transforms into $[2\text{I}@Pd_4L^4_8]$, indicated by strong downfield shifts of the protons pointing inside the outer two cavities. Further addition of halide results in a strong downfield shift of protons f, caused by the interaction of chloride anions with the periphery of the cage. 178
- Figure 7.166** HR-MS of $[2\text{I}+\text{BF}_4@Pd_4L^4_8]$ with a variable number of tetrafluoroborate counter anions..... 179
- Figure 7.167** ^{19}F NMR of $[2\text{I}+\text{BF}_4@Pd_4L^4_8]$ (564 MHz, CD_3CN , 298 K). The signal at -151.70 ppm represents free BF_4 in solution..... 179
- Figure 7.168** ^1H NMR titration (400 MHz, 298 K, CD_3CN) of $[3\text{BF}_4@Pd_4L^4_8]$ with NBu_4ClO_4 . No change in chemical shift could be observed in the ^1H NMR spectra. 179
- Figure 7.169** ^1H NMR titration (400 MHz, 298 K, CD_3CN) of $[3\text{BF}_4@Pd_4L^4_8]$ with NBu_4PF_6 . No change in chemical shift occur. Thus, tetrafluoroborate is not exchanged by hexafluorophosphate anions..... 180
- Figure 7.170** ^1H NMR titration (500 MHz, 335 K, CD_3CN) of $[3\text{BF}_4@Pd_4L^4_8]$ with NBu_4N_3 180
- Figure 7.171** ^1H NMR titration (500 MHz, 335 K, CD_3CN) of $[3\text{BF}_4@Pd_4L^4_8]$ with NBu_4NO_3 181
- Figure 7.172** ^1H NMR titration (500 MHz, 335 K, CD_3CN) of $[3\text{BF}_4@Pd_4L^4_8]$ with NBu_4SCN 181
- Figure 7.173** ^1H NMR titration (400 MHz, 335 K, CD_3CN) of $[3\text{PF}_6@Pd_4L^4_8]$ with NBu_4BF_4 182
- Figure 7.174** ^1H NMR titration (500 MHz, 323 K, CD_3CN) of $[2\text{Cl}@Pd_4L^4_8]$ with AgBF_4 (17.5 mM). No change in chemical shift could be observed. Even after the addition of 100 equiv. of silver(I) ions, only signals of the $[2\text{Cl}@Pd_4L^4_8]$ species are visible. The decrease in intensity is due to dilution..... 182
- Figure 7.175** ^1H NMR titration (500 MHz, 323 K, CD_3CN) of $[2\text{Br}@Pd_4L^4_8]$ with AgBF_4 (17.5 mM). No formation of the tetrafluoroborate anion-containing cage $[2\text{BF}_4@Pd_4L^4_8]$ was observed. 183
- Figure 7.176** ^1H NMR titration (500 MHz, 323 K, CD_3CN) of $[2\text{I}+\text{BF}_4@Pd_4L^4_8]$ with AgBF_4 (17.5 mM). Excess addition of silver(I) cations lead to precipitation of AgI under full recovery of $[3\text{BF}_4@Pd_4L^4_8]$ 183
- Figure 7.177** ^1H NMR spectra (400 MHz, 335 K, CD_3CN) of a) $[3\text{BF}_4@Pd_4L^4_8]$, b) $[2\text{Cl}@Pd_4L^4_8]$, and addition of different neutral guest molecules to the chloride-containing interpenetrated coordination cage $[2\text{Cl}@Pd_4L^4_8]$: c) benzene (20 eq.) d) naphthalene (10 eq.) e) azulene

(10 eq.), f) adamantane (10 eq.), g) ferrocene (10 eq.), h) [2.2]paracyclophane (10 eq.), i) 1,5-cyclooctadiene (10 eq.), j) DABCO (10 eq.) and an equilibration time of 3 weeks. No change in chemical shift could be observed after the addition of the neutral guest molecules to the [2Cl@Pd₄L₈⁴] cage, indicating no incorporation inside the interpenetrated coordination cage.

- 184
- Figure 7.178** ¹H NMR spectra (400 MHz, 298 K, CD₃CN) of a) [2Br@Pd₄L₈⁴] before and after the addition of different neutral guest molecules: b) benzene (20 eq.), d) DABCO (20 eq.), d) ferrocene (20 eq.), and e) [2.2] paracyclophane (20 eq.). No significant change in the NMR spectra could be overserved after several days at room temperature..... 184
- Figure 7.179** ¹H NMR spectrum of ligand L^{5a} (500 MHz, 298 K, CDCl₃). 185
- Figure 7.180** ¹H-¹H COSY spectrum of ligand L^{5a} (500 MHz, 298 K, CD₃CN). 186
- Figure 7.181** ¹³C NMR spectrum of ligand L^{5a} (75 MHz, 298 K, CDCl₃). 186
- Figure 7.182** ¹H NMR spectrum of ligand L^{5b} (500 MHz, 298 K, CDCl₃). 187
- Figure 7.183** ¹H-¹H COSY spectrum of ligand L^{5b} (500 MHz, 298 K, CD₃CN). 188
- Figure 7.184** ¹³C NMR spectrum of ligand L^{5b} (500 MHz, 298 K, CDCl₃). 188
- Figure 7.185** ¹H NMR spectra (300 MHz, CD₃CN, 298 K) of ligand L^{5a} and ligand L^{5b} before and after the addition of different palladium salts ([Pd(CH₃CN)₄](BF₄)₂ or [Pd(CH₃CN)₄](PF₆)₂) and heating at 70 °C overnight. No signals in the ¹H NMR spectra were observed after the addition of palladium cations. 189
- Figure 7.186** ¹H NMR spectra of ligand L^{5a} and Ligand L^{5b} (300 MHz, DMSO-d₆, 298 K) before and after the addition of different palladium salts ([Pd(CH₃CN)₄](BF₄)₂ or [Pd(CH₃CN)₄](PF₆)₂). Addition of palladium(II) cations to ligand L^{5a} and heating the mixture to 70 °C over night leads to a shifting of all signals, indicating the formation of a monomeric [Pd₂L^{5a}₄] cage. A clean formation of a discrete species could not be observed for ligand L^{5b} in the presence of the used palladium salts. 189
- Figure 7.187** ¹H NMR spectra of ligand L^{5a} and ligand L^{5b} (300 MHz, Aceton-d₆, 298 K) before and after the addition of different palladium salts and heating the sample at 70 °C overnight. In all cases, a precipitation was visible in the NMR tube. 189
- Figure 7.188** ESI MS of monomeric [Pd₂L^{5a}₄] cage in DMSO. The spectra clearly shows a series of species [Pd₂L^{5a}₄+nBF₄]⁽⁴⁻ⁿ⁾ (n=0-2) containing a variable number of tetrafluoroborate counter anions. 190
- Figure 7.189** ESI MS of monomeric [Pd₂L^{5a}₄] cage, assembled from ligand L^{5a} and [Pd(CH₃CN)₄](PF₆)₂ in DMSO. 190
- Figure 7.190** Front (left) and side (right) view with distance between nitrogen atoms for a) ligand L³, b) ligand L¹, c) ligand L⁴, d) ligand L^{5a} and e) ligand L^{5b}. Values for ligand L¹ were obtained from a crystal structure, while the other values were gained from a molecular model (DFT B3LYP/6-31g(d)). 191
- Figure 7.191** ¹H NMR spectra (400 MHz, CD₃CN, 298 K) of a mixture of [2Cl@Pd₄L¹₈] and [3BF₄@Pd₄L^{6a}₈] after 5 min, 7 days and 21 days after preparing the mixture (blue square). No

- change in the NMR spectra were observed. Hence, no exchange of the chloride anion between these interpenetrated cages occurs. 192
- Figure 7.192** ^1H NMR spectra (400 MHz, CD_3CN , 298 K) of a mixture of $[\text{2Cl@Pd}_4\text{L}^1_8]$ and $[\text{3BF}_4\text{@Pd}_4\text{L}^{6b}_8]$ after 5 min, 7 and 21 days (blue spare). The $[\text{3BF}_4\text{@Pd}_4\text{L}^{6b}_8]$ coordination cage shows very broad signals in the NMR spectrum, due to the formation of several diastereomeric interpenetrated coordination cages (oxygen substituent in pseudo-axial or pseudo-equatorial position).^[78] Since no change in the NMR spectra was observed, a halide exchange does not take place between these two cage structures..... 193
- Figure 7.193** ^1H NMR spectra (400 MHz, CD_3CN , 298 K) of a mixture of $[\text{2Cl@Pd}_4\text{L}^1_8]$ and $[\text{3BF}_4\text{@Pd}_4\text{L}^{6c}_8]$ after 5 min, 7 and 21 days (blue spare). Due to no change in the ^1H NMR spectrum over time, the interpenetrated coordination cage based on an acridone ligand $[\text{2Cl@Pd}_4\text{L}^1_8]$ does not exchange the chloride anion in the outer two pockets of the cage. 193
- Figure 7.194** ^1H NMR spectra (400 MHz, CD_3CN , 298 K) of a mixture of $[\text{2Cl@Pd}_4\text{L}^1_8]$ and $[\text{3BF}_4\text{@Pd}_4\text{L}^7_8]$ after 5 min, 7 and 21 days (blue spare). No halide exchange between the two interpenetrated cages occurs. 193
- Figure 7.195** ^1H NMR spectra (400 MHz, CD_3CN , 298 K) of a mixture of $[\text{2Cl@Pd}_4\text{L}^1_8]$ and $[\text{3BF}_4\text{@Pd}_4\text{L}^8_8]$ after 5 min, 7 and 21 days (blue spare). No halide exchange between the two interpenetrated cages takes place..... 194
- Figure 7.196** ^1H NMR spectra (400 MHz, CD_3CN , 298 K) of a mixture of $[\text{2Cl@Pd}_4\text{L}^{6a}_8]$ and $[\text{3BF}_4\text{@Pd}_4\text{L}^1_8]$ after 2 h, 20 h, 4 and 8 days. The intensity of the halide-containing $[\text{3BF}_4\text{@Pd}_4\text{L}^1_8]$ was decreased (highlighted in blue), while signals corresponding to the chloride-containing cage $[\text{2Cl@Pd}_4\text{L}^1_8]$ arise (yellow). After, 20 h only the coordination cages $[\text{2Cl@Pd}_4\text{L}^1_8]$ and $[\text{3BF}_4\text{@Pd}_4\text{L}^{6a}_8]$ are found in the mixture, indicating a halide exchange. 194
- Figure 7.197** ^1H NMR spectra (400 MHz, CD_3CN , 298 K) of a mixture of $[\text{2Cl@Pd}_4\text{L}^{6b}_8]$ and $[\text{3BF}_4\text{@Pd}_4\text{L}^1_8]$ after 2 h, 20 h, 4, 8 and 14 days. After 4 days the composition of the mixture changes to $[\text{2Cl@Pd}_4\text{L}^1_8]$ and $[\text{3BF}_4\text{@Pd}_4\text{L}^{6b}_8]$, confirming a halide exchange. Highlighted: yellow: $[\text{2Cl@Pd}_4\text{L}^1_8]$, blue: $[\text{3BF}_4\text{@Pd}_4\text{L}^1_8]$ 194
- Figure 7.198** ^1H NMR spectra (400 MHz, CD_3CN , 298 K) of a mixture of $[\text{2Cl@Pd}_4\text{L}^{6c}_8]$ and $[\text{3BF}_4\text{@Pd}_4\text{L}^1_8]$ after 2 h, 20 h, 4, 8 and 14 days. After 4 days the composition of the mixture completely changed to $[\text{2Cl@Pd}_4\text{L}^1_8]$ and $[\text{3BF}_4\text{@Pd}_4\text{L}^{6c}_8]$, confirming a halide exchange. Highlighted: yellow: $[\text{2Cl@Pd}_4\text{L}^1_8]$, purple: $[\text{2Cl@Pd}_4\text{L}^{6c}_8]$ 195
- Figure 7.199** ^1H NMR spectra (400 MHz, CD_3CN , 298 K) of a mixture of $[\text{2Cl@Pd}_4\text{L}^7_8]$ and $[\text{3BF}_4\text{@Pd}_4\text{L}^1_8]$ after 2 h, 20 h, 4, 8 and 14 days. Slowly, the intensity of the $[\text{2Cl@Pd}_4\text{L}^7_8]$ coordination cage was decreased (green), while the intensity of $[\text{2Cl@Pd}_4\text{L}^1_8]$ increased. Highlighted: yellow: $[\text{2Cl@Pd}_4\text{L}^1_8]$, green: $[\text{2Cl@Pd}_4\text{L}^7_8]$ 195
- Figure 7.200** ^1H NMR spectra (400 MHz, CD_3CN , 298 K) of a mixture of $[\text{2Cl@Pd}_4\text{L}^8_8]$ and $[\text{3BF}_4\text{@Pd}_4\text{L}^1_8]$ after 2 h, 20 h, 4, 8 and 14 days. Since no change in the NMR spectra was observed, a halide exchange does occur between these two cage structures..... 195

- Figure 7.201** ^1H NMR spectra (400 MHz, CD_3CN , 298 K) of a mixture of $[\text{3BF}_4@Pd_4L^1_8]$ and $[\text{3BF}_4@Pd_4L^{6a}_8]$. Upon addition of chloride anions (1.0 eq.) only $[\text{3BF}_4@Pd_4L^1_8]$ transforms into $[\text{2Cl}@Pd_4L^1_8]$, while only a small amount of $[\text{2Cl}+\text{BF}_4@Pd_4L^1_8]$ is present. After 1.5 h, only two species can be observed in the NMR spectra ($[\text{2Cl}@Pd_4L^1_8]$ and $[\text{3BF}_4@Pd_4L^{6a}_8]$). Highlighted: yellow: $[\text{2Cl}@Pd_4L^1_8]$, *pink:* $[\text{3BF}_4@Pd_4L^{6a}_8]$ **196**
- Figure 7.202** ^1H NMR spectra (400 MHz, CD_3CN , 298 K) of a mixture of $[\text{3BF}_4@Pd_4L^1_8]$ and $[\text{3BF}_4@Pd_4L^{6b}_8]$. After adding tetrabutylammonium chloride (1.0 eq.), the intensity of $[\text{3BF}_4@Pd_4L^1_8]$ over time decreases, while $[\text{2Cl}@Pd_4L^1_8]$ increases. Highlighted: yellow: $[\text{2Cl}@Pd_4L^1_8]$, *blue:* $[\text{3BF}_4@Pd_4L^1_8]$ **196**
- Figure 7.203** ^1H NMR spectra (400 MHz, CD_3CN , 298 K) of a mixture of $[\text{3BF}_4@Pd_4L^1_8]$ and $[\text{3BF}_4@Pd_4L^{6c}_8]$. After addition of tetrabutylammonium chloride (1.0 eq.), all possible structures were observed in the NMR spectrum. After 14 days, $[\text{2Cl}@Pd_4L^1_8]$ and $[\text{3BF}_4@Pd_4L^{6c}_8]$ were present in the solution (blue box). The affinity for halide anions in $[\text{3BF}_4@Pd_4L^1_8]$ is higher than in $[\text{3BF}_4@Pd_4L^{6c}_8]$. Highlighted: yellow: $[\text{2Cl}@Pd_4L^1_8]$ **197**
- Figure 7.204** ^1H NMR spectra (400 MHz, CD_3CN , 298 K) of a mixture of $[\text{3BF}_4@Pd_4L^1_8]$ and $[\text{3BF}_4@Pd_4L^7_8]$. Upon addition of chloride anions (1.0 eq.) a mixture of all possible cage structures were observed ($[\text{3BF}_4@Pd_4L^1_8]$, $[\text{3BF}_4@Pd_4L^7_8]$, $[\text{2Cl}@Pd_4L^1_8]$ and $[\text{2Cl}+\text{2BF}_4@Pd_4L^7_8]$). Over time the intensity of $[\text{2Cl}@Pd_4L^1_8]$ increases, while the intensity of $[\text{2Cl}+\text{2BF}_4@Pd_4L^7_8]$ decreases, indicating a stronger affinity towards halide anions for the interpenetrated coordination cage containing ligand L^1 . Highlighted: yellow: $[\text{2Cl}@Pd_4L^1_8]$, *blue:* $[\text{3BF}_4@Pd_4L^1_8]$, *green:* $[\text{2Cl}+\text{BF}_4@Pd_4L^8_8]$ **197**
- Figure 7.205** ^1H NMR spectra (400 MHz, CD_3CN , 298 K) of a mixture of $[\text{3BF}_4@Pd_4L^1_8]$ and $[\text{3BF}_4@Pd_4L^8_8]$. Upon addition of 1.0 equivalents of chloride anions, a mixture of all four possible structures were present in the mixture ($[\text{3BF}_4@Pd_4L^1_8]$, $[\text{3BF}_4@Pd_4L^8_8]$, $[\text{2Cl}@Pd_4L^1_8]$ and $[\text{2Cl}+\text{BF}_4@Pd_4L^{8a}_8]$). No significant changes were observed over time. This indicates a similar binding affinity to the chloride anions of both interpenetrated coordination cages. Highlighted: yellow: $[\text{2Cl}@Pd_4L^1_8]$, *pink:* $[\text{2Cl}+\text{BF}_4@Pd_4L^8_8]$ **198**

10 LIST OF TABLES

Table 1.1 Supramolecular interaction and their energy contribution. ^[2]	5
Table 2.1 Experimental and computed binding free enthalpies, volumes and packing coefficients for all tested guests. a) Volume of the neutral guest was gained from Spartan <i>via</i> EDF2/6-31G* computation b) The packing coefficient (PC) was calculated as the quotient of $V_{\text{guest}}/V_{\text{cavity}} * 100$. The volume of the cavity was calculated using VOIDOO (details see experimental section 7.3.7). (This table does not include all neutral guest, which are encapsulated inside the coordination cage. Further experiments need to be performed to give reliable results for the missing molecules). Reproduced from Reference ^[90] with permission from The Royal Society of Chemistry.	30
Table 2.2 Experimental and computed binding free enthalpies, dispersive contributions, volumes and packing coefficients for selected guests (solvent: acetonitrile). <i>a: CPK volume of EDF2/6-31G* optimized model; b: Packing Coefficients, see Chapter 7.3.8 for detailed information on calculations; c: in kJ/mol; d: not computed.</i> Reproduced from Reference ^[90] with permission from The Royal Society of Chemistry.	35
Table 3.1 Conditions and results for control experiments. 3.1: 1,3-cyclohexadiene, 3.2: 2,3-dioxabicyclo[2.2.2]oct-5ene, 3: 1,4-cyclohexadiene. 10 eq. of 3.1 or 3.3, CD ₃ CN, ambient temperature. *Results obtained from a mixture of 3.1 and free ligand in various temperatures were not reproducibly. However, formation of 3.2 can be ruled out. Currently, the influence of the ligand is under further investigation.....	43
Table 4.1 Selected distances extracted from the X-ray structures of [Pd ₂ L ₂] ₄ and some of its host-guest complexes.	62
Table 5.1 Conditions for cage formation reactions. <i>General procedure:</i> To a solution or suspension of the ligand; a solution of the palladium salt (0.5 eq.) was added. The resulting mixture was heated at 70 °C for 24 h. *: No signals in the aromatic region of the ¹ H NMR spectrum.....	74
Table 7.1 Crystal data and structure refinement for [2Cl+benzene@Pd ₄ L ₁₈].	124
Table 7.2 Crystal data and structure refinement for [2Cl+benzene@Pd ₄ L ₁₈].	125
Table 7.3 Crystal data and structure refinement for [2Cl+DABCO@Pd ₄ L ₁₈] ⁶⁺	127
Table 7.4 Redox potentials $E_p^{(\text{red/ox})}$ vs. Ag/Ag ⁺ of cyclic voltammetry measurements. a) Oxidation of halide (chloride/bromide) was not observed.....	130
Table 7.5 Crystal data and structure refinement.	160

11 REFERENCES

- [1] Jean-Marie Lehn, *Nobel Lecture* **1987**.
- [2] J. W. Steed, J. L. Atwood, *Supramolecular Chemistry*, Wiley, Chichester, UK, **2009**.
- [3] P. D. Beer, P. A. Gale, D. K. Smith, *Supramolecular Chemistry*, Oxford Univ. Press, Oxford, **2003**.
- [4] C. R. Calladine, H. R. Drew, B. F. Luisi, A. A. Travers, J. Wissmann, *DNA. Das Molekül und seine Funktionsweise*, Elsevier Spektrum Akad. Verl., München, **2006**.
- [5] J. M. Berg, L. Stryer, J. L. Tymoczko, G. J. Gatto, *Biochemistry*, WH Freeman, **2015**.
- [6] G. R. Desiraju, *Nature* **2001**, *412*, 397.
- [7] F. Diederich, P. J. Stang, R. R. Tykwinski, *Modern supramolecular chemistry. Strategies for macrocycle synthesis*, Wiley-VCH, Weinheim, **2008**.
- [8] C. J. Pedersen, *J. Am. Chem. Soc.* **1967**, *89*, 7017.
- [9] B. Dietrich, J. M. Lehn, J. P. Sauvage, *Tetrahedron Letters* **1969**, *10*, 2885.
- [10] D. J. Cram, T. Kaneda, R. C. Helgeson, G. M. Lein, *J. Am. Chem. Soc.* **1979**, *101*, 6752.
- [11] C. A. Schalley, *Analytical methods in supramolecular chemistry*, Wiley-VCH, Weinheim, **2007**.
- [12] C. Dietrich-Buchecker, J. Sauvage, J. Kintzinger, *Tetrahedron Letters* **1983**, *24*, 5095.
- [13] C. Dietrich-Buchecker, J.-P. Sauvage (Eds.) *Molecular Catenanes, Rotaxanes and Knots. A journey through the world of molecular topology*, Wiley-VCH, Weinheim, New York, **1999**.
- [14] a) C. O. Dietrich-Buchecker, J. P. Sauvage, *Chem. Rev.* **1987**, *87*, 795; b) D. B. Amabilino, J. F. Stoddart, *Chem. Rev.* **1995**, *95*, 2725.
- [15] G. Schill, A. T. Blomquist, *Catenanes, Rotaxanes, and Knots*, Elsevier Science, Burlington, **1971**.
- [16] E. Wasserman, *J. Am. Chem. Soc.* **1960**, *82*, 4433.
- [17] K. S. Chichak, S. J. Cantrill, A. R. Pease, S.-H. Chiu, G. W. V. Cave, J. L. Atwood, J. F. Stoddart, *Science* **2004**, *304*, 1308.
- [18] G. Rapenne, C. Dietrich-Buchecker, and J. P. Sauvage, *J. Am. Chem. Soc.* **1999**, 994.
- [19] J.-F. Ayme, J. E. Beves, D. A. Leigh, R. T. McBurney, K. Rissanen, D. Schultz, *Nat. Chem.* **2011**, *4*, 15.
- [20] a) C. Peinador, V. Blanco, J. M. Quintela, *J. Am. Chem. Soc.* **2009**, *131*, 920; b) C. D. Pentecost, K. S. Chichak, A. J. Peters, G. W. V. Cave, S. J. Cantrill, J. F. Stoddart, *Angew. Chem. Int. Ed.* **2007**, *46*, 218.
- [21] P. L. Anelli, N. Spencer, J. F. Stoddart, *J. Am. Chem. Soc.* **1991**, *113*, 5131.

- [22] V. Balzani, M. Clemente-Leon, A. Credi, B. Ferrer, M. Venturi, A. H. Flood, J. F. Stoddart, *PNAS* **2006**, *103*, 1178.
- [23] M. C. Jiménez, C. Dietrich-Buchecker, J.-P. Sauvage, *Angew. Chem. Int. Ed.* **2000**, *39*, 3284.
- [24] J. D. Badjic, V. Balzani, A. Credi, S. Silvi, J. F. Stoddart, *Science* **2004**, *303*, 1845.
- [25] N. Koumura, R. W. Zijlstra, R. A. van Delden, N. Harada, B. L. Feringa, *Nature* **1999**, *401*, 152.
- [26] T. Kudernac, N. Ruangsupapichat, M. Parschau, B. Maciá, N. Katsonis, S. R. Harutyunyan, K.-H. Ernst, B. L. Feringa, *Nature* **2011**, *479*, 208.
- [27] V. Balzani, A. Credi, F. M. Raymo, J. F. Stoddart, *Angew. Chem. Int. Ed.* **2000**, *39*, 3348.
- [28] M. Albrecht, *Die Naturwissenschaften* **2007**, *94*, 951.
- [29] G. Whitesides, J. Mathias, C. Seto, *Science* **1991**, *254*, 1312.
- [30] K. Ariga, J. P. Hill, M. V. Lee, A. Vinu, R. Charvet, S. Acharya, *Sci. Technol. Adv. Mater.* **2008**, *9*, 14109.
- [31] D. J. Tranchemontagne, Z. Ni, M. O'Keeffe, O. M. Yaghi, *Angew. Chem. Int. Ed.* **2008**, *47*, 5136.
- [32] J. C. Solem, *Robotics and Autonomous Systems* **2002**, *38*, 69.
- [33] D. G. Bucknall, H. L. Anderson, *Science* **2003**, *302*, 1904.
- [34] M. M. Conn, J. Rebek, *Chem. Rev.* **1997**, *97*, 1647.
- [35] Lindsey J.S., *ChemInform* **1991**, *22*, 2455.
- [36] J.-M. Lehn, *Supramolecular Chemistry. Concepts and perspectives*, VCH, Weinheim, New York, **1995**.
- [37] M. D. Pluth, K. N. Raymond, *Chem. Soc. Rev.* **2007**, *36*, 161.
- [38] a) M. Fujita, M. Tominaga, A. Hori, B. Therrien, *Acc. Chem. Res.* **2005**, *38*, 369; b) S. R. Seidel, P. J. Stang, *Acc. Chem. Res.* **2002**, *35*, 972; c) Smulders, Maarten M. J., I. A. Riddell, C. Browne, J. R. Nitschke, *Chem. Soc. Rev.* **2013**, *42*, 1728; d) R. Chakrabarty, P. S. Mukherjee, P. J. Stang, *Chem. Rev.* **2011**, *111*, 6810; e) T. R. Cook, P. J. Stang, *Chem. Rev.* **2015**, *115*, 7001; f) K. Severin, *Chem. Commun.* **2006**, 3859; g) M. D. Ward, *Chem. Commun.* **2009**, 4487; h) M. Fujita, K. Umemoto, M. Yoshizawa, N. Fujita, T. Kusu-kawa, K. Biradha, *Chem. Commun.* **2001**, 509; i) S. Zarra, D. M. Wood, D. A. Roberts, J. R. Nitschke, *Chem. Soc. Rev.* **2015**, *44*, 419; j) S. J. Park, J. W. Lee, S. Sakamoto, K. Yamaguchi, J.-I. Hong, *Chem. Eur. J.* **2003**, *9*, 1768; k) H. Amouri, C. Desmarests, J. Moussa, *Chem. Rev.* **2012**, *112*, 2015.
- [39] R. Custelcean, *Chem. Soc. Rev.* **2014**, *43*, 1813.
- [40] S. Turega, M. Whitehead, B. R. Hall, M. F. Haddow, C. A. Hunter, M. D. Ward, *Chem. Commun.* **2012**, *48*, 2752.
- [41] S. Leininger, B. Olenyuk, P. J. Stang, *Chem. Rev.* **2000**, *100*, 853.
- [42] M. Han, D. M. Engelhard, G. H. Clever, *Chem. Soc. Rev.* **2014**, *43*, 1848.
- [43] A. Schmidt, A. Casini, F. E. Kühn, *Coord. Chem. Rev.* **2014**, *275*, 19.

- [44] M. Yoshizawa, M. Fujita, *Pure Appl. Chem.* **2005**, *77*, 378.
- [45] G. H. Clever, P. Punt, *Acc. Chem. Res.* **2017**, *50*, 2233.
- [46] E. Riedel, *Anorganische Chemie*, W. de Gruyter, Berlin, New York, **2004**.
- [47] T. R. Schulte, M. Krick, C. I. Asche, S. Freye, G. H. Clever, *RSC Adv.* **2014**, *4*, 29724.
- [48] a) W. Meng, B. Breiner, K. Rissanen, J. D. Thoburn, J. K. Clegg, J. R. Nitschke, *Angew. Chem. Int. Ed.* **2011**, *50*, 3479; b) J. L. Bolliger, A. M. Belenguer, J. R. Nitschke, *Angew. Chem. Int. Ed.* **2013**, *52*, 7958; c) J. L. Bolliger, T. K. Ronson, M. Ogawa, J. R. Nitschke, *J. Am. Chem. Soc.* **2014**, *136*, 14545; d) A. Galano, A. Pérez-González, L. del Olmo, M. Francisco-Marquez, J. R. León-Carmona, *J Mol Model* **2014**, *20*, 2412; e) N. Hafezi, J. M. Holcroft, K. J. Hartlieb, E. J. Dale, N. A. Vermeulen, C. L. Stern, A. A. Sarjeant, J. F. Stoddart, *Angew. Chem.* **2015**, *127*, 466; f) T. Kusukawa, M. Fujita, *J. Am. Chem. Soc.* **2002**, *124*, 13576; g) H.-K. Liu, W.-Y. Sun, D.-J. Ma, W.-X. Tang, K.-B. Yu, *Chem. Commun.* **2000**, 591; h) A. H. Mahmoudkhani, A. P. Côté, Shimizu, George K H, *Chem. Commun.* **2004**, 2678; i) C. M. McGuirk, M. J. Katz, C. L. Stern, A. A. Sarjeant, J. T. Hupp, O. K. Farha, C. A. Mirkin, *J. Am. Chem. Soc.* **2015**, *137*, 919; j) K. Omoto, S. Tashiro, M. Kuritani, M. Shionoya, *J. Am. Chem. Soc.* **2014**, 17946; k) T. K. Ronson, A. B. League, L. Gagliardi, C. J. Cramer, J. R. Nitschke, *J. Am. Chem. Soc.* **2014**, 15615; l) H. Takezawa, T. Murase, M. Fujita, *J. Am. Chem. Soc.* **2012**, *134*, 17420; m) D. M. Wood, W. Meng, T. K. Ronson, A. R. Stefankiewicz, Sanders, J. K. M. Sanders, J. R. Nitschke, *Angew. Chem. Int. Ed.* **2015**, *54*, 3988.
- [49] P. Mal, B. Breiner, K. Rissanen, J. R. Nitschke, *Science* **2009**, *324*, 1697.
- [50] M. M. J. Smulders, J. R. Nitschke, *Chem. Sci.* **2012**, *3*, 785.
- [51] a) C. J. Hastings, M. D. Pluth, R. G. Bergman, K. N. Raymond, *J. Am. Chem. Soc.* **2010**, *132*, 6938; b) T. Murase, S. Horiuchi, M. Fujita, *J. Am. Chem. Soc.* **2010**, *132*, 2866.
- [52] D. M. Vriezema, M. Comellas Aragone`s, J. A. A. W. Elemans, J. J. L. M. Cornelissen, A. E. Rowan, R. J. M. Nolte, *Chem. Rev.* **2005**, *105*, 1445.
- [53] M. Yoshizawa, J. K. Klosterman, M. Fujita, *Angew. Chem. Int. Ed.* **2009**, *48*, 3418.
- [54] B. Linton, A. D. Hamilton, *Chem. Rev.* **1997**, *97*, 1669.
- [55] S. J. Dalgarno, N. P. Power, J. L. Atwood, *Coord. Chem. Rev.* **2008**, *252*, 825.
- [56] T. Murase, Y. Nishijima, M. Fujita, *J. Am. Chem. Soc.* **2012**, *134*, 162.
- [57] T. Kusukawa, T. Nakai, T. Okano, M. Fujita, *Chem. Lett.* **2003**, *32*, 284.
- [58] T. Murase, H. Takezawa, M. Fujita, *Chem. Comm.* **2011**, *47*, 10960.
- [59] a) I. A. Riddell, M. M. J. Smulders, J. K. Clegg, J. R. Nitschke, *Chem. Commun.* **2011**, *47*, 457; b) M. B. Duriska, S. M. Neville, J. Lu, S. S. Iremonger, J. F. Boas, C. J. Kepert, S. R. Batten, *Angew. Chem. Int. Ed.* **2009**, *48*, 8919.
- [60] Y. R. Hristova, Smulders, Maarten M. J., J. K. Clegg, B. Breiner, J. R. Nitschke, *Chem. Sci.* **2011**, *2*, 638.
- [61] A. M. Johnson, M. C. Young, X. Zhang, R. R. Julian, R. J. Hooley, *J. Am. Chem. Soc.* **2013**, *135*, 17723.

- [62] G. H. Clever, S. Tashiro, M. Shionoya, *Angew. Chem. Int. Ed.* **2009**, *48*, 7010.
- [63] a) Lewis, James E. M., E. L. Gavey, S. A. Cameron, J. D. Crowley, *Chem. Sci.* **2012**, *3*, 778; b) P. Liao, B. W. Langloss, A. M. Johnson, E. R. Knudsen, F. S. Tham, R. R. Julian, R. J. Hooley, *Chem. Comm.* **2010**, *46*, 4932.
- [64] M. Frank, M. D. Johnstone, G. H. Clever, *Chem. Eur. J.* **2016**, *22*, 14104.
- [65] R. Zhu, J. Lübben, B. Dittrich, G. H. Clever, *Angew. Chem. Int. Ed.* **2015**, *54*, 2796.
- [66] M. Han, Y. Luo, B. Damaschke, L. Gomez, X. Ribas, A. Jose, P. Peretzki, M. Seibt, G. H. Clever, *Angew. Chem. Int. Ed.* **2016**, *55*, 445.
- [67] a) W. M. Bloch, Y. Abe, J. J. Holstein, C. M. Wandtke, B. Dittrich, G. H. Clever, *J. Am. Chem. Soc.* **2016**; b) W. M. Bloch, J. J. Holstein, W. Hiller, G. H. Clever, *Angew. Chem. Int. Ed.* **2017**, *56*, 8285; c) W. M. Bloch, G. H. Clever, *Chem. Comm.* **2017**, *53*, 8506.
- [68] M. Frank, L. Krause, R. Herbst-Irmer, D. Stalke, G. H. Clever, *Dalton Trans.* **2014**, *43*, 4587.
- [69] M. Frank, J. Ahrens, I. Bejenke, M. Krick, D. Schwarzer, G. H. Clever, *J. Am. Chem. Soc.* **2016**, *138*, 8279.
- [70] D. M. Engelhard, S. Freye, K. Grohe, M. John, G. H. Clever, *Angew. Chem. Int. Ed.* **2012**, *51*, 4747.
- [71] M. D. Johnstone, M. Frank, G. H. Clever, F. M. Pfeffer, *Eur. J. Org. Chem.* **2013**, *26*, 5848.
- [72] M. Fukuda, R. Sekiya, R. Kuroda, *Angew. Chem. Int. Ed.* **2008**, *47*, 706.
- [73] R. Sekiya, R. Kuroda, *Chem. Commun.* **2011**, *47*, 12346.
- [74] R. Sekiya, M. Fukuda, R. Kuroda, *J. Am. Chem. Soc.* **2012**, *134*, 10987.
- [75] S. Freye, J. Hey, A. Torras-Galán, D. Stalke, R. Herbst-Irmer, M. John, G. H. Clever, *Angew. Chem. Int. Ed.* **2012**, *51*, 2191.
- [76] S. Freye, D. M. Engelhard, M. John, G. H. Clever, *Chem. Eur. J.* **2013**, *19*, 2114.
- [77] S. Freye, R. Michel, D. Stalke, M. Pawliczek, H. Frauendorf, G. H. Clever, *J. Am. Chem. Soc.* **2013**, *135*, 8476.
- [78] M. Frank, J. Hey, I. Balcioglu, Y.-S. Chen, D. Stalke, T. Suenobu, S. Fukuzumi, H. Frauendorf, G. H. Clever, *Angew. Chem. Int. Ed.* **2013**, *52*, 10102.
- [79] M. Frank, J. M. Dieterich, S. Freye, R. A. Mata, G. H. Clever, *Dalton Trans.* **2013**, *42*, 15906.
- [80] Utilization of platinum(II) cations instead of palladium(II) cations gives exclusively monomeric coordination cages.
- [81] M. Han, R. Michel, B. He, Y.-S. Chen, D. Stalke, M. John, G. H. Clever, *Angew. Chem. Int. Ed.* **2013**, *52*, 1319.
- [82] A. M. Johnson, R. J. Hooley, *Inorg. Chem.* **2011**, *50*, 4671.
- [83] A. M. Johnson, O. Moshe, A. S. Gamboa, B. W. Langloss, J. F. K. Limtiaco, C. K. Larive, R. J. Hooley, *Inorg. Chem.* **2011**, *50*, 9430.
- [84] M. Sailer, A. W. Franz, T. J. J. Müller, *Chem. Eur. J.* **2008**, *14*, 2602.
- [85] H. J. Dauben, L. L. McCoy, *J. Am. Chem. Soc.* **1959**, *81*, 4863.

- [86] K. Sonogashira, *J. Organomet. Chem.* **2002**, 653, 46.
- [87] S. Löffler, J. Lübben, L. Krause, D. Stalke, B. Dittrich, G. H. Clever, *J. Am. Chem. Soc.* **2015**, 137, 1060.
- [88] a) I. Krossing, I. Raabe, *Angew. Chem. Int. Ed.* **2004**, 43, 2066; b) R. V. Honeychuck, W. H. Hersh, *Inorg. Chem.* **1989**, 28, 2869.
- [89] C. A. Hunter, *Angew. Chem. Int. Ed.* **2004**, 43, 5310.
- [90] S. Löffler, A. Wuttke, B. Zhang, J. J. Holstein, R. A. Mata, G. H. Clever, *Chem. Commun.* **2017**, 53, 11933.
- [91] *Spartan'08*, Wavefunction, Inc. Irvine, CA, **2009**.
- [92] G. J. Kleywegt, T. A. Jones, *Acta Crystallogr D Biol Crystallogr* **1994**, 50, 178.
- [93] The cyclobutanone does not bind in the central pocket of the interpenetrated coordination cage. Due to the small size, no stabilizing interaction between the host and the guest can be formed and an encapsulation is not observed.
- [94] M. R. Willcott, *J. Am. Chem. Soc.* **2009**, 131, 13180.
- [95] H.-J. Werner, F. R. Manby, P. J. Knowles, *J. Chem. Phys.* **2003**, 118, 8149.
- [96] S. Grimme, *J. Chem. Phys.* **2003**, 118, 9095.
- [97] T. H. Dunning, *J. Chem. Phys.* **1989**, 90, 1007.
- [98] K. A. Peterson, D. Figgen, M. Dolg, H. Stoll, *J. Chem. Phys.* **2007**, 126, 124101.
- [99] S. Grimme, J. Antony, S. Ehrlich, H. Krieg, *J. Chem. Phys.* **2010**, 132, 154104.
- [100] P. R. Schreiner, L. V. Chernish, P. A. Gunchenko, E. Y. Tikhonchuk, H. Hausmann, M. Serafin, S. Schlecht, J. E. P. Dahl, R. M. K. Carlson, A. A. Fokin, *Nature* **2011**, 477, 308.
- [101] A. Wuttke, R. A. Mata, *J. Comput. Chem.* **2017**, 38, 15.
- [102] R. Sure, S. Grimme, *J. Chem. Theory Comput.* **2015**, 11, 3785.
- [103] J. Clayden, N. Greeves, S. G. Warren, P. Wothers, *Organic Chemistry*, Oxford Univ. Press, Oxford, **2009**.
- [104] K. Feng, L.-Z. Wu, L.-P. Zhang, C.-H. Tung, *Tetrahedron* **2007**, 63, 4907.
- [105] C. Kaneko, A. Sugimoto, S. Tanaka, *Synthesis* **1974**, 1974, 876.
- [106] a) G. R. Ziegler, C. A. Welch, C. E. Orzech, S. Kikkawa, S. I. Miller, *J. Am. Chem. Soc.* **1963**, 85, 1648; b) V. L. Paddock, R. J. Phipps, A. Conde-Angulo, A. Blanco-Martin, C. Giró-Mañas, L. J. Martin, A. J. P. White, A. C. Spivey, *J. Org. Chem.* **2011**, 76, 1483.
- [107] S. Löffler, J. Lübben, A. Wuttke, R. A. Mata, M. John, B. Dittrich, G. H. Clever, *Chem. Sci.* **2016**, 7, 4676.
- [108] H. F. Lodish, *Molecular Cell Biology*, W.H. Freeman, New York, **2008**.
- [109] E. R. Kay, D. A. Leigh, *Angew. Chem. Int. Ed.* **2015**, 54, 10080.
- [110] S. K. Samanta, D. Samanta, J. W. Bats, M. Schmittel, *J. Org. Chem.* **2011**, 76, 7466.
- [111] T. Muraoka, K. Kinbara, T. Aida, *Nature* **2006**, 440, 512.
- [112] S. Liu, D. V. Kondratuk, S. A. L. Rousseaux, G. Gil-Ramirez, M. C. O'Sullivan, J. Cremers, T. D. W. Claridge, H. L. Anderson, *Angew. Chem.* **2015**, 127, 5445.

- [113] T. D. Nguyen, H.-R. Tseng, P. C. Celestre, A. H. Flood, Y. Liu, J. F. Stoddart, J. I. Zink, *PNAS* **2005**, *102*, 10029.
- [114] K. Hirose, K. Ishibashi, Y. Shiba, Y. Doi, Y. Tobe, *Chemistry* **2008**, *14*, 5803.
- [115] a) H.-B. Yang, K. Ghosh, B. H. Northrop, Y.-R. Zheng, M. M. Lyndon, D. C. Muddiman, P. J. Stang, *J. Am. Chem. Soc.* **2007**, *129*, 14187; b) X. Yan, T. R. Cook, J. B. Pollock, P. Wei, Y. Zhang, Y. Yu, F. Huang, P. J. Stang, *J. Am. Chem. Soc.* **2014**, *136*, 4460.
- [116] M. Krick, J. Holstein, C. Wurtele, G. H. Clever, *Chem. Commun.* **2016**, *52*, 10411.
- [117] a) Y. Fang, T. Murase, S. Sato, M. Fujita, *J. Am. Chem. Soc.* **2013**, *135*, 613; b) J. S. Mugridge, G. Szigethy, R. G. Bergman, K. N. Raymond, *J. Am. Chem. Soc.* **2010**, *132*, 16256; c) H. Kitagawa, Y. Kobori, M. Yamanaka, K. Yoza, K. Kobayashi, *PNAS* **2009**, *106*, 10444.
- [118] a) N. Kishi, Z. Li, Y. Sei, M. Akita, K. Yoza, J. S. Siegel, M. Yoshizawa, *Chem. Eur. J.* **2013**, *19*, 6313; b) N. Kishi, Z. Li, K. Yoza, M. Akita, M. Yoshizawa, *J. Am. Chem. Soc.* **2011**, *133*, 11438.
- [119] T. Murase, S. Sato, M. Fujita, *Angew. Chem. Int. Ed.* **2007**, *46*, 5133.
- [120] L. C. Palmer, J. Rebek, *Org. Biomol. Chem.* **2004**, *2*, 3051.
- [121] F. London, *Trans. Faraday Soc.* **1937**, *33*, 8b.
- [122] S. Grimme, *Chemistry* **2012**, *18*, 9955.
- [123] S. Grimme, R. Huenerbein, S. Ehrlich, *ChemPhysChem* **2011**, *12*, 1258.
- [124] S. Löffler, *Endohedral Functionalization of Coordination Cages*. Master Thesis, **2013**.
- [125] K. Miyashita, M. Minagawa, Y. Ueda, Y. Tada, N. Hoshino, T. Imanishi, *Tetrahedron* **2001**, *57*, 3361.
- [126] J. Ribas Gispert, *Coordination Chemistry*, Wiley-VCH, Weinheim, **2008**.
- [127] M. Krick, J. J. Holstein, A. Wuttke, R. A. Mata, G. H. Clever, *Eur. J. Org. Chem.* **2017**, *2017*, 5141.
- [128] S. Pramanik, S. De, M. Schmittel, *Angew. Chem. Int. Ed.* **2014**, *53*, 4709.
- [129] G. H. Clever, M. Shionoya, *Chemistry* **2010**, *16*, 11792.
- [130] Warren L. DeLano, *The PyMol Molecular Graphics System*, DeLano Scientific LLC, San Carlos, CA (USA).
- [131] R. R. Gagne, C. A. Koval, G. C. Lisensky, *Inorg. Chem.* **1980**, *19*, 2854.
- [132] S. Mecozzi, J. J. Rebek, *Chem. Eur. J.* **1998**, *4*, 1016.
- [133] A. D. Becke, *Chem. Phys.* **1993**, *98*, 5648.
- [134] M. A. Spackman, D. Jayatilaka, *CrystEngComm*, **2009**, *11*, 19.
- [135] R. A. Kendall, T. H. Dunning, R. J. Harrison, *J. Chem. Phys.* **1992**, *96*, 6796.
- [136] H.-J. Werner, P. J. Knowles, G. Knizia, F. R. Manby, Schütz M. Molpro, version 2012.1, a package of ab initio programs **2012**, see <http://www.molpro.net>.
- [137] Due to free rotation of the single bond, the pyrdine residue has several possibilities of orientation. For comparison, the nitrogen-nitrogen distances were measured from the same position as depicted in this scheme.

- [138] M. J. Frisch, G. W. Trucks, H. B. Schlegel, G. E. Scuseria, M. A. Robb, J. R. Cheeseman, G. Scalmani, V. Barone, B. Mennucci, G. A. Petersson, H. Nakatsuji, M. Caricato, X. Li, H. P. Hratchian, A. F. Izmaylov, J. Bloino, G. Zheng, J. L. Sonnenberg, M. Hada, M. Ehara, K. Toyota, R. Fukuda, J. Hasegawa, M. Ishida, T. Nakajima, Y. Honda, O. Kitao, H. Nakai, T. Vreven, J. A. Montgomery Jr., J. E. Peralta, F. Ogliaro, M. J. Bearpark, J. Heyd, E. N. Brothers, K. N. Kudin, V. N. Staroverov, R. Kobayashi, J. Normand, K. Raghavachari, A. P. Rendell, J. C. Burant, S. S. Iyengar, J. Tomasi, M. Cossi, N. Rega, N. J. Millam, M. Klene, J. E. Knox, J. B. Cross, V. Bakken, C. Adamo, J. Jaramillo, R. Gomperts, R. E. Stratmann, O. Yazyev, A. J. Austin, R. Cammi, C. Pomelli, J. W. Ochterski, R. L. Martin, K. Morokuma, V. G. Zakrzewski, G. A. Voth, P. Salvador, J. J. Dannenberg, S. Dapprich, A. D. Daniels, Ö. Farkas, J. B. Foresman, J. V. Ortiz, J. Cioslowski, D. J. Fox, *Gaussian Inc.*, Wallingford, CT, USA,, **2009**.
- [139] G. H. Clever, W. Kawamura, M. Shionoya, *Inorg. Chem.* **2011**, *50*, 4689.
- [140] A. Burkhardt, T. Pakendorf, B. Reime, J. Meyer, P. Fischer, N. Stübe, S. Panneerselvam, O. Lorbeer, K. Stachnik, M. Warmer et al., *Eur. Phys. J. Plus* **2016**, *131*, 25.
- [141] W. Kabsch, *Acta Cryst.* **2010**, *D66*, 125.
- [142] G. M. Sheldrick, *Acta Cryst.* **2015**, *A71*, 3.
- [143] G. M. Sheldrick, *Acta Cryst.* **2008**, *A64*, 112.
- [144] C. B. Hübschle, G. M. Sheldrick, B. Dittrich, *J. Appl. Cryst.* **2011**, *44*, 1281.
- [145] T. Kottke, D. Stalke, *J. Appl. Cryst.* **1993**, *26*, 615.
- [146] M. Bruker SAINT v8.30C, *Madison* **2013**.
- [147] G. M. Sheldrick, *Acta Cryst.* **1990**, *A46*, 467.
- [148] G. M. Sheldrick SADABS 2012/1, Göttingen, 2012. **2012**.
- [149] G. M. Sheldrick, XPREP Version 2012/1 for Windows **2005**.
- [150] G. M. Sheldrick SADABS, Universität Göttingen, Germany **2000**.
- [151] T. R. Schneider, G. M. Sheldrick, *Acta Cryst.* **2002**, *D58*, 1772.
- [152] A. D. Becke, *Phys. Rev. A* **1988**, *38*, 3098.
- [153] J. P. Perdew, *Phys. Rev. B* **1986**, *33*, 8822.
- [154] K. Eichkorn, F. Weigend, O. Treutler, R. Ahlrichs, *Theor. Chem. Acc.* **1997**, *97*, 119.
- [155] F. Weigend, R. Ahlrichs, *Phys. Chem. Chem. Phys.* **2005**, *7*, 3297.
- [156] F. Weigend, *Phys. Chem. Chem. Phys.* **2006**, *8*, 1057.
- [157] TURBOMOLE V7.0 2015, a development of University of Karlsruhe and Forschungszentrum Karlsruhe GmbH, 1989-2015, TURBOMOLE GmbH, since 2007, available from <http://www.turbomole.com>.
- [158] D. Andrae, U. Haeussermann, M. Dolg, H. Stoll, H. Preuss, *Theor. Chim. Acta* **1990**, *77*, 123.
- [159] M. Schütz, G. Hetzer, H.-J. Werner, *J. Chem. Phys.* **1999**, *111*, 5691.
- [160] G. Hetzer, M. Schütz, H. Stoll, H.-J. Werner, *J. Chem. Phys.* **2000**, *113*, 9443.

-
- [161] a) F. Weigend, A. Köhn, C. Hättig, *J. Chem. Phys.* **2002**, *116*, 3175; b) F. Weigend, *J. Comput. Chem.* **2008**, *29*, 167.
- [162] a) R. Gulde, P. Pollak, F. Weigend, *J. Chem. Theory Comput.* **2012**, *8*, 4062; b) C. Hättig, *Phys. Chem. Chem. Phys.* **2005**, *7*, 59.
- [163] J. Pipek, P. G. Mezey, *J. Chem. Phys.* **1989**, *90*, 4916.
- [164] J. W. Boughton, P. Pulay, *J. Comput. Chem.* **1993**, *14*, 736.
- [165] G. Hetzer, P. Pulay, H.-J. Werner, *Chem. Phys. Lett.* **1998**, *290*, 143.
- [166] M. Schütz, G. Rauhut, H.-J. Werner, *J. Phys. Chem. A* **1998**, *102*, 5997.
- [167] F. Eckert, A. Klamt, *AIChE Journal* **2002**, *48*, 369.
- [168] F. Weigend, M. Häser, H. Patzelt, R. Ahlrichs, *Chem. Phys. Lett.* **1998**, *294*, 143.
- [169] D. Ardura, R. López, T. L. Sordo, *J. Phys. Chem. B* **2005**, *109*, 23618.
- [170] G. H. Clever, S. Tashiro, M. Shionoya, *J. Am. Chem. Soc.* **2010**, *132*, 9973.
- [171] N. S. Lawrence, G. J. Tustin, M. Faulkner, T. G. Jones, *Electrochimica Acta* **2006**, *52*, 499.
- [172] S. Grimme, S. Ehrlich, L. Goerigk, *Comput. Chem.* **2011**, *32*, 1456.
- [173] A. Klamt, G. Schüürmann, *J. Chem. Soc., Perkin Trans. 2*, **1993**, 799.
- [174] F. Neese, *WIREs Comput. Mol. Sci.* **2012**, *2*, 73.

CURRICULUM VITAE

Personal Information

Name Susanne Löffler
Adress Hohe Str. 93
44139 Dortmund, Germany
Date of Birth 18.07.1988
Place of Birth Dresden
Nationality German
Email susanne.loeffler@tu-dortmund.de
Phone +49 176 8212 3444

Education

2014 – current

Georg-August-Universität Göttingen, Since 2016 Technische Universität Dortmund
GAUSS PhD

“*Host-Guest Chemistry of Acridone-based Coordination Cages*”, Supervisor: Guido H. Clever

2011 – 2013

Georg-August-Universität Göttingen

M. Sc. IN CHEMISTRY

“*Endohedral Functionalization of Coordination Cages*”, Supervisor: Guido H. Clever

2008 – 2011

Georg-August-Universität Göttingen

B. Sc. IN CHEMISTRY

“*Synthesis and Characterization of Hydrogen-Bonded Phenols*”, Supervisor: Oliver S. Wenger

Publications

- „*Influence of Size, Shape, Heteroatom Content and Dispersive Contributions on Guest Binding in a Coordination Cage*“ S. Löffler, A. Wuttke, R.A. Mata, B. Zhang, G. H. Clever, *Chem. Comm.*, **2017**, 53, 11933.
- „*Internal Dynamics and Guest Binding of a Sterically Overcrowded Host*“ S. Löffler, J. Lübben, A. Wuttke, R.A. Mata, M. John, B. Dittrich, G. H. Clever, *Chem. Sci.*, **2016**, 7, 4676.
- “*Triggered Exchange of Anionic for Neutral Guests inside a Cationic Coordination Cage*” S. Löffler, J. Lübben, L. Krause, D. Stalke, B. Dittrich, G. Clever, *J. Am. Chem. Soc.*, **2015**, 137, 1060.
- “*Electron transfer between hydrogen-bonded pyridylphenols and a photoexcited rhenium(I) complex*” W. Herzog, C. Bronner, S. Löffler, B. He, D. Kratzert, D. Stalke, A. Hauser, O. Wenger, *Chem. Phys. Chem.*, **2013**, 14, 1168.

Teaching/Supervising Experience

Teaching assistant, Technische Universität Dortmund (2016-present)

Supervising undergraduate dissertations

Development and organization of inorganic practical teaching course ("Methods of Inorganic and Organic Chemistry")

Supervising students in the laboratory (in groups and individually)

Teaching assistant, Georg – August Universität Göttingen (2009-2015)

Teaching assistant in "General Inorganic and Organic Chemistry", "Inorganic Chemistry for Biologists" and "General Chemistry for medics"

Duties include: holding weekly seminars, operating and training students in laboratory equipment, preparation and correction of exams and lab reports

Working Experiences

October 2013 – March 2014

Scientific assistant in the research group of Prof. Dr. G. H. Clever at the Georg-August Universität, *Göttingen*, Germany

October 2012 – January 2013

Internship at Bayer Shering Pharma, under supervision of Dr. C. S. Hilger, *Berlin*, Germany

October 2009 – January 2013

Student assistant at the Georg-August Universität (teaching, mentoring), *Göttingen*, Germany

Qualification and Knowledge

Preparation

organic and inorganic syntheses (6+years)

column chromatography

preparative gel permeation chromatography (GPC)

high performance liquid chromatography (HPLC)

Analytical techniques

NMR (1D, 2D, DOESY, EXSY, kinetic measurements), ESI-MS, FT-IR, UV/VIS, CV, ITC, X-ray structure determination

Software Skills

MS Office, data analysis (Origin, MestReNova, TopSpin), Chemdraw, Mercury, ShelXle, PyMol, Spartan, Adobe Illustrator, Touch typing

Administration

Comprehensive knowledge according to Ordinance on Hazardous Substance



Susanne Löffler

Dortmund, February 19, 2018